

POLISH SOCIETY OF THEORETICAL AND APPLIED MECHANICS

**JOURNAL OF THEORETICAL
AND APPLIED MECHANICS**

No. 3 • Vol. 56

Quarterly

WARSAW, JULY 2018

JOURNAL OF THEORETICAL AND APPLIED MECHANICS

(until 1997 Mechanika Teoretyczna i Stosowana, ISSN 0079-3701)

Beginning with Vol. 45, No. 1, 2007, *Journal of Theoretical and Applied Mechanics* (JTAM) has been selected for coverage in Thomson Reuters products and custom information services. Now it is indexed and abstracted in the following:

- **Science Citation Index Expanded** (also known as SciSearch®)
- **Journal Citation Reports/Science Edition**

Advisory Board

MICHAŁ KLEIBER (Poland) – Chairman

- JORGE A.C. AMBROSIO (Portugal) ★ ANGEL BALTOV (Bulgaria) ★ ROMESH C. BATRA (USA)
★ ALAIN COMBESURE (France) ★ JÜRI ENGELBRECHT (Estonia) ★ WITOLD GUTKOWSKI (Poland)
★ JÓZEF KUBIK (Poland) ★ ZENON MRÓZ (Poland) ★ RYSZARD PARKITNY (Poland)
★ EKKEHARD RAMM (Germany) ★ EUGENIUSZ ŚWITOŃSKI (Poland) ★ HISAAKI TOBUSHI (Japan)
★ ANDRZEJ TYLIKOWSKI (Poland) ★ DIETER WEICHERT (Germany) ★ JOSE E. WESFREID (France)
★ JÓZEF WOJNAROWSKI (Poland) ★ JOSEPH ZARKA (France)
★ VLADIMIR ZEMAN (Czech Republic)

Editorial Board

Editor-in-Chief – **WŁODZIMIERZ KURNIK**

Section Editors: IWONA ADAMIEC-WÓJCIK, PIOTR CUPIAŁ, KRZYSZTOF DEMS,
WITOLD ELSNER, ELŻBIETA JARZĘBOWSKA, OLEKSANDR JEWBUSZENKO,
PIOTR KOWALCZYK, ZBIGNIEW KOWALEWSKI, TOMASZ KRZYŻYŃSKI, STANISŁAW KUKLA,
TOMASZ ŁODYGOWSKI, EWA MAJCHRZAK, WIESŁAW NAGÓRKO, JANUSZ NARKIEWICZ,
PIOTR PRZYBYŁOWICZ, BŁAŻEJ SKOCZEŃ, ANDRZEJ STYCZEK,
JACEK SZUMBARSKI, UTZ VON WAGNER (Germany), JERZY WARMIŃSKI

Language Editor – PIOTR PRZYBYŁOWICZ

Technical Editor – EWA KOISAR

Secretary – ELŻBIETA WILANOWSKA



Articles in JTAM are published under Creative Commons Attribution – Non-commercial 3.0. Unported License <http://creativecommons.org/licenses/by-nc/3.0/legalcode>. By submitting an article for publication, the authors consent to the grant of the said license.



The journal content is indexed in Similarity Check, the Crossref initiative to prevent plagiarism.

* * * * *

Editorial Office

Al. Armii Ludowej 16, room 650

00-637 Warszawa, Poland

phone (+48 22) 825 7180, (+48) 664 099 345, e-mail: biuro@ptmts.org.pl

www.ptmts.org.pl/jtam.html

* * * * *



Publication supported by Ministry of Science and Higher Education of Poland

(Journal of Theoretical and Applied Mechanics: 1) digitalizacja publikacji i monografii naukowych w celu zapewnienia i utrzymania otwartego dostępu do nich przez sieć Internet, 2) stworzenie anglojęzycznych wersji wydawanych publikacji, 3) wdrożenie procedur zabezpieczających oryginalność publikacji naukowych oraz zastosowane techniki zabezpieczeń – są finansowane w ramach umowy 699/P-DUN/2018 ze środków Ministra Nauki i Szkolnictwa Wyższego przeznaczonych na działalność upowszechniającą naukę)

STIFFNESS AND DAMPING CHARACTERISTICS OF MR FLUID-BASED SANDWICH BEAMS: EXPERIMENTAL STUDY

MATEUSZ ROMASZKO, BOGDAN SAPIŃSKI

AGH University of Science and Technology, Department of Process Control, Cracow, Poland

e-mail: matek28t@poczta.fm; deep@agh.edu.pl

The study investigates the behaviour of three-layered cantilever sandwich beams filled with magnetorheological fluids (MRFs) differing in the iron particle content by volume. Outer layers are made of aluminium, the space between them is sealed with silicone rubber. Two types of beams are considered: fully filled beams and partially filled beams, subjected to the magnetic field. The aim of the study is to determine stiffness and damping characteristics in relation to the magnetic field strength and the actual location where the magnetic field acts upon the beam. For this purpose, measurements have been taken of the beam free vibration response for various magnetic field strength levels and for various positions of the electromagnet located along the beam axis. Basing on the developed measurement data processing algorithm, the influence of the vibration amplitude on the natural frequency and a dimensionless damping coefficient have been determined. Finally, the equivalent natural frequency and the dimensionless damping coefficient have been derived accordingly, and the stiffness and damping ratio have been determined in function of the magnetic field strength, the electromagnet position and the MRF iron particle content by volume.

Keywords: magnetorheological fluid, beam, magnetic field, vibration, stiffness, damping

1. Introduction

Beams, plates and shell elements are widely used as structural components in a variety of mechanical systems. Their operation, however, gives rise to some undesired phenomena, such as noise or vibrations, leading to damage due to material fatigue. In most systems, stiffness and damping characteristics of their structural components are associated with the type of the manufacturing material. Stiffness and damping characteristics mostly remain unchanged except when the elements have sustained some damage or when they were exposed to action of external factors. In order that stiffness and damping characteristics should be effectively controlled, their structural components are modified to integrate some smart materials, such as magnetorheological fluids (MRF), electrorheological fluids (ERF), piezoelectric elements or other. Yalcintas and Dai (1999, 2004) analyzed dynamic responses of a MRF adaptive structure and compared it with that of ERF containing structure, and established that MRF-based adaptive structure could yield natural frequencies two times higher than ERF-based adaptive structures. Sun *et al.* (2003) determined dynamic characteristics of MRF sandwich beams experimentally and recalling the energy approach. Yeh and Shih (2006) modified the theoretical model of a simply-supported MRF-based adaptive beam under an axial harmonic load, recalling DiTaranto (1965) sandwich beam theory for a symmetric three-layer beam. The incremental harmonic balance method was utilised to identify dynamic instability regions. The study investigated how the magnetic field and beam dimensions should affect the buckling load, natural frequency, loss factor and dynamic instability. Rajamohan *et al.* (2010c) derived the finite element approach and Ritz formulation for a sandwich beam with MRF treatment and showed their validity through tests done on cantilever sandwich beams. Rajamohan *et al.* (2011) formulated an optimal control strategy based

on a linear quadratic regulator and a full dynamic observer to suppress vibration of a cantilever beam with full and partial MRF treatments under a limited magnetic field. All those studies investigated beams with uniform MRF layers subjected to a uniform magnetic field.

A few papers published recently demonstrated that non-uniform MRF treatment could be beneficial for vibration suppression under the transverse excitation. Lara-Prieto *et al.* (2010) conducted an experimental study of the dynamic response of a MRF sandwich cantilever beam under the action of a uniform and non-uniform magnetic field, showing that the natural frequency of the beam tends to decrease as the permanent magnets are moved towards the beam free end. Rajamohan *et al.* (2010a) formulated equations governing the behaviour of partially treated MRF sandwich beams in varied configurations and for different boundary conditions using the finite element approach and Ritz formulation. The results clearly suggest that the natural frequencies and the transverse displacement response of partially treated MRF beams are strongly influenced not only by the magnetic field strength but also by the location and length of the MRF pocket. Next, Rajamohan *et al.* (2010b) considered various configurations of sandwich beams partially treated with MRF, including a beam with a cluster of MRF pockets, a beam with arbitrarily located MRF pockets and with different end conditions. An optimisation problem was formulated by combining finite element analysis with optimisation algorithms based on sequential quadratic programming and a genetic algorithm to identify optimal locations of MRF treatment to achieve the maximal modal damping in the first five modes of flexural vibration. The results showed that the optimal location of the MRF treatment was strongly related to the beam end conditions and the vibration mode. Rajamohan and Ramamoorthy (2012) investigated the vibration behaviour of a multi-layer beam structure comprising an axially non-homogeneous MRF layer in terms of natural frequencies and the loss factor associated with particular modes for varied locations of MRF treatment, varied boundary conditions and subjected to magnetic fields of varied strength levels. It was established that natural frequencies and the loss factor of non-homogeneous MRF beams were strongly influenced not only by strength of the applied magnetic field but also by the actual location of the MRF treatment.

The previous research work of the authors was focused on homogeneous aluminium beams (Romaszko *et al.*, 2015) and three layer beams containing MRF: two fully filled beams (Romaszko *et al.*, 2011; Snamina *et al.*, 2012a,b) and two partially filled beams (Snamina *et al.*, 2012b). The present study summarises experimental investigation of four sandwich beams filled with MRFs (two fully and two partially filled beams). In the present study, the authors employ a newly designed electromagnet (Romaszko and Lacny, 2015). Besides, the end of each beam is clamped in a holder placed at the moving part of the electrodynamic shaker. A slight modification is introduced to investigate forced vibrations with vertical kinematic excitation of the holder (Romaszko *et al.*, 2014). The same boundary conditions are preserved – the cantilever beam. The size of the electromagnet pole pieces cover 80 mm of beam length. Moreover, the gap between the poles is constant this time. The electromagnet is characterized by generation of a larger magnetic field strength and dynamically responding time implies faster reaction, and that is the key parameter for vibration control (Romaszko, 2013). Besides, in the current study the algorithm for determining natural frequency versus vibration amplitude of the beam and dimensionless damping coefficient versus the vibration amplitude is enriched with an additional parameter. It refers to the number of periods of damped vibrations. This parameter behaves similarly to a low-pass filter. The modified experimental set up enabled the authors to repeat and extend the experiments under new conditions.

The authors of the present study investigated experimentally the behaviour of four MRF treated sandwich beams (two fully treated and two partially treated). Two fully treated beams were filled with different types of MRF (characterized by various iron particle content by volume). The objective of the study was to determine the dynamic properties of those beams, particularly their stiffness – natural frequency and damping characteristics – dimensionless damping coefficient.

The influence of the vibration amplitude on the natural frequency and a dimensionless damping coefficient were determined. Then the equivalent natural frequency and the dimensionless damping coefficient were derived accordingly and the stiffness and damping ratio were obtained as a function of the magnetic field strength (taking into account also the non-homogeneous magnetic field), the electromagnet position and the MRF iron particle content by volume.

The work is organised as follows. Section 2 outlines the structure and fabrication technique of beams. Section 3 summarises the experimental set-up and the scenario of experiments (free vibration response measurements). Section 4 presents the experimental data processing algorithm. Section 5 discusses stiffness and damping characteristics of the beams in terms of magnetic field strength levels, electromagnet position and MRF iron particle content by volume. Final conclusions are given in Section 6.

2. Description of the beams

2.1. Structure

The structural design and dimensions of the beam are shown in Fig. 1. Two outer layers made of aluminium are 400 mm long, 30 mm wide and 2 mm high. The space between the layers is sealed with silicone rubber (2 mm in height, 1.5 mm in width). The inside of Beam 1 and Beam 2 is fully filled with a MRF manufactured by Lord Corporation. Beam 1 contains 122-2ED fluid (MRF1) while Beam 2 with 132DG fluid (MRF2). MRF1 and MRF2 differ in the iron particle content by volume (MRF1 contains 22%, MRF2 – 32%). An increase in the particle content in MRF gives rise to an increase in viscosity, density, and changes magnetisation properties and the yield point. Weight of Beam 1 and Beam 2 minus the fluid is 146 g. When filled, Beam 1 weights 196 g and Beam 2 – 211 g. In the case of partially filled Beam 3 and Beam 4, the space between the aluminium layers is divided into five identical pockets, one of them filled with fluid MRF2 (pocket 1 in Beam 3 and pocket 3 in Beam 4). Weight of Beam 3 and Beam 4 minus the fluid is 146.5 g and 159 g when filled.

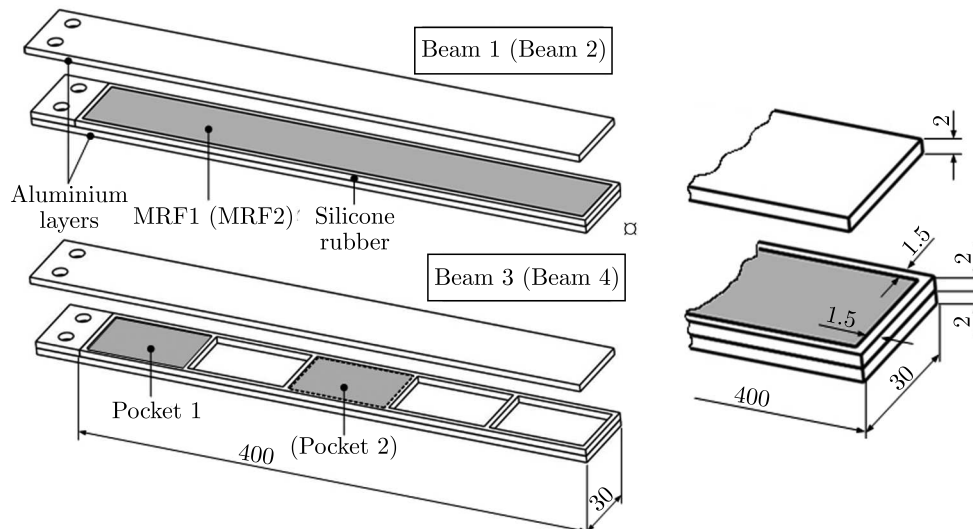


Fig. 1. Structure of the beams

2.2. Fabrication

The beam fabrication involved four stages. At stage 1, the aluminium sheet 30 mm in width was used and two elements 426 mm in length were cut out. During stage 2, those elements were carefully cleaned and silicone rubber was attached to their edges. In the case of Beam 3 and

Beam 4, four transverse stripes of silicone rubber were attached with an adhesive, thus forming five equal pockets. One of the edges of pocket 3 in Beam 4 had silicone sealing removed at two points, along a section 2 mm in length. That procedure was unnecessary in the case of Beam 3 (pocket 1). Afterwards, the second layer of aluminium was attached. Stage 3 consisted in Beam 1 and Beam 2 of filling with MRF1 and MRF2 respectively, using a syringe. A similar procedure was adopted when handling Beam 3, and its pocket 1 was filled with MRF2. In stage 4, an aluminium insert was provided between the outer layers from the fixture end in Beam 1, Beam 2 and Beam 3. In the case of Beam 4, this operation was performed during stage 3 whilst in stage 4, pocket 3 was filled with MRF2, via one of the two opening. The other opening was used to ensure air removal from thus filled pocket. Pocket 3 having been filled, the openings were sealed with silicone rubber.

3. Measurements of the free vibration response

A schematic diagram of the experimental set-up is shown in Fig. 2. One end of the investigated beam is clamped in a holder located in the moving part of the electrodynamic shaker (not used in this study). The suspension of the shaker armature and the upper platform with holder have sufficient stiffness, which does not affect beam free vibration. The magnetic field is generated by the current flowing in the electromagnet. The location of the electromagnet y_m is determined by the distance between the beam fastening point and the mid-point of the electromagnet core of length $e = 80$ mm. The electromagnet is allowed to move freely along the beam length. The measurement and control system incorporates a PC computer, an I/O board RT-DAC4 (INTECO Ltd.), a DC power supply, an amplifier specially designed for this application and a laser sensor SENSO PART RLA-70S1-L8. The system is supported by MATLAB/Simulink software. The power amplifier and I/O board enable control of the magnetic field strength H . The laser sensor measures the displacement z of the beam free end.

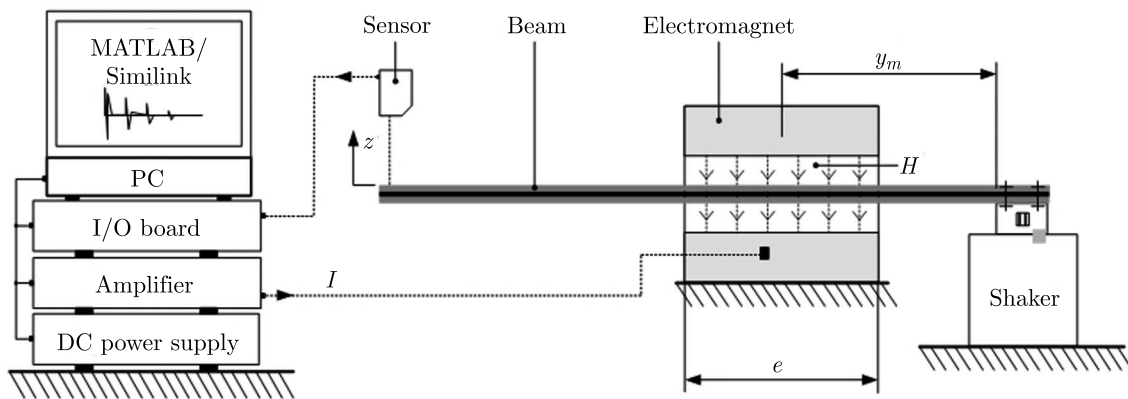


Fig. 2. Schematic diagram of the experimental set-up

Measurements of the beam free vibration response were taken by deflecting its free end from the equilibrium position and recording the displacement z at a sampling frequency of 1 kHz. The measurements were performed for current levels in the electromagnet: 0, 1, 2.4, 3, 3.3, 3.5 A; the corresponding field strength levels H were: 0, 45, 101, 127, 140, 148 kA/m (Romaszko and Lacny, 2015). In the case of Beam 1 and Beam 2, measurements were carried out with the following position of the electromagnet y_m : 40, 60, 80, 100, 120, 140 mm (Fig. 3a). For Beam 3 and Beam 4, the electromagnet position was assumed to be $y_m = 40$ mm and $y_m = 200$ mm, respectively. These values of y_m were related to which pocket was actually filled with MRF (see Fig. 3b). On account of the electromagnetic structure and action of a non-homogeneous magnetic

field, the beam free vibrations were impossible to register when the electromagnet position was $y_m > 140$ mm.

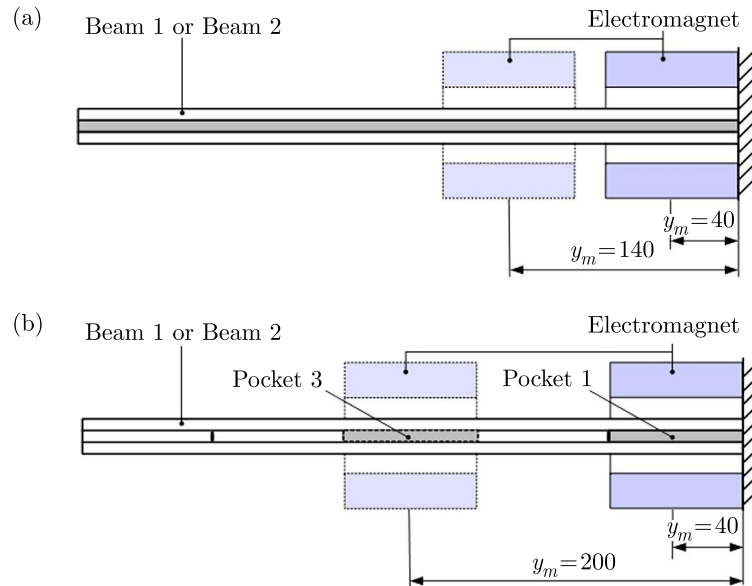


Fig. 3. Electromagnet position in the beams: (a) fully filled, (b) partially filled

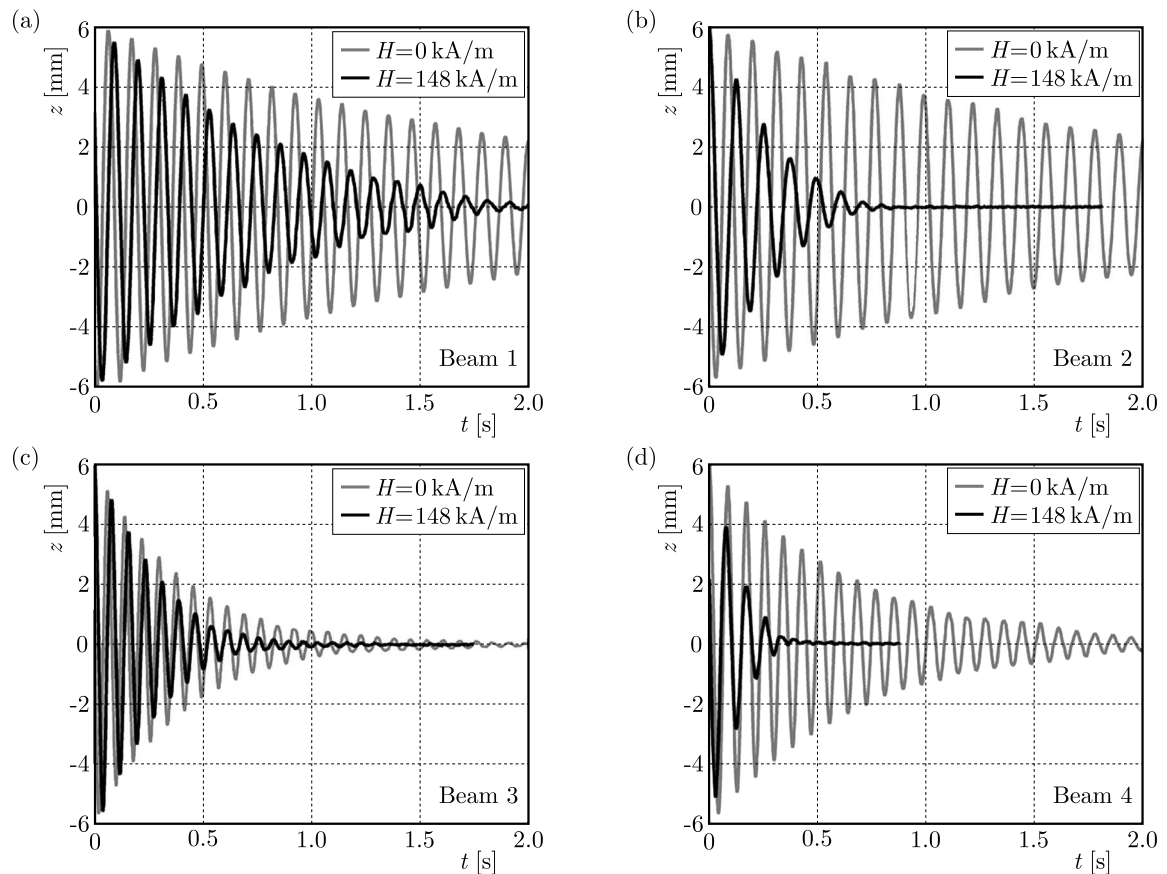


Fig. 4. Free vibration responses

Example free vibration responses of the free end of each beam are shown in Fig. 4, when $H = 0$ kA/m and $H = 148$ kA/m. The plots for Beam 1 and Beam 2 are obtained for the electromagnet position $y_m = 140$ mm. It appears that the decay time tends to decrease with

an increased magnetic field strength level. Comparison of the decay time plots for Beam 1 and Beam 2 taken for the same magnetic field strength level clearly reveals that for Beam 2 the decay time is shorter, which can be attributed to the fact that MRF2 filling Beam 2 has a higher iron particles content than MRF1, which enhances damping. The analysis of measurement data suggests that for the maximal magnetic field strength ($H = 148$ kA/m) the highest damping is registered for Beam 4. In order that interpretation of results should not be obscured by the presence of eddy currents (in aluminium layers) affecting the beam vibration parameters, further measurements were performed to investigate the behaviour of Beam 1 (not filled with MRF1) under the action of a magnetic field. The results showed that magnetic field strength had no effect on the beam vibration parameters.

4. Processing of the experimental data

The registered free vibration responses of the beams have been used to determine the natural frequency f_0 and the dimensionless damping coefficient ζ in function of the vibration amplitude Z . Thus obtained stiffness and damping characteristics were used to derive an equivalent natural frequency f_{0z} and an equivalent damping coefficient ζ_z in relation to the magnetic field strength level H and the electromagnet position y_m .

In the first place, beam vibrations are damped by the MRF filling the beam. Damping properties of the MRF layer can be controlled through the action of the magnetic field. Several energy dispersion mechanisms are involved, including internal friction in aluminium layers and in sealing rubber, friction between the MRF layers and aluminium layers and friction between iron particles suspended in the carrier fluid. Further, energy dispersion is enhanced by external damping. Damping of the beam vibration is not strictly equivalent to viscous damping. It is suggested, therefore, that the measurement data should be processed in accordance with the algorithm, which yields the approximate natural frequency f_0 and the dimensionless damping coefficient ζ for the first mode in relation to the amplitude Z of the registered displacement z . The data processing algorithm involves five steps.

Step 1 defines width of the window k and the number N of amplitudes Z to be found. The amplitude Z is found in the range of 0.5-6 mm and that enables determination of the number N of amplitudes. The number k corresponds to the number of periods of damped vibrations. Next, the signal z is subjected to low-pass and high-pass filtering using the 1st order analogue filters. The critical frequency is chosen such that the frequency band from 2-80 Hz should remain.

In Step 2, the subsequent amplitudes Z_n are found.

In Step 3, the window is introduced with the width k , which is shifted along the time axis. The beginning of the window is set at the time instant when the amplitude occurs Z_n ($n = 1, 2, \dots, N$). For each subsequent amplitude Z_n that is thus located, the time instant t_n when it occurs is recorded. An example of the free vibration response is shown in Fig. 5, revealing the movable window of the width k , the amplitudes that have been found Z_n, Z_{n+k} and the time instants they occur.

The introduced quantity Δ_{nk} is used to determine the logarithmic damping decrement. It is assumed that in the interval between the time instants t_n and t_{n+k} when the respective amplitudes Z_n and Z_{n+k} are registered, the beam damping can be approximated by viscous damping. That is why the damping coefficient and natural frequency in the investigated interval are constant. The quantity Δ_{nk} is expressed by the formula

$$\Delta_{nk} = 2\pi f_{0n} \zeta_n k T_n \quad (4.1)$$

where ζ_n and f_{0n} denote the dimensionless damping coefficient and frequency of undamped vibration (natural frequency). In the investigated interval, beginning at the instant t_n and

corresponding to the occurrence of amplitude Z_n , the average period of damped vibrations T_n is derived from the formula

$$T_n = \frac{t_{n+k} - t_n}{k} \quad (4.2)$$

It is worth while to mention that for a very low damping ($\zeta \ll 1$), the frequency of damped vibration is f_{dn} nearing the natural frequency f_{0n} ($f_{dn} \approx f_{0n}$). Therefore, the dimensionless damping coefficient in function of the amplitude for the window having the width of k periods can be expressed by an approximate formula

$$\zeta(Z) \Big|_{Z=\frac{1}{2}(Z_n+Z_{n+k})} \cong \frac{1}{2k\pi} \Delta_{nk} \quad (4.3)$$

In the event when value of the damping coefficient is difficult to estimate, an exact formula will be recommendable. Recalling the relationship between the natural frequency with no damping f_{0n} and with damping f_{dn} , the dimensionless damping factor is derived in function of the amplitude for the window having the width equal to k periods

$$\zeta(Z) \Big|_{Z=\frac{1}{2}(Z_n+Z_{n+k})} = \frac{\Delta_{nk}}{\sqrt{\Delta_{nk}^2 + 4k^2\pi^2}} \quad (4.4)$$

Accordingly, the natural frequency f_0 can be written by the formula

$$f_0(Z) \Big|_{Z=\frac{1}{2}(Z_n+Z_{n+1})} = \frac{f_d(Z)}{\sqrt{1 - \zeta^2(Z)}} \quad (4.5)$$

Thus, we get the dimensionless damping coefficient ζ and the natural frequency f_0 in the window having the width of k periods and starting at the time instant t_n when the amplitude Z_n occurs. This procedure marks the end of Step 3.

In Step 4, it is checked whether the number being the difference between the number N of sought amplitudes and the window width k should be greater than the ordinal number of the iterative procedure i (for example $N - k > i$). When this condition is not satisfied, the indicator i is incremented and the window is moved to the right with the step equal to one period of damped vibration (to the next amplitude Z_{n+1}), thus marking the beginning of the next iteration. The calculation procedure for the new window position is identical as in Step 3. The window is moved until the moment when the amplitude Z_{n+k} in the window is the ultimate amplitude thus found, in other words, until the condition $N - k > i$ gets satisfied. The number of the thus determined values of $\zeta(Z)$ and $f_0(Z)$ is associated with the number of observed amplitudes Z and width of the window k , and is equal to $N - k$. Having the algorithm procedure completed, the actual value of i implicates the number of the thus determined values of $\zeta(Z)$ and $f_0(Z)$. The width of the window k determines the shape of $f_0(Z)$ and $\zeta(Z)$ plots. The parameter k operates as a low-pass filter – averaging and smoothing both the natural frequency f_0 and dimensionless damping coefficient ζ versus vibration amplitude Z .

Step 5: taking into account the variable window width k , the thus derived characteristics can be smoothed demonstrating how the natural frequency f_0 and the dimensionless damping coefficient ζ should vary in function of the amplitude Z . Then the parameters are established. They express the beam vibration response depending on the field strength and the actual location of magnetic field action. The thus calculated parameters are the equivalent natural frequency f_{0z} and the equivalent damping coefficient ζ_z . Both quantities are computed as the arithmetic mean of dimensionless damping coefficients and natural frequencies computed for each window, using formulas (4.4) and (4.5). The final formulas expressing the equivalent natural frequency f_{0z} and the equivalent damping coefficient ζ_z are written as

$$f_{0z} = \frac{1}{N - k} \sum_{i=1}^{N-k} f_{0i} \quad \zeta_z = \frac{1}{N - k} \sum_{i=1}^{N-k} \zeta_i \quad (4.6)$$

Thus the final Step 5 is completed. The parameters f_{0z} and ζ_z characterising vibration of the beams filled with MRF1 and MRF2 are derived for all cases when the free vibration responses have been registered. The same procedure is applied to derive the parameters f_{0z} and ζ_z for Beam 3 and Beam 4.

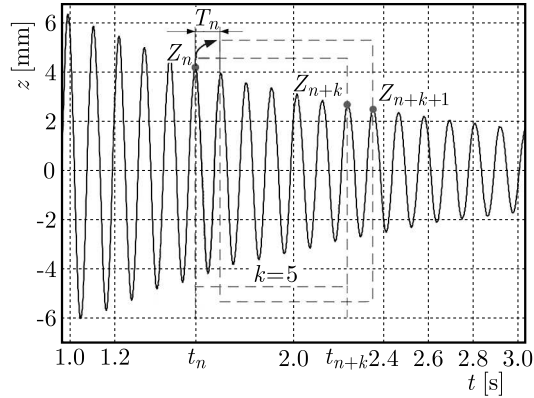


Fig. 5. Procedure of finding the natural frequency and dimensionless damping coefficient

This data processing algorithm would yield characteristics of stiffness and damping in function of the vibration amplitude Z and of the equivalent dimensionless stiffness and equivalent damping coefficient in function of the magnetic field strength and the electromagnet position.

5. Results and discussion

Stiffness and damping characteristics in function of the vibration amplitude Z are not included in this paper. However, their determination has been necessary to calculate the equivalent fundamental frequency and the equivalent damping coefficient in function of the magnetic field strength and the electromagnet position. Recalling respective formulas (4.6), the equivalent fundamental frequency f_{0z} and the equivalent dimensionless damping coefficient ζ_z have been derived accordingly. The variability pattern of the equivalent fundamental natural frequency $f_{0z}(H, y_m)$ and the equivalent dimensionless damping coefficient $\zeta_z(H, y_m)$ in function of the magnetic field strength H and the electromagnet position y_m for Beam 1 and Beam 2 are shown in Figs. 6 and 7. The actual value of the equivalent fundamental natural frequency f_{0z} is derived from formula (4.6)₁ whilst the equivalent dimensionless damping coefficient from formula (4.6)₂. The domain of the function $f_{0z}(H, y_m)$ and $\zeta_z(H, y_m)$ becomes the variability range of the parameters H and y_m . The values of parameter H vary from 0 to 148 kA/m, and the variability range of y_m is from 40 to 140 mm. This domain results from the test conditions. The characteristics $f_{0z}(H, y_m)$ for Beam 1 and Beam 2 are shown in Fig. 6. In the off-state when $H = 0$, the equivalent fundamental frequency $f_{0z}(0, y_m)$ for Beam 1 and Beam 2 is 9.35 and 8.8 Hz, respectively. In the off-state the iron particles suspended in the carrier fluid are able to move freely. The magnetic moments associated with each particle of the MRF are directed randomly. That is why the difference in f_{0z} for Beam 1 and Beam 2 can be attributable to the difference in the beam mass (Beam 1 is lighter than Beam 2 due to a lower iron particle content). Therefore, the equivalent natural frequency f_{0z} registered for a lighter beam-Beam 1 is higher. For fully filled beams operated in the on-state, the critical electromagnet position is observed at $y_m = 100$ mm. In plots in Fig. 6, this boundary is indicated by a grey plane dividing the stiffness characteristics into two areas. Area 1 is contained between the electromagnet positions from 40 and 100 mm. This separation is associated with the influence of the magnetic field strength H on the value of the equivalent fundamental frequency f_{0z} . When the field strength is the maximum

$H = 148 \text{ kA/m}$ and the electromagnet is moved from the beam fastening ($y_m = 40 \text{ mm}$) towards its free end, the frequency f_{0z} tends to increase (the stiffening effect). This increase continues until the electromagnet reaches its critical position $y_m = 100 \text{ mm}$. When the electromagnet is moved still further from the beam fastening, the frequency f_{0z} tends to decrease. For the electromagnet position $y_m = 140 \text{ mm}$ and magnetic field strength $H = 148 \text{ kA/m}$, the equivalent frequency f_{0z} is lower than in the off-state. For any electromagnet position within area 1, an increase in the magnetic field strength results in an increase in the equivalent fundamental frequency f_{0z} . Within this area, the stiffening effect is observed for the two beams. The increase of the equivalent fundamental frequency is also observed in area 2 for the magnetic field strength H falling in a specific range. For Beam 1, this range is from $H = 0$ to $H = 75 \text{ kA/m}$, for Beam 2 is from 0 to 45 kA/m . A further increase in H leads to a decrease in f_{0z} for the two fully filled beams. The beam damping effect predominates over the stiffening effect. Two hypotheses have been put forward to account for this behavior.

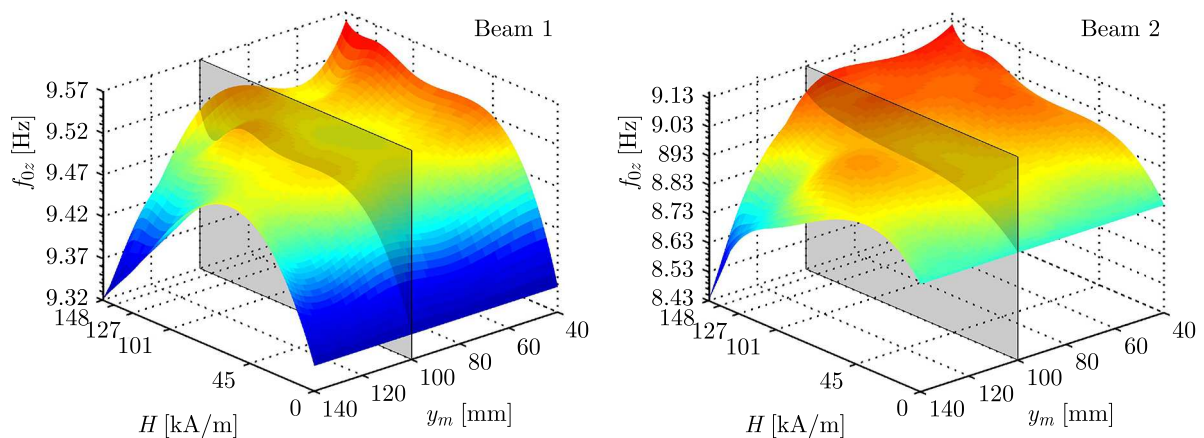


Fig. 6. Equivalent natural frequency f_{0z} vs. the magnetic field strength H and electromagnet position y_m

The first hypothesis emphasises the increasing influence of field non-homogeneity on the edges of the area between the electromagnet poles. The influence of field non-homogeneity on the beam motion is enhanced with the increasing amplitude of vibration, that is for beam points further away from the fastening (increased y_m). Each iron particle in the MRF has two poles which can be assigned a given 'magnetic charge'. The signs of these poles are different, therefore each particle forms a magnetic dipole. When subjected to an external magnetic field, it will be directed in accordance with the field lines. When the external field is non-homogeneous, an iron particle will be attracted to the stronger field region. Moved from its equilibrium position, the beam will move in the direction in which the modulus of the magnetic field strength vector should increase. The field forces acting upon the iron particles in the MRF act opposite to elasticity forces, thus reducing the frequency of the beam natural vibration.

In accordance with the other hypothesis, the storage modulus of the MRF in this area is smaller than the loss modulus. That is why the MRF contained in the beams exhibits properties of a viscous material rather than an elastic material (Lara-Prieto *et al.*, 2010), which leads to a relatively fast increase in the beam damping effect, illustrated by plots of $\zeta_z(H, y_m)$ in further Sections. The extreme values of f_0 are obtained for the MRF in the on-state. The highest value of f_{0z} for fully filled beams is registered for $H = 148 \text{ kA/m}$, $y_m = 40 \text{ mm}$, approaching 9.56 Hz and 9.11 Hz for Beam 1 and Beam 2, respectively. The smallest value of f_0 for fully filled beams is observed for $H = 148 \text{ kA/m}$, $y_m = 140 \text{ mm}$, reaching 9.32 Hz and 8.43 Hz for Beam 1 and Beam 2, respectively. The equivalent natural frequency f_{0z} for MRF in the off-state ($H = 0$) being taken as the reference value, the control of parameters H and y_m allows the value of f_{0z}

to be increased or decreased. It can be increased by 2.25% and 3.25%, respectively, for Beam 1 and Beam 2, or decreased by 0.3% and 4.2%. These changes in the equivalent frequency f_{0z} illustrate the influence of the iron particle content. The largest changes are observed for Beam 2 filled with MRF2 because the iron particle content in this fluid is larger.

Figure 7 plots the characteristics $\zeta_z(H, y_m)$ for Beam 1 and Beam 2. It can be readily seen that both increasing the field strength H and moving the electromagnet further away from the beam fastening (increasing y_m) lead to an increase in the equivalent dimensionless damping coefficient ζ_z . A sharp increase in ζ_z is observed in area 2, alongside a rapid decrease in f_{0z} (Fig. 6), as mentioned in previous Sections. The smallest value of the dimensionless damping coefficient ζ_z is registered when the MRF is in the off-state, approaching 0.0088 and 0.0090 for Beam 1 and Beam 2, respectively. The value of the equivalent dimensionless damping coefficient ζ_z is the highest for $H = 148$ kA/m, $y_m = 140$ mm, reaching 0.0251 for Beam 1 and 0.0739 for Beam 2. In the off-state, there are no significant changes between the dimensionless damping coefficient values for MRF treated beams differing in the iron particle content. Application of a magnetic field with the strength H and the appropriate electromagnet position y_m make the equivalent dimensionless damping coefficient for Beam 2 increase by 721%. For Beam 2, the equivalent dimensionless damping coefficient rises by 185%. It shows that the increasing of the iron particle content by volume from 22% in MRF1 to 32% in MRF2 results in a significant increase in the beam damping effect.

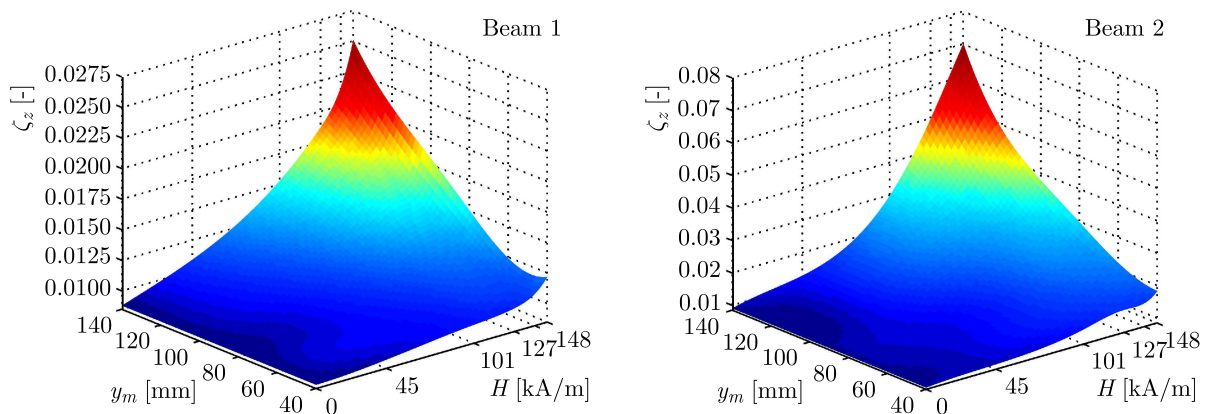


Fig. 7. Equivalent dimensionless damping coefficient ζ_z vs. the magnetic field strength H and electromagnet position y_m

The test results provided in the present study can be compared with the results presented in the previous authors' works (Romaszko *et al.*, 2011; Snamina *et al.*, 2012b). There is a satisfactory convergence comparing current equivalent natural frequencies and equivalent dimensionless damping coefficients with the previous ones. The former measurements were made when the beams were not fixed to the vibration shaker armature and the magnetic field was produced by a newly engineered electromagnet. It implied satisfactory repetition, no disturbance from the shaker armature suspension, no aging, no liquid sedimentation, no leakage and recreation the appropriate magnetic field strength.

Figure 8 plots the equivalent natural frequency f_{0z} and the equivalent dimensionless damping coefficient ζ_z for partially filled beams. Results obtained for Beam 2 for the electromagnet position $y_m = 40$ mm and $y_m = 140$ mm are also given, for easy comparison with the fully treated beams. As the iron particle content by volume for Beam 2 is higher than for Beam 3 and Beam 4, Beam 2 exhibits lower stiffness. Increasing the magnetic field strength leads to an increase in the natural frequency (stiffening effect). Shifting the field interaction zone towards the beam free end causes the beam stiffness to decrease with an increased magnetic field strength. That is clearly seen for Beam 4 (partially filled) and Beam 2 (fully filled) when $y_m = 140$ mm. The most

considerable changes in the natural frequency are observed for Beam 4. For the maximum field strength $H = 148 \text{ kA/m}$, the frequency f_{0z} is reduced by 6.4% in relation to $H = 0$. Experiments showed that the equivalent dimensionless damping coefficient for $H = 0$ for Beam 3 was $\zeta_z = 0.0305$ and for Beam 4 $\zeta_z = 0.0216$. It appears, therefore, that placing the MRF in pocket 3 in the off-state vastly reduced the potential of energy dissipation of the vibrating beam, unlike in the case when the beam was subjected to the magnetic field of strength $H > 75 \text{ kA/m}$. For the maximum field strength $H = 148 \text{ kA/m}$, the damping coefficient for Beam 4 is nearly twice as large as for Beam 3. Comparison of the equivalent dimensionless damping coefficient values $\zeta_z(0)$ and $\zeta_z(148)$ implicates that the slightest increase is registered for beams whose sections subjected to the action of magnetic field are located near the fastening point ($y_m = 40 \text{ mm}$). For Beam 2, there is a two-fold increase of the damping coefficient when $y_m = 40 \text{ mm}$, for Beam 3 this increase is 1.5-fold. When the beam zone affected by the magnetic field shifts towards the beam free end, the dimensionless damping coefficient increases considerably. For Beam 2, a nearly 8-fold increase is observed when $y_m = 140 \text{ mm}$, for Beam 4, nearly 5 fold. Plots shown in Fig. 9 lead us to the conclusion that it is not the volume of the MRF used that determines the actual shape of the stiffness and damping characteristics. Engineering a specially designed beam with five pockets and filling the appropriate pocket with a MRF result in major changes in the relevant characteristics.

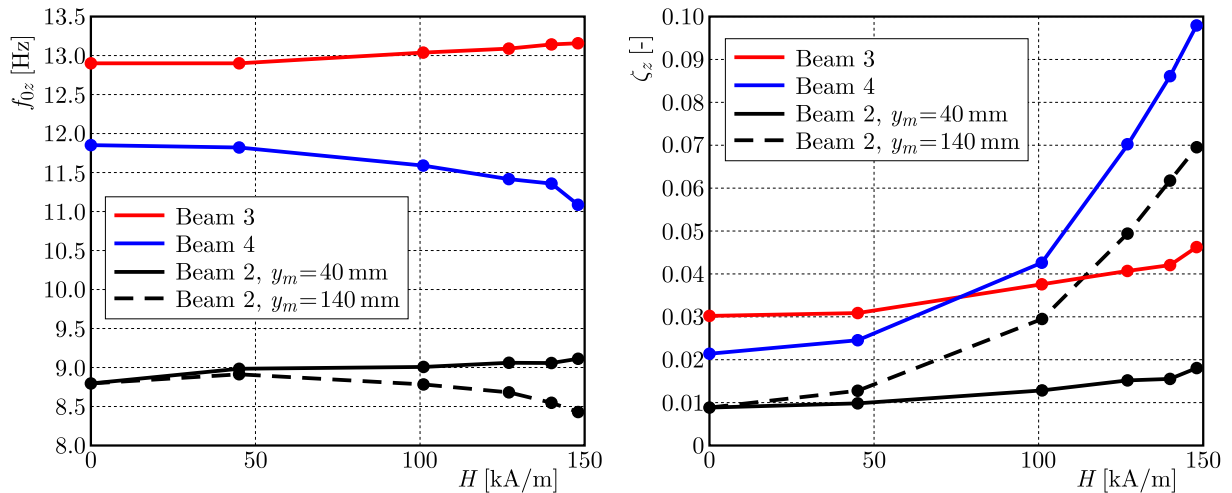


Fig. 8. Equivalent natural frequency f_{0z} and equivalent dimensionless damping coefficient ζ_z vs. magnetic field strength H

6. Conclusions

The study investigates the dynamic behaviour of cantilever sandwich beams (with one or five pockets) filled with MRFs varying in their iron particles content by volume. The purpose of the study is to determine stiffness and damping characteristics of the beams by measuring the free vibration response of the beams subjected to action of a magnetic field of varied strength and varied electromagnet positions. A measurement data processing algorithm has been proposed, allowing us to establish how the vibration amplitude should influence the natural frequency and the equivalent dimensionless damping coefficient. The equivalent natural frequency and the equivalent dimensionless damping coefficient have been derived accordingly.

The results of investigations lead us to the following conclusions.

- The most complex energy dissipation mechanism in beams is explained by recalling the viscous damping model and the developed data processing algorithm.

- The natural frequency and the dimensionless damping coefficient tend to increase as the free vibrations decay. The higher the magnetic field strength and the further the electromagnet from the beam fastening point, the more significant this increase is.
- The effect of field non-homogeneity is revealed particularly when the electromagnet is in the position defined as $y_m > 100$ mm (see the grey-coloured plane in the stiffness and damping plots). This non-homogeneity causes a rapid increase in the dimensionless damping coefficient. At the same time, the natural frequencies of Beam 1, Beam 2, Beam 4 decrease.
- Plots of the natural frequency and the equivalent dimensionless damping coefficient clearly show that for the beam containing the MRF with a higher solids content, the variability range of the natural frequency and of the dimensionless damping factor is wider. It appears that the actual shape of the stiffness and damping characteristics for Beam 1, Beam 2 (fully filled with the MRF) and Beam 3, Beam 4 (partially treated) is associated with the location of the MRF in the beam (pocket number), not with the MRF volume.
- In the case of partially filled beams (Beam 3 and Beam 4), the factor affecting the stiffness and damping plots in the largest extent is the number (location) of MRF-containing pocket. The widest variability range of the equivalent natural frequency and the equivalent dimensionless damping coefficient is registered for Beam 4 (which has the mid pocket filled).
- The presented results are consistent with the previous ones and reveal satisfactory repetition, no disturbance from the shaker armature suspension, no aging, no liquid sedimentation, no leakage. The newly designed electromagnet enables one to recreate the appropriate magnetic field strength level.

In further work, the authors are going to investigate complex vibration modes of the beams.

Acknowledgement

This work has been supported by AGH University of Science and Technology under research program No. 11.11.130.766.

References

1. DiTARANTO R.A., 1965, Theory of vibratory bending for elastic and viscoelastic layered finite-length beams, *Journal of Applied Mechanics*, **87**, 881-886
2. LARA-PRIETO V., PARKIN R., JACKSON M., SILBERSCHMIDT V., KESY Z., 2010b, Vibration characteristics of MR cantilever sandwich beams: experimental study, *Journal of Smart Materials and Structures*, **19**, 1
3. RAJAMOHAN V., RAKHEJA S., SEDAGHATI R., 2010a, Vibration analysis of a partially treated multi-layer beam with magnetorheological fluid, *Journal of Sound and Vibration*, **329**, 3451-3469
4. RAJAMOHAN V., RAMAMOORTHY M., 2012, Dynamic characterization of non-homogeneous magnetorheological fluids based multi-layer beam, *Applied Mechanics and Materials*, **110-116**, 105-112
5. RAJAMOHAN V., SEDAGHATI R., RAKHEJA S., 2010b, Optimum design of a multilayer beam partially treated with magnetorheological fluid, *Journal of Smart Materials and Structures*, **19**, 1
6. RAJAMOHAN V., SEDAGHATI R., RAKHEJA S., 2010c, Vibration analysis of a multi-layer beam containing magnetorheological fluid, *Journal of Smart Materials and Structures*, **19**, 1
7. RAJAMOHAN V., SEDAGHATI R., RAKHEJA S., 2011, Optimal vibration control of beams with total and partial MR-fluid treatments, *Journal of Smart Materials and Structures*, **20**, 11

8. ROMASZKO M., 2013, Free vibration control of a cantilever MR fluid based sandwich beam, *Proceedings of the 14th International Carpathian Control Conference (ICCC)*, Rytro, Poland, May 26-29, 2013
9. ROMASZKO M., LACNY L., 2015, Magnetic field analysis of the actuator in a semi-active vibration control of the beam with MR fluid, *Applied Mechanics and Materials*, **759**, 37-44
10. ROMASZKO M., PAKULA S., SAPINSKI B., SNAMINA J., 2011, Vibration parameters of sandwich beams with two types of MR fluid, *Mechanics and Control*, **30**, 3, 151-156
11. ROMASZKO M., SAPINSKI B., SIOMA A., 2015, Forced vibrations analysis of a cantilever beam using the vision method, *Journal of Theoretical and Applied Mechanics*, **53**, 1, 243-254
12. ROMASZKO M., SNAMINA J., PAKULA S., 2014, Composite beam's parameters identification based on frequency responses, *Proceedings of the 15th International Carpathian Control Conference (ICCC)*, Velke Karlovice, Czech Republic, May 28-30
13. SNAMINA J., SAPINSKI B., WSZOŁEK W., ROMASZKO M., 2012a, Investigation on vibrations of a cantilever beam with magnetorheological fluid by using the acoustical signal, *Acta Physica Polonica A*, **121**, 1-A, 188-190
14. SNAMINA J., SAPINSKI B., ROMASZKO M., 2012b, Vibration parameter analysis of sandwich cantilever beams with multiple MR fluid segments, *Engineering Modeling*, **12**, 43, 247-254
15. SUN Q., ZHOU J.X., ZHANG L., 2003, An adaptive beam model and dynamic characteristics of magnetorheological materials, *Journal of Sound and Vibration*, **261**, 465-481
16. YALCINTAS M., DAI H., 1999, Magnetorheological and electrorheological materials in adaptive structures and their performance comparison, *Journal of Smart Materials and Structures*, **8**, 560-573
17. YALCINTAS M., DAI H., 2004, Vibration suppression capabilities of magnetorheological materials based adaptive structures, *Journal of Smart Materials and Structures*, **13**, 1-11
18. YEH Z.F., SHIH Y.S., 2006, Dynamic characteristics and dynamic instability of magnetorheological material-based adaptive beams, *Journal of Composite Materials*, **40**, 1333-1359

Manuscript received November 8, 2016; accepted for print September 21, 2017

BIFURCATION AND CHAOS ANALYSIS OF A GEAR-ROTOR-BEARING SYSTEM

XIANGFENG GOU

School of Mechanical Engineering, Tianjin Polytechnic University, Tianjin, China
Tianjin Key Laboratory of Advanced Mechatronics Equipment Technology, Tianjin, China
School of Mechanical Engineering, Lanzhou Jiaotong University, Lanzhou, China
e-mail: 20150022@tjpu.edu.cn

LINGYUN ZHU

School of Mechanical Engineering, Tianjin Polytechnic University, Tianjin, China
School of Mechanical Engineering, Lanzhou Jiaotong University, Lanzhou, China

CHANGJUN QI

School of Mechanical Engineering, Lanzhou Jiaotong University, Lanzhou, China

To study chaos and bifurcation of a gear system, a five-degree-of-freedom nonlinear dynamic model of a gear-rotor-bearing system is established. It consists of a gear pair, supporting shafts, bearings and other auxiliary components. The effects of frequency, backlash, bearing clearance, comprehensive transmission error and stiffness on nonlinear dynamics of the system are investigated according to bifurcation diagrams, phase portraits and Poincaré maps by a numerical method. Some nonlinear phenomena such as grazing bifurcation, Hopf bifurcation, inverse-Hopf bifurcation, chaos and coexistence of attractors are investigated. Different grazing bifurcations and their causes are discussed. The critical parameters are identified, too.

Keywords: gear-rotor-bearing, dynamics, bifurcation, chaos

1. Introduction

Gear systems play a major role in mechanical engineering and other engineering fields. There are plenty of researches on nonlinear dynamics of gear systems since Kahraman and Singh (1990) researched nonlinear dynamics of a spur gear pair where the backlash was represented by a truncated series expansion. They developed a 3-DOF dynamic model including non-linearities associated with radial clearances in the radial rolling element bearings and backlash between a spur gear pair in 1991. Ranghothama and Narayanan (1999) investigated periodic motions and chaotic motions of a nonlinear geared rotor-bearing system. Theodossiades and Natsiavas (2001) investigated the response and stability characteristics of a gear pair system supported on oil journal bearings. Choi *et al.* (2001) analyzed dynamic characteristics of a geared rotor-bearing system with the transfer matrix method. Chen *et al.* (2011) developed a multi-degree-of-freedom nonlinear dynamic gear system with dynamic backlash, friction and time varying stiffness. Chang-Jian (2010a,b) established a dynamical model of a HSFDM mounted gear-bearing system, a dynamical model of a gear-bearing system under nonlinear suspension, Chang-Jian and Chang (2012a,b) – a dynamical model of the porous squeeze film damper mounted on a gear-bearing system and a dynamical model of a gear pair system equipped with journal bearings under turbulent flow. Cui *et al.* (2012) established a dynamical model of a geared rotor system with a nonlinear oil film force and a nonlinear mesh force. Xiang *et al.* (2016) proposed a period

expansion method to build a 6-DOF nonlinear dynamic model of a spur gear pair with time varying stiffness, gear backlash and surface friction.

The motor and other auxiliary components mounted on the input and output shafts as rotor are abstracted as rotors coupled with the gear-bearing system in this paper. A 5-DOF nonlinear dynamic model which is closer to the engineering practice is developed to research the bifurcation and chaos of the system. It is a multiple clearance and multi-parameter coupled system.

2. Nonlinear dynamic model of a gear-rotor-bearing system

A simplified theoretical model of a gear-rotor-bearing system is illustrated in Fig. 1. The gear meshing part is simplified as two rotors coupled with viscous dampers and nonlinear springs. Three nonlinear factors such as time-varying stiffness, backlash and the comprehensive transmis-

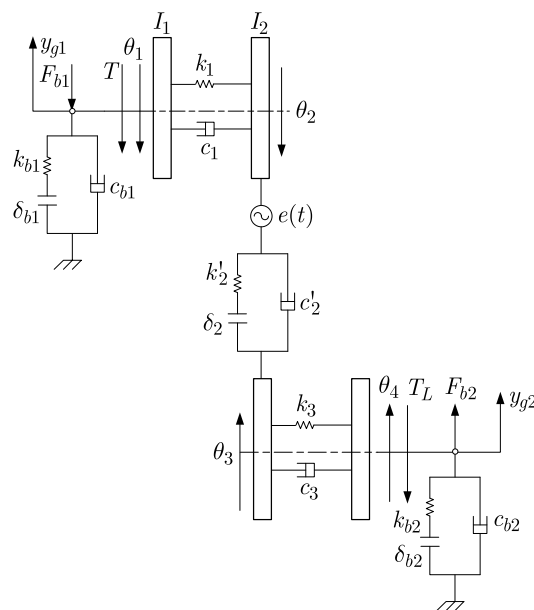


Fig. 1. Dynamic model of the gear-rotor-bearing system

sion error are considered in it. Axial vibration, transverse vibration and longitudinal vibration are not taken into account. Torsional vibration displacements between meshing gears are studied only. The torsional vibration displacement of the two gears and rotors is denoted as θ_i ($i = 1, 2, 3, 4$), respectively. The mass moment of inertia of the two gears is I_i ($i = 2, 3$) and the moment of inertia of the two rotors is I_i ($i = 1, 4$), respectively. The base circle radius of the two gears is r_{bi} ($i = 2, 3$), respectively. Torsional damping is c_1 and c_3 and the torsional stiffness of the two rotation shafts is k_1 and k_3 , respectively. The mesh stiffness and damping coefficient is k'_2 and c'_2 , respectively. The force of gears by bearings on the input and output shafts is F_{bi} ($i = 1, 2$), respectively. The torque of the input and output shafts is T and T_L , respectively. The damping coefficient of the bearings on the input and output shafts is c_{bi} ($i = 1, 2$), respectively. The average support stiffness of the bearings on the input and output shafts is k_{bi} ($i = 1, 2$), respectively. The backlash function $f(\cdot)$ is usually used to represent gear clearance. The bearing clearance functions on the input and output shafts is $\bar{f}(\cdot)$ ($i = 1, 2$), respectively. The actual backlash is δ_2 . The bearing clearance on the input and output shafts is δ_{bi} ($i = 1, 2$), respectively. The displacement of the center of the two gears is y_{gi} ($i = 1, 2$), respectively. The time-varying comprehensive transmission error of the gear pair is $e(t)$. The absolute rotational equations of the system can be derived according to the 2nd Newton's law

$$\begin{aligned}
I_1 \ddot{\theta}_1 + c_1(\dot{\theta}_1 - \dot{\theta}_2) + k_1(\theta_1 - \theta_2) &= T \\
I_2 \ddot{\theta}_2 - c_1(\dot{\theta}_1 - \dot{\theta}_2) - k_1(\theta_1 - \theta_2) + R_{b2} c'_2 [R_{b2} \dot{\theta}_2 - R_{b3} \dot{\theta}_3 - \dot{e}(t) - (\dot{y}_{g1} - \dot{y}_{g2})] \\
+ R_{b2} k'_2 f [R_{b2} \theta_2 - R_{b3} \theta_3 - e(t) - (y_{g1} - y_{g2})] &= 0 \\
I_3 \ddot{\theta}_3 - c_3(\dot{\theta}_3 - \dot{\theta}_4) + k_1(\theta_1 - \theta_2) - R_{b3} c'_2 [R_{b2} \dot{\theta}_2 - R_{b3} \dot{\theta}_3 - \dot{e}(t) - (\dot{y}_{g1} - \dot{y}_{g2})] \\
- R_{b3} k'_2 f [R_{b2} \theta_2 - R_{b3} \theta_3 - e(t) - (y_{g1} - y_{g2})] &= 0 \\
I_4 \ddot{\theta}_4 + c_3(\dot{\theta}_3 - \dot{\theta}_4) + k_3(\theta_3 - \theta_4) &= -T_L
\end{aligned} \tag{2.1}$$

The theoretical backlash is defined as $2b$, and b is selected as the feature size. The relative rotational equation of the system can be written as in Eqs. (2.2) by subtracting every two in Eqs. (2.1) with the following expressions $\gamma = b/R_{b2}$, $q_1 = (\theta_1 - \theta_2)/\gamma$, $q_2 = [R_{b2}\theta_2 - R_{b3}\theta_3 - e(t) - (y_{g1} - y_{g2})]/b$ and $q_3 = (\theta_3 - \theta_4)/\gamma$

$$\begin{aligned}
\ddot{q}_1 + \left(\frac{c_1}{I_1} + \frac{c_1}{I_2}\right) \dot{q}_1 + \left(\frac{k_1}{I_1} + \frac{k_1}{I_2}\right) q_1 - \frac{R_{b2}^2 c'_2}{I_2} \dot{q}_2 - \frac{R_{b2}^2 k'_2}{I_2} f(q_2) &= \frac{T}{I_1 \gamma} \\
\ddot{q}_2 - \frac{c_1}{I_2} \dot{q}_1 - \frac{k_1}{I_2} q_1 - \frac{R_{b3} c_3}{I_3 R_{b2}} \dot{q}_3 - \frac{R_{b3} k_3}{I_3 R_{b2}} q_3 + \left(\frac{R_{b2}^2 c'_2}{I_2} + \frac{R_{b3}^2 c'_2}{I_3}\right) \dot{q}_2 \\
+ \left(\frac{R_{b2}^2 k'_2}{I_2} + \frac{R_{b3}^2 k'_2}{I_3}\right) f(q_2) &= \frac{-\ddot{e}(t) - (\ddot{y}_{g1} - \ddot{y}_{g2})}{b} \\
\ddot{q}_3 + \left(\frac{c_3}{I_3} + \frac{c_3}{I_4}\right) \dot{q}_3 + \left(\frac{k_3}{I_3} + \frac{k_3}{I_4}\right) q_3 - \frac{R_{b2} R_{b3} c'_2}{I_3} \dot{q}_2 - \frac{R_{b2} R_{b3} k'_2}{I_3} f(q_2) &= \frac{T_L}{I_4 \gamma}
\end{aligned} \tag{2.2}$$

The dimensionless torsional vibration equation of the system can be obtained by defining $\tau = \omega_n t$, $\dot{q}_{(1,2,3)} = \dot{q}_{(1,2,3)}/\omega_n^2$, $\dot{y}_{(g1,g2)} = b\omega_n \dot{q}_{(4,5)}$ where $\omega_n = \sqrt{k'_2 I_2 I_3 / (I_3 R_{b2}^2 + I_2 R_{b3}^2)}$

$$\begin{aligned}
\ddot{q}_1 + \xi_{11} \dot{q}_1 - \xi_{12} \dot{q}_2 + k_{11} q_1 - k_{12} [1 + k \cos(\tau + \varphi)] f(q_2) &= F_{mi} + F_{ai} \sin(\tau + \varphi_i) \\
\ddot{q}_2 - \xi_{21} \dot{q}_1 + \xi_{22} \dot{q}_2 - \xi_{23} \dot{q}_3 - k_{21} q_1 + k_{22} [1 + k \cos(\tau + \varphi)] f(q_2) - k_{23} q_3 \\
= -\omega^2 \varepsilon \sin(\tau + \varphi) - \ddot{q}_4 + \ddot{q}_5 & \\
\ddot{q}_3 - \xi_{31} \dot{q}_2 + \xi_{32} \dot{q}_3 - k_{31} [1 + k \cos(\tau + \varphi)] f(q_2) + k_{32} q_3 &= F_{ml} + F_{al} \sin(\tau + \varphi_o)
\end{aligned} \tag{2.3}$$

The dimensionless parameters are defined as

$$\begin{aligned}
\xi_{11} &= \frac{c'_2 R_{b2}^2 R_{b3}}{I_1 I_2 \omega_n} & \xi_{12} &= \frac{R_{b2}^2 c'_2}{I_2 \omega_n} & \xi_{23} &= \frac{c_3 R_{b3}}{I_3 R_{b2} \omega_n} \\
\xi_{21} &= \frac{c_1}{I_2 \omega_n} & \xi_{22} &= \frac{c'_2 (I_3 R_{b2}^2 + I_2 R_{b3}^2)}{I_2 I_3 \omega_n} & \xi_{31} &= \frac{c'_2 R_{b2}^2 R_{b3}}{I_3 R_{b2} \omega_n} \\
\xi_{32} &= \frac{c_3 (I_3 + I_4)}{I_3 I_4 \omega_n} & k_{11} &= \frac{k_1 (I_1 + I_2)}{I_1 I_2 \omega_n^2} & k_{12} &= \frac{R_{b2}^2 k'_2}{I_2 \omega_n^2} \\
k_{21} &= \frac{k_1}{I_2 \omega_n^2} & k_{22} &= \frac{k'_2 (I_3 R_{b2}^2 + I_2 R_{b3}^2)}{I_2 I_3 \omega_n^2} & k_{23} &= \frac{k_3 R_{b3}}{I_3 R_{b2} \omega_n^2} \\
k_{31} &= \frac{k'_2 R_{b2}^2 R_{b3}}{I_3 R_{b2} \omega_n^2} & k_{32} &= \frac{k_3 (I_3 + I_4)}{I_3 I_4 \omega_n}
\end{aligned}$$

in equations (2.3). The time-varying mesh stiffness is $k(t) = 1 + k \sin(\omega t + \varphi)$ (Kahraman and Singh, 1990) where the dimensionless mesh frequency is $\omega = \omega_e/\omega_n$ and ω_e is the mesh frequency of the gear. The dynamical transmission error is $e(t) = 1 + \varepsilon \sin(\omega t + \varphi)$ (Kahraman and Singh, 1990). The dimensionless loads can be defined as

$$F_{mi} = \frac{T}{I_1 \gamma} \quad F_{ai} = \frac{T \sin(\omega t + \varphi_i)}{I_1 \gamma} \quad F_{ml} = \frac{T_L}{I_4 \gamma} \quad F_{al} = \frac{T_L \sin(\omega t + \varphi_o)}{I_4 \gamma}$$

where φ_i and φ_o is the initial phase angular of the excitation and response, respectively.

Transverse vibration equations of the system can be formulated according to the 2nd Newton's law

$$\begin{aligned}
 m_{g1}\ddot{y}_{g1} + c_{b1}\dot{y}_{g1} - c'_2[R_{b2}\dot{\theta}_2 - R_{b3}\dot{\theta}_3 - \dot{e}(t) - (\dot{y}_{g1} - \dot{y}_{g2})] + k_{b1}\bar{f}_{b1}(y_{g1}) \\
 - k'_2f[R_{b2}\theta_2 - R_{b3}\theta_3 - e(t) - (y_{g1} - y_{g2})] = -F_{b1} \\
 m_{g2}\ddot{y}_{g2} + c_{b2}\dot{y}_{g2} + c'_2[R_{b2}\dot{\theta}_2 - R_{b3}\dot{\theta}_3 - \dot{e}(t) - (\dot{y}_{g1} - \dot{y}_{g2})] + k_{b2}\bar{f}_{b2}(y_{g2}) \\
 + k'_2f[R_{b2}\theta_2 - R_{b3}\theta_3 - e(t) - (y_{g1} - y_{g2})] = F_{b2}
 \end{aligned} \tag{2.4}$$

where the mass of the gear and rotor on the drive and driven shaft is m_{g1} and m_{g2} , respectively.

The dimensionless transverse vibration equations of the system can be obtained when the dimensionless parameters are defined as

$$\begin{aligned}
 \xi_{41} &= \frac{c_{b1}}{2m_{g1}\omega_n} & \xi_{42} &= \frac{c'_2}{2m_{g1}\omega_n} & \xi_{51} &= \frac{c_{b2}}{2m_{g2}\omega_n} & \xi_{52} &= \frac{c'_2}{2m_{g2}\omega_n} \\
 k_{41} &= \frac{k_{b1}}{m_{g1}\omega_n^2} & k_{42} &= \frac{k'_2}{m_{g2}\omega_n^2} & k_{51} &= \frac{k_{b2}}{m_{g2}\omega_n^2} & k_{52} &= \frac{k'_2}{m_{g2}\omega_n^2} \\
 \bar{F}_{b1} &= \frac{F_{b1}}{m_{g1}b\omega_n^2} & \bar{F}_{b2} &= \frac{F_{b2}}{m_{g2}b\omega_n^2}
 \end{aligned}$$

and

$$\begin{aligned}
 \ddot{q}_4 + 2\xi_{41}\dot{q}_4 + k_{41}\bar{f}_{b1}(q_4) - 2\xi_{42}\dot{q}_2 - k_{42}f(q_2) = -\bar{F}_{b1} \\
 \ddot{q}_5 + 2\xi_{51}\dot{q}_5 + k_{51}\bar{f}_{b2}(q_5) + 2\xi_{52}\dot{q}_2 + k_{52}f(q_2) = \bar{F}_{b2}
 \end{aligned} \tag{2.5}$$

A 5-DOF dimensionless dynamical equation of the gear-rotor-bearing system can be obtained by coupling the torsional vibration and transverse vibration. It can be written as the state equation by defining $x_1 = q_1$, $x_2 = \dot{x}_1$, $x_3 = q_2$, $x_4 = \dot{x}_3$, $x_5 = q_3$, $x_6 = \dot{x}_5$, $x_7 = q_4$, $x_8 = \dot{x}_7$, $x_9 = q_5$, $x_{10} = \dot{x}_9$

$$\begin{aligned}
 \dot{x}_1 &= x_2 \\
 \dot{x}_2 &= F_{mi} + F_{ai} \sin(\tau + \varphi_i) - \xi_{11}x_2 + \xi_{12}x_4 - k_{11}x_1 + k_{12}[1 + k \cos(\tau + \varphi)]f(x_3) \\
 \dot{x}_3 &= x_4 \\
 \dot{x}_4 &= -\dot{x}_8 + \dot{x}_{10} + \xi_{21}x_2 - \xi_{22}x_4 + \xi_{23}x_6 + k_{21}x_1 - k_{22}[1 + k \cos(\tau + \varphi)]f(x_3) \\
 &\quad + k_{23}x_5 - \omega^2\varepsilon \sin(\tau + \varphi) \\
 \dot{x}_5 &= x_6 \\
 \dot{x}_6 &= F_{ml} + F_{al} \sin(\tau + \varphi_o) + \xi_{31}x_4 - \xi_{32}x_6 + k_{31}[1 + k \cos(\tau + \varphi)]f(x_3) - k_{33}x_5 \\
 \dot{x}_7 &= x_8 \\
 \dot{x}_8 &= -\bar{F}_{b1} - 2\xi_{41}x_8 - k_{41}f_{b1}(x_7) + 2\xi_{42}x_4 + k_{42}f(x_3) \\
 \dot{x}_9 &= x_{10} \\
 \dot{x}_{10} &= \bar{F}_{b2} - 2\xi_{51}x_{10} - k_{51}f_{b2}(x_9) - 2\xi_{52}x_4 - k_{52}f(x_3)
 \end{aligned} \tag{2.6}$$

Backlash is one of the main nonlinear factors in the gear system. The backlash function of the gear pair can be written as follows if the dimensionless backlash is defined as $D = \delta_2/(2b)$

$$f(x) = \begin{cases} x - D & \text{for } x > D \\ 0 & \text{for } -D \leq x \leq D \\ x + D & \text{for } x < -D \end{cases} \tag{2.7}$$

The rolling bearing is composed of the inner ring, outer ring and rolling elements. Clearance exists between the inner ring and rolling elements or rolling elements and the outer ring. It is

one of the main nonlinear factors in the system, too. The bearing clearance functions can be drawn up as follows if the dimensionless bearing clearance is defined as $D_{bi} = \delta_{bi}/(2b)$ ($i = 1, 2$)

$$\begin{aligned} \bar{f}_{b1}(x_7) &= \begin{cases} x_7 - D_{b1} & \text{for } x_7 > D_{b1} \\ 0 & \text{for } -D_{b1} \leq x_7 \leq D_{b1} \\ x_7 + D_{b1} & \text{for } x_7 < -D_{b1} \end{cases} \\ \bar{f}_{b2}(x_9) &= \begin{cases} x_9 - D_{b2} & \text{for } x_9 > D_{b2} \\ 0 & \text{for } -D_{b2} \leq x_9 \leq D_{b2} \\ x_9 + D_{b2} & \text{for } x_9 < -D_{b2} \end{cases} \end{aligned} \tag{2.8}$$

3. Bifurcation and chaos of the system

A gearbox of a metro train is selected as the research object. The material of the gear is 40Cr. The related parameters of the gearbox are given in Table 1. The lengths of two shafts are 450 mm. The elastic modulus of the shafts is $2 \cdot 10^{11}$ Pa, the Poisson ratio is 0.3. Each shaft is supported by two bearings, 7306. The preload load of the bearing is 200 N. The torque is 150 N·m. The related parameters of bearings are given in Table 2. The calculated dimensionless parameters are given in Table 3. Other dimensionless coefficients of the time-varying stiffness can be calculated by computer programs according to the meshing parameters real-timely.

Table 1. Parameters of the baseline example gear pair

System parameters	Pinion	Gear	System parameters	Pinion	Gear
Number of teeth z	40	156	Radius of base circle r_b [mm]	56.4	219.9
Mass [kg]	1.82	2.63	Mass moment of inertia of gear [$\times 10^{-3}$ kg·m ²]	2.6	3.1
Module [mm]	3	3	Mass moment of inertia of rotor [$\times 10^{-3}$ kg·m ²]	3.4	2.8
Backlash [μ m]	100	100	Meshing damping ratio	0.1	0.1
Width of gear [mm]	52	48	Pressure angle α [°]	20	20

Table 2. Parameters of bearings

System parameters	Value	System parameters	Value
Inner radius [mm]	30	Race way curvity of inner ring	0.52
Outer radius [mm]	62	Race way curvity of outer ring	0.525
Radius of rolling [mm]	9.525	Radial clearance [μ m]	60
Number of rolling elements	11		

Table 3. Value of dimensionless parameters

Param.	Value	Param.	Value	Param.	Value	Param.	Value	Param.	Value
k_{11}	1.05	k_{33}	1.05	ξ_{11}	0.1	ξ_{32}	0.1	k_{52}	0.6
k_{12}	0.6	k_{31}	0.3	ξ_{12}	0.1	ξ_{31}	0.1	ξ_{52}	0.125
k_{21}	0.6	k_{41}	1.1	ξ_{22}	0.2	ξ_{41}	0.01	\bar{F}_{b2}	0.1
k_{23}	0.7	k_{42}	0.6	ξ_{21}	0.05	ξ_{42}	0.125	F_{ai}	0.1
k_{22}	0.8	k_{51}	1.1	ξ_{23}	0.05	ξ_{51}	0.01	F_{ml}	0.1
F_{mi}	0.05	\bar{F}_{b1}	0.1	F_{al}	0.2				

3.1. Effect of the mesh frequency

The bifurcation diagram of the relative displacement via the frequency, $\omega \in [0.5, 2.5]$ as $D = 1.0$ and $D_b = D_{b1} = D_{b2} = 0.6$ is illustrated in Fig. 2. The bifurcation and chaos of the system with the increasing frequency will be discussed in three regions precisely.

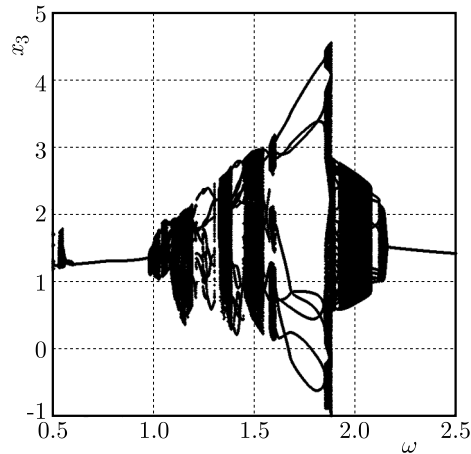


Fig. 2. Bifurcation diagram of the system via the mesh frequency

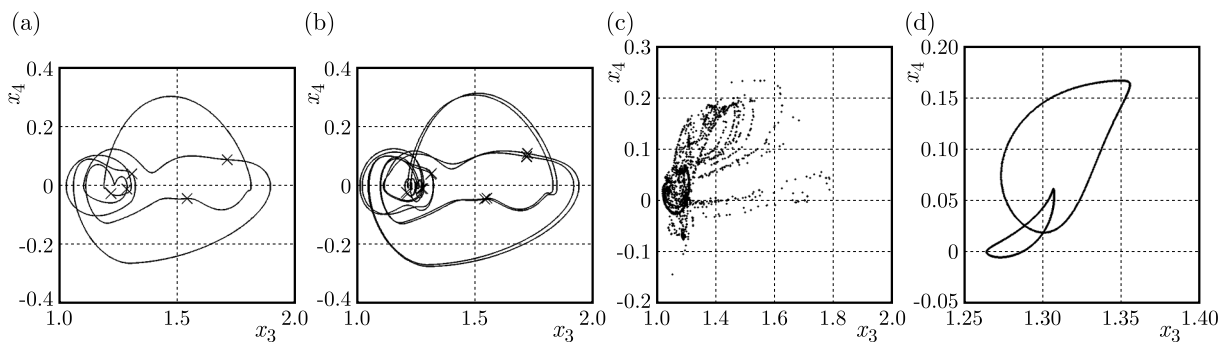


Fig. 3. Diagrams of Poincaré mapping and phase portraits: (a) $\omega = 0.5$, (b) $\omega = 0.502$, (c) $\omega = 0.545$, (d) $\omega = 0.56$. Here, the diagram of Poincaré mapping in *a* and *b* is represented by \times

Firstly, the bifurcation and chaos of the system as $\omega \in [0.5, 0.62]$ is studied. The motion of the system is stable period-5 motion as $\omega = 0.5$. The diagram of Poincaré mapping and phase portrait is illustrated in Fig. 3a as $\omega = 0.5$ and the diagram of Poincaré mapping is represented by \times . There are 5 discrete points in the diagram of Poincaré mapping. Doubling periodic bifurcation occurs and the period-5 motion doubles to period-10 motion when the frequency ω increases to $\omega = 0.501$. The diagram of Poincaré mapping and phase portrait is illustrated in Fig. 3b as $\omega = 0.502$. The period-10 degenerates to period-5 when the frequency ω increases to 0.503. The period-5 motion transits to period-1 motion when ω increases to 0.505. Doubling periodic bifurcation occurs with an increase in the mesh frequency and the period-1 motion doubles to stable period-2 motion as $\omega = 0.5125$. Saddle-node bifurcation leads the system to chaotic motion as $\omega = 0.5315$. The diagram of Poincaré mapping is illustrated in Fig. 3c as $\omega = 0.545$. The chaotic motion of the system exists in a small range and it evolves in quasi-periodic motion by Hopf bifurcation when ω increases to 0.556. A diagram of Poincaré mapping is presented in Fig. 3d. There are two closed tori in the diagram of Poincaré mapping. Inverse Hopf bifurcation occurs when ω increases to 0.565 and it leads the quasi-periodic motion to period-2 motion. Inverse-doubling periodic bifurcation leads the period-2 motion to period-1 motion when ω increases in 0.602. The period-1 motion exists in a considerable range of frequency.

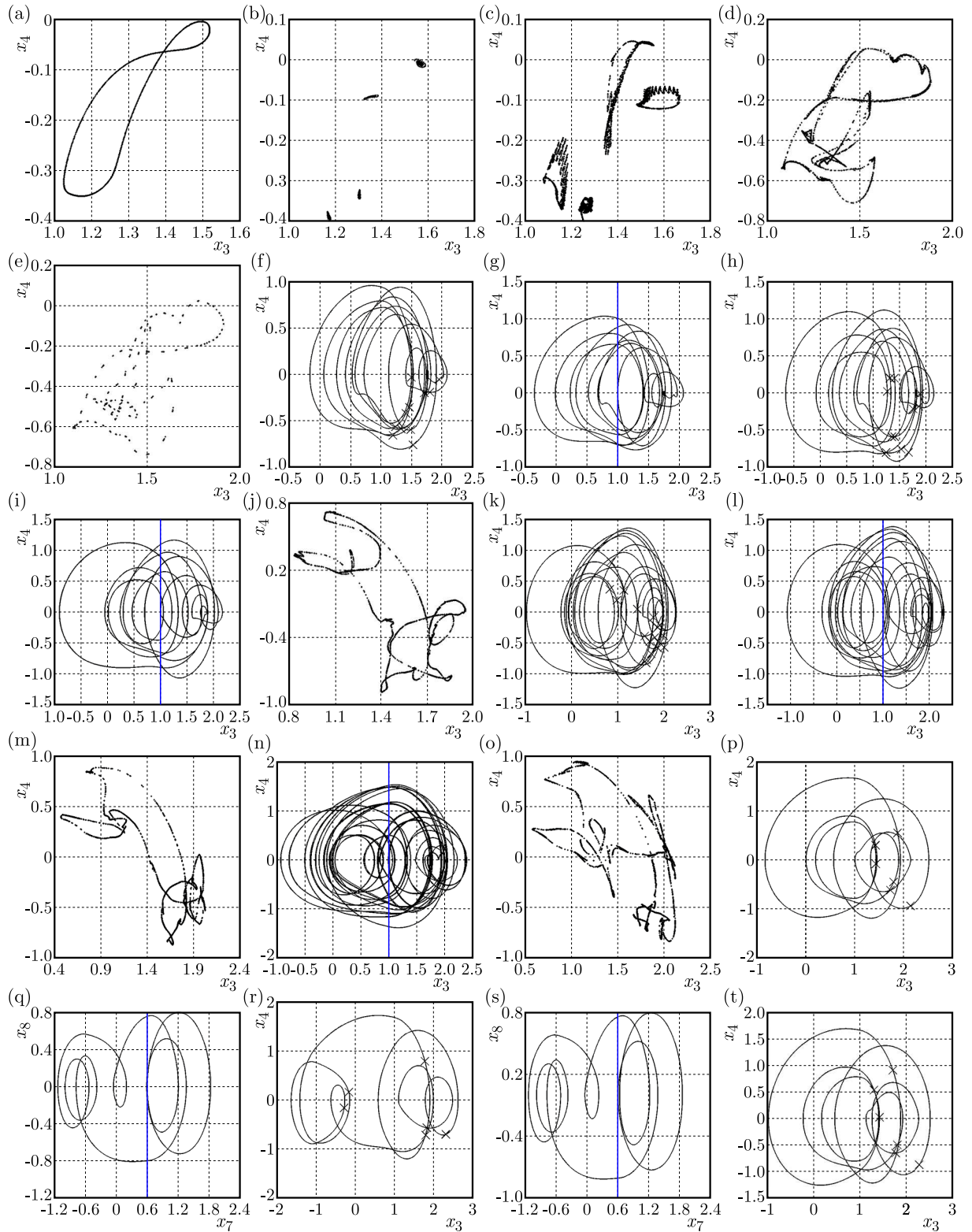


Fig. 4. Phase portraits and diagrams of Poincaré mapping: (a) $\omega = 0.99$, (b) $\omega = 1.004795$, (c) $\omega = 1.005$, (d) $\omega = 1.041$, (e) $\omega = 1.05$, (f) $\omega = 1.0625$, (g) $\omega = 1.06508242$, phase portrait, grazing at the gear surface; (h) $\omega = 1.08$, (i) $\omega = 1.09205$, phase portrait, grazing at the gear surface; (j) $\omega = 1.1$, (k) $\omega = 1.13$, (l) $\omega = 1.1332$, phase portrait, grazing at the gear surface; (m) $\omega = 1.135$, (n) $\omega = 1.1675$, phase portrait, grazing at the gear surface; (o) $\omega = 1.18$, (p) $\omega = 1.2$, (q) $\omega = 1.2087$, phase portrait, grazing at the bearing surface; (r) $\omega = 1.21$, (s) $\omega = 1.213$, phase portrait, grazing at the bearing surface; (t) $\omega = 1.22$. Here, the diagram of Poincaré mapping in the phase portrait is represented by \times and the blue line represents the grazing boundary

Secondly, the bifurcation and chaos of the system as $\omega \in [0.9, 1.3]$ is discussed. The motion of the system is a stable period-1 motion as $\omega < 0.9747$. Hopf bifurcation occurs when the frequency increases to $\omega = 0.9747$ and it leads the period-1 motion to quasi-periodic motion. Diagram of Poincaré mapping is illustrated in Fig. 4a as $\omega = 0.99$. There is a closed torus in it. The quasi-periodic motion transients to 4 saddle-nodes and they transform to chaos quickly. Diagrams of Poincaré mapping is illustrated in Fig. 4b and Fig. 4c as $\omega = 1.004795$ and $\omega = 1.005$. The chaos transients into the period-4 motion when the frequency increases to $\omega = 1.017$. Saddle-node bifurcation leads the period-4 motion to chaos when the frequency increases to $\omega = 1.040798$. The diagram of Poincaré mapping is illustrated in Fig. 4d as $\omega = 1.041$. Phase lock occurs when the frequency increases to $\omega = 1.0495$ and the diagram of Poincaré mapping is illustrated in Fig. 4e as $\omega = 1.05$. The phase lock transients into period-11 motion when the frequency increases to $\omega = 1.0623$. The phase portrait and diagram of Poincaré mapping is illustrated in Fig. 4f as $\omega = 1.0625$ and the diagram of Poincaré mapping is represented by \times . The phase trajectory of the system is tangent to the boundary $x_3 = 1.0$. It implies the grazing occurred in the tooth surface as $\omega = 1.06508242$ and its phase portrait is illustrated in Fig. 4g. The phase portrait and diagram of Poincaré mapping is illustrated in Fig. 4h as $\omega = 1.08$ after the tooth surface grazing. The number of the periodic motion is not changed but the phase trajectory is changed by the grazing. The phase portraits and diagrams of Poincaré mapping before and after the grazing are shown in Fig. 4f and Fig. 4h. The grazing occurs in the tooth surface again when the frequency increases to $\omega = 1.09205$ and it leads the periodic motion to chaos. The phase portrait of the grazing is illustrated in Fig. 4i. The diagram of Poincaré mapping of the chaos is illustrated in Fig. 4j as $\omega = 1.1$ after the tooth surface grazing. The chaotic motion changes to period-17 motion by phase lock when the frequency increases to $\omega = 1.1255$. The phase portrait and diagram of Poincaré mapping is illustrated in Fig. 4k as $\omega = 1.13$, and there are 17 discrete points in the diagram of Poincaré mapping. The grazing in the tooth surface leads the periodic motion to chaos when the frequency increases to $\omega = 1.1332$, and the phase portrait of the grazing is illustrated in Fig. 4l. The diagram of Poincaré mapping of the chaotic motion is illustrated in Fig. 4m as $\omega = 1.135$ after the tooth surface grazing. The motion of the system goes to period-23 motion when the frequency increases to $\omega = 1.154$. The periodic motion exists in a narrow region only. The grazing occurs in the tooth surface again when the frequency increases to $\omega = 1.1657$ and it leads the periodic motion to chaotic motion. The phase portrait of the grazing is illustrated in Fig. 4n. The diagram of Poincaré mapping of the chaotic motion is illustrated in Fig. 4o as $\omega = 1.18$ after the tooth surface grazing. The chaos transients to period-6 motion when the frequency increases to $\omega = 1.1927$. The phase portrait and diagram of Poincaré mapping is illustrated in Fig. 4p as $\omega = 1.2$, and there are 6 discrete points in the diagram of Poincaré mapping. The grazing occurs in the bearing and it leads the phase trajectory of the period-6 motion change when the frequency increases to $\omega = 1.2087$. The phase portrait of the grazing of the bearing is illustrated in Fig. 4q, and the clearance of the bearing is $D_b = 0.6$. The phase portrait and diagram of Poincaré mapping after bearing grazing is illustrated in Fig. 4r as $\omega = 1.21$. The number of the periodic motion of the system is not changed but the topological shape of the motion is changed by the grazing in the bearing. Grazing occurs in the bearing when the frequency increases to $\omega = 1.213$ again, and the phase portrait is illustrated in Fig. 4s. The period-6 motion trajectory is changed by the bearing grazing again. The phase portrait and diagram of Poincaré mapping after bearing grazing is illustrated in Fig. 4t as $\omega = 1.22$. A conclusion can be drawn that the bearing grazing leads the phase trajectory of the system change but it can not change the number of the system motion. Period-doubling bifurcation occurs when the frequency increases to $\omega = 1.25$ and it leads the period-6 motion to period-12 motion. Inverse period-doubling bifurcation occurs when the frequency increases to $\omega = 1.2645$ and the period-12 motion transients into period-6 motion.

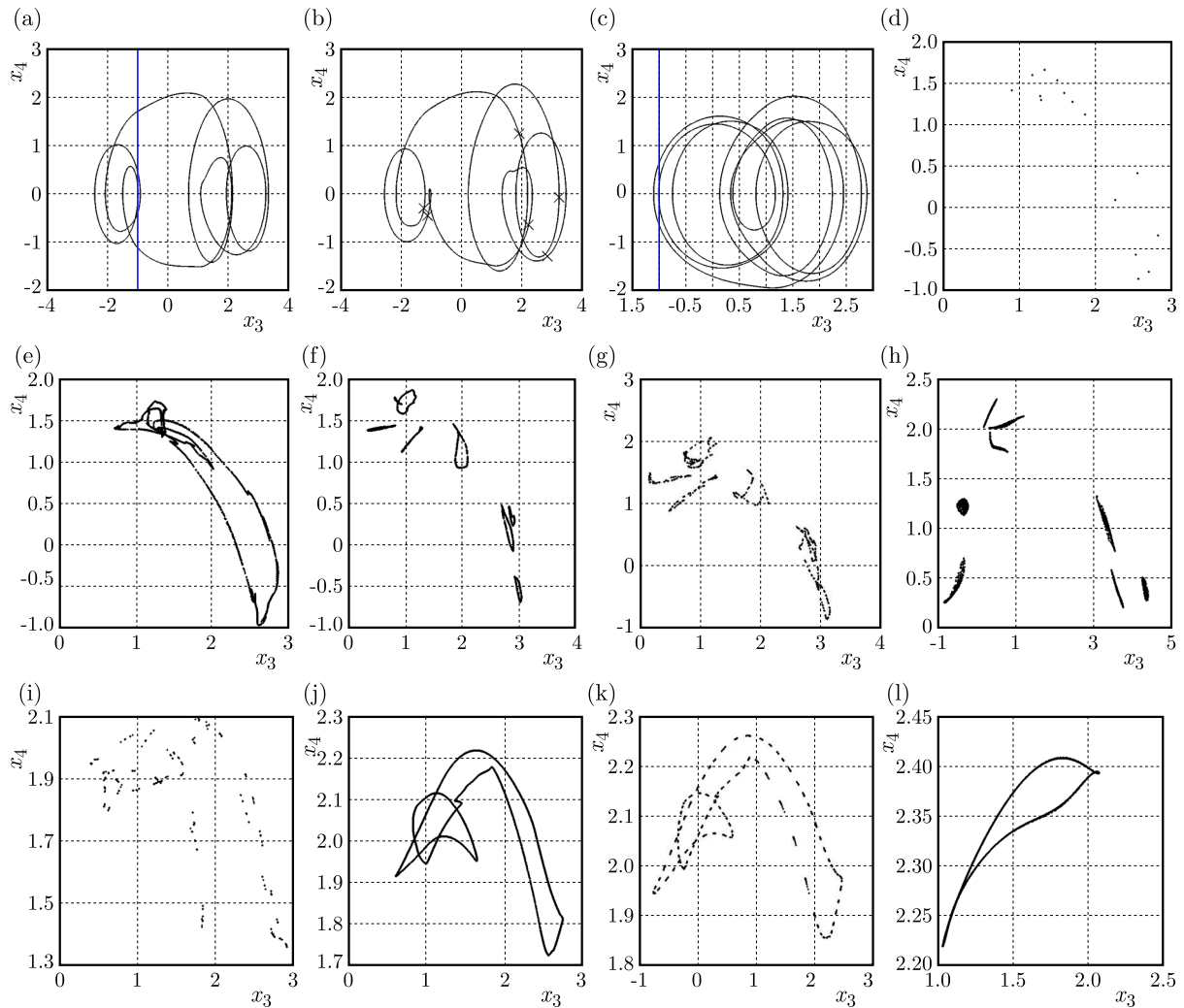


Fig. 5. Phase portraits and diagrams of Poincaré mapping: (a) $\omega = 1.3607$, phase portrait, grazing at the tooth back; (b) $\omega = 1.38$, (c) $\omega = 1.443$, phase portrait, grazing at the tooth back; (d) $\omega = 1.45$, (e) $\omega = 1.46$, (f) $\omega = 1.575$, (g) $\omega = 1.59$, (h) $\omega = 1.845$, (i) $\omega = 1.85$, (j) $\omega = 1.94$, (k) $\omega = 1.98$, (l) $\omega = 2.14$. Herein, the diagram of Poincaré mapping in the phase portrait is represented by \times and the blue line represents the grazing boundary

Finally, the bifurcation and chaos of the system as $\omega \in [1.3, 2.5]$ is studied. The motion of the system is stable period-6 as $1.2645 < \omega < 1.3607$. Grazing occurs at the tooth back and the phase trajectory of the system is changed. The phase portrait of the tooth back grazing is shown in Fig. 5a. The diagram of Poincaré mapping and phase portrait after tooth back grazing is illustrated in Fig. 5b as $\omega = 1.38$. The phase trajectory is changed and the number of periodic motion is not changed comparing Fig. 5b to Fig. 4t by the tooth back grazing. Grazing occurs at the tooth back again when the frequency increases to $\omega = 1.443$ and the period-6 motion evolves into period-15 motion. The phase portrait of the tooth back grazing is shown in Fig. 5c as $\omega = 1.443$. The diagram of Poincaré mapping after the tooth back grazing is illustrated in Fig. 5d as $\omega = 1.45$. The period-15 motion evolves into chaotic motion by saddle-node bifurcation when the frequency increases to $\omega = 1.4521$ and the diagram of Poincaré mapping is illustrated in Fig. 5e as $\omega = 1.46$. Saddle-node bifurcation occurs when the frequency increases to $\omega = 1.5412$ and it changes the chaotic motion into period-8 motion. Hopf bifurcation occurs when the frequency increases to $\omega = 1.5697$ and the period-8 motion degenerates to quasi-periodic motion. The diagram of Poincaré mapping is illustrated in Fig. 5f as $\omega = 1.575$. There are 8 closed tori in the figure. The torus loses its smoothness and breaks with the increasing

frequency gradually, and the quasi-periodic motion degenerates to phase lock when the frequency increases to $\omega = 1.583$. The diagram of Poincaré mapping is illustrated in Fig. 5g as $\omega = 1.59$. The phase lock degenerates to the period-8 motion when the frequency increases to $\omega = 1.6016$. The period-8 motion goes to chaotic motion by period-doubling bifurcation with an increase in the frequency. The diagram of Poincaré mapping is illustrated in Fig. 5h as $\omega = 1.845$. The phase lock appears again when the frequency increases to $\omega = 1.85$. The diagram of Poincaré mapping is illustrated in Fig. 5i as $\omega = 1.85$ and it degenerates to period-28 motion when the frequency increases to $\omega = 1.889$. Hopf bifurcation occurs when the frequency increases to $\omega = 1.921$ and it leads the period-28 motion to a quasi-periodic motion. The diagram of Poincaré mapping is illustrated in Fig. 5j as $\omega = 1.94$. There are 2 closed tori in the figure. The stability of the quasi-periodic motion is lost with an increase in the frequency, and the phase lock appears when the frequency increases to $\omega = 1.976$. The diagram of Poincaré mapping is illustrated in Fig. 5k as $\omega = 1.98$. The phase lock evolves into period-8 motion when the frequency increases to $\omega = 2.0799$. Hopf bifurcation occurs when the frequency increases to $\omega = 2.12$ and it leads the period-8 motion to quasi-periodic motion again. The diagram of Poincaré mapping is illustrated in Fig. 5l as $\omega = 2.14$. There is a closed torus in the figure. Inverse-Hopf bifurcation occurs when the frequency increases to $\omega = 2.1587$ and the quasi-periodic motion degenerates to stable period-1 motion. The period-1 motion exists in a wide region.

The system exhibits complicate dynamical characteristics with an increase in the frequency as above all. Saddle-node bifurcation, Hopf bifurcation, inverse-Hopf bifurcation, period-doubling bifurcation, grazing and so on take place in the process of change of the frequency. Grazing occurs in many areas such as the tooth surface, tooth back and the bearing. The phase trajectory of the system is changed but the number of periodic motion is not changed by the bearing grazing. Not only the phase trajectory but also the number of the periodic motion is changed by grazing at the tooth surface and the tooth back, probably. The gear-rotor-bearing system is a multi-clearance nonlinear system. Clearances exist in the tooth back and the contact surface of the bearing. This may lead to grazing motion in different regions. But the stable simplicity periodic motion can be found in the gear-rotor-bearing system according to the above analysis when the frequency is taken to a reasonable value. The motion of the system remains stable period-1 motion when the frequency is in the range of $\omega \in [0.602, 0.9747]$ and $\omega > 2.1587$.

3.2. Effect of the time-varying stiffness

The bifurcation diagram of the relative displacement via the amplitude of the time-varying stiffness k is illustrated in Fig. 6 when the values of dimensionless parameters are taken from Table 3 and $\omega = 1.05$. The motion of the system is a long-periodic motion when the amplitude of the time-varying stiffness is $k < 0.1032$ as shown in Fig. 6. The long-periodic motion evolves into quasi-periodic motion by Hopf bifurcation when the amplitude of the time-varying stiffness is $k = 0.1032$. The quasi-periodic motion degenerates to long-periodic motion again when the amplitude of the time-varying stiffness increases to $k = 0.1173$. The long-periodic motion degenerates to quasi-periodic motion by Hopf bifurcation again when the amplitude of the time-varying stiffness increases to $k = 0.1332$. Two tori in these two quasi-periodic motions are irregular and the irregularity leads the quasi-periodic motion unstable. The motion of the system shocks between the long-periodic motion and the quasi-periodic motion when the amplitude of the time-varying stiffness k exists in the range of $[0.1332, 0.2556]$. The motion of the system moves to period-10 motion by inverse-Hopf bifurcation as $k = 0.2556$. The phase portrait and diagram of Poincaré mapping are illustrated in Fig. 7a as $k = 0.26$. There are 10 discrete points, which implies that the motion of the system is stable period-10 motion. Grazing occurs in two bearings and it makes the phase trajectory of the system change. Phase portraits of the grazing are illustrated in Fig. 7b and Fig. 7c. The phase portrait and diagram of Poincaré mapping after

grazing is illustrated in Fig. 7d as $k = 0.28$. The periodic motion trajectory is changed slightly but the motion property is not changed by the grazing comparing Fig. 7a to Fig. 7d. It is said that the grazing of the bearing makes the motion trajectory change only. Grazing occurs in the reverse direction of two bearings simultaneously. It implies that grazing is caused by the lean of the shaft in the meshing process, probably. The motion of the system is possibly changed by the assemblment precision of the gear system and the lean of the shaft in the movement. The high assemblment precision of the gear system is used to obtain high movement stability in the meshing in practical engineering.

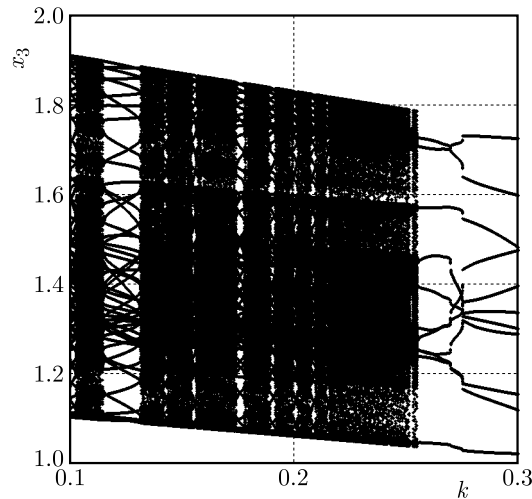


Fig. 6. Bifurcation diagram of system via the amplitude of the time-varying stiffness

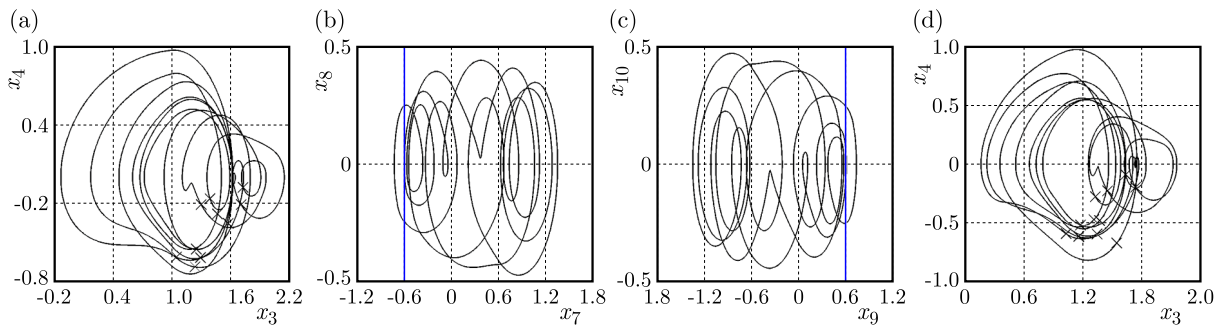


Fig. 7. Phase portraits and diagrams of Poincaré mapping: (a) $k = 0.26$, (b) $k = 0.272$, phase portrait, grazing in the bearing; (c) $k = 0.272$, phase portrait, grazing in the bearing; (d) $k = 0.26$. Here, the diagram of Poincaré mapping is represented by \times and the blue line represents the grazing boundary

The motion of the system exhibits nonlinear characteristics when the stiffness is small but a stable periodic motion can be obtained as the stiffness is large when other parameters are the same. The quench is used to improve the meshing stiffness. High meshing stiffness is used to obtain stable periodic motion in practical engineering.

3.3. Effect of the bearing clearance

The bearing clearance D_b has an essential influence on the dynamical behavior of the gear-rotor-bearing system. The bifurcation diagrams of the relative displacement via the bearing clearance D_b are illustrated in Fig. 8 when the values of dimensionless parameters are taken from Table 3 and $\omega = 1.05$. Figure 8a is the bifurcation diagram of the system for the increasing bearing clearance and Fig. 8b is the bifurcation diagram of the system for the decreasing bearing clearance.

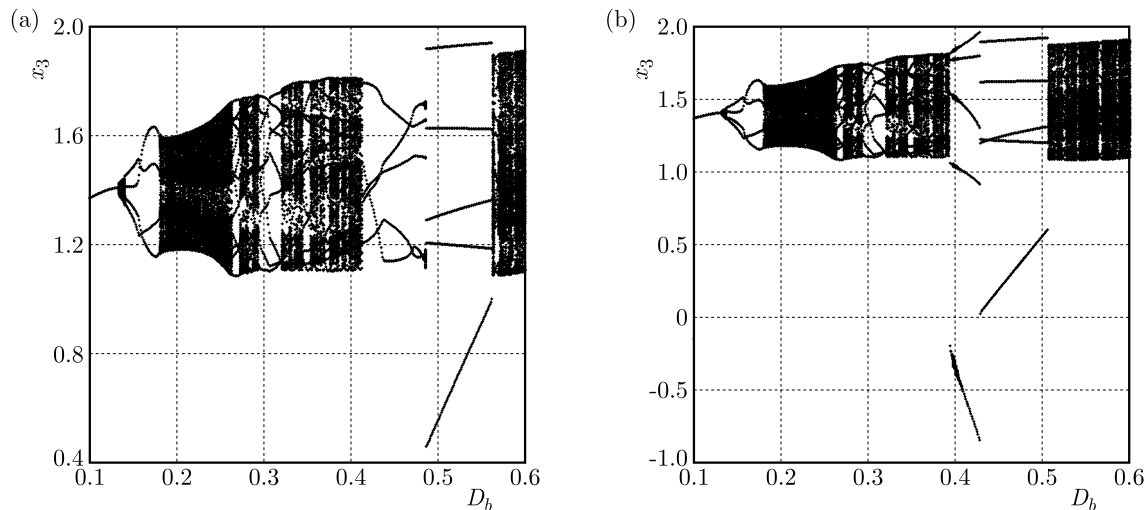


Fig. 8. Bifurcation diagrams of system via the bearing clearance, $D_b = [0.1, 0.6]$: (a) with the increasing of the bearing clearance; (b) with the decreasing of the bearing clearance

The motion of the system is stable period-1 when the bearing clearance is lower than 0.132 as shown in Fig. 8a. Hopf bifurcation leads the period-1 motion to quasi-periodic motion when the bearing clearance increases to $D_b = 0.132$. It is a closed limit torus in the diagram of Poincaré mapping. The smoothing of the limit torus loses gradually, the distortion and breakage occur. The motion of the system evolves into period-4 motion when the bearing clearance increases. The period-4 motion evolves into quasi-periodic motion by Hopf bifurcation when the bearing clearance increases to $D_b = 0.1815$. It is an irregular closed limit torus. The irregularity of the closed limit torus directs the motion of the system unstable. The motion of the system shocks between the periodic motion and quasi-periodic motion in the region of $D_b \in [0.23, 0.295]$. The quasi-periodic motion evolves into period-13 motion when the bearing clearance increases to $D_b = 0.261$. The period-13 motion changes to quasi-periodic motion when the bearing clearance increases to $D_b = 0.272$. The quasi-periodic motion evolves into period-9 motion when the bearing clearance increases to $D_b = 0.294$. The motion of the system shocks between the periodic motion and quasi-periodic motion in the region of $D_b \in [0.321, 0.413]$. The motion of the system evolves into period-5 motion by the phase lock when the bearing clearance is greater than 0.413. The periodic motion evolves into quasi-periodic motion when the bearing clearance increases to $D_b = 0.4798$ but it exists in a narrow region. It degenerates to period-5 motion again when the bearing clearance increases to $D_b = 0.484$. The phase lock occurs again when the bearing clearance increases to $D_b = 0.5618$.

There is a coexistence of attractors in the region of $D_b \in [0.3935, 0.5612]$ according to Fig. 8. The diagrams of Poincaré mapping are shown in Fig. 9 for $D_b = 0.4, 0.44, 0.5, 0.52$, respectively. Different colors represent different attractors of the coexistence. The red one represents the attractor with the increasing bearing clearance and the black one represents the attractor with the decreasing bearing clearance. The coexistence of attractors for periodic motion and phase lock, periodic motion and quasi-periodic motion, periodic motion and periodic motion and so on in the region is discovered.

The bearing clearance affects the nonlinear dynamic behavior of the system. The motion of the system is stable when the value of the bearing clearance is small, and it is complicated when the clearance is big according to the analysis above. The motion of the system is stable period-1 motion when the bearing clearance is less than 0.12. The motion of the system is stable periodic motion but there is coexistence of attractors when the bearing clearance is in the region of $D_b \in [0.41, 0.5]$. This coexistence means strong nonlinear characteristics because the motion

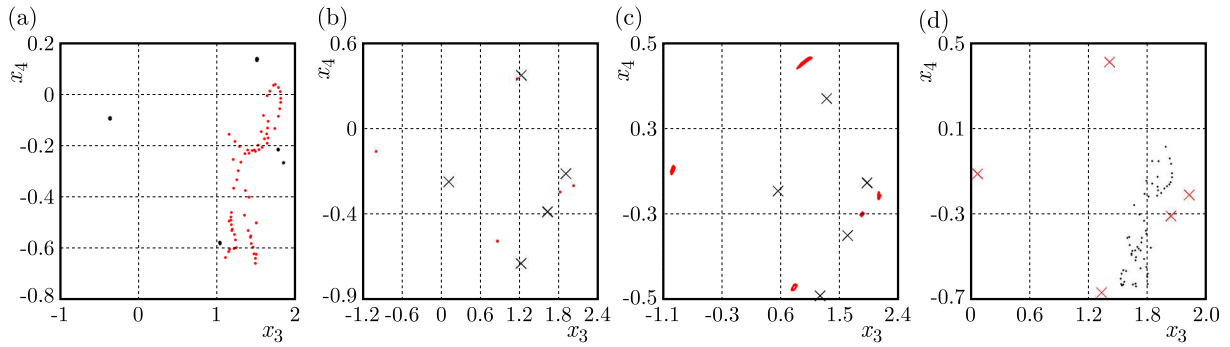


Fig. 9. Diagrams of Poincaré mapping: (a) $D_b = 0.4$, (b) $D_b = 0.44$, (c) $D_b = 0.5$, (d) $D_b = 0.52$. Here, red color represents the diagram of Poincaré mapping with the increasing bearing clearance and black color represents the one with the decreasing bearing clearance

form will change with a change in the initial value. A small value of the bearing clearance should be selected to obtain stable motion of the gear system. The bearing clearance should be selected as 40%-50% of the backlash if the small bearing clearance can not be obtain by manufacturing precision. Noise and vibration increase when the degree of wear reaches a certain degree in engineering practice. Big bearing clearance causes strong impact and vibration because of wear of rolling elements. So a small bearing clearance should be selected and the worn bearing should be replaced to decrease the impact and vibration and increase the stability of the system.

3.4. Effect of the comprehensive transmission error and backlash

The bifurcation diagrams of the relative displacement versus the amplitude of the comprehensive transmission error ε are illustrated in Fig. 10a. The values of dimensionless parameters are taken from Table 3 and $\omega = 1.05$. The motion of the system is stable period-5 when the amplitude of the comprehensive transmission error is less than 0.7316 as shown in Fig. 10a. There are 5 discrete points in the diagram of Poincaré mapping. The periodic motion evolves

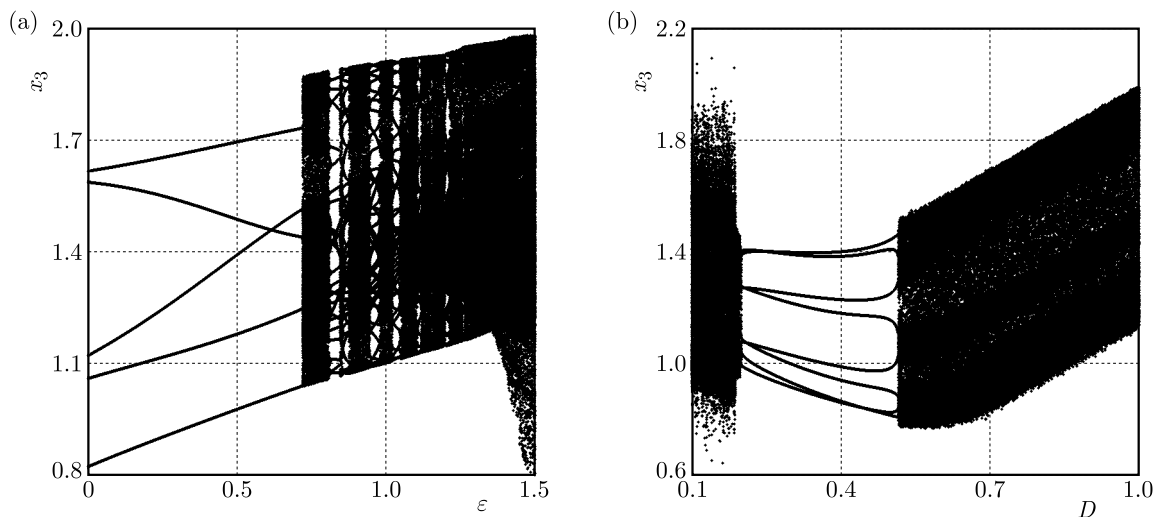


Fig. 10. Bifurcation diagrams of the system: (a) vs. the transmission error, (b) vs. backlash

into chaotic motion when the amplitude of the comprehensive transmission error increases to $\varepsilon = 0.7316$. The motion of the system shocks between the long-periodic motion and chaotic motion with the increasing amplitude of the comprehensive transmission error. The region of the long-periodic motion becomes narrow and the region of the chaotic motion becomes wide

with a gradual increase in the amplitude of the comprehensive transmission error. The motion of the system is chaotic in this region. The morphology of the chaotic motion change when the amplitude of the comprehensive transmission error increases to $\varepsilon = 1.4108$.

The motion of the system becomes instable with an increase in the amplitude of error (comprehensive transmission error of the system). Chaotic motion, shock of chaotic motion and periodic motion occur with an increase in the amplitude of the error, and the instability of the system becomes worse. The motion of the system preserves stable when the value of the amplitude of the error is low. So the manufacturing and assemblment precision of the gear should be improved to obtain stability of the system.

The bifurcation diagram of the relative displacement versus the backlash D is illustrated in Fig. 10b. The motion of the system is period-8 when the backlash is in the region of $D \in [0.2004, 0.5154]$. There are 8 discrete points. The motion of the system is chaotic when the backlash is less than 0.2004 and greater than 0.5154. Backlash is an important factor to lead the motion of the system to chaos. Chaos is caused by rattling when the backlash is small, and it is caused by impact when the backlash is big. So a reasonable backlash must be selected to improve the stability of the gear system.

4. Conclusion

A nonlinear dynamic model of a gear-rotor-bearing system is established when the time-varying stiffness, tooth surface friction, backlash, bearing clearance and the comprehensive transmission error are considered. The effects of frequency, backlash, bearing clearance, comprehensive transmission error and stiffness on dynamic characteristics of the system are analyzed. Some conclusions can be drawn according to the analysis.

Firstly, there are some complicated nonlinear phenomena such as grazing bifurcation, quasi-periodic bifurcation, chaos and coexistence of attractors in the system. Stable periodic motion can be obtained by low backlash, bearing clearance, comprehensive transmission error, high manufacturing and assemblment precision of the gear and mesh stiffness.

Secondly, the phase trajectory and the number of periodic motion can be changed by the grazing at the tooth surface and the tooth back. Different kinds of grazing motions may be produced by clearances existing in the gear back and the contact surface of the bearing. But a stable periodic motion can be obtained when the frequency is taken to a reasonable value.

Finally, the phase trajectory of the system should be changed but the number of the periodic motion can not be changed by the bearing grazing. A small value of the bearing clearance should be selected to obtain stable motion of the gear system. Sometimes, grazing occurs in the reverse direction of two bearings simultaneously. This means that the grazing is caused by the lean of the shaft in the meshing process. The motion of the system is changed by the assemblment precision of the gear system and the lean of the shaft in the movement. High assemblment precision of the gear system should be secured to obtain high movement stability of the meshing in the engineering practice.

Acknowledgments

This work was financially supported by the National Natural Science Foundation of China (grant No. 51365025), by Natural Science Key Foundation of Tianjin, China (grant No. 16JCZDJC38500) and by the Natural Science Foundation of Tianjin, China (grant No. 17JCQNJC04300).

References

1. CHANG-JIAN C.J., 2010a, Non-linear dynamic analysis of a HSFDF mounted gear-bearing system, *Nonlinear Dynamics*, **62**, 333-347

2. CHANG-JIAN C.J., 2010b, Strong nonlinearity analysis for gear-bearing system under nonlinear suspension – bifurcation and chaos, *Nonlinear Analysis: Real World Applications*, **11**, 1760-1774
3. CHANG-JIAN C.J., CHANG S.M., 2012a, Bifurcation and chaos analysis of the porous squeeze film damper mounted gear-bearing system, *Computers and Mathematics with Applications*, **64**, 5, 798-812
4. CHANG-JIAN C.J., CHANG S.M., 2012b, Chaotic responses on gear pair system equipped with journal bearings under turbulent flow, *Applied Mathematical Modelling*, **36**, 6, 2600-2613
5. CHEN S.Y., TANG J.Y., LUO C.W., 2011, Nonlinear dynamic characteristics of geared rotor bearing systems with dynamic backlash and friction, *Mechanism and Machine Theory*, **46**, 4, 466-478
6. CHOI S.T., MAU S.Y., 2001, Dynamic analysis of geared rotor-bearing systems by the transfer matrix method, *Journal of Mechanical Design*, **123**, 562-579
7. CUI Y.H., LIU Z.S., WANG Y.L., 2012, Nonlinear dynamic of a geared rotor system with nonlinear oil film force and nonlinear mesh force, *Journal of Vibration and Acoustics, Transactions of the ASME*, **134**, 4, 1313-1320
8. KAHRAMAN A., SINGH R., 1990, Non-linear dynamics of a spur gear pair, *Journal of Sound and Vibration*, **142**, 1, 49-75
9. KAHRAMAN A., SINGH R., 1991, Non-linear dynamics of a geared rotor-bearing system with multiple clearances, *Journal of Sound and Vibration*, **144**, 3, 135-156
10. RANGHOTHAMA A., NARAYANAN S., 1999, Bifurcation and chaos in geared rotor bearing system by incremental harmonic balance method, *Journal of Sound and Vibration*, **226**, 3, 469-492
11. THEODOSSIADES S., NATSIAVAS S., 2001, On geared rotor dynamic systems with oil journal bearings, *Journal of Sound and Vibration*, **243**, 4, 721-745
12. XIANG L., JIA Y., HU A., 2016, Bifurcation and chaos analysis for multi-freedom gear-bearing system with time-varying stiffness, *Applied Mathematical Modelling*, **40**, 10506-10520

Manuscript received December 25, 2016; accepted for print September 23, 2017

COARSE-GRAINING MODELS FOR MOLECULAR DYNAMICS SIMULATIONS OF FCC METALS

POURYA DELAFROUZ, HOSSEIN NEJAT PISHKENARI

Department of Mechanical Engineering, Sharif University of Technology, Tehran, Islamic Republic of Iran
e-mail: nejat@sharif.edu

In this paper, four coarse-graining (CG) models are proposed to accelerate molecular dynamics simulations of FCC metals. To this aim, at first, a proper map between beads of the CG models and atoms of the all-atom (AA) system is assigned, afterwards mass of the beads and the parameters of the CG models are determined in a manner that the CG models and the original all-atom model have the same physical properties. To evaluate and compare precision of these four CG models, different static and dynamic simulations are conducted. The results show that these CG models are at least 4 times faster than the AA model, while their errors are less than 1 percent.

Keywords: accelerated molecular dynamics, coarse-grain models, FCC metals, EAM potential

1. Introduction

One of the important challenges of working at the nanoscale is to analyze materials properties. Because experimental researches in characterization and analysis of materials characteristics at nano-scale are significantly expensive, improvement of theoretical modeling methods is an in-progress research field. Also, there are some important subjects which experimental setups and techniques cannot capture. On the other hand, it seems necessary to assess the system behavior and amend the experimental setup based on the results of modeling and simulation techniques before any practical attempt. Consequently, computational modelling techniques, with their great potential to model and predict atomic features of nano-structures, entice the interest of many researchers in nanotechnology. The necessity for this predictive capability has empowered computational modeling and simulation methods to become an important component for inspecting phenomena in different nano-scale engineering applications. The most popular computational methods used in simulations at micro and nano scales are classic and non-classic continuum theories (Chandramouli, 2014), molecular dynamics (MD) (Leach, 2001; Muc, 2011) and Monte-Carlo (Berg, 2005; Samani and Pourtakdoust, 2014). Molecular dynamics (MD) is a powerful technique in the computational study of nano-scale structures and processes, which can provide data on the time dependent performance of a molecular system.

Augmented by quantum mechanical computations of interatomic potentials that explain the interaction of atoms, molecular dynamics can model behavior of a variety of materials with all-atom detail. However, the all-atom (AA) molecular dynamics method is not able to model many phenomena because it is practically limited to system sizes less than a few tens of nanometers and simulation times less than a few hundreds of nanoseconds (Chen *et al.*, 2011). These restrictions have attracted a lot of attention in the development of techniques to accelerate molecular dynamics simulations. To accelerate long-time molecular simulations, different methods including increasing the integration time step, reducing the computational cost per step, or combinations of these methodologies have been developed (Poursina and Anderson, 2014). These improvements may be achieved through clustering atoms to make a larger rigid

bead or by employing continuum theories in combination with atomistic modeling. Totally, there are two main schemes for accelerating molecular dynamics simulations: multi-scale modeling (Cranford and Buchler, 2010; Park and Klein, 2007; Jovanovic and Filipovic, 2006) and coarse-graining (CG) methods (Ouldridge, 2012; Yang and Ou, 2014; Hedrich and Hedrich, 2010).

As noted by Yang and To (2015), numerous multiscale techniques have been proposed to achieve the accuracy of full atomistic simulations with a reduced computational cost (Tadmor *et al.*, 2013; Burbery *et al.*, 2017). These methods couple atomistic and continuum models to link different spatial and time scales from nanometer and femtosecond to meter and second (Paćko and Uhl, 2011; Karma and Tournet, 2016).

FCC metals are commonly used in MEMs/NEMs systems as a main material. Although there exists a lot of researches employing the molecular dynamics technique for the modeling of FCC metals (Pishkenari and Meghdari, 2010; Lao *et al.*, 2013; Pishkenari, 2015), faster techniques with enough accuracy are highly demanded for modeling these metals (Park and Klein, 2007; Oren *et al.*, 2016).

In this paper, we have proposed four effective CG models based on the first technique introduced in the previous paragraph, for simulation of FCC metals. To this aim, at first, the proper atomic structure is defined and based on this new atomic structure, mass of the beads is determined. Then, the potential parameters are determined in a manner that the original model and the coarse-grained models have the same physical properties like cohesive energy, bulk modulus and elastic constants. After developing CG models, the bulk properties of an FCC metal such as elastic constants, bulk modulus and potential energy are determined and compared with the results of the AA model. As a case-study, to show the speed and accuracy of the developed coarse-graining models in prediction of mechanical properties of nano-scale systems, we have studied longitudinal and transversal vibrations of nanowires. The results demonstrate that the error of the CG models is reduced when the surface effects decrease.

The main goal of this paper is introduction of a novel coarse-grain model in order to accelerate the molecular dynamics simulations. The way of implementing these methods for modeling of nanowires are as same as using the molecular dynamics method with few changes. Owing to decreasing the number of beads in these methods, nanowires of larger size can be modeled with better accuracy compared to the Finite Element model. As an example, the error of calculating the natural transversal frequency among the all-atom model and one of the CG model is less than 0.6 percent for a nanowire with 65.28 nm length and 13.056 nm thickness while it is 4 times faster. Hence, these CG models are faster than the Molecular Dynamics method and more accurate than the Finite Element method. The rest of the paper is organized as follows. In Section 2, four CG models for analyzing FCC metals are introduced. In that Section, proper mapping, mass of beads and potential parameters are developed. In Section 3, size-dependency of the proposed models is investigated by various static and dynamic simulations. The last Section is devoted to concluding remarks.

2. Proposed CG method

The term “coarse graining” is used for methods based on replacing some atoms with one bead in order to reduce the number of degrees of freedom. Since the number of degrees of freedom in a CG model is significantly lower than in the main atomic system, simulation of the CG system needs considerably less computational resources; consequently, the simulation time and the system size can be substantially decreased (Cascella and Dal Peraro, 2009; Marrink *et al.*, 2007).

To develop a CG model for analyzing FCC metals, three steps must be done. At first, the location of the beads must be assigned. After choosing a proper atomic structure, the mass of the beads is specified and, finally, inter-atomic potential parameters are determined.

2.1. Mapping

One way to arrange the locations of beads is to choose an FCC crystalline structure as the CG model having a different lattice constant in comparison with the main atomic structure. In this way, a new FCC metal is made of the representative beads. Herein, the lattice constant of the CG model is set as twice of the lattice constant of the AA model, i.e. $a_{CG} = 2a_{AA}$, where a_{AA} and a_{CG} are respectively the lattice constants of the AA and CG models. Figure 1 shows this mapping for a cubic structure with an edge of $2a_{AA}$.

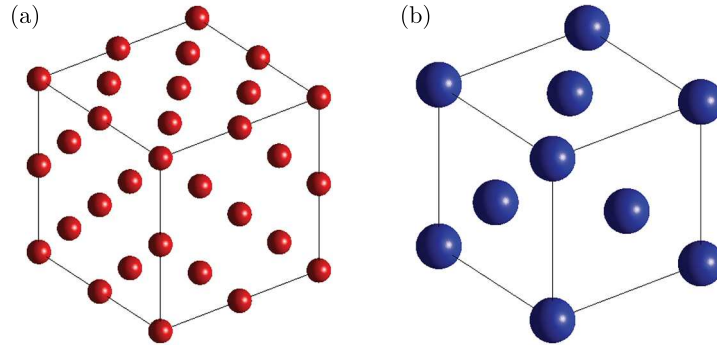


Fig. 1. 3-D display of (a) the AA model and (b) the CG model

The number of the beads in the resultant CG structure is about one-eighth of the number of atoms in the original structure. It should be mentioned that all of the four CG models have the same arrangement of the beads. After introducing the proposed mapping, the mass of the beads must be specified.

2.2. Mass of beads

By calculating contributions of each atom to the assigned beads, the mass of the beads can be determined. At first, we describe how the mass of the internal beads, named as bulk beads, can be calculated. Based on the structure of the CG and AA models, there is an atom that is in the same place where the bead is and its entire mass contributes to the corresponding bead. There are also 12 atoms surrounding the bead with a distance $(\sqrt{2}/2)a_{AA}$ from the bead and being shared with another bead equally. Also, there are 6 atoms with distance a_{AA} from the bulk bead each of which are shared among 6 beads. Consequently, the mass of the bulk bead can be calculated as below

$$M_{bulk} = \left(1 + 12 \cdot \frac{1}{2} + 6 \cdot \frac{1}{6}\right) m_{atom} = 8m_{atom} \quad (2.1)$$

where m_{atom} is the atomic mass of the FCC material. In addition to bulk beads, there are other new beads including surface beads, edge beads and corner beads.

For the surface beads, there is an atom at the same place where the bead is. There are 8 atoms at the distance $(\sqrt{2}/2)a_{AA}$ from the surface bead each of which is shared between two beads. There are also 4 atoms on the surface with the distance a_{AA} from the surface bead, and they are shared among 5 beads. Also there exists one atom of the system with the distance a_{AA} from the surface bead that is shared among 6 beads. So the mass of the surface bead can be calculated as follows

$$M_{surface} = \left(1 + 8 \cdot \frac{1}{2} + \frac{1}{6} + 4 \cdot \frac{1}{5}\right) m_{atom} = \frac{179}{30} m_{atom} \approx 5.97m_{atom} \quad (2.2)$$

The number of atoms with the distance $(\sqrt{2}/2)a_{AA}$ from the edge bead is 5, and each of them is shared between two beads. There are 4 atoms with the distance a_{AA} from the edge bead.

Two of them are on the surface and are shared among 4 beads while the remaining atoms are shared among 5 beads are at the edge. By noticing one atom at the same place where the edge bead is, the mass of the bead is calculated as follows

$$M_{edge} = \left(1 + 5 \cdot \frac{1}{2} + 2 \cdot \frac{1}{4} + 2 \cdot \frac{1}{5}\right)m_{atom} = 4.4m_{atom} \quad (2.3)$$

The mass of the corner bead can be calculated as follows. There are 3 atoms that are shared between two beads with the distance $(\sqrt{2}/2)a_{AA}$ from each atom. There are also 3 atoms with the distance a_{AA} from the corner bead, and each of them are shared among 4 beads. Hence, the mass of the corner bead is obtained as follows

$$M_{corner} = \left(1 + 3 \cdot \frac{1}{2} + 3 \cdot \frac{1}{4}\right)m_{atom} = 3.25m_{atom} \quad (2.4)$$

In addition to the four aforementioned beads, there are some new beads with different atomic neighborhood. To determine the mass of these new beads, a system is created with both AA and CG structures. Then all of atoms with the distance which is equal or less than one lattice constant from each bead are determined. Also, the number of beads, inheriting from each atom, must be calculated. With this data, mass allocation for each bead can be computed and used in MD simulations. LAMMPS software (Plimpton, 1995) is used as the main solver in our simulations.

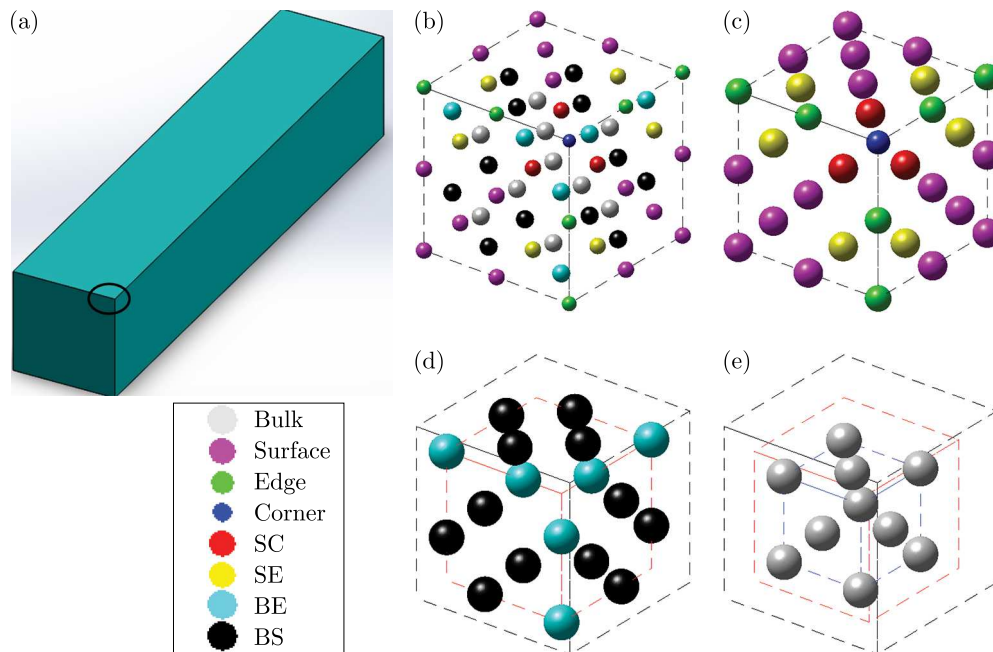


Fig. 2. Eight types of beads in the last CG model: (a) one corner of a nanowire which can be zoomed in to display different bead types, (b) a cubic box on the corner of the nanowire with the edge of $2a_{CG}$ (all types of beads are shown in this part of figure simultaneously), (c) external layer of the beads of the corner, (d) the first internal layer of the beads of the corner, (e) the second internal layer of the beads of the corner

By using the mentioned algorithm, 8 types of beads are obtained (Fig. 2). Four of them are previously mentioned as the bulk, surface, edge and corner beads. The rest of them is as follows:

- Beads shared between the surface and corner: these beads are on the surface with the distance a_{AA} from the corner and their mass is $M_{SC} = 6.0667m_{atom}$.
- Beads shared between the surface and edge: there are beads with mass of $M_{SE} = 6.0167m_{atom}$. These beads are on the surface with the distance a_{AA} from the edge.

- Beads shared between the bulk (internal material) and edge: these internal beads have the distance a_{AA} from the edge and their mass is $M_{BE} = 8.0667m_{atom}$.
- Beads shared between the bulk and surface: these internal beads have the distance a_{AA} from the surface and their mass is $M_{BS} = 8.033m_{atom}$.

Currently, we can introduce 4 CG models based on the mass assignment. Table 1 lists the specifications of these CG models. Although the second and third coarse-graining methods have the same mass assignments, their potential parameters are different (see the next Section).

Table 1. Four different CG models

CG model	Mass assignment
CG ₁	One bead type: $M_{bulk} = 8m_{atom}$
CG ₂	Four bead types: $M_{bulk} = 8m_{atom}$, $M_{surface} = 5.9667m_{atom}$, $M_{edge} = 4.4m_{atom}$, $M_{corner} = 3.25m_{atom}$
CG ₃	Four bead types: $M_{bulk} = 8m_{atom}$, $M_{surface} = 5.9667m_{atom}$, $M_{edge} = 4.4m_{atom}$, $M_{corner} = 3.25m_{atom}$
CG ₄	Eight bead types: $M_{bulk} = 8m_{atom}$, $M_{surface} = 5.9667m_{atom}$, $M_{edge} = 4.4m_{atom}$, $M_{corner} = 3.25m_{atom}$, $M_{SC} = 6.0667m_{atom}$, $M_{SE} = 6.0167m_{atom}$, $M_{BE} = 8.0667m_{atom}$, $M_{BS} = 8.033m_{atom}$

In this Section, we have introduced 8 types of beads which was developed for a cubic system. In the next Section, the potential parameters are determined for the CG models.

2.3. Potential parameters

The most widely used potential for the modeling of FCC metals is EAM (Zhou *et al.*, 2004). In this potential, the total potential energy can be expressed as

$$E = \frac{1}{2} \sum_{i,j,i \neq j} \varphi_{ij}(r_{ij}) + \sum_i F_i(\rho_i) \quad (2.5)$$

This potential model has two parts. The first part is φ_{ij} that is known as pair energy between atoms i and j , and the second part is embedding energy $F_i(\rho_i)$ that describes the effect of electron density ρ_i . The electron density can be obtained as below

$$\rho_i = \sum_{i,j \neq i} f_i(r_{ij}) \quad (2.6)$$

where $f_i(r_{ij})$ is the electron density produced by atom j at the position of atom i .

Herein, at first, the potential parameters for the first model (CG₁) is introduced. For the first model, each bead is representative of eight atoms, hence the cohesive energy per bead in the CG model should be 8 times bigger than the cohesive energy per atom in the AA model. Consequently, to have the same potential energy for both CG₁ and AA models at any arbitrary point, the potential energy obtained from Eq. (2.5) for the first CG model, must be multiplied by 8 to reproduce the correct potential energy.

On the other hand, since the lattice constant of the CG models is $a_{CG} = 2a_{AA}$, the distance between beads is also twice the distance between atoms. Thus, every part of the potential which is a function of distance, must be modified to be a function of distance divided by 2. Totally, the potential function for the first CG model, can be represented as follows

$$\varphi_{CG_1}(r_{ij}) = 8\varphi_{AA}\left(\frac{r_{ij}}{2}\right) \quad \rho_{CG_1}(r_{ij}) = \rho_{AA}\left(\frac{r_{ij}}{2}\right) \quad F_{CG_1}(\rho_i) = 8F_{AA}(\rho_i) \quad (2.7)$$

For the second CG model, the mass assignment for the beads is different from the first CG model; however, the potential parameters for these models are considered to be the same. For the third and fourth CG models, the potential parameters are modified based on the mass proportions. This means that each bead is not necessary representative of 8 atoms, and only bulk atoms are representative of eight atoms and other beads are representative of M_{bead}/m_{atom} atoms. Therefore, it is reasonable to replace number 8 in Eq. (2.7) with M_{bead}/m_{atom} as follows

$$\begin{aligned}\varphi_{(CG_1)}(r_{ij}) &= \frac{M_{bead}}{m_{atom}} \varphi_{AA}\left(\frac{r_{ij}}{2}\right) & \rho_{CG_1}(r_{ij}) &= \rho_{AA}\left(\frac{r_{ij}}{2}\right) \\ F_{CG_1}(\rho_i) &= \frac{M_{bead}}{m_{atom}} F_{AA}(\rho_i)\end{aligned}\quad (2.8)$$

For this model, a different pairwise potential is required for calculating the interaction between two different beads. So, the EAM potential relation for alloys can be used (Zhou *et al.*, 2004), which has the following relation

$$\varphi^{ab}(r) = \frac{1}{2} \left[\frac{\rho^b(r)}{\rho^a(r)} \varphi^{aa}(r) + \frac{\rho^a(r)}{\rho^b(r)} \varphi^{bb}(r) \right] \quad (2.9)$$

Equation (2.9) shows the pairwise potential function for alloys a and b . Since electron density is equal for all beads, the average of the two pairwise potential function should be considered for the interaction between two beads.

Thus, in this paper, four different CG models which have the following specifications are considered:

1. CG₁: one type of bead,
2. CG₂: four types of beads having four different mass values while using the same potential parameters,
3. CG₃: four types of beads having four different mass values and potential parameters tuned based on the mass of the beads,
4. CG₄: eight types of beads having eight different mass values and potential parameters tuned based on the mass of the beads.

After introducing the CG models, the validity of them must be checked. For this purpose, bulk simulations such as calculating elastic properties are performed firstly. In our simulations, gold is studied as one of the FCC metals. To simulate a bulk material, periodic boundary conditions are used in three dimensions to remove the effect of boundaries. A cubic central box with an edge length of $10a_{AA}$ is considered. Our goal is to compare the total potential energy, bulk modulus and elastic properties obtained from the CG models with those obtained from the AA method and experiment (Simmons and Wang, 1971). For evaluating the elastic constants, a specified strain is applied to the system and stress changes caused by the strain are measured. By dividing the stress changes by strain, different elastic constants are calculated. Generally, a material has 36 elastic constants; however, for FCC metals, due to symmetry, there are only three different elastic constants. As can be expected, our simulation results demonstrate that all CG models predict the bulk properties exactly as same as the AA model. In fact, all of the CG models behave completely similar, since for the bulk materials there exists only one bead type. Therefore, all CG models are appropriate for the modeling of the bulk FCC materials.

In the following Section, some static and dynamic simulations are performed so as to check the size-dependency of these models. To this aim, in different nanowires, the natural frequency of longitudinal and transversal vibrations by employing these models is calculated. Then the results are compared with the results of the AA model. Investigation of how accurate these CG models can predict the mechanical properties of an FCC metal having free surfaces is studied in the next Section.

3. Case study

In this Section, the accuracy of the CG models in the prediction of mechanical properties of small-size nanowires is examined. To this aim, Young's modulus in static longitudinal deformation and the natural frequency in longitudinal and transversal vibrations of nanowires are studied. Figure 3 depicts a gold nanowire with clamped-free boundary conditions.

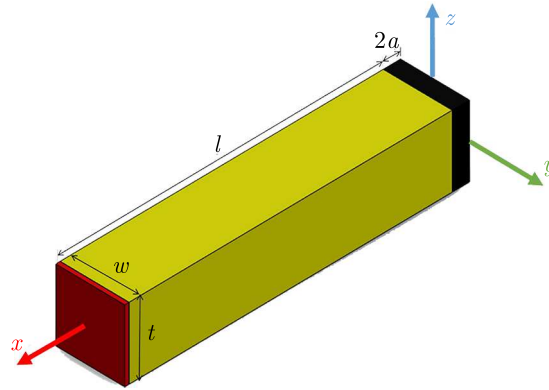


Fig. 3. A gold nanowire. Three zones are recognizable at each setup: the boundary zone having a length $2a_{AA}$ (shown by black color), moving zone having a length a_{AA} (shown by yellow color), and the excitation zone displayed in red color

3.1. Longitudinal deformation

Herein, Young's modulus through static analysis is calculated and the size effect on the accuracy of 4 CG models is investigated. Then, longitudinal vibrations of the nanowire are studied.

3.1.1. Calculating Young's modulus

Young's modulus is calculated based on the potential energy changes followed by strain changes. For this purpose, five different strains are applied to the nanowire, and variations of the potential energy per unit volume are calculated for these strains as follows

$$\Delta u = \frac{1}{2} E \varepsilon^2 \quad (3.1)$$

where Δu stands for potential energy changes per volume, E is Young's modulus and ε is the strain. By fitting a quadratic curve to the data, Young's modulus is calculated. Figure 4 shows the results for a gold nanowire with $56a_{AA}$ in length and $14a_{AA}$ in thickness.

According to the relative error of the CG models, the most accurate model is the fourth model, which is predictable due to more corrections applied to bead masses and potential parameters in this model. Furthermore, as it is expected, the errors of the first and second CG models are the same. In fact, in static simulations, the mass distribution plays no significant role, and the difference between the first two models and two other models is only because of the distinct potential parameter of the beads. Next, Young's modulus is calculated for different sizes of nanowires and the accuracy of these 4 CG models is examined.

Nanowires with thickness of $14a_{AA}$ and with various lengths are considered for checking the effect of length. The length of these nanowires varies from 4 to 10 times larger than their thicknesses. The results of these simulations show that the error of the CG models is approximately constant for different lengths. Since there is no change in the surface effects by changing length of the nanowire, it is expected that the error of the models does not change significantly with variations of the length.

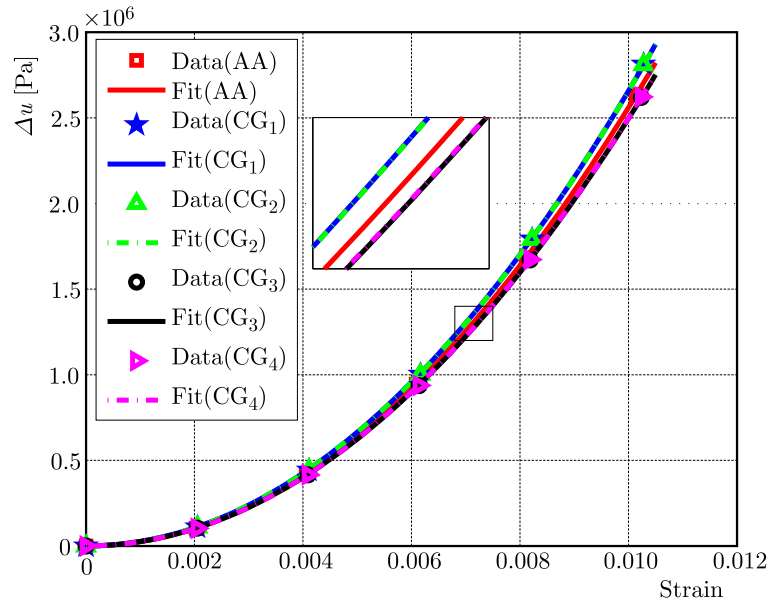


Fig. 4. Variations of the potential energy per volume with respect to strain for a gold nanowire with length of $56a_{AA}$ and thickness of $14a_{AA}$

Thickness is another size parameter influencing the error of the models. The nanowire length is set to be 8 times larger than its thickness. The results depict that the error of the CG models in the prediction of Young's modulus decreases as the nanowire thickness increases. The reason for this behavior is that the surface effects decrease as the nanowire thickness increases. The first and second models use the same potential parameters. Nevertheless, their mass assignments are different. Therefore, it is expected that their behavior in the static and dynamic simulations are similar and different, respectively. Since in this Section a static simulation is performed, the results of these two methods are the same.

3.1.2. Calculating the natural frequency of longitudinal vibration

Here we aim at the investigation of the size effect on the exactness of the proposed CG models in the estimation of the dynamic behavior of the nanowires in longitudinal vibrations. In this regard, the effect of length, thickness, and the scaling parameter on the first longitudinal vibrational frequency of the clamped-free gold nanowire is studied. The details of simulation setup are explained as follows:

- After minimization, two lattices (one lattice in the CG models) at one end of the nanowire are fixed and temperature of the nanowire is maintained at 0.01 K employing the Nosé-Hoover thermostat (Nosé, 1984; Hoover, 1985). It should be mentioned that the higher the temperature of the system is, the greater its kinetic energy is, that may yield incorrect results. Therefore, the nanowire temperature is controlled at 0.01 K.
- The other end of the nanowire is displaced with a constant speed. This displacement is about 1% of the nanowire length to avoid nonlinearity and plastic deformation.
- Then the excited atoms are fixed (at a new position), and temperature of the nanowire is controlled at 0.01 K.
- At the last stage, the end of the nanowire is released to vibrate freely. The corresponding frequency of longitudinal vibrations can be calculated by fitting a sinusoidal function to its end-point displacement (Pishkenari *et al.*, 2015, 2016).

Figure 5 shows the x position of the nanowire free end for a nanowire with length of $80a_{AA}$ and thickness of $20a_{AA}$. According to Fig. 5, all CG methods similar to the AA model pre-

dict oscillating behavior for motion of the nanowire free end. The natural frequencies that are calculated from Fig. 5 are listed in Table 2.

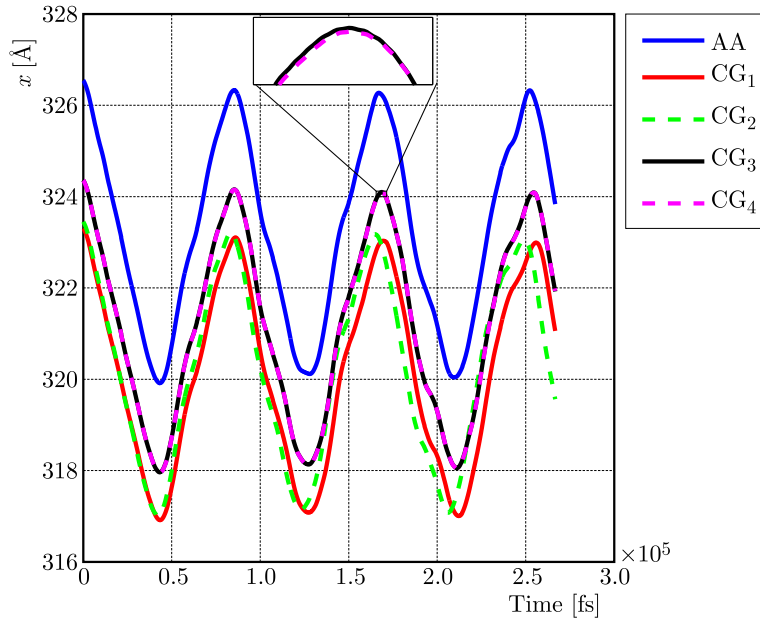


Fig. 5. Position x of the nanowire free end in the fourth step of simulation. The nanowire length and thickness are $80a_{AA}$ and $20a_{AA}$, respectively

Table 2. Natural frequency of longitudinal vibrations for the proposed CG models and the relative error in the estimation of the natural frequency in addition to computation time

	AA	CG ₁	CG ₂	CG ₃	CG ₄
Longitudinal natural frequency [GHz]	75.4	74.8	77.1	75.1	75.1
Relative error [%]	—	0.80	2.3	0.40	0.40
CPU time [s]	15356	2021	3666	3832	3917

Based on the relative error of the CG models, the most accurate models are the third and fourth ones. Despite the fact that we expect the error of the second model to be smaller than the first one, the first model is more accurate in this simulation setup. It should be mentioned that the error of the CG models highly depends on the nanowire thickness, and the dependency is different in four CG models. It is worthy to note that functionality of the first, third and fourth CG models on the size parameters of the nanowire is nearly similar (where always the third and fourth models are more precise than the first one), but behavior of the second model is completely distinct. In fact, for a considerable range of nanowire thickness, the second model may give less exact results with respect to the first model (follow the next Sections).

Further simulations are done to investigate the effect of the size parameters on the error of the CG models. Length, thickness and scale parameter are the three size parameters that their effects are studied in this Section.

Length effect: In the simulations, the nanowire length is changed from $48a_{AA}$ to $120a_{AA}$ while its thickness is set as $12a_{AA}$. The results show that the nanowire length does not influence the accuracy of four CG models. This behavior is due to the fact that the surface effects do not significantly change with the nanowire length. A striking point observed in this figure is that at this nanowire thickness the second model is the most precise one.

Thickness effect: Figure 6 illustrates the effect of thickness on the precision of the CG models. In Fig. 6a, the nanowire thickness is varied from $8a_{AA}$ to $20a_{AA}$ and its length is set to be 10 times larger than its thickness. In Fig. 6b, the nanowire length is set to be $100a_{AA}$ and its thickness is varied from $8a_{AA}$ to $20a_{AA}$.

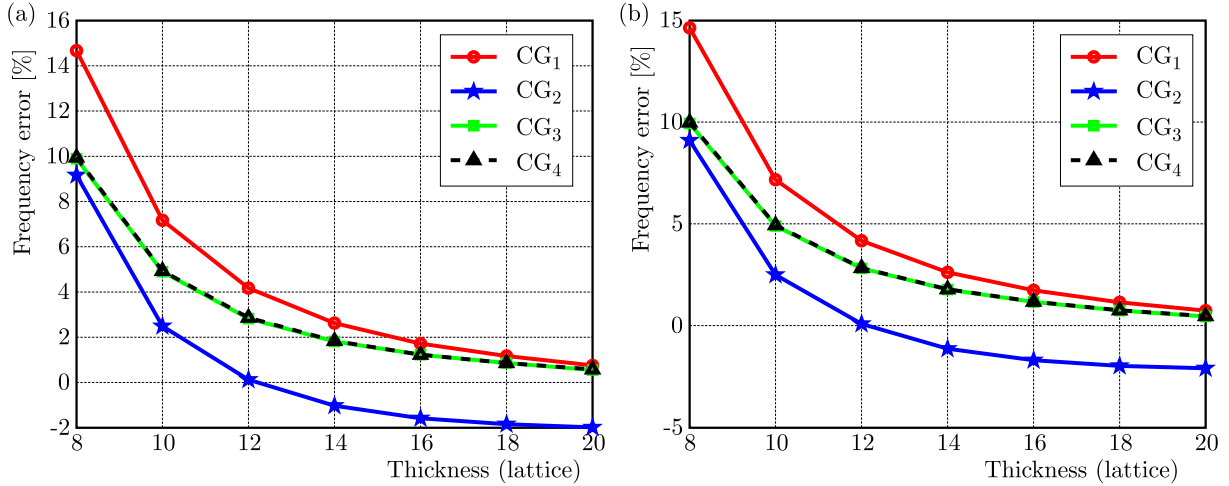


Fig. 6. Error of the estimated longitudinal first natural frequency of the gold nanowire for different CG models: (a) length of the nanowires is 10 times larger than its thickness, (b) nanowire length is set as $100a_{AA}$

Based on Fig. 6, the error of the CG models in the prediction of the longitudinal natural frequency decreases to zero by increasing thickness of the nanowire. The reason for this behavior is that the surface effects reduce as nanowire thickness increases. It should be noted that the second model cannot properly predict the natural frequency for nanowire thicknesses over $14a_{AA}$. In this model, the exterior beads have different masses with respect to the interior beads, while the potential parameters of all beads are the same. Due to limitations in computational facilities, simulations of larger nanowires are not possible in this work. However, for larger thickness, it is expected that the error of the second model converges to zero because all coarse-grained models behave similar to bulk materials.

Scale parameter effect: To examine another effect of nanowire size on the accuracy of the CG models, a nanowire with length of $40a_{AA}$ and thickness of $8a_{AA}$ is considered as the base nanowire, and all of its dimensions are multiplied by a scale parameter. The results show that the frequency error decays to zero for three of the CG models. It should be noted that the surface-to-volume ratio reduces as the nanowire size increases, hence the surface effects should vanish for larger values of the scale parameter. For the second CG model, at first the frequency error descends from positive values to negative values and then it ascends gradually. It is expected that the error of the second model eventually converges to zero for larger values of the scale parameter because the bulk simulations proved that all of the CG models behave as same as the AA model. It should be mentioned that our computational facilities limit our simulations to scale parameter 4.

3.2. Transversal vibrations

In this Section, transversal vibration of the nanowire is investigated. The nanowire free end is displaced and released in the z direction. By fitting a sinusoidal function on motion of this point in the direction of excitation, the transversal natural frequency is measured (Pishkenari *et al.*, 2016). The initial displacement of the beam is equal to 1% of the total nanowire length to avoid large-displacement nonlinear effects. Herein, we will examine the effect of nanowire length and thickness as well as the scale parameter on the accuracy of four CG models.

Length effect: for investigating this effect, a nanowire with thickness of $16a_{AA}$ is considered and its length is varied from $64a_{AA}$ to $160a_{AA}$. As previously discussed, the surface effect does not change with variation of the nanowire length, hence the error of the models remains approximately constant as the nanowire length is altered in these simulations.

Thickness effect: in this Section, the effect of nanowire thickness is studied. The thickness of the nanowire varies from $8a_{AA}$ to $20a_{AA}$. The length of the nanowire for simulations in Figs. 7a and 7b are set to be 10 times larger than the nanowire thickness and $100a_{AA}$, respectively.

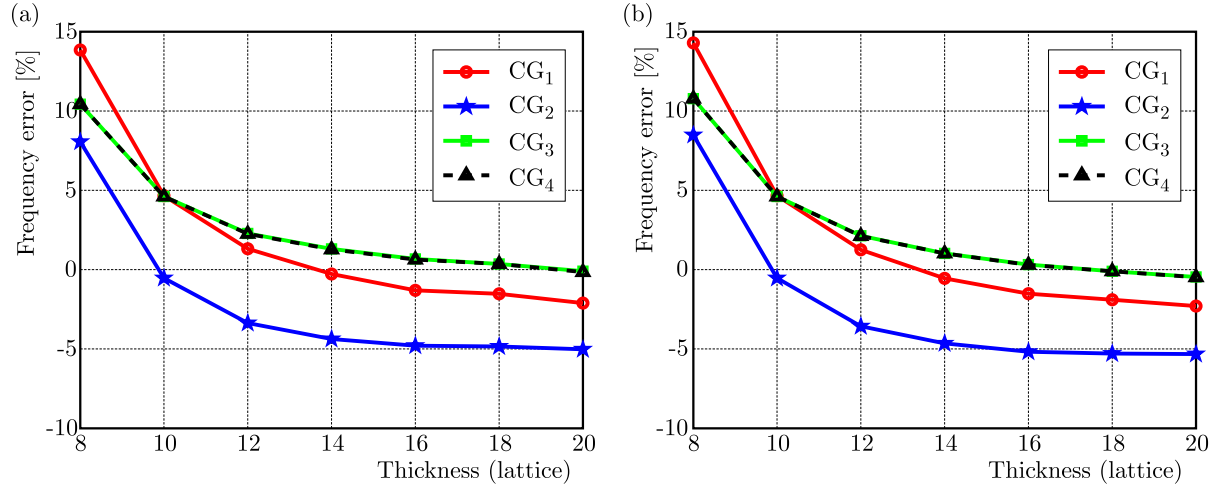


Fig. 7. The error of 4 CG models in estimating the transversal natural frequency as a function of nanowire thickness: (a) length of the nanowire is 10 times larger than its thickness, (b) nanowire length is set to be $100a_{AA}$

Increasing the thickness decreases the surface effect and, therefore, the error of the CG models decays to 0. It should be noted that the error of the first and second CG models does not converge to zero at this thickness interval. However, based on the results of bulk materials, it is expected that the error of these models eventually converges to zero for larger values of the nanowire length whose simulation is beyond capability of our computational resources.

The scale parameter effect: the effect of the scale parameter on the accuracy of the CG models is investigated here. The base nanowire in these simulations has length of $40a_{AA}$ and thickness of $8a_{AA}$. According to the results, the error of the CG models at first descends from positive values to negative values and then slowly ascends. As the nanowire size increases, its properties become closer to behavior of the bulk material. Consequently, the error of the CG models should eventually converge to zero for larger values of the scale parameter. Totally, the third and fourth models have the least error. In this part, the natural frequency of a nanowire with $160a_{AA}$ in length and $32a_{AA}$ in thickness is evaluated. The AA model for the nanowire has more than 670000 atoms, however, the CG model of the nanowire has less than 90000 beads. According to the dimension of the nanowire, approximately 3 million steps are needed to calculate the natural transversal frequency of the nanowire. It causes a seventeen-day simulation for the AA model. Our model can decrease the time to about 4 days while its error is less than 0.6%. When nanowire size rises, not only the number of the beads increases, but also steps of simulations go up. Hence, evaluating the natural frequency for a larger-size nanowire by the AA model is very time-consuming and it is not possible for us to compare our results for larger-size nanowires. Nevertheless, the CG models are capable of modeling these nanowires.

4. Conclusions

In this paper, 4 different CG models are introduced:

1. CG model with one type of bead and one type of potential parameter.
2. CG model with four types of bead and one type of potential parameter.
3. CG model with four types of bead and four types of potential parameter.
4. CG model with eight types of bead and eight types of potential parameter.

To reveal the ability of the CG models for reproduction of results of the original atomic system, we have conducted different simulations. At first, it is shown that these models can predict behavior of the bulk material, including elastic constants, bulk modulus and potential energy, exactly as same as the AA model. Then we have applied longitudinal and transversal displacements to the free end of a nanowire and compared Young's modulus as well as the longitudinal and transversal vibrational frequency of the CG models with the AA model. The results exhibit that the CG models can properly estimate the results of the AA model. Nevertheless, the accuracy of the proposed CG models in calculating mechanical properties of the nanowire highly depends on the nanowire size.

Totally, among four proposed CG models, the error of the second model highly and nonlinearly depends on the nanowire size. Also the error of the second model at a considerable size interval is relatively larger than in other models. The simulation results of the third and fourth models are approximately the same but the third method is slightly faster. These two models are the most accurate models. The error of these models in prediction of the longitudinal and transversal frequencies for nanowires with thickness more than $18a_{AA}$ is less than one percent, while they accelerate the simulations 4 to 8 times. Therefore, the best proposed CG model is the third one. Although the accuracy of the first model is less than in the third model, it is approximately 2 times faster. Therefore, in some cases where speed is more important than accuracy, the first model can be used.

References

1. BERG B.A., 2005, Introduction to Markov chain Monte Carlo simulations and their statistical analysis, *Markov Chain Monte Carlo, Lecture Notes Series*, **7**, 1
2. BURBERY N., DAS R., FERGUSON W., 2017, Dynamic behaviour of mixed dislocations in FCC metals under multi-oriented loading with molecular dynamics simulations, *Computational Materials Science*, **137**, 39-54
3. CASCELLA M., DAL PERARO M., 2009, Challenges and perspectives in biomolecular simulations: from the atomistic picture to multiscale modeling, *CHIMIA International Journal for Chemistry*, **63**, 14-18
4. CHANDRAMOULI P.N., 2014, *Continuum Mechanics*, Yes Dee Publishing Pvt Ltd.
5. CHEN Y., ZIMMERMAN J., KRIVTSOV A., MCDOWELL D.L., 2011, Assessment of atomistic coarse-graining methods, *International Journal of Engineering Science*, **49**, 1337-1349
6. CRANFORD S., BUEHLER M.J., 2010, *Coarse-Graining Parameterization and Multiscale Simulation of Hierarchical Systems. Part I: Theory and Model Formulation*, DTIC Document
7. HEDRIH K.R.S., HEDRIH A.N., 2010, Eigen modes of the double DNA chain helix vibrations, *Journal of Theoretical and Applied Mechanics*, **48**, 219-231
8. HOOVER W.G., 1985, Canonical dynamics: equilibrium phase-space distributions, *Physical Review A*, **31**, 1695

9. JOVANOVIĆ A.S., FILIPOVIĆ N., 2006, Innovative modeling methods in damage assessment: application of dissipative particle dynamics to simulation of damage and self-healing of polymer-coated surfaces, *Journal of Theoretical and Applied Mechanics*, **44**, 637-648
10. KARMA A., TOURET D., 2016, Atomistic to continuum modeling of solidification microstructures, *Current Opinion in Solid State and Materials Science*, **20**, 25-36
11. LAO J., TAM M.N., PINISETTY D., GUPTA N., 2013, Molecular dynamics simulation of FCC metallic nanowires: a review, *JOM*, **65**, 175-184
12. LEACH A.R., 2001, *Molecular Modelling: Principles and Applications*, Pearson education
13. MARRINK S.J., RISSELADA H.J., YEFIMOV S., TIELEMAN D.P., DE VRIES A.H., 2007, The MARTINI force field: coarse grained model for biomolecular simulations, *The Journal of Physical Chemistry B*, **111**, 7812-7824
14. MUC A., 2011, Modelling of carbon nanotubes behaviour with the use of a thin shell theory, *Journal of Theoretical and Applied Mechanics*, **49**, 531-540
15. NOSÉ S., 1984, A unified formulation of the constant temperature molecular dynamics methods, *The Journal of Chemical Physics*, **81**, 511-519
16. OREN E., YAHIEL E., MAKOV G., 2016, Dislocation kinematics: a molecular dynamics study in Cu, *Modelling and Simulation in Materials Science and Engineering*, **25**, 025002
17. OULDRIDGE T.E., 2012, *Coarse-Grained Modelling of DNA and DNA Self-Assembly*, Springer
18. PAĆKO P., UHL T., 2011, Multiscale approach to structure damage modelling, *Journal of Theoretical and Applied Mechanics*, **49**, 243-264
19. PARK H.S., KLEIN P.A., 2007, Surface Cauchy-Born analysis of surface stress effects on metallic nanowires, *Physical Review B*, **75**, 085408
20. PISHKENARI H.N., 2015, Atomic interactions between metallic tips and surfaces in NC-AFM, *Journal of Physics D: Applied Physics*, **48**, 125301
21. PISHKENARI H.N., AFSHARMANESH B., AKBARI E., 2015, Surface elasticity and size effect on the vibrational behavior of silicon nanoresonators, *Current Applied Physics*, **15**, 1389-1396
22. PISHKENARI H.N., AFSHARMANESH B., TAJADDODIANFAR F., 2016, Continuum models calibrated with atomistic simulations for the transverse vibrations of silicon nanowires, *International Journal of Engineering Science*, **100**, 8-24
23. PISHKENARI H.N., MEGHDARI A., 2010, Surface defects characterization with frequency and force modulation atomic force microscopy using molecular dynamics simulations, *Current Applied Physics*, **10**, 583-591
24. PLIMPTON S., 1995, Fast parallel algorithms for short-range molecular dynamics, *Journal of Computational Physics*, **117**, 1-19
25. POURSINA M., ANDERSON K.S., 2014, An improved fast multipole method for electrostatic potential calculations in a class of coarse-grained molecular simulations, *Journal of Computational Physics*, **270**, 613-633
26. SAMANI M., POURTAKDOUST S.H., 2014, Analysis of two-stage endo-atmospheric separation using statistical methods, *Journal of Theoretical and Applied Mechanics*, **52**, 1115-1124
27. SIMMONS G., WANG H., 1971, *Single Crystal Elastic Constants and Calculated Aggregate Properties*, 2nd ed., Cambridge, Mass., M.I.T. Press
28. TADMOR E., LEGOLL F., KIM W., DUPUY L., MILLER R., 2013, Finite-temperature quasi-continuum, *Applied Mechanics Reviews*, **65**, 010803, 2013
29. YANG S., QU J., 2014, An investigation of the tensile deformation and failure of an epoxy/Cu interface using coarse-grained molecular dynamics simulations, *Modelling and Simulation in Materials Science and Engineering*, **22**, 065011

30. YANG Q., TO A.C., 2015, Multiresolution molecular mechanics: A unified and consistent framework for general finite element shape functions, *Computer Methods in Applied Mechanics and Engineering*, **283**, 384-418
31. ZHOU X., JOHNSON R., WADLEY H., 2004, Misfit-energy-increasing dislocations in vapor-deposited CoFe/NiFe multilayers, *Physical Review B*, **69**, 144113

Manuscript received January 1, 2017; accepted for print September 25, 2017

NONLINEAR MODELING AND ANALYSIS OF A SHOCK ABSORBER WITH A BYPASS

URSZULA FERDEK, JAN ŁUCZKO

Cracow University of Technology, Faculty of Mechanical Engineering, Kraków, Poland
e-mail: uferdek@mech.pk.edu.pl; jluczko@mech.pk.edu.pl

The model of a mono-tube shock absorber with a bypass is proposed in this paper. It is shown that the application of an additional flow passage (bypass) causes changes to the damping force characteristics when the excitation amplitudes are large. In such cases, the damping force values increase, thereby improving safety of the ride. For small excitation amplitudes, the shock absorber behaves in a similar fashion as shock absorbers without a bypass, ensuring a high comfort level of the ride on roads with smooth surfaces.

Keywords: shock absorber, hydraulic damper, vehicle suspension, nonlinear, vibrations

1. Introduction

The problems with the modelling and analysis of hydraulic dampers are discussed in several papers. It results from the fact of their wide applications (especially in the automotive industry) as well as from frequent employment of new damper designs (Norgaard and Cimins, 2009; King, 2014; Marking, 2014). These new concepts, often intuitively introduced, require successive theoretical solutions. One of such ideas is the application of an additional flow passage, meaning bypasses. Such solutions are introduced in order to improve safety of the ride, mainly in cross-country vehicles. When such vehicles run onto a large obstacle, the oil flow through a bypass becomes blocked off. As a result, the damping force increases suddenly, changing the damper characteristics. The constructional parameters of the damper with a bypass should be selected in such a way as to have – during travelling on smooth surfaces – the characteristic not worse than the characteristic of a hydraulic damper without a bypass.

Good comfortable rides are provided by dampers of ‘soft’ characteristics while dampers of ‘hard’ characteristics increase the safety, assuring better control and higher braking forces. In order to bring together these contradictory requirements, semi-active systems (Ferdek and Łuczko, 2015, 2016) usually magneto-rheological (Sapiński and Rosół, 2007; Gołdasz, 2015) are often applied. Compared to passive systems, semi-active dampers provide the possibility of adjusting the damping force to specific conditions of the ride. However, they have more complicated construction and due to that, they are more expensive both in production and in operations.

Currently used dampers have a flow passage which can be situated inside the piston rod (King, 2014) or outside the working cylinder (Norgaard and Cimins, 2009; Marking, 2014). Such bypasses can have an additional pressure valve controlling the oil flow. The application of the bypass changes the dampers characteristics. When a vehicle is going on relatively smooth surfaces, the displacement of the piston rod is small, and the oil flow between the chambers occurs both through the piston bleed orifices and through the bypass. This in turn creates a soft damper characteristic ensuring comfort of the ride. When the vehicle has to clear large obstacles, it means large piston strokes, the oil is not flowing through the bypass, and the damping force significantly increases (‘hard’ characteristic).

The analysis of the car model requires the introduction of a relatively simple hydraulic damper model properly describing its basic properties and allowing simultaneously the investigation of the influence of essential parameters within the wide range of their changes. Tests of modelling twin-tube dampers (Ramos *et al.*, 2005; Alonso and Comas, 2006), mono-tube dampers (Talbot and Starkey, 2002; Titurus *et al.*, 2010; Farjoud *et al.*, 2012) and others have been undertaken. They mainly differ in the approach to describing the oil flow through valves. Alonso and Comas (2006) investigated the twin-tube damper model taking into account the cavitation problem and the damper chambers elasticity. Talbot and Starkey (2002) investigated the mono-tube damper modelling the influence of the shim stack by the preliminarily pressed spring. They assumed that the laminar oil flow was a result of leakage in the piston-cylinder system, in contrast to the turbulent flow through the orifice system in the piston. Farjoud *et al.* (2012) investigated the influence of the shim stack properties on characteristics of the mono-tube damper. The authors compared the obtained results with the experimental ones. In the paper by Czop and Sławik (2011), the model of the twin-tube shock absorber was tested and experimentally verified.

There is a separate group of research papers dealing with the cavitation problem being a result of sudden oil pressure changes in hydraulic dampers. In the papers by Cho *et al.* (2002), Van de Ven (2013) and by Manring (1997) various descriptions of the effective bulk modulus were given.

Papers dealing with modelling of dampers with a bypass are relatively rare. Apart from patents (Norgaard and Cimins, 2009; King, 2014; Marking, 2014), only in the paper by Lee and Moon (2006) the model of the displacement-sensitive shock absorber was discussed. Depending on the piston displacement, the flow control was realised by a proper configuration of the inner cylinder surface.

The purpose of the hereby paper is to demonstrate that the introducing of an additional flow passage to a classical hydraulic damper causes a change of the damping force characteristics. In the case of high excitation amplitudes, an increased value of the damping force improves the safety of the ride. While in the case of small excitation amplitudes, the damper behaves in a similar fashion as the classical shock absorber, where an increased oil flow causes a decrease in the damping force providing higher riding comfort. To assure the proper functioning of the model within the wide range of amplitudes and excitation frequencies, the pressure influence on the oil compressibility modulus is taken into account. The proposed model of the damper is different than the presented in the paper by Lee and Moon (2006) and allows the investigation of the influence of a more number of constructional parameters of the shock absorber within the wide range of their changes.

2. Model of a variable damping shock absorber

The scheme of the hydraulic shock absorber with a bypass as well as its model is presented in Fig. 1. Two chambers are in the main cylinder: chamber K_1 above the piston (rebound chamber) and chamber K_2 below the piston (compression chamber). Narrow orifices through which oil flows between both chambers are inside the piston. Some orifices are constantly open while the others are the most often covered by the shim stack. An additional external flow passage connects chambers K_1 and K_2 , and distances h_1 and h_2 determine placements of the bypass orifices. The shock absorber is rigidly connected with a reserve cylinder, consisting of chamber K_3 filled with oil and chamber K_4 filled with gas under a high pressure of 2-3 MPa. The floating piston of a relatively small mass separates both chambers. Two phases of the piston rod motion are essential in the damper operations: the compression phase and rebound (expansion) phase. During the compression, the piston rod is moving down causing the pressure increase in

chamber K_2 and the oil flow into chambers K_1 and K_3 . During the rebound process, due to the pressure increase in chamber K_1 , the oil returns to chamber K_2 .

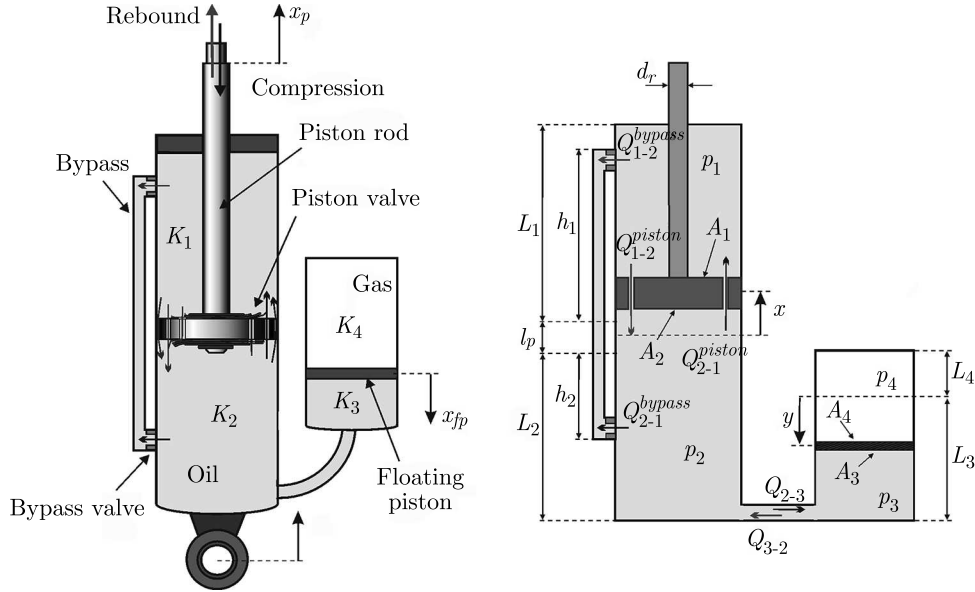


Fig. 1. The scheme and the model of the damper with a bypass

In the case of minor displacements and pressures, the oil flows only through bleed orifices not covered by plates through leakages and, eventually, through the bypass if the pressure controlled valve is not installed. Along with the pressure increase, the valves in the piston and bypass are gradually opened. During the rebound phase, the oil flows through differently designed piston orifices (of a different cross-sectional area) than in the compression phase, which – finally – causes the damper characteristic asymmetry. Asymmetrical characteristics of the shock absorber are desirable for comfort of the passengers (Silveira *et al.*, 2014). When the piston exceeds the distance h_1 (during compression) or h_2 (during rebound), the proper entrance to the bypass becomes blocked, and the oil flows only through bleed orifices in the main piston.

The oil flow from chamber K_2 to K_3 occurs through a relatively short and stiff conduit of a significant cross-section. Coordinate x_p determines the piston motion, x_c – motions of both cylinders, while x_{fp} – the floating piston motion. The relative displacements of corresponding pistons are determined by coordinates $x = x_p - x_c$ and $y = x_{fp} - x_c$. The motion of both pistons is measured from the static equilibrium position. Notation p_i is used for pressures in chambers K_i ($i = 1, \dots, 4$), A_i – for surfaces of the main and floating pistons ($A_3 = A_4$) and V_i – for volumes of chambers K_i .

The resistance force depends mainly on the resultant pressure force acting on the piston, it corresponds to the oil pressures p_1 and p_2 in chambers K_1 and K_2 . Taking into consideration the Coulomb friction force F_{f1} (Lee and Moon, 2006; Farjoud *et al.*, 2012; Goldasz, 2015) between the piston rod and the main cylinder, the damping force can be described as

$$F = (p_1 - p_0)A_1 - (p_2 - p_0)A_2 + F_{f1} \operatorname{sgn} \dot{x} \quad (2.1)$$

where p_0 is the nominal working pressure. In the simulations, the signum function is approximated (Czop and Sławik, 2011) as follows: $\operatorname{sgn} \dot{x} = \tanh(\dot{x}/v_{ref})$, where v_{ref} is the reference velocity value (in simulations $v_{ref} = 0.005$ m/s). In order to determine the shock absorber characteristics, the most often a harmonic excitation is assumed in the form: $x(t) = a \sin \omega t$, where a and ω are the amplitude and frequency of the excitation.

In order to determine pressures p_1 and p_2 , the processes occurring in the chambers should be considered with a special attention directed to the proper description of the oil flows between

the chambers. It will be assumed that the fluid is compressible, taking into account changes of the bulk modulus, especially in the low pressures range. The equation

$$\frac{d\rho_i}{dp_i} = \frac{1}{\beta_i} \rho_i \quad (2.2)$$

describes the oil density change ρ_i in chamber K_i caused by the pressure change p_i ($i = 1, 2, 3$). It is usually assumed that the bulk modulus value β_i is constant ($\beta_i = \beta$, where β is the bulk modulus for the given pressure value, e.g. for the working pressure). This assumption is justified within the limited pressure changes, i.e. in a limited range of the amplitude and piston velocity. For large displacements and velocities, the pressure in one chamber significantly increases while in the other decreases. The assumption of the constant value of the bulk modulus can lead to physically inadmissible solutions of the analysed equations, sometimes even to negative pressure values. In reality, the bulk modulus for large pressures insignificantly increases, and for very small pressures the cavitation effect occurs, during which – due to liquid evaporation – gas bubbles are formed. The accurate description of this phenomenon is more complex and depends on several other factors. The effect of cavitation is a sudden compressibility increase; meaning a bulk modulus decrease. Cho *et al.* (2002) proposed different descriptions of the bulk modulus depending on the pressure and the oil aeration degree. Comparisons with experimental results were also presented. Van de Ven (2013) provided selected equations for the effective bulk modulus β_e . The simplest equation proposed by Merritt (1967) is of the following form

$$\beta_e = \beta \frac{1}{R\beta/\kappa p + 1} \quad (2.3)$$

where R is the volume fraction of the air at the atmospheric pressure p_a , while κ is the adiabatic index. Hayward provides a slightly different equation

$$\beta_e = \beta \frac{R + \bar{p}^\kappa}{R\beta/\kappa p + \bar{p}^\kappa} \quad (2.4)$$

where $\bar{p} = p/p_a$. Another equation was proposed by Cho *et al.* (2002)

$$\beta_e = \beta \frac{R + \bar{p}^\kappa \exp[(p_a - p)/\beta]}{R\beta/\kappa p + \bar{p}^\kappa \exp[(p_a - p)/\beta]} \quad (2.5)$$

The shock absorber of properly selected parameters operates within the range of high pressures (~ 2 MPa), and then the compressibility modulus changes only insignificantly. However, in the designing process, the damper parameters can be changing in wide ranges. When the parameters are incorrectly selected, a malfunction of the shock absorber – manifested by large pressure changes – can occur. In such cases, there is a necessity of applying the proper equation for the effective bulk modulus.

The following one-parameter model is proposed in the hereby paper

$$\beta_e(p) = \beta \tanh \frac{p}{p_s} \quad (2.6)$$

Along with decreasing of the parameter p_s value (reference pressure) the bulk modulus faster obtains the limit value β . Figure 2 presents comparisons of the effective bulk modulus diagrams obtained for models: (2.3)-(2.6), for two relatively small values of the parameter R . For the given values of the parameter p_s , the proposed model (2.6) indicates the best compatibility with model (2.4). Within the working pressures range ($p_0 = 2$ MPa) the bulk modulus is close to β , and for low pressures it fastly approaches zero. The advantage of formula (2.6) constitutes the possibility

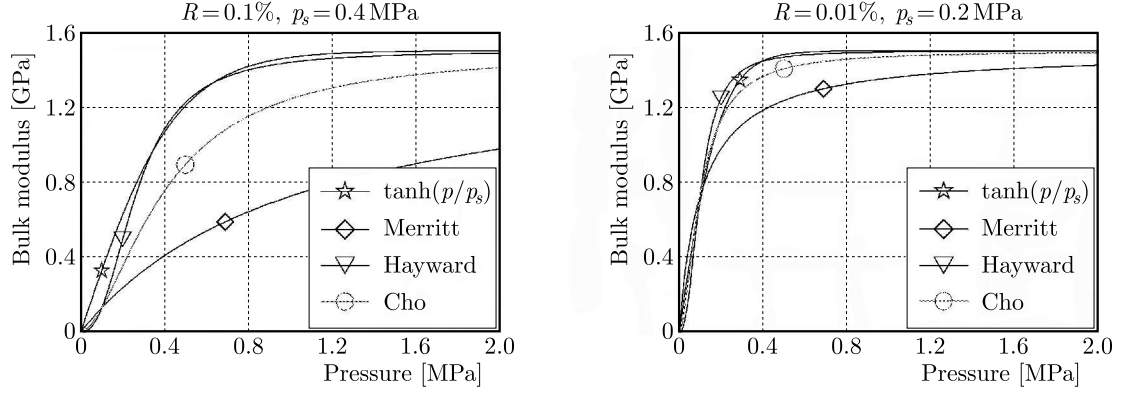


Fig. 2. Bulk modulus versus pressure for different values of R and p_s

of obtaining an analytical equation describing the oil density. After substituting formula (2.6) into equation (2.2), the following expression is obtained

$$\rho_i = \rho_0 \left[\frac{\sinh(p_i/p_s)}{\sinh(p_0/p_s)} \right]^{p_s/\beta} \quad (2.7)$$

where ρ_0 is the oil density under the working pressure p_0 .

In order to determine the oil pressure in chambers K_i , equations of the general form can be used

$$\dot{\rho}_i V_i + \rho_i \dot{V}_i = Q_i \quad (2.8)$$

where $Q_i = \dot{m}_i$ are mass flow rates. Volumes of chambers K_i ($i = 1, 2, 3$) can be calculated as follows

$$V_1 = A_1(L_1 - x) \quad V_2 = A_2(L_2 + x) \quad V_3 = A_3(L_3 - y) \quad (2.9)$$

where distances L_1 and L_2 are lengths of chambers K_1 and K_2 in the working cylinder for $x = 0$, while L_3 and L_4 are lengths of chambers K_3 and K_4 in the external cylinder for $y = 0$. The relative displacement y of the floating piston can be determined from the differential equation

$$m_{fp} \ddot{y} = (p_4 - p_3)A_3 - F_{f2} \operatorname{sgn} \dot{y} \quad (2.10)$$

where m_{fp} is the floating piston mass, and F_{f2} is the friction force between this floating piston and the reserve cylinder. Gas pressure p_4 is determined from the equation of the polytropic process: $p_4 V_4^n = p_0 V_{40}^n$ (Farjoud *et al.*, 2012; Ferdek and Łuczko, 2012), where: $V_4 = A_4(L_4 + y)$ and $V_{40} = A_4 L_4$. Hence, it follows

$$p_4 = p_0 \frac{L_4^n}{(L_4 + y)^n} \quad (2.11)$$

After using equation (2.2) and transforming equations (2.8), the equations describing the oil pressures in the chambers K_i ($i = 1, 2, 3$) take the form

$$\dot{p}_1 = \frac{\beta_1}{V_1} \left(\frac{Q_1}{\rho_1} + A_1 \dot{x} \right) \quad \dot{p}_2 = \frac{\beta_2}{V_2} \left(\frac{Q_2}{\rho_2} - A_2 \dot{x} \right) \quad \dot{p}_3 = \frac{\beta_3}{V_3} \left(\frac{Q_3}{\rho_3} + A_3 \dot{y} \right) \quad (2.12)$$

where the moduli $\beta_i = \beta_e(p_i)$ in the respective chambers are determined by formula (2.6) and the densities by (2.7). System (2.12) of non-linear differential equations of the first order and differential equation (2.10) of the second order constitute the base for the determination of characteristic (2.1) of the mono-tube hydraulic shock absorber with and without the bypass.

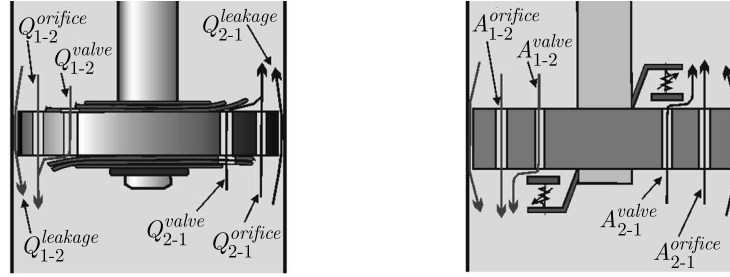


Fig. 3. Diagram showing the flow paths

One can denote Q_{j-i} ($j = 1, i = 2$ or $j = 2, i = 1$) – the mass flow rate from chamber K_j (e.g. rebound for $j = 1$) to chamber K_i (e.g. compression $i = 2$). In the case of the flow in the reverse direction: $Q_{j-i} = 0$ (then $Q_{i-j} \neq 0$). Since the oil flow between these chambers occurs through orifices in the piston (Fig. 3) and through the bypass, the flow rate can be written as

$$Q_{j-i} = Q_{j-i}^{piston} + Q_{j-i}^{bypass} \quad (2.13)$$

where the flow rate Q_{j-i}^{piston} is the sum of three flow rates (Fig. 3)

$$Q_{j-i}^{piston} = Q_{j-i}^{leakage} + Q_{j-i}^{orifice} + Q_{j-i}^{valve} \quad (2.14)$$

representing the flow rates resulting from leakage past piston, flow through bleed orifices and flow through valves in the piston. The oil flow in the reversed direction, from chamber K_i to K_j , determined by the mass flow rate Q_{i-j} , causes a mass decrease in chamber K_i . Thus, the oil mass change in chamber K_i can be written in the following form

$$Q_i = Q_{j-i} - Q_{i-j} \quad (2.15)$$

Since, from the law of mass conservation between mass flow rates the following relation occurs: $Q_1 + Q_2 + Q_3 = 0$. It is enough to determine the mass flow rates Q_1 and Q_3 determining mass changes in chambers K_1 and K_3 . It results that $Q_2 = -Q_1 - Q_3$. The negative value of Q_i is related to the oil outflow from chamber K_i .

Assuming the laminar flow (Talbot and Starkey, 2002), the mass flow rate Q_{2-1} leakage from the compression chamber to the rebound chamber can be determined from the equation

$$Q_{2-1}^{leakage} = \pi d_p \left(\frac{b_{pc}^3 (p_2 - p_1)}{12 l_p \nu} - \frac{\rho_2 b_{pc} \dot{x}}{2} \right) \quad (2.16)$$

where b_{pc} is clearance, d_p – piston diameter, l_p – piston length, ν – coefficient of kinematic viscosity. The first component of equation (2.16) determines the flow rate caused by the pressure difference while the second by the relative piston velocity. In the case when the piston moves up (for $\dot{x} > 0$), the flow rate caused by the pressure difference is decreasing. Equation (2.16) is correct only for $Q_{2-1}^{leakage} > 0$. Otherwise, the flow rate is determined from the following equation

$$Q_{1-2}^{leakage} = \pi d_p \left(\frac{b_{pc}^3 (p_1 - p_2)}{12 l_p \nu} + \frac{\rho_1 b_{pc} \dot{x}}{2} \right) \quad (2.17)$$

In order to determine the remaining component of equation (2.11) for the turbulent flow (Titurus *et al.*, 2010), the equation of a general form is used

$$Q_{j-i} = C_d A_{j-i} \sqrt{2 \rho_j (p_j - p_i)} \quad (2.18)$$

where C_d is the discharge coefficient while A_{j-i} is the effective cross-sectional area of the proper orifice through which the oil flows from chamber K_j to K_i . Equation (2.18) is correct for $p_j > p_i$. After introduction of the function

$$\vartheta(p_j, p_i, \rho_j) = C_d H(p_j - p_i) \sqrt{2\rho_j(p_j - p_i)} \quad (2.19)$$

where $H(\cdot)$ is the unit step function, equation (2.13) obtains the form

$$Q_{j-i} = Q_{j-i}^{leakage} + (A_{j-i}^{orifice} + A_{j-i}^{valve} + A_{j-i}^{bypass}) \vartheta(p_j, p_i, \rho_j) \quad (2.20)$$

Out of parameters: $A_{j-i}^{orifice}$, A_{j-i}^{valve} , A_{j-i}^{bypass} , determining the effective areas of respective orifices, only the parameter $A_{j-i}^{orifice}$ is of a constant value. After referring the orifice area to the area of the compression side of the piston, this area depends on the dimensionless parameter α_{j-i} in the following way

$$A_{j-i}^{orifice} = \alpha_{j-i} A_2 \quad (2.21)$$

Values of the remaining areas depend on the oil pressure in the neighbouring chambers of the shock absorber and on the relative piston displacement.

The flow through the compression intake or through the rebound intake is controlled by pressures p_1 and p_2 . Bleed orifices are the most often covered by a stack of circular plates (Fig. 3) deflecting under the influence of the resultant pressure force, and gradually uncovering the orifices. The effective cross-sectional area depends mainly on the pressure difference $p_1 - p_2$ in the shock absorber chambers as well as on geometrical and physical parameters of the plates. The accurate determination of the area change law requires the accurate modelling of the specific technical solution. Disregarding inertia of the plates, the valve can be modelled by means of a stiff plate preliminarily pressed down by a spring of a progressive characteristic. For minute pressure differences and until the resultant pressure force is lower than the preload force, the bleed orifice remains closed. Only after exceeding the preload force, the orifice is gradually uncovered. The parameter A_{j-i}^{valve} (effective area) decides which flow depends on the spring deflection. It can not, however, exceed the total area of the orifice cross-section. A function θ_1 will be used for description of a change in the area. This function is defined as follows

$$\theta_1(p_j - p_i, \sigma, k) = H(p_j - p_i - \sigma) \tanh \frac{p_j - p_i - \sigma}{k} \quad (2.22)$$

where the parameter σ determines the pressure difference value above which the plates start to deflect uncovering the bleed orifice joining the neighbouring chambers ($\theta_1 \neq 0$ only for $p_j - p_i > \sigma$), while the parameter k characterises elastic properties of the shim stack. Using the hyperbolic tangent function in equation (2.22) ensures that the effective area A_{j-i}^{valve} will not exceed the area of the orifice cross-section. The efficient (variable) valve area, it means the parameter A_{j-i}^{valve} , is determined by

$$A_{j-i}^{valve} = \delta_{j-i} A_2 \theta_1(p_j - p_i, \sigma^{valve}, k^{valve}) \quad (2.23)$$

where the dimensionless parameter δ_{j-i} is the ratio of the orifice cross-sectional area to the area of the compression side of the piston. Values of dimensionless coefficients δ_{2-1} and δ_{1-2} (also α_{2-1} and α_{1-2}), deciding respectively on flows in the compression and rebound process, can be different (the most often $\delta_{12} < \delta_{21}$) for ensuring a higher resistance force during rebound (for $\dot{x} > 0$) in relation to the force created during the compression process (for $\dot{x} < 0$).

The opening or closing of the bypass is controlled by the relative piston displacement x . The bypass whose openings are of a round cross-section of radius r is gradually closed within

the range $(h_2 - r, h_2 + r)$ in the rebound phase and within the range $(-h_1 - r, -h_1 + r)$ in the compression process. To describe the variable area A_{j-i}^{bypass} , the function defined below is suitable

$$\theta_2(x, h_1, h_2, r) = \begin{cases} 0 & \text{for } x \geq h_2 + r \\ \theta_0[(x - h_2)/r] & \text{for } h_2 - r < x < h_2 + r \\ 1 & \text{for } -h_1 + r \leq x \leq h_2 - r \\ \theta_0[(-x - h_1)/r] & \text{for } -h_1 - r < x < -h_1 + r \\ 0 & \text{for } x \leq -h_1 - r \end{cases} \quad (2.24)$$

where the function θ_0 takes into account the round shape of the bypass orifices and is defined as

$$\theta_0(\xi) = \frac{1}{\pi} \left(\arccos \xi - \xi \sqrt{1 - \xi^2} \right) \quad (2.25)$$

Assuming that the valve controlled by the pressure difference is additionally assembled in the bypass, after using functions (2.22) and (2.24), the effective bypass area is described by

$$A_{j-i}^{bypass} = \gamma_{j-i} A_2 \theta_1(p_j - p_i, \sigma^{bypass}, k^{bypass}) \theta_2(x, h_1, h_2, r) \quad (2.26)$$

where $\gamma_{j-i} A_2$ determines the bypass cross-sectional area. The flow from the compression chamber K_2 to the reserve chamber K_3 can be described in a similar way. However, due to a significant diameter of the conduit which joining these chambers and the rarely used pressure valve, the mass flow rate is described by the following equation

$$Q_{j-i} = A_{j-i}^{conduit} \vartheta(p_j, p_i, \rho_j) \quad (2.27)$$

where $j = 2, i = 3$ or $j = 3, i = 2$. The parameter $A_{2-3}^{conduit} = A_{3-2}^{conduit}$ describes the cross-sectional area of the conduit joining chambers K_2 and K_3 .

3. Effect of model parameters on the characteristics of the shock absorber

The basic characteristics of the shock absorber are dependences of damping forces (2.1) on piston displacements and its relative velocity. The damping force depends mainly on the oil pressure in the compression and rebound chambers. The determination of characteristics requires integration of non-linear differential equations (2.10) and (2.12) describing the floating piston motion and the pressures. For the numerical integration, the Runge-Kutta method of the 5-th order has been used.

The values of the characteristic parameters of the shock absorber are given in Table 1. The majority of these values results from the analysis of the existing structural solutions of mono-tube dampers. The values of the excitation parameters are changed within the specified ranges. The special attention is directed towards parameters influencing the mass flow rate and characterising the bypass. Apart from dimensional parameters given in Table 1, a significant influence on the solutions have dimensionless parameters $\alpha_{1-2}, \alpha_{2-1}, \delta_{1-2}, \delta_{2-1}, \gamma_{1-2}, \gamma_{2-1}$ characterising cross-section areas of the respective orifices. A number of these parameters can be limited by assuming that the areas of orifices – active in the rebound process – are proportional to the corresponding areas in the compression process. After introducing a coefficient λ (in numerical calculations: $\lambda = 0.6$), it can be assumed: $\alpha_{1-2} = \lambda\alpha, \alpha_{2-1} = \alpha, \delta_{1-2} = \lambda\delta, \delta_{2-1} = \delta$. It is also convenient to introduce dimensionless parameters k_p and k_b characterising the valve stiffness in the piston ($k^{valve} = k_v p_0$) and in the bypass ($k^{bypass} = k_b p_0$), respectively, as well as the dimensionless parameter S_v related to the preload force in the piston ($\sigma^{valve} = S_v p_a$). Investigations of the bypass parameters influence are limited to the case of the symmetric distribution of bypass

Table 1. Parameters of the shock absorber model

Symbol	Description	Value	Unit
A_1	Cross-sectional area of chamber K_1	24.6	cm ²
A_i	Cross-sectional area of chambers K_2 , K_3 and K_4	28.3	cm ²
d_p	Diameter of piston	6	cm
d_r	Diameter of piston rod	2.2	cm
d_c	Diameter of conduit	1	cm
l_p	Piston length	1.5	cm
b_{pc}	Clearance	0.1	mm
h	Distance between bypass orifices	2-5	cm
F_{f1}	Friction force between piston and cylinder	10	N
F_{f2}	Friction between floating piston and oil tank	1	N
m_{fp}	Floating piston mass	0.1	kg
p_0	Nominal working pressure	2	MPa
p_a	Atmospheric pressure	0.1	MPa
C_d	Discharge coefficient	0.6	–
β	Fluid bulk modulus at atmospheric pressure	1.5	GPa
β	Kinematic viscosity of hydraulic oil	32	cSt
β	Oil density at atmospheric pressure	890	kg/m ³
a	Amplitude	1-8	cm
f	Excitation frequency	1-12	Hz

orifices ($h_1 = h_2 = h$, and $\gamma_{1-2} = \gamma_{2-1} = \gamma_1$) and for the elastic valve without preliminary deflections ($\sigma^{bypass} = 0$).

The influence of damping forces on the piston relative displacement x is presented in Fig. 4. The curves illustrate the effect of the excitation amplitude a (for $f = \omega/2\pi = 1.4$ Hz) and the effect of frequency f (for $a = 3$ cm) on the damper characteristics. The assumed excitation frequency $f = 1.4$ Hz corresponds to the first frequency of natural vibrations in several models of vehicles. Excited vibrations, within the resonance range enclosing this frequency, worsen the ride comfort.

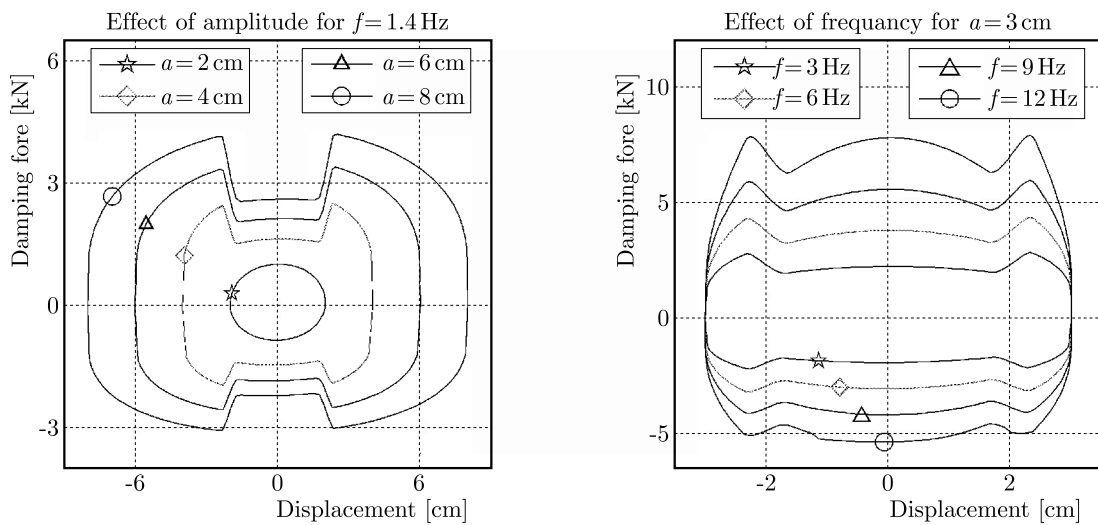


Fig. 4. Influence of the amplitude and excitation frequency on the damping force characteristics ($\alpha = 0.004$, $\gamma = 0.015$, $\delta = 0.04$, $S_v = 5$, $k_p = 2$, $k_b = 0.5$, $h = 2$ cm)

The presented curves are determined for relatively large amplitude values. They are aimed at clear observation of the bypass influence. For the assumed parameter $h = 2$ cm the flow through the bypass is not blocked by the piston, only for the amplitude $a = 2$ cm. However, along with an increase of the amplitude and the excitation frequency, the damping forces grow, but within the range of the active flow through the bypass they are significantly lower (for $-h + r < x < h - r$). Only after surpassing this range, the damping force suddenly increases, which is caused by covering the openings of the additional orifice. Thus, within this range, the damper changes its properties and becomes the so-called ‘hard’ damper, which improves the safety level when a vehicle travels on surfaces with large irregularities. When a vehicle travels on good surfaces (for small amplitudes), the bypass is active all the time, and the damping force is not suddenly increasing.

The influence of the excitation amplitude on the damping force characteristics presented in Fig. 4 is qualitatively similar to the results of experiments discussed by Lee and Moon (2006).

The excitation frequency is related to the ride velocity, and this usually depends on the road class. When the damper performance is investigated within the high frequency range, respectively lower excitation amplitudes should be assumed, e.g. by limiting the maximum piston velocities. Characteristics of shock absorbers are the most often determined within the velocity range not exceeding $v_0 \approx 1$ m/s. In the case of harmonic motion, this leads to the condition: $2\pi fa \leq v_0$. Out of all characteristics shown in Fig. 4, the curves obtained for $f = 9$ Hz and $f = 12$ Hz do not satisfy this condition. The effect of high piston velocities, especially for $f = 12$ Hz, $a = 3$ cm, constitute large changes of the oil pressure in the damper chambers. For the excitation parameters selected in such a way, the oil pressure in the rebound chamber during the compression phase suddenly decreases causing a significant decrease of the bulk modulus. The assumption of a constant bulk modulus, in this drastic case, would lead to a negative pressure p_1 , physically unacceptable. Pressure values for the proposed description of the bulk modulus (2.6) are always positive. The excitation frequency $f = 12$ Hz in several vehicle models (Lee and Moon, 2006) is contained in the second resonance range, corresponding to higher velocities for which the excitation amplitudes satisfy the discussed above limitation. For such amplitudes (smaller than 2 cm) the bypass is not blocked by the piston, and the damper characteristic is close to the ‘soft’ one.

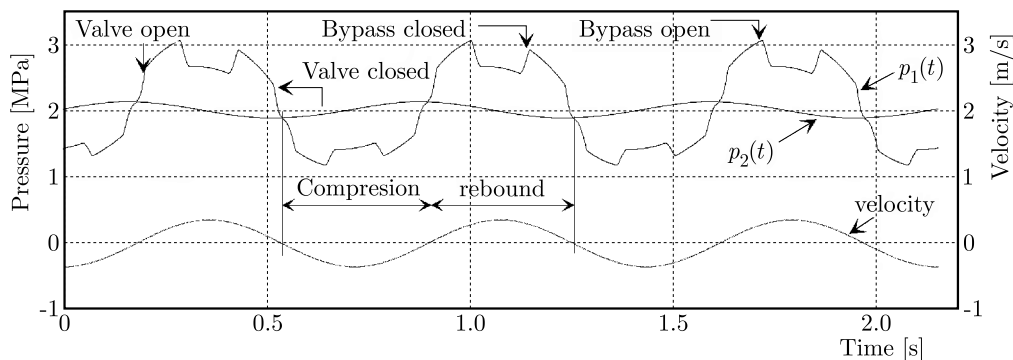


Fig. 5. Time histories of pressures ($f = 1.4$ Hz, $a = 4$ cm, $h = 2$ cm, $\alpha = 0.004$, $\gamma = 0.015$, $\delta = 0.04$, $S_v = 5$, $k_p = 2$, $k_b = 0.5$)

The typical diagrams of pressure p_1 time waveforms in the rebound chamber K_1 and pressure p_2 in the compression chamber K_2 are shown in Fig. 5. Oil pressure p_3 and gas p_4 time histories in chambers K_3 and K_4 are similar to the pressure p_2 diagram. It is easy to determine time intervals corresponding to the compression and rebound, by analysing the sign of the relative piston velocity. Pressure p_1 in the rebound chamber has the decisive influence on the damping force. Changes of the remaining pressures are similar to the harmonic waveforms, which is the

result of connecting the compression chamber with the reservoir of accumulative properties. When observing the pressure $p_1(t)$ diagram, the characteristic points in which pressure changes are either softer or more sudden can be noticed in the rebound and compression phases. This is the effect of opening or closing valves in the piston or bypass.

The functions of the mass flow rates on the relative piston displacement as well as diagrams of the effective (variable) areas deciding on flows through the corresponding valves are shown in Fig. 6. The shown functions: $Q^{leakage} = Q_{2-1}^{leakage} - Q_{1-2}^{leakage}$, $Q^{orifice} = Q_{2-1}^{orifice} - Q_{1-2}^{orifice}$, $Q^{valve} = Q_{2-1}^{valve} - Q_{1-2}^{valve}$, $Q^{bypass} = Q_{2-1}^{bypass} - Q_{1-2}^{bypass}$ characterise the oil flow into the rebound chamber. Negative values of the mass flow rates are related to a mass decrease. It means that they correspond to the oil outflow from chamber K_1 . Diagrams of the total flow rates $Q_{2-1} - Q_{1-2}$ and $Q_{2-3} - Q_{3-2}$ (mass change in chamber K_3) are also seen in Fig. 6. The respective areas (except areas characterising leakages) are defined in a similar fashion. Cyclic repetitions of curves pathways in Fig. 6 signify the motion periodicity.

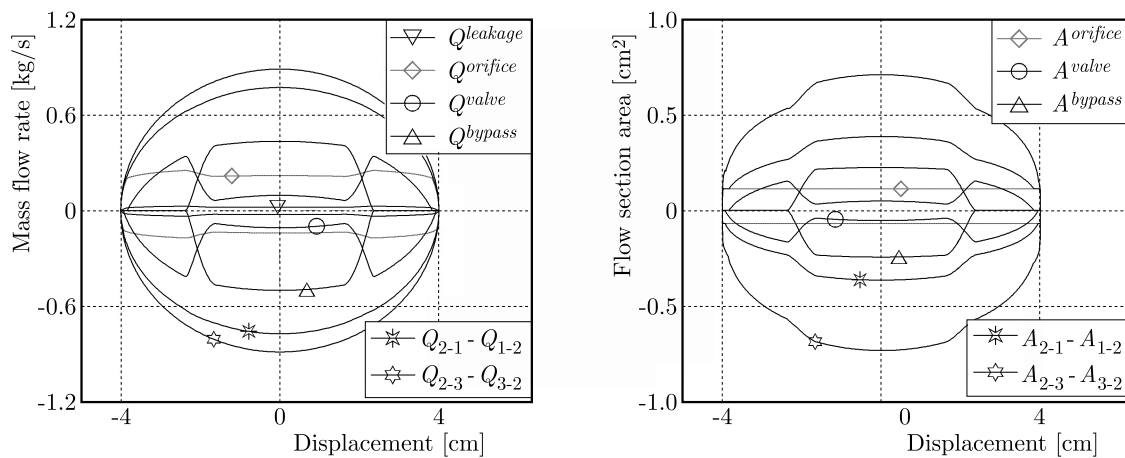


Fig. 6. Mass flow rates and effective areas ($f = 1.4$ Hz, $a = 4$ cm, $h = 2$ cm, $\alpha = 0.004$, $\gamma = 0.015$, $\delta = 0.04$, $S_v = 5$, $k_p = 2$, $k_b = 0.5$)

The presented diagrams allow one to better understand the oil flow processes between individual chambers of the damper. The most interesting of which are diagrams concerning flows through valves placed in the piston (Q^{valve} , A^{valve}) and in the bypass (Q^{bypass} , A^{bypass}). At the moment of bypass opening, the pressure p_1 suddenly decreases in the rebound chamber, which also causes the pressure difference to decrease in the neighbouring chambers. In effect, both the area A^{valve} and the flow rate Q^{valve} through the valve in the piston are thereby decreasing. For insignificantly higher values of the parameter S_v (e.g. for $S_v \approx 7$), characterising the preload force, this valve is closed within small displacements. The fact that the total flow rates Q_{2-1} and Q_{2-3} are changing very regularly, regardless of values of the parameters characterising the valves, is very interesting.

The diagrams of the damping force versus displacement and the relative piston velocity are presented in Figs. 7-9. The shown characteristics successively illustrate the influence of the dimensionless parameters α , δ and S_v , deciding on flows through the orifices placed in the piston. The force dependence on displacements is in all cases qualitatively similar to those discussed earlier. Much more interesting are diagrams of the damping force versus velocity. Inflection points determining the velocity ranges in which the characteristics have different waveforms are seen in the diagrams.

The parameter α determining the areas of constant orifices (it is assumed that $\alpha_{2-1} = \alpha$, $\alpha_{1-2} = \lambda\alpha$) is essential within the range of small velocities (Fig. 7). Along with the increasing parameter α , the inclination angle of the curve $F(\dot{x})$ decreases. This means that the damping forces for the given velocity are smaller, which is beneficial from the point of view of the ride

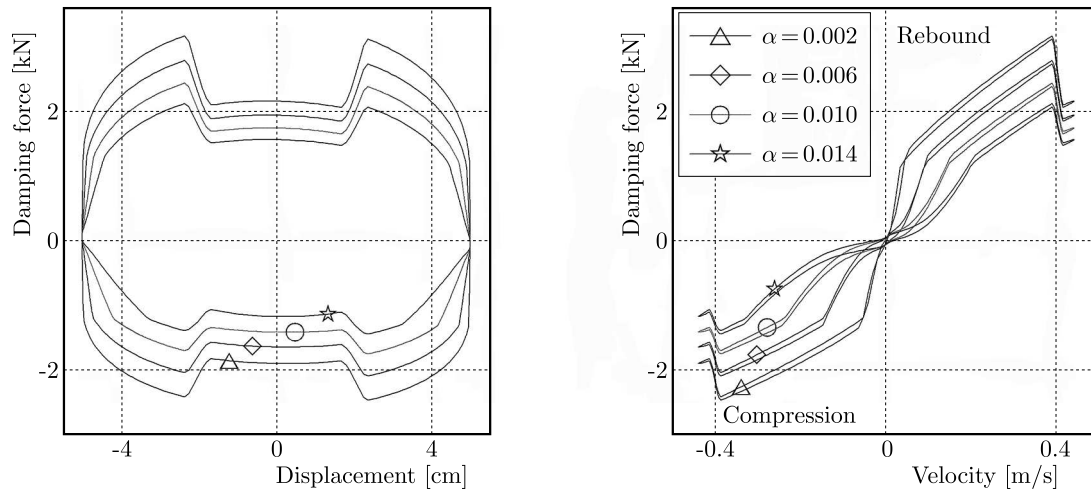


Fig. 7. Influence of the parameter α on the damping force characteristic ($f = 1.4$ Hz, $a = 5$ cm, $h = 2$ cm, $\delta = 0.04$, $\gamma = 0.012$, $S_v = 5$, $k_p = 2$, $k_b = 0.5$)

comfort. In the diagrams of forces versus velocities, narrow hysteresis loops occur, which means that the damper behaves differently in positive and negative ranges of relative displacements. For the excitation frequency $f = 1.4$ Hz (within the first resonance range) the loop width is nearly constant in the whole velocity range. When the frequency increases, the loop width significantly increases for low piston velocities and decreases for higher velocities. Thus, the characteristics are non-symmetrical. This asymmetry results mainly from various areas of the orifices through which the oil flows in the compression and rebound processes. The parameter λ decides about the model characteristic asymmetry. For $\lambda < 1$ (in simulations $\lambda = 0.6$), the damper offers higher resistances in the rebound process (for $\dot{x} > 0$) than in the compression one.

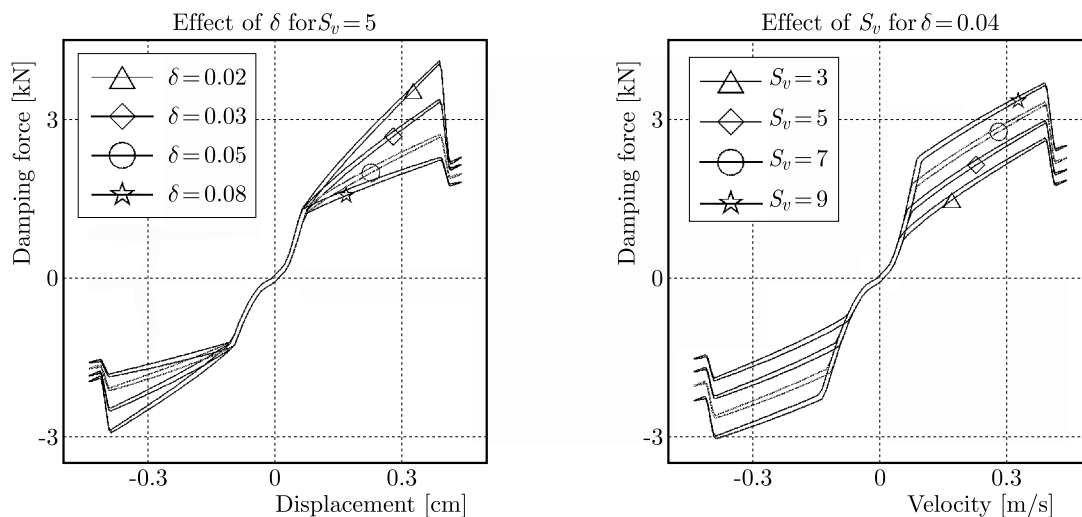


Fig. 8. Influence of the parameters δ and S_v on the force characteristics ($f = 1.4$ Hz, $a = 5$ cm, $h = 2$ cm, $\alpha = 0.004$, $\gamma = 0.012$, $k_p = 2$, $k_b = 0.5$)

The dimensionless parameter δ ($\delta_{2-1} = \delta$, $\delta_{1-2} = 0.8\delta$) determines the maximum areas of the orifices controlled by the pressure difference. It influences the characteristic in the higher velocities range (Fig. 8). When the piston velocity increases, the pressure difference in chambers K_1 and K_2 also increases and, in consequence, the valves in the piston are opening and the damping force decreases. For larger values of the parameter δ , in the compression as well as in the rebound process, the inclination of curves determining the damping force dependence on

velocity decreases. For high piston velocity near the piston zero position, the damping force of the shock absorber abruptly changes. The reason of this sudden change constitutes unblocking (or blocking) of flows through the bypass, which entails a decrease (or increase) in the pressure difference in the neighbouring chambers. The dimensionless parameter S_v characterises the preload force and decides about the location of the characteristic inflection point. This means that the point in which the inclination angle of curves changes (Fig. 8). When the parameter S_v changes, the characteristic shape related to opening of the orifices changes for higher velocities \dot{x} . Simultaneously, the maximum values of the damping force increase.

The damper performance within the range of large relative displacements of the piston depends additionally on parameters characterising the bypass, i.e. on the parameter γ ($\gamma_{2-1} = \gamma_{1-2} = \gamma$) (determining the orifice cross-section area), on distance h (it is assumed that $h_1 = h_2 = h$) determining placement of bypass openings in the working cylinder, and on the parameter k_b (characterising elastic properties of the valve).

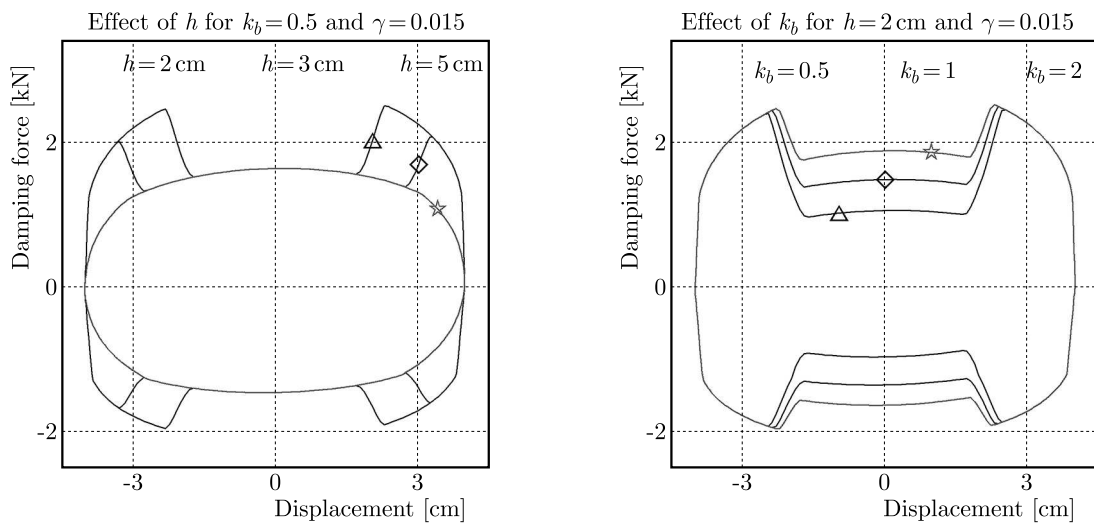


Fig. 9. Influence of the parameters h and k_b on the force characteristics ($f = 1.4$ Hz, $a = 4$ cm, $\beta = 0.004$, $\beta = 0.04$, $k_p = 2$)

Figure 9 shows the influences of the parameters h and k_b on the damping force as a function of piston displacements. The sudden change of the damping force occurs in two ranges of the displacements: $-h - r < x < -h + r$ and $h - r < x < h + r$. In these both ranges the area change is given by equation (2.24).

Since for higher values of the parameter h the oil flow through the bypass can be blocked only in the case of large piston displacements, the shock absorber in a wide range of vibration amplitudes behaves in a similar fashion as the classic shock absorber without the bypass (curve for $h = 5$ cm). The change of the characteristic occurs only when the amplitude exceeds a certain limited value, dependent on the parameter h . Along with a decrease of k_b , the damping force decreases significantly in the range of small displacements. For higher values of the parameter k_b , the bypass valve is not fully open, that is to say the effective area A bypass is smaller.

Summing up the above conclusions, the application of more stiff valves causes a decrease of the force step change (improves safety of the ride), however, it occurs at the expense of increasing damping forces within the range of small displacements (disadvantageous for the ride comfort). In some (currently produced) shock absorbers, the user can independently change the parameters of the bypass valve (parameter k_b), i.e. can adjust the damper characteristic for the conditions of the ride.

4. Conclusions

The non-linear model describing behaviour of the mono-tube shock absorber with a bypass, applied in passive systems of car suspensions, is proposed in this paper. Controlling of the oil flow between the damper chambers depending on the present pressure as well as on relative displacements of the piston is considered. A change in the oil bulk modulus caused by the pressure change is taken into account, and a relevant description allowing for efficient numerical simulations is provided. The developed model allows one to investigate the most important properties of mono-tube hydraulic shock absorbers in a wide range of amplitudes and excitation frequencies.

Several numerical simulations have been performed and their most important results are presented in this work. The influence of structural parameters of the shock absorber on the damping force characteristics is investigated in detail. Quantitative analysis indicates a significant influence of parameters depending on geometrical and physical properties of structural elements of valves in the main piston and in the bypass of the shock absorber. Although the results obtained are qualitatively consistent with the results of other authors, it is advisable to experimentally verify the assumptions used in the modeling process.

The application of bypasses allows one to obtain satisfactorily high damping forces for large relative displacements of the piston. In such a case, the shock absorber meets the requirements of a 'hard' damper, improving by that safety of the ride. When the relative displacements are small, the bypass is active and a 'soft' damper characteristic provides a high comfort level of the ride.

The global analysis of the efficiency of application of bypasses to vehicle shock absorbers requires development of a vehicle model with the tested damper and investigation of the influence various types of excitations on indices defining the comfort, (e.g. max or RMS value of velocity of the so-called spring-supported mass) as well as safety of the ride (e.g. dynamic component of the reaction exerted on the wheel of the vehicle). Determining such system responses for a sinusoidal signal with a variable frequency (e.g. sweep type), impulse or random signals allow one to better understand the shock absorber performance in various situations.

References

1. ALONSO M., COMAS Á., 2006, Modelling a twin tube cavitating shock absorber, *Proceedings of the Institution of Mechanical Engineers, Part D: Journal of Automobile Engineering*, **220**, 8, 1031-1040
2. CHO B.H., LEE H.W., OH J.S., 2002, Estimation technique of air content in automatic transmission fluid by measuring effective bulk modulus, *International Journal of Automotive Technology*, **3**, 2, 57-61
3. CZOP P., SŁAWIK D., 2011, A high-frequency first-principle model of a shock absorber and servo-hydraulic tester, *Mechanical Systems and Signal Processing*, **25**, 6, 1937-1955
4. FARJOD A., AHMADIAN M., CRAFT M., BURKE W., 2012, Nonlinear modeling and experimental characterization of hydraulic dampers: effects of shim stack and orifice parameters on damper performance, *Nonlinear Dynamics*, **67**, 2, 1437-1456
5. FERDEK U., ŁUCZKO J., 2012, Modeling and analysis of a twin-tube hydraulic shock absorber, *Journal of Theoretical and Applied Mechanics*, **50**, 2, 627-638
6. FERDEK U., ŁUCZKO J., 2015, Performance comparison of active and semi-active SMC and LQR regulators in a quarter-car model, *Journal of Theoretical and Applied Mechanics*, **53**, 4, 811-822
7. FERDEK U., ŁUCZKO J., 2016, Vibration analysis of a half-car model with semi-active damping, *Journal of Theoretical and Applied Mechanics*, **54**, 2, 321-332

8. GOLDASZ J., 2015, Theoretical study of a twin-tube magnetorheological damper concept, *Journal of Theoretical and Applied Mechanics*, **53**, 4, 885-894
9. KING L., 2014, Adjustable internal bypass shock absorber featuring a fluid flow regulator, U.S. Patent No. 8,820,495
10. LEE C.T., MOON B.Y., 2006, Simulation and experimental validation of vehicle dynamic characteristics for displacement-sensitive shock absorber using fluid-flow modelling, *Mechanical Systems and Signal Processing*, **20**, 2, 373-388
11. MANRING N.D., 1997, The effective fluid bulk-modulus within a hydrostatic transmission, *Journal of Dynamic Systems, Measurement, and Control*, **119**, 3, 462-466
12. MARKING J., 2014, Bypass for a suspension damper, U.S. Patent No. 8,627,932
13. MERRITT H.E., 1967, *Hydraulic Control Systems*, John Wiley & Sons
14. NORGAARD B.M., CIMINS D.J., 2009, Fluid flow regulation of a vehicle shock absorber/damper, U.S. Patent No. 7,628,259
15. PURDY D.J., 2000, Theoretical and experimental investigation into an adjustable automotive damper, *Proceedings of the Institution of Mechanical Engineers, Part D: Journal of Automobile Engineering*, **214**, 265-283
16. RAMOS J.C., RIVAS A., BIERA J., SACRAMENTO G., SALA J.A., 2005, Development of a thermal model for automotive twin-tube shock absorbers, *Applied Thermal Engineering*, **25**, 11, 1836-1853
17. SAPIŃSKI B., ROSÓŁ M., 2007, MR damper performance for shock isolation, *Journal of Theoretical and Applied Mechanics*, **45**, 1, 133-145
18. SILVEIRA M., PONTES B.R., BALTHAZAR J.M., 2014, Use of nonlinear asymmetrical shock absorber to improve comfort on passenger vehicles, *Journal of Sound and Vibration*, **333**, 7, 2114-2129
19. TALBOTT M.S., STARKEY J., 2002, An experimentally validated physical model of a high-performance mono-tube damper, SAE Technical Paper
20. TITURUS B., DU BOIS J., LIEVEN N., HANSFORD R., 2010, A method for the identification of hydraulic damper characteristics from steady velocity inputs, *Mechanical Systems and Signal Processing*, **24**, 8, 2868-2887
21. VAN DE VEN J.D., 2013, On fluid compressibility in switch-mode hydraulic circuits – Part I: Modeling and analysis, *Journal of Dynamic Systems, Measurement and Control*, **135**, 2, 021013

Manuscript received April 3, 2017; accepted for print October 17, 2017

SELECTED PROBLEMS OF DAMAGE DETECTION IN INTERNALLY SUPPORTED PLATES USING ONE-DIMENSIONAL DISCRETE WAVELET TRANSFORM

MICHAŁ GUMINIAK, ANNA KNITTER-PIĄTKOWSKA

Poznan University of Technology, Poznań, Poland

e-mail: michal.guminiak@put.poznan.pl; anna.knitter-piatkowska@put.poznan.pl

The paper is concerned with damage detection in plates while using the Discrete Wavelet Transform (DWT). Rectangular plate structures resting on a Winkler or elastic half-space type foundation, with free boundaries are examined. Plate bending is described and solved by the Boundary Element Method in a direct approach. Defects are introduced by additional edges forming slots in relation to the basic plate domain. Numerical investigation is conducted basing on signal analysis of the structural static response and by taking advantage of multi-resolution analysis (MRA) of the signal function which can be represented in a multi-scale manner. The obtained signal is decomposed with the use of Daubechies or Coiflet wavelet families. The white noise generator is used to model measurement inaccuracy which is an inevitable element of a real experiment. The efficiency of DWT of the contaminated signal in damage detection is studied.

Keywords: Kirchhoff plates, Boundary Element Method, Discrete Wavelet Transform

1. Introduction

The aim of the present work is to detect the localization of defects provided that they exist in the considered plate structure. This problem has focused much attention and has been extensively investigated by many scientists. Some approaches are based on e.g. optimization of loads (Mróz and Garstecki, 2005), information on natural frequencies (Dems and Mróz, 2001), heat transfer (Ziopaja *et al.*, 2011) or inverse analysis (Garbowski *et al.*, 2011; Knitter-Piątkowska and Garbowski, 2013). Variety of methods are based on comparison of the response of damaged and undamaged structures. It is a serious difficulty since the experiments on these two structures must be carried out with identical boundary and loading conditions. Moreover, a global response of a structure is insensitive to the localized damage. Therefore, the uncertainty following from variation of the conditions in experiments can be larger than the precision of measuring gauges. A new impact came from a modern signal processing method, namely wavelet transformation (WT) (Wang and Deng, 1999) also in its discrete form (DWT) (Knitter-Piątkowska *et al.*, 2014). WT can surprisingly well extract the desired detailed information from numerous data representing the global response of a damaged structure. Moreover, the information on the undamaged structure is not necessary.

Numerical investigation is carried out basing on signal analysis of the structural static response. Plate bending is described and solved by the Boundary Element Method in a direct form (Guminiak, 2016). The problem of damage detection in plates supported on the boundary and inside its domain was described in detail and illustrated e.g. in the paper (Knitter-Piątkowska *et al.*, 2017). The boundary integral equations were derived in a singular and non-singular approach (Guminiak, 2016). There were considered rectangular plates resting on the half-space flexible foundation with bilateral constraints and on the Winkler-type flexible supports with unilateral

(with the possibility of disconnection of the plate and the foundation) and bilateral (without such possibility) constraints. Defects in plates were modeled as slots near the plate boundary. As a structural response, vertical displacements or influence line of deflections were taken into consideration. Decomposition of the obtained signal was carried out using DWT with Daubechies 4, Coiflet 6 and Coiflet 12 families of wavelets. Multiresolution signal analysis using Mallat pyramid algorithm was applied (Mallat, 1999).

Although the considered problem is two-dimensional from the point of view of deformation description, the applied one-dimensional DWT leads to efficient results in defect detection. Considered examples quite correctly identify the presence and position of damage. For the selected example, white noise has been introduced too.

2. Theoretical consideration on wavelet transform

In the presented paper, the wavelet transform will be implemented, in which for the representation of the signal $f(t)$ a linear combination of wavelet functions is used. Therefore, they are well-suited for dealing with signals having discontinuities. The theory of the wavelet transformation (WT) was presented in many papers e.g. (Dodge, 2003). Foundations of WT will be recalled below. First, let us consider the continuous wavelet transform of the signal $f(t)$ in the time and frequency domain

$$Wf(a, b) = \int_{-\infty}^{\infty} f(t) \overline{\psi}_{a,b}(t) dt \quad (2.1)$$

where the overbar denotes the complex conjugate of the function under it. The function $\psi(t)$ is usually called the wavelet (mother) function and belongs to the field of $L^2(\mathbf{R})$. Additionally, the function $\psi(t)$ must satisfy the condition of admissibility (Mallat, 1999). This condition can be written in form of inequality

$$\int_0^{\infty} \frac{1}{\omega} |\Psi(\omega)|^2 d\omega < \infty \quad (2.2)$$

The function $\Psi(\omega)$ can be treated as the Fourier transform of the function $\psi(t)$:

$$\Psi(\omega) = \int_{-\infty}^{\infty} \psi(t) e^{-i\omega t} dt \quad (2.3)$$

The function $\Psi(\omega)$ is oscillatory and its average value is equal to zero, which leads to the equality

$$\int_{-\infty}^{\infty} \psi(t) dt = 0 \quad (2.4)$$

The mother wavelet may have real or complex-valued character. In the considered cases, real-valued wavelets will be applied. For signal decomposition, a set of wavelets (wavelet family) is applied. This set of functions is obtained by translating and scaling of the function ψ

$$\psi_{a,b} = \frac{1}{\sqrt{|a|}} \psi\left(\frac{t-b}{a}\right) \quad (2.5)$$

where t denotes a time or space coordinate, a is the scale parameter and b the translation parameter. The parameters a and b take real values ($a, b \in \mathbf{R}$) and, additionally, $a \neq 0$. The

element $1/\sqrt{a}$ is the scale factor which ensures constant wavelet energy regardless of the scale. It means that the norm $\|\psi_{a,b}\| = \|\psi\| = 1$. In the presented numerical solutions of plate bending problems the leading role takes the Discrete Wavelet Transform (DWT). According to this approach, the wavelet family can be obtained by substitution $a = 1/2^j$ and $b = k/2^j$ into equation (2.5). As a result, the following relation is obtained

$$\psi_{j,k}(t) = \sqrt{2^j} \psi(2^j t - k) \quad (2.6)$$

in which k and j are the scale and translation parameters, respectively. The meaning of these parameters for the simplest Haar wavelet is illustrated e.g. in papers (Guminiak, 2016; Dobrzycki and Mikulski, 2016).

Discrete signal decomposition can be written according to the Mallat pyramid algorithm in the known form (Mallat, 1999)

$$f_J = S_J + D_J + \dots + D_n + \dots + D_1 \quad n = J - j \quad (2.7)$$

where each component in signal representation is associated with a specific range of frequency and provides information at the scale level ($j = 1, \dots, J$). The discrete parameter J describes the level of multi-resolution analysis (MRA), S_J is a smooth signal representation, D_n and S_n are details and rough parts of the signal and D_1 corresponds with the most detailed representation of the signal. To fulfill the dyadic requirements of DWT, the function f_J must be approximated by $N = 2^J$ discrete values. The multi-resolution analysis according to the Mallat pyramid algorithm is illustrated in Fig. 1 and e.g. in papers (Mallat, 1999) and (Knitter-Piątkowska *et al.*, 2017).

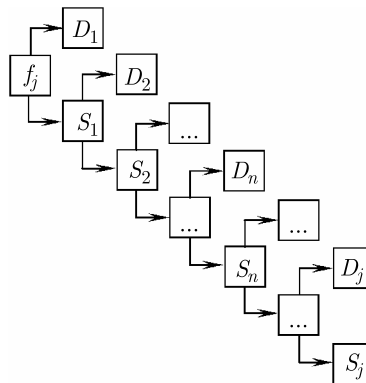


Fig. 1. Mallat pyramid algorithm (Mallat, 1999; Knitter-Piątkowska *et al.*, 2017)

In the current analysis of defect detection, Daubechies and Coiflet wavelets will be applied. These family of wavelets are orthogonal, continuous and have a compact support. Daubechies wavelets are asymmetrical and Coiflet wavelets are nearly symmetric. Both families have sharp edges. These wavelet families do not require a large number of coefficients hence they are widely used in solving a broad range of problems e.g. image analysis or defect detection. The order of Daubechies wavelet family functions has the range between 2 and 20 and they are even numbers only. The Coiflet function accepts the even integers 6, 12, 18, 24 and 30. Daubechies wavelet of the second order corresponds to the simplest Haar wavelet. Basis and scaling functions of Daubechies 4 and Coiflet 6 wavelets are presented in Fig. 2.

3. Simulation of measurement errors in numerical data

Measurement (observational) error is the difference between the measured value of quantity and its true value (Dodge, 2003). Measurement errors are an inevitable element of any real experiment

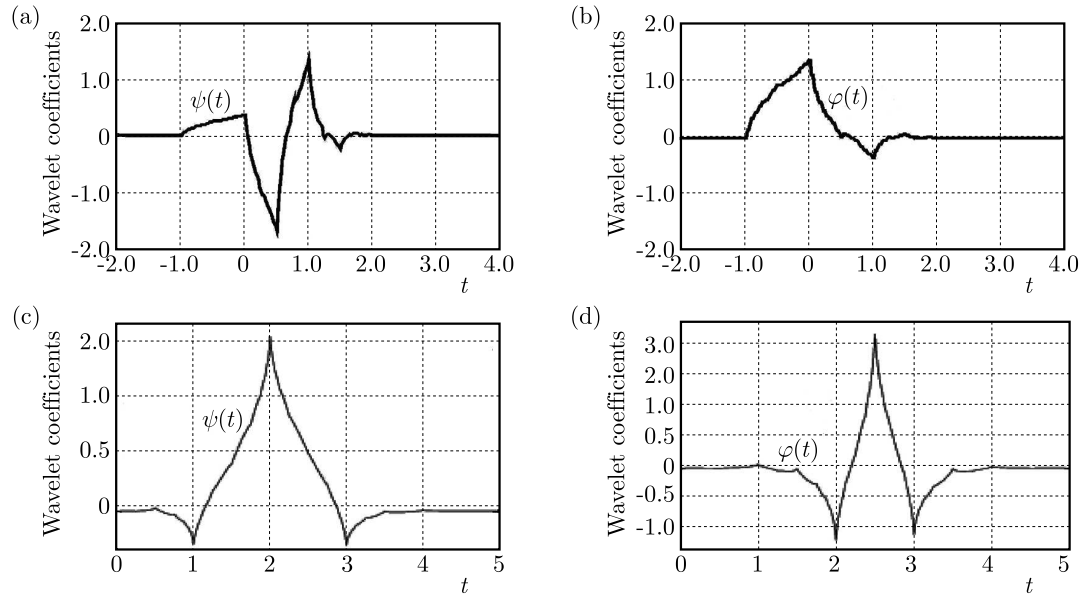


Fig. 2. Basis function (mother): (a) Daubechies 4, (c) Coiflet 6 wavelet and scaling function (father), (b) Daubechies 4 and (d) Coiflet 6 wavelet

and may be caused inter alia by measuring devices, measuring methods, measuring person, miscalculations or the influence of the environment on the previously mentioned causes. To investigate the efficiency of DWT of a contaminated signal in damage detection and localization, measurement errors are accounted for by introduction of white noise to the output from computer simulated experiments. An example of randomly generated white noise is illustrated in Fig. 3.

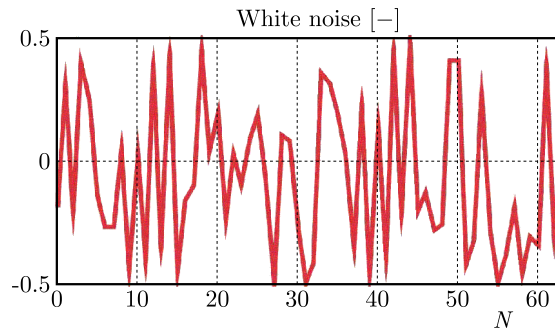


Fig. 3. White noise, values from -0.5 to 0.5

To adjust the size of the disturbance to the intensity of the analyzed response signal of the structure, white noise has been scaled by multiplying it by the constant number corresponding to the order of designated signal magnitude.

4. Problem formulation of defect detection

The aim of this work is to detect the localization of a defect provided that the defect (damage) exists in the considered plate structure. Numerical investigation is conducted being based on signal analysis of the structural static response. The plate material is assumed as linear-elastic. Plates are resting on elastic foundations: the Winkler type with bilateral and unilateral constraints and the elastic half-space with bilateral constraints. The plate bending is described and solved by the Boundary Element Method in the direct approach. The static fundamental solution (Green function) for a pure infinite plate is used (Guminiak, 2016)

$$w^*(r) = \frac{1}{8\pi D} r^2 \ln(r) \quad (4.1)$$

which is a solution to the biharmonic equation

$$\nabla^4 w^*(r) = \frac{1}{D} \delta(r) \quad (4.2)$$

for a thin isotropic plate, where $D = Eh^3/[12(1 - \nu^2)]$ is plate stiffness, h is plate thickness, E and ν are the Young modulus and Poisson ratio, $\delta(r)$ is the Dirac delta and $r = \sqrt{x^2 + y^2}$.

4.1. Modeling of the elastic internal support

Mathematical description of behaviour of an elastic flexible foundation is usually given in form of an equation which connects reaction forces of the foundation q_0 with displacements w

$$w(P) = \int_{\Omega_0} q_0(Q) g_0(P, Q) d\Omega_0 \quad (4.3)$$

For the simplest Winkler-type foundation in the discrete approach, a set of finite number of single independent and flexible supports is taken into account. Each of them has its stiffness k . For this type of foundation, the flexibility function has the following form

$$g_0(P, Q) = \frac{1}{k} \delta(P, Q) \quad (4.4)$$

where $\delta(P, Q)$ is the Dirac delta. After discretization, the Winkler-type foundation is described by the following diagonal stiffness matrix

$$\mathbf{K}_0 = \text{diag}(k) \quad (4.5)$$

The elastic half-space foundation with the elastic modulus E_0 and the Poisson ratio ν_0 is considered. For this type of foundation, after its discretization using sub-domains of the constant type, the flexibility function has the form

$$g_0(P, Q) = \frac{1 - \nu_0^2}{\pi E_0 r} \quad (4.6)$$

and deformation of the foundation is expressed as

$$w_i = \frac{1 - \nu_0^2}{\pi E_0} \sum_{j=1}^J q_0(j) \int_{S_j} \frac{1}{r_{PQ}} dS_j \quad (4.7)$$

In matrix notation, equation (4.7) will have the form

$$\mathbf{w}_0 = \mathbf{D}_0 \mathbf{q}_0 \quad (4.8)$$

where \mathbf{D}_0 is the fully-populated flexibility matrix of the foundation. Using matrix equation (4.8), the reaction forces of the foundation can be obtained

$$\mathbf{q}_0 = \mathbf{K}_0 \mathbf{w}_0 \quad (4.9)$$

where $\mathbf{K}_0 = \mathbf{D}_0^{-1}$ is the fully-populated stiffness matrix of the foundation $\mathbf{K}_0 = [k_{ij}]$.

The integral

$$\int_{S_j} \frac{1}{r_{PQ}} dS_j \quad (4.10)$$

can be calculated analytically (Fig. 4)

$$\int_{\Omega_0} \frac{1}{r} d\Omega_0 = x_p \ln\left(\frac{y_p + r_1}{y_k + r_4}\right) - y_k \ln\left(\frac{x_p + r_4}{x_k + r_3}\right) + x_k \ln\left(\frac{y_k + r_3}{y_p + r_2}\right) - y_p \ln\left(\frac{x_k + r_2}{x_p + r_1}\right) \quad (4.11)$$

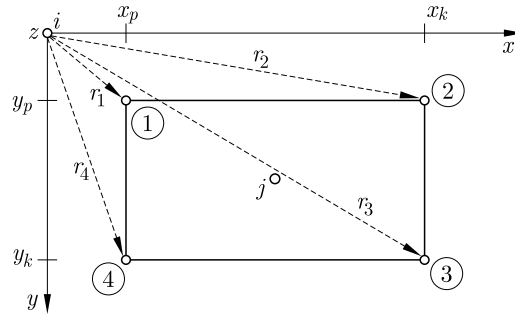


Fig. 4. Analytical calculation of integral (4.10) – assumed designations

4.2. Boundary and domain integral equations

Let the reaction forces of the foundation be realized as: a) set of concentrated forces $R_0^{(j)}$ or b) forces $q_0(j)$ distributed over the plate sub-domains. The Bézine technique (Bézine and Gamby, 1978) is introduced to derive the boundary-domain integral equations

$$\begin{aligned}
 c(\mathbf{x})w(\mathbf{x}) + \int_{\Gamma} \left[T_n^*(\mathbf{y}, \mathbf{x})w(\mathbf{y}) - M_{ns}^*(\mathbf{y}, \mathbf{x})\frac{dw(\mathbf{y})}{ds} - M_n^*(\mathbf{y}, \mathbf{x})\varphi_n(\mathbf{y}) \right] d\Gamma(\mathbf{y}) \\
 = \int_{\Gamma} [\tilde{T}_n(\mathbf{y})w^*(\mathbf{y}, \mathbf{x}) - M_n(\mathbf{y})\varphi_n^*(\mathbf{y}, \mathbf{x})] d\Gamma(\mathbf{y}) - \sum_{j=1}^J R_0^{(j)}w^*(j, \mathbf{x}) + \int_{\Omega} p(\mathbf{y})w^*(\mathbf{y}, \mathbf{x}) d\Omega(\mathbf{y})
 \end{aligned} \quad (4.12)$$

$$\begin{aligned}
 c(\mathbf{x})\varphi_n(\mathbf{x}) + \int_{\Gamma} \left[\bar{T}_n^*(\mathbf{y}, \mathbf{x})w(\mathbf{y}) - \bar{M}_{ns}^*(\mathbf{y}, \mathbf{x})\frac{dw(\mathbf{y})}{ds} - \bar{M}_n^*(\mathbf{y}, \mathbf{x})\varphi_n(\mathbf{y}) \right] d\Gamma(\mathbf{y}) \\
 = \int_{\Gamma} [\tilde{\bar{T}}_n(\mathbf{y})\bar{w}^*(\mathbf{y}, \mathbf{x}) - M_n(\mathbf{y})\bar{\varphi}_n^*(\mathbf{y}, \mathbf{x})] d\Gamma(\mathbf{y}) - \sum_{j=1}^J R_0^{(j)}\bar{w}^*(j, \mathbf{x}) + \int_{\Omega} p(\mathbf{y})\bar{w}^*(\mathbf{y}, \mathbf{x}) d\Omega(\mathbf{y})
 \end{aligned}$$

for case a) and

$$\begin{aligned}
 c(\mathbf{x})w(\mathbf{x}) + \int_{\Gamma} \left[T_n^*(\mathbf{y}, \mathbf{x})w(\mathbf{y}) - M_{ns}^*(\mathbf{y}, \mathbf{x})\frac{dw(\mathbf{y})}{ds} - M_n^*(\mathbf{y}, \mathbf{x})\varphi_n(\mathbf{y}) \right] d\Gamma(\mathbf{y}) \\
 = \int_{\Gamma} [\tilde{T}_n(\mathbf{y})w^*(\mathbf{y}, \mathbf{x}) - M_n(\mathbf{y})\varphi_n^*(\mathbf{y}, \mathbf{x})] d\Gamma(\mathbf{y}) \\
 - \sum_{j=1}^J \left(\int_{\Omega_0(j)} q_0(j)w^*(j, \mathbf{x}) d\Omega_0(j) \right) + \int_{\Omega} p(\mathbf{y})w^*(\mathbf{y}, \mathbf{x}) d\Omega(\mathbf{y})
 \end{aligned} \quad (4.13)$$

$$\begin{aligned}
 c(\mathbf{x})\varphi_n(\mathbf{x}) + \int_{\Gamma} \left[\bar{T}_n^*(\mathbf{y}, \mathbf{x})w(\mathbf{y}) - \bar{M}_{ns}^*(\mathbf{y}, \mathbf{x})\frac{dw(\mathbf{y})}{ds} - \bar{M}_n^*(\mathbf{y}, \mathbf{x})\varphi_n(\mathbf{y}) \right] d\Gamma(\mathbf{y}) \\
 = \int_{\Gamma} [\tilde{\bar{T}}_n(\mathbf{y})\bar{w}^*(\mathbf{y}, \mathbf{x}) - M_n(\mathbf{y})\bar{\varphi}_n^*(\mathbf{y}, \mathbf{x})] d\Gamma(\mathbf{y}) \\
 - \sum_{j=1}^J \left(\int_{\Omega_0(j)} q_0(j)\bar{w}^*(j, \mathbf{x}) d\Omega_0(j) \right) + \int_{\Omega} p(\mathbf{y})\bar{w}^*(\mathbf{y}, \mathbf{x}) d\Omega(\mathbf{y})
 \end{aligned}$$

for case b), where \mathbf{x} is the source point, \mathbf{y} is the field point and $r = |\mathbf{y} - \mathbf{x}|$. The second boundary-domain integral equations (4.12)₂ for case a) and (4.13)₂ for case b) can be obtained replacing the unit concentrated force $P^* = 1$ by the unit concentrated moment $M_n^* = 1$. Such

a replacement is equivalent to the differentiation of the first boundary integral equation (4.12)₁ or (4.13)₁ with respect to the coordinate n at a point \mathbf{x} belonging to the plate domain, and letting this point approach the boundary and taking n coincide with the normal to it. The force $\tilde{T}_n(\mathbf{y})$ can be treated as an equivalent shear force $V_n(\mathbf{y})$ on a fragment of the boundary which is located far from the corner, or it plays the role of the corner force $R_n(\mathbf{y})$ which is distributed on a small fragment of the boundary close to the corner. In the case of the free edge, we must combine the rotation angle in the tangent direction $\varphi_s(\mathbf{y})$ with the fundamental function $M_{ns}^*(\mathbf{y})$. Since the relation between $\varphi_s(\mathbf{y})$ and the deflection is known: $\varphi_s(\mathbf{y}) = dw(\mathbf{y})/ds$, the angle of rotation $\varphi_s(\mathbf{y})$ can be evaluated while using a finite difference scheme of the deflection with two or more adjacent nodal values. In this analysis, the employed finite difference scheme includes the deflections of two adjacent nodes.

4.3. Construction of the set of algebraic equation

The set of algebraic equations in matrix notation has the following form

$$\begin{bmatrix} \mathbf{G}_{BB} & \mathbf{G}_{BS} & \mathbf{G}_{Bw}\mathbf{K}_0 \\ \mathbf{\Delta} & -\mathbf{I} & \mathbf{0} \\ \mathbf{G}_{wB} & \mathbf{G}_{wS} & \mathbf{G}_{ww}\mathbf{K}_0 \end{bmatrix} \begin{Bmatrix} \mathbf{B} \\ \varphi_s \\ \mathbf{w} \end{Bmatrix} = \begin{Bmatrix} \mathbf{F}_B \\ \mathbf{0} \\ \mathbf{F}_R \end{Bmatrix} \quad (4.14)$$

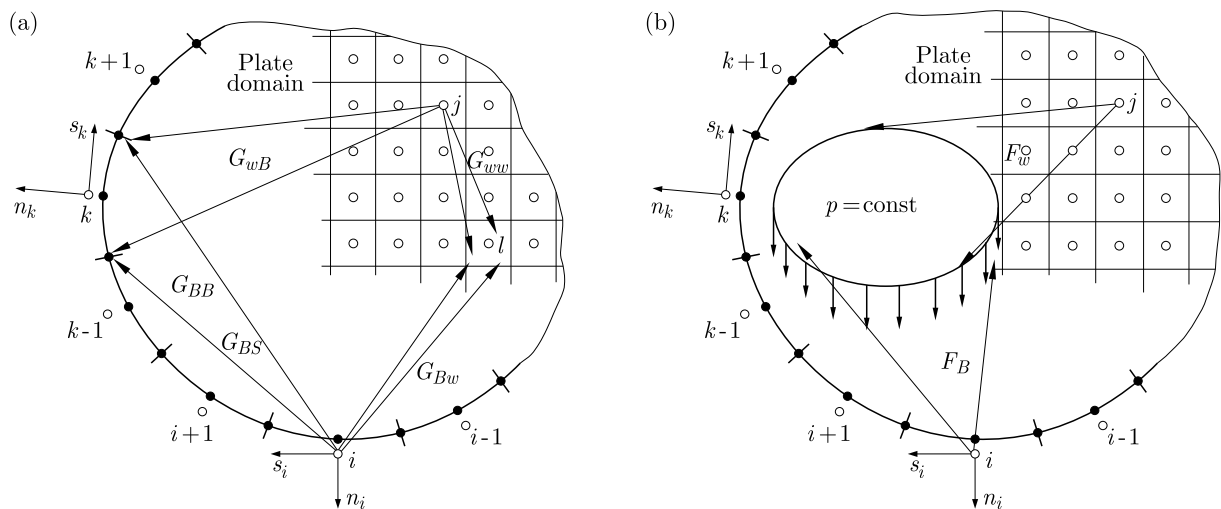


Fig. 5. Construction of the characteristic matrix

Suitable designations of sub-matrices occurring in matrix equation (4.14) are presented in Fig. 5 for (a) characteristic matrix and (b) right-hand-side vector, where: \mathbf{G}_{BB} and \mathbf{G}_{BS} are the matrices of dimension $(2N \times 2N)$ and of dimension $(2N \times S)$ grouping boundary integrals and depending on the type of the boundary, where N is the number of boundary nodes (or the number of constant type elements). S is the number of boundary elements along the free edge; \mathbf{G}_{Bw} is the matrix of dimension $(2N \times M)$ grouping values of the fundamental function w^* established at the internal collocation points; $\mathbf{\Delta}$ is the matrix grouping difference operators connecting the angle of rotations in the tangent direction with deflections of suitable boundary nodes if the plate has a free edge; \mathbf{G}_{wB} is the matrix of dimension $(M \times 2N)$ grouping the boundary integrals of the appropriate fundamental functions, where M is the number of the internal collocation points and N is the number of the boundary nodes; \mathbf{G}_{wS} is the matrix of dimension $(M \times S)$ grouping the boundary integrals of the appropriate fundamental functions; \mathbf{G}_{ww} is the matrix of dimension $(M \times M)$ grouping the values of the fundamental function w^* established at the internal collocation points; \mathbf{F}_B is the right-hand side vector in which all

elements are calculated in the coordinate systems connected with the boundary physical nodes over the loading area; \mathbf{F}_w is the right-hand side vector whose all elements are calculated in the coordinate systems connected with the internal collocation points over the loading area; \mathbf{K}_0 is the stiffness matrix of the foundation.

4.4. Calculation of deflection and internal forces inside the plate domain

The solution of the set of equations (4.14) allows one to determine suitable boundary variables and values of deflection at the internal collocation points associated with flexible constraints. Then, using the same boundary and domain integral equation (4.12)₁ or (4.13)₁, deflection at an arbitrary point of plate domain can be calculated. The collocation point is located inside the plate domain, hence the coefficient $c(\mathbf{x})$ is equal to one. Plate deflection can be expressed as the sum of the deflection depending on boundary variables, the deflections (or reactions) at the internal collocation points and the external loading, respectively

$$w = w(\bar{\mathbf{B}}) + w(\mathbf{w}) + w(p) \quad (4.15)$$

To calculate deflection at a selected point, equations (4.12)₁ or (4.13)₁ can be directly used for Winkler and elastic half-space type of foundations, respectively.

5. Numerical examples

Rectangular plate structures with free boundaries are considered. Defects are introduced by additional edges forming slots or holes in relation to the basic plate domain. The Boundary Element Method is applied to solve a thin plate bending problem. Each plate edge is divided into 30 boundary elements of the constant type. The collocation point is located slightly outside the plate edge, which is estimated by the parameter $\varepsilon = \bar{\delta}/d$, where δ is the real distance of the collocation point from the plate edge and d is the element length. For each example, it is assumed $\varepsilon = 0.001$. Diagonal boundary terms in the characteristic matrix are calculated analytically and the rest of them use 12-point Gauss quadrature. Plate properties are $E = 205.0$ GPa, $\nu = 0.3$, $h = 0.04$ m. The plates are loaded statically. The static concentrated external load $P = 10.0$ kN which is moving along the line parallel to the global coordinate x is replaced by an equivalent uniformly distributed loading p acting over the square surface of dimensions 0.05 m \times 0.05 m. Except for that, plates subjected only to a uniformly distributed loading $q = 10.0$ kN/m² acting on the surface are considered too. The examined plates are resting on the Winkler and elastic half-space types of foundation. The stiffness coefficient of the Winkler foundation is $k = 5000.0$ kN/m³ and the properties of the elastic half-space are $E_0 = 30000$ kN/m², $\nu_0 = 0.4$. As a structural response, the influence line of deflections and vertical displacements are taken into account. The data is gathered in one measurement point in equal time intervals or in 64 points. Decomposition of the obtained signal is carried out using DWT with Daubechies 4, Coiflet 6 and Coiflet 12 families of wavelets. For the selected example, white noise is introduced too.

5.1. Example 1

The plate resting on the Winkler foundation loaded by a static concentrated force P which is moving along the edge parallel to the x direction is considered and presented in Fig. 6. The measurement point D has the following coordinates: $x_D = 2.2$ m and $y_D = 0.2$ m. The introduced plate defect is described by the parameter: $e = 0.005$ m.

The results of calculation for bilateral constraints are presented in Fig. 7 for (a) Daubechies 4 and (b) Coiflet 12 families of wavelets, respectively. Detail 1 of the decomposed response signal is analysed. It is visible that in both cases the damage location is clearly depicted by the evident

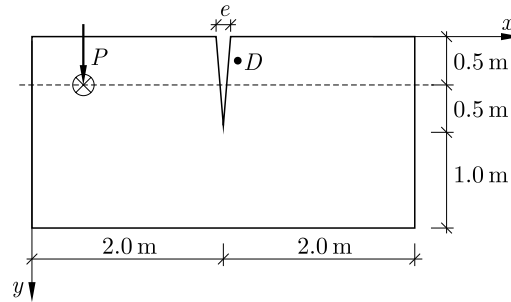


Fig. 6. Considered plate structure

disturbances and high picks. Nonetheless, noteworthy is the fact that in Coiflet 12 DWT, the transformed signal is smoother and the boundary disturbances in transformation window are slightly smaller (Fig. 7b).

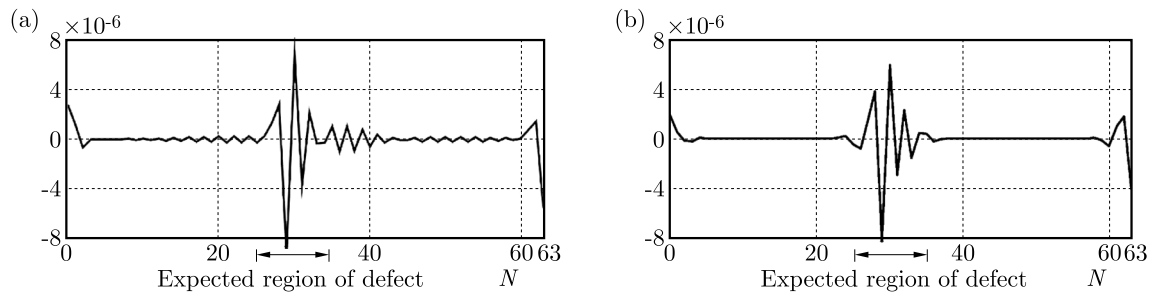


Fig. 7. DWT (Daubechies 4, Coiflet 12, detail 1) signal: vertical displacements measured at the point D , N – number of measurements

The results of calculation for unilateral constraints are presented in Fig. 8 for (a) Daubechies 4 and (b) Coiflet 12 families of wavelets, respectively. Detail 1 of the decomposed response signal has been analysed. However, in this analysis, expected disturbances of the transformed signal do not properly indicate the damage location. The highest pick is unfortunately elsewhere. Presumably, at a finite number of iterations with exclusion of nodes in which the reaction force is negative, the problem formulation in terms of the BEM causes bad conditioning of the characteristic matrix.

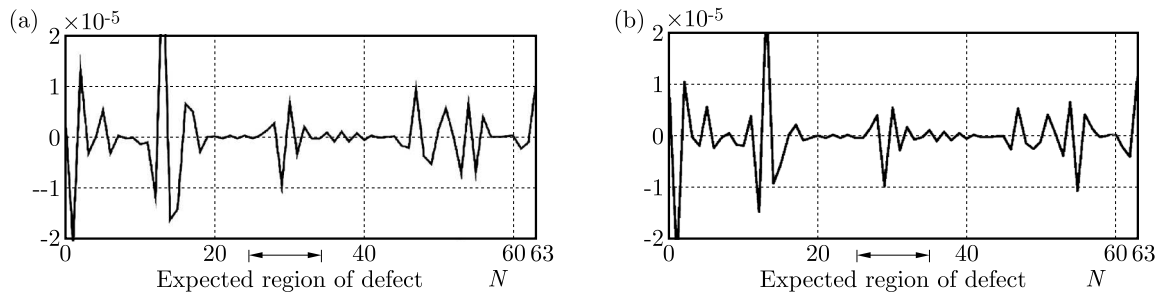


Fig. 8. DWT (Daubechies 4, Coiflet 12, detail 1) signal: vertical displacements measured at the point D , N – number of measurements

5.2. Example 2

The plate resting on the Winkler foundation with bilateral constrains and loaded by a static uniformly distribute loading q is considered and presented in Figs. 9 and 12. Damage is identified by the parameter $e = 0.005$ m.

a) External loading q is acting on the square whose corners (A , B , C and D) have coordinates x and y , respectively (Fig. 9): $A(0.6\text{ m};0.6\text{ m})$, $B(1.4\text{ m};0.6\text{ m})$, $C(0.6\text{ m};1.4\text{ m})$ and $D(1.4\text{ m};1.4\text{ m})$.

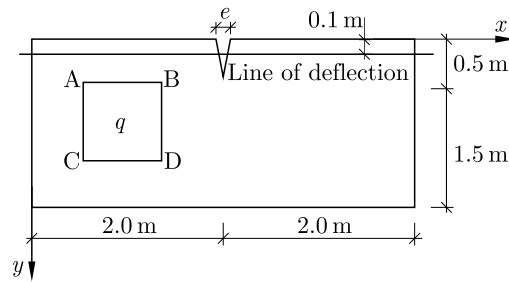


Fig. 9. Considered plate structure

The results of calculation are presented in Fig. 10 for (a) Daubechies 4 and (b) Coiflet 6 families of wavelets, respectively. Detail 1 of the decomposed response signal has been analysed. The damage is undoubtedly located properly in both transforms by a high pick.

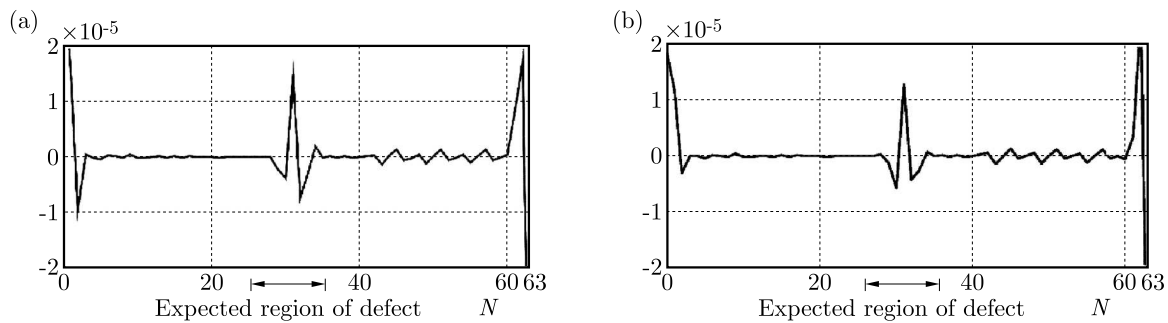


Fig. 10. DWT (Daubechies 4, Coiflet 6, detail 1) signal: vertical displacements, N – number of measurement points

In this example, randomly generated white noise has been introduced. The maximum intensity of the introduced disturbance has 5% of the response signal measured value (relative to the highest measured value). The results of calculation are presented in Fig. 11 for (a) Daubechies 4 and (b) Coiflet 6 families of wavelets respectively. The DWT (detail 1) of the vertical displacements has been analysed. In both cases, the damage is properly localized by a high pick, however, previous experiments show that 5% noise in the transformed data is for DWT the upper limit of damage detection capability. While considering more contaminated signals, one can apply signal denoising techniques, e.g. the wavelet shrinkage method (Dobrzycki and Mikulski, 2016).

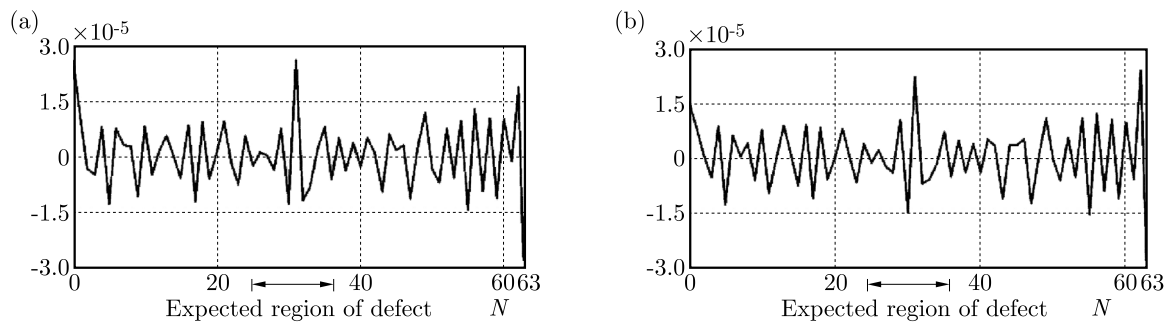


Fig. 11. DWT (Daubechies 4, Coiflet 6, detail 1) signal: vertical displacements, N – number of measurement points

b) External loading q is acting on the square whose corners (A , B , C and D) have coordinates x and y , respectively (Fig. 12): $A(2.6\text{ m};0.2\text{ m})$, $B(3.4\text{ m};0.2\text{ m})$, $C(2.6\text{ m};1.0\text{ m})$ and $D(3.4\text{ m};1.0\text{ m})$.

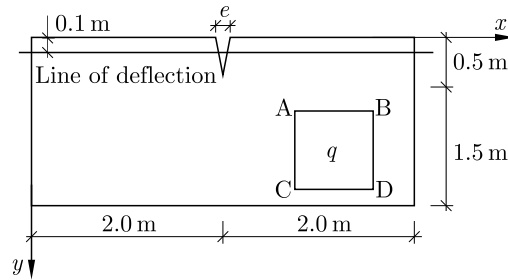


Fig. 12. Considered plate structure

The results of calculation are presented in Fig. 13 for (a) Daubechies 4 and (b) Coiflet 6 families of wavelets respectively. Detail 1 of the transformed vertical displacements signal is shown. In both cases, the damage existence and location are properly detected.

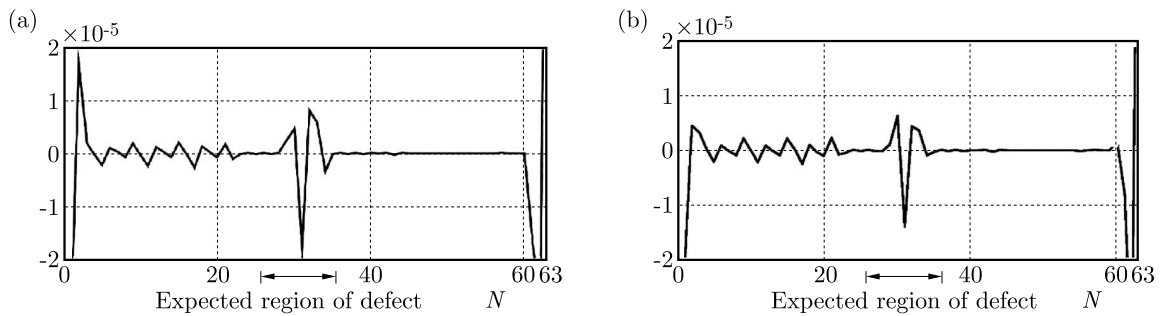


Fig. 13. DWT (Daubechies 4, Coiflet 6, detail 1) signal: vertical displacements, N – number of measurement points

5.3. Example 3

The plate resting on the elastic half-space foundation, loaded by a static concentrated force P which is moving along the edge parallel to the x direction is considered. The plate geometry and loading is presented in Fig. 14. The measurement point D has following coordinates: $x_D = 2.2\text{ m}$ and $y_D = 0.2\text{ m}$. The introduced plate defect is described by the parameter: $e = 0.01\text{ m}$. Bilateral constraints are assumed in the analysis. The results of calculation are presented in Fig. 15 for (a) Daubechies 4 and (b) Coiflet 12 wavelet families, respectively. The DWT (detail 1) of the vertical displacements influence line is shown. The damage location is clearly depicted by the evident disturbances of the transformed data in both cases. It is worth to emphasize that while using Coiflet 12 DWT, the transformed signal is smoother and the disturbance region is slightly shorter (Fig. 15b).

5.4. Example 4

The plate resting on the elastic half-space foundation with bilateral constrains and loaded by a static uniformly distribute loading q is considered. The plate geometry is the same as presented in Figs. 12 and 16. The damage is identified by the parameter $e = 0.005\text{ m}$. The analysis has been carried out for the bilateral constraints.

a) External loading q is acting on the square whose corners (A , B , C and D) have coordinates x and y , respectively (Fig. 16): $A(2.6\text{ m};0.2\text{ m})$, $B(3.4\text{ m};0.2\text{ m})$, $C(2.6\text{ m};1.0\text{ m})$ and $D(3.4\text{ m};1.0\text{ m})$. The results of DWT (detail 1) of the vertical displacement signals measured in 64 points are

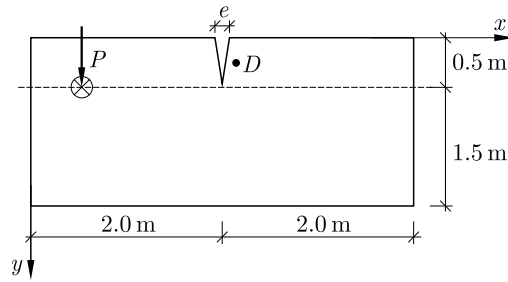


Fig. 14. Considered plate structure

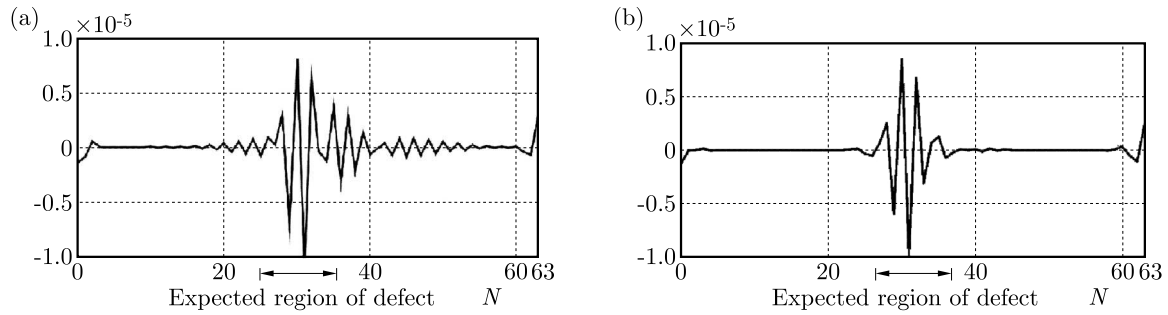


Fig. 15. DWT (Daubechies 4, Coiflet 12, detail 1) signal: vertical displacements measured at the point D , N – number of measurements

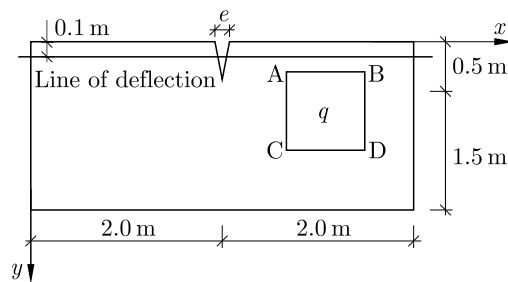


Fig. 16. Considered plate structure

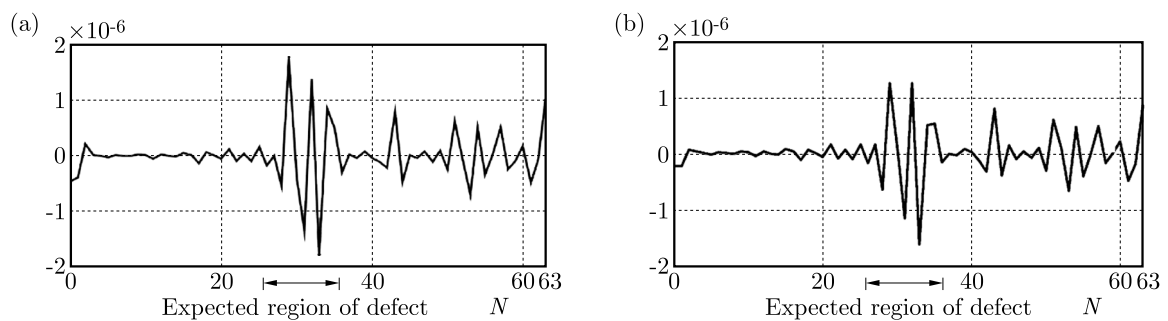


Fig. 17. DWT (Daubechies 4, Coiflet 12, detail 1) signal: vertical displacements, N – number of measurement points

presented in Fig. 17 for (a) Daubechies 4 and (b) Coiflet 12 wavelets. The damage location can be clearly determined by high picks in both cases despite quite large disturbances on the right hand side in the windows of transformation.

b) External loading q is acting on the square whose corners (A , B , C and D) have coordinates x and y , respectively (Fig. 12): $A(2.8\text{ m};1.0\text{ m})$, $B(3.6\text{ m};1.0\text{ m})$, $C(2.8\text{ m};1.8\text{ m})$ and $D(3.6\text{ m};1.8\text{ m})$. The results of DWT (detail 1) of the vertical displacement signals measured in 64 points are

presented in Fig. 18 for (a) Daubechies 4 and (b) Coiflet 6 families of wavelets, respectively. In both cases, the damage existence and location are properly detected by high picks of the transformed signal.

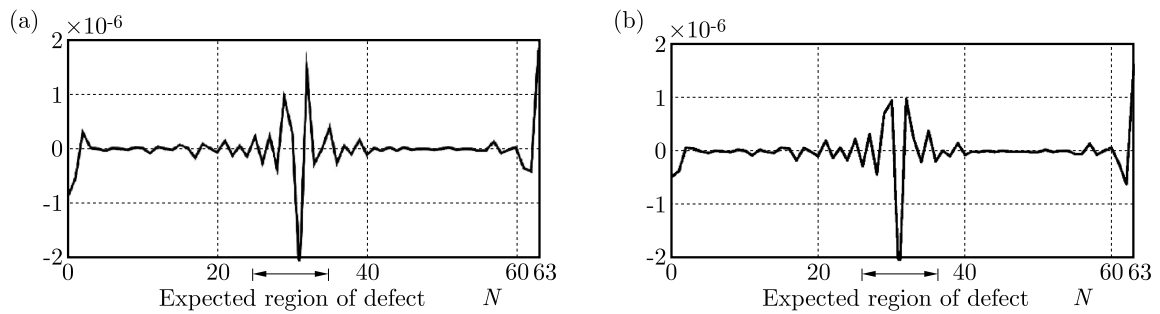


Fig. 18. DWT (Daubechies 4, Coiflet 6, detail 1) signal: vertical displacements measured along the line of deflection, N – number of measurement point

6. Concluding remarks

The implementation of a discrete dyadic wavelet transformation to identification of signal discontinuity in the analysis of plates resting on internal flexible supports is presented in this paper. The novelty is the introduction of defects by additional edges forming slots or holes in the relation to the basic plate domain. Thin (Kirchhoff) plate bending is described by boundary-domain integral equations and solved using the Boundary Element Method (BEM). The BEM is particularly useful to carry out a numerical experiment of plate bending considering abnormal shapes of the plate edge having the character of cracks or tears. Although the considered issue is two-dimensional from the point of view of deformation description, the applied one-dimensional DWT leads to efficient results in defect detection. The proposed method does not provide detection of defects localized inside the plate domain. The measured response signal is assumed as the influence line of deflection considered at a selected point and the deflection line. The minimum number of measurements has been assumed as sixty four. The damage is properly localized while using asymmetric Daubechies 4 wavelet as well as nearly symmetrical Coiflet 6 or 12 wavelet in signal decomposition. Detail 1, as the most detailed representation of the transformed signal, is taken into consideration. The efficiency of DWT in damage detection and localization does not depend on the position of the uniformly distributed load, yet the distance of the measurement point from the damaged area in the case of the influence line of deflection is crucial. White noise as an inaccuracy of the measured signal has also been considered in the selected example. The position of defects has been quite correctly identified by a high pick of the transformed (both Daubechies and Coiflet wavelet) data, however it should be noted that 5% noise in the transformed data is for DWT the upper limit of damage detection capability. While considering more contaminated signals, one can apply signal denoising techniques, e.g. the wavelet shrinkage method.

References

1. BÉZINE G., GAMBY D.A., 1978, A new integral equations formulation for plate bending problems, *Advances in Boundary Element Method*, Pentech Press, London
2. DEMS K., MRÓZ, Z., 2001, Identification of damage in beam and plate structures using parameter-dependent frequency changes, *Engineering Computations*, **18**, 1/2, 96-120

3. DOBRZYCKI A., MIKULSKI S., 2016, Using of continuous wavelet transform for de-noising signals accompanying electrical treeing in epoxy resins, *Przegląd Elektrotechniczny (Electrotechnical Review)*, **92**, 4, 26-29, DOI: 10.15199/48.2016.04.07
4. DODGE Y., 2003, *The Oxford Dictionary of Statistical Terms*, Oxford University Press
5. GARBOWSKI T., MAIER G., NOVATI G., 2011, Diagnosis of concrete dams by flat-jack tests and inverse analysis based on proper orthogonal decomposition, *Journal of Mechanics of Materials and Structures*, **6**, 1-4, 181-202
6. GUMINIAK M., 2016, Static and free vibration analysis of thin plates of the curved edges by the boundary element method considering an alternative formulation of boundary conditions, *Engineering Transactions*, **64**, 1, 3-32
7. KNITTER-PIĄTKOWSKA A., GARBOWSKI, T., 2013, Damage detection through wavelet transform and inverse analysis, *VI International Conference on Adaptive Modelling and Simulation (ADMOS 2013)*, J. Moitinho de Almeida, P. Diez, C. Tiago, and N. Pares (Edit.), Barcelona, 389-400
8. KNITTER-PIĄTKOWSKA A., GUMINIAK M., HLOUPIS G., 2017, Crack identification in plates using 1-D discrete wavelet transform, *Journal of Theoretical and Applied Mechanics*, **55**, 2, 481-496
9. KNITTER-PIĄTKOWSKA A., GUMINIAK M., PRZYCHODZKI M., 2014, *Damage Detection in Truss Structure Being the Part of Historic Railway Viaduct Wavelet Transformation*, T. Łodygowski, J. Rakowski and P. Litewka (Edit.), CRC Press/Balkema, Taylor and Francis Group
10. MALLAT S.G., 1989, A theory for multiresolution signal decomposition: the wavelet representation, *IEEE Transactions on Pattern Analysis and Machine Intelligence*, **11**, 7, 674-693
11. MALLAT S.G., 1999, *A Wavelet Tour of Signal Processing*, Academic Press, San Diego
12. MRÓZ Z., GARSTECKI A., 2005, Optimal loading conditions in design and identification of structures. Part 1: Discrete formulation, *International Journal of Structural and Multidisciplinary Optimization*, **29**, 11-18
13. WANG Q., DENG X., 1999, Damage detection with spatial wavelets, *International Journal of Solids and Structures*, **36**, 3443-3448
14. ZIOPAJA K., POZORSKI Z., GARSTECKI A., 2011, Damage detection using thermal experiments and wavelet transformation, *Inverse Problems in Science and Engineering*, **19**, 1, 127-153

Manuscript received June 7, 2017; accepted for print October 26, 2017

TIG AND LASER BEAM WELDED JOINTS – SIMPLIFIED NUMERICAL ANALYSES

BARBARA NASIŁOWSKA

Military University of Technology, Institute of Optoelectronics, Warsaw, Poland
e-mail: barbara.nasilowska@wat.edu.pl

AGNIESZKA DEREWONKO, ZDZISŁAW BOGDANOWICZ

Military University of Technology, Faculty of Mechanical Engineering, Warsaw, Poland
e-mail: agnieszka.derewonko@wat.edu.pl; zbogdanowicz@wat.edu.pl

Regardless of the welding method, a new joint and the surrounding area are inevitably subjected to thermo-physical perturbation. The paper presents analyses of many different issues involved in welding and potential solutions including adoption of simplifying assumptions, application of numerical algorithms and development of reliable representative models. The Finite Element Method is used to determine residual stress distribution, using results from thermo-physical tests and widely known mechanical properties of metals subjected to welding processes. Experimental and numerical methods for determining residual stress are compared for welds generated using both TIG (Tungsten Inert Gas, Gas Tungsten Arc Welding) and a laser beam. This data reveals that it is necessary to precisely define location of the analyzed welded fragment to correctly determine thermal boundary conditions.

Keywords: TIG, laser beam, welded joints, steel 904L, numerical analysis, residual stress

1. Introduction

During a welding process, the areas around the joints are subjected to thermal and structural changes. Uneven distribution of both temperature and heat flow contributes to a diversity of thermal and mechanical properties of metals. Steel, while being heated only in a narrow areas of joints, increases in volume, thereby resisting to adjacent areas of cold steel and causing thermal stress (Jiao *et al.*, 2014). Thermal stress affects the structural balance, which adds mechanical stress to the already deformed element.

Residual stress in welded joints is an indicator of fatigue life. Two methods are traditionally used to determine these types of stress (Susmel and Tovo, 2008; Zamiri Akhlaghi, 2009). The first method uses mathematical analysis of the nominal stress in constant-amplitude load cases. With the second method, called “hot spot” (Susmel and Tovo, 2008; Zamiri Akhlaghi, 2009), the nominal stress is determined empirically or experimentally using the finite element method (FEM).

Structural changes induced during welding include formation of a geometry notch at the point of stress concentration (Blacha and Karolczuk, 2016). The stress is most concentrated in the “hot spot” at the bottom of the geometry notch of the welded area, potentially resulting in fracture initiation (Kluger and Łagoda, 2016). Stress in pipes of austenitic stainless steel 304 and duplex steel S32750 subjected to a circumferential weld were analyzed in the previous study. Surface tensile stresses in the axis of a circumferential weld prepared using the TIG (Tungsten Inert Gas, Gas Tungsten Arc Welding) method were 250-350 MPa and 350-450 MPa for welds prepared from 304 austenitic stainless steel and S32750 duplex steel, respectively (Lee and Chang, 2014).

Numerical and experimental evaluation of the heat affected zone as well as the stress of thermal loads and phase transformations in the front welded joint executed with a laser beam, is presented in papers edited by Piekarska and Kubiak (2011, 2013). Temperature-dependent thermo-physical parameters were adopted for a low-carbon weldable steel. Analysis of a three-dimensional numerical model of the temperature field in a welded joint included the movement of the liquid metal in the weld pool and the latent heat associated with the changes of the material state (Tan and Shin, 2015).

Distribution of the residual stress in the cross section at the place of the laser beam impact on the top (face) and bottom (ridge) surface of welds for different welding parameters $v = 100$ m/h, $P = 3.5$ kW (a) and $v = 30$ m/h, $P = 2.0$ kW (b) have also been established in the literature (Tan and Shin, 2015).

Numerical simulation of the residual stress in flat elements made of low-alloy steel butt-welded with a laser beam is shown in (Tan and Shin, 2015; Voss, 2011) in order to illustrate the stress generated in the elements during welding and cooling down to 293 K. Studies have shown that the highest tensile stresses appear in the central part of the welded joint element after cooling (Murakawa, 2013; Ma *et al.*, 2014; Benasciutti *et al.*, 2014; Dong *et al.*, 2014).

The effect of the initial stress generated in the manufacturing process of SUS316 austenitic stainless steel pipeline (diameter 200 mm, length 800 mm, wall thickness 10 mm) on the joint welded with a laser beam ($P = 12$ kW, $v = 1$ m/min) in experimental and mathematical aspects was compared by Voss (2011).

The results revealed that initial stress in the steel prior to the welding process increased the residual stress after welding by approximately 10%. Despite the widespread use of 904L austenitic stainless steel, there is no thorough comparison between the efficacies of numerical analysis and experimental research in determining the residual stress when welded by using both the TIG and laser beam methodologies.

2. Experiment

The research has been carried out on samples of 904L stainless steel welded by the TIG method using infusible MTC MT-904L tungsten electrode ($\emptyset 2.5$ mm) and G/W 20 25 5 CuL (20% Cr, 25% Ni, 4.5% Mo, 1.5% Cu) weld, according to production technology used i.al. for manufacturing chemical apparatus at the Department of Mechanical Chemical Equipment, Azoty Group in Tarnów.

Table 1. Parameters of 904L welding austenitic stainless steel with a laser beam

Welding parameters	IU	Data
Focal length of lens	mm	260
Spot on sample surface	mm	$\emptyset 0.4$
Power	kW	$P = 4.5$
Welding speed	m/min	$v = 1.4$
Protective gas	–	helium

The weld has been made with three weldments (Fig. 1c). After chamfering the edges V (Fig. 1a), welding with two weldments from the face side was performed (Fig. 1c – 1 and 2), then the ridge was cut (Fig. 1b – grinding) and welded (Fig. 1c – 3).

Joints made with a laser beam ($45 \times 15 \times 5$ mm) were prepared using CO₂ laser TRIUMF 1005, with parameters shown in Table 1, at the Centre for Laser Technologies of Metals.

The experimental tests of the residual stress of welded joints were conducted at the Institute of Non-Ferrous Metals, Light Metals Division in Skawina (Fig. 2).

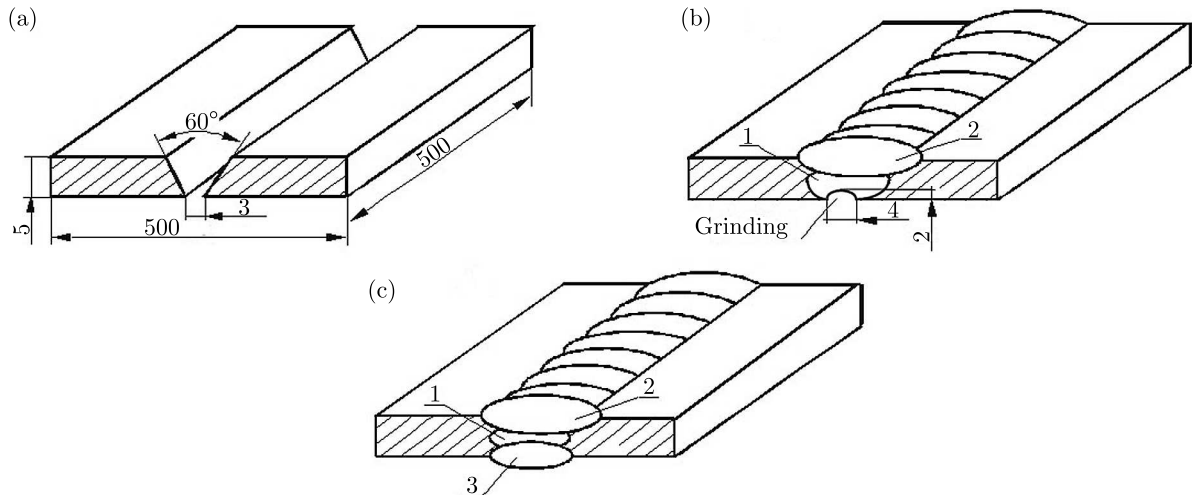


Fig. 1. Geometry of components preparation of a metal sheet before TIG welding of steel 904L (a) and scheme of ridge cutting (b) and welding (c) according to technology used at the Chemical Equipment Plant Construction – Group Azoty in Tarnów

Measurements of the residual stresses (second type σ^S – balancing within the crystallites area) have been performed on the surface of the samples in the weld (W), the heat affected zone (HAZ) and the base material (BM) for welds made using the TIG and laser beam methods. σ_x transverse and longitudinal σ_y distributions of the residual stress were assessed, and numerical analyses were performed using FEA (finite element analysis).

3. Subject of research

The subject of research was austenitic stainless steel 904L (containing %: Ni 24-26, Cr 19-21, Mo 4-5, 1.2-2.0 Cu, $Mn \leq 2.0$, $N \leq 0.15$, $Si \leq 0.7$, $P \leq 0.030$, $S \leq 0.010$, $C \leq 0.02$), supplied by the Department of Mechanical Chemical Equipment Group Azoty in Tarnów, produced by Outokumpu Stainless AB in Stockholm, Sweden (Fig. 2) (PN-EN 10088).

4. Experimental study of residual stress

Test results of the residual stress for a joint made with a laser beam are shown in Fig. 3a. The stress component perpendicular to the axis of the joint σ_x for the joint (S) and the heat affected zone (HAZ) are compressive stresses. However, a component parallel to the axis of the joint σ_y is tensile stress with the highest value detected in the HAZ equal to $\sigma_y = 296$ MPa.

For welds made by the TIG method, the component σ_x is tensile. The maximum value of it is 282 MPa, and in the heat affected zone $\sigma_x = 123$ MPa.

In the zone of the base material (BM) there occurred compressive stresses for samples welded with the laser beam method $\sigma_x = -279$ MPa, $\sigma_y = -250$ MPa, and with the TIG method $\sigma_x = -143$ MPa, $\sigma_y = -279$ MPa (Fig. 3).

5. Numerical FEM analysis of welded joints

Attempts to carry out numerical analyses of the weld cooling phase after the process of TIG and laser beam welding are presented in (Fig. 4). The cooling was achieved by introducing a non-linear function of temperature in time in the form of piecewise linear representation. Thermo-

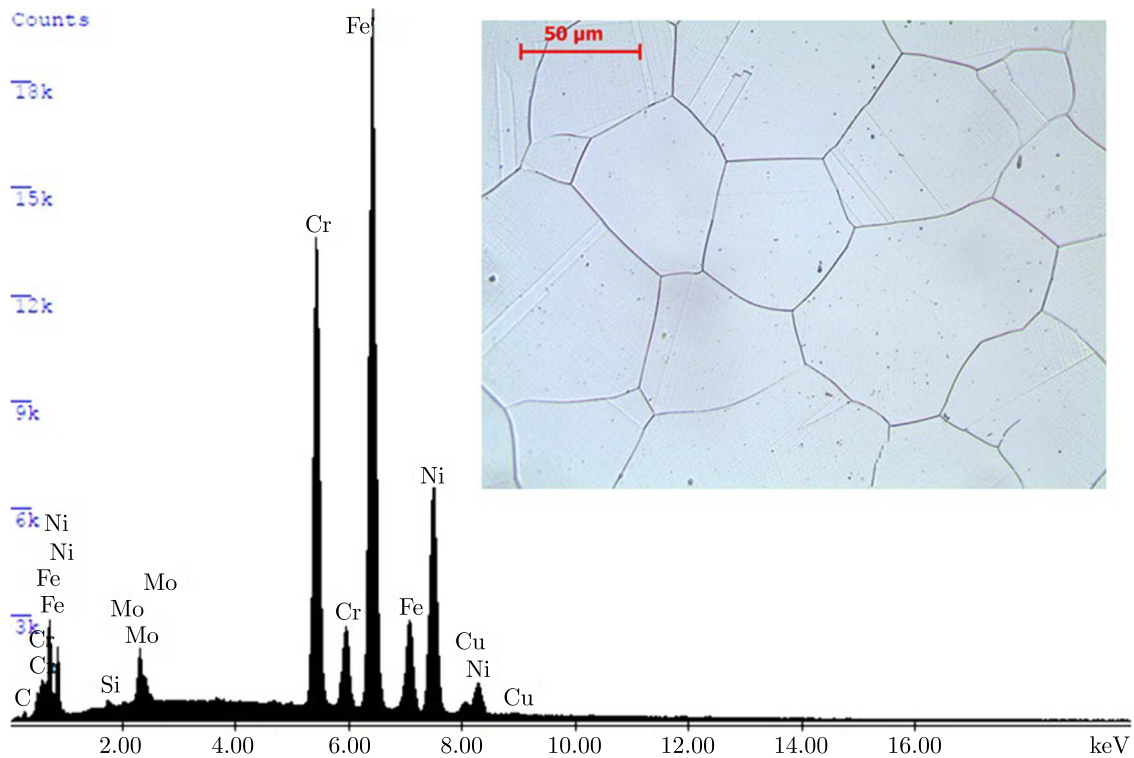


Fig. 2. An example of chemical composition of steel 904 L

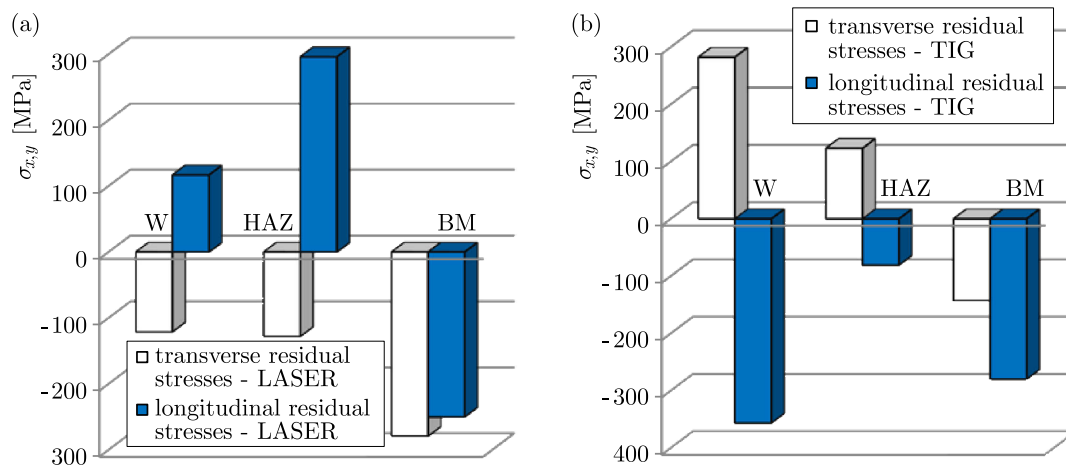


Fig. 3. Residual stress in the weld (W), in the heat affected zone (HAZ) and in the base material (BM) of joints made with the laser beam and TIG methods in the x -axis (a) and y -axis (b)

-mechanical coupling occurring between thermal and mechanical boundary conditions was applied in the analyses.

The fully coupled problems, where the thermal solution affects the structural solution and the structural solution affects the thermal solution, are presented by a general scheme shown in Fig. 4.

The coupling between thermal and mechanical phenomena depends on material properties and temperature distribution resulting from the welding process, which is the source of data for analysis of transient heat transfer. Mechanical equilibrium equations are introduced assuming a quasi-stationary load process.

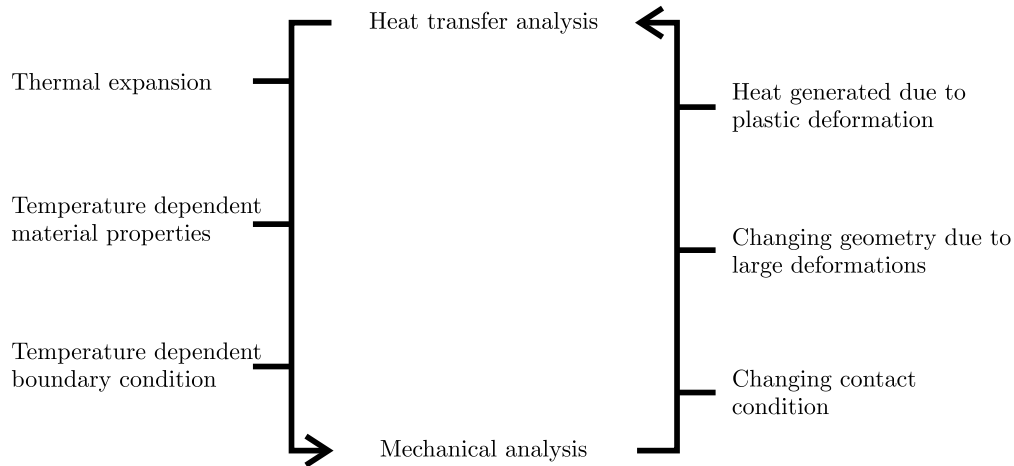


Fig. 4. Schematic of coupled thermo-mechanical analyses

Mathematical formulation of heat transfer with the diffusion and convection part in the tensor form is based on the energy conservation law

$$\rho c_p \frac{\partial T}{\partial t} + \rho c_p \mathbf{T} \nabla T - \nabla^T (\mathbf{\Lambda} \nabla T) = Q \quad (5.1)$$

where ρ is mass density, c_p – specific heat, $\mathbf{\Lambda}$ – conductivity tensor, T – temperature, t – time and Q is a heat source or heat sink. v is the velocity field calculated by coupling a momentum balance application mode such as incompressible Navier-Stokes. The gradient operator ∇ is given by $\nabla = \left(\frac{\partial}{\partial x}, \frac{\partial}{\partial y}, \frac{\partial}{\partial z} \right)$.

The initial condition and prescribed temperature in transient analysis are defined by

$$T = T_i(x, t) \quad T(x, 0) = T_i(x) \quad (5.2)$$

where x denotes space coordinates.

Thermal boundary conditions for weld cooling are described by convective heat transfer to the environment. They are given by

$$-\lambda \frac{\partial T}{\partial n} = h(T - T_\infty) \quad (5.3)$$

where h is the film coefficient, T_∞ – environmental temperature.

The temperature $\mathbf{T}(x, t)$ in the given element is interpolated from nodal values $\mathbf{T}(t)$ of the element by shape functions $\mathbf{N}(x)$ (Marc®, 2011)

$$\mathbf{T}(x) = [\mathbf{N}(x)]^T \mathbf{T} \quad (5.4)$$

The equation used for heat transfer is given by (Marc®, 2011)

$$\mathbf{C}(\mathbf{T}) \dot{\mathbf{T}} + \mathbf{K}(\mathbf{T}) \mathbf{T} = \mathbf{Q} \quad (5.5)$$

where \mathbf{T} is the vector of nodal temperatures (time derivative of the temperature vector), \mathbf{Q} – heat flux vector for the node, $\mathbf{C}(\mathbf{T})$ – matrix of heat capacity, $\mathbf{K}(\mathbf{T})$ – conductivity and convection matrix, $\mathbf{C}(\mathbf{T})$ and $\mathbf{K}(\mathbf{T})$ are dependent on temperature.

The Galerkin method is used to write a coupled set of first order ordinary differential equation (5.6) of the heat transfer problem.

The transient solution is obtained by using a backward difference scheme

$$\left[\frac{1}{\Delta t} \mathbf{C}(\mathbf{T}^*) + \mathbf{K}(\mathbf{T}^*) \right] \mathbf{T}^n = \mathbf{Q}(\mathbf{T}^*) + \frac{1}{\Delta t} \mathbf{C}(\mathbf{T}^*) \mathbf{T}^{n-1} \quad (5.6)$$

where \mathbf{T}^* is an average nodal temperature vector.

In the time increment Δt , the first iteration within the increment n and is taken as an extrapolated value of the previous two increments: $n - 1$ and $n - 2$

$$\mathbf{T}^* = \frac{1}{2}(3\mathbf{T}^{n-1} + \mathbf{T}^{n-2}) \quad (5.7)$$

\mathbf{T}^* follows from

$$\mathbf{T}^* = \frac{1}{2}(\mathbf{T}^{n-1} + \mathbf{T}^n) \quad (5.8)$$

for next iterations. The iterations are stopped when

$$\|\mathbf{T}_{i-1}^* - \mathbf{T}_i^*\|_{max} \leq \Delta \mathbf{T}_{tol3} \quad (5.9)$$

where $\Delta \mathbf{T}_{tol3}$ is the maximum error in the estimated nodal temperature.

The changing geometry due to thermal deformation caused an effect called the large strain. The element and load matrices are derived using an Updated Lagrangian formulation.

The geometric shape was mapped based on the images of metallographic transverse specimens of a weld made with the laser beam (Fig. 5a) and TIG (Fig. 5b) methods.

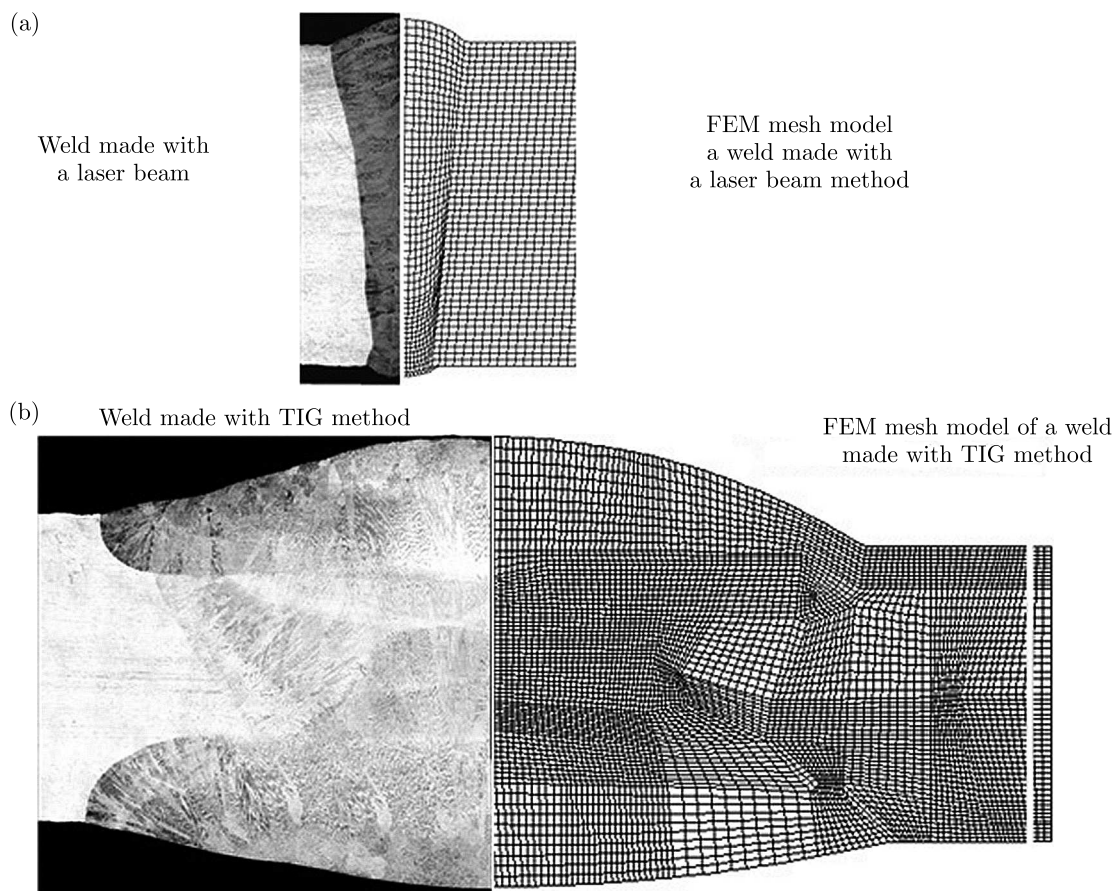


Fig. 5. Finite element mesh of welds made with the laser beam (a) and TIG (b) methods

It is assumed that the shape of the model made with both TIG and the laser beam method is not symmetrical.

The geometry of the finite models reflecting a part of the actual shape of the welds made with the laser and TIG methods has been divided into 280 560 and 408 625 isoparametric hexahedral (solid) finite elements described with trilinear shape functions, respectively. The stiffness of the solid element is formed using eight-point Gaussian integration. The use of such elements allows for coupled thermomechanical analysis.

The average edge length of a single finite element in this area is 0.02 mm. Due to necessity to create elements with small dimensions of the weld area, it is possible to map only a part of the welded metal sheets with a width of 5 mm.

To create the model, the following simplifications have been introduced:

- a) neglecting non-essential external influences (e.g. welding grips),
- b) simplification of shapes of the areas under consideration,
- c) neglecting the welding shrinkage,
- d) assumption that materials density is constant in time and homogeneous in the whole area,
- e) neglecting phase transitions and liquid-solid transformation,
- f) assumption of homogeneity of the part contained in a given area for:
 - Young's modulus $E(T)$ (PN-EN 19988)
 - Poisson's ratio $\nu(T)$ (Jiao *et al.*, 2014)
 - thermal conductivity $\lambda(T)$ (Nasiłowska, 2016)
 - thermal diffusivity T (Nasiłowska, 2016)
 - specific heat T (Nasiłowska, 2016).

Four zones are extracted:

- a) base material (BM),
- b) heat affected zone (HAZ),
- c) joint core (S1, W1-weld),
- d) residual weld zone (S2, W2-weld).

The physical properties of the austenitic stainless steel are defined based on standards (PN-EN 19988), analysis of the literature (Piekarska, 2007; Ranatowski, 2009) and our in-house studies (Bogdanowicz *et al.*, 2015). These properties, both mechanical and thermal are introduced as a function of temperature. The same parameters have been adopted for each designated zone of the weld.

The temperature load as a function of time has been introduced in each zone of the weld. Nonlinear curves for the weld prepared with the laser beam (Piekarska, 2007) and TIG (Ranatowski, 2009) methods are shown in Figs. 6a and 6b.

In the case of welding with the laser beam, in the core of the weld (W1) and in the residual weld zone (W2), the maximum temperature exceeds the melting point of the steel. Therefore, each of these two curves is divided into two parts: above and below the melting point assumed as 1420 K. In the other two zones, the maximum temperatures do not exceed the melting point of the steel; therefore, they are left in the form shown in Fig. 6.

It is assumed that the environment (air) affects the surface of the weld model on its face and the ridge side, and cools the joint. The ambient temperature of 293 K has been assumed in the two control points by using the POINT FLUX option. It is assumed that cooling influences only the nodes of the upper and lower walls of the sample discrete model.

In order to map the real welding conditions, there are boundary conditions (support) given based on the structure of the welding torches.

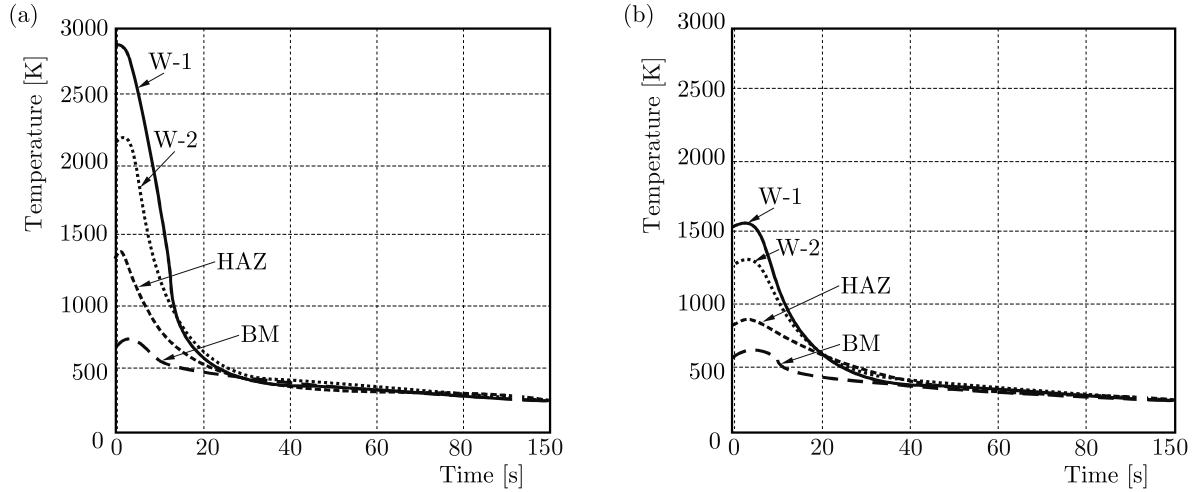


Fig. 6. The temperature distribution as a function of welding time for the zones of a weld made with the laser beam (a) and TIG (b) methods

One of the major challenges is to appropriately represent the mechanical boundary conditions. Due to thermal deformations generated in the cooling process and the fact that only a small part of the welded sheets is modelled, it is necessary to use other forms of simulation for the impacts of the operating handles in which the sheets are mounted during the welding process. The influence of the rest of the structure is mapped by introducing springs with an appropriate stiffness defined by

$$k_i = \frac{E(T)A}{l_s L} \quad (5.10)$$

where k_i is the modulus of elasticity of the spring, A – area of the cross section of the sample respective wall (front or side), $E(T)$ – Young's modulus of the base material in function of time, l_s – the number of springs.

The length L is determined according to the part of the steel sheet which it replaces, i.e., both the front and back wall of the sample

$$L = \frac{1000 - \text{sample width}}{2} \quad (5.11)$$

whereas for the side walls

$$L = \frac{1000 - \text{sample length}}{2} \quad (5.12)$$

The determined factors of the spring elasticity are assigned to this type of elements in which the length is equal to 1 mm. All degrees of freedom are removed from the nodes at the end of the spring. A schematic method for introducing the mechanical boundary conditions is illustrated in Fig. 7. The positioning of the springs is asymmetrical to ensure lack of rigid movement.

Layers of the reduced stress calculated according to the Huber-Mises-Hencky yield criterion for the models of welds made with the laser beam and TIG methods are shown in Figs. 8 and 9.

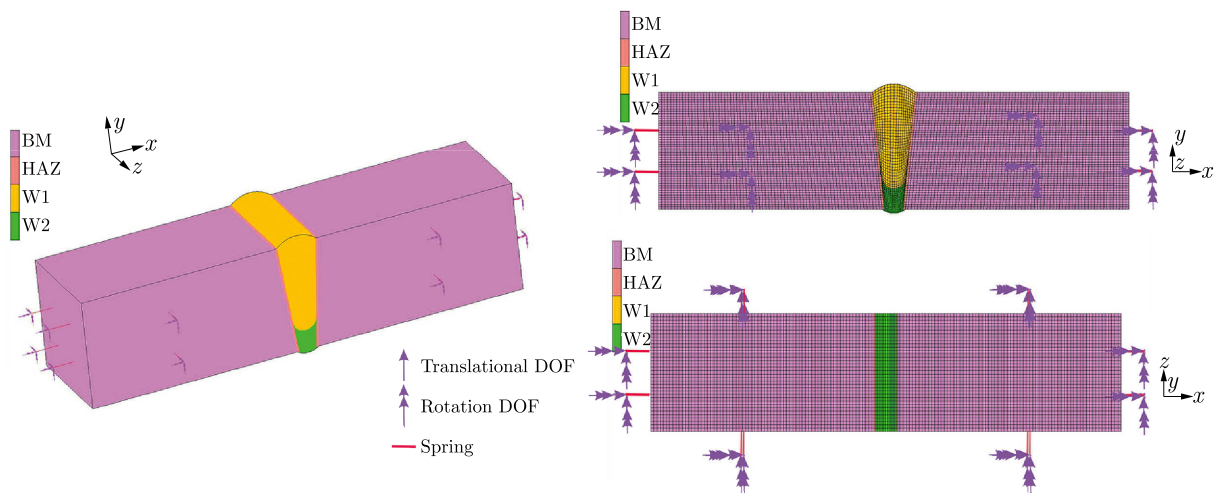


Fig. 7. Schematic of boundary conditions for the weld model created with the laser beam method

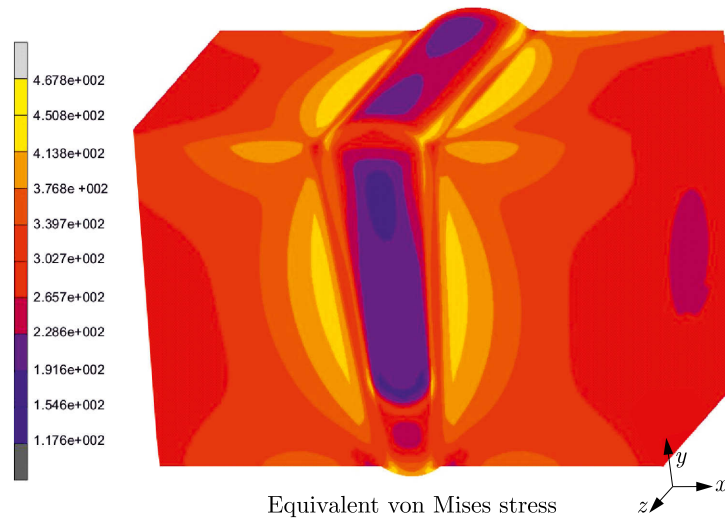


Fig. 8. Layers of the reduced stress calculated according to the Huber-Mises-Hencky yield criterion for the model of weld made with the laser beam method

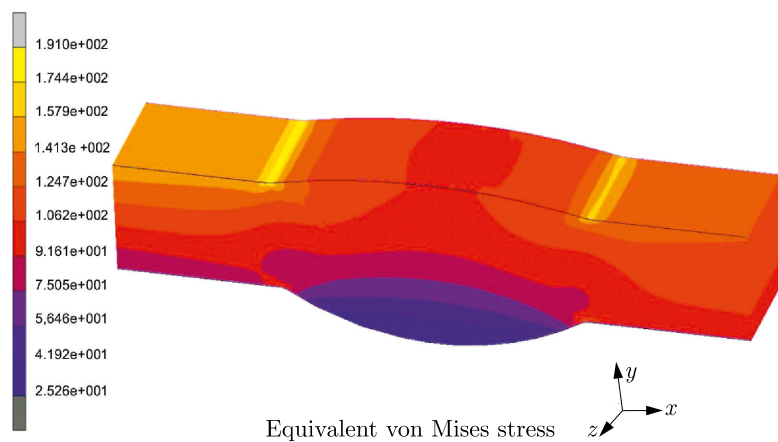


Fig. 9. Layers of the reduced stress calculated according to the Huber-Mises-Hencky yield criterion for the model of weld made with the TIG method

The analysis of the distribution of stress calculated according to the Huber-Mises-Hencky yield criterion (red) determined with FEM (for welds made with the laser beam and TIG methods) has been compared with the experimental results (Figs. 10a and 10b). Based on the components of residual stress in both the x and y axis directions and formula (5.13), the reduced stress is calculated (Dyląg *et al.*, 2007)

$$\sigma_{red} = \sqrt{\sigma_x^2 + \sigma_y^2 - \sigma_x \sigma_y} \quad (5.13)$$

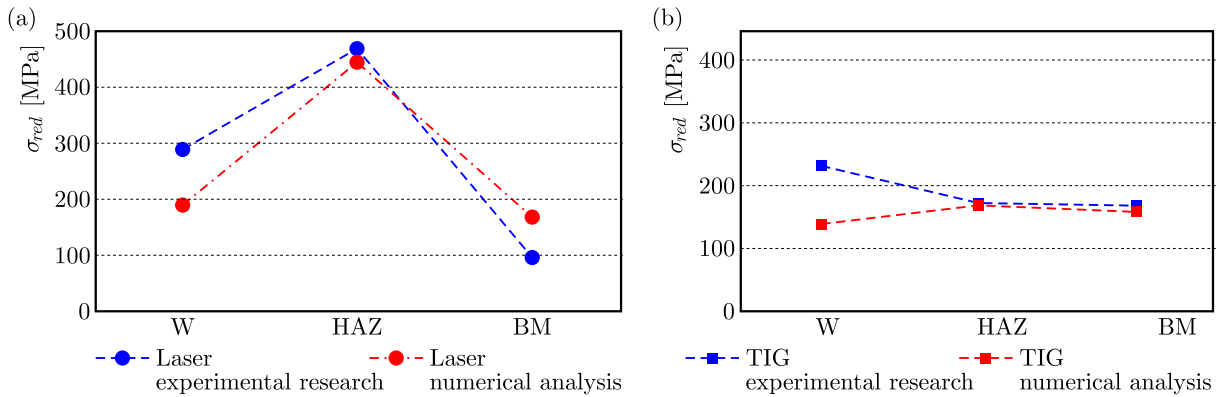


Fig. 10. Distribution of the reduced and computational stress determined experimentally and with the use of the finite element analysis of the weld (W), the heat affected zone (HAZ), and the base material (BM) of the samples made with the laser beam (a) and TIG (b) methods

The results of the experimental tests and the numerical analyses show a compliance that falls within some margin of error (Dyląg *et al.*, 2007). The differences may be due to previously described oversimplification of the model.

6. Conclusion

904L welded austenitic stainless steel is of great importance in demanding structural engineering and, therefore, it is crucial to detect and remove any errors resulting from design and manufacturing processes. To achieve this goal, it is essential to effectively determine residual stress occurring in sensitive locations of welded joints.

The distribution of stress has been determined using the FEM, based on established thermo-physical results (Nasiłowska, 2016) and mechanical properties (PN-EN 19988). Analysis of the numerical distribution of stress in comparison to experimental results shows a compliance within a margin of the measurement error. The most accurate results have been obtained for welds made with the laser beam.

The observed differences between the numerical analysis and experimental research are likely to result from oversimplification of the model.

In conclusion, this analysis suggests that future numerical simulations should take into account liquid-solid transformation and more precisely define thermal boundary conditions.

References

1. BENASCIUTTI D., LANZUTTI A., RUPIL G., HAEBERLE E., 2014, Microstructural and mechanical characterisation of laser-welded lap joints with linear and circular beads in thin low carbon steel sheets, *Materials and Design*, **62**, 205-216

2. BLACHA Ł., KAROLCZUK A., 2016, Validation of the weakest link approach and the proposed Weibull based probability distribution of failure for fatigue design of steel welded joints, *Engineering Failure Analysis*, **67**, 1, 46-62
3. BOGDANOWICZ Z., NASIŁOWSKA B., JÓZWIĄK P., ZASADA D., 2015, Structure and mechanical properties of 1.4539 austenitic steel joints made by TIG and laser-beam welding, *Solid State Phenomena*, **224**, 99-104
4. DONG D., LIU Y., YANG Y., LI J., MA M., JIANG T., 2014, Microstructure and dynamic tensile behavior of DP600 dual phase steel joint by laser welding, *Materials Science and Engineering*, **594**, 17-25
5. DYŁĄG Z., JAKUBOWICZ A., ORŁÓŚ Z., 2007, *Strength of Materials* (in Polish), vol I, WNT Warszawa
6. JIAO X., YANG Y., ZHOU C., 2014, Seam tracking technology for hyperbaric underwater welding, *Chinese Journal of Mechanical Engineering*, **22**, 2, 265-269
7. KLUGER K., ŁAGODA T., 2016, Fatigue life estimation for selected materials in multiaxial stress states with mean stress, *Journal of Theoretical and Applied Mechanics*, **54**, 2, 385-396
8. LEE C.-H., CHANG K.-H., 2014, Comparative study on girth weld-induced residual stress between austenitic and duplex stainless steel pipe welds, *Applied Thermal Engineering*, **63**, 140-150
9. MA J., KONG F., LIU W., CARLSON B., KOVACEVIC R., 2014, Study on the strength and failure modes of laser welded galvanized DP980 steel lap joints, *Journal of Materials Processing Technology*, **214**, 8, 1696-1709
10. Marc® 2011, Volume A: Theory and User Information, Copyright 2011 MSC. Software Corporation
11. MURAKAWA H., 2013, Residual stress and distortion in laser welding, *Handbook of Laser Welding Technologies*, 374-398
12. NASIŁOWSKA B., 2016, Fatigue life and fractures in 1.4539 austenitic steel welded joints prepared using TIG and laser beam welding methods, PhD Thesis, Military University of Technology, Warsaw, 43-47
13. OGLE M.H., MADDOX S.J., 1998, Joints in aluminium, *Seventh International Conference Joints in Aluminium – INALCO'98*, Cambridge, UK
14. PIEKARSKA W., 2007, *Numerical Analysis of Thermomechanical Phenomena in the Laser Beam Welding – the Temperature Field, Phase Transformations and Stresses* (in Polish), Czestochowa University of Technology, Czestochowa
15. PIEKARSKA W., KUBIAK M., 2011, Three-dimensional model for numerical analysis of thermal phenomena in laser – arc hybrid welding process, *International Journal of Heat and Mass Transfer*, **54**, 23-24, 4966-4974
16. PIEKARSKA W., KUBIAK M., 2013, Modeling of thermal phenomena in single laser beam and laser – arc hybrid welding processes using projection method, *Applied Mathematical Modelling*, **37**, 415, 2051-2062
17. PN-EN 10088 – 1:2014 – 12 – Stainless steels, Part 1: List of stainless steels
18. RANATOWSKI E., 2009, *Calculational Mechanics of Welding – Physical Fundamentals of the Process* (in Polish), University Publications, University of Technology and Life Sciences in Bydgoszcz
19. SUSMEL L., TOVO R., 2008, Modified Wöhler curve method and Eurocode 3: accuracy in predicting the multiaxial fatigue strength of welded joint, [In:] *Lifetime Estimation of Welded Joints*, T. Łagoda (Edit.), 203-207
20. TAN W., SHIN Y.C., 2015, Multi-scale modeling of solidification and microstructure development in laser keyhole welding process for austenitic stainless steel, *Computational Materials Science*, **98**, 15, 446-458

21. VOSS O., 2011, *Untersuchung relevanter Einflussgrößen auf die numerische Schweissimulation*, TU Braunschweig, Shaker Verlag, Aachen, 36
22. ZAMIRI AKHLAGHI F., 2009, *Fatigue Life Assessment of Welded Bridge Details Using Structural Hot Spot Stress Method. A Numerical and Experimental Case Study*, Master Thesis, Chalmers University of Technology, Göteborg, Sweden

Manuscript received July 3, 2017; accepted for print October 26, 2017

A CONTINUUM DESCRIPTION OF FAILURE WAVES

HAMID SAID, JAMES GLIMM

Stony Brook University, Department of Applied Mathematics and Statistics, Stony Brook, USA
e-mail: hsaid@ams.sunysb.edu

Shattering of a brittle material such as glass occurs dynamically through a propagating failure wave, which however, can not be assigned to any of the classical wave. In this paper, we build a thermodynamically consistent theory based on the idea that a failure wave is analogous to a deflagration wave. Our theory admits, as special cases, the classical models of Feng and Clifton. Two fundamental thermodynamic functions form the basis of our theory. This approach allows for the construction of a new variational principle and a Lagrangian formulation. Finally, the theory is linearized to interpret specific experimental observations.

Keywords: brittle fracture, failure wave, internal variable, dissipative systems, variational principle

1. Introduction

Fracture is one of the two main modes of material damage. Brittle fracture and comminuted fracture waves (also called failure waves) are an extreme version of these phenomena, arising in engineering applications such as modeling low-frequency earthquakes (Sapozhnikov *et al.*, 2007), armor damage prevention (Walley, 2013), determining the fracture strength of ceramics (Ccalister and Rethwisch, 2011), and developing blast technology in underground mining (Zhang, 2016). Likewise, applications of brittle fracture arise in medicine: kidney stone treatment via shock wave lithography (Neuberg *et al.*, 2006), quantifying comminution in bone fracture (Beardsley *et al.*, 2005), and modeling tooth structure and function (Lee *et al.*, 2011). It is known that failure waves represent a dynamic wave mode of brittle elastic fracture that do not correspond to any of the classical elastic or inelastic waves of solid mechanics. Behind the wave front the material is in a comminuted or microfractured state (Bless and Brar, 2007; Feng *et al.*, 2000).

Our main result is the derivation of failure wave modeling from a consistent thermodynamic framework based on a diffusive process. Our equations include the classic work of Feng *et al.* (2000) and Clifton (1993) as special cases. We identify Clifton's model as the zero dissipation limit endpoint in a one parameter family of Feng models. Our analysis suggests that anisotropy of diffusion (longitudinal vs transverse) is significant, which we argue is related to an observable quantity, the shard size of the comminuted rubble. Furthermore, we present a new data analysis corresponding to the width and rise time of the failure wave. The thermodynamic framework results in a new formulation of a variational principle and the Lagrange equations with dissipation.

The dynamic response of glass to impact has been investigated by researchers for many years (see selected references (Feng *et al.*, 2012; Bless and Brar, 2007; Kanel *et al.*, 2005; Bourne and Rosenberg, 1996). Experiments have conclusively demonstrated that once glass experiences impact (e.g. uni-axial compression) close to, but below the Hugoniot elastic limit, the sample initially deforms elastically at the shock front and subsequently fails dramatically through the formation of multiple microcracks into a comminuted (rubblized) zone. This delay in time is

interpreted as the result of a self-propagating failure wave moving at subsonic speed behind the initial elastic shock. The material behind the failure wave suffers a total loss in tensile strength, and a large reduction in shear strength, while little to no change occurs in the longitudinal stress across the failure front. Researchers have used plate impact, rod impact and projectile penetration experiments to investigate the properties of failure fronts in various types of glass.

Various models have been developed to describe the failure wave: its formation, the speed at which the wave propagates, and the stability of the failure front. However, a consistent thermodynamic basis for the dynamics governing the failure wave is still lacking. Partom proposed a simple phenomenological model, which relates the rate of damage accumulation to the gradient of damage (Partom, 1998). Kanel *et al.* (1991) also suggested a phenomenological model where the failure wave is a moving control surface and the shear strength behind this surface is set to zero. A more fundamental model was proposed by Clifton (1993) who described the failure wave as a propagating phase boundary within a system of conservation laws. All these models do, in fact, provide multiple perspectives into the dynamics of the failure wave, and do agree, to varying degrees, with experimental observations. Here we model the propagation of the failure wave as analogous to a slow combustion process, a point of view presented by Feng (2000) and later adopted by Chen *et al.* (2003) (in collaboration with Feng).

In 2000, R. Feng (Feng, 2000) proposed a physically based diffusive field equation to describe the propagation of the failure wave. As he observed, since there is an increase in the lateral stress associated with the arrival of the failure wave, while the longitudinal stress remains unchanged, the propagation of a failure wave is not the result of momentum balance. Rather, it is the progressive percolation of microfissures that drives the propagation of the failure wave; hence, leading to a diffusive model. In fact, Feng observes that the propagation of the failure wave resembles that of a (subsonic) deflagration wave. He, therefore, writes a field equation of parabolic type for an unknown V_d

$$\frac{\partial V_d}{\partial t} = \nabla \cdot [\mathbf{D}(\mathbf{x}, t) \cdot \nabla V_d] + \beta(\mathbf{x}, t) \quad (1.1)$$

where $t \in \mathbb{R}^+$ and $\mathbf{x} \in \mathbb{R}^3$ denote the time and space coordinates, and \mathbf{D} and β are the second order damage diffusivity tensor and evolution function, respectively. The variable V_d is a damage related quantity: the increase in the specific volume of the material if it is damaged and then completely unloaded. Feng's model simulations were successful in reproducing the profile of the lateral stress measurements for different glass specimens.

The main critique of Feng's diffusive model is that field equation (1.1) is not derived from a consistent thermodynamic formulation. In this work, we show that Feng's equation can be recovered in a theoretical derivation from thermodynamically consistent postulates.

The paper is organized as follows. In Section 2, we formulate the equations of motion and the constitutive theory based on two functions: the (Helmholtz) free energy and the rate of entropy production. This derivation is based on the principle of conservation of momentum, and the first and second law of thermodynamics. This two-function approach is related to but distinct from Biot's derivation of the equations of classical thermoelasticity (Biot, 1956). Biot's formulation (Biot, 1956), which in contrast to our theory, depends on a modified (Biot's) free energy, rather than the thermodynamically correct free energy. In our context, all the dynamics and thermodynamics of the system under study are contained in these two functions, and as such they specify the equations of motion, which are of hyperbolic-parabolic type. The evolution-diffusion equation are then linearized to obtain an anisotropic extension of Feng's model. In this context, we analyze the two distinct diffusion coefficients and compare our new theoretical predictions for the width and time rise of the failure waves to experiment. Lastly, we show that in the appropriate limit Feng's model reduces to Clifton's conservative model. In Section 3, we introduce a thermodynamic potential as a sum of the Lagrangian and a dissipation function. The minimization of the sum leads to the equations of motion and constitutive relations. The equations of

motion can thus be written as Lagrange's equations with dissipation. In Section 4, we linearize the equations of motion, thereby illustrating the two components of the dissipative Lagrangian formalism and offering insight into the nature of the interaction of the reversible effects upon the irreversible process in the system. As a consequence, we provide a theoretical explanation for the disparity in the experimental values pertaining to the change in the longitudinal strain across the failure wave as observed by Feng. Finally, Section 5 offers concluding remarks.

2. The equations of motion

We formulate the governing equations in Lagrangian coordinates as is customary in solid mechanics. See (Gurtin *et al.*, 2010; Marsden and Hughes, 1994) for more details. Let the body $\mathcal{B}_0 \subset \mathbb{R}^n$ denote the undeformed reference configuration. A point $\mathbf{X} \in \mathcal{B}_0$ is called a Lagrangian or material point. We represent the coordinates on \mathcal{B}_0 by $\{X_i\}$, $i = 1, 2, \dots, n$. Furthermore, by defining a time-dependent diffeomorphism $\phi : \mathcal{B}_0 \times \mathbb{R}^+ \rightarrow \mathcal{B}_t \subset \mathbb{R}^n$ to be a motion of \mathcal{B}_0 , we can represent an Eulerian or spatial point occupied by \mathbf{X} at time t by $\mathbf{x} = \phi(\mathbf{X}, t)$, and so we have $\mathbf{X} = \phi(\mathbf{x}, 0)$.

Define the displacement vector $\mathbf{U} = \mathbf{U}(\mathbf{X}, t)$ in Lagrangian coordinates by

$$\mathbf{U}(\mathbf{X}, t) = \mathbf{x} - \mathbf{X} \quad U_i(\mathbf{X}, t) = x_i - X_i \quad i = 1, 2, \dots, n$$

where $\mathbf{x} = \phi(\mathbf{X}, t)$.

Moreover, define the deformation gradient $\mathbf{F} = \partial\mathbf{x}/\partial\mathbf{X}$, and so

$$\mathbf{F} = \mathbf{I} + \nabla\mathbf{U} \quad F_{ij} = \delta_{ij} + U_{i,j} \quad i, j = 1, 2, \dots, n \quad (2.1)$$

2.1. Constitutive theory

In this Section, we develop the thermodynamics of elasticity coupled to diffusive internal variables based on the work of Biot (1956), Maugin (1990) and Ziegler (2012). The derivation is based on the determining two fundamental thermodynamic functions. Such a two function approach was first proposed by Biot to obtain the equations of thermoelasticity (Biot, 1956). Biot observed that by minimizing the sum of two quantities – a modified free energy (sometimes referred to as Biot's potential) and the dissipation function – he was able to produce the classical equations of thermoelasticity. However, the relation of Biot's thermoelastic potential to fundamental thermodynamic principles is not clear.

For isothermal processes such as the one we are studying, the Helmholtz free energy is the appropriate fundamental thermodynamic potential representing the thermodynamic state of the system (Lebon *et al.*, 2008), and minimizing the free energy produces the balance of forces for isothermal processes (Fung and Tong, 2001). Moreover, in the case of failure waves, there is entropy production associated with the irreversible process of the growth and propagation of microcracks into the material (Maugin, 1990). In fact, as we will show, the rate of entropy production is proportional to the dissipation function. Therefore, the Helmholtz free energy and the dissipation function constitute the basis of our two-function approach. A more general treatment of this approach can be found in (Ziegler, 2012). We rely on Internal Variable Theory and classical theory of irreversible thermodynamics to construct our two functions.

Internal Variable Theory (IVT) has many applications including the description of elastoplastic fracture and modeling viscoelastic behavior (Ziegler, 2012; Murakami, 2012). The dialated volume V_d in Feng's model can be interpreted as an internal variable. We adopt this approach and introduce an internal variable $\mathbf{\Gamma}$. We assert that the propagation of the failure wave is represented by an evolution-diffusion equation for the internal variable $\mathbf{\Gamma}$. The tensorial nature of $\mathbf{\Gamma}$ and its interpretation as it pertains to the failure wave phenomenon will be discussed below. In

keeping with our analogy to thermoelasticity and combustion theory, the diffusion of $\mathbf{\Gamma}$ can be viewed in some respects as analogous to the diffusion of heat in a body as briefly mentioned by Chen *et al.* (2003).

We first begin by considering the specific Helmholtz free energy denoted Ψ , and assume the system to be at constant temperature Θ_0 .

In the theory of thermoelasticity, the Helmholtz free energy Ψ is a function of the deformation gradient \mathbf{F} and temperature Θ such that (Guertn *et al.*, 2010)

$$\mathbf{S} = \rho_0 \frac{\partial \Psi}{\partial \mathbf{F}} \quad s = -\frac{\partial \Psi}{\partial \Theta}$$

where \mathbf{S} is the first Piola-Kirchhoff stress tensor, s is the entropy, and ρ_0 is the mass density of the undeformed material.

In our context we assume that Ψ depends on \mathbf{F} and $\mathbf{\Gamma}$ with

$$\mathbf{S} = \rho_0 \frac{\partial \Psi}{\partial \mathbf{F}} \tag{2.2}$$

Note that

$$S_{ij} = \rho_0 \frac{\partial \Psi}{\partial U_{k,l}} \frac{\partial U_{k,l}}{\partial F_{ij}} = \rho_0 \frac{\partial \Psi}{\partial U_{k,l}} \frac{\partial F_{kl}}{\partial F_{ij}} = \rho_0 \frac{\partial \Psi}{\partial U_{i,j}} = \rho_0 \frac{\partial \Psi}{\partial (\nabla \mathbf{U})}$$

Before examining the associated variable to $\mathbf{\Gamma}$, we make the following two key assumptions: (i) the Helmholtz free energy Ψ not only depends on \mathbf{F} (or equivalently on $\nabla \mathbf{U}$) and the internal variable $\mathbf{\Gamma}$, but also on the gradient of the internal variable $\nabla \mathbf{\Gamma}$ as done by Maugin (1990), (ii) function Ψ is convex in $\nabla \mathbf{\Gamma}$ and $\mathbf{\Gamma}$. We motivate these assumptions below. For now, we can write symbolically

$$\Psi = \Psi(\nabla \mathbf{U}, \mathbf{\Gamma}, \nabla \mathbf{\Gamma}) \tag{2.3}$$

Free energy functions that depend on the gradient of the internal variable have been used extensively in non-local damage models (Nedjar, 2002; Liebe, 2001). For instance, Nedjar (2002) utilizes essentially the same free energy as in equation (2.3) for a scalar damage variable. However, the main difference with our present work lies in the definition of the dissipation function. The dissipation function we employ is a direct result of Onsager's principle; however, Nedjar postulates the existence of a pseudo-potential of damage dissipation. But the relation of this potential to entropy production is not clear. Furthermore, while the thermodynamic framework outlined in (Nedjar, 2002) can allow for rate-dependent material damage, the quasi-static problem was only considered in detail, as opposed to the dynamic problem in this work.

Consider the time derivative of Ψ

$$\rho_0 \dot{\Psi} = \mathbf{S} : \overline{\nabla \mathbf{U}} - \mathbf{Z} \dot{\mathbf{\Gamma}} - \nabla \cdot (\mathbf{B} \dot{\mathbf{\Gamma}}) \tag{2.4}$$

where we have defined

$$\mathbf{Z} = -\rho_0 \frac{\delta \Psi}{\delta \mathbf{\Gamma}} = \mathbf{A} - \nabla \cdot \mathbf{B} \quad \mathbf{A} = -\rho_0 \frac{\partial \Psi}{\partial \mathbf{\Gamma}} \quad \mathbf{B} = -\rho_0 \frac{\partial \Psi}{\partial (\nabla \mathbf{\Gamma})} \tag{2.5}$$

We consider \mathbf{Z} to be the associated variable to $\mathbf{\Gamma}$. The variable \mathbf{Z} is interpreted as an internal force corresponding to the internal variable $\mathbf{\Gamma}$ (Maugin, 1990).

The second law of thermodynamics (or equivalently the Clausius-Duhem inequality) determines physically permissible processes. In Lagrangian coordinates, it reads (Fung and Tong, 2001)

$$\frac{d}{dt} \int_{\Omega} \rho_0 s \, d\Omega + \int_{\partial \Omega} \dot{\Sigma} \, da \geq 0 \tag{2.6}$$

where s is the entropy (per unit mass) of the system, Ω is the domain of the system, and $\dot{\Sigma}$ is the entropy flow vector on the boundary. As the problem is isothermal, the only relevant entropy is that associated with Γ . Locally, (2.6) simplifies to

$$\rho_0 \dot{s} + \nabla \cdot \dot{\Sigma} \geq 0 \tag{2.7}$$

By substituting $\Psi = \mathcal{E} - s\theta_0$ (\mathcal{E} being the internal energy of the system), and the balance of energy equation: $\rho_0 \dot{\mathcal{E}} = \mathbf{S} : \dot{\mathbf{F}}$ into the above equation, and taking into consideration equations (2.5) we obtain

$$\mathbf{Z}\dot{\Gamma} + \nabla \cdot (\mathbf{B}\dot{\Gamma} + \theta_0 \dot{\Sigma}) \geq 0 \tag{2.8}$$

By making the choice

$$\dot{\Sigma} = -\frac{\mathbf{B}\dot{\Gamma}}{\theta_0} \tag{2.9}$$

we arrive at the fundamental inequality

$$\mathbf{Z}\dot{\Gamma} \geq 0 \tag{2.10}$$

In general, diffusion can be expressed in terms of a flux \mathbf{h} across the boundary. For instance, in thermomechanics, \mathbf{h} is given by Fourier’s law, which in turn gives rise to an entropy flux $\dot{\Sigma}$ defined as $\dot{\Sigma} = \mathbf{h}/\theta$.

In the context of our problem, there is no heat exchange at the boundary. So the diffusion of the internal variable is associated with a flux other than the heat flux across the boundary. Equation (2.9) gives an explicit expression for this flux: it is the entropy flux associated with the internal variable Γ . Therefore, by analogy to heat flow across the boundary, we obtain an explicit expression for the total rate of energy released from the surface of the material during the propagation of the failure wave

$$H = \int_{\partial\Omega} \mathbf{h} \cdot \mathbf{n} \, da = \int_{\partial\Omega} \mathbf{B}\dot{\Gamma} \cdot \mathbf{n} \, da \tag{2.11}$$

where \mathbf{n} is the unit outer normal. Note it was by assuming $\Psi = \Psi(\dots, \nabla\Gamma)$ that we got $\mathbf{B} \neq \mathbf{0}$, which gives a nonzero entropy flux $\dot{\Sigma}$.

Had we only assumed $\Psi = \Psi(\nabla\mathbf{U}, \Gamma)$, then we would expect $\dot{\Sigma} = \mathbf{0}$ and an equation similar to (2.10) would still hold (by replacing \mathbf{Z} with \mathbf{A}) (Ziegler 2012; Lebon, 2008). Thus, there still could be dissipation in the medium, but not diffusion of the internal variable.

Next we consider the dissipation function. It is known that the Helmholtz free energy determines the reversible processes occurring in the system. If in addition to reversible processes, the evolution of the system under consideration produces entropy (i.e. an accompanied irreversible process), then one needs to supplement the free energy with a scalar dissipation function \mathcal{D} . This approach has been used in thermomechanics by Ziegler (2012) and Biot (1955, 1956), and in a more general context by Maugin¹ (1992).

The constitutive law for the dissipation function \mathcal{D} varies according to the system under study. In applications, the function \mathcal{D} is positive and depends on the rate variables, as well as on the thermodynamic state variables (Ziegler, 2012). As a postulate, we exclude the viscous

¹In fact the dissipation function was first introduced by Rayleigh (1945) in his study of dissipative processes in classical mechanics. He required such a function to be non-negative and quadratic in the velocities.

related strain rate $\dot{\nabla}\bar{\mathbf{U}}$ from \mathcal{D} . Moreover, as the system is isothermal, the only remaining rate variable is $\dot{\mathbf{\Gamma}}$, and so we write

$$\mathcal{D} = \mathcal{D}(\dot{\mathbf{\Gamma}}, w) \quad (2.12)$$

where w represents the state variables.

Before investigating the functional form of \mathcal{D} in the case of failure waves, we need to determine the forces associated with $\dot{\mathbf{\Gamma}}$. Following Ziegler (2012) and Maugin (1990), we assume that the function \mathcal{D} is such that

$$\frac{\partial \mathcal{D}}{\partial \dot{\mathbf{\Gamma}}} + \frac{\delta \Psi}{\delta \mathbf{\Gamma}} = \mathbf{0} \quad (2.13)$$

or equivalently

$$\rho_0 \frac{\partial \mathcal{D}}{\partial \dot{\mathbf{\Gamma}}} = \mathbf{Z} \quad (2.14)$$

In other words, the dissipative force associated with $\dot{\mathbf{\Gamma}}$ through \mathcal{D} is identified as the opposite of the quasiconservative force associated with $\mathbf{\Gamma}$ through Ψ^2 .

For failure waves, we assume the dependence of \mathcal{D} on w in (2.12) vanishes, and furthermore, we assume a quadratic dependence of \mathcal{D} on $\dot{\mathbf{\Gamma}}$ similar to the thermoelastic theory of Biot (1956)

$$\rho_0 \mathcal{D} = \rho_0 \mathcal{D}(\dot{\mathbf{\Gamma}}) = \frac{1}{2} \mathbf{\Lambda} \cdot (\dot{\mathbf{\Gamma}} \cdot \dot{\mathbf{\Gamma}}) \geq 0 \quad (2.15)$$

For example, if $\mathbf{\Gamma}$ is an n -vector, then the above equation in component form reads

$$\rho_0 \mathcal{D}(\dot{\mathbf{\Gamma}}) = \frac{1}{2} A_{ij} \dot{\Gamma}_i \dot{\Gamma}_j \geq 0 \quad i, j = 1, 2, \dots, n \quad (2.16)$$

The classical theory of irreversible thermodynamics relates the function \mathcal{D} to the rate of production on internal entropy $\dot{s}^{(i)}$. Onsager's principle defines $\dot{s}^{(i)}$ in terms of fluxes and forces associated to the fluxes. In the absence of thermal effects, the flux and force are identified with $\dot{\mathbf{\Gamma}}$ and \mathbf{Z} , respectively. So we write (Fung and Tong, 2001)

$$\rho_0 \Theta_0 \dot{s}^{(i)} = \dot{\mathbf{\Gamma}} \cdot \mathbf{Z} \geq 0 \quad (2.17)$$

If the fluxes and forces are related by a linear phenomenological relation

$$\mathbf{Z} = \mathbf{\Lambda} \cdot \dot{\mathbf{\Gamma}} \quad (2.18)$$

then,

$$\rho_0 \dot{s}^{(i)} = \frac{1}{\Theta_0} \dot{\mathbf{\Gamma}} \cdot \mathbf{Z} = \frac{1}{\Theta_0} \mathbf{\Lambda} \cdot \dot{\mathbf{\Gamma}} \cdot \dot{\mathbf{\Gamma}} = \frac{2\rho_0}{\Theta_0} \mathcal{D} \quad (2.19)$$

where by Onsager reciprocal relations we have $\mathbf{\Lambda} = \mathbf{\Lambda}^T$. Furthermore, we assume $\mathbf{\Lambda}$ is invertible. So not only does the dissipation produce entropy, the rate of entropy production is in fact proportional to the dissipation function. Hence, we can treat \mathcal{D} as the source of entropy production. A more general treatment of dissipation functions can be found in (Ziegler, 2012; Gurtin *et al.*, 2010).

²According to, Ziegler this is a statement that the net internal forces associated to the internal variables in an arbitrary process is equal to zero, which is a consequence of energy conservation.

Expanding equation (2.13) gives us

$$\rho_0 \frac{\partial \mathcal{D}}{\partial \dot{\mathbf{\Gamma}}} + \frac{\partial \Psi}{\partial \mathbf{\Gamma}} - \left(\frac{\partial \mathbf{P}}{\partial (\nabla \mathbf{U})} \cdot \nabla_{\mathbf{X}}(\nabla \mathbf{U}) + \frac{\partial \mathbf{P}}{\partial \mathbf{\Gamma}} \cdot \nabla_{\mathbf{X}} \mathbf{\Gamma} + \frac{\partial \mathbf{P}}{\partial (\nabla \mathbf{\Gamma})} \cdot \nabla_{\mathbf{X}}(\nabla \mathbf{\Gamma}) \right) = 0 \tag{2.20}$$

where $\mathbf{P} = -(1/\rho_0)\mathbf{B}$ and symbol $\nabla_{\mathbf{X}}$ means derivative with respect to \mathbf{X} while holding other variables constant. Moreover, we define the damage diffusion tensor \mathbf{K} as

$$\frac{1}{\rho_0} \mathbf{K} = \frac{\partial \mathbf{P}}{\partial (\nabla \mathbf{\Gamma})} = \frac{\partial^2 \Psi}{\partial (\nabla \mathbf{\Gamma}) \partial (\nabla \mathbf{\Gamma})} \tag{2.21}$$

Tensor \mathbf{K} is defined analogously to the classical elasticity tensor, and hence it is symmetric. Furthermore, since Ψ is convex in $\nabla \mathbf{\Gamma}$ tensor \mathbf{K} must be positive definite, thereby ensuring well-defined diffusion.

Before we formulate the hyperbolic-parabolic equations, we discuss the order and nature of the variable $\mathbf{\Gamma}$. In general, the order and physical meaning of an internal variable depends on the system under study. In the classical theory of material damage, a scalar variable $d \in [0, 1]$ called a *damage variable* is introduced such that $d = 0$ corresponds to intact material, and $d = 1$ corresponds to fully fractured material (Maugin, 1992). However, in the context of our problem, the incident shock wave introduces lateral shear in the brittle material because of Poisson’s ratio, which is released by the arrival of the failure wave as a drop in shear strength. It is reasonable then to assume that the difference in shear stress is driving the damage from a mechanical point of view. So it is natural to introduce a second order tensor to describe the diffusion of the damage $\mathbf{\Gamma}$. Variable $\mathbf{\Gamma}$ represents the strain due to the 3D anisotropic fracture and microcracks. The associated force (in this case a measure of shear stress) is given by the first equation of (2.5).

For notational simplicity, we rewrite the symmetric rank two indices i, j of $\mathbf{\Gamma}$ as a single index $i = 1, \dots, [n(n + 1)]/2$. This choice yields a rank four tensor \mathbf{K} and rank two tensor $\mathbf{\Lambda}$.

2.2. Coupled hyperbolic-parabolic equations

We are now in position to write down the system of partial differential equations of hyperbolic-parabolic type describing the formation and propagation of failure waves

$$\rho_0 \frac{\partial^2 \mathbf{U}}{\partial t^2} - \nabla \cdot \mathbf{S} \Big|_{\mathbf{\Gamma}=\mathbf{0}} = \rho_0 \mathbf{r} \qquad \frac{\partial \mathcal{D}}{\partial \dot{\mathbf{\Gamma}}} + \frac{\delta \Psi}{\delta \mathbf{\Gamma}} = 0 \tag{2.22}$$

where $\mathbf{r}(\mathbf{X}, t)$ is a (specific) body force. Equation (2.22)₁ describes the motion of the initial nonlinear shock, hence we have a vanishing $\mathbf{\Gamma}$.

By using the constitutive equations for functions Ψ and \mathcal{D} , particularly equations (2.2), (2.16), and (2.21), the coupled system³ (2.22) can be rewritten as

$$\begin{aligned} \rho_0 \frac{\partial^2 U_i}{\partial t^2} - C_{ijkl} \frac{\partial^2 U_k}{\partial X_j \partial X_l} &= \rho_0 r_i \\ \Lambda_{i'k'} \frac{\partial \Gamma_{k'}}{\partial t} - \frac{\partial}{\partial X_j} \left(K_{i'jk'l} \frac{\partial \Gamma_{k'}}{\partial X_l} \right) &= f_{i'}(U_{m,n}, \Gamma_{m'}, \Gamma_{m',n}) \end{aligned} \tag{2.23}$$

where $\mathbf{C}|_{\mathbf{\Gamma}=\mathbf{0}} = \mathbf{C}(\nabla \mathbf{U}, \mathbf{\Gamma} = \mathbf{0}) = \mathbf{C}(\nabla \mathbf{U})$ is the elasticity tensor, \mathbf{f} is a nonlinear function in its arguments, and tensor \mathbf{K} depends on the state variables $\nabla \mathbf{U}$, $\mathbf{\Gamma}$, $\nabla \mathbf{\Gamma}$. In the above equations,

³Strictly speaking there is one-way coupling only: the parabolic part is coupled with the hyperbolic equation since the hyperbolic part is independent of variable $\mathbf{\Gamma}$.

'prime' indices range from 1 to $n(n+1)/2$ while the rest range from 1 to n . In component form, the elasticity tensor is given to be

$$C_{ijkl} = \left. \frac{\partial S_{ij}}{\partial U_{k,l}} \right|_{\Gamma=0} = \rho_0 \left. \frac{\partial^2 \Psi}{\partial U_{i,j} \partial U_{k,l}} \right|_{\Gamma=0}$$

Hence, we have obtained a nonlinear coupled hyperbolic-parabolic system of PDEs. It should be realized that diffusion will be inactive (i.e. each term in equation (2.23)₂ is identically zero) if the stress due to initial impact does not overcome a certain threshold σ_0 .

System (2.23) is constrained by entropy inequality (2.10)

$$\mathbf{Z}\dot{\Gamma} \geq 0$$

which only allows for physically admissible solutions.

The initial and boundary conditions that must accompany the system of equations (2.23) are given to be

$$\mathbf{U}(\mathbf{X}, 0) = \mathbf{U}^0(\mathbf{X}) \quad \mathbf{U}_t(\mathbf{X}, 0) = \mathbf{U}^1(\mathbf{X}) \quad \Gamma(\mathbf{X}, 0) = \Gamma^0(\mathbf{X}) \quad \mathbf{X} \in \mathcal{B}_0 \quad (2.24)$$

and

$$\mathbf{U} \Big|_{\mathbf{x} \in \partial \mathcal{B}_0} = \mathbf{h}^1 \quad \Gamma \Big|_{\mathbf{x} \in \partial \mathcal{B}_0} = \mathbf{h}^2 \quad \forall t > 0 \quad (2.25)$$

where the functions $\mathbf{U}^0(\mathbf{X})$, $\mathbf{U}^1(\mathbf{X})$, $\Gamma^0(\mathbf{X})$, \mathbf{h}^1 , \mathbf{h}^2 are all given. The dynamics (2.23) of the problem is completely determined by the two functions: Ψ and \mathcal{D} .

For the full 3D problem, the internal variable Γ has 6 independent components, $\nabla \Gamma$ has 6×3 components, and hence the rank 4 symmetric tensor \mathbf{K} has $(19 \times 18)/2$ independent components. We obtain a simple non-isotropic model for diffusion if we assume that the material under study is isotropic, and consider a 1D shock wave in the longitudinal direction $X \doteq X_1$; in such a case the two lateral directions mirror one another. In addition, if we take a scalar variable Γ to represent the damage, as done by Feng, then the matrix \mathbf{K} reduces to a 3×3 matrix and the matrix $\mathbf{\Lambda}$ reduces to a scalar, which we denote λ . Finally, we assume that the matrix \mathbf{K} is diagonalized in the longitudinal direction X and the two transverse components.

2.3. Feng's model

By the considerations given in the preceding paragraph, we have $U_2 = U_3 = 0$, and the unknown variables are written as $U_1 \doteq U = U(X, t)$ and $\Gamma = \Gamma(\mathbf{X}, t)$. We obtain Feng's diffusive field equation as follows. We retain the definition of \mathcal{D} and expand (2.3) to second order around the natural undamaged state (i.e. $\nabla \mathbf{U} = \mathbf{\Gamma} = \nabla \Gamma = 0$). In this state, the forces associated with state variables (i.e. equations (2.2) and (2.5)) vanish, and we assume that no coupling exists between the state variables. Thus the free energy and dissipation function are written as

$$\rho_0 \Psi_F = \frac{c_1}{2} U_X^2 + \frac{c_2}{2} \Gamma^2 + \frac{1}{2} K_{ij} \nabla_i \Gamma \nabla_j \Gamma + \frac{c_3}{4} U_X^4 \quad \rho_0 \mathcal{D}_F = \frac{1}{2} \lambda \dot{\Gamma}^2 \quad (2.26)$$

where the constant c_1 is the 1D linear elastic coefficient (e.g. Young's modulus) and the constant c_3 specifies the nonlinear elastic properties. An expression for scalar $c_2 = c_2(\mathbf{X}, t) \geq 0$ is given by Feng (2000) depending on the principle eigenvalue of \mathbf{K} (see also Chen *et al.*, 2003). Furthermore, we allow \mathbf{K} to depend on the variables \mathbf{X} and t .

With these specifications, equation (2.23)₂ gives

$$\lambda \frac{\partial \Gamma}{\partial t} - \frac{\partial}{\partial X_j} \left(K_{ij} \frac{\partial \Gamma}{\partial X_i} \right) = -c_2 \Gamma \quad (2.27)$$

For a nonzero λ , (2.27) can be written as

$$\frac{\partial \Gamma}{\partial t} - \frac{\partial}{\partial X_j} \left(D_{ij} \frac{\partial \Gamma}{\partial X_i} \right) = c_4 \Gamma \tag{2.28}$$

where $c_4 = -c_2/\lambda$ and $D_{ij} = (1/\lambda)K_{ij}$

$$\mathbf{D} = \begin{bmatrix} d_1 & 0 \\ 0 & d_2 \end{bmatrix} = \begin{bmatrix} \frac{k_1}{\lambda} & 0 \\ 0 & \frac{k_2}{\lambda} \end{bmatrix} \tag{2.29}$$

where the coefficients d_2 and k_2 are multiples of the identity matrix $\mathbf{I}_{2 \times 2}$.

According to Feng, d_1 determines the speed of the failure wave. We claim that d_2 determines the shard size in the damaged material. First, however, we discuss the evolution of d_1 and d_2 during the failure process.

In 2D projectile impact experiments in which a failure wave propagates as a spherical wave outwards, it is known (Wei and Samulyak, 2014) that after the abrupt cessation of the failure front isolated radial cracks start to form moving away from the impact point. We speculate that similar phenomena for a planar shock impact should occur parametrically as the shock impact is varied, with a transition from a failure wave to isolated cracks occurring at the critical shock strength. To explain such behavior, we must have that during the propagation of the failure wave, the speed of diffusion associated with d_2 , denoted v_l (defined analogously to (2.30)), is larger than the crack trip velocity v_0 . As the failure wave propagates away from the impact point speed v_l decreases until $v_l = v_0$ at which point the failure process stops, and the cracks "escape" the percolation in the lateral direction and as, a result, isolated radial cracks begin.

Chen *et al.* (2003) observe that in order to obtain a planar failure wave in a uniaxially compressed material: "percolation of microdamage [is] much faster in all the lateral (transverse) directions than in the longitudinal direction..." (see Fig. 1). Hence, in terms of the diffusion coefficients we must have $d_2 > d_1$ before the cessation of the failure wave. Chen *et al.* (2003), however, model only the isotropic case by assuming $d_1 = d_2$, and they express d_1 in terms of a measure of shear stress. The point here is that according to their model the speed of the failure wave is governed only by d_1 .

In diffusion-driven processes such as combustion, the speed of propagation is determined by the reaction rate or, the equivalently reaction time, and the diffusion coefficient (Clavin and Searby, 2016)

$$v_f \simeq \sqrt{d_1 \dot{\omega}} \quad \text{or equivalently} \quad v_f \simeq \sqrt{\frac{d_1}{\tau}} \tag{2.30}$$

where $\dot{\omega}$ and τ are the reaction rate and reaction time, respectively. By identifying v_f with the speed of the failure wave obtained by experiments, we can calculate the reaction time. Moreover, once v_f is specified we are able to specify the width of the wave δ_1 through

$$\delta_1 \doteq \frac{d_1}{v_f} \tag{2.31}$$

As a new analysis of existing experiments, we compare our theoretical predictions for the values of τ and δ_1 for K8 glass and soda lime glass with the experiments examined by Feng. Experimental data are taken from plots of (Feng, 2000). We have interpreted τ as the time rise in the lateral stress to find the experimental value of δ_1 .

Finally, we assert that the second eigenvalue d_2 of tensor D_{ij} determines the fineness of fracture in the failed brittle material. If we define a measure of length δ_2 in the following way

$$\delta_2 \doteq \frac{d_2}{v_f}$$

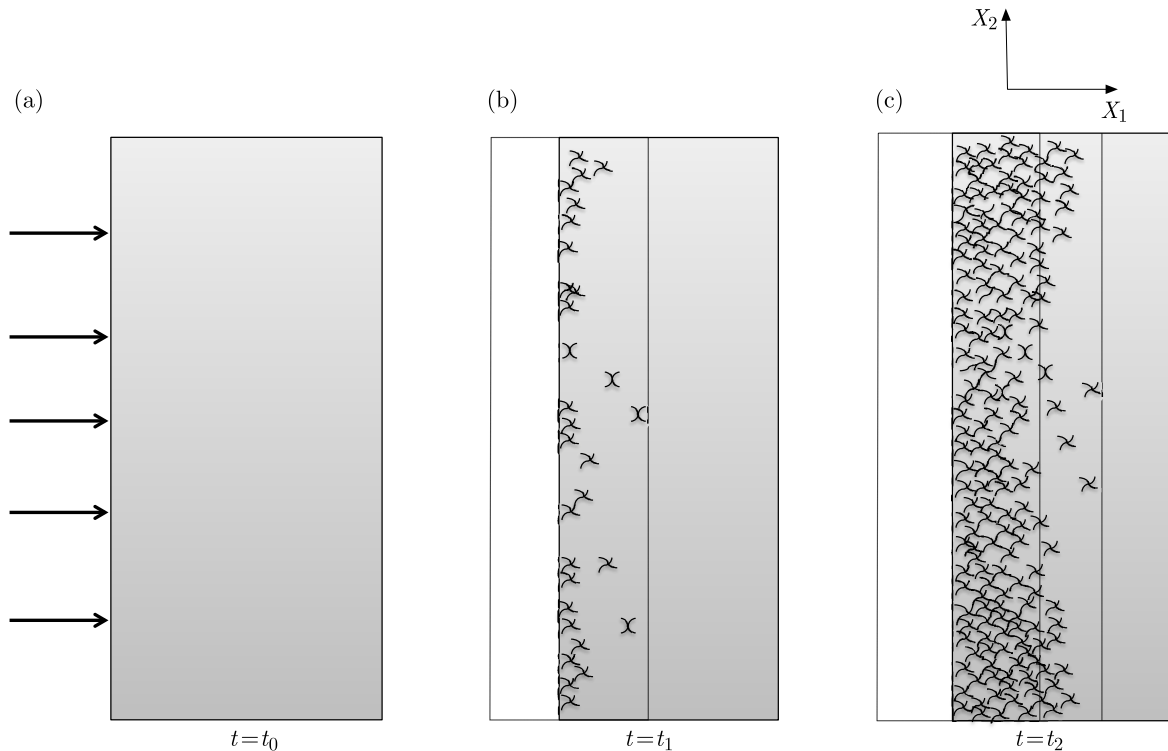


Fig. 1. A schematic figure illustrating the percolation of microcracks in an elastically compressed brittle material: (a) initial compression due to the incident shock wave; at t_0 we have $\Gamma = 0$; (b) at a later time t_1 microcracks begin to appear; the damage field $\Gamma \neq 0$; (c) at $t_2 > t_1$ failure propagates into the material due to microcrack nucleation shown here schematically as perpendicular to the incident shock; percolation in X_2 -direction is faster than in X_1 -direction. The dashed line represents the failure front

Table 1. Comparison of model prediction with experimental data for K8 glass with $v_f = 3320$ m/s, $d_1 = 6.6$ m²/s. Gauge positioned at 4.5×10^{-3} m from the loading surface

	τ [s]	δ_1 [m]
Experimental value	$0.75 \cdot 10^{-6}$	$2.49 \cdot 10^{-3}$
Theoretical prediction	$0.6 \cdot 10^{-6}$	$2 \cdot 10^{-3}$

Table 2. Comparison of model prediction with experimental data for soda lime glass with $v_f = 3090$ m/s, $d_1 = 7.4$ m²/s. Gauge positioned at $3.3 \cdot 10^{-3}$ m from the loading surface

	τ [s]	δ_1 [m]
Experimental value	$0.9 \cdot 10^{-6}$	$2.8 \cdot 10^{-3}$
Theoretical prediction	$0.8 \cdot 10^{-6}$	$2.4 \cdot 10^{-3}$

then scalar δ_2 gives an estimate for the fineness of fracture. Although, to the extent of our knowledge, there are not any experimental measurements available for the shard size, it can be measured in principle via impact experiments.

2.4. Clifton's model

The theory of deflagration can be formulated as a strictly hyperbolic system as found in (Courant and Friedrichs, 1999; Chorin and Marsden, 1990). However, if diffusion and finite reaction rates are considered, then combustion is obtained in the sense given by Zeldovich: a coupled hyperbolic-parabolic system of PDEs (Clavin and Searby, 2016; Bebernes and Eberly,

2013). In the latter formulation of the theory, the flame propagates with finite width and the flame speed depends on the diffusion coefficient and the reaction rate. In the absence of heat transfer and assuming an infinite reaction rate leading to a sharp flame front, Zeldovich’s theory reduces to the hyperbolic system. This same sharp front limit can be achieved with zero viscous and thermal dissipations (Maugin, 1992; Courant and Friedrichs, 1999). We show that in this zero dissipation limit for the propagation of the failure wave, Feng’s model reduces to Clifton’s conservative model.

Clifton (1993) models the failure wave as a propagating phase boundary, which he calls a transformation shock. According to Clifton, the phase change occurs across a sharp front. Across the phase boundary, he imposes Rankine-Hugoniot conditions for the usual isentropic conservation laws in one space dimension, and derives an expression for the speed of the front. The task that lies before us, therefore, is to find the conditions under which the theory in Section 2.2 reduces to the conservation laws proposed by Clifton.

Dissipation effects due to entropy production vanish for conservative systems, hence by taking $\mathbf{\Lambda} \rightarrow \mathbf{0}$, we obtain $\mathcal{D} = 0$ in equation (2.16) – assuming $\dot{\mathbf{\Gamma}}$ is bounded on \mathcal{B}_0 . Moreover, since the entropy flux across the boundary $\dot{\mathbf{\Sigma}}$ must also vanish, we conclude

$$\mathbf{B} = -\rho_0 \frac{\partial \Psi}{\partial \nabla \mathbf{\Gamma}} = \mathbf{0}$$

which implies $\mathbf{K} = \mathbf{0}$, and

$$\frac{\partial s}{\partial t} = \frac{\partial s^{(i)}}{\partial t} = 0 \tag{2.32}$$

Furthermore, by assuming the nonhomogenous term f to be identically zero, equation (2.23)₂ trivially vanishes. We claim that equations (2.23)₁ and (2.32), produce the 1D conservation laws considered by Clifton.

It is sufficient to show that (2.32) is equivalent to the law of conservation of energy (Dafermos, 2005)

$$\frac{\partial}{\partial t} \rho_0 \left(\mathcal{E} + \frac{1}{2} v^2 \right) - \frac{\partial}{\partial X} (vS) = 0 \tag{2.33}$$

where we have defined \mathcal{E} as the internal energy, S is the scalar valued Piola-Kirchhoff stress, and $v = \partial U / \partial t$.

Gibbs equation with an internal variable reads (Lebon *et al.*, 2008)

$$d\mathcal{E} = \Theta_0 ds + \frac{1}{\rho_0} S dU_X - A d\Gamma$$

with $A = -\rho_0 \partial \Psi / \partial \Gamma$ in (2.5). However, by (2.14) we have $A = 0$. Thus, Gibbs equation reduces to

$$d\mathcal{E} = \Theta_0 ds + \frac{1}{\rho_0} S dU_X \tag{2.34}$$

Assuming $\mathcal{E} = \mathcal{E}(s, U_X)$ combined with (2.34) we obtain

$$\frac{\partial \mathcal{E}}{\partial t} = \Theta_0 \frac{\partial s}{\partial t} + \frac{1}{\rho_0} S \frac{\partial U_X}{\partial t} = \Theta_0 \frac{\partial s}{\partial t} + \frac{1}{\rho_0} S \frac{\partial v}{\partial X}$$

Therefore

$$\frac{\partial}{\partial t} \rho_0 \left(\mathcal{E} + \frac{1}{2} v^2 \right) = \rho_0 \frac{\partial \mathcal{E}}{\partial t} + \rho_0 v \frac{\partial v}{\partial t} = \rho_0 \Theta_0 \frac{\partial s}{\partial t} + S \frac{\partial v}{\partial X} + v \frac{\partial S}{\partial X}$$

where we have used the balance of momentum equation $\rho_0 \partial v / \partial t = \partial S / \partial X$. By substituting for (2.32), we obtain the conservation of energy equation (2.33).

We have established the classical conservation laws

$$\frac{\partial U_X}{\partial t} - \frac{\partial v}{\partial X} = 0 \quad \rho_0 \frac{\partial v}{\partial t} - \frac{\partial S}{\partial X} = 0 \quad \rho_0 \frac{\partial}{\partial t} \left(\mathcal{E} + \frac{1}{2} v^2 \right) - \frac{\partial}{\partial X} (vS) = 0 \quad (2.35)$$

In one space dimension, if we choose $\Gamma = V_d$ and write Feng’s equation in form (2.27), then the limit $\lambda \rightarrow 0$ implies $\mathcal{D}_F = 0$ and equation (2.32) is satisfied. Moreover, we assume that the nonhomogeneous term is zero (i.e. $c_2 = 0$) as postulated earlier; then by the above argument, we obtain system (2.35) and, hence, Feng’s model reduces to the Clifton model.

Field equations (2.35) satisfy the Rankine-Hugoniot jump relations, which is the starting point considered by Clifton for modeling failure waves. We have, therefore, demonstrated that Clifton’s model can be recovered from Feng’s model in the limit $\Lambda \rightarrow \mathbf{0}$. In this limit, the entropy is constant and, therefore, entropy production associated with the irreversible process of the growth of microcracks is zero over time, making Clifton’s model an idealization of the process of the propagation of failure waves.

3. Variational principle and Lagrangian formalism

In this section we formulate a novel variational principle which produces equations (2.23). We show that minimizing the sum of the Lagrangian function and the dissipation function leads to the equations of motion. Furthermore, we demonstrate that system (2.23) can be rewritten as Lagrange’s equations with dissipation similar to dissipative systems in classical mechanics.

We start with a simplified variational principle where all surface and boundary terms vanish. While this is only a special case, the main physical and mathematical insights still hold. Appendix A presents the complete variational principle that includes all boundary terms, and is formulated in terms of generalized coordinates.

For the body \mathcal{B}_0 , define the total (Helmholtz) free energy ψ , the total kinetic energy \mathcal{K} , and the total dissipative function \mathcal{D}

$$\psi = \int_{\mathcal{B}_0} \rho_0 \Psi \, dV \quad \mathcal{K} = \frac{1}{2} \int_{\mathcal{B}_0} \rho_0 \frac{\partial U_i}{\partial t} \frac{\partial U_i}{\partial t} \, dV \quad \mathcal{D} = \frac{1}{2} \int_{\mathcal{B}_0} A_{ij} \dot{\Gamma}_i \dot{\Gamma}_j \, dV$$

Furthermore, we define the Lagrangian \mathcal{L}

$$\mathcal{L} = \psi - \mathcal{K} = \mathcal{L}(\nabla \mathbf{U}, \dot{\mathbf{U}}, \mathbf{\Gamma}, \nabla \mathbf{\Gamma}) = \int_{\mathcal{B}_0} L \, dV$$

With the above definitions, the variational principle for the equations of motion is

$$\delta I = \delta \int_{t_1}^{t_2} (\mathcal{L} + \mathcal{D}) \, dt = 0 \quad (3.1)$$

where t_1 and t_2 represent fixed instants of time. The variation is taken with respect to the displacement \mathbf{U} and the internal variable $\mathbf{\Gamma}$.

We demonstrate that variational principle (3.1) produces the system of equations (2.23).

We define the variation of the dissipation function $\delta \mathcal{D}$ in a similar fashion to Biot

$$\delta \mathcal{D} = \int_{\mathcal{B}_0} A_{ij} \dot{\Gamma}_i \delta \Gamma_j \, dV \quad (3.2)$$

The justification of equation (3.2) becomes evident when we introduce generalized coordinates, as done in Appendix A.

Thus,

$$\begin{aligned} & \int_{t_1}^{t_2} (\delta \mathcal{D} + \delta \psi) dt - \frac{1}{2} \int_{t_1}^{t_2} \delta \int_{\mathcal{B}_0} \rho_0 \frac{\partial U_i}{\partial t} \frac{\partial U_i}{\partial t} dV dt = 0 \\ & \int_{t_1}^{t_2} \left\{ \delta \mathcal{D} + \int_{\mathcal{B}_0} \rho_0 \left(\frac{\delta \Psi}{\delta U_i} \delta U_i + \frac{\delta \Psi}{\delta \Gamma_i} \delta \Gamma_i \right) dV \right\} dt - \int_{t_1}^{t_2} \int_{\mathcal{B}_0} \rho_0 \frac{\partial U_i}{\partial t} \frac{\partial (\delta U_i)}{\partial t} dV dt = 0 \\ & \int_{t_1}^{t_2} \left\{ \delta \mathcal{D} + \int_{\mathcal{B}_0} \rho_0 \left[-\nabla_j \cdot \left(\frac{\partial \Psi}{\partial U_{i,j}} \right) \delta U_i + \frac{\delta \Psi}{\delta \Gamma_i} \delta \Gamma_i \right] dV \right\} dt + \int_{t_1}^{t_2} \int_{\mathcal{B}_0} \rho_0 \frac{\partial^2 U_i}{\partial t^2} \delta U_i dV dt = 0 \\ & \int_{t_1}^{t_2} \left\{ \int_{\mathcal{B}_0} \left(-\nabla \cdot \mathbf{S} + \rho_0 \frac{\partial^2 \mathbf{U}}{\partial t^2} \right) \delta \mathbf{U} dV + \int_{\mathcal{B}_0} \left(\mathbf{\Lambda} \cdot \dot{\mathbf{\Gamma}} + \rho_0 \frac{\delta \Psi}{\delta \mathbf{\Gamma}} \right) \delta \mathbf{\Gamma} dV \right\} dt = 0 \end{aligned}$$

Since the last equation holds for all variations $\delta \mathbf{U}$ and $\delta \mathbf{\Gamma}$, we are left with the desired system of equations (2.23) with $\mathbf{r} = \mathbf{0}$.

Therefore, the associated Lagrange equations to variational principle (3.1), which is equivalent to the governing system of PDEs (2.23), is written as

$$\frac{\delta \mathcal{L}}{\delta \eta_i} - \frac{d}{dt} \left(\frac{\partial \mathcal{L}}{\partial \dot{\eta}_i} \right) + \frac{\partial \mathcal{D}}{\partial \dot{\eta}_i} = 0 \tag{3.3}$$

where we have defined the vector variable $\boldsymbol{\eta} = (\mathbf{U}, \mathbf{\Gamma})$. Notice that the form of equation (3.3) is identical to the form of Lagrange’s equations of motion in classical mechanics for dissipative systems (Goldstein, 1965).

There exist dissipative Hamiltonian and bracket formulations corresponding to the above dissipative Lagrangian system. The construction of said formalisms can be found in the thesis of the first author.

4. Linear theory

In this Section, we linearize equations (2.23) and note the interaction of the reversible effects upon the irreversible process of material failure.

We begin by requiring that the free energy Ψ be a quadratic form in $\nabla \mathbf{U}$ and $\mathbf{\Gamma}$ and quadratic in $\nabla \mathbf{\Gamma}$ as follows

$$\rho_0 \Psi = \frac{1}{2} \mathbf{C} \cdot (\nabla \mathbf{U} \cdot \nabla \mathbf{U}) + \mathbf{b} \cdot (\nabla \mathbf{U} \cdot \mathbf{\Gamma}) + \frac{1}{2} \mathbf{c} \cdot (\mathbf{\Gamma} \cdot \mathbf{\Gamma}) + \frac{1}{2} \mathbf{K} \cdot (\nabla \mathbf{\Gamma} \cdot \nabla \mathbf{\Gamma}) \tag{4.1}$$

where \mathbf{C} is the (linear) elasticity tensor, \mathbf{b} are the constant coupling reversible effects to the irreversible ones, and \mathbf{c} is a dissipative constant. Clearly, the four coefficients in equation (4.1) are given in terms of Taylor’s formula. Moreover, we retain the definition of the quadratic dissipation function \mathcal{D} as given in (2.16). We notice that by adding a nonlinear quartic term in $\nabla \mathbf{U}$ and setting $\mathbf{b} = \mathbf{0}$, we obtain the free energy for Feng’s model in three dimensions (compare with (2.26)).

With the above identifications, we substitute the Lagrangian function

$$\mathcal{L} = \int_{\mathcal{B}_0} \rho_0 \left(\Psi - \frac{1}{2} \frac{\partial U_i}{\partial t} \frac{\partial U_i}{\partial t} \right) dV$$

and dissipation function \mathcal{D} into equations of motion (3.3) to obtain

$$\begin{aligned} \rho_0 \frac{\partial^2 \mathbf{U}}{\partial t^2} - \nabla \cdot (\mathbf{C} \cdot \nabla \mathbf{U}) &= 0 \\ \mathbf{\Lambda} \frac{\partial \mathbf{\Gamma}}{\partial t} - \nabla \cdot (\mathbf{K} \nabla \mathbf{\Gamma}) + \mathbf{b} \nabla \mathbf{U} + \mathbf{c} \mathbf{\Gamma} &= 0 \end{aligned} \tag{4.2}$$

where we have evaluated $\rho_0 \partial \Psi / [\partial(\nabla \mathbf{U})]$ at $\mathbf{\Gamma} = \mathbf{0}$ in equation (4.2)₁. In the above linear system of PDEs, we have obtained a linear diffusion equation coupled to a linear wave equation.

We notice that for a nonzero \mathbf{b} , equation (4.2)₂ picks up the reversible contribution $\mathbf{b} \nabla \mathbf{U}$, as observed. Hence, for $\mathbf{b} = \mathbf{0}$, equation (4.2)₂ is purely dissipative with no additional elastic effects, which is precisely what Chen *et al.* (2003) consider in their model: “The failure wave behind the shock wave front will not cause additional strain at the macroscopic level under the plate impact conditions...”.

The constant tensor \mathbf{b} , therefore, measures the *coupling* of the irreversible effects to the reversible effects. One expects that in an ideal situation, the constant \mathbf{b} should be set to zero, but due to varying material properties and/or different experimental configurations, residual elastic effects in the dissipative process may appear as a result, hence a non-zero \mathbf{b} . This observation explains the inconsistencies in the data observed by Feng as they pertain to the rise in the longitudinal strains behind the failure wave (Feng, 2000).

5. Conclusions

We have formulated a theory describing failure waves in a brittle elastic material at a continuum level based on a thermodynamically consistent theory. We have subsumed and extended in our analysis a prior model proposed by Feng for brittle fracture, and we have recovered Clifton’s model in the dissipationless limit. Our analysis reveals the importance of the coefficient of lateral diffusion d_2 in determining both the shard size and the transition from failure waves to isolated cracks. In this work, we have combined and modified several methodologies previously developed in the context of thermoelasticity, IVT, and irreversible thermodynamics.

In summary, we developed a constitutive theory and the equations of motion in the context of two fundamental thermodynamic functions: the (Helmholtz) free energy Ψ and a dissipation function \mathcal{D} . Feng’s model is recovered by specific choices of the potentials $\Psi = \Psi_F$ and $\mathcal{D} = \mathcal{D}_F$ defining the constitutive theory. Clifton’s model, in turn, can be recovered from Feng’s by taking the limit $\mathbf{\Lambda} \rightarrow \mathbf{0}$. Our two-function approach gives rise to a variational principle and a Lagrangian formalism. Finally, we presented a linear theory to gain insight into the interaction of the reversible and irreversible processes, and discussed its experimental manifestation.

A. Appendix

In this appendix, we derive Lagrange’s equations (3.3) in generalized coordinates from a variational principle that includes boundary terms. We adapt Biot’s method (Biot, 1970) for formulating a variational principle for thermoelasticity to our problem.

We begin by stating the complete variational principle

$$\delta \int_{t_1}^{t_2} (\psi - \mathcal{K} + \mathcal{D}) dt = \int_{t_1}^{t_2} R dt \tag{A.1}$$

where

$$R = \int_{\partial\mathcal{B}_0} (S_{ij}n_j\delta U_i - B_{ij}n_j\delta\Gamma_i) dA + \int_{\mathcal{B}_0} \rho_0 r_i \delta U_i dV$$

We start by expressing the unknown vectors \mathbf{U} and $\mathbf{\Gamma}$ in terms of k generalized coordinates $\mathbf{q} = (q_1, \dots, q_k)$. We write

$$\mathbf{U} = \mathbf{U}(q_1, \dots, q_k, \mathbf{X}, t) \quad \mathbf{\Gamma} = \mathbf{\Gamma}(q_1, \dots, q_k, \mathbf{X}, t) \tag{A.2}$$

The variations of variables \mathbf{U} and $\mathbf{\Gamma}$ are given in terms of variation $\delta\mathbf{q}$

$$\delta U_i = \frac{\partial U_i}{\partial q_j} \delta q_j \quad \delta \Gamma_i = \frac{\partial \Gamma_i}{\partial q_j} \delta q_j \tag{A.3}$$

First, we look at $\int_{\mathcal{B}_0} \Lambda_{ij} \dot{\Gamma}_i \delta \Gamma_j dV$

$$\begin{aligned} \int_{\mathcal{B}_0} \Lambda_{ij} \dot{\Gamma}_i \delta \Gamma_j dV &= \int_{\mathcal{B}_0} \Lambda_{ij} \dot{\Gamma}_i \frac{\partial \Gamma_j}{\partial q_m} \delta q_m dV = \int_{\mathcal{B}_0} \Lambda_{ij} \dot{\Gamma}_i \frac{\partial \dot{\Gamma}_j}{\partial \dot{q}_m} \delta q_m dV \\ &= \frac{\partial}{\partial \dot{q}_m} \int_{\mathcal{B}_0} \frac{1}{2} \Lambda_{ij} \dot{\Gamma}_i \dot{\Gamma}_j \delta q_m dV \quad \text{for} \quad \frac{\partial \Gamma_j}{\partial q_m} = \frac{\partial \dot{\Gamma}_j}{\partial \dot{q}_m} \end{aligned}$$

So, if we define

$$\mathcal{D} = \frac{1}{2} \int_{\mathcal{B}_0} \Lambda_{ij} \dot{\Gamma}_i \dot{\Gamma}_j dV \tag{A.4}$$

we obtain

$$\int_{\mathcal{B}_0} \Lambda_{ij} \dot{\Gamma}_i \delta \Gamma_j dV = \frac{\partial \mathcal{D}}{\partial \dot{q}_m} \delta q_m \doteq \delta \mathcal{D} \tag{A.5}$$

Next, we examine the variation of ψ . We assume that ψ is independent of the generalized velocities $\dot{\mathbf{q}}$. Moreover, below we keep the boundary terms when integrating by parts

$$\begin{aligned} \delta \psi &= \rho_0 \int_{\mathcal{B}_0} \left(\frac{\partial \Psi}{\partial U_{i,j}} \delta U_{i,j} + \frac{\partial \Psi}{\partial \Gamma_i} \delta \Gamma_i + \frac{\partial \Psi}{\partial \Gamma_{i,j}} \delta \Gamma_{i,j} \right) dV \\ &= \int_{\mathcal{B}_0} \left(-S_{ij,j} \delta U_i + \rho_0 \frac{\delta \Psi}{\delta \Gamma_i} \delta \Gamma_i \right) dV + \int_{\partial\mathcal{B}_0} (T_i \delta U_i - B_{ij} n_j \delta \Gamma_i) dA = \frac{\partial \psi}{\partial q_m} \delta q_m \end{aligned}$$

with $T_i = S_{ij}n_j$ is the force per unit area applied at the boundary of \mathcal{B}_0 , and $B_{ij} = -\rho_0 \partial \Psi / \partial \Gamma_{i,j}$ is associated with the entropy flux (see Section 2.1). In addition, we define the generalized force Q_i as

$$Q_i = \int_{\partial\mathcal{B}_0} \left(T_j \frac{\partial U_j}{\partial q_i} - B_{lj} n_j \frac{\partial \Gamma_l}{\partial q_i} \right) dA + \int_{\mathcal{B}_0} \rho_0 r_j \frac{\partial U_j}{\partial q_i} dV$$

where $\mathbf{r}(\mathbf{X}, t)$ is a body force (see Section 2.2), so that

$$R = Q_i \delta q_i$$

Lastly, we look at the variation of the kinetic energy \mathcal{K} . In Section 3, we calculated $\delta\mathcal{K}$

$$-\delta\mathcal{K} = \int_{\mathcal{B}_0} \rho_0 \ddot{U}_i \delta U_i dV = \int_{\mathcal{B}_0} \rho_0 \ddot{U}_i \frac{\partial U_i}{\partial q_m} \delta q_m dV$$

Since $\frac{\partial U_i}{\partial q_m} = \frac{\partial \dot{U}_i}{\partial \dot{q}_m}$, we obtain

$$\ddot{U}_i \frac{\partial U_i}{\partial q_m} = \frac{d}{dt} \left(\dot{U}_i \frac{\partial \dot{U}_i}{\partial \dot{q}_m} \right) - \dot{U}_i \frac{\partial \dot{U}_i}{\partial q_m}$$

Thus, we arrive at

$$-\delta\mathcal{K} = \int_{\mathcal{B}_0} \rho_0 \ddot{U}_i \delta U_i dV = \left\{ \frac{d}{dt} \left(\frac{\partial \mathcal{K}}{\partial \dot{q}_m} \right) - \frac{\partial \mathcal{K}}{\partial q_m} \right\} \delta q_m$$

Finally, by substituting the above three variations into variational principle (A.1) we obtain

$$\delta \int_{t_1}^{t_2} (\psi - \mathcal{K} + \mathcal{D}) dt = \int_{t_1}^{t_2} \left[\frac{\partial \psi}{\partial q_i} + \frac{d}{dt} \left(\frac{\partial \mathcal{K}}{\partial \dot{q}_i} \right) - \frac{\partial \mathcal{K}}{\partial q_i} + \frac{\partial \mathcal{D}}{\partial \dot{q}_i} \right] \delta q_i dt = \int_{t_1}^{t_2} Q_i \delta q_i dt$$

Since the time interval $[t_1, t_2]$ is arbitrary, we are left with

$$\frac{d}{dt} \left(\frac{\partial \mathcal{K}}{\partial \dot{q}_i} \right) - \frac{\partial \mathcal{K}}{\partial q_i} + \frac{\partial \mathcal{D}}{\partial \dot{q}_i} + \frac{\partial \psi}{\partial q_i} = Q_i \quad (\text{A.6})$$

We can rewrite equation (A.6) in the form of Lagrange's equations with dissipation by first introducing the full potential energy of the system

$$\mathcal{V} = \int_{\mathcal{B}_0} \rho_0 \Psi dV + \int_{\mathcal{B}_0} \rho_0 r_j U_j dV + \int_{\partial \mathcal{B}_0} (T_i U_i - B_{ij} n_j \Gamma_i) dA$$

and defining the Lagrangian $\mathcal{L} \doteq \mathcal{V} - \mathcal{K}$

$$\frac{\delta \mathcal{L}}{\delta q_i} - \frac{d}{dt} \left(\frac{\partial \mathcal{L}}{\partial \dot{q}_i} \right) + \frac{\partial \mathcal{D}}{\partial \dot{q}_i} = 0 \quad (\text{A.7})$$

This concludes the derivation.

We note that by substituting the expression for the variations of ψ , \mathcal{K} and \mathcal{D} into variational principle (A.1), we obtain the full nonlinear system (2.23).

Acknowledgements

The authors thank Roman Samulyak for his helpful comments. Hamid Said wishes to thank the generous support of Kuwait University through the graduate scholarship. James Glimm's research is supported in part by the Army Research Organization, award #W911NF1310249.

References

1. BEARDSLEY C.L., ANDERSON D.D., MARSH J.L., BROWN T.D., 2005, Interfragmentary surface area as an index of comminution severity in cortical bone impact, *Journal of Orthopaedic Research*, **23**, 3, 686-690
2. BEBERNES J., EBERLY D., 2013, *Mathematical Problems from Combustion Theory*, Applied Mathematical Sciences, Vol. 83, Springer Science & Business Media

3. BIOT M.A., 1955, Variational principles in irreversible thermodynamics with application to viscoelasticity, *Physical Review*, **97**, 6, 1463
4. BIOT M.A., 1956, Thermoelasticity and irreversible thermodynamics, *Journal of Applied Physics*, **27**, 3, 240-253
5. BIOT M.A., 1970, *Variational Principles in Heat Transfer: a Unified Lagrangian Analysis of Dissipative Phenomena*, DTIC Document
6. BLESS S.J., BRAR N.S., 2007, Failure waves and their effects on penetration mechanics in glass and ceramics, [In:] *Shockwave Science and Technology Reference Library*, 105-141, Springer
7. BOURNE N.K., ROSENBERG Z., 1996, The dynamic response of soda-lime glass, *Proceedings of the Conference of the American Physical Society Topical Group on Shock Compression of Condensed Matter*, **370**, 1, 567-572
8. CALLISTER W.D., RETHWISCH D.G., 2011, *Materials Science and Engineering*, Vol. 5, John Wiley & Sons, NY
9. CHEN Z., FENG R., XIN X., SHEN L., 2003, A computational model for impact failure with shear-induced dilatancy, *International Journal for Numerical Methods in Engineering*, **56**, 14, 1979-1997
10. CHORIN A.J., MARSDEN J.E., 1990, *A Mathematical Introduction to Fluid Mechanics*, 3rd edit., Springer
11. CLAVIN P., SEARBY G., 2016, *Combustion Waves and Fronts in Flows: Flames, Shocks, Detonations, Ablation Fronts and Explosion of Stars*, Cambridge University Press
12. CLIFTON R.J., 1993, Analysis of failure waves in glasses, *Applied Mechanics Reviews*, **46**, 12, 540-546
13. COURANT R., FRIEDRICHS K.O., 1991, *Supersonic Flow and Shock Waves*, Applied Mathematical Sciences, Vol. 21, Springer Science & Business Media
14. DAFERMOS C., 2005, *Hyperbolic Conservation Laws in Continuum Physics*, Springer-Verlag, Berlin
15. FENG R., 2000, Formation and propagation of failure in shocked glasses, *Journal of Applied Physics*, **87**, 4, 1693-1700
16. FENG X.W., LIU Z.F., CHEN G., YAO G.W., 2012, Experimental investigation on delayed failure of alumina under shock compression, *Advances in Applied Ceramics*, **111**, 4, 237-242
17. FUNG Y.-C., TONG P., 2001, *Classical and Computational Solid Mechanics*, Vol. 1, World Scientific
18. GOLDSTEIN H., 1965, *Classical Mechanics*, Pearson Education India
19. GURTIN M.E., FRIED E., ANAND L., 2010, *The Mechanics and Thermodynamics of Continua*, Cambridge University Press
20. KANEL G.I., RASORENOV S.V., FORTOV V.E., 1991, The failure waves and spallations in homogeneous brittle materials, *Shock Compression of Condensed Matter*, **199**, 1, 451-454
21. KANEL G.I., RAZORENOV S.V., SAVINYKH A.S., RAJENDRAN A., CHEN Z., 2005, A study of the failure wave phenomenon in glasses compressed at different levels, *Journal of Applied Physics*, **98**, 11, 113523
22. LEBON G., JOU D., CASAS-VÁZQUEZ J., 2008, *Understanding Non-Equilibrium Thermodynamics*, Springer
23. LEE J.J.-W., CONSTANTINO P.J., LUCAS P.W., LAWN B.R., 2011, Fracture in teeth a diagnostic for inferring bite force and tooth function, *Biological Reviews*, **86**, 4, 959-974
24. LIEBE T., STEINMANN P., BENALLAL A., 2001, Theoretical and computational aspects of a thermodynamically consistent framework for geometrically linear gradient damage, *Computer Methods in Applied Mechanics and Engineering*, **190**, 49, 6555-6576
25. MARSDEN J.E., HUGHES T. JR., 1994, *Mathematical Foundations of Elasticity*, Courier Corporation

26. MAUGIN G.A., 1990, Internal variables and dissipative structures, *Journal of Non-Equilibrium Thermodynamics*, **15**, 2, 173-192
27. MAUGIN G.A., 1992, *The Thermomechanics of Plasticity and Fracture*, Vol. 7, Cambridge University Press
28. MURAKAMI S., 2012, *Continuum Damage Mechanics: a Continuum Mechanics Approach to the Analysis of Damage and Fracture*, Springer
29. NEDJAR B., 2002, A theoretical and computational setting for a geometrically nonlinear gradient damage modelling framework, *Computational Mechanics*, **30**, 1, 65-80
30. NEUBERG J.W., TUFFEN H., COLLIER L., GREEN D., POWELL T., DINGWELL D., 2006, The trigger mechanism of low-frequency earthquakes on Montserrat, *Journal of Volcanology and Geothermal Research*, **153**, 1, 37-50
31. PARTOM Y., 1998, Modeling failure waves in glass, *International Journal of Impact Engineering*, **21**, 9, 791-799
32. RAYLEIGH L., 1945, *Theory of Sound*, Vol. 1, Macmillan, London, reprinted 1945 by Dover, New York
33. SAPOZHNIKOV O.A., MAXWELL A.D., MACCONAGHY B., BAILEY M.R., 2007, A mechanistic analysis of stone fracture in lithotripsy, *The Journal of the Acoustical Society of America*, **121**, 2, 1190-1202
34. WALLEY S.M., 2013, An introduction to the properties of silica glass in ballistic applications, *Strain*, **50**, 470-500
35. WEI H., SAMULYAK R., 2014, Mass-conservative network model for brittle fracture, *Journal of Coupled Systems and Multiscale Dynamics*, **2**, 2, 79-90
36. ZHANG Z.-X., 2016, *Rock Fracture and Blasting: Theory and Applications*, Butterworth-Heinemann
37. ZIEGLER H., 2012, *An Introduction to Thermomechanics*, Vol. 21, Elsevier

Manuscript received April 27, 2017; accepted for print October 26, 2017

SMOOTHED PARTICLE HYDRODYNAMICS MODELLING OF THE RAYLEIGH-PLATEAU INSTABILITY

MICHAŁ OLEJNIK, KAMIL SZEWC

Institute of Fluid-Flow Machinery, Polish Academy of Sciences, Gdańsk, Poland
e-mail: michal.olejnik@imp.gda.pl; kamil.szewc@gmail.com

The break-up of liquid ligaments and formation of droplets are elementary phenomena in multiphase flows which are of high importance in industrial and medical applications. From the numerical point of view, they require proper interface and surface tension treatment. In the present work, we apply Smoothed Particle Hydrodynamics, a meshless approach, to simulate the break-up of a liquid cylinder inside the gaseous phase, i.e. the Rayleigh-Plateau instability. Results obtained in 3D show that even a relatively coarse resolution allows one to predict correctly the size of droplets formed in the process. The detailed analysis of the break-up time in 2D setup implies that a certain level of spatial discretisation needs to be reached to determine this moment precisely.

Keywords: meshless methods, SPH, capillary jet break-up, interfacial flows

1. Introduction

Multiphase flows have been of interest for both academic and industrial communities for a long period of time. Accurate interface tracking and surface tension modelling are of particular importance due the influence on the flow solution as a whole. Another challenge has been the ability to properly treat high density ratios, frequently appearing in industrial problems. Over the years, many different approaches have been developed to tackle this matter, including Volume of Fluid, Level Set and Front Tracking methods, for a comprehensive overview see the handbook by Tryggvason (2011).

Among existing methods for fluid flow modelling, Smoothed Particle Hydrodynamics (SPH) remains a relatively new alternative. It is a particle based meshless method of Lagrangian nature. SPH was originally developed in the 1970s for astrophysical problems, and later adapted for fluid mechanics simulations (Monaghan, 2012), where it gained more and more interest over the recent years. Branches where its meshless nature is notably favorable are free-surface flows (Violeau and Rogers, 2016) and general two-fluid flows with interfacial surfaces (Das and Das, 2010b; SzeWC *et al.*, 2013; Olejnik *et al.*, 2016). SPH advantages in the latter case are mainly the easiness in dealing with high density ratios and straightforward treatment of the interface. Recently, applications of SPH have appeared in the area of microfluidics (Wieth *et al.*, 2016).

In the present paper, we focus on a particular application of SPH to interfacial flows which is the Rayleigh-Plateau (R-P) instability. This fundamental phenomenon leads to atomisation of liquid jets and, likewise, the Kelvin-Helmholtz instability (Boeck *et al.*, 2007) is one of the basic mechanisms of the regime change in complex multiphase flows. Another area where breaking-up liquid ligaments is of high concern is the formation of droplets of a desired size in drug delivery and lab-on-a-chip devices (Abate *et al.*, 2009; Guzowski *et al.*, 2013). In our work, we test feasibility of SPH in these problems. Although attempts in this matter have already been made for the case of gravity-driven dripping break-up, see Sirotkin and Yoh (2012), they focused on qualitative results and influence of dimensionless numbers. In the present study, we pay special attention to the resolution needed for accurate prediction of the liquid ligament break-up time.

2. SPH for multiphase flows

2.1. Basics of the method

The general idea behind SPH lies in interpolation theory. Let us consider any scalar (for simplicity) field A . The integral formula

$$A(\mathbf{r}) = \int_{\Omega} A(\mathbf{r}') \delta(\mathbf{r} - \mathbf{r}') d\mathbf{r}', \quad (2.1)$$

where $\delta(\mathbf{r})$ is the Dirac delta function, can be used to express the field value at the point \mathbf{r} in space Ω . To obtain SPH approximation, we first replace $\delta(\mathbf{r})$ with the weighting kernel function $W(\mathbf{r}, h)$ which should be normalised, symmetrical and converging to $\delta(\mathbf{r})$ with $h \rightarrow 0$ (Mognaghan, 1992). Argument h is the so-called smoothing length and it determines the interpolation range. In our work, we use the quintic kernel proposed by Wendland (1995)

$$W(\mathbf{r}, h) = C \begin{cases} \left(1 - \frac{q}{2}\right)^4 (2q + 1) & \text{for } q < 2 \\ 0 & \text{otherwise} \end{cases} \quad (2.2)$$

where $q = |\mathbf{r}|/h$ and C is the normalisation constant ($C = 7/4\pi h^2$ in 2D and $C = 21/16\pi h^3$ in 3D), as guaranteeing good stability of computations (Dehnen and Aly, 2012; Szewc *et al.*, 2012a).

The second step consists in discretisation of the space into a set of particles of the volume $\Omega_b = m_b/\rho_b$, where m_b is mass and ρ_b is density of the b -th particle. As a result, the integral from Eq. (2.1) is approximated by a sum, i.e.

$$A(\mathbf{r}) \simeq \sum_b A(\mathbf{r}_b) W(\mathbf{r} - \mathbf{r}_b, h) \Omega_b \quad (2.3)$$

In the shorthand notation, the SPH approximation $\langle A \rangle_a$ of the field A at any point a is defined as

$$\langle A \rangle_a = \sum_b A_b W_{ab}(h) \Omega_b \quad (2.4)$$

where $A_b = A(\mathbf{r}_b)$ and $W_{ab}(h) = W(\mathbf{r}_a - \mathbf{r}_b, h)$. Thanks to the properties of $W(\mathbf{r}, h)$, differentiation can be shifted from the field to the kernel function yielding

$$\langle \nabla A \rangle_a = \sum_b A_b \nabla W_{ab}(h) \Omega_b \quad (2.5)$$

Further derivatives can be obtained in a similar way.

Using the above method, various kinds of differential equations can be rewritten into the SPH formalism and solved by calculating interactions between particles, hence its wide application. More detailed information on the derivation of SPH and basics of the method can be found in the handbook by Violeau (2012).

2.2. Governing equations

The set of governing equations for viscous flow consists of the Navier-Stokes (momentum) equation

$$\frac{d\mathbf{u}}{dt} = -\frac{1}{\rho} \nabla p + \frac{\mu}{\rho} \Delta u + \mathbf{a} \quad (2.6)$$

and the continuity equation

$$\frac{d\rho}{dt} = -\rho \nabla \cdot \mathbf{u} \quad (2.7)$$

where \mathbf{u} denotes the velocity vector, ρ is fluid density, p is pressure and μ is dynamic viscosity. In Eq. (2.6), \mathbf{a} stands for the interfacial term, detailed in Section 2.3. Due to the Lagrangian nature of SPH, we also include the advection equation

$$\frac{d\mathbf{r}}{dt} = \mathbf{u} \quad (2.8)$$

Depending on the purpose and assumptions, different SPH formalisms for the fluid flow can be obtained by using Eqs. (2.4) and (2.5). In the present study, we use a formulation proposed by Hu and Adams (2006). To the best of our knowledge, their approach is well suited for modelling multiphase flows with large density ratios (Szewc *et al.*, 2012b). The pressure term in Eq. (2.6) will become

$$\left\langle \frac{\nabla p}{\rho} \right\rangle_a = \frac{1}{m_a} \sum_b \left(\frac{p_a}{\theta_a^2} + \frac{p_b}{\theta_b^2} \right) \nabla_a W_{ab}(h) \quad (2.9)$$

where θ is the inverse of the particle volume. The viscous term of Eq. (2.6), obtained by combining SPH formalism and Finite Difference Method, takes the form

$$\left\langle \frac{\mu}{\rho} \Delta \mathbf{u} \right\rangle_a = \frac{1}{m_a} \sum_b \frac{2\mu_a\mu_b}{\mu_a + \mu_b} \left(\frac{1}{\theta_a^2} + \frac{1}{\theta_b^2} \right) \frac{\mathbf{r}_{ab} \cdot \nabla_a W_{ab}(h)}{\mathbf{r}_{ab}^2 + 0.01h^2} \mathbf{u}_{ab} \quad (2.10)$$

where $\mathbf{u}_{ab} = \mathbf{u}_a - \mathbf{u}_b$. The key feature of the approach proposed by Hu and Adams (2006) is the treatment of the continuity equation. Instead of rewriting Eq. (2.7) into the SPH language, density is found from

$$\langle \rho \rangle_a = m_a \sum_b W_{ab}(h) = m_a \theta_a \quad (2.11)$$

This allows the density field to be represented only by the spatial distribution of particles and not by their masses. Thanks to this, densities of particles near the interface are not affected by the other fluid, which is important in multiphase flow modelling. Note that Eq. (2.11) requires the whole domain to be filled with SPH particles, hence it is not suitable for multiphase computations in which the lighter phase is neglected, e.g. see the approach proposed by Ordoubadi *et al.* (2017).

In this work, we use the Weakly Compressible SPH approach (WCSPH). The set of equations is closed with the state equation

$$p = \frac{s^2 \rho_0}{\gamma} \left[\left(\frac{\rho}{\rho_0} \right)^\gamma - 1 \right] \quad (2.12)$$

where s is the artificial speed of sound, ρ_0 is the reference (initial) density and γ is a numerical parameter. Values of c and γ are chosen to ensure density fluctuations at a level of 1% or below. In multiphase flow modelling, it is a common practice to treat the liquid as incompressible with $\gamma = 7$, and the gas as compressible with $\gamma = 1.4$. We follow this approach in this study.

2.3. Surface tension

The influence of surface tension is modelled with the Continuum Surface Force method (CSF), originally proposed by Brackbill *et al.* (1992), with SPH implementation due to Morris (2000). In this approach, surface tension forces are converted into a force per unit volume

$$\mathbf{F}_s = \mathbf{f}_s \delta_s \quad (2.13)$$

where δ_s is a suitably chosen surface delta function and

$$\mathbf{f}_s = \sigma \kappa \hat{\mathbf{n}} \quad (2.14)$$

is the force per unit area, σ is the surface tension coefficient, κ is the local curvature of the interface and $\hat{\mathbf{n}}$ is the unit vector normal to the interface. Using the so-called color function c (say, $c = 0$ for the first phase and $c = 1$ for the second one) $\hat{\mathbf{n}}$ can be calculated using the formula

$$\hat{\mathbf{n}} = \frac{\mathbf{n}}{|\mathbf{n}|} = \frac{\nabla c}{|\nabla c|} \quad (2.15)$$

The vector \mathbf{n} is obtained from

$$\mathbf{n}_a = \varrho_a \sum_b (\tilde{c}_b - \tilde{c}_a) \nabla_a W_{ab}(h) \Omega_b \quad (2.16)$$

where \tilde{c} stands for the smoothed color function, i.e.

$$\tilde{c}_a = \sum_b c_b W_{ab}(h) \Omega_b \quad (2.17)$$

The local curvature is obtained from

$$\kappa = -\nabla \cdot \hat{\mathbf{n}} \quad (2.18)$$

Assuming that $\delta_s = |\mathbf{n}|$, the influence of surface tension can be included in Eq. (2.6) by adding the term

$$\mathbf{a}_a = \frac{\sigma}{\varrho_a} \kappa_a \mathbf{n}_a \quad (2.19)$$

Following Morris (2000), we also exclude from calculations of surface tension effects particles for which $|\mathbf{n}_a|$ is below the threshold of $0.01/h$. This greatly improves accuracy of curvature estimation on fringes of the interfacial area.

2.4. Interface correction

As already mentioned, SPH does not require any special treatment of the interface. In some cases, however, particles of two immiscible phases can penetrate into the bulk of the other phase. This is particularly visible in problems involving high density ratios. To prevent this unphysical phenomenon, we enforce a small repulsive interaction between different phases (Szewc *et al.*, 2013), by adding to Eq. (2.6) the term

$$\Xi_a = \frac{\varepsilon}{m_a} \sum_{\substack{b \\ c_b \neq c_a}} \left(\frac{1}{\theta_a^2} + \frac{1}{\theta_b^2} \right) \nabla_a W_{ab}(h) \quad (2.20)$$

where ε is a numerical parameter. This correction, however, may change the characteristics of the flow if used improperly. Detailed analysis of this approach and the spurious interface fragmentation in the case of gas bubbles rising in the liquid can be found in the work of Szewc *et al.* (2015).

3. Results

In order to validate the SPH approach for modelling of the break-up of liquid jets, we decided to perform simulations of the case presented by Dai and Schmidt (2005). We consider a fully periodic, cubic domain of the edge of length L containing a column of liquid l surrounded by the gaseous phase g . The column is placed in the centre of the domain according to

$$\left(y - \frac{L}{2}\right)^2 + \left(z - \frac{L}{2}\right)^2 \leq r_0^2 \quad (3.1)$$

where $r_0 = 0.1L$ and $x \in [0, L]$. The density and viscosity ratios are respectively $\rho_l/\rho_g = 1000$ and $\mu_l/\mu_g = 100$. The initial perturbation of the liquid velocity field is given as

$$u_x = u_0 \sin \frac{2\pi x}{L} \quad u_y = 0 \quad u_z = 0 \quad (3.2)$$

where u_0 is the initial velocity amplitude. Dimensionless numbers describing this case are the Weber number

$$\text{We} = \frac{\rho_l r_0 u_0^2}{\sigma} \quad (3.3)$$

and the Reynolds number

$$\text{Re} = \frac{\rho_l u_0 r_0}{\mu_l} \quad (3.4)$$

In our study, we take $\text{We} = 1.4$ and $\text{Re} = 18$. The time is made dimensionless with

$$t_c = \sqrt{\frac{\rho_l (r_0)^D}{\sigma}} \quad (3.5)$$

where D stands for the number of spatial dimensions. In the 2D case, we simply consider the central slice of the domain in the xy plane.

In the present study, instead of raw particles data we analyse data interpolated onto a regular grid. The reason for this is that the studied phenomena involve very thin liquid ligaments. Even for relatively fine resolution positions of SPH particles may be slightly perturbed, which creates impression of a misshapen interface. The grid used for post-processing has the cell size of Δr , which is the initial spacing between the particles. The interpolation is performed with SPH formulation with the same weighting function, i.e. the Wendland kernel, that has been employed in calculations. This way, without distorting any information, detailed analysis is made significantly easier. Since in this work the shape of the interface is of utmost interest, we treat it as the isoline or isosurface of the color function $c = 0.5$. To obtain the isoline/isosurface Python libraries Matplotlib (2D cases, (Hunter, 2007)) and Mayavi (3D cases, (Ramachandran and Varoquaux, 2011)) have been used. Figure 1 shows an exemplary result of such treatment.

3.1. 3D case

The SPH simulations have been performed for $L/h = 64$ and $L/h = 128$ with $h/\Delta r = 1.5625$ which resulted in 10^6 particles filling the whole domain, while 31 600 of them were forming the liquid cylinder for the lower resolution, and $8 \cdot 10^6$ to 252 800 respectively for the higher one. Figure 2 presents results obtained from SPH simulation with $L/h = 64$ for different values of the interface sharpness correction term, Eq. (2.20), against the reference material (Dai and Schmidt, 2005). The general agreement is good, however, some discrepancies can be observed at later stages of simulations. The ligament break-up for SPH calculations occurs around $t^+ = 5.5$,

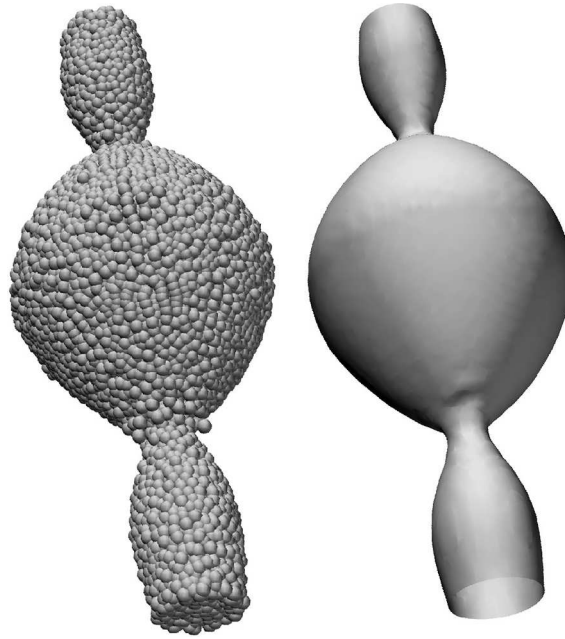


Fig. 1. Positions of SPH particles representing the liquid vs. isosurface of the color function $c = 0.5$ interpolated onto a uniform grid

while for the reference material it is $t^+ = 6.49$. The main reason for this discrepancy is that in the SPH computations we do not use the Adaptive Mesh Refinement (AMR) or any similar techniques, contrary to calculations by Dai and Schmidt (2005). We should also mention that in the cited work, due to the use of AMR, the break-up time was defined as the moment when the liquid ligament between droplets reaches radius of $0.05r_0$. Note that AMR in grid-based methods is a standard technique, while in SPH it is still a novelty in development, see Vacondio *et al.* (2016) or Olejnik *et al.* (2017). Furthermore, with an increase in the value of ε we observe a decrease in the diameter of the liquid bridge between the droplets at $t^+ = 4.49$. This tendency is the outcome of additional interfacial pressure repelling phases from each other, see Eq. (2.20). The quantitative comparison is shown in Fig. 3. It shows the disturbance growth process quantified as

$$\frac{r_{max}(t) - r_0}{r_0} \quad (3.6)$$

where $r_{max}(t)$ is the maximum distance of the liquid phase measured from the axis of symmetry. The results show high agreement with the reference data, independently of the value of ε used. The higher resolution also does not yield significantly different results. We can conclude that even a coarse resolution is sufficient to correctly predict the size of formed droplets. As shown in Fig. 4, the resolution does influence their shape. For $L/h = 128$, the curvature of the central droplet is lower than for $L/h = 64$. All in all, the quality of SPH simulation of the considered case proves that the method is suitable for simulations of the capillary jet break up provided that the resolution is high enough. The issue of the interface correction term and its influence on the flow requires further investigation.

3.2. 2D case

Since SPH simulations in 3D are costly, for the purpose of a more detailed analysis we decided to settle on the 2D setup. To determine the influence of the resolution on the moment of break-up, the calculations have been performed for $h/\Delta r = 2$ and different values of the

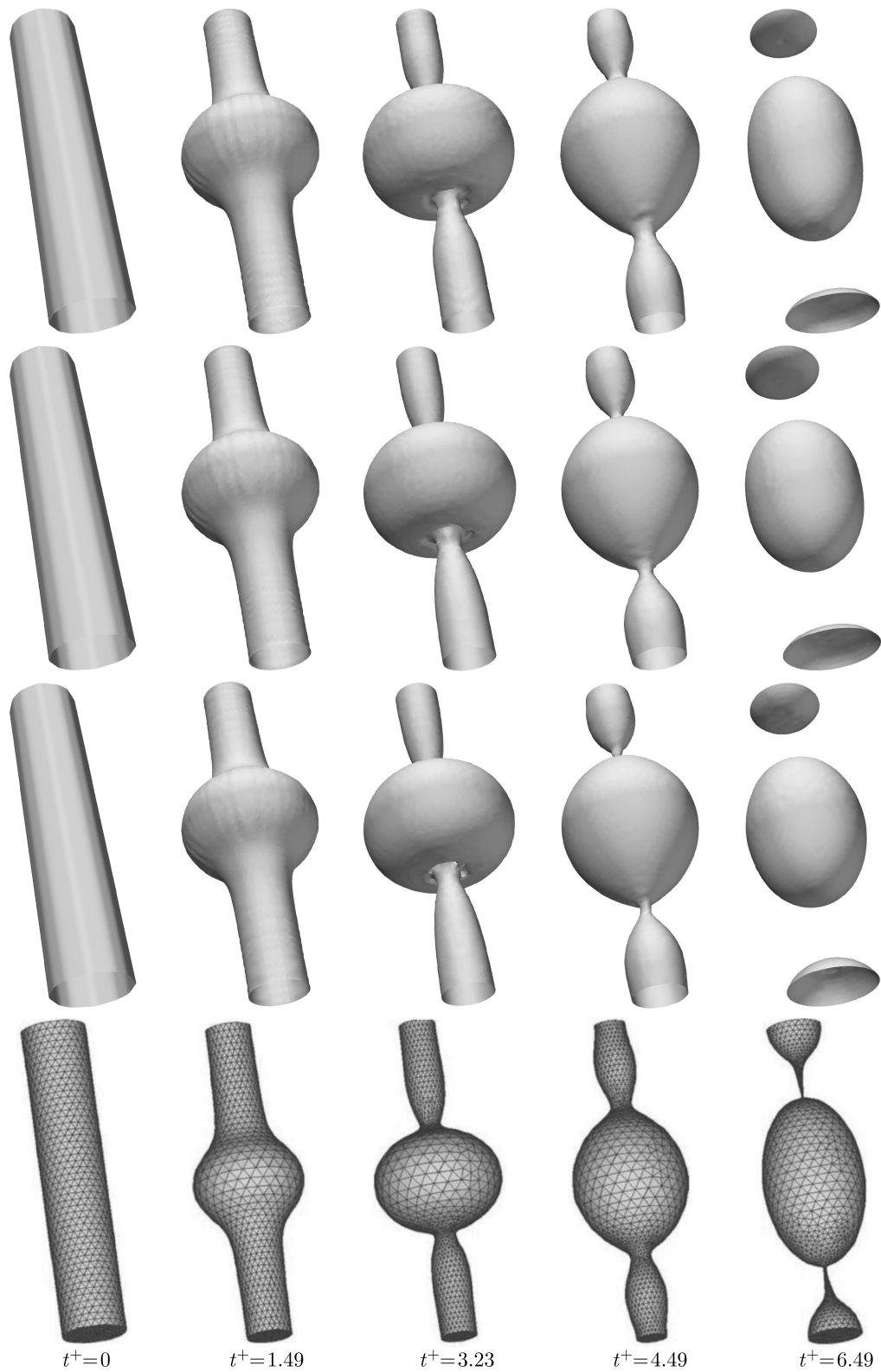


Fig. 2. Results of SPH simulation of the R-P instability without the interface sharpness correction term (1st row), with $\varepsilon = 0.5$ (2nd row) and $\varepsilon = 0.75$ (3rd row). The 4th row presents the reference data of Dai and Schmidt (2005) reprinted with the permission from Elsevier

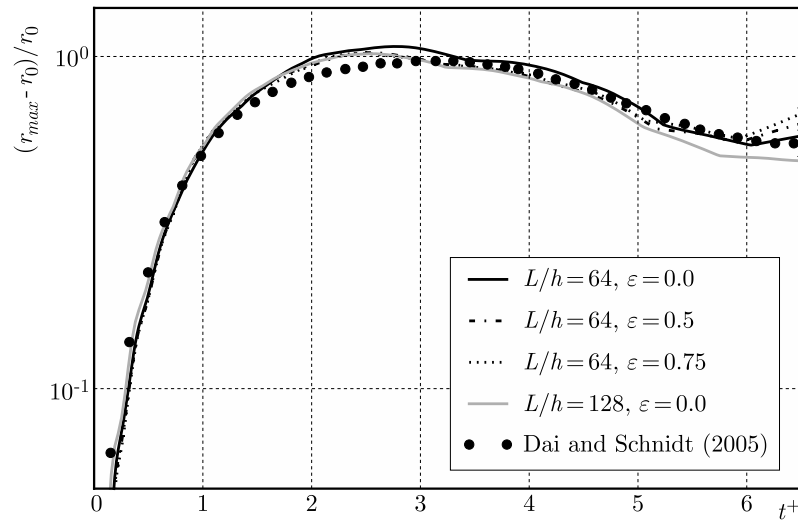


Fig. 3. Disturbance growth in time; SPH results compared to the reference material from Dai and Schmidt (2005)

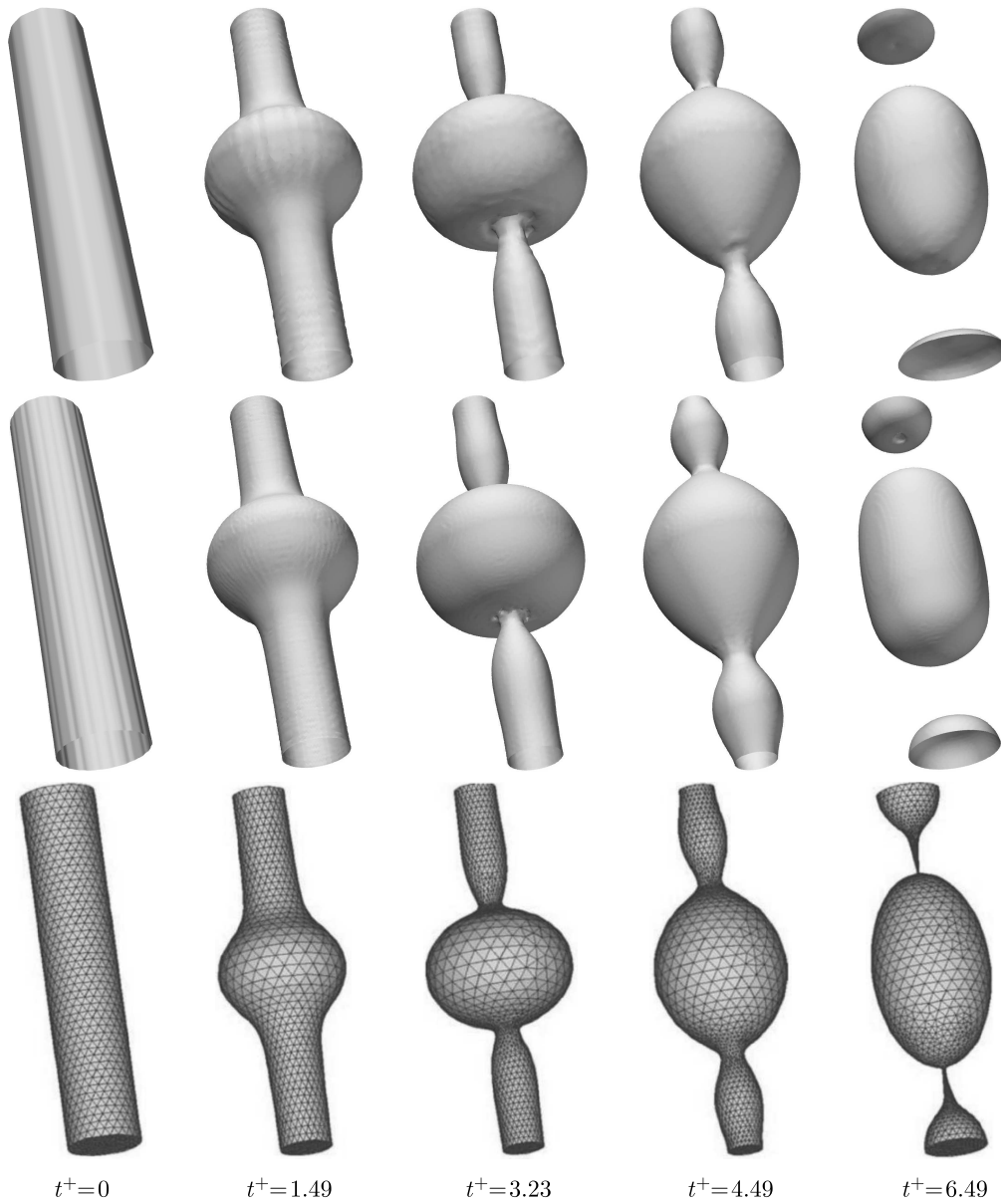


Fig. 4. Results of SPH simulation of the R-P instability without the interface sharpness correction term for $L/h = 64$ (top row) and $L/h = 128$ (middle row). In comparison to the reference data of Dai and Schmidt (2005) reprinted with the permission from Elsevier

smoothing length, i.e. $L/h = 64, 128, 256, 384$ and 512 . Figure 5 shows the evolution of the interface in the simulation for $L/h = 512$. We defined the break-up time as the moment when the color function drops to the value $c = 0.5$ in any of the points situated on the symmetry line of the liquid column. An example of the interface shape and the values of the color function at such a moment are presented in Fig. 6. As shown in Fig. 7, the outcome is highly dependent on the resolution. For the highest values of h the dependency is almost linear, i.e. the lower resolution, the earlier moment of break-up. Beginning from $L/h = 256$, the growth is barely visible, and it is safe to assume that this resolution is sufficient to fully resolve the flow without computational overhead. Analysis of the disturbance growth in time, defined with Eq. (3.6), confirms this statement. We see that the three highest resolutions tested are in agreement and hard to distinguish while the three lowest ones tend to diverge from them, especially in the later stage of simulation.

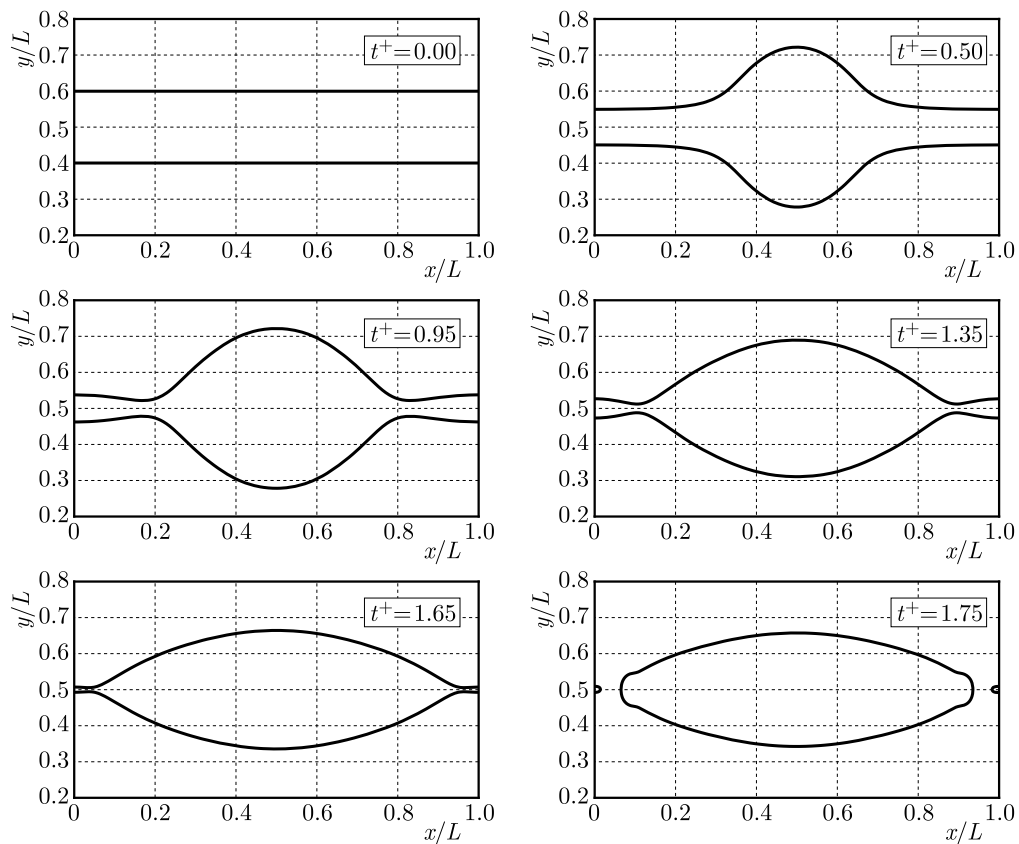


Fig. 5. Evolution of 2D R-P instability. Result of SPH simulation for $L/h = 512$

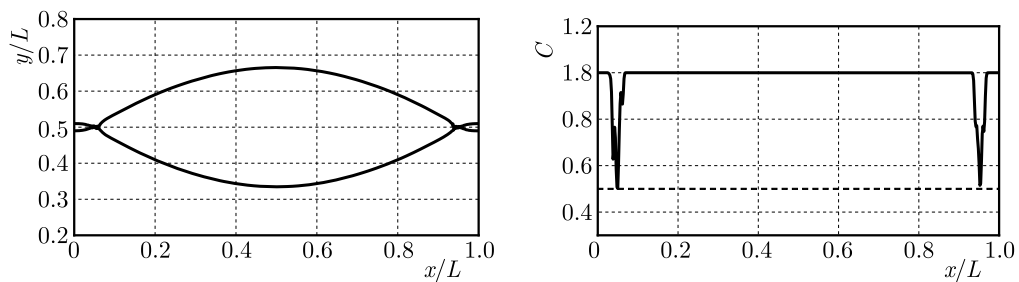


Fig. 6. Definition of the break-up time in SPH simulations; example for $L/h = 256$. Shape of the interface (left) and color function profile (right) at $t^+ = 1.684$

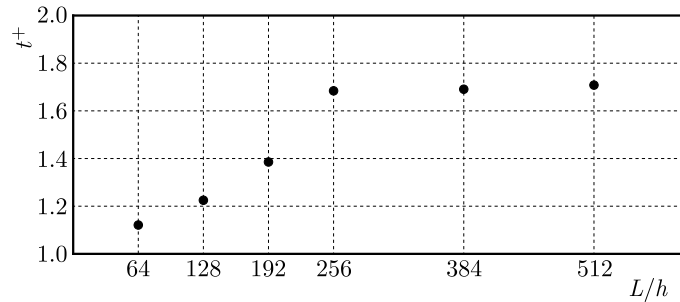


Fig. 7. Dependency of the dimensionless moment of break-up on the resolution

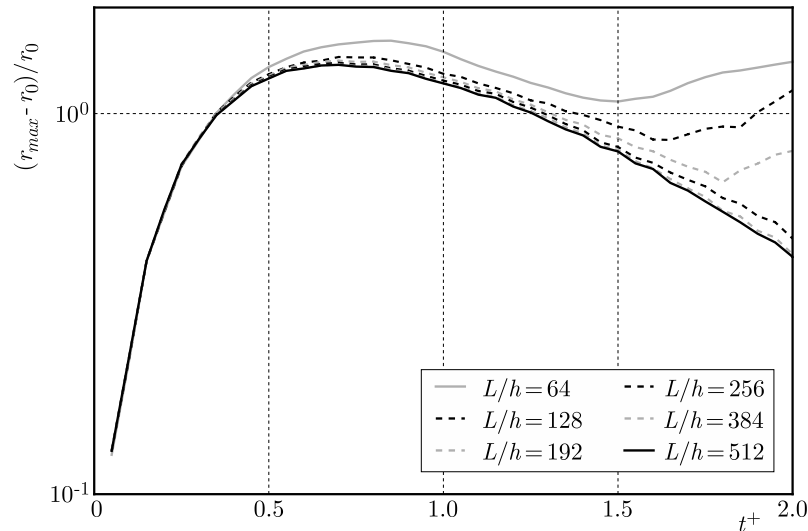


Fig. 8. Disturbance growth in time in the 2D case

4. Conclusions

In the present study, we have successfully applied SPH to simulations of the R-P instability. Results obtained in the 3D case showed that SPH can predict droplets size with a comparable accuracy as a mesh based method using AMR, despite the relatively low resolution used. Analysis of the break-up time in 2D, however, showed that resolution needs to be on a relatively high level to correctly predict this moment. It is worth to note that thanks to the GPU parallelisation, for which SPH is exceptionally suitable (Szewc, 2014), it is still affordable for a desktop class computer.

The method proposed in this paper can naturally be extended for other situations involving generations of microdroplets in the so-called lab-on-a-chip devices (Guzowski *et al.*, 2013). The presence of solid boundaries in such devices is not an issue since reliable implementations of boundary conditions in SPH already exist (Adami *et al.*, 2012). Recent works also show that the wetting phenomena and contact angles can be properly treated within SPH framework (Das and Das, 2010a; Yeganehdoust *et al.*, 2016). This makes SPH an interesting alternative to the traditional mesh based codes as a tool for engineering simulations. Optimisation of devices for e.g. precise and repeatable delivery of microdroplets sequences (Abate *et al.*, 2009) can readily be performed with SPH.

Acknowledgments

K.S. was supported by Électricité de France (EDF) R&D project No. 8160-5910131187. M.O. was supported by the EU FP7 project Nugenia Plus No. 604965. The authors wish to thank Professor Jacek Pozorski for his encouragement and insightful discussions.

References

1. ABATE A.R., POITZSCH A., HWANG Y., LEE J., CZERWINSKA J., WEITZ D.A., 2009, Impact of inlet channel geometry on microfluidic drop formation, *Physical Review E*, **80**, 026310
2. ADAMI S., HU X.Y., ADAMS N.A., 2012, A generalized wall boundary condition for smoothed particle hydrodynamics, *Journal of Computational Physics*, **231**, 7057-7075
3. BOECK T., LI J., LÓPEZ-PAGÉS E., YECKO P., ZALESKI S., 2007, Ligament formation in sheared liquid-gas layers, *Theoretical and Computational Fluid Dynamics*, **21**, 59-76
4. BRACKBILL J.U., KOTHE D.B., ZEMACH C., 1992, A continuum method for modeling surface tension, *Journal of Computational Physics*, **100**, 335-354
5. DAI M., SCHMIDT S.P., 2005, Adaptive tetrahedral meshing in free-surface flow, *Journal of Computational Physics*, **208**, 228-252
6. DAS A.K., DAS P.K., 2010a, Equilibrium shape and contact angle of sessile drops of different volumes – Computation by SPH and its further improvement by DI, *Chemical Engineering Science*, **65**, 4027-4037
7. DAS A.K., DAS P.K., 2010b, Incorporation of diffuse interface in smoothed particle hydrodynamics: Implementation of the scheme and case studies, *International Journal for Numerical Methods in Fluids*, **67**, 671-699
8. DEHNEN W., ALY H., 2012, Improving convergence in smoothed particle hydrodynamics simulations without pairing instability, *Monthly Notices of Royal Astronomical Society*, **425**, 1068-1082
9. GUZOWSKI J., JAKIELA S., KORCZYK P.M., GARSTECKI P., 2013, Custom tailoring multiple droplets one-by-one, *Lab on a Chip*, **13**, 4308-4311
10. HU X.Y., ADAMS N.A., 2006, A multi-phase SPH method for macroscopic and mesoscopic flows, *Journal of Computational Physics*, **213**, 844-861
11. HUNTER J.D., 2007, Matplotlib: A 2D Graphics Environment, *Computing in Science and Engineering*, **9**, 90-95
12. MONAGHAN J.J., 1992, Smoothed Particle Hydrodynamics, *Annual Review of Astronomy and Astrophysics*, **30**, 543-574
13. MONAGHAN J.J., 2012, Smoothed Particle Hydrodynamics and its diverse applications, *Annual Review of Fluid Mechanics*, **44**, 323-346
14. MORRIS J.P., 2000, Simulating surface tension with smoothed particle hydrodynamics, *International Journal for Numerical Methods in Fluids*, **33**, 333-353
15. OLEJNIK M., SZEWC K., POZORSKI J., 2016, Modelling of the flow regime transition with the Smoothed Particle Hydrodynamics, *Proceedings of 9th International Conference on Multiphase Flow*, Florence, Italy, paper No. 1037
16. OLEJNIK M., SZEWC K., POZORSKI J., 2017, SPH with dynamical smoothing length adjustment based on the local flow kinematics, *Journal of Computational Physics*, **348**, 23-44
17. ORDOUBADI M., YAGHOUBI M., YEGANEHDOUST F., 2017, Surface tension simulation of free surface flows using smoothed particle hydrodynamics, *Scientia Iranica, Transactions B: Mechanical Engineering*, **24**, 2019-2033
18. RAMACHANDRAN P., VAROQUAUX G., 2011, Mayavi: 3D visualization of scientific data, *Computing in Science and Engineering*, **13**, 40-51
19. SIROTKIN F.V., YOH J.J., 2012, A new particle method for simulating breakup of liquid jets, *Journal of Computational Physics*, **231**, 1650-1674
20. SZEWC K., 2014, Smoothed Particle Hydrodynamics simulations using Graphics Processing Units, *TASK Quarterly*, **18**, 67-80

21. SZEWC K., POZORSKI J., MINIER J.-P., 2012a, Analysis of the incompressibility constraint in the SPH method, *International Journal for Numerical Methods in Engineering*, **91**, 343-369
22. SZEWC K., POZORSKI J., MINIER J.-P., 2013, Simulations of single bubbles rising through viscous liquids using Smoothed Particle Hydrodynamics, *International Journal of Multiphase Flow*, **50**, 98-105
23. SZEWC K., POZORSKI J., MINIER J.-P., 2015, Spurious interface fragmentation in multiphase SPH, *International Journal for Numerical Methods in Engineering*, **103**, 625-649
24. SZEWC K., TANIÈRE A., POZORSKI J., MINIER J.-P., 2012b, A study on application of Smoothed Particle Hydrodynamics to multi-phase flows, *International Journal of Nonlinear Sciences and Numerical Simulation*, **13(6)**, 383-395
25. TRYGGVASON G., SCARDOVELLI R., ZALESKI S., 2011, *Direct Numerical Simulations of Gas-Liquid Multiphase Flows*, Cambridge University Press
26. WENDLAND H., 1995, Piecewise polynomial, positive definite and compactly supported radial functions of minimal degree, *Advances in Computational Mathematics*, **4**, 389-396
27. WIETH L., KELEMEN K., BRAUN S., KOCH R., BAUER H.J., SCHUCHMANN H.P., 2016, Smoothed Particle Hydrodynamics (SPH) simulation of a high-pressure homogenization process, *Microfluidics and Nanofluidics*, **20**, 42
28. VACONDIO R., ROGERS B.D., STANSBY P.K., MIGNOSA P., 2016, Variable resolution for SPH in three dimensions: Towards optimal splitting and coalescing for dynamic adaptivity, *Computer Methods in Applied Mechanics and Engineering*, **300**, 442-460
29. VIOLEAU D., 2012, *Fluid Mechanics and the SPH Method*, Oxford University Press, Oxford
30. VIOLEAU D., ROGERS B.D., 2016, Smoothed particle hydrodynamics (SPH) for free-surface flows: past, present and future, *Journal of Hydraulic Research*, **54**, 1-26
31. YEGANEHDOUST F., YAGHOUBI M., EMDAD H., ORDOUBADI M., 2016, Numerical study of multiphase droplet dynamics and contact angles by smoothed particle hydrodynamics, *Applied Mathematical Modelling*, **40**, 8493-8512

Manuscript received July 12, 2017; accepted for print October 27, 2017

EXPERIMENTAL INVESTIGATION ON THE PIEZOELECTRIC ENERGY HARVESTER AS A SELF-POWERED VIBRATION SENSOR

DARIUSZ GRZYBEK, PIOTR MICEK

*AGH University of Science and Technology, Faculty of Mechanical Engineering and Robotics, Cracow, Poland
e-mail: dariusz.grzybek@agh.edu.pl; miecek-pt@agh.edu.pl*

The article presents an experimental study of a system consisting of a piezoelectric energy harvesting device, Graetz bridge rectifier, capacitor, voltage comparator and radio transmitter. In the presented experimental study, the recovered electrical energy is accumulated in the capacitor and is used to send signals by a radio transmitter. In the first part, the application of piezoelectric energy harvesting devices based on the cantilever beam in wireless monitoring systems is discussed. In the second part, the mathematical model of energy conversion in the piezoelectric energy harvesting devices is presented. In the third part, the characteristics obtained during laboratory research are presented.

Keywords: piezoelectric energy harvesting, piezoelectric composite, wireless sensor, vibration

1. Introduction

An effective monitoring of some building structures demands measurements of selected parameters in many places of the monitored structure. Such a problem exists, among other things, in Structural Health Monitoring (SHM) systems, which are used for behaviour monitoring of several objects, e.g. bridges, aircrafts, ships (Lynch and Lohg, 2006). SHM systems can be composed of tens or hundreds of sensors, each of which has to be powered. The monitoring system of three bridges in Hong Kong: Tsing Ma, Ting Kau and Kap Shui Mun contains 300 sensors measuring several variables (deformations, displacements, acceleration, temperature) (Chan *et al.*, 2006). The monitoring system containing 63 sensors measures the stress in the girders of Taylor bridge in Canada (Kim *et al.*, 2007). The monitoring system of the span vibration of Golden Gate bridge in the USA contains 64 sensors (De Roeck *et al.*, 2000). The conventional supply of sensors in such a monitoring system requires the use of either kilometres of wires or a large number of batteries. It should also be noted that in the case of batteries, there is a necessity to replace these batteries, which increases operating costs of monitoring systems and makes the whole system not eco-friendly (Soobum *et al.*, 2009). Hence, nowadays, the development of wireless power of sensors is needed in the monitoring systems.

The use of natural properties of piezoelectric materials to conversion of mechanical energy into electric energy in places where sensors are mounted is a promising field of wireless power development. The piezoelectric effects are used to active damping of vibration, see e.g. (Pietrzakowski, 2000; Przybyłowicz, 1999). The direct piezoelectric effect in piezoelectric materials is the base of building devices converting energy called piezoelectric generators. The generators, in which the main element is a cantilever beam composed of piezoelectric materials and carrying materials, are one of the structures which can be used for energy harvesting from the mechanical vibration of a building. The subject of recent examinations are piezoelectric beam generators constructed from a basic material which does not indicate piezoelectric characteristics, e.g. steel, and from a piezoelectric material which can be piezoelectric ceramic, e.g. PZT-4H (Roundy and

Wright, 2004), composite made from piezoelectric ceramics and polymer warp, e.g. MFC (Upadrashta and Yang, 2016), piezoelectric polymer e.g. PVDF (Li *et al.*, 2016) or a structure made of nanowires (Yu *et al.*, 2012).

The use of relatively flexible piezoelectric composite materials allows one to subject the generator beams to loads varying over time which cause large strains of piezoelectric elements (Yang and Tang, 2009). Macro Fiber Composite (MFC) is one of the piezoelectric composites which is used in the piezoelectric generators. MFC contains the piezoceramic phase in the form of square cross-section fibers placed in the polymer matrix. The piezoelectric MFC composite is usually joined with the base material by means of gluing. The latest research indicates that the maximum electrical power harvested by the generator in which the cantilever beam is made of the MFC and of the steel base material is up to a few mW. For example, the piezoelectric beam generator contains MFC of the following dimensions: $85 \times 28 \times 0.3$ mm, presented in (Song *et al.*, 2014), produces 1.7 mW for a frequency of 30 Hz, which was the resonant frequency of that generator.

The range of harvested electric power restricts the field of potential applications to supply miniaturized electronic devices with an ultra low power demand. The ideal schema of a typical wireless sensor node powered by the piezoelectric generator is presented in Fig. 1.

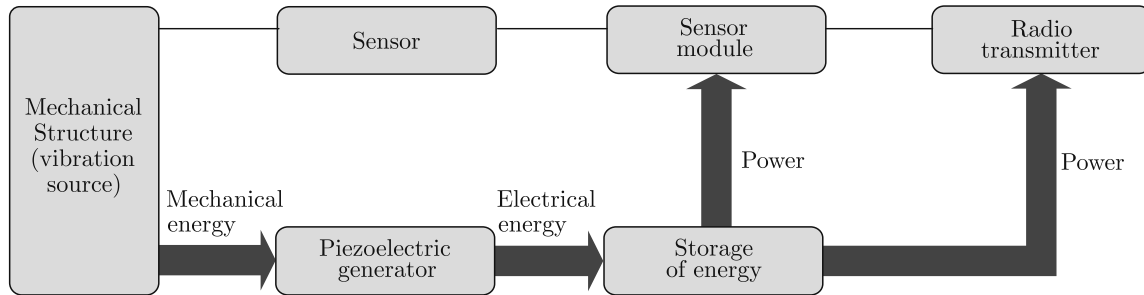


Fig. 1. Schema of a typical wireless sensor node powered by a piezoelectric generator (Woiias *et al.*, 2009)

The generated electric energy through a piezoelectric generator is consumed mainly by a sensor and a radio transmitter. The electrical energy, generated by the piezoelectric beam generators, is enough to supply commercial low-powered micro sensors with commercial ultra low-power radio transmitters in wireless nodes which enable transfer of periodical data, if only the frequency of the vibration source is close to the resonant frequency of the generator. This condition is difficult to fulfil in buildings whose vibrations are excited by natural processes, e.g. wind. One possible solution is broadening of the generator frequency range by e.g. the application of several beams with various dimensions in the generator structure (Ferrari *et al.*, 2008). The wireless sensor node enabling the periodical data transfer powered by the piezoelectric generator has to have an electronic system to control and store recovered energy which is needed for the transfer of a proper energy amount. The designing of such a control and store system is the subject of recent scientific research.

The abovementioned remarks are the base of a concept of a wireless monitoring system in which several piezoelectric beam generators work as both harvesters and sensors. The piezoelectric beam generator does not supply any sensor, but the electrical energy harvested by this generator is accumulated in the capacitor and is used to send signals by the radio transmitter. Such a defined harvester/sensor consists of the following elements: the piezoelectric beam generator, Graetz bridge rectifier, capacitor, voltage comparator and radio transmitter. In this study, the characteristics of capacitor charging and radio transmission are compared in the frequency domain and evaluated with respect to time between the radio signals for different excitation levels.

2. Mathematical model of a piezoelectric energy harvester

In this Section, the basic mathematical model of piezoelectric energy conversion by a MFC glued on the top of a steel beam is presented. The basic purpose of this Section is the determination of the dependence between the displacement of the free end of the harvester beam and the course of voltage across the capacitor. The schema of the electrical circuit used to charge the capacitor is presented in Fig. 2.

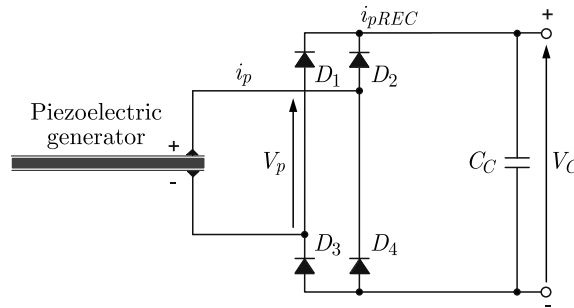


Fig. 2. Schema of the electrical circuit used to the energy harvesting: V_p – generated voltage by the piezoelectric patch, i_{pREC} – rectified current intensity, C_c – capacitance of the capacitor, V_c – voltage across the capacitor

The harvester beam is fabricated from stainless steel and a piezoelectric composite which is the Macro Fiber Composite (MFC). The beam structure of the generator is achieved by gluing steel and the MFC (Fig. 3).

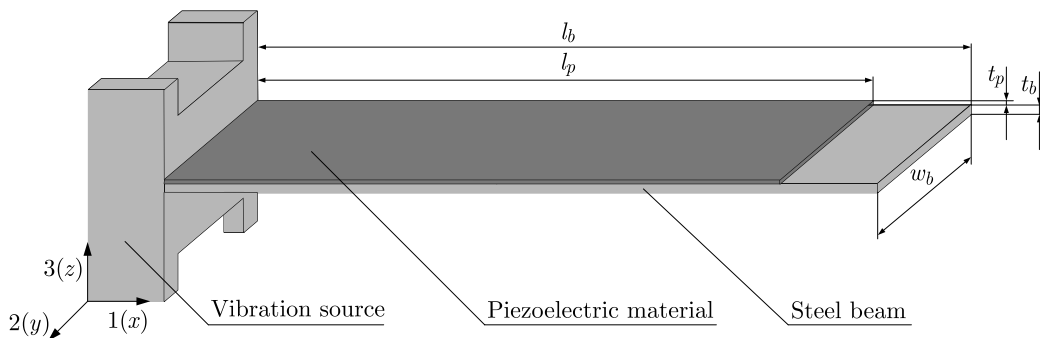


Fig. 3. Piezoelectric harvester beam structure: l_b – length of the beam, l_p – length of the MFC patch, w_b – width of the beam, t_b – thickness of the beam, t_p – thickness of the MFC patch

The Macro Fiber Composite (MFC) presented in Fig. 4 has been selected as a piezoelectric material applied in the harvester beam.

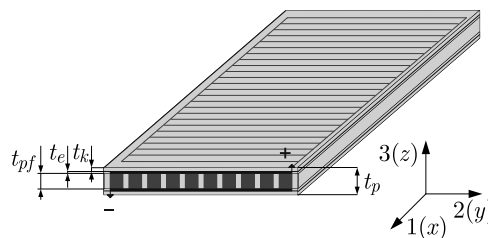


Fig. 4. Macro Fiber Composite (MFC): t_{pf} – thickness of the piezoelectric fiber, t_e – thickness of the electrode layer (copper + epoxy), t_k – thickness of the kapton layer

The basic equations describing the energy conversion in a piezoelectric material are given by (Nye, 1957)

$$\begin{aligned} S_p(t) &= s_{pq}^{(E)} T_q(t) + d_{pk}^T E_k(t) & \text{for } p = 1, \dots, 6 & \quad q = 1, \dots, 6 & \quad k = 1, 2, 3 \\ D_i(t) &= d_{iq} T_q(t) + \varepsilon_{ik}^{(T)} E_k(t) & \text{for } i = 1, 2, 3 \end{aligned} \quad (2.1)$$

where S is strain, T is stress, D is electric induction, E is electric field intensity, s is the compliance constant, d is the electromechanical coupling constant, ε is the permeability tensor.

In the case in which electric induction is perpendicular to stress in piezoelectric fibers (along axis 1 in Fig. 4), the basic equations are the following

$$S_1(t) = s_{11}^{(E)} T_1(t) + d_{31} E_3(t) \quad D_3(t) = d_{31} T_1(t) + \varepsilon_{33}^{(T)} E_3(t) \quad (2.2)$$

The dependence among electrical and mechanical variables in the piezoelectric material

$$E(t) = -\frac{V_p(t)}{t_{pf}} \quad i_p(t) = w_p l_p \frac{dD(t)}{dt} \quad (2.3)$$

where w_p is width of the active area of the piezoelectric material.

After introduction of (2.3) into (2.2) and their transformation

$$\begin{aligned} V_p(t) &= \frac{s_{11}^{(E)} t_{pf}}{d_{31}} T_1(t) - \frac{t_{pf}}{d_{31}} S_1(t) \\ i_p(t) &= d_{31} w_p l_p \frac{dT_1(t)}{dt} - \frac{\varepsilon_{33}^{(T)} w_p l_p}{t_{pf}} \frac{dV_p(t)}{dt} \end{aligned} \quad (2.4)$$

The average stress in the piezoelectric material (Roundy *et al.*, 2003) is

$$T_1(t) = \frac{1}{l_p} \int_0^{l_p} \frac{M(x) t_d}{I} dx \quad (2.5)$$

where M is the bending moment in the beam, t_d is the distance from the centre of the steel beam to the centre of the piezoelectric layer, I is the moment of inertia.

The bending moment in the beam is

$$M(x) = F_z(t)(l_b - x) \quad (2.6)$$

where F_z is the theoretical external force acting on the free end of the harvester beam, x is the distance from the beam fixing to the free end of the harvester beam.

F_z is calculated on the basis of the displacement of the free end of the harvester beam

$$F_z(t) = \frac{3Y_{MFC} I}{l_b^3} y_{out}(t) \quad (2.7)$$

where Y_{MFC} is Young's modulus of the Macro Fiber Composite, y_{out} is the displacement of the free end of the harvester beam.

The distance from the centre of the steel beam to the centre of the piezoelectric layer is

$$t_d = \frac{1}{2} t_b + t_k + t_e + \frac{1}{2} t_p \quad (2.8)$$

Stress calculated from (Roundy *et al.*, 2003) is

$$T_1(t) = \frac{3Y_{MFC} t_d}{l_b^3} \left(l_b - \frac{l_p}{2} \right) y_{out}(t) \quad (2.9)$$

After introduction of (2.9) to (2.4) and its transformation

$$\begin{aligned} V_p(t) &= \frac{s_{11}^{(E)} t_{pf}}{d_{31}} \frac{3Y_{MFC} t_d (2l_b - l_p)}{2l_b^3} y_{out}(t) - \frac{t_{pf}}{d_{31}} S_1(t) \\ i_p(t) &= d_{31} w_p l_p \frac{3Y_{MFC} t_d (2l_b - l_e)}{2l_b^3} \frac{dy_{out}(t)}{dt} - \frac{\varepsilon_{33}^{(T)} w_p l_p}{t_{pf}} \frac{dV_p(t)}{dt} \end{aligned} \quad (2.10)$$

After introduction of the assumption that the electrical circuit is not connected to the load resistance, the rectified current intensity i_{pREC} generated by the piezoelectric generator is equal to the charging intensity i_c of the capacitor

$$i_{pREC}(t) = i_c(t) = C_c \frac{dV_c(t)}{dt} \quad (2.11)$$

The dependence between the voltage across the capacitor V_c and the displacement of the free end of the harvester beam y_{out} is

$$\frac{dV_c(t)}{dt} = \frac{1}{C_c} d_{31} w_p l_p \frac{3Y_{MFC} t_d (2l_b - l_e)}{2l_b^3} \frac{dy_{out}(t)}{dt} - \frac{1}{C_c} \frac{\varepsilon_{33}^{(T)} w_p l_p}{t_{pf}} \frac{dV_p(t)}{dt} \quad (2.12)$$

On the basis of (2.12), the piezoelectric harvesting device and electrical circuit (Fig. 2) can be defined as a multioutput system in which the displacement of the free end of the harvester beam y_{out} is the input and voltage across the capacitor V_c , the voltage generated by the piezoelectric patch V_p is the output (Fig. 5).

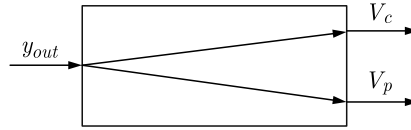


Fig. 5. Energy harvesting circuit as a multioutput system

Two research problems appear in such a definition of the piezoelectric harvesting device:

- what is the dependence between the courses of the displacement of the free end of the harvester beam y_{out} and voltage across the capacitor V_c ,
- what is the dependence between the courses of voltage across the capacitor V_c and voltage generated by the piezoelectric V_p .

The energy accumulated in the capacitor will be used in the presented concept of wireless monitoring systems to supply the radio transmitter. Hence, the next research problem appears:

- what is the dependence between the courses of voltage across the capacitor V_c and the period of time among radio signals which are transmitted by the radio transmitter.

These research problems are the subject of experimental experiments presented in Section 3.

3. Experimental study

3.1. Experimental setup

In this study, the energy harvesting device based on the cantilever beam and P2-type Macro Fiber Composite (MFC) material has been designed and fabricated. The MFC patch (from Smart Material Corporation) was glued on the top of a steel cantilever beam. Material and geometric parameters of the MFC patch and the steel beam are listed in Table 1.

Table 1. Material and geometric parameters of the MFC patch (Smart Material Corporation, 2017)

Parameter	Unit	Value
Young's modulus Y_{MFC}	N/m ²	$30.336 \cdot 10^9$
Piezoelectric constant d_{31}	C/N	$-170 \cdot 10^{-12}$
Permittivity ϵ_{33}	F/m	$13\,800.13 \cdot 10^{-12}$
Length l_p	mm	85
Width w_p	mm	14
Thickness t_p	mm	0.3

Table 2. Geometric parameters of the MFC patch (Deraemaeker *et al.*, 2009)

Parameter	Unit	Value
Thickness of piezoelectric fiber t_{pf}	mm	0.18
Thickness of electrode layer t_e	mm	0.018
Thickness of kapton layer t_k	mm	0.04

The MFC patch consists of piezoceramic fibers, copper electrodes, epoxy and kapton. The geometric parameters of these parts of the MFC patch are listed in Table 2.

The thickness, length and width of the base stainless steel beam were correspondingly the following 1.24 mm, 130 mm and 18 mm. The MFC was connected to a full-bridge rectifier which in turn was connected to an energy harvesting circuit EH301A. EH301A circuit powered the radio transmitter in specific time periods. The steel beam with MFC, the full-bridge rectifier, EH301A circuit and radio transmitter created a system which is called the harvester/sensor in the following Section of this article. The standard full-bridge rectifier (Graetz bridge) converted the generated by the energy harvesting device the AC voltage into DC voltage. Figure 6 presents the schema of the whole system of the harvester/sensor.

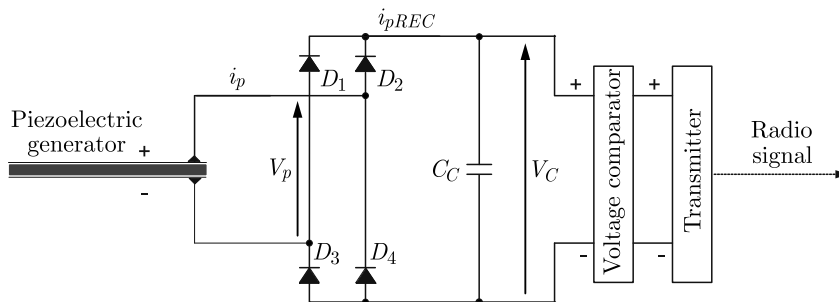


Fig. 6. Schema of the whole system of the harvester/sensor

As a voltage comparator, EH301A, developed by Advanced Linear Devices (EH300A data-sheet, 2017) has been applied. When the energy harvesting device starts to supply energy into the inputs of the EH301A module in the form of electrical charge impulses, these charge packets are collected and accumulated in a storage capacitor (Yang and Tang, 2009). Figure 7 presents the waveform of the voltage across the capacitor in the EH301A. The start of the voltage, $+V$, increases from the point 0.0 V. When $+V$ reaches 5.2 V, the output of EH301A starts to supply the radio transmitter and $+V$ decreases. When $+V$ decreases to 3.1 V, the output of EH301A stops to supply the radio transmitter and the charging cycle restarts. The time periods t_1 and t_2 are limited by the energy from the piezoelectric harvesting devices minus the energy losses by the EH301A Series Module. The period time t_3 is dependent upon the power consumption of the radio transmitter. In the experiments, the EH301A device has been modified by the replacement

of the capacitor from Advanced Linear Devices with a capacitor of 200 nF. The reduction of time periods t_1 and t_2 was the aim of that replacement.

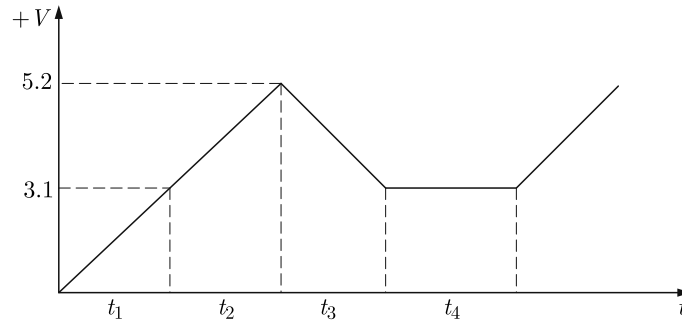


Fig. 7. Voltage waveform in the capacitor in the EH301A

The radio transmitter applied in the structure of the harvester/sensor is a part of the transmission system consisting of the PT2262 radio transmitter and the PT2272 radio receiver (Fig. 8).

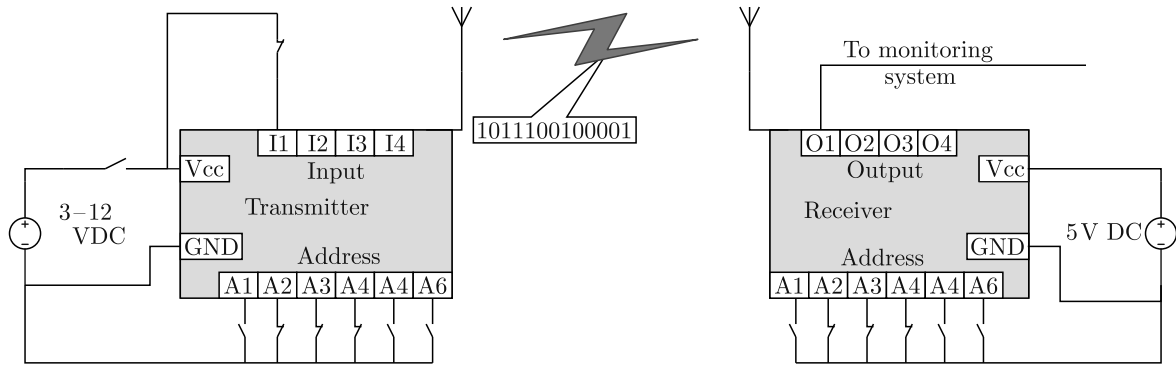


Fig. 8. Schema of the radio transmission system

The operating frequency has been set on 38 Hz both for the radio transmitter and radio receiver. The radio transmitter has 4 digital inputs which allow for sending of 4 different states (0 or 1). The start of the supply of the radio transmitter by the voltage comparator causes sending of the signal to the radio receiver. The voltage comparator starts supply to the radio transmitter when the voltage reaches of 3.1 V (Fig. 8).

The experimental setup consisting of the energy harvesting device with the radio transmission system as well as the system generating vibrations of the fixed beam end is presented in Fig. 9.

3.2. Results of the laboratory experiments

The basic purposes of the laboratory experiments are defined in the last part of Section 2. In the discussion of the results (in the next parts), the following definitions are used:

- the displacement of the free end of the harvester beam (y_{out}) is defined by the output frequency ω_{out} and the output amplitude A_{out} ,
- the displacement of the fixed end of the harvester beam y_{in} is defined by the input frequency ω_{in} and the input amplitude A_{in} .

In the first step, a dependence between the input frequency ω_{in} and the output amplitude A_{out} has been experimentally determined. Such a dependence for the input amplitude of 0.2 mm is presented in Fig. 10.

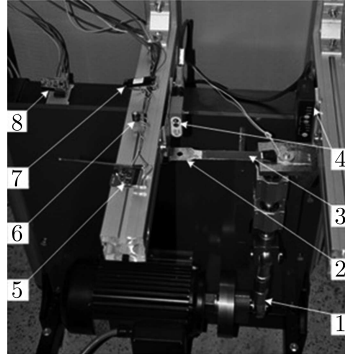


Fig. 9. Experimental setup: 1 – system of vibration generation, 2 – steel cantilever beam, 3 – piezoelectric composite (MFC), 4 – laser sensors of displacement, 5 – radio transmitter, 6 – capacitor, 7 – EH301A Series Module, 8 – radio receiver

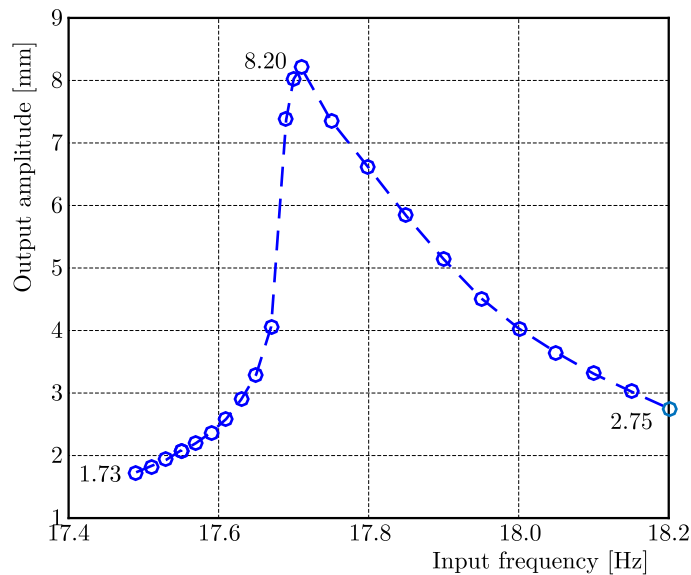


Fig. 10. Output amplitude (A_{out}) versus the input frequency ω_{in} for a constant input amplitude y_{in} : 0.2 mm

The maximum output amplitude appears for the resonant frequency of the fabricated beam (17.7 Hz). In the next step, the characteristics are experimentally determined: RMS voltage generated by the piezoelectric V_{pRMS} versus the resistive load R_l and RMS current generated by the piezoelectric i_{pRMS} versus the resistive load R_l (Fig. 11). These characteristics are obtained for the input frequency ω_{in} : 17.7 Hz.

On the basis of Fig. 11a, it can be seen that an increase in the load resistance R_l causes an approximately proportional increase in the rectified voltage generated by the piezoelectric patch V_{pRMS} in the voltage range from 0 to 5 V. Such a range of the generated voltage V_{pRMS} has been chosen regarding the range of voltage across the capacitor V_c which was applied in the testing device. The rectified current generated by the piezoelectric patch i_{pRMS} is approximately constant in the rectified voltage range from 0 to 5 V (Fig. 11b). Hence, in the following part of this article, the piezoelectric patch is treated as a current source controlled by the displacement of the fixed end of the harvester beam.

The comparison between the course of voltage generated by the piezoelectric patch and the voltage across the capacitor obtained in the experiment is presented in Fig. 12.

The courses shown in Fig. 12 have been obtained in the circuit without any load resistance R_l . It has been found that the voltage across the capacitor is approximately equal to the Root Mean

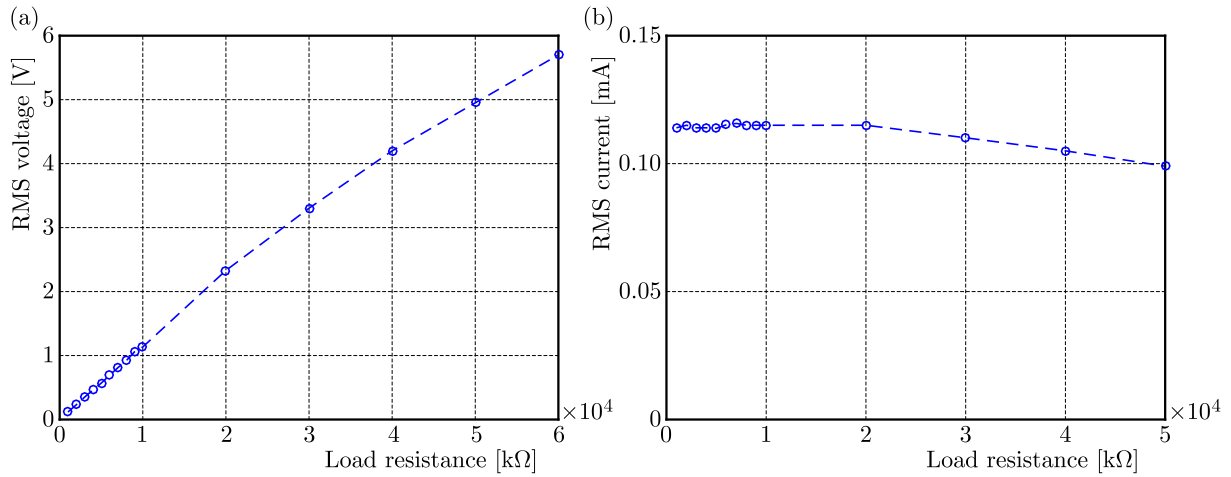


Fig. 11. RMS voltage and RMS current generated by the MFC harvester versus resistive load: (a) RMS voltage V_{pRMS} , (b) RMS current i_{pRMS}

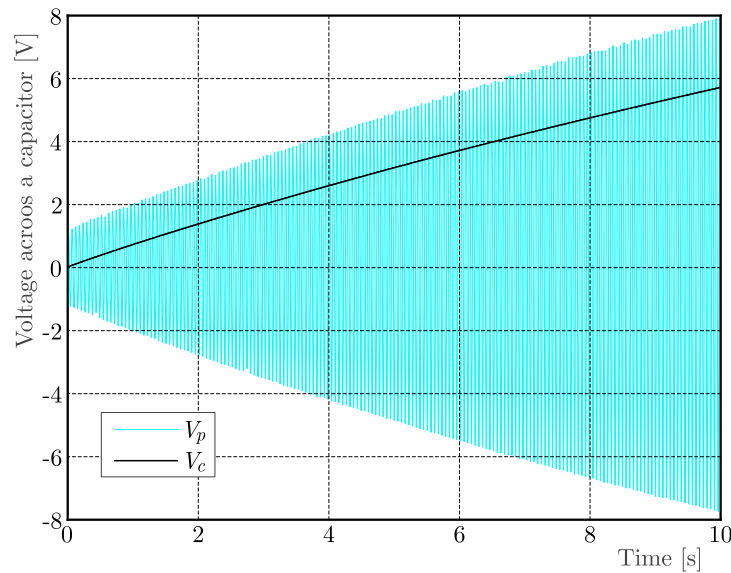


Fig. 12. Voltage generated by the piezoelectric patch V_p versus voltage across the capacitor V_c for a constant output amplitude $A_{out} = 8.20$ mm and a constant input frequency $\omega_{in} = 17.70$ Hz

Square of the voltage generated by the piezoelectric patch. It can be seen that an increase in voltage across the capacitor V_c caused an increase in voltage generated by the piezoelectric patch V_p . Hence, the charged capacitor can be treated as a load connected to the piezoelectric patch. The charging time of the capacitor strongly depends on the output amplitude A_{out} . The dependence between the output amplitude A_{out} and the charging time of the capacitor is presented in Fig. 13. The measurements of the charging time have begun when the voltage across a capacitor was equal to 3.1 V and were finished when the voltage achieved 5.2 V. It can be seen that this dependence can be approximated by an exponential course.

The course of voltage generated by the piezoelectric patch V_p and the course of voltage across the capacitor V_c , as well as the course of voltage delivered to the radio transmitter V_r and the number of received signals in the radio receiver are presented in Fig. 14. On the basis of the courses presented in Fig. 14, it can be seen that the number of transmitted radio signals is equal to the number of charging cycles of the capacitor, which is a part of the system presented in the previous Section, see Fig. 6. Hence, the charging time of the capacitor (to 5.2 V) is equal to

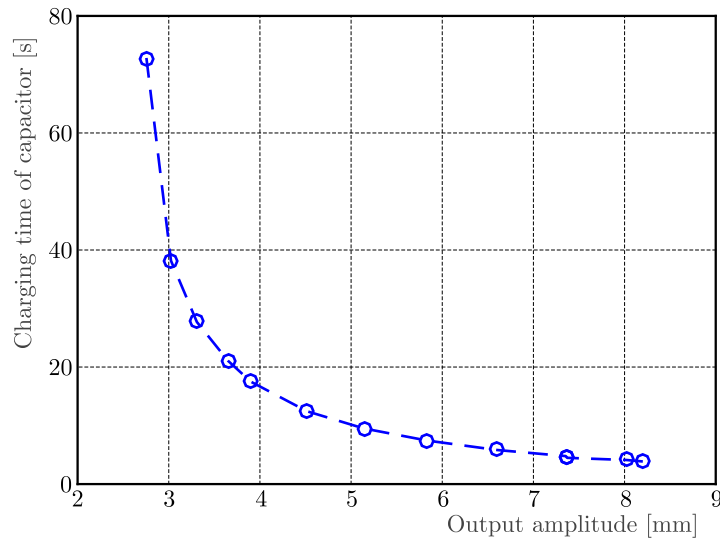


Fig. 13. Dependence between the output amplitude of the free end of the generator beam A_{out} and charging time of the capacitor

the period of time among the radio signals which are transmitted by the radio transmitter. This observation allows one to find that the dependence between the output amplitude A_{out} of the harvester beam and the time among signals transmitted by the radio transmitter is the same as the dependence between the output amplitude of the free end of the generator beam A_{out} and the charging time of the capacitor, which is presented in Fig. 13.

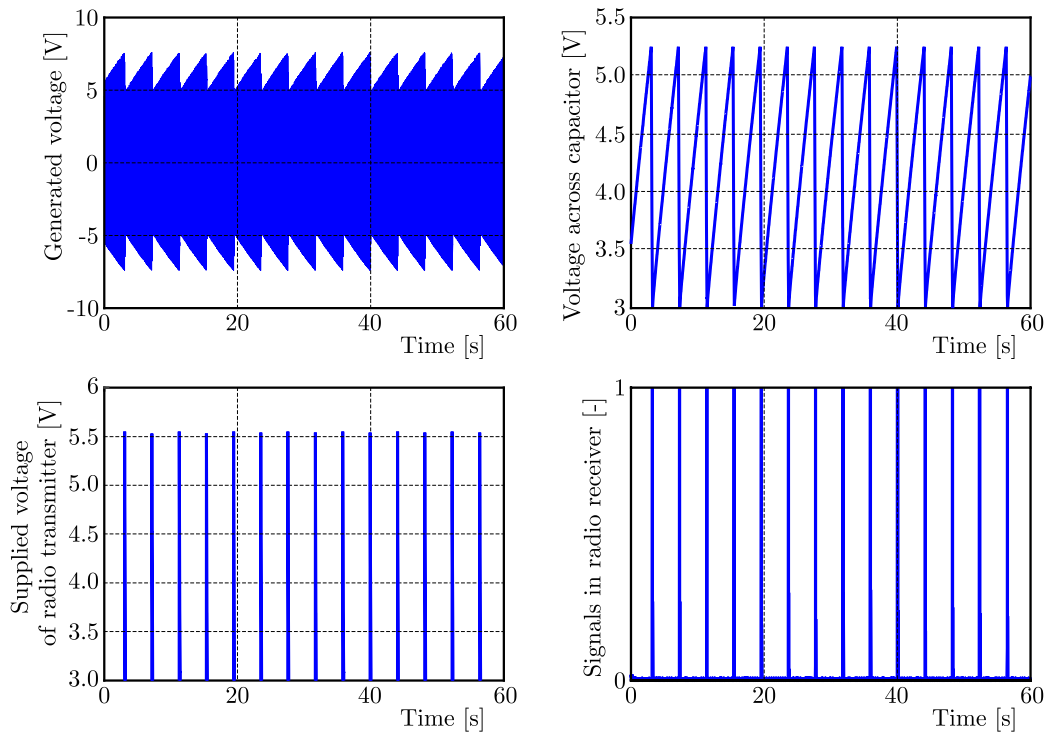


Fig. 14. Characteristics for the constant output amplitude $A_{out} = 8.20$ mm

The course of voltage across the capacitor V_c and the course of voltage delivered to the radio transmitter V_r in the same time for several values of output amplitudes are presented in Fig. 15.

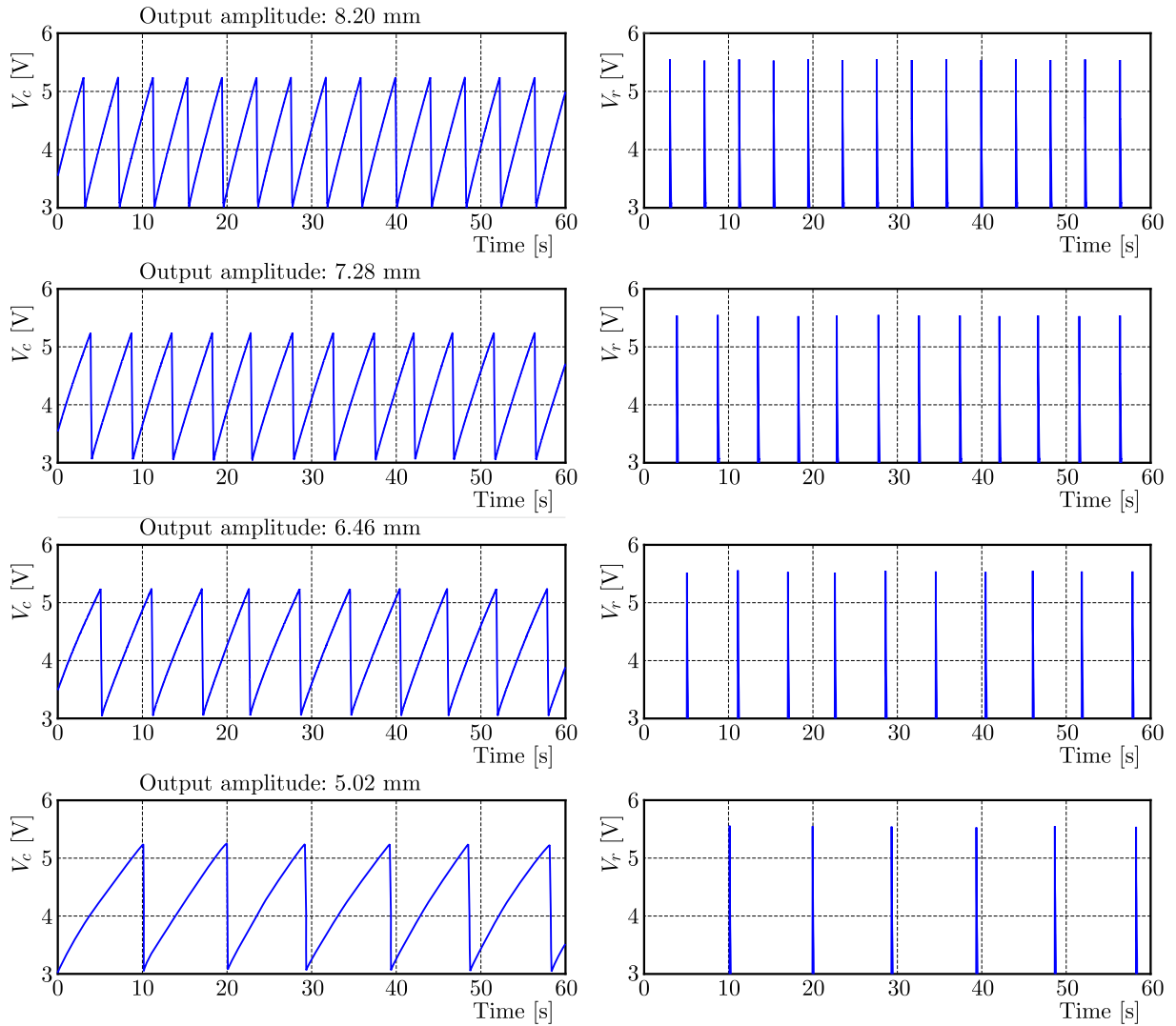


Fig. 15. Voltage across the capacitor V_c and voltage delivered to the radio transmitter V_r for several values of the output amplitude

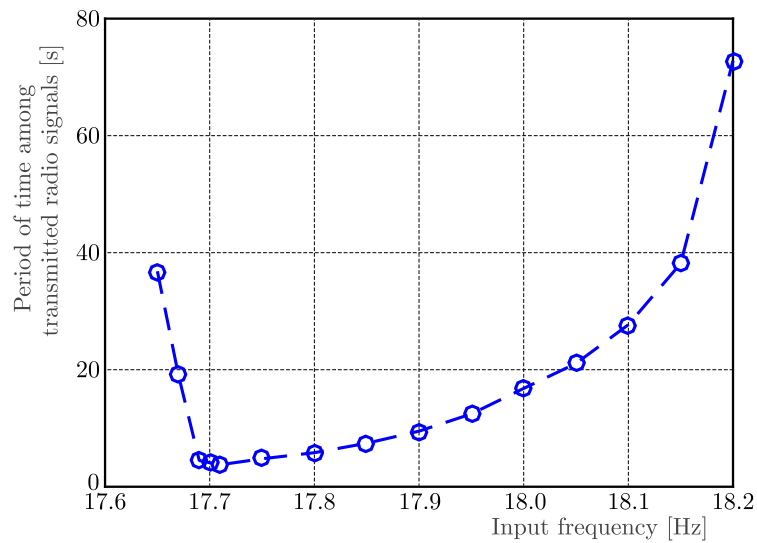


Fig. 16. Dependence between the input frequency A_{out} and the period of time among transmitted radio signals for the constant input amplitude of 0.2 mm

The output amplitude is strongly dependent upon the input frequency ω_{in} , so the time of radio transmitter supply is also dependent upon this frequency (Fig. 16).

The action of piezoelectric harvester/sensor will be changed in the operating time because the problem of electric fatigue appears in piezoelectric materials (Goy *et al.*, 2006). This problem should be the subject of next research.

4. Summary

On the basis of the conducted experiments whose selected results are shown in the previous Section, the following conclusions have been established:

- the piezoelectric patch can be treated as a current source controlled by the displacement of the fixed end of the harvester beam,
- an increase in voltage across the capacitor causes an increase in voltage generated by the piezoelectric patch. Hence, the charged capacitor can be treated as a load for the harvester,
- periods of time among received radio signals are strongly dependent upon the output amplitude of the free end of the harvester beam. The dependence between the time of radio transmitter supply can be approximated by an exponential course,
- the definition of frequency of the free end of the harvester beam is possible on the basis of periods of time among the signals received by the radio receiver for a constant input amplitude.

The study has been completed under the AGH-UST's research program No 11.11.130.958 sponsored through statutory research funds, AGH University of Science and Technology, Faculty of Mechanical Engineering and Robotics, Department of Process Control.

References

1. CHAN T.H., YU L., TAM H.Y., NI Y.Q., LIU S.Y., CHUNG W.H., CHENG L.K., 2006, Fiber Bragg grating sensors for structural health monitoring of Tsing Ma bridge: Background and experimental observation, *Engineering Structures*, **28**, 5, 648-659
2. DE ROECK G., PEETERS B., MAECK J., 2000, Dynamic monitoring of civil engineering structures, *Proceedings of IASS-IACM*
3. DERAEMAERKER A., NASSER H., BENJEDDOU A., PREUMONT A., 2009, Mixing rules for the piezoelectric properties of macro fiber composites (MFC), *Journal of Intelligent Material Systems and Structures*, **20**, 12, 1475-1482
4. EH300A datasheet, 2017, <http://www.aldinc.com/pdf/EH300.pdf>
5. FERRARI M., FERRARI V., GUIZZETTI M., MARIOLI D., TARONI A., 2008, Piezoelectric multifrequency energy converter for power harvesting in autonomous microsystems, *Sensors and Actuators A: Physical*, **142**, 1, 329-335
6. GOY O., MUELLER R., GROSS D., 2006, Interaction of point defects in piezoelectric materials – numerical simulation in the context of electric fatigue, *Journal of Theoretical and Applied Mechanics*, **44**, 4, 819-836
7. KIM S., PAKZAD S., CULLER D., DEMMEL J., FENVES G., GLASER S., TURON M., 2007, Health monitoring of civil infrastructures using wireless sensor networks, *Proceedings of 6th International Symposium on Information Processing in Sensor Networks*, 254-263
8. LEE S., YOUNG B. D., JUNG B.C., 2009, Robust segment-type energy harvester and its application to a wireless sensor, *Smart Materials and Structures*, **18**, 9, 095021

9. LI S., CROVETTO A., PENG Z., ZHANG A., HANSEN O., WANG M., WANG F., 2016, Bi-resonant structure with piezoelectric PVDF films for energy harvesting from random vibration sources at low frequency, *Sensors and Actuators A: Physical*, **247**, 547-554
10. LYNCH J. P., LOHG K. J., 2006, A summary review of wireless sensors and sensor networks for structural health monitoring, *The Shock and Vibration Digest*, **38**, 2, 91-128
11. NYE J.F., 1957, *Physical Properties of Crystals*, Oxford at the Clarendon Press, Oxford
12. PIETRZAKOWSKI M., 2000, Multiple piezoelectric segments in structural vibration control, *Journal of Theoretical and Applied Mechanics*, **38**, 1, 35-50
13. PRZYBYŁOWICZ P.M., 1999, Application of piezoelectric elements to semiadaptive dynamic eliminator of torsional vibration, *Journal of Theoretical and Applied Mechanics*, **37**, 2, 319-334
14. ROUNDY S., WRIGHT P. K., 2004, A piezoelectric vibration based generator for wireless electronics, *Smart Materials and Structures*, **13**, 5, 1131-1142
15. ROUNDY S., WRIGHT P. K., RABAEY J. M., 2003, *Energy Scavenging for Wireless Sensor Networks*, Springer Science Business Media, New York
16. Smart Material Corp., 2017, Macro-fibre composites technical data, www.smartmaterial.com
17. SONG H. J. CHOI Y. T., WERELEY N. M., PUREKAR A., 2014, Comparison of monolithic and composite piezoelectric material-based energy harvesting devices, *Journal of Intelligent Material Systems and Structures*, **25**, 14, 1825-1837
18. SOOBUM L., BYENG D.Y., BYUNG C.J., 2009, Robust segment-type energy harvester and its application to a wireless sensor, *Smart Materials and Structures*, **18**, 9, 095021
19. UPADRASHTA D., YANG Y., 2016, Experimental investigation of performance reliability of macro fiber composite for piezoelectric energy harvesting applications, *Sensors and Actuators A*, **244**, 223-232
20. WOIAS P., WISCHKE M., EICHORN CH., FUCHS B., 2009, An energy-autonomous wireless temperature monitoring system powered by piezoelectric energy harvesting, *Proceedings of PowerMEMS*, 209-212
21. YANG Y., TANG L., LI H., 2009, Vibration energy harvesting using macro-fiber composites, *Smart Materials and Structures*, **18**, 11, 115025
22. YU A., JIANG P., WANG Z.L., 2012, Nanogenerator as self-powered vibration sensor, *Nano Energy*, **1**, 3, 418-423

MECHANICAL BUCKLING OF FUNCTIONALLY GRADED POLYETHYLENE/CLAY NANOCOMPOSITES COLUMNS BASED ON THE ENGESSER-TIMOSHENKO BEAM THEORY

MOHAMMAD HOSSEIN YAS, MAHDI KARAMI KHORRAMABADI

Department of Mechanical Engineering, Razi University, Kermanshah, Iran

e-mail: yas@razi.ac.ir; mehdi_karami2001@yahoo.com

This paper deals with mechanical buckling of polyethylene/clay nanocomposite beams of functionally graded and uniformly distributed of nanoclay subjected to axial compressive load with simply supported conditions at both ends. The Young moduli of functionally graded and uniformly distributed nanocomposites are calculated using a genetic algorithm procedure and then compared with experimental results. The formulation is modified to include the effect of nanoparticles weight fractions in the calculation of the Young modulus for uniform distribution. Also, it is modified to take into account the Young modulus as a function of the thickness coordinate. The displacement field of the beam is assumed based on the Engesser-Timoshenko beam theory. Applying the Hamilton principle, governing equations are derived. The influence of nanoparticles on the buckling load of the beam is presented. To investigate the accuracy of the present analysis, a compression study with the experimental results is carried out.

Keywords: mechanical buckling, functionally graded nanocomposite, montmorillonite, genetic algorithm theory

1. Introduction

Nanomaterials have aroused interest among scientific communities in the field of physics, chemistry and engineering. Some of these materials are nanoparticles, nanowires and nanotubes (Jia *et al.*, 2014; Nam *et al.*, 2001; Lei *et al.*, 2013; Pakdaman *et al.*, 2013; Grigoriadi *et al.*, 2014). Compared to experimental studies, the number of publications dealing with theoretical prediction of properties in polymer/clay nanocomposites is relatively small. Fornes and Paul (2003) applied the Halpin-Tsai and Mori-Tanaka reinforcement theories to predict the modulus of nylon based nanocomposites. The modulus obtained using Mori-Tanaka calculation increased with nanoclay reinforcement as predicted. The Halpin-Tsai formula gave higher values to the modulus but could still be used to predict its value.

Some efforts have been focused on the modeling of mechanical properties of nanoclay-reinforced polymer composites (Sheng *et al.*, 2004) and nanoparticle-reinforced polymer composites (Smith *et al.*, 2002; Brown *et al.*, 2003). These modeling efforts have demonstrated the need for the development of a model that would predict mechanical properties of nanoparticle/polyimide composites as a function of the nanoparticle size and weight fraction as well as the molecular structure of the nanoparticle/polyimide interface. Genetic algorithms (GA) are a family of computational models inspired by evolution. These algorithms encode a potential solution or a specific problem on a simple chromosome-like data structure and apply recombination operators to these structures so as to preserve critical information. Structural stability is considered to be the one of the most important engineering issues in the design and application of slender structures. Buckling and post-buckling behaviour are the two main types of structural instability, they often govern failure of structures under static or dynamic compressive loading

conditions, thus, have been investigated by several researchers in the past decades. Vodenitcharova and Zhang (2006) presented analyses of pure bending and bending-induced local buckling of a nanocomposite beam based on a continuum mechanical model and found that single-walled carbon nanotube (SWCNT) buckled at smaller bending angles and greater flattening ratios in thicker matrix layers. Based on the classical laminated plate theory and third-order shear deformation theory, Arani *et al.* (2011) analytically and numerically studied buckling behaviour of laminated composite plates. The optimal orientation of CNTs to achieve the highest critical load and corresponding mode shape were calculated for different kinds of boundary conditions as well as aspect ratios of the plates. Shen (2011) presented a postbuckling analysis of cylindrical shells reinforced by SWCNTs subjected to axial compression and lateral or hydrostatic pressure in thermal environments. The results revealed that the mid-plane symmetric functionally graded distribution of reinforcements could increase the buckling load as well as postbuckling strength of the shells and confirmed that the postbuckling equilibrium path for both FG- and UD-CNTRC cylindrical shells under axial compression was unstable. Mosallaie Barzoki *et al.* (2012) analyzed the torsional buckling of electro-thermo-mechanical cylindrical shells reinforced by polymer piezoelectric double-walled boron nitride nanotubes. They expressed properties of the electro-thermo-mechanical smart composite materials using a micro-mechanical approach. Their results stated that the buckling load increased with increasing the foam core. Eltaher *et al.* (2013) illustrated the size dependent effect on static and buckling behaviour of an FG nano-beam based on the nonlocal elasticity theory. They used the finite element method to discretize this model and obtained a numerical approximation for equilibrium equations. Yin *et al.* (2015) studied static bending and buckling of an FGPR nanoscale beam based on the nonlocal Timoshenko beam model. The results revealed that the deflections of the FGPR beam increased with the nonlocal parameters, and the buckling loads decreased with it. Li *et al.* (2015) investigated the relationship between the critical buckling loads of the functionally graded material (FGM) Levinson beams (LBs) and those of the corresponding homogeneous Euler-Bernoulli beams (HEBBs). Barati *et al.* (2014) studied buckling of functionally graded beams with imperfectly integrated surface piezoelectric layers under low velocity and found that the piezoelectric actuators induced tensile piezoelectric force produced by applying negative voltages that significantly affected the stability of the functionally graded Engesser-Timoshenko beam with piezoelectric actuators. Heydari (2011) presented a new analytical method for buckling analysis of rectangular and annular beams made up of functionally graded materials with constant thickness and Poisson's ratio. The results revealed that dimensionless first mode shape of buckling for prismatic functionally graded beams was similar to prismatic homogeneous beams. Simsek and Yurtcu (2013) studied static bending and buckling of a functionally graded (FG) nanobeam based on the nonlocal Timoshenko and Euler-Bernoulli beam theory. The results showed that the new nonlocal beam model produced larger deflection and smaller buckling load than the classical (local) beam model. Rychlewska (2014) presented the critical buckling loads for axially functionally graded (FG) beams subjected to a distributed axial load and found that the critical buckling loads of a homogeneous beam calculated by the proposed approach were in good agreement with those available in literature. Houari *et al.* (2013) investigated the size-dependent buckling behaviour of functionally graded (FG) nanobeams on the basis of the nonlocal continuum model. The effects of the nonlocal parameter, aspect ratio, various material compositions on the stability responses of the FG nanobeams were discussed. Ghiasian *et al.* (2015) studied nonlinear thermal dynamic buckling of FGM beams and found that for beams with stable post-buckling equilibrium path, no dynamic buckling occurred according to the Budiansky-Roth criterion. Sun *et al.* (2016) investigated thermal buckling and post-buckling of FGM Timoshenko beams on a nonlinear elastic foundation. The results revealed that post-buckling behaviour of a FGM Timoshenko beam exhibited bifurcations under both uniform and non-uniform temperature rise. Kiani and Eslami (2010) studied buckling of beams made of functionally graded materials under various types of

thermal loading. The formulations were compared using reduction of results for the functionally graded beams to those of isotropic homogeneous beams given in the literature. Kiani and Eslami (2013) investigated buckling of beams made of functionally graded materials (FGM) under thermomechanical loading. The results revealed that in each case of thermal loading, the Timoshenko beam theory predicted lower values for critical buckling temperature in comparison with the Euler beam theory. Majumdar and Das (2016) determined thermal buckling loads of various functionally graded material beams with both ends clamped. The effect of the limit thermal load at which the effective elastic modulus and/or thermal expansion coefficient become theoretically zero was considered. Rafiee *et al.* (2009) experimentally investigated buckling of graphene/epoxy nanocomposite beam structures. They revealed that graphene nanocomposites showed potential to provide significant enhancement in buckling stability, which is an important consideration for the design of ultra light-weight and highly optimized structural elements used in aerospace applications.

The present work deals with mechanical buckling of polyethylene/clay nanocomposite beams with functionally graded (FG) and uniformly distributed nanoclay. The beams are subjected to axial compressive load and are simply supported at both ends. By using a genetic algorithm procedure, Young's modulus of functionally graded and uniformly distributed nanocomposites is calculated and then compared with experimental data. The displacement field of the beam is assumed based on the Engesser-Timoshenko beam theory. Applying the Hamilton principle, the governing equations are derived. The influence of nanoparticles on the buckling load of the beam is presented. To investigate the accuracy of the present analysis, a compression study is carried out with the experimental results.

2. Experimental data

2.1. Materials

The polymer matrix used in this study was a linear low-density polyethylene (LDPE) with the trade name LL209AA from Arak Petrochemical Co. (Iran), with the melt flow index (MFI) of $1.5 \cdot 10^{-6}$ kg/s and density of $\rho = 920$ kg/m³. The nanofiller was K10 modified montmorillonite (MMT) from Sigma-Aldrich, Germany. Also, the polyethyleneglycol which has been used in this study was polyethyleneglycol 40 from Merk-KGaA, Germany.

2.2. Mechanical properties

The tensile properties were evaluated according to ASTM D638 using dumbbell-shaped samples and a Gotech universal testing machine (Model GT-AI5000L), a tensile tester with a crosshead speed of $8.33 \cdot 10^{-4}$ m/s. The material compositions of the nanocomposites are listed in Table 1. In this table, wt. is considered as the weight percent.

Table 1. Sample compositions

Sample	LDPE [wt.%]	Compatibilizer [wt.%]	MMT [wt.%]
1	85	15	–
2	82	15	3
3	80	15	5
4	78	15	7

The effect of nanoparticles with different weight fractions on the elastic modulus is shown in Fig. 1.

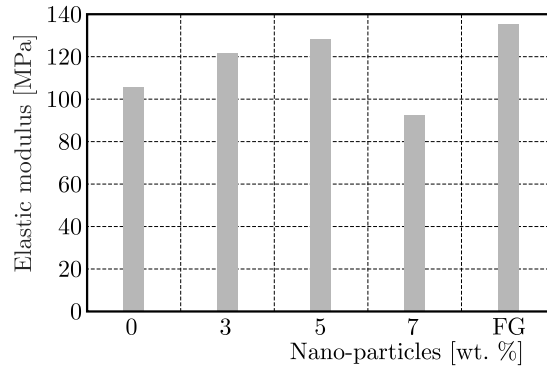


Fig. 1. The effect of nanoparticles with different weight fractions on the elastic modulus

As noticed, the elastic modulus begins to increase up to 5 wt.% of nanoclay. As the clay weight fraction exceeds 5 wt.%, the elastic modulus levels off, but for the functionally graded distribution, the elastic modulus is generally larger than the corresponding values for the uniform distribution of nanoclay. In fact, the elastic modulus of the functionally graded sample is the total result of the tensile test. The elastic moduli of all samples are calculated by using the machine software. Figure 2 illustrates the effect of nanoparticles with different weight fractions on the yield strength.

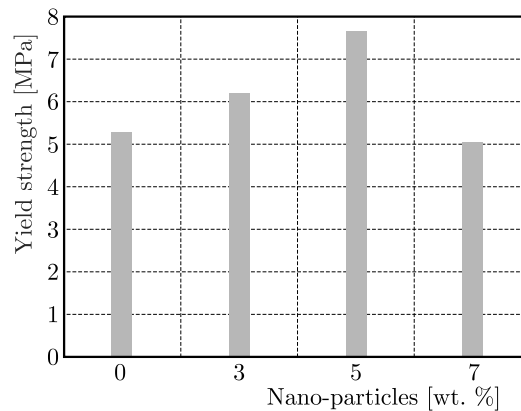


Fig. 2. The effect of nanoparticles with different weight fractions on the yield strength

As observed, the yield strength begins to increase up to 5 wt.% of nanoclay. As the weight fraction of nanoclay exceeds 5 wt.%, the yield strength levels off.

2.3. Buckling tests

We used a beam apparatus from TQ, England (Model SM1005) to study mechanical buckling of columns made of functionally graded and uniformly distributed nanocomposites. The test specimens have a rectangular cross section $0.02\text{ m} \times 0.004\text{ m}$ and length of 0.2 m with both ends simply supported.

3. Modeling

3.1. Genetic Algorithm

The GA is an unorthodox search or optimization algorithm, which was first suggested by Holland (1975). As the name suggests, the GA was inspired by the processes observed in natural evolution. It attempts to mimic these processes and utilizes them for solving a wide range of

optimization problems. In general, GA performs directed random searches through a given set of criteria. These criteria are required to be expressed in terms of an objective function, which is usually referred to as a fitness function. The GA method requires that the set of alternatives to be searched be finite. To apply them to an optimization problem where this requirement is not met, the set involved must be discretized and appropriate finite subset must be selected. It is further required that the alternatives be coded in chromosomes of some specific finite length which consists of symbols from some finite alphabet. These are called chromosomes; the symbols that form them are called genes, and their set is called a gene pool. The GA method searches for the best alternative (in the sense of a given fitness function) through chromosome evolution. The basic steps in the GA are shown in Fig. 3.

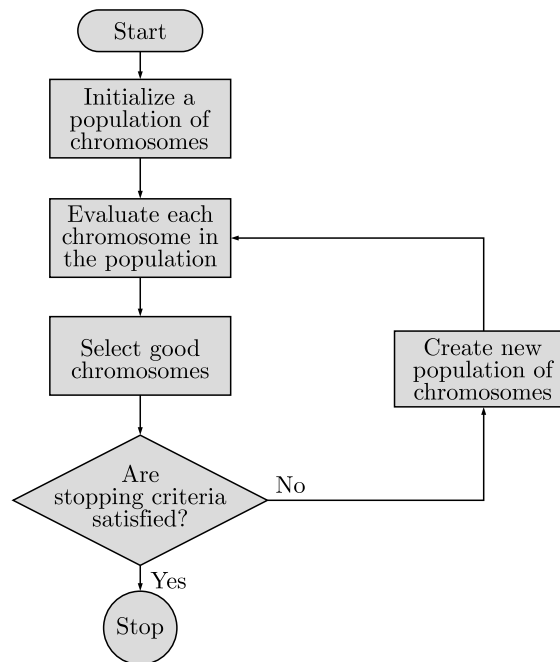


Fig. 3. High level description of the GA

First, the initial population of chromosomes is randomly selected. Then each chromosome in the population is evaluated in terms of its fitness (expressed by the fitness function). Next, a new population of chromosomes is selected from the given population by giving a greater chance to select chromosomes with higher fitness. This is called the reproduction operation. The new population may contain duplicates. If given stopping criteria (e.g., no change in the old and new population, specified computing time, etc.) are not met, some specific, genetic-like operations are performed on chromosomes of the new population. These operations produce new chromosomes, called offsprings s . The same steps of this process, evaluation and reproduction operations are then applied to chromosomes of the resulting population. The whole process is repeated until the given stopping criteria are met. The solution is expressed by the best chromosome in the final population.

3.2. Theoretical predictions

First, it is assumed that the material properties can be described by a simple polynomial depending on the nanoclay weight percentage. The coefficients of this polynomial function are found by maximizing the accuracy. The $1 - R_{adj}^2$ is introduced as the fitness function which is to be minimized. R_{adj}^2 is the accuracy criterion of an arbitrary mechanical property function (such as Young's modulus). R_{adj}^2 is defined as a process which is demonstrated below. The mechanical

property is a function of the nanoclay weight percent and R_{adj}^2 is a function of coefficients which are introduced below. M_i and W are considered as the mechanical properties and the nanoclay weight percent, respectively. M_i is expressed as a polynomial function of W as follows

$$M_i = \sum_{j=0}^4 a_{ji} W^j \quad (3.1)$$

Now, the coefficients a_{ji} are found by maximizing the accuracy of the polynomial function. The equations can be written as

$$R_{adj}^2 = 1 - \frac{VAR_E}{VAR_T} \quad (3.2)$$

in which

$$\begin{aligned} VAR_E &= \frac{SS_{Err}}{n - k - 1} & VAR_T &= \frac{SS_{Tot}}{n - 1} \\ SS_{Tot} &= \sum_{i=1}^n (y_i - \bar{y})^2 & SS_{Err} &= \sum_{i=1}^n (y_i - M_i)^2 \\ \bar{y} &= \frac{1}{n} \sum_{i=1}^n y_i & M_i(W) &= a_{0i} + a_{1i}W + a_{2i}W^2 + a_{3i}W^3 \end{aligned} \quad (3.3)$$

In these equations, $n = 4$ is the number of experiments, $k = 0$ is the number of duplicated experiments and y_i denotes the experimentally measured mechanical properties. a_{ji} coefficients are obtained after approximately 40 generations by minimization of $1 - R_{adj}^2$ through using MATLAB. Obtaining the a_{ji} coefficients, the Young modulus of the uniformed distribution can be expressed as a function of the nanoclay weight percent as follows

$$E = -3.401W + 4.97W^2 - 0.677W^3 + 105.338 \quad (3.4)$$

Here, W is the nanoclay weight percent (wt.% and W have the same value, e.g., wt.% = $W = 3$). To validate the presented results, comparison studies are carried out for the Young modulus of the uniformly distributed nanocomposites as presented in Table 2.

Table 2. Comparison of Young's modulus for uniformly distributed nanocomposites

Nanoclay weight percent	Theoretical predictions [MPa]	Experimental results [MPa]
pure	105.338	105.338
3%	121.586	121.582
5%	127.958	127.939
7%	92.85	92.795

The comparison between theoretical predictions and the experimental data shows high accuracy of the present analysis. Equation (3.4) can also be used to derive a suitable relation for Young's modulus of the functionally graded distribution. The specimen with functionally graded distribution consists of four perfectly bonded sheets with a total thickness of 4 mm. Each sheet has 1 mm in thickness with different nanoparticles weight fractions (pure, 1 wt.%, 3 wt.% and 5 wt.%). The Young modulus can be written as

$$E(z) = \begin{cases} -3.401(2z + \text{sgn}(z)) + 4.97(2z + \text{sgn}(z))^2 \\ \quad - 0.677(2z + \text{sgn}(z))^3 + 105.338 & \text{for } 0 \leq z < 4 \\ 92.85 & \text{for } z = 4 \end{cases} \quad (3.5)$$

As mentioned before, the Young modulus is assumed to vary as a function of the thickness coordinate z . By using a simple change of the variable as $z = \bar{z} + 2$, the coordinate \bar{z} changes within $-2 \leq \bar{z} \leq 2$. Equation (3.5) can be verified via employing the buckling analysis of the functionally graded nanocomposite beam under axial compressive load.

4. Formulation of the problems

The formulation is presented based on the assumptions of the Engesser-Timoshenko beam theory. Based on this theory, the displacement field can be written as (Wang and Reddy, 2000)

$$u(x, \bar{z}) = \bar{z}\phi(x) \quad w(x, \bar{z}) = w_0(x, \bar{z}) \quad (4.1)$$

In view of the displacement field given by Eqs. (4.1), the strain displacement relations are (Wang and Reddy, 2000)

$$\varepsilon_{xx} = \frac{\partial u}{\partial x} = \bar{z} \frac{d\phi}{dx} \quad \gamma_{xz} = \frac{\partial u}{\partial \bar{z}} + \frac{\partial w}{\partial x} = \phi + \frac{dw}{dx} \quad (4.2)$$

Consider a functionally graded beam under axial compressive load with a rectangular cross-section as shown in Fig. 4.

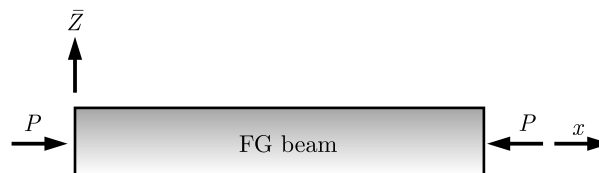


Fig. 4. Simply supported beam under compressive load

Thickness, length and width of the beam are denoted by h , L and b , respectively. The xy -plane coincides with the midplane of the beam and the \bar{z} -axis located along the thickness direction. The Young modulus E is assumed to vary as a function of the thickness coordinate variable \bar{z} ($-2 \leq \bar{z} \leq 2$). The constitutive relations for the functionally graded Engesser-Timoshenko beam are given by (Reddy, 2004)

$$\sigma_{xx} = E(\bar{z})\varepsilon_{xx} \quad \sigma_{xz} = G(\bar{z})\gamma_{xz} \quad (4.3)$$

where σ_{xx} , σ_{xz} , $E(\bar{z})$ and $G(\bar{z})$ are the normal stress, shear stress, the Young and shear modulus, respectively. The shear modulus can be written as (Thomas *et al.*, 2013)

$$G(\bar{z}) = \frac{E(\bar{z})}{2(1 + \nu)} \quad (4.4)$$

where ν is the Poisson ratio, estimated with the aid of the relation (Kozlov *et al.*, 2012)

$$\frac{\sigma_y}{E} = \frac{1 - 2\nu}{6(1 + \nu)} \quad (4.5)$$

where σ_y is the yield strength and equals 6.645 MPa from a tensile test. In fact, the total yield strength for the whole functionally graded sample can be obtained from the tensile test and calculated by using the machine software like the elastic modulus for the functionally graded sample. Also, the Poisson ratio assumed to be constant through thickness of the beam (Lei *et al.*, 2013). So, equation (4.5) can be used to estimate the Poisson ratio for the whole sample. Also, u and w are the displacement components in the x - and \bar{z} -directions, respectively.

The potential energy can be expressed as (Wang and Reddy, 2000)

$$U = \frac{1}{2} \int_v (\sigma_{xx} \varepsilon_{xx} + \sigma_{xz} \gamma_{xz}) dv \quad (4.6)$$

Substituting Eq. (4.2) and Eq. (4.3) into Eq. (4.6) and neglecting higher-order terms, we obtain

$$U = \frac{1}{2} \int_v \left\{ \left[\left(E(\bar{z}) \left(\bar{z} \frac{d\phi}{dx} \right) \right) \left(\bar{z} \frac{d\phi}{dx} \right) + \left[G(\bar{z}) \left(\phi + \frac{dw}{dx} \right) \right] \left(\phi + \frac{dw}{dx} \right) \right] \right\} dv \quad (4.7)$$

The width of the beam is assumed to be constant, which is obtained by integrating along y over v . Then Eq. (4.7) becomes

$$U = \frac{1}{2} \int_0^L \left\{ D \left(\frac{d\phi}{dx} \right)^2 + \frac{A}{2(1+\nu)} \left[\phi^2 + \left(\frac{dw}{dx} \right)^2 + 2\phi \frac{dw}{dx} \right] \right\} dx \quad (4.8)$$

where

$$A = bK_s \int_{-h/2}^{+h/2} G(\bar{z}) dz \quad D = b \int_{-h/2}^{+h/2} \bar{z}^2 E(\bar{z}) dz \quad (4.9)$$

where A , D and K_s are the shear rigidity, flexural rigidity and shear correction factor, respectively. The beam is subjected to the axial compressive load P as shown in Fig. 4. The work done by the axial compressive load can be expressed as (Wang and Reddy, 2000)

$$W = \frac{1}{2} \int_0^L P \left(\frac{\partial w}{\partial x} \right)^2 dx \quad (4.10)$$

We apply the Hamilton principle to derive the equilibrium equations of the beam as follows (Reddy, 2004)

$$\int_0^t (T - U + W) dt = 0 \quad (4.11)$$

where T is kinetic energy. Substituting Eq. (4.8) and Eq. (4.10) into Eq. (4.11) leads to the following equilibrium equations of the functionally graded Engesser-Timoshenko beam

$$(P - A) \frac{d^2 w}{dx^2} - A \frac{d\phi}{dx} = 0 \quad D \frac{d^2 \phi}{dx^2} - A \left(\phi + \frac{dw}{dx} \right) = 0 \quad (4.12)$$

5. Stability analysis

The boundary conditions for the simply supported Engesser-Timoshenko column are given by

$$w = \frac{d^2 w}{dx^2} = \frac{d\phi}{dx} \quad x = 0, L \quad (5.1)$$

By differentiating Eq. (4.12)₂ and then using Eq. (4.12)₁, we obtain

$$D \frac{d^3 \phi}{dx^3} = P \frac{d^2 w}{dx^2} \quad (5.2)$$

Equation (4.12)₁ can be solved for $d\phi/dx$

$$\frac{d\phi}{dx} = \frac{P - A \frac{d^2w}{dx^2}}{A} \quad (5.3)$$

Substituting Eq. (5.3) into (5.2) and applying the boundary conditions, the buckling load of the Engesser-Timoshenko beam is derived as follows

$$p_{cr} = \frac{\left(\frac{\pi}{L}\right)^2 D}{1 + \left(\frac{\pi}{L}\right)^2 \frac{D}{K_s A}} \quad (5.4)$$

where K_s can be expressed as (Lei *et al.*, 2013)

$$K_s = \frac{5}{6 - (\nu_1 V_1 + \nu_2 V_2)} \quad (5.5)$$

where ν_1 and ν_2 are Poisson's ratios of the nanoclay and the matrix, respectively, whereas V_1 and V_2 are the nanoclay and the matrix volume fractions, respectively. The quantity of $(\nu_1 V_1 + \nu_2 V_2)$ for the presented nanocomposite is infinitesimal, and the shear correction factor can be assumed to $K_s = 5/6$ (Ke *et al.*, 2013).

6. Results and discussion

The mechanical buckling of simply supported functionally graded Engesser-Timoshenko nanocomposite beams are studied in this paper. The material compositions of the nanocomposite beams are listed in Table 1 and the material properties are listed in Table 2. The effect of nanoparticles with different weight fractions on the theoretical buckling load are shown in Fig. 5. It is noticed that the buckling loads for the Engesser-Timoshenko beams with uniform distribution of the nanocomposite are generally lower than the corresponding values for the beams with functionally graded distribution of the nanocomposite. Also, it is seen that the buckling loads for the Engesser-Timoshenko beams with the uniform distribution of nanoparticles increase by increasing the nanoparticles weight percent up to 5 wt.%. By increasing the amount of nanoclay more than 5 wt.%, the buckling load is found to decrease.

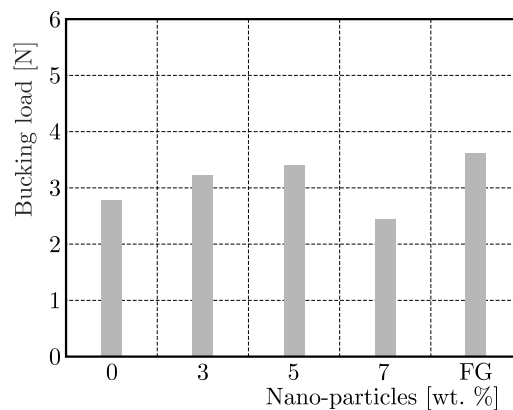


Fig. 5. The effect of nanoparticles with different weight fractions on the buckling load

The comparison between the theoretical and experimental data of the buckling load for uniform by distributed and functionally graded nanocomposites is shown in Table 3. As observed, there is good agreement between the results. Thus the presented approach to analysis of mechanical buckling of uniformly distributed and functionally graded nanocomposites has high accuracy.

Table 3. Compression between the theoretical and experimental data of the buckling load

Nanoclay weight percent	Theoretical buckling load [N]	Experimental buckling load [N]
pure	2.76	2.9
3%	3.19	3.3
5%	3.36	3.6
7%	2.43	2.7
FG	3.55	3.9

7. Conclusions

Mechanical buckling of polyethylene/clay nanocomposite columns with uniform and functionally graded distributions of nanoclay based on the Engesser-Timoshenko beam theory is studied. Some conclusions can be drawn as follows:

- The elastic modulus for the FG distribution of nanoclay is generally larger than the corresponding value for the uniform distribution of nanoclay.
- By increasing the nanoparticles weight fractions, the mechanical properties increase up to 5 wt.% of nanoclay. By increasing the amount of nanoclay more than 5 wt.%, the mechanical properties are found to decrease.
- GA is an acceptable optimization research technique which can be used with confidence to identify mechanical properties of nanocomposites with maximum accuracy.
- The buckling load of the uniformly distributed Engesser-Timoshenko nanocomposite beam is generally lower than the corresponding value for the functionally graded distribution.
- The buckling load of uniformly distributed nanoparticles of the Engesser-Timoshenko beam increases by increasing the nanoparticles weight percent up to 5 wt.% and then, for the amount of nanoclay more than 5 wt.%, the buckling load is found to decrease.

References

1. ARANI A., MAGHAMIKIA S., MOHAMMADIMEHR M., AREFMANESH A., 2011, Buckling analysis of laminated composite rectangular plates reinforced by SWCNTs using analytical and finite element methods, *Journal of Mechanical Science and Technology*, **25**, 809-820
2. BARATI F., FARAHANI H., NEZAMABADI A., VEISKARAMI M., 2014, Buckling analysis of functionally graded beams with imperfectly integrated surface piezoelectric layers under low velocity, *International Journal of Advances in Applied Mathematics and Mechanics*, **2**, 64-73
3. BROWN D., MELE P., MARCEAU S., ALBEROLA N.D., 2003, A molecular dynamics study of a model nanoparticle embedded in a polymer matrix, *Macromolecules*, **36**, 1395-1406
4. ELTAHER M.A., EMAM S.A., MAHMOUD F.F., 2013, Static and stability analysis of nonlocal functionally graded nanobeams, *Composite Structures*, **96**, 82-88
5. FORNES T.D., PAUL D.R., 2003, Modeling properties of nylon 6/clay nanocomposites using composite theories, *Polymer*, **44**, 4993-5013
6. GHIASIAN S.E., KIANI Y., ESLAMI M.R., 2015, Nonlinear thermal dynamic buckling of FGM beams, *European Journal of Mechanics – A/Solids*, **54**, 232-242
7. GRIGORIADI K., GIANNAKAS A., LADAVOS A., BARKOULA N.M., 2012, Thermomechanical behavior of polymer/layered silicate clay nanocomposites based on unmodified low density polyethylene, *Polymer Engineering Science*, **53**, 301-308

8. HEYDARI A., 2011, Buckling of functionally graded beams with rectangular and annular sections subjected to axial compression, *International Journal Advanced Design and Manufacturing Technology*, **5**, 25-31
9. HOLLAND J.H., 1975, *Adaptation in Natural and Artificial Systems*, University of Michigan Press, Ann Arbor, Michigan, U.S.A.
10. HOUARI M.S.A., BOUSALHA A.A., BESSAIM A., ADDA BEDIA E.A., TOUNSI A., 2013, Buckling of functionally graded nanobeams based on the nonlocal new first-order shear deformation beam theory, *International Congress on Materials and Structural Stability*, 427-428
11. JIA W.L., ZHAO L., HOU L., JI W.L., SHI W., QU G. H., 2014, Theoretical analysis of carbon nanotube photomixer-generated terahertz power, *Acta Physica Sinica*, **63**, 72-77
12. KE L.L., YANG J., KITIPORNCHAI S., 2013, Dynamic stability of functionally graded carbon nanotube-reinforced composite beams, *Mechanics of Advanced Materials and Structures*, **20**, 28-37
13. KIANI Y., ESLAMI M.R., 2010, Thermal buckling analysis of functionally graded material beams, *International Journal of Mechanics and Materials in Design*, **6**, 229-238
14. KIANI Y., ESLAMI M.R., 2013, Thermomechanical buckling of temperature-dependent FGM beams, *Latin American Journal of Solids and Structures*, **10**, 223-245
15. KOZLOV G., DZHANGURAZOV B., ZIAKOV G., MIKITAEV A., 2012, The nanocomposites polyethylene/organoclay permeability to gas description within the frameworks of percolation and multifractal models, *Chemistry and Chemical Technology*, **6**, 163-166
16. LEI Z.X., LIEW K.M., YU J.L., 2013a, Buckling analysis of functionally graded carbon nanotube-reinforced composite plates using the element – kp-Ritz method, *Composite Structures*, **98**, 160-168
17. LEI Z.X., LIEW K.M., YU J.L., 2013b, Free vibration analysis of functionally graded carbon nanotube-reinforced composite plates using the element-kp-Ritz method in thermal environment, *Composite Structures*, **106**, 128-138
18. LEI D., MENGGEN Q. Q. G., ZHANG H. L., ZHI Y. B., 2013c, Field emission properties from a carbon nanotube array with parallel grid, *Acta Physica Sinica*, **62**, 48-50
19. LI S., WANG X., WAN Z., 2015, Classical and homogenized expressions for buckling solutions of functionally graded material Levinson beams, *Acta Mechanica Solida Sinica*, **28**, 592-604
20. MAJUMDAR A., DAS D., 2016, A study on thermal buckling load of clamped functionally graded beams under linear and nonlinear thermal gradient across thickness, *Proceedings of the Institution of Mechanical Engineers, Part L: Journal of Materials: Design and Applications*, **1**, 23-32
21. MOSALLAIE BARZOKI A.A., GHORBANPOUR ARANI A., KOLAHCHI A., MOZDIANFARD M.R., 2012, Electro-thermo-mechanical torsional buckling of a piezoelectric polymeric cylindrical shell reinforced by DWBNNTs with an elastic core, *Applied Mathematical Modelling*, **36**, 2983-2995
22. NAM P.H., MAITI P., OKAMOTO M., 2001, Hierarchical structure and properties of intercalated polypropylene/clay nanocomposite, *Polymer*, **42**, 9633-9640
23. PAKDAMAN A.S., MORSHEDIAN J., JAHANI Y., 2013, Effect of organoclay and silane grafting of polyethylene on morphology, barrierity, and rheological properties of HDPE/PA6 blends, *Journal of Applied Polymer Science*, **127**, 1211-1220
24. RAFIEE M.A., RAFIEE J., YU Z.Z., KORATKAR N., 2009, Buckling resistant graphene nanocomposites, *Applied Physics Letters*, **95**, 223103
25. REDDY J.N., 2004, *Mechanics of Laminated Composite Plates and Shells Theory and Analysis*, CRC, New York, U.S.A.
26. RYCHLEWSKA J., 2014, Buckling analysis of axially functionally graded beams, *Journal of Applied Mathematics and Computational Mechanics*, **13**, 103-108
27. SHEN H.S., 2011a, Postbuckling of nanotube-reinforced composite cylindrical shells in thermal environments. Part I: Axially-loaded shells, *Composite Structures*, **93**, 2096-2108

28. SHEN H.S., 2011b, Postbuckling of nanotube-reinforced composite cylindrical shells in thermal environments. Part II: Pressure-loaded shells, *Composite Structures*, **93**, 2496-2503
29. SHENG N., BOYCE M.C., PARKS D.M., 2004, Multiscale micromechanical modeling of polymer/clay nanocomposites and the effective clay particle, *Polymer*, **45**, 487-506
30. SIMSEK M., YURTSU H.H., 2013, Analytical solutions for bending and buckling of functionally graded nanobeams based on the nonlocal Timoshenko beam theory, *Composite Structures*, **97**, 378-386
31. SMITH G.D., BEDROV D., LI L., BYUTNER O.A., 2002, A molecular dynamics simulation study of the viscoelastic properties of polymer nanocomposites, *Journal of Chemical Physics*, **20**, 9478-9489
32. SUN Y., LI S.R., BATRA R.C., 2016, Thermal buckling and post-buckling of FGM Timoshenko beams on nonlinear elastic foundation, *Journal of Thermal Stresses*, **39**, 11-26
33. THOMAS B., INAMDAR P., ROY, T., NADA B.K., 2013, Finite element modeling and free vibration analysis of functionally graded nanocomposite beams reinforced by randomly oriented carbon nanotubes, *International Journal on Theoretical and Applied Research in Mechanical Engineering*, **2**, 97-102
34. VODENITCHAROVA T., ZHANG L.C., 2006, Bending and local buckling of a nanocomposite beam reinforced by a single-walled carbon nanotube, *International Journal of Solids and Structures*, **43**, 3006-3024
35. WANG C.M., REDDY J.N., 2000, *Shear Deformable Beams and Plates*, Elsevier, Oxford, England
36. YIN G.H., DENG Q.T., YANG Z.C., 2015, Bending and buckling of functionally graded Poisson's ratio nanoscale beam based on nonlocal theory, *Iranian Journal of Science and Technology*, **39**, 559-565

Manuscript received March 1, 2017; accepted for print November 5, 2017

STUDY ON THE EFFECTS OF PREHEATED WALL/PLATES IN MICROTHRUSTER SYSTEMS

ELYAS LEKZIAN, HAMID PARHIZKAR, ASGHAR EBRAHIMI

Aerospace Faculty, Malek Ashtar University of Technology, Tehran, Iran

e-mail: lekzian@mut.ac.ir; hparhiz@mut.ac.ir; ebrahimi@mut.ac.ir

In the present paper, effects of pre-heated walls/plates on microthrusters performance are studied using a DSMC/NS solver. Three microthruster configuration types are studied. Type 1 is a cold gas microthruster. Microthruster type 2 has pre-heated walls. Pre-heated plates are inserted inside the chamber of microthruster type 3. It is observed that in microthruster type 2 the flow is accelerated and the specific impulse is elevated. However, by insertion of the pre-heated plates in microthruster type 3, viscous effects have stronger negative influence and the thrust is decreased. By implementing temperature gradients on walls in type 2 and on plates in type 3, it is observed that a higher temperature gradient enhances performance parameters of microthrusters. Among all types of microthrusters, microthruster type 2 with pre-heated walls has the highest thrust and specific impulse. Microthruster type 3 with a temperature gradient of 300-500 K has the minimum thrust due to a considerable decrease in the mass flow rate.

Keywords: DSMC/NS solver, pre-heated walls/plates, microthruster, performance parameters, temperature gradient

1. Introduction

Lots of micro devices such as microchannels, micro heat sinks, microturbines, microengines, and microthrusters were developed with advancement in fabrication. Due to advantages of micro-electro-mechanical-systems (MEMS) compared to their macro counterparts, they find increased applications in a variety of industrial and medical fields (Gad-el-Hak, 2005a,b). These miniaturized devices utilize smaller volumes while offering the possibility of parallel operation on a chip and reduce the risk of the whole system failure. In addition to advantages of scale miniaturization, they utilize little energy, offer high sensitivity and work with great accuracy. Besides the present applications of MEMS in electrical, structural, fluidic, transport and control aspects (Gad-el-Hak, 2005a,b), the potential applications such as attitude control of small satellites using micro thrusters in deep space (Janson *et al.*, 1999; Platt, 2002; Osiander *et al.*, 2005; Mihailovic *et al.*, 2011) are a field of interest.

In 1960s, low thrust devices were analyzed experimentally (Milligan, 1964; Rothe, 1971). Then numerical methods were proposed by Rae (1971) and Boyd *et al.* (1992) in order to investigate converging-diverging nozzles numerically. Boyd used a DSMC method and proved that this method was accurate enough to analyze the flow especially in the expanding section of the thruster with a near vacuum exit boundary conditions. Small nozzles were studied by Bayt (1999). He modeled a MEMS based nozzle by using Navier-Stokes simulations and observed that by a decrease of Reynolds number the propulsive efficiency was decreased due to an increase in boundary layer thickness. A microthruster utilized in GP-B spacecraft was studied by Jafryt and Beukelt (1994). They studied back pressure effects on the behavior of flow in the nozzle. Ivanov *et al.* (1999) studied the effects of the throat Reynolds number on the specific impulse. They demonstrated that an increase of losses could lead to over-prediction of the specific impulse at

the exit of the nozzle. Alexeenko *et al.* (2002) investigated an axisymmetric 3D micronozzle by the DSMC method and Navier-Stokes solver. Their results showed that gas expansion increased the specific impulse. Xie (2007) demonstrated that flow in MEMS nozzles was simulated accurately by the DSMC method and the Navier-Stokes equations even when adding slip boundary conditions became invalid when the average Knudsen number was about 0.01 in his special case. Surface roughness of the micro nozzle was studied by Torre *et al.* (2010). They observed shocks near the walls due to roughness. Sun *et al.* (2009) conducted a DSMC-FVM method to simulate the flow inside a micro nozzle. They investigated the effect of inlet pressure on the flow field inside the nozzle. They concluded that when the inlet pressure was increased, the distance between the throat and the point that propellant velocity surpassed sonic velocity became smaller.

In the present study, pressure driven microthrusters are investigated. Numerical simulation of the flow passing through the thruster is introduced first. A DSMC/NS solver is utilized. Due to lack of experimental data at microscales, the solver is first verified by a simulated micronozzle. The solver is then utilized to simulate microthrusters. Effects of heating the flow by increasing the wall temperature and by insertion of high temperature plates inside the domain are studied, and performance parameters are then investigated. Next, the effects of the temperature gradient on the performance parameters are analyzed. At the end, the thrust and specific impulse of all microthrusters configurations are compared.

2. Basic theory

2.1. DSMC solver

DSMC method enables numerical solution of the Boltzmann equations. The method benefits from the statistical solution of the particles behavior represented by kinetic theory (Bird, 1994).

For an accurate DSMC simulation, four issues must be considered: The cell size, time step, number of particles per cell and the mean collision separation distance. The cell size must be $1/3$ of the mean free path (Hadjiconstantinou, 2000; Pfeiffer *et al.*, 2013) to prevent errors in diffusion. In the present study, the method proposed by Nance *et al.* (1998) is utilized to determine the grid distribution. The time step must be smaller than the mean collision time in order to properly distinguish the particle free movement from a pair collision. In order to obtain physical and meaningful solutions, Bird (2007) propose that the particle per cell (PPC) would be around 7. However, Le *et al.* (2006) showed that for the low speed portion of the flow near the inlet of the computational domain, an average of 20 particles per cell gives precise solutions. In this paper, the study is begun with $PPC=7$, and then a PPC independence study is conducted. Another parameter that affects the results is the mean collision separation distance. According to Moss and Bird (2005), the mean separation distance has to be smaller than the mean free path in each cell throughout the computational domain.

The DSMFOAM solver of OPENFOAM-2.3.1 is used in DSMC simulations. The boundary condition proposed by Liu *et al.* (2006) is applied in simulation. The boundary condition in microchannel systems strongly affects the results, as described by Nance *et al.* (1998). Current boundary treatment is simple and stable. Many publications (Liou and Fang, 2000; Wang and Li, 2004; Roohi *et al.*, 2009) demonstrated the accuracy of this boundary condition. The solver is capable of parallel operation and can model any geometry and any number of gas species. For calculation of post collision velocities and modeling of particle collisions, the Variable Hard Sphere (VHS) model is used. This model is widely applied because of its simplicity and good approximation of intermolecular collisions (Le *et al.*, 2006).

2.2. NS solver

By using the Chapman-Enskog procedure, the Navier stokes equations can be derived from the Boltzmann equations. The conservation of mass, momentum and energy are used (OPENFOAM, 2014). Maxwell velocity slip boundary conditions including thermal creep effects are implemented on the walls and plates (O'Hare *et al.*, 2007)

$$\mathbf{V}_g - \mathbf{V}_w = -\frac{2 - \sigma_u}{\sigma_u} \frac{\lambda}{\mu} \boldsymbol{\tau} - \frac{3 \text{Pr}(\gamma - 1)}{4 \gamma p} \mathbf{q} \quad (2.1)$$

where σ_u is the momentum accommodation coefficient. Subscripts g and w denote the gas adjacent to the wall and the wall, respectively. The parameter γ is the specific heat ratio and Pr is the Prandtl number. The shear stress is $\boldsymbol{\tau} = \mathbf{S} \cdot (\mathbf{n} \cdot \boldsymbol{\Pi})$ and the heat flux is $\mathbf{q} = \mathbf{Q} \cdot \mathbf{S}$. The tensor $\mathbf{S} = \mathbf{I} - \mathbf{nn}$, where \mathbf{I} is the identity tensor, and \mathbf{n} is the normal unit vector to the wall. \mathbf{Q} is the heat flux vector along the wall, and $\boldsymbol{\Pi}$ is the stress tensor at the wall. The parameter μ is the gas viscosity and can be calculated using both the power law and the Sutherland law. The power law model is slightly less accurate than the Sutherland law at moderate temperatures. Therefore, the Sutherland law is used for calculation of gas viscosity as follows (Le and Roohi, 2015)

$$\mu = A_S \frac{\sqrt{T^3}}{T + T_S} \quad (2.2)$$

The parameter A_S and T_S are constants, $A_S = 1.41 \cdot 10^{-6} \text{ Pas/K}^2$, $T_S = 111 \text{ K}$ for nitrogen. Maxwellian definition can be used for calculation of the molecular mean free path λ (Le *et al.*, 2012), but for the VHS collision model the molecular mean free path can be calculated as follows (Bird, 1994)

$$\lambda = \frac{2(5 - 2\omega)(7 - 2\omega)}{15} \sqrt{\frac{m}{2\pi kT}} \frac{\mu}{\rho} \quad (2.3)$$

where ω is the temperature exponent of the viscosity coefficient in the power law viscosity model, $\omega = 0.74$ for nitrogen (Bird, 1994). The parameter m is molecular mass, and k is Boltzmann constant. It has been observed that the temperature of the rarefied gas adjacent to the wall is not equal to the wall temperature. Therefore, temperature jump boundary conditions are implemented on the walls when a dilute gas is simulated by the NS equations. In the present study, the second order Smoluchowski temperature jump boundary condition is used as follows (Karniadakis *et al.*, 2006)

$$T_g - T_w = -\frac{2 - \sigma_T}{\sigma_T} \frac{2\gamma}{\gamma + 1} \frac{1}{\text{Pr}} \lambda \frac{\partial T}{\partial n} - \frac{2 - \sigma_T}{\sigma_T} \frac{2\gamma}{\gamma + 1} \frac{1}{\text{Pr}} \frac{\lambda^2}{2} \frac{\partial^2 T}{\partial n^2} \quad (2.4)$$

where σ_T is the thermal accommodation coefficient and n is the unit vector normal to the wall. Momentum and thermal accommodation coefficients are equal to unity in order to simulate diffuse reflector walls.

For NS simulation of the flow, RhoCentralFoam solver in OPENFOAM-2.3.1 is used. RhoCentralFoam is a density-based compressible flow solver based on central-upwind schemes of Kurganov and Tadmor.

3. Solver algorithm

To make use of the DSMC/NS solver, a parameter is required to be defined in order to distinguish the continuum and molecular regions. In the present study, the local Knudsen number is utilized to distinguish rarefied and continuum regions. The local Knudsen number is defined as below

$$\text{Kn}_{local} = \frac{\lambda_{local}}{\varphi \left(\frac{\Delta\varphi}{\Delta x} \right)^{-1}} \quad (3.1)$$

where φ is one of the macroscopic properties in each cell including: velocity, temperature, or density. In the NS solver, the parameter λ_{local} is calculated using equation (2.3). In the DSMC solver, the local mean free path is determined as below (Bird, 1994)

$$\lambda_{local} = \frac{1}{\sqrt{2}\pi d^2 n} \quad (3.2)$$

where $d = 4.17 \cdot 10^{-10}$ m is the nitrogen molecular diameter, and n is the density number within each cell. The local Knudsen number is determined as follows: $\text{Kn}_{local} = \max(\text{Kn}_{local_T}, \text{Kn}_{local_u}, \text{Kn}_{local_\rho})$ (Boyd *et al.*, 1995). Based on the procedure proposed by Schwartzentruber *et al.* (2007), the DSMC/NS solver simulation cycle is as follows:

- Entire computational domain is solved by the NS solver,
- Local Knudsen number is calculated and the continuum and rarefied regions are distinguished,
- Rarefied regions are solved by the DSMC solver,
- Local Knudsen number is recalculated, and the interface of the continuum and rarefied region is changed,
- Steps 3 and 4 are repeated until location of the interface region does not change.

4. Validation

4.1. DSMC solver validation

There is no experimental study on microthruster systems at micro scales. Therefore, in order to verify the accuracy of the DSMC solver, simulation results are compared with Liu *et al.* (2006). After a careful grid study based on the method proposed by Nance *et al.* (1998), the domain is divided into 400 cells in the x direction and 150 cells in the y direction by using a structured grid. The temperature and Mach number contours are depicted in Fig. 1a. The centerline temperature and Mach number are presented in Fig. 1b, and the results are compared with those presented in Liu *et al.* (2006).

Considering that the mean separation distance between the simulation particles must be smaller than the mean free path in each cell, two different particles per cell (PPC) (PPC = 15, PPC = 20) are chosen. As seen in Fig. 1b, a similar Mach number and temperature distribution is achieved. Therefore, correct simulation results are obtained by both PPC = 15 and PPC = 20. Also, agreements of the results with those of Liu *et al.* (2006) shows that the DSMC solver is accurate and the results are trustworthy.

4.2. DSMC/NS solver validation

In the previous Section, the entire domain is solved by the DSMC solver. In this Section, the DSMC/NS solver is used to obtain the solution. As mentioned earlier, the local Knudsen number needs to be determined. The domain is divided into 400×150 cells using a structured grid (Fig. 2a). Figure 2b shows the density based local Knudsen number which is the maximum local Knudsen number. It is observed that the boundary layer region in the divergent section of the micronozzle is in the rarefied regime since the local Knudsen number in this part is more than 0.05 (Boyd *et al.*, 1995). Due to expansion of flow in the divergent section, the rarefied region is increased toward the end of nozzle. It is demonstrated by Darbandi and Roohi (2011) that solving the flow using the NS solver in the divergent section is not accurate even in the

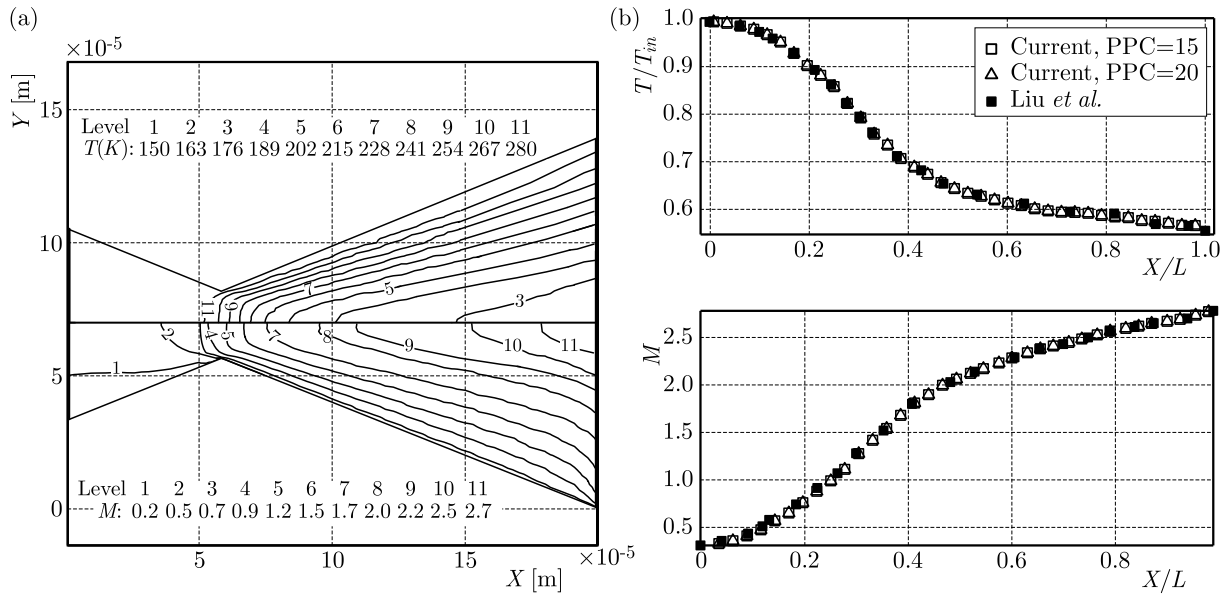


Fig. 1. (a) Temperature, Mach contours and graphs of the micronozzle; (b) current temperature and Mach number compared with Liu *et al.* (2006)

centerline. Therefore, the DSMC solver is used to simulate the entire divergent section and the NS solver is used for simulation of the convergent section of the micronozzle. The convergent section of the domain is divided into 100×150 cells and the divergent section is divided into 300×150 cells. Careful grid study is carried out based on the reference (Nance *et al.*, 1998) to choose pre-mentioned grid division of the domain. Pressure and temperature are considered as inlet boundary conditions of the micronozzle at the convergent section. The solution at the end of the convergent section is considered as the inlet boundary conditions of the divergent section. This data is considered as the initial data for calculation of pressure, temperature and flux by averaging over the inlet of the divergent section.

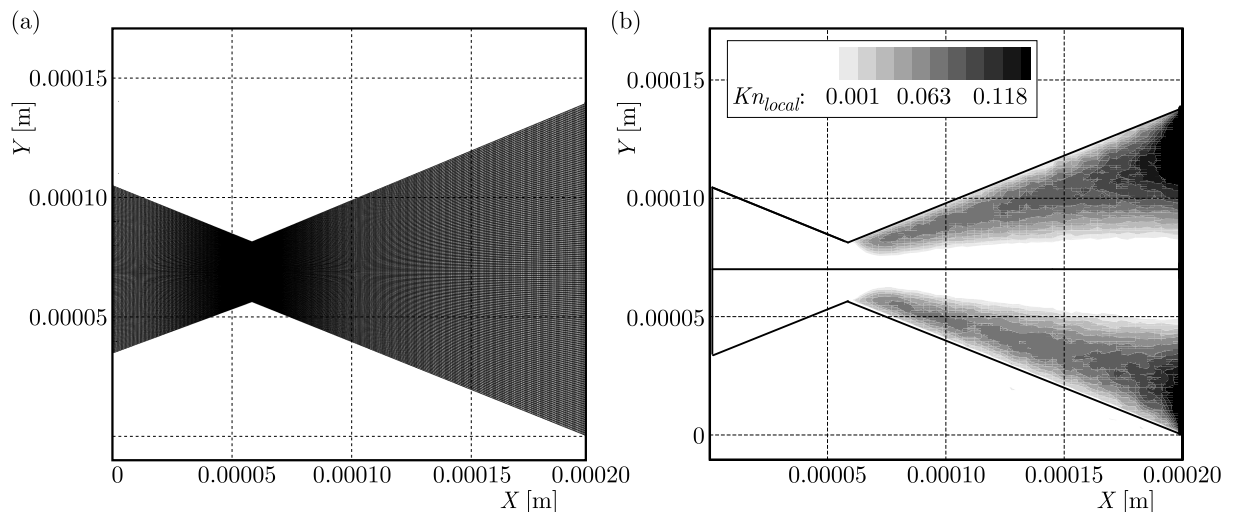


Fig. 2. Grid and Knudsen number distribution of the micronozzle: (a) structured grid, (b) Knudsen number contours using the DSMC solver (up) and the NS solver (bottom)

Figure 3 shows temperature distribution along the micronozzle centerline achieved by the DSMC and DSMC/NS solvers.

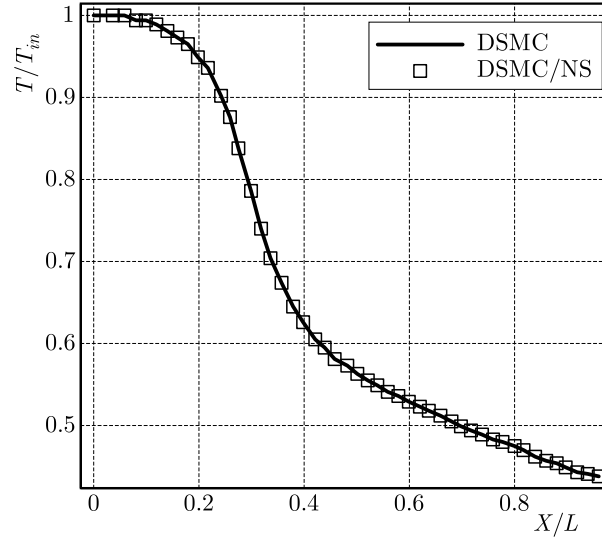


Fig. 3. Temperature distribution using the DSMC and DSMC/NS

It is observed that the result of the DSMC/NS solver is exactly the same as of the DSMC solver. Although the domain can be solved by the DSMC solver, the DSMC/NS solver is developed to reduce computational cost. DSMC simulation of the above micronozzle (using an Intel Core i5 computer with 3 GB RAM) takes 35 hours while using the DSMC/NS solver the time of computations is reduced to 23 hours (21 hours for the DSMC solver and 2 hours for the NS solver).

5. Microthruster problem statement

In this Section, the DSMC/NS solver is used to simulate microthruster systems. The chosen microthruster device is shown in Fig. 4. The thruster consists of a rectangular channel which is connected to a converging-diverging nozzle. A buffer zone is attached to the end of the diverging nozzle to consider variation of parameters at the nozzle exit (Wu *et al.*, 2001).

Three types of microthrusters are considered. In type 1, a cold gas microthruster is simulated (Fig. 4 without heater plates). Type 2 is the case when the flow is heated by increasing the wall temperature up to 900 K (see Fig. 4 without heater plates, the wall temperature is 900 K). The increasing of the wall temperature can be performed by using hot wire coated walls (Kundu *et al.*, 2013). For type 3, heater plates (with temperature 900 K) are inserted into the thruster (see Fig. 4 with heater plates). The overall geometry (but not the exact dimensions), the structure and idea of heating the fluid flow in type 3 is adapted from Kundu *et al.* (2013), Hitt *et al.* (2001) but not exactly with the same components. They fabricated and tested such a microthruster. Geometrical details of the three types of microthrusters are mentioned in Table 1.

Table 1. Dimensional parameters of the three types of microthrusters

	L_1	L_2/L_1	L_3/L_1	L_4/L_1	L_5/L_1	H_1	H_2/H_3	H_3/H_1
Type 1	0.6 mm	0.4	0.62	0.83	–	0.3 mm	0.5	0.33
Type 2					0.17			
Type 3					0.17			

The gas inside the thrusters is nitrogen. In all types of the thrusters mentioned above, the inlet temperature of 300 K is imposed. Since the velocity at the thruster exit is supersonic, no outlet pressure is set at the exit.

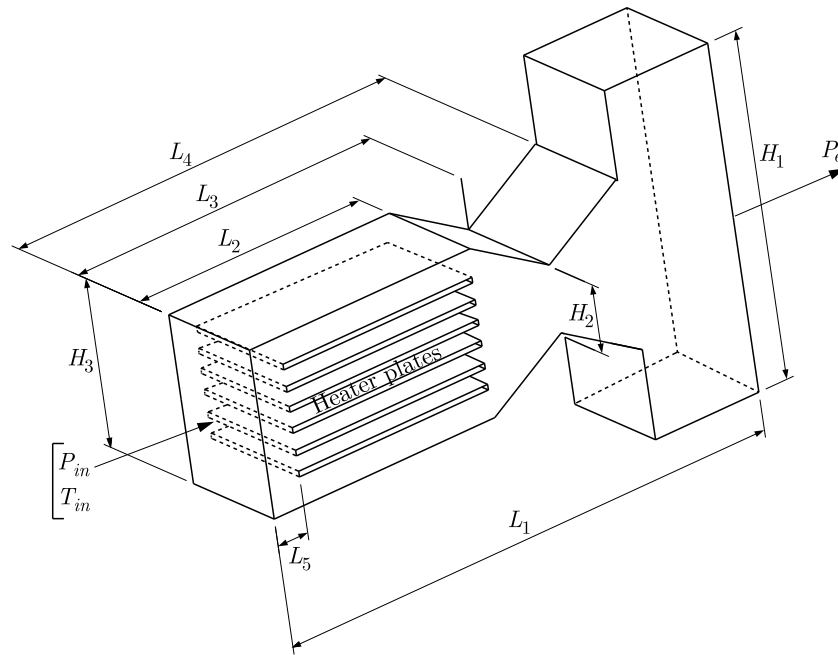


Fig. 4. Geometry of the microthruster

5.1. Flow properties comparison of type 1, 2, and 3

Temperature contours for the three types of microthrusters are shown in Fig. 5. Type 1 is considered as the reference case. In type 1, the temperature is decreased in the divergent section due to gas expansion. In type 2, the temperature is increased and reaches to the maximum value (less than 900 K) in the centerline and then it decreases. In type 3, the temperature is increased (to the maximum temperature of 900 K of pre-heated plates), it remains constant in the pre-heated plates section and then is decreased.

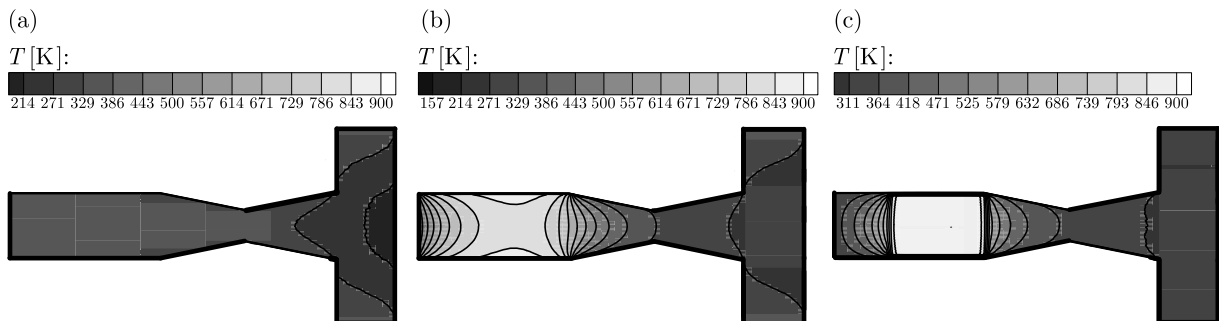


Fig. 5. Temperature contours for three types of microthrusters: (a) type 1 – cold gas, (b) type 2 – pre-heated walls, (c) type 3 – pre-heated plates

For accurate analysis of types 1, 2, and 3, the flow properties along the microthruster centerline are presented and compared in Fig. 6. These graphs illustrate the effect of pre-heated walls/plates inside the device on the gas flow properties. A significant pressure reduction occurs when the flow passes over heater plates in type 3 while the pressure along the centerline changes more smoothly in type 2 and 1. At the beginning and at the end of the heater plates the temperature is increased and decreased rapidly in type 3, whereas the temperature is increased more smoothly in type 2. In the convergent section, it is seen that the heater plates of type 3 microthruster system affect the downstream temperature flow field and increase the temperature downstream the plates. It can be concluded that the pressure loss at the heater plates in type 3 is converted into a temperature increase.

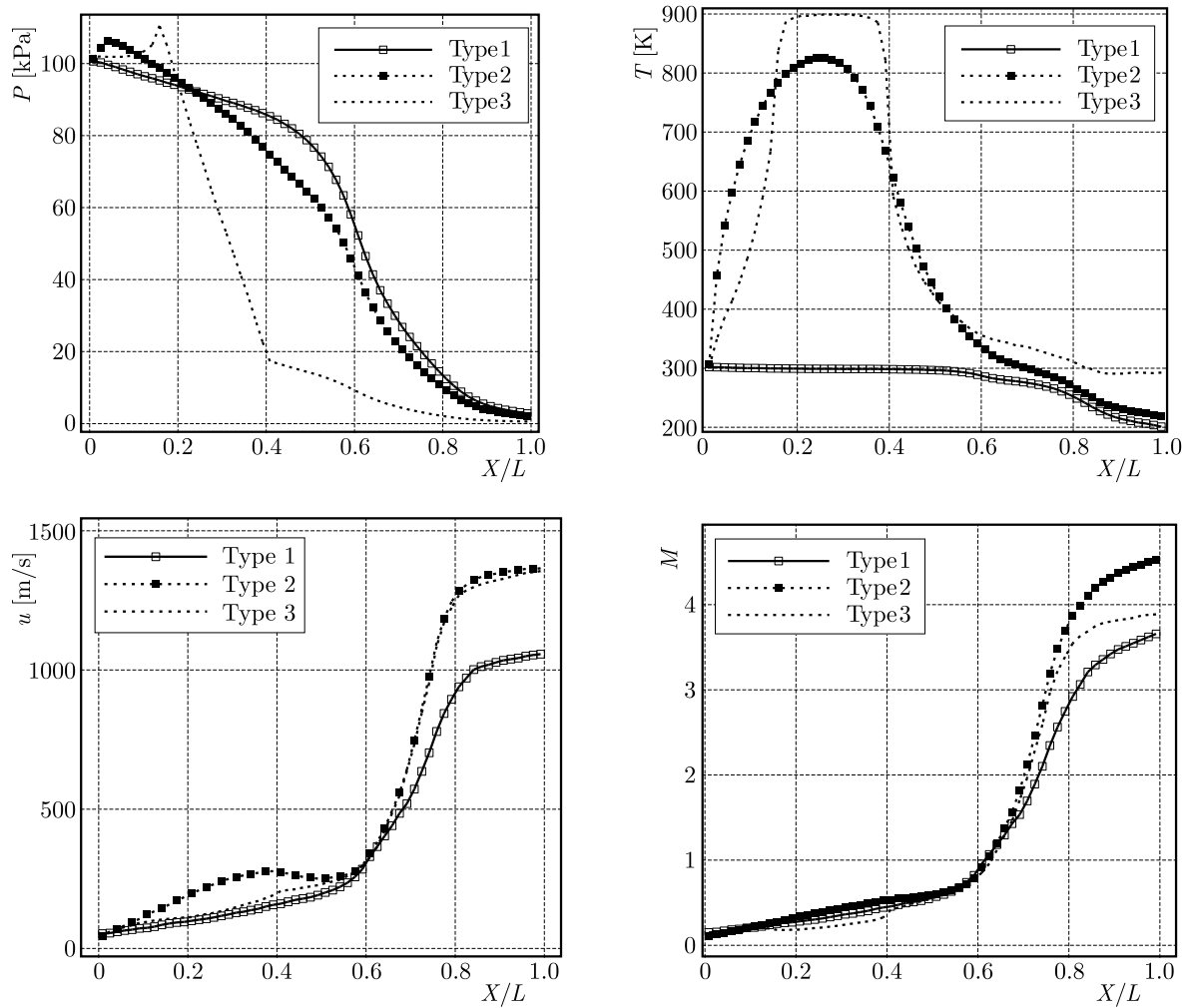


Fig. 6. Flow properties comparison of three types of microthrusters

The temperature at the diverging section of the micro propulsion device type 2 is almost similar to the cold gas microthruster. The exit velocity for type 2 and 3 is identical and greater than type 1. Therefore, the heating process accelerates the flow. Heating the flow also affects the Mach number at the exit. In type 2 and 3, the choking place of flow is not changed, but the exit Mach number of type 2 is greater than type 3. Such behavior is expected because the flow velocity at the exit is almost identical for type 2 and 3, but the temperature at the nozzle exit is higher in type 3 than type 2. Therefore, the exit Mach number of type 2 is greater than type 3.

5.2. Microthrusters performance results

Thrust, specific impulse, exit velocity and the mass flow rate are compared for three types of microthrusters. The total thrust is the sum of thrusts of each cell at the exit. The thrust is calculated using $F = \dot{m}V_{exit}$. The specific impulse is calculated as $I_{sp} = F/(\dot{m}g)$.

Quick comparison of the performance of three preceding microthruster systems is provided in Table 2. It is observed that the thrust and the specific impulse are highest in type 2. Therefore, a higher temperature would result in a higher thrust and specific impulse. Meanwhile, the minimum of thrust occurs in type 3, where the heater plates are inserted in. In type 3, the viscous effects of heater plates dominate the gas expansion and reduce the thrust due to significant viscous effects of the plates. In type 2, the flow is heated and accelerated but there are no

heater plates in the domain to increase the frictional forces. Hence, the performance parameters of type 2 are higher than the two others.

Table 2. Comparison of performance of three types of microthrusters

	\dot{m} [g/s]	V_{exit} [m/s]	F [mN]	I_{sp} [s]
Type 1	12.3	980	11.1	106.7
Type 2	11.8	1310	14.7	144.7
Type 3	7.4	1290	7.1	121.3

5.3. Effects of temperature gradient

Kundu *et al.* (2013) showed that there was a temperature gradient in a hydrogen peroxide monopropellant microthruster at the chamber section. Therefore, in this Section, the effect of temperature gradient on the thruster performance is studied. Three cases of temperature gradients are implemented on the wall of micropropulsion device type 2 and on the heater plates of microthruster type 3 (see Table 3).

Table 3. Comparison of performance of three types of microthrusters

Type of microthruster	Gradient case	Temperature at the beginning of wall/heater plates [K]	Temperature at end of wall/heater plates [K]
Type 2/type 3	Linear: 1	300	500
	Linear: 2	300	700
	Linear: 3	300	900

Grid/PPC studies have been carefully carried out for all gradient cases. In this Section, only the results obtained from simulation are presented. Temperature gradients of microthrusters 2 and 3 without the gradient and with the gradient (case 3) are depicted in Fig. 7.

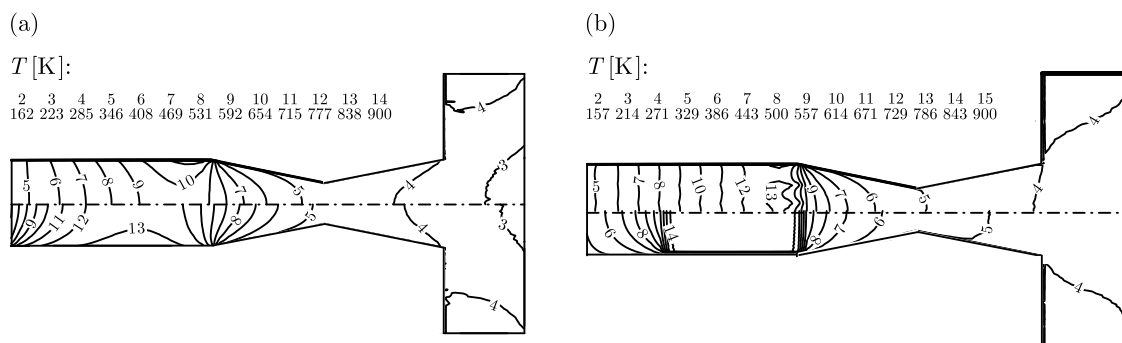


Fig. 7. Comparison of temperature contours for gradient case 3 and constant temperature: (a) gradient case (up), constant pre-heated wall (900 K) (bottom) for microthruster 2, (b) gradient case (up), constant pre-heated plate (900 K) (bottom) for microthruster 2

It is observed that the exit temperature of microthruster 2 is slightly larger than the exit temperature of microthruster 2 with gradient case 3. The same temperature behavior is seen for thruster type 3. Table 4 provides a quick review of the microthrusters performance.

It is demonstrated that temperature gradient case 3 has a higher thrust and specific impulse for both types of microthrusters (type 2 and 3).

Table 4. Performance comparison of three types of microthrusters

Type of microthruster	Gradient case	Mass flow rate [gs^{-1}]	Exit velocity [ms^{-1}]	Thrust [mN]	Specific impulse [s]
2	Linear: 1	12.1	1030	12.3	119.7
	Linear: 2	12	1211	13.7	130.4
	Linear: 3	11.7	1305	14.6	142.3
3	Linear: 1	6.85	1003	4.41	85.1
	Linear: 2	6.9	1111	5.4	99.8
	Linear: 3	7.2	1263	6.8	118.5

6. Performance comparison with/without temperature gradient

Figure 8 compares the thrust, specific impulse, mass flow rate and the exit velocity of all types of microthrusters with the constant temperature and with temperature gradient cases.

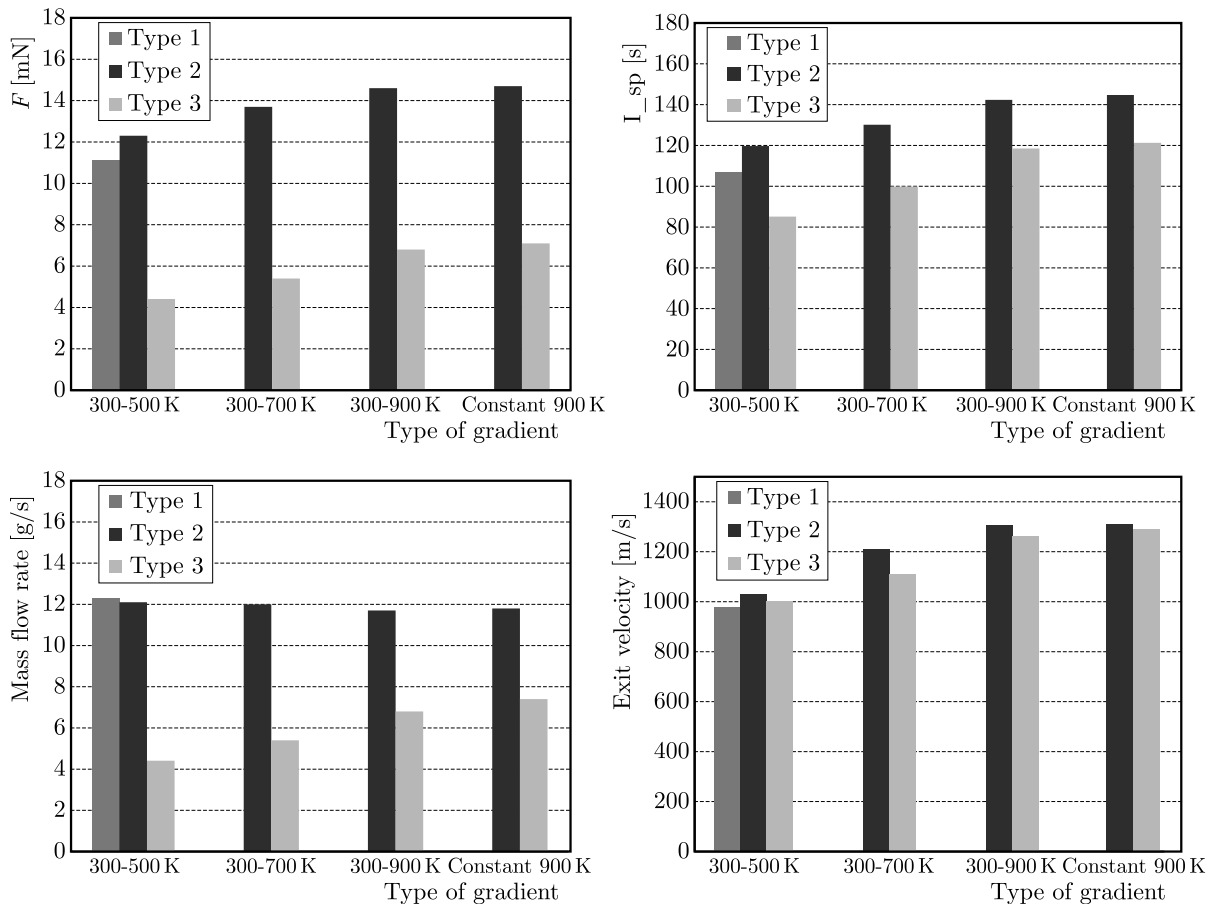


Fig. 8. Comparison of performance parameters of three types of microthrusters with constant pre-heated walls/plates and with gradient cases

It is observed that the highest thrust and specific impulse occurs in microthruster 2 with the constant wall temperature of 900 K. Insertion of pre-heated plates into microthruster 3 decreases the thrust. Pre-heated plates/walls increase the exit velocity. However, by implementing a higher temperature gradient to walls/plates, the microthrusters performance is elevated.

7. Conclusion

A DSMC/NS solver has been used in this paper. Accuracy of simulations has been first verified by simulation of a micronozzle. Then the flow inside three different microthruster system configurations has been simulated. A cold gas microthruster as type 1, pre-heated wall propulsion device as type 2, and a thruster with pre-heat plates inside the domain as type 3 have been simulated. It is observed that an increase in the fluid temperature accelerates the flow. Insertion of pre-heated plates inside the domain increases pressure loss, whereas heating up the walls of the thruster does not increase the frictional forces and, consequently, does not increase the pressure loss. It is demonstrated that type 2 has higher performance parameters than type 1 and 3. Also, temperature gradients have been implemented into the pre-heated walls and plates. It is observed that a higher gradient would elevate the thrust and specific impulse. Among all simulated cases, microthruster of type 2 with constant pre-heated walls (no temperature gradient) has better performance than all other cases. Microthruster 2 benefits from heating up which accelerates the flow, whereas it does not suffer from the frictional forces caused by the heater plates in type 3.

References

1. ALEXEENKO A., LEVIN D., GIMELSHEIN S., COLLINS R., MARKELOV G., 2002, Numerical simulation of high-temperature gas flows in a millimeter-scale thruster, *Journal of Thermophysics and Heat Transfer*, **16**, 1, 10-16
2. BAYT R.L., 1999, Analysis, fabrication and testing of a MEMS-based micropropulsion system, PhD, Aerospace Computational Design Laboratory, Department of Aeronautics and Astronautics, Massachusetts Institute of Technology
3. BIRD G., 2007, *Sophisticated DSMC, Notes Prepared for a Short Course at the DSMC07 Meeting*, Santa Fe, USA
4. BIRD G.A., 1994, *Molecular Gas Dynamics and the Direct Simulation of Gas Flows*, USA, Oxford Science Publications
5. BOYD I.D., CHEN G., CANDLER G.V., 1995, Predicting failure of the continuum fluid equations in transitional hypersonic flows, *Physics of Fluids*, **7**, 1, 210-219
6. BOYD I.D., PENKO P.F., MEISSNER D.L., DEWITT K.J., 1992, Experimental and numerical investigations of low-density nozzle and plume flows of nitrogen, *AIAA Journal*, **30**, 10, 2453-2461
7. DARBANDI M., ROOHI E., 2011, Study of subsonic-supersonic gas flow through micro/nanoscale nozzles using unstructured DSMC solver, *Microfluidics and Nanofluidics*, **10**, 2, 321-335
8. GAD-EL-HAK M., 2005a, *MEMS: Applications*, USA, CRC Press
9. GAD-EL-HAK M., 2005b, *MEMS: Introduction and Fundamentals*, USA, CRC Press
10. HADJICONSTANTINOU N.G., 2000, Analysis of discretization in the direct simulation Monte Carlo, *Physics of Fluids*, **12**, 10, 2634-2638
11. HITT D.L., ZAKRZWSKI C.M., THOMAS M.A., 2001, MEMS-based satellite micropropulsion via catalyzed hydrogen peroxide decomposition, *Smart Materials and Structures*, **10**, 6, 1163
12. IVANOV M., MARKELOV G., KETSDEVER A., WADSWORTH D., 1999, Numerical study of cold gas micronozzle flows, *37th Aerospace Sciences Meeting and Exhibit*, Reno, NV, U.S.A., American Institute of Aeronautics and Astronautics
13. JAFRYT Y., BEUKELT J.V., 1994, Investigation of nozzle and plume expansions of a small helium thruster, *Rarefied Gas Dynamics: Space Science and Engineering*, **160**, 136

14. JANSON S.W., HELVAJIAN H., HANSEN W.W., LODMELL J., 1999, Microthrusters for nanosatellites, *Second International Conference on Integrated Micro Nanotechnology for Space Applications*, Pasadena
15. KARNIADAKIS G.E., BESKOK A., ALURU N., 2006, *Microflows and Nanoflows: Fundamentals and Simulation*, Springer New York
16. KUNDU P., SINHA A.K., BHATTACHARYYA T.K., DAS S., 2013, Nanowire embedded hydrogen peroxide monopropellant MEMS thruster, *Journal of Microelectromechanical Systems*, **22**, 2, 406-417
17. LE M., HASSAN I., ESMAIL N., 2006, DSMC simulation of subsonic flows in parallel and series microchannels, *Journal of Fluids Engineering*, **128**, 6, 1153-1163
18. LE N.T., ROOHI E., 2015, A new form of the second-order temperature jump boundary condition for the low-speed nanoscale and hypersonic rarefied gas flow simulations, *International Journal of Thermal Sciences*, **98**, 51-59
19. LE N.T., WHITE C., REESE J.M., MYONG R.S., 2012, Langmuir-Maxwell and Langmuir-Smoluchowski boundary conditions for thermal gas flow simulations in hypersonic aerodynamics, *International Journal of Heat and Mass Transfer*, **55**, 19, 5032-5043
20. LIOU W., FANG Y., 2000, Implicit boundary conditions for direct simulation Monte Carlo method in MEMS flow predictions, *CMES – Computer Modeling in Engineering and Sciences*, **1**, 4, 119-128
21. LIU M., ZHANG X., ZHANG G., CHEN Y., 2006, Study on micronozzle flow and propulsion performance using DSMC and continuum methods, *Acta Mechanica Sinica*, **22**, 5, 409-416
22. MIHAILOVIC M., MATHEW T., CREEMER J., ZANDBERGEN B., SARRO P., 2011, MEMS silicon-based resistojet micro-thruster for attitude control of nano-satellites, *Solid-State Sensors, Actuators and Microsystems Conference (TRANSDUCERS)*, Beijing, IEEE: 262-265
23. MILLIGAN M.W., 1964, Nozzle characteristics in the transition regime between continuum and free molecular flow, *AIAA Journal*, **2**, 6, 1088-1092
24. MOSS J.N., BIRD G.A., 2005, Direct simulation Monte Carlo simulations of hypersonic flows with shock interactions, *AIAA Journal*, **43**, 12, 2565-2573
25. NANCE R.P., HASH D.B., HASSAN H., 1998, Role of boundary conditions in Monte Carlo simulation of microelectromechanical systems, *Journal of Thermophysics and Heat Transfer*, **12**, 3, 447-449
26. O'HARE L., LOCKERBY D.A., REESE J.M., EMERSON D.R., 2007, Near-wall effects in rarefied gas micro-flows: some modern hydrodynamic approaches, *International Journal of Heat and Fluid Flow*, **28**, 1, 37-43
27. OPENFOAM, (2014), *OPENFOAM: The Open Source CFD Toolbox*
28. OSIANDER R., DARRIN M.A.G., CHAMPION J.L., 2005, *MEMS and Microstructures in Aerospace Applications*, USA, CRC Press
29. PFEIFFER M., MIRZA A., FASOULAS S., 2013, A grid-independent particle pairing strategy for DSMC, *Journal of Computational Physics*, **246**, 28-36
30. PLATT D., 2002, A monopropellant milli-Newton thruster system for attitude control of nanosatellites, *AIAA/USU Conference on Small Satellites*, Utah
31. RAE W.J., 1971, Some numerical results on viscous low-density nozzle flows in the slender-channel approximation, *AIAA Journal*, **9**, 5, 811-820
32. ROOHI E., DARBANDI M., MIRJALILI V., 2009, Direct simulation Monte Carlo solution of subsonic flow through micro/nanoscale channels, *Journal of Heat Transfer*, **131**, 9, 092402
33. ROTHE D.E., 1971, Electron-beam studies of viscous flow in supersonic nozzles, *AIAA Journal*, **9**, 5, 804-811

34. SCHWARTZENTRUBER T.E., SCALABRIN L.C., BOYD I.D., 2007, A modular particlecontinuum numerical method for hypersonic non-equilibrium gas flows, *Journal of Computational Physics*, **225**, 1, 1159-1174
35. SUN Z.-X., LI Z.-Y., HE Y.-L., TAO W.-Q., 2009, Coupled solid (FVM)-fluid (DSMC) simulation of micro-nozzle with unstructured-grid, *Microfluidics and Nanofluidics*, **7**, 5, 621-631
36. SUN Z.-X., TANG Z., HE Y.-L., TAO W.-Q., 2011, Proper cell dimension and number of particles per cell for DSMC, *Computers and Fluids*, **50**, 1, 1-9
37. TORRE F.L., KENJERES S., KLEIJN C.R., MOEREL J.-L.P., 2010, Effects of wavy surface roughness on the performance of micronozzles, *Journal of Propulsion and Power*, **26**, 4, 655-662
38. WANG M., LI Z., 2004, Simulations for gas flows in microgeometries using the direct simulation Monte Carlo method, *International Journal of Heat and Fluid Flow*, **25**, 6, 975-985
39. WU J., LEE W., LEE F., WONG S., 2001, Pressure boundary treatment in internal gas flows at subsonic speed using the DSMC method, *Rarefied Gas Dynamics: 22nd International Symposium*, USA, American Institute of Physics, 408-416
40. XIE C., 2007, Characteristics of micronozzle gas flows, *Physics of Fluids*, **19**, 3, 037102

Manuscript received December 31, 2016; accepted for print November 7, 2017

DUAL-CONTROL MISSILE GUIDANCE: A SIMULATION STUDY

WITOLD BUŻANTOWICZ, JAN PIETRASIENSKI

Military University of Technology, Faculty of Mechatronics and Aerospace, Warsaw, Poland

e-mail: witold.buzantowicz@wat.edu.pl; jan.pietrasienski@wat.edu.pl

Theoretical considerations and a simulation study concerning description and analysis of new autopilot structures and issues relating to conversion of guidance commands into deflections of a complex system of control surfaces aimed at minimizing the miss distance value are presented in this paper. Due to nonlinear and nonstationary nature of the phenomena associated with the guidance process, a significant role is assigned to simulation studies. A comparative analysis has been made of the guidance processes of three models of a dual-control missile, which differ in terms of formulae implemented in the control command converters.

Keywords: dual-control missile, autopilot, guidance, miss distance

1. Introduction

Recent years have seen a significant increase in the possibilities offered by the air attack, both in terms of the impact on the enemy and the tactics used. Common use is made of jamming, anti-missile maneuvers, long-distance guided glide bombs and anti-radiation missiles. The intensive development of aircraft as well as maneuvering and aeroballistic missiles, and the increasingly common use of unmanned aircraft systems on today's battlefields, demand that ways are found to counteract these threats. Areas in which progress has been made include solutions for producing the lift force and methods of controlling anti-aircraft missiles. In particular, this concerns the design of dual-control missiles which have sets of aerodynamic fins both in front of and behind the missile center of mass. The aim of these solutions is to extend maneuvering possibilities of the missiles, thereby to increase the effectiveness of control during the terminal guidance phase.

Dual-control missiles were subjected to scientific analysis in the early 1990s (Hull *et al.*, 1990; Ochi *et al.*, 1991). Research in this area has been carried out by centers in, for example, Israel (Idan *et al.*, 2007; Shima and Golan, 2006, 2007), the United States (Schroeder, 2001; Shtessel and Tournes, 2009), China (Hua *et al.*, 2016; Yan and Ji, 2012), Japan (Ochi, 2003) and Spain (Ibarrondo and Sanz-Aránguez, 2016). These studies have largely concentrated on the optimum distribution of signals between control channels with attention being given both to problems of minimizing the miss distance and to general strategies for controlling and guiding missiles to aerial targets.

The high maneuverability of modern airstrike weapons enables them to react effectively to fire, including through anti-missile maneuvers. This situation is particularly disadvantageous during the terminal guidance phase, as it requires a very rapid reaction on the part of the missile, involving significant rotations of its airframe. This disturbs working conditions of the seeker, increasing dynamic errors of the coordinate determination system (Grycewicz *et al.*, 1984; Siouris, 2004; Yanushevsky, 2007; Gapiński and Krzysztofik, 2014). These errors are incorporated into the missile control commands, leading to increased miss distances and, thus, to reduced effectiveness of fire against the target. The minimization of miss distances is especially critical against ballistic missiles, which are generally destroyed by a direct hit, using the kinetic energy of

the guided missile. In these situations, the miss distance cannot exceed geometrical dimensions of the target.

It, therefore, becomes necessary to seek for solutions enabling stabilization of the operating conditions of the on-board seeker. Every change in the angle of attack and the use of aerodynamic control moment to produce rotation of the airframe achieved through deflection of the fins brings about transitional processes in the system that have an adverse effect on the operating conditions of the seeker installed in the nose section.

The use of a dual-control aerodynamic scheme is interesting in view of the increased technical control possibilities offered and, thus, the extended possibilities available for the guidance process itself. For example, the sets of fins in the control planes may deflect in the same direction (“divert mode”) or in opposite directions (“opposite mode”) – that is, the angles of deflection of the control surfaces located in front of and behind the center of mass of the missile airframe may have either the same or different signs.

This study focuses on issues related to improving the operating conditions of the seeker installed on an anti-aircraft missile. Specifically, the terminal phase of the guidance of the missile to an aerial target – the phase of particular relevance to effective combating of modern highly maneuverable air attacks.

The structure of the paper is as follows. In Section 2, a mathematical model is given for the dynamics of dual-control missile flight. The models of the elements making up the guidance loop are presented in Section 3. In Sections 4 and 5, formulae are proposed for the conversion of control commands, with selected simulation results. Conclusions and closing remarks constitute the final Section.

2. Dual-control missile dynamics model

We consider a cruciform, roll-stabilized missile with dual controls located in front of and behind the center of mass (Fig. 1).

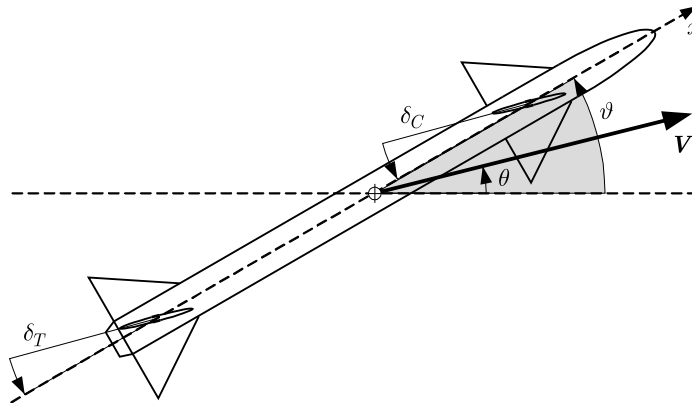


Fig. 1. Dual-control missile configuration

The motion of the missile is considered independently in the control planes. Selected questions will be addressed in the case of motion in the pitch plane.

The dynamics of the missile in the pitch plane is described by the following system of equations

$$\dot{\mathbf{x}}(t) = \mathbf{A}\mathbf{x}(t) + \mathbf{B}\mathbf{q}(t) \quad \mathbf{y}(t) = \mathbf{C}\mathbf{x}(t) \quad (2.1)$$

where \mathbf{x} is a state vector

$$\mathbf{x} \in \mathbb{R}^{5 \times 1} : \quad \mathbf{x} = [\theta \quad \omega \quad \vartheta \quad \delta_C \quad \delta_T]^T \quad (2.2)$$

\mathbf{y} is a vector of output signals

$$\mathbf{y} \in \mathbb{R}^{2 \times 1} : \quad \mathbf{y} = \begin{bmatrix} \omega & \vartheta \end{bmatrix}^T \quad (2.3)$$

and \mathbf{q} is a control vector

$$\mathbf{q} \in \mathbb{R}^{5 \times 1} : \quad \mathbf{q} = \begin{bmatrix} 0 & 0 & 0 & \delta_C^{com} & \delta_T^{com} \end{bmatrix}^T \quad (2.4)$$

The symbols in equations (2.2)-(2.4) have the following meanings: θ is the pitch angle of the missile velocity vector; ω is the angular rate of the missile airframe; ϑ is the pitch angle of the missile airframe; δ_C^{com} and δ_C are the commanded and actual deflections of the canards; δ_T^{com} and δ_T are the commanded and actual deflections of the tail fins.

The matrices \mathbf{A} , \mathbf{B} and \mathbf{C} are defined as follows

$$\begin{aligned} \mathbf{A} \in \mathbb{R}^{5 \times 5} : \quad \mathbf{A} &= \begin{bmatrix} -A_1 & 0 & A_1 & A_5^C & A_5^T \\ A_3 & -A_4 & -A_3 & -A_2^C & -A_2^T \\ 0 & 1 & 0 & 0 & 0 \\ 0 & 0 & 0 & -1/\tau_C & 0 \\ 0 & 0 & 0 & 0 & -1/\tau_T \end{bmatrix} \\ \mathbf{B} \in \mathbb{R}^{5 \times 5} : \quad \mathbf{B} &= \begin{bmatrix} 0 & 0 & 0 & 0 & 0 \\ 0 & 0 & 0 & 0 & 0 \\ 0 & 0 & 0 & 0 & 0 \\ 0 & 0 & 0 & 1/\tau_C & 0 \\ 0 & 0 & 0 & 0 & 1/\tau_T \end{bmatrix} \\ \mathbf{C} \in \mathbb{N}^{2 \times 5} : \quad \mathbf{C} &= \begin{bmatrix} 0 & 1 & 0 & 0 & 0 \\ 0 & 0 & 1 & 0 & 0 \end{bmatrix} \end{aligned} \quad (2.5)$$

where τ_C and τ_T are the time constants for the canards and tail fin servos. The coefficients of the matrix \mathbf{A} take the following forms

$$\begin{aligned} A_1 &= \frac{\rho V}{2m} f_1(M, \alpha) \\ A_2^C &= \frac{\rho V^2}{2I} f_2^C(M, \delta_C) & A_2^T &= \frac{\rho V^2}{2I} f_2^T(M, \delta_T) \\ A_3 &= \frac{\rho V^2}{2I} f_3(M, \alpha) & A_4 &= \frac{\rho V}{2I} f_4(M, \omega) \\ A_5^C &= \frac{\rho V}{2m} f_5(M, \delta_C) & A_5^T &= \frac{\rho V}{2m} f_5(M, \delta_T) \end{aligned} \quad (2.6)$$

where $V = |\mathbf{V}|$ is the module of the missile velocity vector, ρ is the air density, and $\alpha \equiv \vartheta - \theta$ is the airframe angle of attack. Nonlinear functions $f_i(\cdot)$, $i \in \{1, \dots, 5\}$ describe the missile aerodynamics. These depend on, among others, geometric parameters of the airframe, Mach's number M , and values of the variables α , ω , δ_C , and δ_T . They have a complex form whose derivation lies outside the scope of this work. The polynomial approximations $\hat{f}_i(\cdot)$, $i \in \{1, \dots, 5\}$ are taken for $M > 1.15$, and the following are assumed to hold

$$\begin{aligned} f_1(M, \alpha) &\approx S_B \hat{f}_1 \\ f_2^C(M, \delta_C) &\approx S_C l_C \hat{f}_2^C & f_2^T(M, \delta_T) &\approx S_T l_T \hat{f}_2^T \\ f_3(M, \alpha) &\approx S_B l_B \hat{f}_3 & f_4(M, \omega) &\approx S_B l_B^2 \hat{f}_4 \\ f_5(M, \delta_C) &\approx S_C \hat{f}_5 & f_5(M, \delta_T) &\approx S_T \hat{f}_5 \end{aligned} \quad (2.7)$$

where S_B, S_C, S_T and l_B, l_C, l_T are the characteristic surfaces and linear characteristic dimensions of the airframe, canards, and tail fins, respectively. The system of equations (2.1) is supplemented with the kinematic equation

$$a_{av} = V\dot{\theta} \tag{2.8}$$

where a_{av} is the available acceleration relative to the normal of the missile velocity vector, and V is the module of that vector.

The gravitational force acting on the missile during its flight is treated as an external signal the compensation of which is made in the numerical calculations by means of the adjustment

$$\dot{\theta}_G = -\frac{g}{V} \cos \theta \tag{2.9}$$

where $g = 9.81 \text{ m/s}^2$ is the gravitational acceleration.

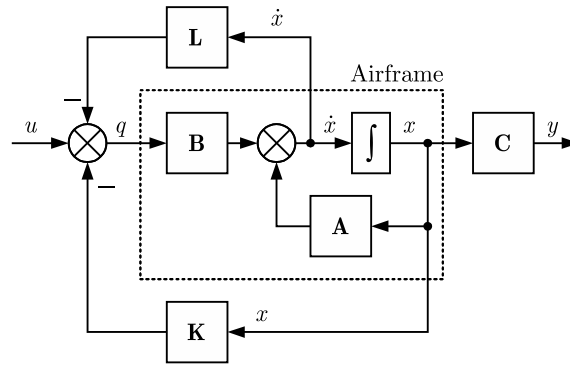


Fig. 2. Block diagram of the dual-control missile stabilization system in the pitch plane

A system for stabilization of the static and dynamic characteristics of the airframe is applied in the form of feedback loops, based on the angular rate and linear acceleration (Fig. 2). Consequently, a vector-matrix equation is obtained to describe motion of the dual-control missile in the pitch plane, taking account the stabilization system

$$\dot{\mathbf{x}} = (\mathbf{I} + \mathbf{BL})^{-1}(\mathbf{A} - \mathbf{BK})\mathbf{x} + (\mathbf{I} + \mathbf{BL})^{-1}\mathbf{Bu} \tag{2.10}$$

where \mathbf{I} is the identity matrix, and \mathbf{u} is the control command vector

$$\mathbf{u} \in \mathbb{R}^{5 \times 1} : \quad \mathbf{u} = \begin{bmatrix} \mathbf{0}^{3 \times 1} \\ \mathbf{u}_\kappa \end{bmatrix} \quad \wedge \quad \mathbf{u}_\kappa = \begin{bmatrix} \kappa_C \\ \kappa_T \end{bmatrix} \tag{2.11}$$

where, in turn, κ_C is the command applied to the canards, κ_T is the command applied to the tail fins, and \mathbf{K} and \mathbf{L} are matrices in the feedback paths

$$\mathbf{K}, \mathbf{L} \in \mathbb{R}^{5 \times 5} : \quad \mathbf{K} = \begin{bmatrix} 0 & 0 & 0 & 0 & 0 \\ 0 & 0 & 0 & 0 & 0 \\ 0 & 0 & 0 & 0 & 0 \\ 0 & K_C & 0 & 0 & 0 \\ 0 & K_T & 0 & 0 & 0 \end{bmatrix} \quad \mathbf{L} = \begin{bmatrix} 0 & 0 & 0 & 0 & 0 \\ 0 & 0 & 0 & 0 & 0 \\ 0 & 0 & 0 & 0 & 0 \\ L_C & 0 & 0 & 0 & 0 \\ L_T & 0 & 0 & 0 & 0 \end{bmatrix} \tag{2.12}$$

where K_C, K_T, L_C and L_T are the gains of component control signals for the canards and the tail fins.

3. Homing loop model

The system under consideration is a homing system based on a proportional navigation method in which control signals are dependent on parameters of the line of sight (Siouris, 2004; Yanushevsky, 2007; Zarchan, 2012)

$$a_{req} = nV_C\dot{\lambda} \quad (3.1)$$

where a_{req} is the required acceleration, n is the navigational constant, V_C is the closing velocity and $\dot{\lambda}$ is the angular rate of the line of sight.

A simplified block diagram of the missile homing system is shown in Fig. 3. The loop elements consist of the target, a seeker with a system for determining the target coordinates (TCD), an autopilot system (AP) and actuators.

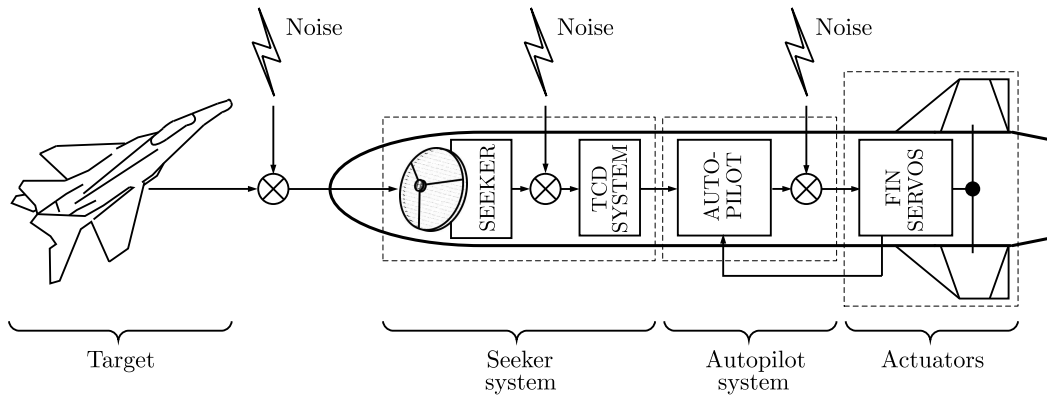


Fig. 3. Block diagram of the missile homing loop

The aerial target is modelled as a mass point whose motion is described by the vector \mathbf{E}

$$\mathbf{E} \in \mathbb{R}^{1 \times 4} : \quad \mathbf{E} = [x_E \quad y_E \quad \theta_E \quad V_E] \quad (3.2)$$

where x_E and y_E are the coordinates of the instantaneous position of the target, θ_E is the pitch angle of the target velocity vector, and V_E is the module of the target velocity vector. The changes in the target velocity and the pitch angle are defined by

$$\dot{V}_E = a_E^L \quad \dot{\theta}_E = \frac{1}{V_E} a_E \quad (3.3)$$

where a_E^L is the longitudinal acceleration and a_E is the lateral acceleration in the pitch plane. The changes in the accelerations a_E^L and a_E are approximated by the first-order dynamics

$$\dot{a}_E^L = \frac{\kappa_E^L - a_E^L}{\tau_E} \quad \dot{a}_E = \frac{\kappa_E - a_E}{\tau_E} \quad (3.4)$$

where κ_E^L and κ_E are the commanded accelerations and τ_E is the time constant. The commanded accelerations are subject to the following restrictions

$$|\kappa_E^L| \leq \bar{\kappa}_E^L \quad |\kappa_E| \leq \bar{\kappa}_E \quad (3.5)$$

The angle of the line of sight is given by

$$\lambda = \arctan \frac{y_E - y}{x_E - x} \quad (3.6)$$

where the coordinates x and y describe the instantaneous position of the missile.

The seeker supplies data to the coordinate determination system. A significant problem relating to the homing process is the determination of the current angular rate of the line of sight as determination of the position of the target is hampered by the fact that the motion of the missile airframe affects the operation of the coordinate determination system. The signal returned by the seeker contains information about the angular rate of the line of sight distorted by the inertia of the system (Grycewicz *et al.*, 1984) via a signal proportional to the angular acceleration of the missile airframe, and by generally understood measurement errors

$$s\lambda_m(s) = \frac{k_S}{\tau_S s + 1} [s\lambda(s) + s\Delta\lambda(s) + s^2\xi\vartheta(s)] \quad (3.7)$$

where ξ is the acceleration gain factor, k_S and τ_S are the gain and the time constant of the seeker drives, and $\Delta\lambda$ denotes the sum of the error signals occurring in the measuring path.

The sector of observation of the seeker's antenna is subject to the following restriction

$$|\vartheta - \lambda_m| \leq \zeta \quad (3.8)$$

4. Control command equations

Under the classical approach, the following control equation may be applied for a missile guided using a method of proportional navigation (Grycewicz *et al.*, 1984)

$$\kappa = \eta_1 \dot{\lambda} + \eta_2 \ddot{\lambda} \quad (4.1)$$

where κ is the control command, η_1 is a navigation function dependent on time and mass-geometrical characteristics of the missile, and η_2 is a variable related to compensation of the errors resulting from the airframe dynamics. Expression (4.1) is insufficient to perform the guidance process of a dual-control missile, as it does not take into account the additional possibilities offered by the dual-control system – in particular, it does not contain a rule for selecting the control mode.

During the guidance of a missile to the target, it is desirable that

$$\omega = \dot{\theta} = n\dot{\lambda} \quad (4.2)$$

namely, that the angular rate of the airframe should be close to the angular rate of the missile velocity vector and should not depend on the dynamics of the missile itself. This requirement is the basis for the formulation of the quantity index

$$J = E \left\{ \int_0^{t_f} (\omega - \dot{\theta})^2 dt \right\} \quad (4.3)$$

where $E\{\cdot\}$ is the mean operator and t_f is the final time. The value of the expression in (4.3) depends on the system ability to reduce the effect of components related to the dynamics of the missile airframe. This value will be smaller when the transitional processes occurring during guidance are shorter and less oscillatory. Figure 4a shows graphs of the angular rates of a dual-control missile airframe normalized to the final value, as they respond to step deflections of the fins (in the divert or opposite mode). The diagram shows the divert mode to be a more desirable control method in terms of the course of the process. A fundamental drawback, however, is that the accelerations available in the divert mode are many times smaller than those available in the opposite mode (Fig. 4b).

Based on Eq. (4.1) and the conditions described above, two forms of the conversion equations have been formulated for the mathematical model of the dual-control missile given by Eq. (2.10).

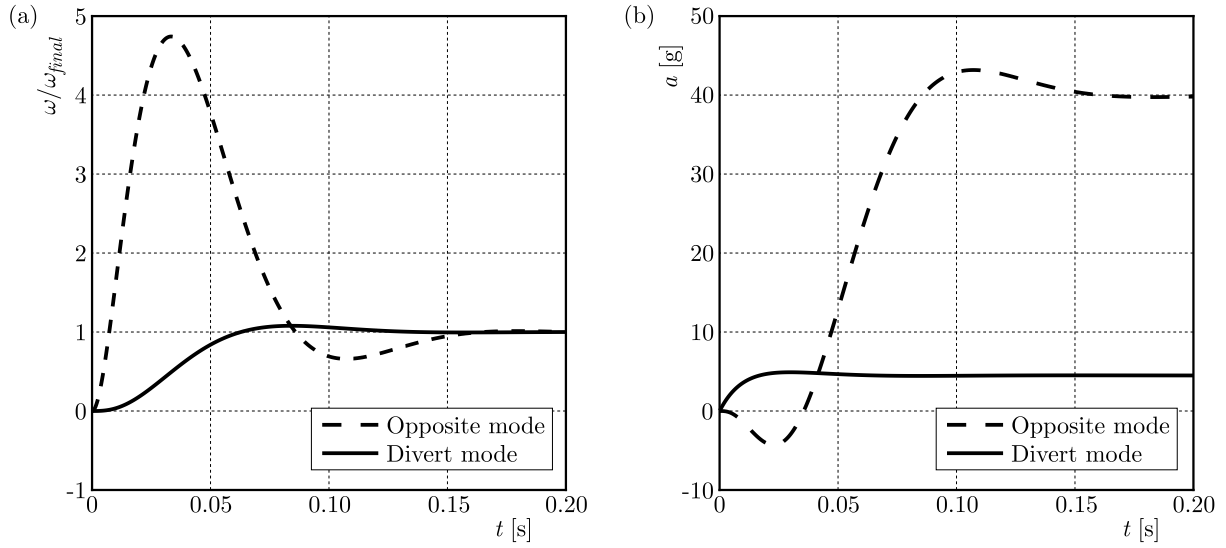


Fig. 4. Normalized angular rates (a) and normal accelerations (b) of the missile airframe

The condition for switching the control commands has been taken to be the result of comparison of the current values for the required and available acceleration.

The rule in the first case is formulated as follows: if the absolute value of the required acceleration in the control plane is greater than the absolute value of the available acceleration in the divert mode, then the switch to the opposite mode takes place. The equation with acceleration-based determination of control commands for the control plane takes the form

$$\mathbf{u}_\kappa = \begin{bmatrix} \kappa_C \\ \kappa_T \end{bmatrix} = \begin{bmatrix} \eta_1 \dot{\lambda}_m + \eta_2 \ddot{\lambda}_m \\ \kappa_T \end{bmatrix} \quad (4.4)$$

$$\kappa_T = \begin{cases} -\eta_1 \dot{\lambda}_m - \eta_2 \ddot{\lambda}_m & \text{for } |a_{req}| > |a_{av}^D| \\ \eta_1 \dot{\lambda}_m + \eta_2 \ddot{\lambda}_m & \text{for } |a_{req}| \leq |a_{av}^D| \end{cases}$$

where a_{av}^D is the available acceleration in the divert mode.

In the second case, an extended acceleration-based conversion model is used, where the values of required acceleration are compared with the values of available acceleration in the divert and canard-control mode. If the absolute value of the required acceleration in the considered control plane is greater than the absolute value of the available acceleration in the divert mode, the switch to canard control takes place. If the absolute value of the required acceleration also exceeds the absolute value of the available acceleration in the canard-control mode, the switch to the opposite mode takes place. In the extended acceleration-based conversion model, Eq. (4.4)₂ for the control command κ_T is replaced by

$$\kappa_T = \begin{cases} -\eta_1 \dot{\lambda}_m - \eta_2 \ddot{\lambda}_m & \text{for } |a_{req}| > |a_{av}^C| \\ 0 & \text{for } |a_{av}^D| < |a_{req}| \leq |a_{av}^C| \\ \eta_1 \dot{\lambda}_\varepsilon^m + \eta_2 \ddot{\lambda}_\varepsilon^m & \text{for } |a_{req}| \leq |a_{av}^D| \end{cases} \quad (4.5)$$

where a_{av}^C is the available acceleration in the canard-control mode.

Equations (4.4) and (4.5) indicate that in the present dual-control system, the canard fins are assigned a primary role. The tail fins regulate the resulting aerodynamic control moment depending on both the relative position of the missile and the target, and on the current state of the variables in the homing loop.

It is assumed that the control commands are overlaid with white noise with Gaussian distribution modelling the fluctuating interference caused by the noise from on-board devices and the environment. The resulting signal is limited by the saturation function

$$\text{sat}(\kappa) = \begin{cases} 1 & \text{for } \kappa > 1 \\ \kappa & \text{for } |\kappa| \leq 1 \\ -1 & \text{for } \kappa < -1 \end{cases} \quad (4.6)$$

where κ is the control command in the general meaning.

5. Simulation of the guidance process

The modelled missile guidance loop consists of systems with highly differentiated dynamics and event rates, including the rate of electromagnetic wave propagation. For these reasons, different methods of numerical integration have been used in forming approximate differential equations for elements of the guidance loop. For the elements subject to a negative feedback loop, Euler's approximations are generally sufficient, given an appropriate choice of the integration step size. Similarly, central-difference formulas computed in an open-loop system have been used to approximate the motion of the target. The proposed command formulas were examined for the terminal guidance phase. A comparison of guidance processes was made for the following missile models: a) dual-control missile No. 1 with the command formula described by equations (4.4); b) dual-control missile No. 2 with the command formula described by equations (4.4)₁ and (4.5); c) dual-control missile No. 3 with tail-fin control, with the following conversion formula

$$\mathbf{u}_\kappa = \begin{bmatrix} \kappa_C \\ \kappa_T \end{bmatrix} = \begin{bmatrix} 0 \\ -\eta_1 \dot{\lambda}_m - \eta_2 \ddot{\lambda}_m \end{bmatrix} \quad (5.1)$$

The following values were used as quantity indices of the guidance process: a) the value of the expression in (4.3); and b) the miss distance d defined as

$$d = \sqrt{(x_E - x)^2 + (y_E - y)^2} \quad (5.2)$$

at the instant at which the closing velocity V_C changed the sign.

It is assumed that the missiles have no thrust during the endgame. The following values of variables have been used in the simulation: $m = 100$ kg, $I = 35$ kgm², $S_B = 0.67$ m², $S_C = S_T = 0.06$ m², $l_B = 0.2$ m, $l_C = l_T = 1.36$ m, $\tau_C = \tau_T = 0.01$ s, $k_S = 1$, $\tau_S = 0.01$ s, $\zeta = 1.3$ rad, $\tau_E = 0.1$ s.

Scenario 1

The missiles are aimed at a non-maneuvering aerial target (Fig. 5). At the time $t = 0$, the target is located at the pitch angle $\theta_E = 0^\circ$ and is moving at $V_E = 400$ m/s at a height of 1 500 m and a distance of 3 000 m from the initial position of the missiles. At $t = 0$, the missiles have a height of 1 000 m, the pitch angle of the airframe is $\vartheta = 5^\circ$, the pitch angle of the velocity vector is $\theta = 5^\circ$, and the initial velocity is $V = 1 000$ m/s. The time of the simulation is $t_{sim} = 2.5$ s.

In the simulation, missiles 1-3 intercept the target at the time $t_1 = t_2 = t_3 = 2.23$ s. The mean values of the quantity indices from 100 sample runs of the scenario are given in Table 1, where

$$\bar{d} = \frac{1}{100} \sum_{i=1}^{100} d_i \quad \bar{J} = \frac{1}{100} \sum_{i=1}^{100} J_i$$

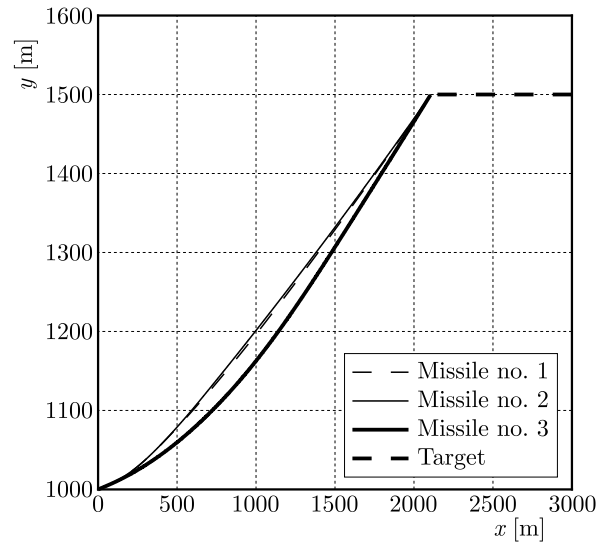


Fig. 5. Missile and target trajectories

Table 1. Guidance results

	d	J
Missile No. 1	0.0054	5.18
Missile No. 2	0.0013	3.49
Missile No. 3	0.0385	9.44

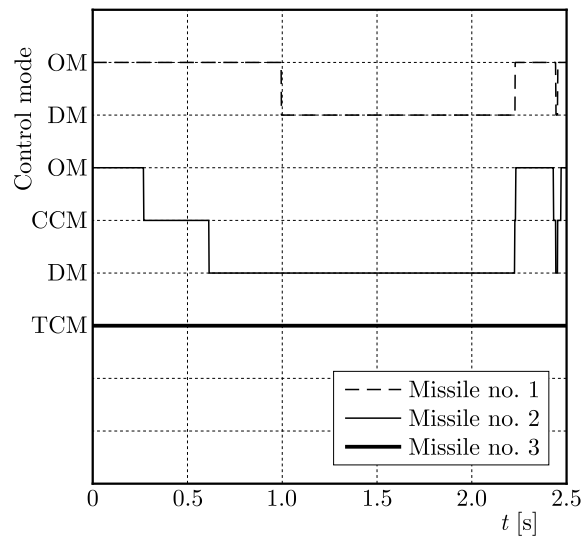


Fig. 6. Control mode comparison for a sample run (OM – opposite mode, DM – divert mode, CCM – canard-control mode, TCM – tail-fin control mode)

Figures 6 and 7 illustrate selected results from one of the simulation tests.

The analysis of the guidance process indicates that more favorable working conditions for the seeker are attained in the case of missiles No. 1 and No. 2 than in the case of missile No. 3: the angular rates of the line of sight stabilize at around 0.5 deg/s (Fig. 7a), while the missile airframes in the divert mode move at angles of attack of approximately zero (Fig. 7b). In the case of missile No. 2, the conditions for transition to the divert mode are attained 0.4 s earlier (Fig. 6) using an indirect control mode (canard-control mode). This leads to the most favorable stabilization index value for seeker working conditions, and the smallest average miss distance among the studied missiles (cf. Table 1).

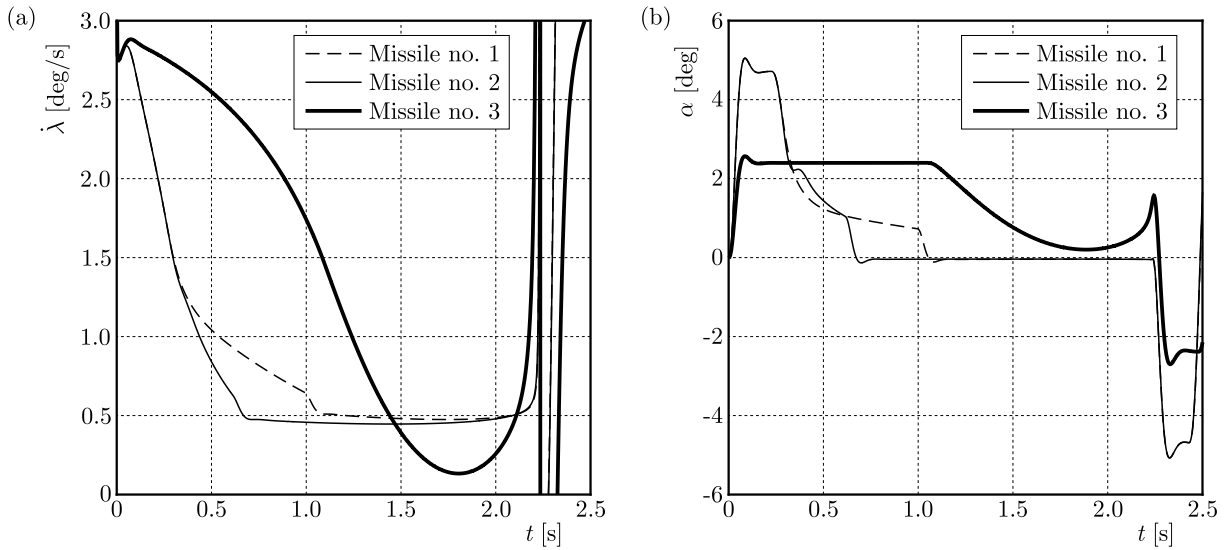


Fig. 7. (a) Angular rates of the line of sight, (b) angles of attack of the missile airframes

Scenario 2

The missiles are aimed at a fast aerial target maneuvering with longitudinal acceleration $a_E^L = \pm 1 g$ and lateral acceleration $a_E = \pm 10 g$ (Fig. 8). At the time $t = 0$, the target is located at the pitch angle $\theta_E = 5^\circ$ and is moving at $V_E = 350$ m/s at a height of 800 m and a distance of 3000 m from the initial position of the missiles. At $t = 0$, the missiles are at a height of 1000 m, the pitch angle of the airframe is $\vartheta = 0^\circ$, the pitch angle of the velocity vector is $\theta = 0^\circ$, and the initial velocity is $V = 1000$ m/s. The time of the simulation is $t_{sim} = 2.5$ s.

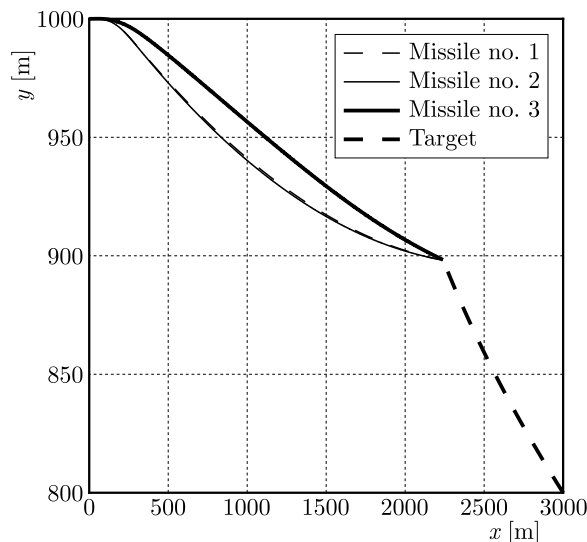


Fig. 8. Missile and target trajectories

The missiles intercept the target at the following times: $t_1 = 2.34$ s for missile No. 1, $t_2 = 2.33$ s for missile No. 2, and $t_3 = 2.32$ s for missile No. 3. The mean values of the quantity indices from 100 sample runs of the scenario are given in Table 2. Figures 9 and 10 illustrate selected results from one of the simulation tests.

In the case of missile No. 2, the conditions for transition to the divert mode are attained most rapidly using the indirect control mode (Fig. 9). In the case of both missile No. 1 and No. 2, it is necessary to switch to other control modes later in the guidance process: the opposite mode in

Table 2. Guidance results

	\bar{d}	J
Missile No. 1	0.2663	67.58
Missile No. 2	0.1054	61.09
Missile No. 3	2.8760	73.73

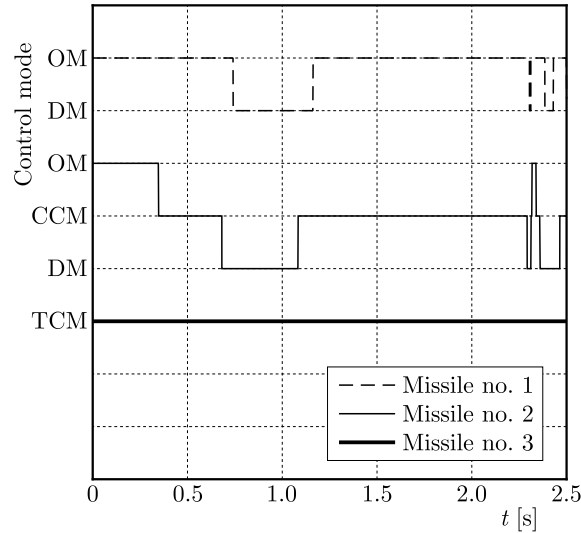


Fig. 9. Control mode comparison for a sample run (OM – opposite mode, DM – divert mode, CCM – canard-control mode, TCM – tail-fin control mode)

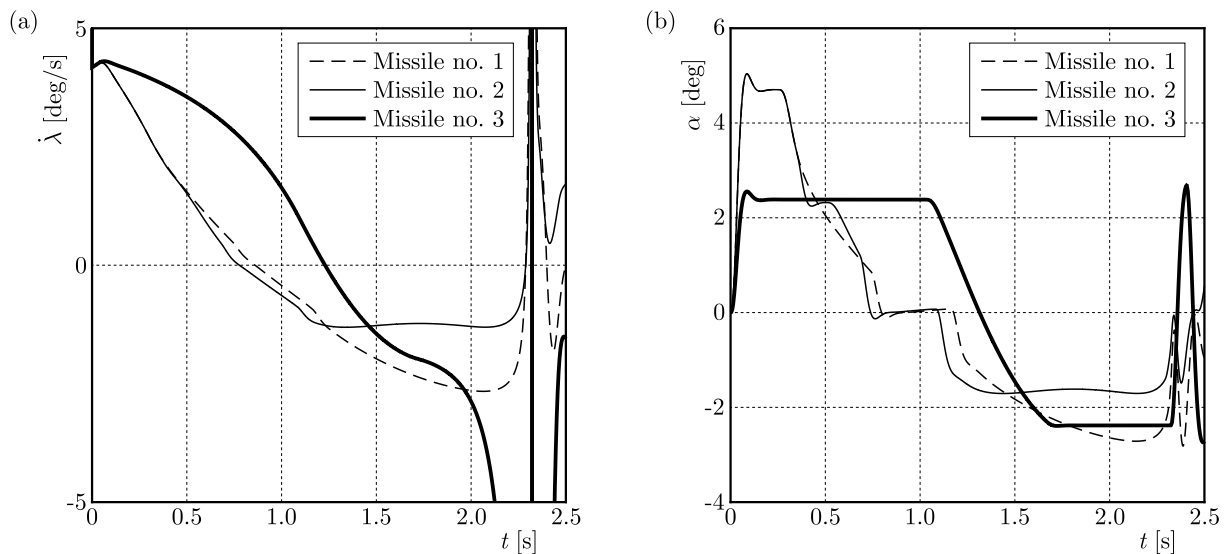


Fig. 10. (a) Angular rates of the line of sight, (b) angles of attack of the missile airframes

the case of missile No. 1, and the canard-control mode in the case of missile No. 2. However, the conditions for transitioning to the divert mode are still satisfied immediately before the strike on the target. This makes it possible to reduce the angular rate of the line of sight (Fig. 10a) leading to a reduction in the miss distance (cf. Table 2). The opposite situation occurs in the case of missile No. 3 in the tail-fin control mode: as the distance to the target decreases, the angular rate of the line of sight continues to increase, reaching a value above 300 deg/s at the moment of strike. The average miss distance of missile No. 3 is larger by an order of magnitude than that of missiles No. 1 and No. 2.

6. Conclusions

The proposed control method provides a wide range of possibilities for reacting to changing conditions of an aerial combat situation.

If the target is such that the missile is not required to perform significant maneuvering, it can be guided in the divert mode with angles of attack close to zero. The use of the divert mode enables the angular rates of the missile airframe to be matched with the angular rates of the missile velocity vector, which is preceded by a short and gentle transitional process. Advantages of this mode of control include its favorable effect on the operating conditions of the sensor elements and a reduction in energy losses resulting from oscillations of the airframe. However, the limited ability to achieve normal accelerations means that guidance using the divert mode exclusively may prove insufficient to complete the task.

When the required values of normal acceleration are such that the divert mode is insufficient, the guidance can be performed using opposing deflections of the fins. This mode of control exhibits all characteristic features of control using traditional configurations (tail fins and canards) with the difference being that it enables higher aerodynamic control moments to be attained, which may be advantageous when the aerial situation requires a maneuver involving significant acceleration. The basic drawback is that the achievement of these accelerations is associated with sudden large reactions of the missile airframe, which disrupts the operating conditions of the seeker, increasing the percentage error in the control signals.

An advantage is found to result from the use of extended acceleration-based conversion with an additional control mode – canard control – as an intermediate mode between the divert and opposite modes. This enables larger accelerations to be achieved than in the case of the divert mode but, at the same time, generates lower values of the angular rates and angles of attack than the opposite mode, with resultant tactical advantages.

References

1. GAPIŃSKI D., KRZYSZTOFIK I., 2014, The process of tracking an air target by the designed scanning and tracking seeker, *Proceedings of 15th International Carpathian Control Conference, ICCO 2014*, Velke Karlovice, Czech Republic, 129-134
2. GRYCEWICZ H., MOSIEWICZ R., PIETRASIEŃSKI J., 1984, *Radio Control Systems* (in Polish), Military University of Technology, Warsaw
3. HUA W.H., MENG Q.L., ZHANG J.P., ZHANG Y.J., 2016, Differential game guidance law for dual and bounded controlled missiles, *Journal of Beijing University of Aeronautics and Astronautics*, **42**, 9, 1851-1856
4. HULL D.G., SPEYER J.L., BURRIS D.B., 1990, Linear-quadratic guidance law for dual control of homing missiles, *Journal of Guidance, Control and Dynamics*, **13**, 1, 137-144
5. IBARRONDO F.B., SANZ-ARÁNGUEZ P., 2016, Integrated versus two-loop guidance-autopilot for a dual control missile with high-order aerodynamic model, *Proceedings of the Institution of Mechanical Engineers, Part G: Journal of Aerospace Engineering*, **230**, 1, 60-76
6. IDAN M., SHIMA T., GOLAN O.M., 2007, Integrated sliding mode autopilot-guidance for dual control missiles, *Journal of Guidance, Control and Dynamics*, **30**, 4, 1081-1089
7. OCHI Y., 2003, Design of a normal acceleration and angle of attack control system for a missile having front and rear control surfaces, *Transactions of the Japan Society for Aeronautical and Space Sciences*, **51**, 598, 621-627
8. OCHI Y., KANAI K., SAKA N., IMADO F., KURODA T., 1991, A design method of normal acceleration control system for a missile with front and rear control surfaces, *Proceedings of Navigation and Control Conference*, New Orleans LA, USA, 196-207

9. SCHROEDER W., 2001, Dual-control scheme for improved missile maneuverability, Patent No. US RE37,331 E
10. SHIMA T., GOLAN O.M., 2006, Bounded differential games guidance law for dual-controlled missiles, *IEEE Transactions on Control Systems Technology*, **14**, 4, 719-724
11. SHIMA T., GOLAN O.M., 2007, Linear quadratic differential games guidance law for dual controlled missiles, *IEEE Transactions on Aerospace and Electronic Systems*, **43**, 3, 834-842
12. SHITESSEL Y.B., TOURNES C.H., 2009, Integrated higher-order sliding mode guidance and auto-pilot for dual-control missiles, *Journal of Guidance, Control and Dynamics*, **32**, 1, 79-94
13. SIOURIS G.M., 2004, *Missile Guidance and Control Systems*, Springer, New York
14. YAN H., JI H., 2012, Integrated guidance and control for dual-control missiles based on small-gain theorem, *Automatica*, **48**, 10, 2686-2692
15. YANUSHEVSKY R., 2007, *Modern Missile Guidance*, 1st Edition, CRC Press, New York
16. ZARCHAN P., 2012, *Tactical and Strategic Missile Guidance*, 6th Edition, AIAA, Reston

Manuscript received July 3, 2017; accepted for print November 14, 2017

COLLOCATION METHOD BASED ON BARYCENTRIC INTERPOLATION ITERATION FOR ANALYSIS OF NONLINEAR MICROBEAMS

MEILING ZHUANG, CHANGQING MIAO

*Key Laboratory of Concrete and Prestressed Concrete Structures of Ministry of Education, Southeast University,
Nanjing, China and*

School of Civil Engineering, Southeast University, Nanjing, China

e-mail: 18036558037@163.com; chqmiao@163.com (corresponding author)

ZHAOQING WANG

Institute of Mechanics, Shandong Jianzhu University, Jinan, China

A powerful computational methodology, named the barycentric Lagrange interpolation iteration collocation method (BLIICM), for solving nonlinear bending problems of a doubly clamped microbeam under electrostatic loads is presented. The nonlinear governing equation of the microbeam is converted into a linear differential equation by assuming the initial function. The barycentric Lagrange interpolation collocation method (BLICM) is used to solve the linear differential equation. The direct linearization formulations and Newton linearization calculation formulations for the nonlinear differential equation have been given. The calculation method and formulation of the nonlinear integral term have been discussed in details. By applying a barycentric Lagrange interpolation differential matrix, a matrix-vector calculation formula of BLIICM has been established. Numerical results of calculation examples show that the advantages of the proposed methodology are efficient, simple and of high precision.

Keywords: nonlinear microbeams, barycentric Lagrange interpolation, collocation method, linearization method, iteration method

1. Introduction

Microbeams are used in microsensors and microactuators fabricated by MEMS technology (Brusa *et al.*, 2004). The main mechanism of microsensor and microactuator can be simplified as a microbeam in micro electro-mechanical systems (MEMS). The geometric dimension of microbeams is normally in micron scale and microbeams mainly bear electric loads and axial forces. The relation between the force of electric potential acting on the microbeam and the deflection of the microbeam is nonlinear. For accurate analysis of microbeam mechanical properties, the elongation effect of the microbeam shall be considered. Considering external forces and geometric nonlinear factors of the microbeam, the governing equation of the microbeam bending established is a nonlinear differential equation. The analytical method used to solve the microbeam nonlinear differential equation is often extremely complicated and sometimes even impossible. With the progress of computer technology, the numerical method has become important for analysis of nonlinear bending of microbeams (Rezazadeh *et al.*, 2009; Zand *et al.*, 2009; Batra *et al.*, 2008).

A high accuracy numerical method is needed to analyze microbeams, because the maximum deflection of the microbeams deformation is in micron to nanometer scales. Nayfeh, Mook, and Lobitz used a numerical-perturbation method to analyze forced vibration of a non-uniform beam (Nayfeh *et al.*, 1974). Refwield (2015) analyzed vibration of nonlinear flat arch. Choi and Lovell

(1997) converted the microbeam boundary value problem into the initial value problem and then used the shoot method to solve it (Choi, 1992). The differential quadrature method is a high precision collocation method widely used to solve Euler-Bernoulli microbeam bending and vibration problems (Shu and Du, 1997; Tomasiello, 1998; Karami and Malekzadeh, 2002). The differential quadrature method is a collocation method that approximates the unknown function based on Lagrange interpolation (Kuang and Chen, 2004; Najjar *et al.*, 2004; Sadeghian *et al.*, 2007). Due to numerical instability of Lagrange interpolation, its calculation result tends to be unstable with an increase of quantity of calculation nodes.

We can obtain a barycentric Lagrange interpolation by transforming the Lagrange interpolation into barycentric form. Rewriting the Lagrange interpolation formula to barycentric form can apparently improve numerical stability of the interpolation (Berrut and Trefethen, 2004). Wang *et al.* (2007) used the barycentric interpolation to approximate the unknown function, establishing differential matrices of the unknown function and each order of its derivative on calculation nodes, proposing a high accuracy grid-free barycentric interpolation collocation method to solve differential equation initial (boundary) value problems, and providing an algorithm program and a large amount of engineering calculation examples (Berrut *et al.*, 2005; Floater and Hormann, 2007; Li and Wang, 2012; Wang *et al.*, 2014a,b). Numerical calculation examples show that the barycentric interpolation collocation method has advantages of convenient use, high efficiency and high accuracy. It is a high accuracy meshless numerical calculation method applicable to numerical calculations for various differential equations.

Based on the barycentric interpolation collocation method and in combination with the linearization method for nonlinear differential equations, this article has established a barycentric Lagrange interpolation iteration collocation method (BLIICM) for solving nonlinear bending problems of doubly clamped microbeams under electrostatic loads, and presents numerical calculation examples to verify effectiveness and computational accuracy of this proposed method.

2. Barycentric Lagrange interpolation and its differentiation matrices

Given a function $v(x)$ defined on the interval $0 = x_1 < x_2 < \dots < x_n = l$ and function values on the nodes $v_j = v(x_j)$, $j = 1, 2, \dots, n$, the barycentric Lagrange interpolation of the function $v(x)$ is

$$v(x) = \frac{\sum_{j=1}^n \frac{w_j}{x - x_j} v_j}{\sum_{j=1}^n \frac{w_j}{x - x_j}} \quad (2.1)$$

where $w_j = 1/\prod_{j \neq k} (x_j - x_k)$, $j = 0, 1, \dots, n$ is the barycentric Lagrange interpolation weight. The barycentric Lagrange interpolation of the function $v(x)$ can be simplified as

$$v(x) = \sum_{j=1}^n L_j(x) v_j \quad L_j(x) = \frac{w_j}{x - x_j} \bigg/ \sum_{j=1}^n \frac{w_j}{x - x_j} \quad (2.2)$$

And then, the m -th order derivative of the function $v(x)$ can be written as

$$v^{(m)}(x) = \frac{d^m v(x)}{dx^m} = \sum_{j=1}^n L_j^{(m)}(x) v_j \quad (2.3)$$

So the m -th order derivative of the function $v(x)$ on the nodes $x_1 < x_2 < \dots < x_n$ can be written as

$$v^{(m)}(x_i) = v_i^{(m)} = \frac{d^m v(x_i)}{dt^m} = \sum_{j=1}^n D_{ij}^{(m)} v_j \quad (2.4)$$

Equation (2.4) can be written in the following matrix form (Wang *et al.*, 2007)

$$\mathbf{v}^{(m)} = \mathbf{D}^{(m)} \mathbf{v} \quad (2.5)$$

where $\mathbf{v}^{(m)} = [v_1^{(m)}, v_2^{(m)}, \dots, v_n^{(m)}]^T$ and $\mathbf{v} = [v_1, v_2, \dots, v_n]^T$ represent the column vector of the m -th order derivative and the value of the function $v(x)$ on the nodes, respectively. Matrix $\mathbf{D}^{(m)}$ indicates the unknown function m -th order barycentric Lagrange interpolation differential matrix on the nodes x_1, x_2, \dots, x_n , which is composed of the elements $D_{ij}^{(m)} = L_j^{(m)}(x_i)$.

3. Calculation models of an MEMS microbeam

As shown in Fig. 1, while a microbeam is loaded electrostatically, the transverse force per unit area is displacement dependent. So the function per unit force of the axial coordinate x is expressed as

$$p = p(v(x)) = \frac{\varepsilon_0 V^2}{2[g - v(x)]^2} \quad (3.1)$$

where V is the applied voltage, g is the gap between the beams and the cover electrode (Fig. 1), and $\varepsilon_0 = 8.854 \cdot 10^{-12}$ F/m is the permittivity of vacuum.

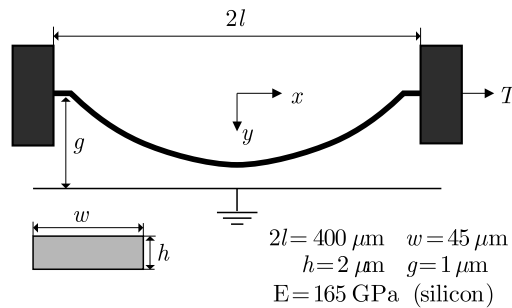


Fig. 1. Diagram of a doubly clamped microbeam

Stretching the induced tension T and tension from the intrinsic strain T_i can be included with the nonlinear loading for the most accurate representation (Nayfeh *et al.*, 1974)

$$EI \frac{d^4 v}{dx^4} - (T + T_i) \frac{d^2 v}{dx^2} = \frac{\varepsilon_0 V^2 w}{2[g - v(x)]^2} \quad (3.2)$$

where T_i is taken as 0.01% of the residual strain of the microbeam and w is the width of the microbeam. According to the relation between the stretching tension and bending deflection of the microbeam, Eq. (3.2) can be written as

$$EI \frac{d^4 v(x)}{dx^4} - \left[\frac{Ewh}{2l} \int_0^l \left(\frac{dv(x)}{dx} \right)^2 dx + T_i \right] \frac{d^2 v(x)}{dx^2} = \frac{\varepsilon_0 V^2 w}{2[g - v(x)]^2} \quad (3.3)$$

Equation (3.3) is solved by the numerical method proposed in this article with the boundary condition

$$v'(0) = v'(2l) = v(0) = v(2l) = 0 \quad (3.4)$$

4. Linearization iteration collocation method for the nonlinear differential equation

Using Eq. (2.2) to approximate the unknown function, nonlinear Eq. (3.4) is usually discreted to nonlinear algebraic equations and then the Newton-Raphson iteration is used to solve these nonlinear algebraic equations to obtain a numerical solution. The discrete form of the barycentric interpolation collocation method for Eq. (3.3) can be written as

$$EI \sum_{j=1}^n L_j''''(x_i) v_j - \left[\frac{Ewh}{2l} \int_0^l \left(\sum_{j=1}^n L_j'(x) v_j \right)^2 dx + T_i \right] \sum_{j=1}^n L_j''(x_i) v_j = \frac{\varepsilon_0 V^2 w}{2 \left(g - \sum_{j=1}^n L_j(x) v_j \right)^2} \quad (4.1)$$

It is very fussy to construct a Newton-Raphson iteration form of nonlinear Eq. (4.1). The linearization iteration collocation method is adopted to solve nonlinear Eq. (4.1). Under a mechanical load, for a given assumed initial function $v_0 = v_0(x)$, under electric load and for the given assumed initial function of $v_0 = v_0(x)$, Eq.(4.1) can be directly linearized to

$$EI \frac{d^4 v(x)}{dx^4} - \left[\frac{Ewh}{2l} \int_0^l \left(\frac{dv_0(x)}{dx} \right)^2 dx + T_i \right] \frac{d^2 v(x)}{dx^2} = \frac{\varepsilon_0 V^2 w}{2[g - v_0(x)]^2} \quad (4.2)$$

Accordingly, the linearized iteration form can be directly constructed as follows

$$EI \frac{d^4 v_k(x)}{dx^4} - \left[\frac{Ewh}{2l} \int_0^l \left(\frac{dv_{k-1}(x)}{dx} \right)^2 dx + T_i \right] \frac{d^2 v_k(x)}{dx^2} = \frac{\varepsilon_0 V^2 w}{2[g - v_{k-1}(x)]^2} \quad k = 1, 2, 3, \dots \quad (4.3)$$

Equation (4.3) is a linear differential equation. Using form (2.5) of the barycentric Lagrange interpolation and characteristic of interpolation basis functions, Eq. (4.3) can be written in form of a matrix

$$\left[EID^{(4)} - (T_{k-1} + T_i) \mathbf{D}^{(2)} \right] \mathbf{v}_k = \mathbf{p}_{k-1} \quad k = 1, 2, 3, \dots \quad (4.4)$$

where

$$\mathbf{p}_{k-1} = \frac{\varepsilon_0 V^2 w}{2[g - \mathbf{v}_{k-1}]^2}$$

is the external force vector of the $(k - 1)$ -th iteration.

The Newton iteration method is another more available way. In the Newton iteration method, the approximating function is the line tangent to the nonlinear electric load

$$p = p(v(x)) = \frac{\varepsilon_0 V^2}{2[g - v(x)]^2}$$

at the initial point \mathbf{v}_0 (advised $\mathbf{v}_0 = 0$), where v_0 is the assumed initial point. Equation (4.2) in a Taylor series about \mathbf{v}_0 and discarding nonlinear terms yields

$$p(v) \approx p(v_0) + p'(v_0)(v - v_0) \quad (4.5)$$

Substituting Eq. (4.5) into Eq. (4.2), we can obtain

$$EI \sum_{j=1}^n L_j'''(x_i) v_j - \left[\frac{Ewh}{2l} \int_0^l \left(\sum_{j=1}^n L_j'(x) v_{j(0)} \right)^2 dx + T_i \right] \sum_{j=1}^n L_j''(x_i) v_j = p(v_0) + p'(v_0)(v - v_0) \quad (4.6)$$

Accordingly, the following iteration differential equation of the Newton linearization method can be obtained

$$EI \sum_{j=1}^n L_j'''(x_i) v_{j(k)} - \left[\frac{Ewh}{2l} \int_0^l \left(\sum_{j=1}^n L_j'(x) v_{j(k-1)} \right)^2 dx + T_i \right] \sum_{j=1}^n L_j''(x_i) v_{j(k)} = p(v_{(k-1)}) + p'(v_{(k-1)})(v_{(k)} - v_{(k-1)}) \quad (4.7)$$

Now, the iteration differential matrix form of Eq.(4.7) can be obtained as follows

$$\left[EID^{(4)} - (T_{k-1} + T_i)D^{(2)} \right] \mathbf{v}_k = \mathbf{p}_{k-1} + \mathbf{p}'_{k-1}(\mathbf{v}_k - \mathbf{v}_{k-1}) \quad k = 1, 2, 3, \dots \quad (4.8)$$

The nonlinear integral term in the microbeam governing Eq. (3.3) is related to stretching tension of the microbeam and its computational accuracy directly affects the error of the final computation result. We use Gauss integration for numerical integration. Barycentric interpolation of the unknown function is substituted in the integral term, and the square expansion of the integral term yields

$$\begin{aligned} T &= \frac{Ewh}{2l} \int_0^l \left(\frac{dv(x)}{dx} \right)^2 dx = \frac{Ewh}{2l} \int_0^l \left(\sum_{j=1}^n L_j'(x) v_j \right)^2 dx \\ &= \frac{Ewh}{2l} \sum_{i=1}^n \sum_{j=1}^n \left(\int_0^l L_i'(x) L_j'(x) dx \right) v_i v_j \end{aligned} \quad (4.9)$$

Introducing notation $A_{ij} = \int_a^b [L_i'(x) L_j'(x)] dx$, we can obtain

$$\int_a^b \left(\frac{dv}{dx} \right)^2 dx = \sum_{i=1}^N \sum_{j=1}^N A_{ij} v_i v_j = \mathbf{v}^T \mathbf{A} \mathbf{v} \quad (4.10)$$

where \mathbf{A} is an $n \times n$ matrix comprising elements A_{ij} and referred to as the barycentric interpolation integral matrix. A_{ij} is a definite integral of arycentric interpolation primary function derivative interactive product, which is constant only if related to the interpolation node and irrelevant of the type of problem to be solved. According to formula (4.10), we can obtain stretching tension of the microbeam after $(k - 1)$ -th iteration

$$T_{k-1} = \frac{Ewh}{2l} \int_0^l \left(\frac{dv_{k-1}(x)}{dx} \right)^2 dx = \frac{Ewh}{2l} \mathbf{v}_{k-1}^T \mathbf{A} \mathbf{v}_{k-1} \quad (4.11)$$

The substitution method (Wang *et al.*, 2007) is used to apply boundary conditions of the MEMS microbeam. Starting from the assumed initial value \mathbf{v}_0 ($\mathbf{v}_0 = \mathbf{0}$) the iteration method is used to solve direct linearization Eq. (4.4) or Newton linearization Eq. (4.8), to obtain a corrected solution \mathbf{v}_1 of the unknown function $v(x)$ on nodes. Then, Eq. (4.11) can be used to obtain the corrected solution T_1 . For a given control accuracy $\varepsilon = 10^{-10}$, if $\|\mathbf{v}_k - \mathbf{v}_{k-1}\|_\infty < \varepsilon$, the corrected solution \mathbf{v}_k is the numerical solution of the MEMS microbeam; otherwise the iteration is kept until the computational control accuracy ε is met and then the numerical solution is obtained.

5. Numerical results

The calculation program is compiled by MATLAB. By making use of the barycentric Lagrange interpolation differential matrix, the matrix-vector calculation formula of BLIICM has been established. Relying on the powerful matrix operation capability of MATLAB, the calculation program can be easily and quickly compiled. Microbeam geometric and physical parameters are shown in Fig. 1. For calculation, the computational domain is $[0, 400]$ and the type of discrete nodes is the Chebyshev node $x_i = 200 + 200 \cos(i\pi/n)$, $i = 0, 1, 2, \dots, n$. In the collocation method, 21 nodes are selected. The control precision of iteration methods is 10^{-10} and the Gauss integral with 6 points is applied.

In this Section, there is no analytical solution to Eq. (3.2). So, we quote the maximum residual error (err) to illustrate the solution accuracy of BLIICM. Here, the maximum residual error is

$$\text{err} = \max_{k=1,2,\dots,n} |EIv^{(4)}(x_k) - (T + T_i)v^{(2)}(x_k) - p(v(x_k))|$$

Based on the numerical results of Fig. 2, Table 1 and Table 2 comprehensively, the following observations can be concluded:

- in terms of the convergence rate, the Newton linearization iteration is apparently faster than the direct linearization iteration,
- in terms of differential equation residual, the Newton linearization iteration method has a higher computational accuracy than the direct linearization iteration method,
- computation results of BLIICM are highly consistent with the results of reference.

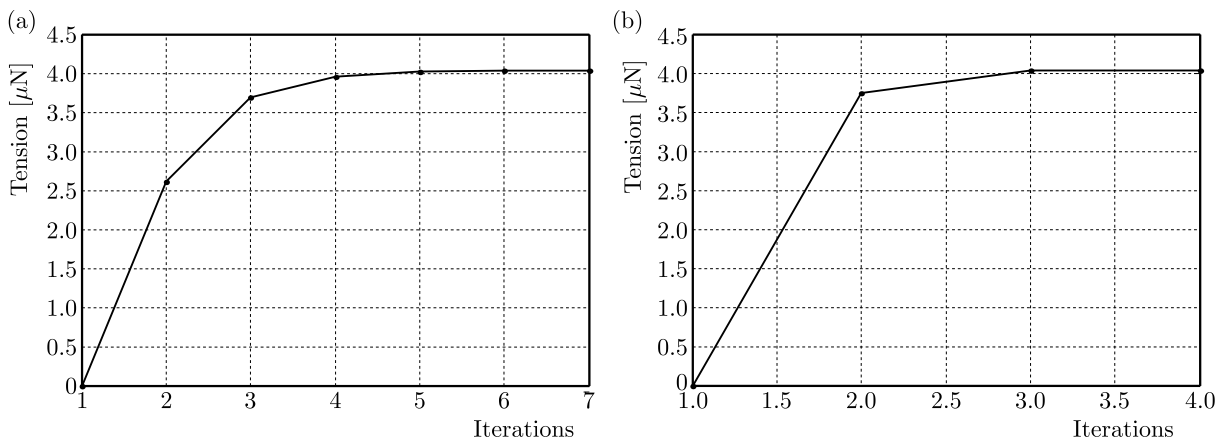


Fig. 2. The iterative process of the direct (a) and Newton (b) linearization method at $V_2 = 40$

Figure 3 shows comparative results of the maximum deflection of the microbeam for three tensional cases with various voltages. It can be seen that the existence of induced tension strengthens the deformation resistance of the microbeam. It is also known that deflection of the microbeam is the smallest while considering the induced tension and the residual tensile strain of 0.01%, and that the deflection of the microbeam is the largest when the axial effects are absent.

Figure 4 shows the relations of the induced tensile force and residual strain of the microbeam with various voltages. It can be seen that the residual strain has a huge effect on the induced tensile force, and this effect is more remarkable with an increase of the electric load. The mechanical properties of the microbeam caused by the residual strain are known that an extremely high dimensional precision applies to the process and installation of the microbeam, and it needs to have a great improvement to the process level in fact.

Table 1. MEMS microbeam calculation results without considering 0.01% residual strain

Voltage [V ²]	Direct iteration method				Newton iteration method			
	Midspan deflection [μm]	Axial force [μN]	Iterations	Residual error	Midspan deflection [μm]	Axial force [μN]	Iterations	Residual error
20	0.0589	0.7843	4	$4.0536 \cdot 10^{-7}$	0.0589	0.7845	3	$2.5976 \cdot 10^{-15}$
30	0.0935	1.9791	5	$6.4801 \cdot 10^{-7}$	0.0936	1.9812	3	$1.2745 \cdot 10^{-14}$
40	0.1335	4.0329	7	$1.3098 \cdot 10^{-6}$	0.1335	4.0359	4	$5.0783 \cdot 10^{-12}$
50	0.1818	7.4771	8	$1.3105 \cdot 10^{-6}$	0.1819	7.4891	4	$1.3164 \cdot 10^{-14}$
60	0.2463	13.7156	10	$5.3423 \cdot 10^{-6}$	0.2463	13.7265	4	$5.2615 \cdot 10^{-12}$

Table 2. BLIICM and Shooting Method numerical results of the MEMS microbeam without considering 0.01% residual strain

Voltage [V ²]	Direct iteration method		Newton iteration method		Shooting method, Zand <i>et al.</i> (2009)	
	Midspan deflection [μm]	Axial force [μN]	Midspan deflection [μm]	Axial force [μN]	Midspan deflection [μm]	Axial force [μN]
1.0	$0.2694 \cdot 10^{-2}$	$0.1629 \cdot 10^{-2}$	$0.2694 \cdot 10^{-2}$	$0.1643 \cdot 10^{-2}$	$0.2694 \cdot 10^{-2}$	$0.1642 \cdot 10^{-2}$
2.0	$0.1091 \cdot 10^{-1}$	$0.2686 \cdot 10^{-1}$	$0.1091 \cdot 10^{-1}$	$0.2678 \cdot 10^{-1}$	$0.1089 \cdot 10^{-1}$	$0.2677 \cdot 10^{-1}$
3.0	$0.2512 \cdot 10^{-1}$	$0.1425 \cdot 10^0$	$0.2512 \cdot 10^{-1}$	$0.1427 \cdot 10^0$	$0.2512 \cdot 10^{-1}$	$0.1427 \cdot 10^0$
4.0	$0.4617 \cdot 10^{-1}$	$0.4821 \cdot 10^0$	$0.4617 \cdot 10^{-1}$	$0.4822 \cdot 10^0$	$0.4617 \cdot 10^{-1}$	$0.4822 \cdot 10^0$
5.0	$0.7570 \cdot 10^{-1}$	$0.1296 \cdot 10^1$	$0.7570 \cdot 10^{-1}$	$0.1297 \cdot 10^1$	$0.7570 \cdot 10^{-1}$	$0.1297 \cdot 10^1$
6.0	$0.1168 \cdot 10^{-1}$	$0.3083 \cdot 10^1$	$0.1168 \cdot 10^{-1}$	$0.3085 \cdot 10^1$	$0.1168 \cdot 10^{-1}$	$0.3085 \cdot 10^1$
7.0	$0.1765 \cdot 10^0$	$0.7039 \cdot 10^1$	$0.1765 \cdot 10^0$	$0.7046 \cdot 10^1$	$0.1765 \cdot 10^0$	$0.7045 \cdot 10^1$
8.0	$0.2821 \cdot 10^0$	$0.1798 \cdot 10^2$	$0.2822 \cdot 10^0$	$0.1800 \cdot 10^2$	$0.2822 \cdot 10^0$	$0.1800 \cdot 10^2$

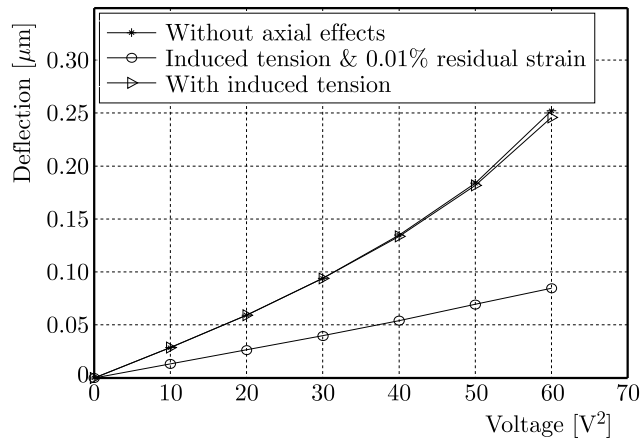


Fig. 3. Maximum deflections for electrical loading and three tensional cases with various voltages

6. Conclusions

Doubly clamped microbeams under electrostatic loads have been analysed by using the collocation method based on the barycentric Lagrange interpolation iteration. Compared with other numerical methods of solving the differential equation, the collocation method in this article has merits of simple calculation formulations, convenient program and a high computation preci-

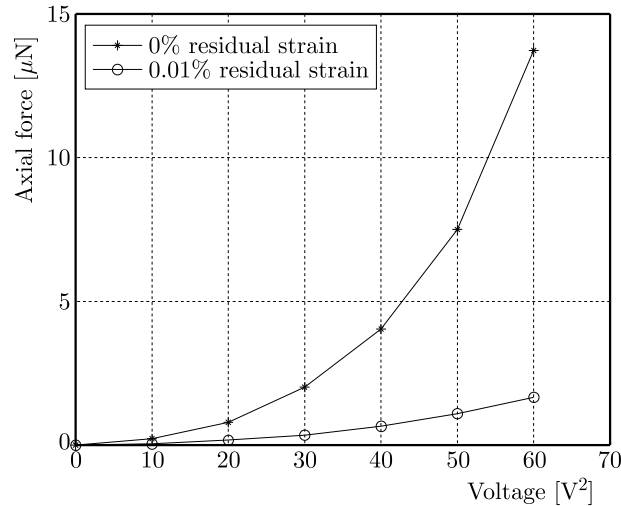


Fig. 4. Induced axial force for electrical loading with and without the residual strain with various voltages

sion. The BLIICM adopting matrix-vector calculation formula has obvious advantages in solving nonlinear problems as it can analyze such problems quickly and accurately.

For the existing stretching effects, the induced tension has a considerable influence in reducing displacements and stresses because the stiffness increases with the increasing transverse load. In a especial case of electrical loading, the residual strain has a strong influence on the induced tensile force. Therefore, analysis of the microbeam geometric nonlinear factor and the inertial nonlinear factor of MEMS microbeam mechanical properties is very important. In particular, the microbeam geometric nonlinear factor and the inertial nonlinear factor are decisive for design and use in MEMS, and sufficient attention should be given to them before implementation.

Acknowledgements

This research has been supported by the National Natural Science Foundation of China under grant No. 51778135 and Aeronautical Science Foundation of China under grant No. 20130969010. This research also has been supported by the Fundamental Research Funds for the Central Universities and Postgraduate Research and Practice Innovation Program of Jiangsu Province under grant No. KYCX18_0113.

References

1. BATRA R.C., PORFIR M., SPINELLO D., 2008, Vibrations of narrow microbeams predeformed by an electric field, *Journal of Sound and Vibration*, **309**, 3-5, 600-612
2. BERRUT J.P., BALTENSPERGER R., MITTELMANN H.D., 2005, Recent developments in barycentric rational interpolation, [In:] *Trends and Applications in Constructive Approximation*, D.H. Mache, J. Szabados, M.G. de Bruin (Edit), 27-51
3. BERRUT J.P., TREFETHEN L.N., 2004, Barycentric Lagrange interpolation, *SIAM Review*, **46**, 3, 501-517
4. BRUSA E., BONA F.D., GUGLIOTTA A., 2004, Modeling and prediction of the dynamic behaviour of microbeams under electrostatic load, *Analog Integrated Circuits and Signal Processing*, **40**, 2, 155-164
5. CHOI B., 1992, *Diaphragm Stretching and Contact Problems for Microelectromechanical Pressure Transducers*, Madison: University of Wisconsin
6. CHOI B., LOVELL E.G., 1997, Improved analysis of microbeams under mechanical and electrostatic loads, *Journal of Micromechanics and Microengineering*, **7**, 1, 24-29

7. FLOATER M.S., HORMANN K., 2007, Barycentric rational interpolation with no poles and high rates of approximation, *Numerische Mathematik*, **107**, 2, 315-331
8. KARAMI G., MALEKZADEH P., 2002, A new differential quadrature methodology for beam analysis and the associated differential quadrature element method, *Computer Methods in Applied Mechanics and Engineering*, **191**, 32, 3509-3526
9. KUANG J.H., CHEN C.J., 2004, Dynamic characteristics of shaped micro-actuators solved using the differential quadrature method, *Journal of Micromechanics and Microengineering*, **14**, 4, 647-655
10. LI S.C., WANG Z.Q., 2012, *Algorithm, Program and Engineering Application on High Precision and Meshless Barycentric Interpolation Collocation Method*, Beijing: Science Press
11. NAJAR F., CHOURA S., ELBORGI S., ABDELRAHMAN E.M., NAYFEH A.H., 2004, Modeling and design of variable-geometry electrostatic microactuators, *Journal of Micromechanics and Microengineering*, **15**, 3, 419-429
12. NAYFEH A.H., MOOK D.T., LOBITZ D.W., 1974, Numerical-perturbation method for the nonlinear analysis of structural vibrations, *AIAA Journal*, **12**, 9, 1222-1228
13. REFWIELD L.W., 2015, Nonlinear flexural oscillations of shallow arches, *AIAA Journal*, **12**, 1, 91-93
14. REZAZADEH G., TAHMASEBI A., ZIAEI-RAD S., 2009, Nonlinear electrostatic behavior for two elastic parallel fixed-fixed and cantilever microbeams, *Mechatronics*, **19**, 6, 840-846
15. SADEGHIAN H., REZAZADEH G., OSTERBERG P.M., 2007, Application of the generalized differential quadrature method to the study of pull-in phenomena of MEMS switches, *Journal of Microelectromechanical Systems*, **16**, 6, 1334-1340
16. SHU C., DU H., 1997, Implementation of clamped and simply supported boundary conditions in the GDQ free vibration analysis of beams and plates, *International Journal of Solids and Structures*, **34**, 7, 819-835
17. TOMASIELLO S., 1998, Differential quadrature method application to initial-boundary-value problems, *Journal of Sound and Vibration*, **218**, 4, 573-585
18. WANG Z.Q., JIANG J., TANG B.T., ZHENG W., 2014, Numerical solution of bending problem for elliptical plate using differentiation matrix method based on barycentric Lagrange interpolation, *Applied Mechanics and Materials*, **638-640**, 1720-1724
19. WANG Z.Q., LI S.P., TANG B.T., 2007., Formulations, algorithms and applications on barycentric interpolation in 1D, *Journal of Shandong Jianzhu University*, **22**, 4, 448-453
20. WANG Z.Q., LI S.C., PING Y., JIANG J., MA T.F., 2014, A highly accurate regular domain collocation method for solving potential problems in the irregular doubly connected domains, *Mathematical Problems in Engineering*, **2014**, 4, 1-9
21. ZAND M.M., AHMADIAN M.T., RASHIDIAN B., 2009, Semi-analytic solutions to nonlinear vibrations of microbeams under suddenly applied voltages, *Journal of Sound and Vibration*, **325**, 1, 382-396

EXPERIMENTAL AND NUMERICAL STUDY OF THE HEAT TRANSFER AND PRESSURE DROP IN TRIANGULAR CHEVRON CHANNELS

HOSSEIN DOLATABADI, ABOLFAZL HAJIZADEH AGHDAM

Department of Mechanical Engineering, Arak University of Technology, Arak, Iran

e-mail: abolfazl_hajizade@yahoo.com

Chevron channels are one of the popular techniques that are extensively used in manufacturing of compacted heat exchangers. The present paper deals with the experimental and numerical analysis on the fluid flow and heat transfer in a triangular chevron channel. The studies are carried out for a uniform wall heat flux equal to 1350 W/m^2 using air as the working fluid. The Reynolds number varies from 1000 to 10000, phase shifts $0^\circ \leq \phi \leq 180^\circ$, and channel heights are $5 \leq D \leq 35 \text{ mm}$. The study shows a significant effect of the optimum structure of the triangular chevron on the heat transfer rate and friction loss over the channel wall. The Nusselt number increases and the Thermal Enhancement Factor (TEF) decreases with the increasing Reynolds number. The best performance is noticed on the phase shift, $\phi = 90^\circ$. For triangular chevron surfaces, the maximum heat transfer is obtained 33.33% up to 37.5% more than for a smooth wall channel.

Keywords: heat transfer, pressure drop, thermal enhancement factor, phase shift

1. Introduction

Chevron channels are basic channel geometry in plate heat exchangers because of their efficient heat exchange capabilities. Today, to increase the heat flux rate in nuclear reactors, turbine blades and electronic equipment, some companies are using chevron surfaces. Chevron surfaces create turbulent sublayer of laminar flows, as a result the heat transfer becomes increased. When the friction factor increases, the fan power will increase for a stable velocity of the fluid flow. To generate more power and enhance system performance of designed turbines, the inlet temperature of the fluid must be increased. In some cases high temperature of the fluid increases the temperature of turbine blades to the melting point. In such situations making use of alloy or super alloys might be a technical solution, but it is justified economically. To reduce temperature of hot surfaces, one has to use surfaces with spatial geometry including ribs or chevron surfaces. The experience proves that chevron surfaces lead to a suitable pressure drop. In solar systems, the fluid flow is laminar so the heat transfer is low, and the chevron surfaces create turbulent sublayers increasing the heat transfer. One can increase the heat transfer in fluids by: 1 – separation of fluids, 2 – making laminar sublayers turbulent, 3 – replacing flows in the hot surface. The first major problem in designing heat exchanger is to save more energy and increase the heat transfer rate as well as reduce friction. Thus, chevron surfaces play an important role here.

The flow and heat transfer in chevron channels have been extensively investigated in the recent years, see for example Yang and Chen (2010), Vanaki *et al.* (2014), Sakr (2015).

Khoshvaght-Aliabadi *et al.* (2016) found a significant improvement in the heat transfer coefficient by using pure water instead of a water-ethylene glycol mixture. However, the Nusselt number increased considerably with a grow in the weight percentage of ethylene glycol in the working fluid. The convective thermal resistance was noticeably reduced by using the SWMCHSs. As an example, a reduction of 113.8% was obtained for the water flow at the mass flow rate of

0.024 kg/s in the SWMCHS with $l = 20$ mm and $a = 1.0$ mm, compared to the straight MCHS at the same conditions.

Yongsiri *et al.* (2014) found that the ribs which induced recirculation gave a higher Nusselt number and friction factor than those which did not. Among the ribs examined, the ones with $\theta = 60$ yielded a comparable heat transfer rate 1.74 times of those in the smooth channel, and $\theta = 120$ yielded a thermal performance factor 1.21 which was higher than those given by others.

Al-Shamani *et al.* (2015) showed interesting results of changing rib groove shapes in thermal and fluid fields. The results proved that trapezoidal grooves with increasing height in the flow direction (Trap+R-TrapG) gave the highest Nusselt number in comparison with other types of trapezoidal channels. 1) By changing types of nano particles (Al_2O_3 , CuO, SiO_2 , and ZnO) the results revealed that SiO_2 led to the highest Nusselt number, then followed by Al_2O_3 , ZnO, and CuO, respectively, while pure water gave the lowest value of Nusselt number. 2) The Nusselt number increased with the increasing volume fraction of nanoparticles. 3) The Nusselt number increased gradually with a decrease in diameter of the nano particles. 4) The Nusselt number increased gradually with growth in the Reynolds number in the range of 10 000-40 000.

Eiamsa-ard and Changcharoen (2011) found that by reducing the degree of sudden changes of the main flow, the flow separation suppresses and thus the corner separation of bubbles in front and rear surfaces of the rib decreases. The streamlines proved that among the ribs with concave surfaces unrecognized corner separation of bubbles appeared, whereas those with modified convex surfaces generated corner separation of bubbles with size comparable to that of the unmodified square rib. All ribs with concave surfaces induced a larger recirculation zone than the others, resulting in high turbulence intensity. With good conformation of the streamlines, the rib with concave-concave surfaces gave the highest Nusselt number and the friction factor while those with convex-concave surfaces provided the lowest friction factor with moderate Nusselt numbers.

Due to the prominent effect of a low friction factor, the rib with the convex-concave surface offers the highest TEF with the maximum value of 1.19.

Xie *et al.* (2014) studied the flow structure and heat transfer in a square passage with offset mid-truncated ribs.

The heated surface of 135° V-shaped mid-truncated ribs provided the highest heat transfer enhancement, while the heated surface of 90° mid-truncated ribs with no staggered arrangement behaved best in reducing the pressure loss penalty.

Moon *et al.* (2014) proved that the new boot-shaped rib gave the best heat transfer performance with an average friction loss performance, and the reverse pentagonal rib gave the best friction loss performance.

Dellil *et al.* (2004) conducted a geometrical parametric study by changing the amplitude-to-wavelength ratio. Comparison of predicted results for a wavy wall with those for a straight channel indicated that the averaged Nusselt number increased until a critical value was reached where the amplitude wave was increased. However, that heat transfer enhancement was accompanied by an increase in the pressure drop.

Characteristics of the fluid flow and heat transfer in a periodic fully developed region of a corrugated duct were numerically obtained using the finite element software by Islamoglu and Parmaksizoglu (2004). Both the heat transfer coefficient and the pressure drop for the corrugated ducts were in good agreement. In addition, the finite element technique can be used to simulate heat exchanger channels.

However, the present study is concerned with a special triangular chevron channel with the focus on variation in the phase shift ϕ and distance of plates D . The experimental and numerical methods have been used to find the best ϕ and D with considering the maximum Nu and TEF as well as the minimum friction factor.

2. Experimental setup

The experimental set up is shown in Fig. 1. The plate geometry is 125×80 mm. A forced-convection air flow was used in the experiments and an equal power input for heated length was established in the bottom walls. To measure the temperature distribution of each chevron wall, nine thermocouples (KTJ model TA-288) were used with 4 mm diameter holes drilled into the side wall (number 8 in Fig. 1). These holes were located at axial distances of (T1), (T2), (T3), (T4), (T5), (T6), (T7), (T8), (T9). The accuracy of the thermocouples was $\pm 1^\circ\text{C}$. A U-manometer was located at the chevron surface to measure pressure drop within the triangular chevron channel (number 4 in Fig. 1). The accuracy of pressure transducer was ± 1 mm $\text{C}_2\text{H}_6\text{O}$. The test section was also isolated to avoid thermal losses. The experimental procedure involved adjusting the flow rate to the desired value (number 1 in Fig. 1). After the fan was turned on and the desired Reynolds number was obtained, the power input of plate heaters (number 6 in Fig. 1) gradually increased and maintained at 1350 W/m^2 to provide sufficient measurement while the fluid property varied. The heat supplied into the chevron walls was adjusted to achieve the desired level by using electric heaters, which were 1.314 mm thick, 80 mm wide and 150 mm long. They were located at the back of the bottom triangular chevron plate. The voltage and current of the electric input to the plate type heaters were controlled by a DC power supply (P.A. Hilton model Ltd H111/07332) unit (number 5 in Fig.). Temperatures were recorded at intervals of 15 min until a steady state was reached. Steady state conditions were assumed to prevail when temperature measurements (number 8 in Fig. 1) on the plates were within $\pm 1^\circ\text{C}$.

These instruments were placed and fitted in a container made of the plexiglas insulator. Figure 1 shows the assembled configuration of the test module with the fluid entrance and exit from the channel. The chevron surfaces are fabricated from blocks of aluminum 1060 alloy whose physical properties are shown in Table 1.

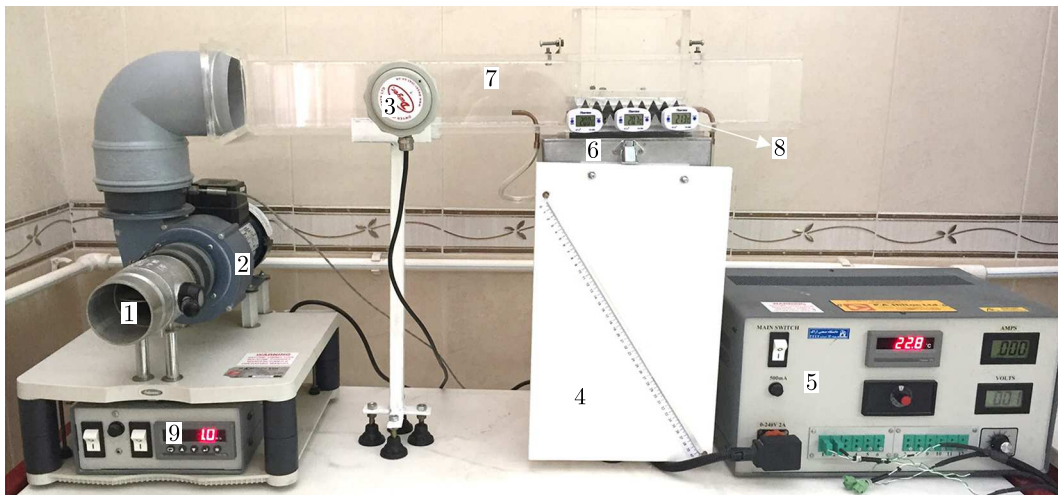


Fig. 1. Assembled configuration of the test module with triangular chevron surfaces

A centrifugal fan which was made of stainless steel and had the inner diameter of 90 mm (number 2 in Fig. 1) sucked the room air at the room temperature and exhausted into the atmosphere through the test section (that made of plexiglass with 8 mm thickness (number 7 in Fig. 1)). The flow was controlled by a control valve placed inside the fan (number 1 in Fig. 1) and the air velocity was calculated by a velocity sensor (Dwyer AVU-3V model HP111 LH) as shown in Fig. 1 (number 3). The display on the DC power controller of the centrifugal fan (P.A. Hilton Ltd H111/00629) is shown (number 9) in Fig. 1. The accuracy of the velocity sensor was ± 0.1 m/s.

Table 1. Physical properties of the aluminum 1060 alloy

Properties		Conditions
		T [°C]
Density [$\times 1000$ kg/m ³]	2.7	25
Poisson's ratio	0.33	25
Elastic modulus [GPa]	70-80	25
Hardness (HB500)	23	25
Thermal expansion	$23.6 \cdot 10^{-6}/^{\circ}\text{C}$	20-100
Thermal conductivity	234 W/mK	25

2.1. Physical model

Geometry of the experimental setup of the channel is shown in Fig. 2. The physical properties of the air have been assumed to remain constant at the average bulk temperature. Impermeable boundary and no-slip wall conditions have been assumed over the channel walls as well as the chevron surfaces. The distance between the apexes of the triangle with the vertical axis coordinates ($D_v = 7.5$ mm) was constant. Length of the channel in front of the test section was $L_{inlet} = 30$ cm and length of the channel behind the test section $L_{outlet} = 25$ cm. Length of the test section was (L_{test}) 15 cm and height and length of the ribs were $H = L = 15$ mm. Location of thermocouples shown with a blue circle was $H_T = 7.5$ mm of the base chevron surface.

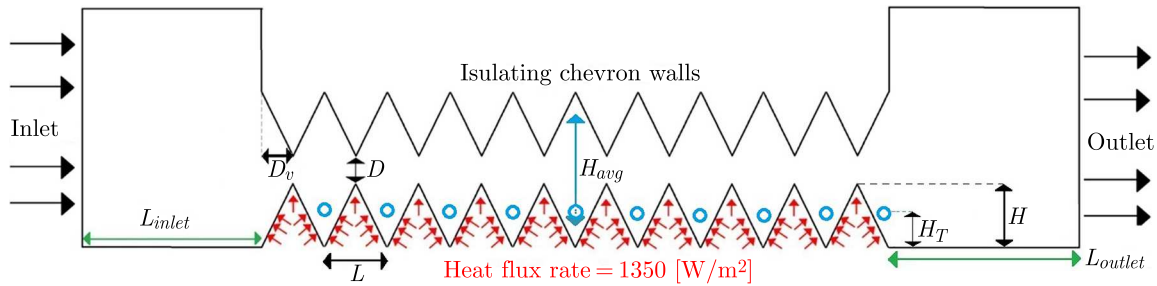


Fig. 2. Geometry of the experimental setup of the channel

The next section creates the entering boundary condition with a heat flux rate of the heater 1350 w/m^2 , The other wall is an insulating one and the inlet section with the input speed (velocity inlet) as well as the fluid outlet (pressure outlet). The inlet temperature of the working fluid (air) was kept constant at 298.15 K.

3. Performance parameters

Parameters of interest in the present work are the Reynolds number, friction factor, Nusselt number and hydraulic diameter

$$D_h = \frac{2H_{avg}W}{H_{avg} + W} \quad (3.1)$$

where H_{avg} is average distance between the chevron surfaces, and W is width of the chevron surfaces.

$$\text{Re} = \frac{\rho u D_h}{\mu} \quad (3.2)$$

where u is velocity of the fluid at the inlet of the test section, D_h is hydraulic diameter and μ is dynamic viscosity

$$f = 2 \frac{\Delta p}{L} \left(\frac{D_h}{\rho u^2} \right) \quad (3.3)$$

The friction factor is computed by the pressure drop ΔP across length of the duct L , and ρ is density of flow.

$$h_x = \frac{\dot{q}}{T_x - T_b} \quad (3.4)$$

where h_x is the local convective heat transfer coefficient, T_x is the local temperature, T_b is the bulk temperature and \dot{q} is heat flux. The heat transfer was measured through the local Nusselt number which can be written as

$$\text{Nu}_x = \frac{h_x D_h}{k} \quad (3.5)$$

where Nu is the Nusselt number and K is conductivity. Then, the average Nusselt number can be obtained by

$$\text{Nu} = \frac{1}{L} \int \text{Nu}_x dx \quad (3.6)$$

and

$$\text{Nu}_s = 0.024 \text{Re}^{0.8} \text{Pr}^{0.4} \quad f_s = 0.085 \text{Re}^{-0.25} \quad (3.7)$$

where Nu_s and f_s stand respectively for the Nusselt number and friction factor of the smooth duct. The Thermal Enhancement Factor (TEF) can be written according to Eiamsa-ard and Changcharoen (2011)

$$\text{TEF} = \frac{\text{Nu}}{\text{Nu}_s} \left(\frac{f}{f_s} \right)^{-\frac{1}{3}} \quad (3.8)$$

4. Numerical model

Numerical analysis of the thermal behavior and flow dynamic characteristics of the chevron channel has been carried out to predict the heat transfer and pressure drop. The governing equations have been solved using a finite volume approach. The time-independent incompressible Navier-Stokes equations and the turbulence model were discretized using the finite volume method. Many investigators predicted turbulent forced convection in a rectangular duct with periodic chevron shapes by utilizing different turbulence models, such as $k - \varepsilon$, $k - \omega$, Reynolds stress model ($k - \varepsilon$) and large eddy simulations (LES) models. The $k - \varepsilon$ model made from the two-equation models when predicting flow patterns of revolving flows.

In the present study, the $k - \varepsilon$ model is used for the turbulence modeling, and the SIMPLE algorithm is used to handle the pressure-velocity coupling. The discretized nonlinear equations are implemented implicitly. To evaluate the pressure field, the pressure-velocity coupling algorithm SIMPLE (Semi Implicit Method for Pressure-Linked Equations) is selected. The following assumptions are applied in the simulations: the flow is steady, fully developed turbulent and two dimensional, the thermal conductivity of the channel wall and chevron material do not change with temperature, and the channel wall and chevron material are homogeneous and isotropic with an enhanced wall treatment function. The solutions are considered to be converged when

the normalized residual values are less than 10^{-6} for all variables, but less than 10^{-5} only for the continuity equation.

A grid independence test has been performed for the channel to analyze the effects of grid sizes on the results, as shown in Fig. 3. It is found that further increase in the grid beyond 51159 cells results in a variation in the Nusselt number less than 1%, thus this grid number is taken as a criterion of grid independence. This fine mesh size is able to provide good spatial resolution for the distribution of most variables within the channel.

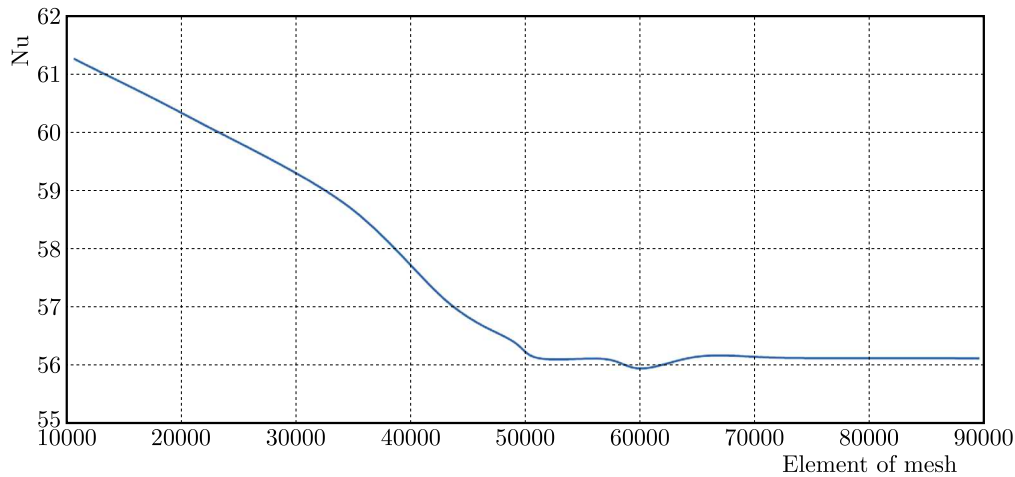


Fig. 3. Investigation of the independency of mesh elements

Figure 4 shows the grid size of mesh elements near the chevron walls. To investigate the independency of the mesh, the number of mesh elements increases near the chevron walls by $y^+ = 2.014253$.

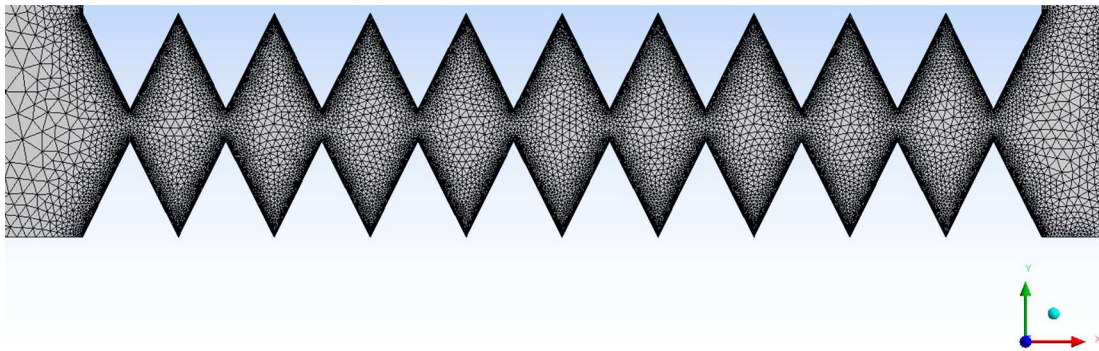


Fig. 4. Grid size of mesh element near the chevron walls

5. Results and discussion

5.1. Phase shift and Reynolds numbers variation in a triangular chevron channel

Figure 5 shows experimental results of temperature variation of the fluid vs. dimensionless distance x/D for a phase shift of 0° and $D = 5$ mm. The air temperature has increased by an increase in the dimensionless distance. The same results are for other phase differences.

Figure 6 illustrates the average fluid temperature across the triangular chevron wall for different Reynolds numbers. The fluid temperature significantly decreases with the increasing Reynolds number. The difference between the numerical and experimental results is about $1\% \leq \text{error} \leq 11\%$, which proves good validation between both results.

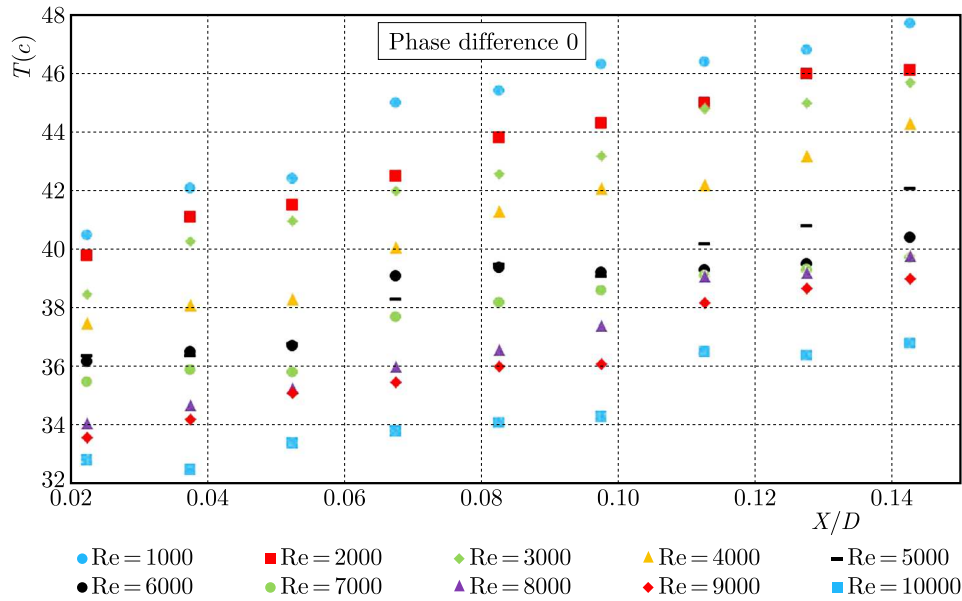


Fig. 5. Experimental results of temperature variation of the fluid vs. dimensionless distance x/D for a phase shift of 0° and $D = 5$ mm

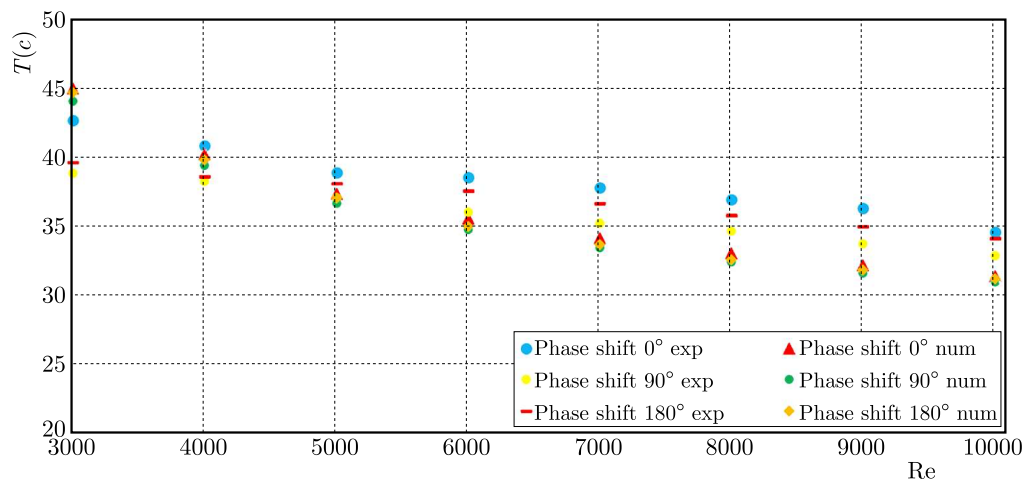


Fig. 6. Variation and validation of the average temperature of the fluid vs. Re in experimental and numerical results at phase shifts 0° , 90° , 180°

The numerical and experimental results of the variation of Nu for three phase shifts and within $3000 \leq Re \leq 10000$ are shown in Fig. 7. The Nusselt number for the chevron channels is higher than for the plain channel because the Nusselt number depends on the heat transfer rate. On the other hand, the values of the Nusselt number are found to increase with an increase in Re in all cases. Best results are obtained for the phase difference 90° . The Nusselt number for $\phi = 90^\circ$ is about 4.8% higher than for $\phi = 0$. In fact, $\phi = 90^\circ$ makes more turbulence interrupts in the development of a thermal boundary layer. The vortices induced in and around the chevron channels are thought to be responsible for the increase of turbulence intensity of the flow which leads to higher heat transfer rates.

Figure 8 shows the experimental and numerical results of the effect of the Reynolds number and the relative phase shift on the friction factor. When the fluid passes through the chevron channel, a considerable pressure drop occurs. The value of the friction factor decreases with the increasing Reynolds number in all cases, as expected, due to suppression of the viscous sub-layer with an increase in Re. Also, the pressure drop in the channel with a phase shift $\phi = 180^\circ$ is

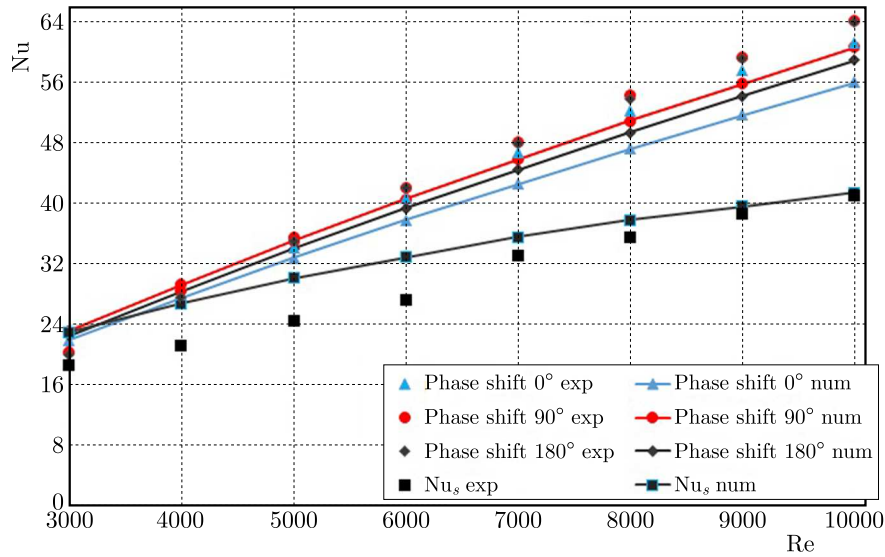


Fig. 7. Variation of Nu vs. Re for phase shifts 0°, 90°, 180° in experimental and numerical results

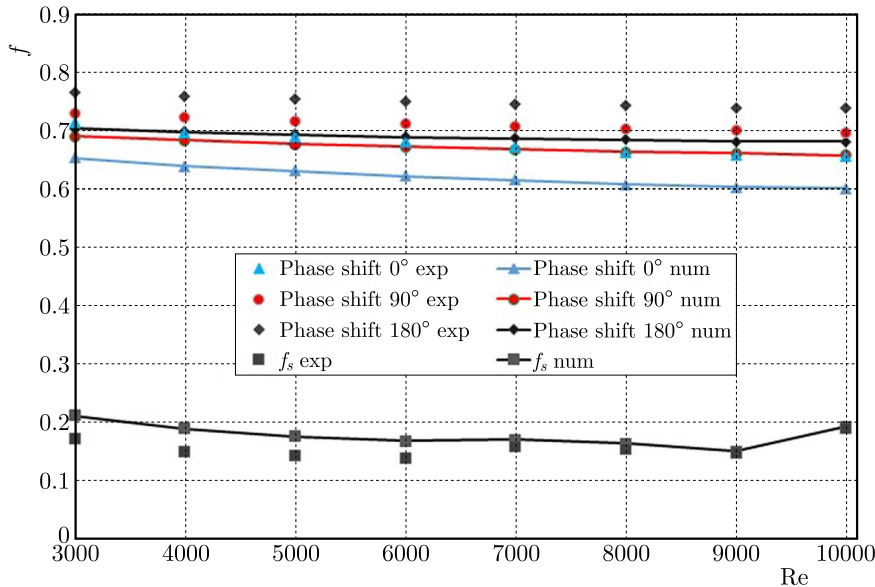


Fig. 8. Variation of f vs. Re for phase shifts 0°, 90°, 180° in experimental and numerical results

greater than in other cases. As expected, the f from the $\phi = 180^\circ$ array is substantially higher than that with $\phi = 0^\circ$ and $\phi = 90^\circ$, whereas the $\phi = 0^\circ$ yields the lowest f . The f value of $\phi = 180^\circ$ is found to be about 4% above $\phi = 90^\circ$ and about 5.4% over the $\phi = 0^\circ$. It can be interpreted that the $\phi = 180^\circ$ causes a higher turbulence intensity in the flow due to more oscillating streamlines than for the other phase shifts (see Fig. 10). But it creates a “stronger” recirculation region and vortices inside the chevron surfaces, so it prevents the fluid from good mixing. Thus, it results in a less increase in the heat transfer in comparison with both $\phi = 90^\circ$ and $\phi = 180^\circ$. Using the phase shift, one can reduce the occurrence of the recirculation providing more surface sweep, therefore, the negative effect of the recirculation region on the heat transfer can be decreased. The shift between the numerical and experimental results for each phase shift is about $1\% \leq \text{error} \leq 11\%$, which proves a good validation.

Figure 9 shows the variation of TEF with Re for all phase shifts. The combined effect of Nu and f values has been simplified by TEF, Eq. (3.8). In general, TEF tends to decrease with the

rise of Re. It is worth noting that the TEF value of the phase shift 90 is the highest and found to be the best among other phase shifts.

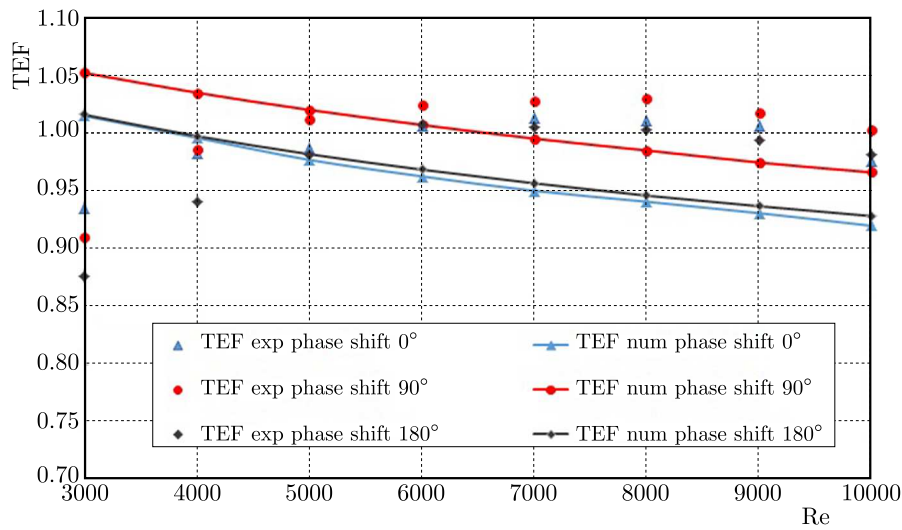


Fig. 9. Variation of TEF vs. Re for phase shifts 0°, 90°, 180° in experimental and numerical results

For phase shifts 0°, 90° and 180°, the maximum TEF values are, respectively, about 1.05, 1.1 and 1.07. It is seen that the phase shift 90° gives the highest TEF at lower Reynolds numbers. At the given chevron surfaces, the phase shift 90° yields TEF around 3-7% higher than that of other two phase shifts. Because of considerably higher Nu and lower f , only for the phase shift 90° will be further investigated in the subsequent Section.

The variation of the dimensionless parameters Nu, f and TEF versus Re for phase shifts 0°, 90° and 180° are presented in Figs. 7, 8 and 9, respectively. For three cases and at all positions, it is observed that there is a relatively good concordance between the experimental data and the numerical results. For very low flow rates, as in the experiment, it is believed that the observed differences between the experimental and numerical data may be partly caused by a small error in the DC source power, heater and the manometer velocity sensor in the system, which can slightly disrupt the turbulence flow. Another possible cause of these differences is the fact that the hot junction of the thermocouples, which are the top of the plate surface, covers a small circular area with a diameter of approximately 1 mm and, therefore, the measured temperature is actually the average temperature of that small surface.

Figure 10 shows the streamlines associated by a modified various phase shift at Re = 10000. By focus on the upstream flow structures of various phase shifts, the phase shift is $\phi = 90^\circ$ and the size of bubbles decrease. The volume of the bubbles, induce larger recirculation zones which provide higher turbulent intensity. This may be related to a decrease of the laminar sub-layer and to the maximum heat transfer for $\phi = 90^\circ$. When the phase shift is close $\phi = 90^\circ$, it creates more vortex and decreases bubbles from triangular chevron surfaces. When the phase shift angle increases, the friction factor also increases because the fluid is oscillating between chevron surfaces. It is clear that the effect of the phase shift on temperature and flow development in the chevron channel is that there are smaller recirculation regions and more separation bubble regions formed in the adjacent inlet/outlet. This effect increases by closing to the phase shift $\phi = 90^\circ$, which means that the influence of the wall on the main stream becomes greater. This generates greater swirl flow in the wavy wall due to transfer vortices of the bulk flow field in the wavy wall. This induces a higher temperature gradient near the wavy wall. Therefore, the net heat transfer rate from the wavy wall to the fluid is increased.

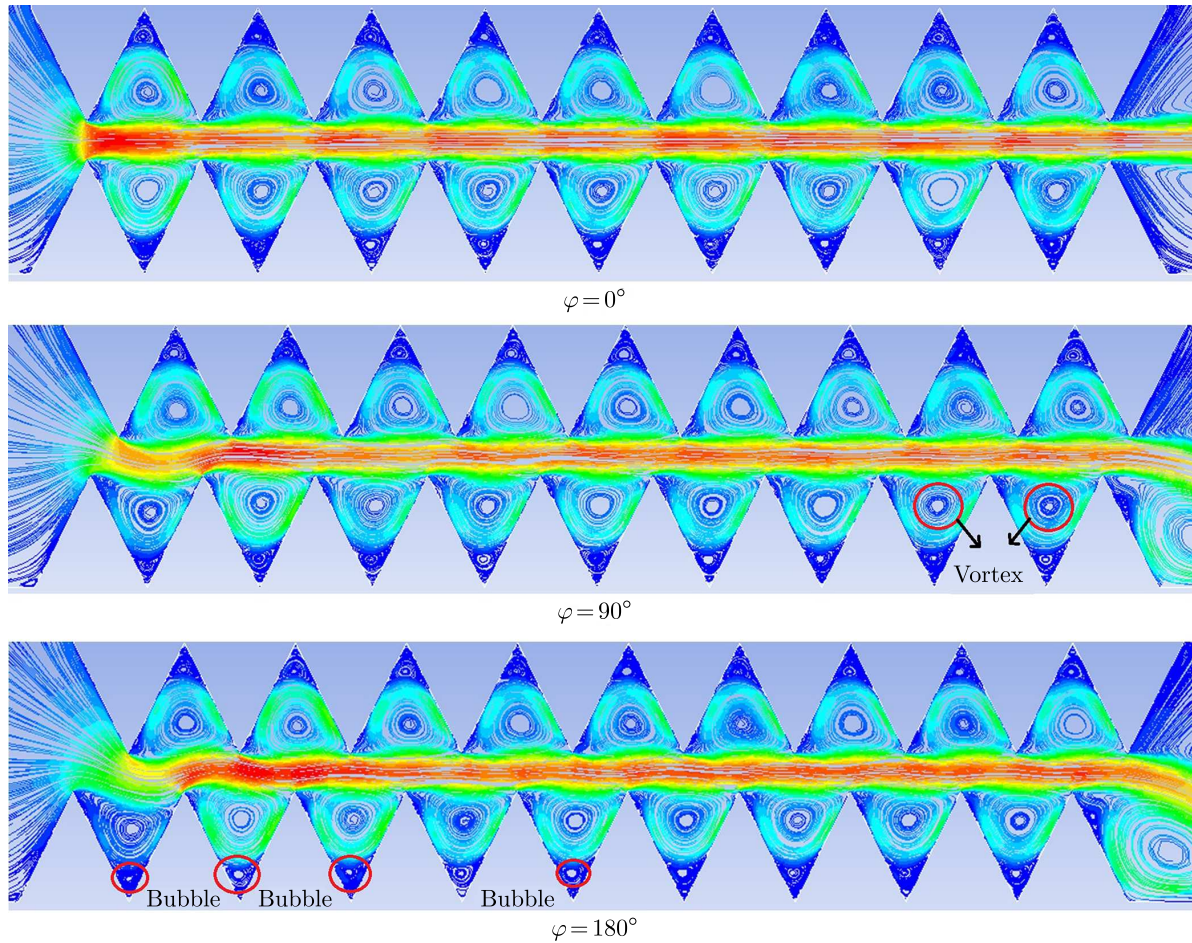


Fig. 10. Streamline of fluids for phase shifts 0° , 90° , 180°

5.2. Effect of distance between triangular chevron surfaces

Figure 11 demonstrates the variation of the average fluid temperature above 7.5 mm from the triangular chevron plate according to numerical and experimental results. In Fig. 11, it is seen that the numerical calculations with the standard wall function are similar to the experimental data with the chevron channel for $Re = 10000$ and $\phi = 180^\circ$. The wall temperature increases when the distance between the surfaces increases. It can be interpreted that the fluid flow becomes more complex near the wall region when D increases. As a result, the velocity of fluids decrease with growing D and the temperature near the wall becomes warmer.

The average numerical and experimental Nusselt number for triangular chevron surfaces at $Re = 10000$ for $\phi = 180^\circ$ is presented in Fig. 12. There is good agreement between numerical and experimental results with an error less than 10% for most of the results. It can be seen that with an increase in the distance between triangular chevron surfaces, the Nusselt number decreases. In fact, the volume of vortices in the laminar sublayer and the velocity of fluids decrease. Figure 12 shows Nu for triangular chevron surfaces. It is greater than for a smooth surface below $D = 15$ mm. When D increases for a constant $Re = 10000$, the velocity of the fluid decreases. As a result, Nu for triangular chevron surfaces is less than that for smooth surfaces above $D = 15$ mm.

Figure 13 shows the variation of the experimental and numerical friction factor along the channel for $Re = 10000$ and $\phi = 180^\circ$. There is a good validation of the numerical and experimental results with an error less than 9% for most of results. The friction factor for triangular

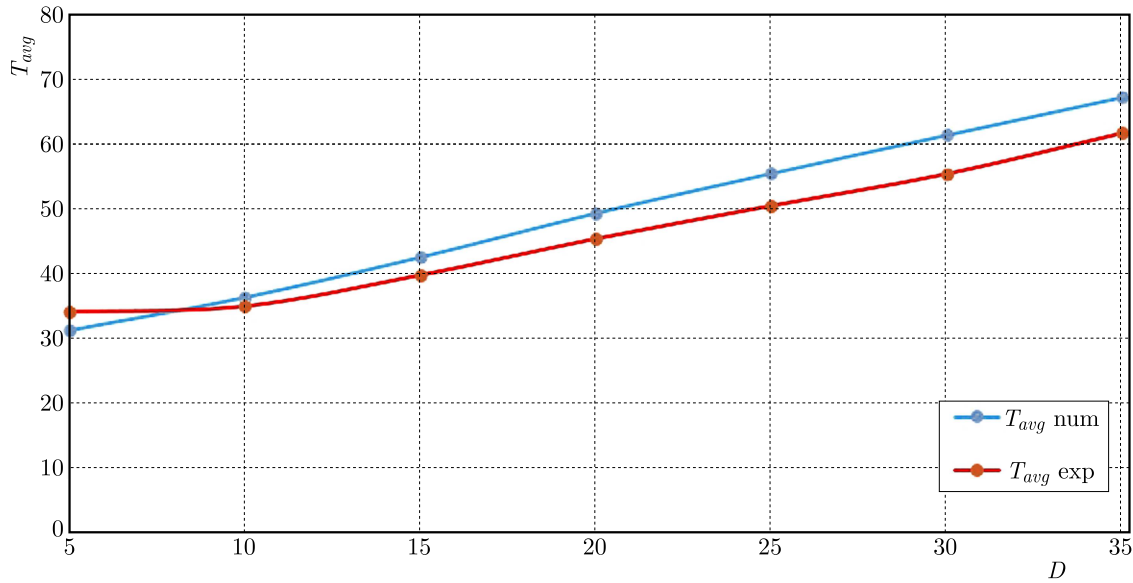


Fig. 11. Experimental and numerical variation of average temperature of the chevron plate vs. different distances

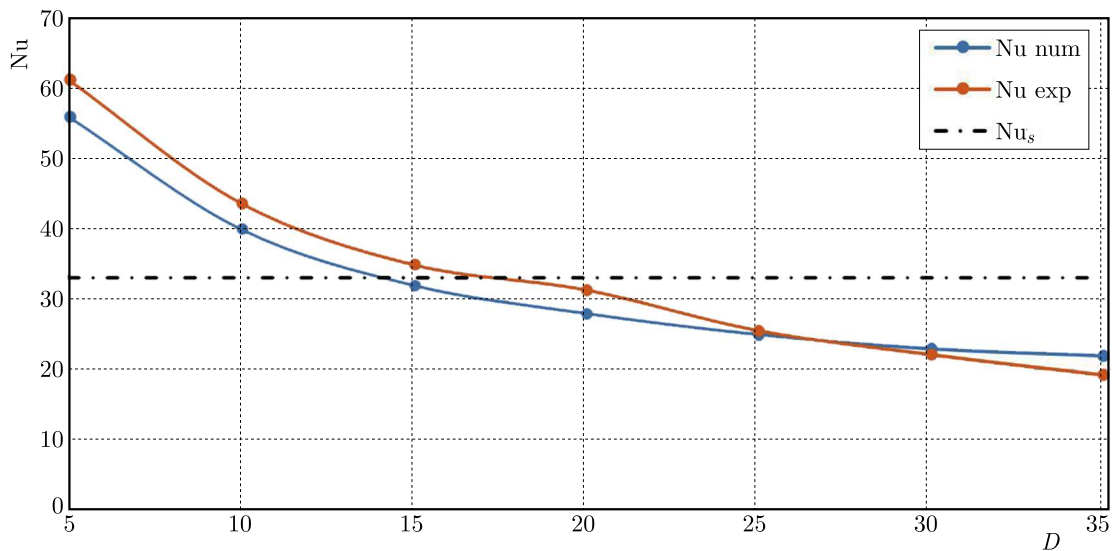


Fig. 12. Experimental and numerical variation of Nu of the chevron plate vs. different distances

chevron surfaces is the highest compared to the smooth surface. It is obvious that the friction factor decreases gradually for all configurations with an increase in the Reynolds number.

Based on the same pumping power consumption, the TEF is shown and compared for differently distanced chevron surfaces tested, see Fig. 14. By considering the heat transfer and the pressure drop simultaneously at $Re = 10000$ and $\phi = 180^\circ$, the working conditions should give a high TEF. It is seen from the figure that the TEF tends to decrease as D increases (for numerical results). Consistently, the investigation reveals a higher thermal enhancement factor at $D = 5$ mm. There appears transfer of additional heat by conduction which provides a better fluid mixing. As a result, to obtain the maximum TEF, one should to get the heat exchanger with the minimum distance between surfaces, see Fig. 14.

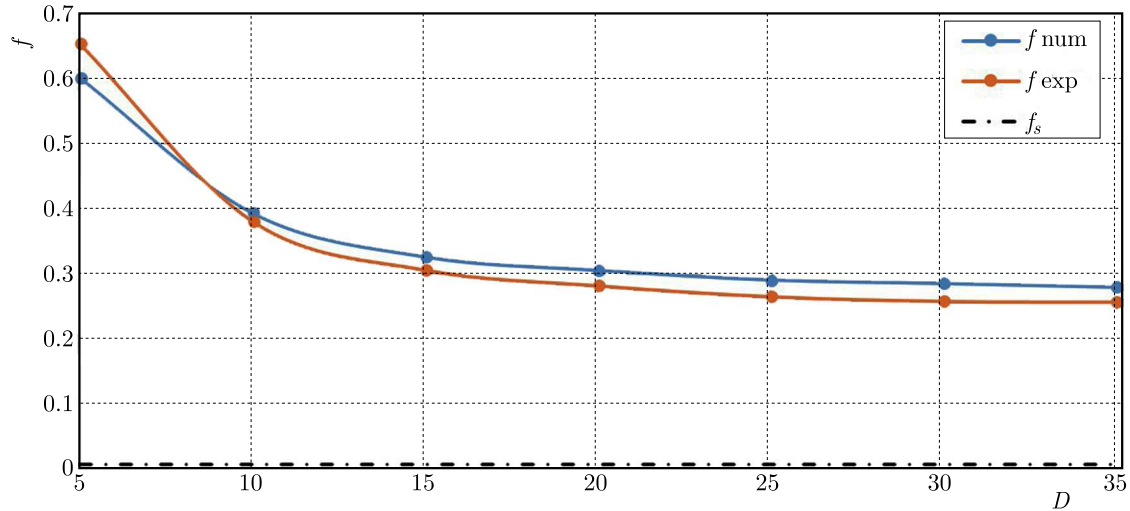


Fig. 13. Experimental and numerical variation of the friction factor for the chevron plate vs. different distances

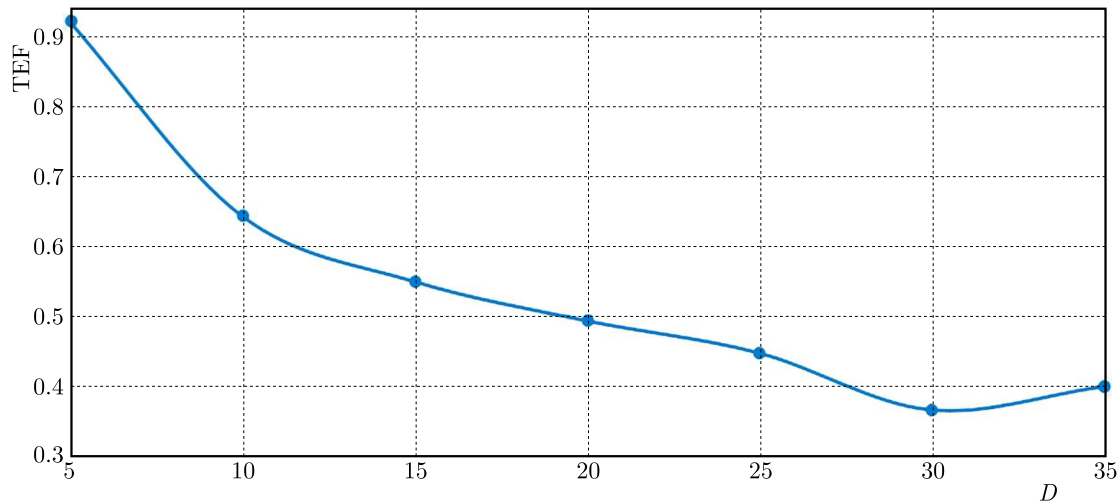


Fig. 14. Variation of TEF for the chevron plate vs. different distances

6. Conclusions

A triangular chevron channel is a good alternative in high heat flux applications or more efficient heat exchange devices used in a variety of engineering structures such as heating and air conditioning systems. In this paper, the effect of phase shift and distance between chevron channels is examined for Reynolds numbers ranging from 1000 to 10 000. The aim of the study is to achieve to the maximum heat transfer and thermal enhancement factor as well as the minimum pressure drop. The best phase shift angle is $\phi = 90^\circ$. Also the distance between chevron surfaces D has been investigated. The results show that $D = 5$ mm is the best distance between chevron surfaces in getting the maximum TEF and Nu, and the minimum f . Decreasing and holding the average base temperature of the chevron surfaces at a constant level, particularly at higher Reynolds numbers has been successfully achieved. Increasing the Reynolds number leads to a more complex fluid flow and the heat transfer rate. When the phase shift gets close to $\phi = 90^\circ$, Nu and TEF reach the maximum rate, whereas f the minimum value. The channels with the phase shift angle $\phi = 90^\circ$ are the most attractive from the viewpoint of energy saving compared to others with the phase shifts $\phi = 0^\circ$ and 180° . For the triangular chevron surfaces, the

maximum heat transfer is obtained from 33.33% up to 37.5%, which is higher than for smooth surfaces.

References

1. AL-SHAMANI A.N., SOPIAN K., MOHAMMED H.A., MAT S., RUSLAN M.H., ABED A.M., 2015, Enhancement heat transfer characteristics in the channel with Trapezoidal rib-groove using nano fluids, *Case Studies in Thermal Engineering*, **5**, 48-58
2. DELLIL A., AZZI A., JUBRAN B.A., 2004, Turbulent flow and convective heat transfer in a chevron wall channel, *Heat and Mass Transfer*, **40**, 793-799
3. EIAMSA-ARD S., CHANGCHAROEN W., 2011, Analysis of turbulent heat transfer and fluid flow in channels with various ribbed internal surfaces, *Journal of Thermal Science*, **20**, 3
4. ISLAMOGLU Y., PARMAKSIZOGLU C., 2004, Numerical investigation of convective heat transfer and pressure drop in a chevron heat exchanger channel, *Applied Thermal Engineering*, **24**
5. KHOSHVAGHT-ALIABADI M., SAHAMMIYAN M., HESAMPOUR M., SARTIPZADEH O., 2016, Experimental study on cooling performance of sinusoidal-chevron minichannel heat sink, *Applied Thermal Engineering*, **92**, 50-61
6. MOON M.-A., PARK M.-J., KOM K.-Y., 2014, Evaluation of heat transfer performances of various rib shapes, *International Journal of Heat and Mass Transfer*, **71**, 275-284
7. SAKR M., 2015, Convective heat transfer and pressure drop in V-chevron channel with different phase shifts, *Heat Mass Transfer*, **51**, 129-141
8. VANAKI SH.M., MOHAMMED H.A., ABDOLLAHI A., WAHID M.A., 2014, Effect of nanoparticle shapes on the heat transfer enhancement in a chevron channel with different phase shift, *Journal of Molecular Liquids*, **196**, 32-42
9. XIE G., LIU J., LIGRANI P.M., SUNDEN B., 2014, Flow structure and heat transfer in a square passage with offset mid-truncated ribs, *International Journal of Heat and Mass Transfer*, **71**, 44-56
10. YANG Y.-T., CHEN P.-J., 2010, Numerical simulation of fluid flow and heat transfer characteristics in channel with V chevron plates, *Heat Mass Transfer*, **46**, 437-445
11. YONGSIRI K.A., EIAMSA-ARD P.B., WONGCHAREE K.C, EIAMSA-ARD S., 2014, Augmented heat transfer in a turbulent channel flow with inclined detached-ribs, *Case Studies in Thermal Engineering*, **3**, 110

Manuscript received September 25, 2017; accepted for print November 29, 2017

EFFECT OF THE LOCAL DAMAGE AND PROFILE ERROR OF THE GEAR ON THE DRIVETRAIN DYNAMIC RESPONSE

AHMED GHORBEL, BACEM ZGHAL, MOEZ ABDENNADHER,
LASSAD WALHA, MOHAMED HADDAR

*Mechanics, Modelling and Manufacturing Laboratory (LA2MP), Mechanical Engineering Department, National Engineers
School of Sfax, Sfax, Tunisia*

e-mail: gh.ahmed.enis@gmail.com

The dynamic modeling of vibration of a drivetrain is used for increasing our information about vibration generating mechanisms, especially in the presence of some kind of gear faults. This paper describes a research work on the automotive driveline modeling, vibration analysis, and the effect of gear defects on the dynamic behavior of the system. Firstly, main drivetrain components including the engine, clutch, single stage spur gearbox and disc brake are modeled, respectively. The nonlinear dynamic model is simulated by a thirteen degrees of freedom (DOF) system and the nonlinear function is due to the dry friction path. Secondly, two types of defects are modeled and introduced into the spur gear system; local damage and profile error. Then, the nonlinear equations of motion are solved by the numerical Runge Kutta method and a comparative study of the dynamic behavior of the system in healthy and defected cases is discussed for each fault type. The influence of the defects on the vibration response is presented in the time and frequency domain. Finally, analysis of the two defects together is presented.

Keywords: dynamic behavior, clutch, gear, brake disc, gear local damage, gear profile error

1. Introduction

All conventional automotive vehicles must have drivetrains. The objective of the drivetrain is to transfer the power developed in a thermal engine to driving wheels. Vibro-impacts in an automotive driveline system are a critical concern to vehicle manufactures based on noise, vibration and reliability considerations.

In this context and in order to determine the vibratory behavior, the modeling and studying a drivetrain system is an important research field addressed by many researchers. Bemporad *et al.* (2001) proposed some simple models with two masses where the first represented the engine and the second the vehicle which included the powertrain, clutch and shafts. Templin and Egardt (2009) investigated a torsional drivetrain model with only two degrees of freedom. A more detailed model was developed by Walha *et al.* (2011) to study the effect of the eccentricity defect on the dynamic behavior of a coupled clutch-helical two stage gear system. Brancati *et al.* (2007) intend to modeled and investigate the effect of oil damping on the dynamic behavior where the considered model was constituted by a flywheel, clutch and gear pairs of an automotive transmission. Wu and Guangqiang (2016) developed a torsional driveline model to analyze torsional vibration and reduce the gear rattle. Ghorbel *et al.* (2017) proposed a linear model with 22 DOFs including the main subsystems of an automotive drivetrain (engine, clutch, two helical gear stage and disc brake) to investigate their dynamic behavior and modal properties.

A nonlinear torsional model of the clutch was developed by Xue-Lai *et al.* (2016) for investigating the influence of each parameter on noise generation. Gaillard and Singh (2000) proposed five models of an automotive clutch with the dry friction path and investigated energy dissipation

for each model. Driss *et al.* (2007) presented a clutch model with 11 DOFs which included three types of nonlinearity. Saleh *et al.* (2015), Krak *et al.* (2015) investigated multi stage stiffness and hysteresis phenomena with spline nonlinearities in the vibrational behavior of the clutch. Also, the influence of clutch characteristics of the gearbox rattling in different engine conditions was studied.

Concerning gearbox modeling, the literature is rich in analytical and experimental works on gear systems. A detailed model of gear dynamic vibration was investigated in many review papers (Chaari *et al.*, 2008; Howard *et al.*, 2011; Kim *et al.*, 2010; Walha *et al.*, 2009). These models are currently heavily used and can include shaft torsional vibration and bearing stiffness. A gear mechanism may undergo several types of defects. The gear faults can be classified into three types: manufacturing defects (eccentricity of wheels, tooth profile errors, etc.), assembly defects (misalignment, parallelism, etc.) and defects appearing during transmission error. In many earlier gear models, defects or errors have not been taken into account, especially the local damage and profile error. The research work by Rincon *et al.* (2012) includes different types of faults that may affect the gearing and studies their influence on the dynamic response. Indeed, Fakhfakh *et al.* (2005) studied the influence of teeth defects of a gear through variation it makes to the mesh stiffness. In another work, Fakhfakh *et al.* (2006) analyzed the dynamic behavior of two stage gears in presence of tooth manufacturing defects. Divandari *et al.* (2012) investigated the effect of profile modifications and errors on the gear system dynamic behavior in the presence of tooth localized defects. Detections of defects become important tools to know health of the gearbox. There are various vibration analysis techniques which can be used for this purpose. Time domain frequency domain techniques and time frequency analysis are the methods that can be employed for gearbox diagnostics (Abouel-seoud *et al.*, 2012; Aherwar and Khalid, 2012; Kobra *et al.*, 2010). In this paper, the time domain response and the Fast Fourier Transform (FFT) are used to investigate the effect of gear faults on the drivetrain dynamic behavior.

A wide range of vehicles are equipped with disc brakes which offer many advantages over drum brakes. The experimental observations of Fosberry and Holubecki (1961) showed that the vibrations of the disc were much larger than those of the caliper of about $20 \mu\text{m}$. Ahmed (2011) developed a detailed theoretical model of the disc brake to reduce squeal phenomena. In another work, a theoretical model was proposed in order to analyze the influence of the disc brake friction model of the dynamic response of one-stage spur gear transmission (Khabou *et al.*, 2014).

It should be noted that although the modeling and analysis of the drivetrain dynamic behavior presented in the paper already exist in the literature, few results actually address the dynamic response which includes the influence of gear defects on a coupled system. In this article, we propose a new nonlinear dynamic model of a drivetrain system that contains thirteen degrees of freedom. Two typical defects of the gear (local damage and profile error) are introduced to study their effect on the dynamic response.

2. Dynamic drivetrain model

In this Section, a simple drivetrain model is presented in Fig. 1. This model is composed of three blocks; clutch, single spur gear stage and disc brake, which are supported by three bearings, one for the input, the second for the shaft linking the clutch with the geared system and the third one for the output shaft. The drivetrain system is driven by an engine which transmits torque $T_e(t)$ to the input shaft by a coupling. A load torque T_d is applied to the brake disc of the output shaft.

Using Fourier series decomposition, the engine torque $T_e(t)$ can be written as follows

$$T_e(t) = T_p + T_{pm} \cos\left(\frac{n_c}{2}\Omega_e t + \phi_{pn}\right) \quad (2.1)$$

where n_c and Ω_e are the number of engine cylinders and the engine rotational speed. T_p , T_{pm} are respectively the average amplitude and the amplitude of the harmonic, and ϕ_{pm} is the associated phase. To simplify the problem, the phase is supposed to be equal to zero.

The system has thirteen degrees of freedom (DOF) which can be defined as follows:

- Rotation along the z axis of the flywheel and cover θ_1 , pressure plate θ_2 , friction disc θ_3 , clutch hub θ_4 , pinion 12 θ_{12} , pinion 21 θ_{21} and brake disc θ_d .
- Translations of the first block (mass m_{b1}) composed of the engine, flywheel, cover and pressure plate along the x and y directions. The corresponding DOFs are x_1 and y_1 .
- Translations of the intermediate block (mass m_{b2}) composed of the friction disc, clutch hub and pinion 12 along the x and y directions. The corresponding DOFs are x_2 and y_2 .
- Translations of the output block (mass m_{b3}) composed of wheel 21 and the disc brake along the x and y directions. The corresponding DOFs are x_3 and y_3 .
- The following inertias are considered: I_1 for the flywheel and cover, I_2 for the pressure plate, I_3 for the friction disc, I_4 for the clutch hub, I_{12} for pinion 12, I_{21} for wheel 21 and I_d for the brake disc.
- The elasticity of three shafts is modelled by torsional stiffnesses, respectively K_1 , K_2 and K_3 . Bearings supporting the input, intermediate and output shafts are respectively modelled by linear stiffnesses k_{xi} and k_{yi} ($i = 1, 2, 3$) acting along the x and y directions.

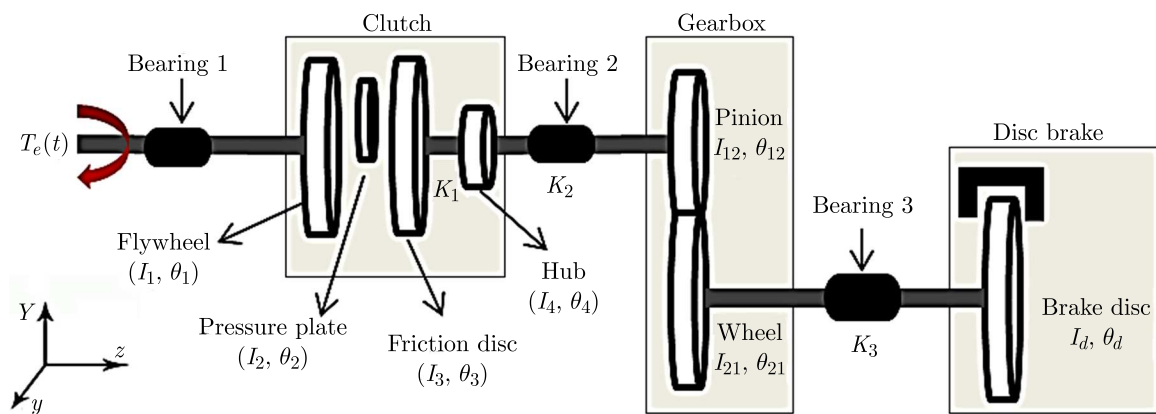


Fig. 1. Vehicle drivetrain model

2.1. Vehicle clutch modelling

The clutch is an important component of the car driveline which can play a significant role in filtering vibrations due to fluctuations of the engine torque. The modeling of a vehicle clutch is affected by a torsional model with a nonlinear function, see Fig. 2. This is due to dry friction. The friction torque $\tilde{T}_f(\dot{\delta})$ is a nonlinear function which depends on the relative velocity $\dot{\delta}$, such that $\dot{\delta}_2$ is the relative velocity between the pressure plate and the friction disc and $\dot{\delta}_3$ describes the relative velocity between the flywheel and the friction disc. K_1 represents the torsional stiffness of the shaft and k_{12} is torsional stiffness between the cover and the pressing plate.

The equation of the friction torque is

$$T_f(\dot{\delta}) = \left(\mu_D + (\mu_S - \mu_D)e^{\varepsilon|\dot{\delta}|} \tanh(\sigma\dot{\delta}) \right) PAR \quad (2.2)$$

where P is the pressure, A is the surface area of contact and R is the mean radius of that surface. μ_s and μ_D are respectively the static and dynamic friction coefficients, ε is a factor which controls the gradient of exponential decaying and σ is the conditioning factor that controls the smoothing level at the discontinuity of this function. The ε and σ values are verified with those by Walha *et al.* (2011), and they are equal to: $\varepsilon = 2$ and $\sigma = 50$.

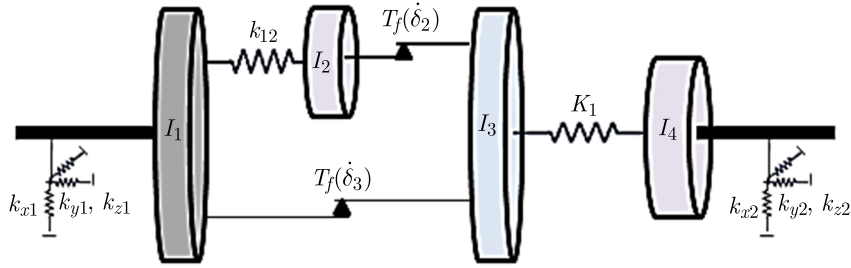


Fig. 2. Dynamic clutch model

2.2. Spur gear system modelling

The gearbox mechanism contains a single stage spur gear (Fig. 3). Toothed wheels 12 and 21 are assumed to be rigid bodies and bearings 2 and 3 are modeled by linear stiffness k_{xi} and k_{yi} ($i = 2, 3$). A periodic variation of the gear mesh stiffness $k(t)$ is another excitation source to the system and it is generated by the time varying number of teeth in contact. Figure 4 shows the evolution of gear mesh stiffness in the healthy case. The spectrum in this case is composed by the meshing frequency f_m and its harmonics.

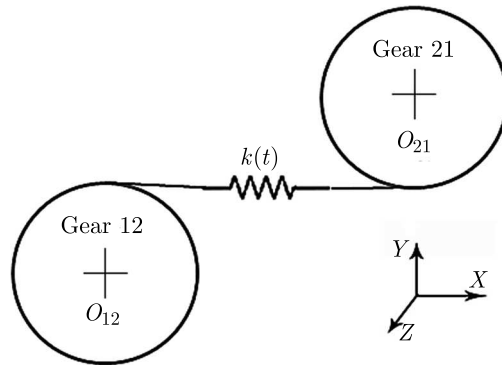


Fig. 3. Single stage spur gear modelling

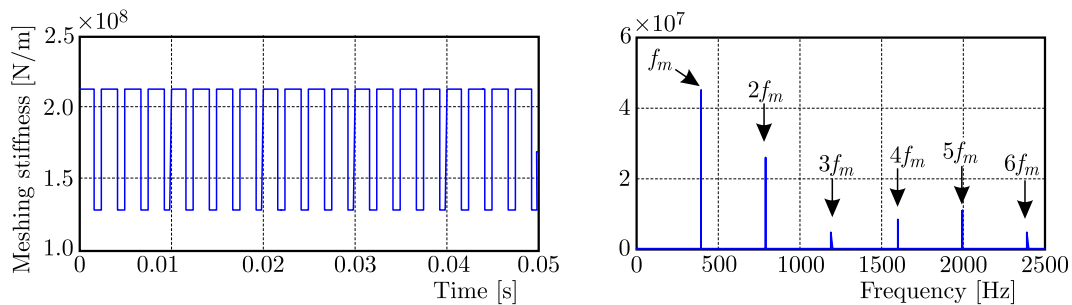


Fig. 4. Gear mesh stiffness for healthy case

The healthy configuration can be described by a step function with no phase and amplitude modifications. If the contact ratio is less than two, the minimum value corresponds to the mesh stiffness of one pair of teeth in contact, whereas the maximum value being twice the minimum amplitude corresponding to two pairs of teeth in contact.

2.3. Disc brake modelling

The braking of the system is done by a disc brake system rigidly assembled with pinion 21. Composed mainly of the disc and two braking plates, the pair of brake pad assemblies is pressed

against the disc in order to generate a frictional torque and, consequently, to slow down its rotation (Fig. 5). The braking torque C_{br} can be expressed by the Coulomb model and it is considered as an externally applied force in the equations of motion of the studied system.

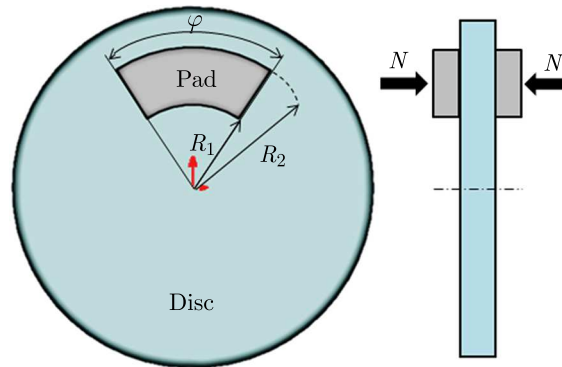


Fig. 5. Disc brake model

The braking torque C_{br} can be expressed as follows

$$C_{br} = \frac{4\mu N\varphi(R_1 + R_2)}{6 \sin(\varphi/2)} \left(1 - \frac{R_1 R_2}{(R_1 + R_2)^2}\right) \quad (2.3)$$

where μ is the friction coefficient of the pad, N is the normal force, φ is the pad opening angle and R_1 and R_2 are, respectively, the outer and inner radii of the pad.

3. Equations of motion

Lagrange's method has been used to formulate the nonlinear differential equation governing the drivetrain system with thirteen degrees of freedom, which is

$$\mathbf{M}_G \ddot{\mathbf{q}} + \mathbf{C} \dot{\mathbf{q}} + \mathbf{K}_G \mathbf{q} = \mathbf{F}_0(t) + \mathbf{F}(q) \quad (3.1)$$

where \mathbf{q} is the vector of degrees of freedom defined by

$$\mathbf{q} = [x_1, y_1, x_2, y_2, x_3, y_3, \theta_1, \theta_2, \theta_3, \theta_4, \theta_{12}, \theta_{21}, \theta_d] \quad (3.2)$$

where x_i and y_i ($i = 1, 2, 3$) are the bearing displacements. θ represents the angular displacement of the wheel and gears (12 and 21) along the direction z .

\mathbf{M}_G is the global mass matrix and expressed by

$$\mathbf{M}_G = \text{diag}(m_{b1}, m_{b1}, m_{b2}, m_{b2}, m_{b3}, m_{b3}, I_1, I_2, I_3, I_4, I_{12}, I_{21}, I_d) \quad (3.3)$$

\mathbf{K}_G is the stiffness matrix and written as

$$\mathbf{K}_G = \mathbf{K}_e(t) + \mathbf{K} \quad (3.4)$$

where $\mathbf{K}_e(t)$ is the linear time varying mesh stiffness matrix and \mathbf{K} designates the constant stiffness matrix of the bearing and shafts and written as

$$\mathbf{K} = \text{diag}(\mathbf{K}^b, \mathbf{K}^{sh}) \quad (3.5)$$

where the matrices \mathbf{K}_b and \mathbf{K}_{sh} are expressed by

$$\mathbf{K}^b = \text{diag}(k_{x1}, k_{y1}, k_{x2}, k_{y2}, k_{x3}, k_{y3})$$

$$\mathbf{K}^{sh} = \begin{bmatrix} k_{12} & -k_{12} & 0 & 0 & 0 & 0 & 0 \\ -k_{12} & k_{12} & 0 & 0 & 0 & 0 & 0 \\ 0 & 0 & K_1 & -K_1 & 0 & 0 & 0 \\ 0 & 0 & -K_1 & K_1 + K_2 & -K_2 & 0 & 0 \\ 0 & 0 & 0 & -K_2 & K_2 & 0 & 0 \\ 0 & 0 & 0 & 0 & 0 & K_3 & -K_3 \\ 0 & 0 & 0 & 0 & 0 & -K_3 & K_3 \end{bmatrix} \quad (3.6)$$

K_i is the torsional stiffness of the shaft i .

The gear mesh stiffness matrix can be written as follows

$$\mathbf{K}(t) = \mathbf{L}_\delta^T \mathbf{L}_\delta k(t) \quad (3.7)$$

where $k(t)$ is the total meshing stiffness. \mathbf{L}_δ is the teeth deflection and can be written as follows

$$\mathbf{L}_\delta = [0, 0, s_1, s_2, -s_1, -s_2, 0, 0, 0, 0, s_3, s_4, 0] \quad (3.8)$$

The constants of deflection s_i , $i = 1, 2, 3, 4$ are given in Table 1, where α is the pressure angle. The base radii of pinions 12 and 21 are respectively R_{b12} and R_{b21} .

Table 1. Coefficients s_i of $K(t)$

s_1	s_2	s_3	s_4
$\sin \alpha$	$\cos \alpha$	R_{b12}	R_{b21}

\mathbf{C} is the damping matrix proportional to the mass and stiffness matrix

$$\mathbf{C} = \lambda \mathbf{M}_G + \eta \tilde{\mathbf{K}}_G \quad (3.9)$$

where $\tilde{\mathbf{K}}_G$ is the average rigidity matrix, independent of time. λ and η are determined experimentally.

The excitation vector is expressed by

$$\mathbf{F}(t, \dot{q}) = [F_{Tx2/3}, F_{Ty2/3}, -F_{Tx2/3}, -F_{Ty2/3}, 0, 0, T_e(t) - T_f(\dot{\delta}_3), -T_f(\dot{\delta}_2), T_f(\dot{\delta}_2) + T_f(\dot{\delta}_3), 0, 0, 0, -T_d + C_{br}] \quad (3.10)$$

The terms $F_{Tx2/3}$ and $F_{Ty2/3}$ are tangential forces applied by the second block on the third block along the direction x and y

$$F_{Tx2/3} = -\mu_D P A \frac{\dot{x}_3 - \dot{x}_2}{\|\dot{x}_3 - \dot{x}_2\|} \quad F_{Ty2/3} = -\mu_D P A \frac{\dot{y}_3 - \dot{y}_2}{\|\dot{y}_3 - \dot{y}_2\|} \quad (3.11)$$

4. Effect of damage in spur gear on the dynamic response

A elements in various mechanical driveline systems have a specific vibration pattern that depends on work conditions and construction. Variation in the vibration pattern in any position of the system indicates the initiation of defect in the machine. The main objective of vibration analysis is to identify the condition of the drivetrain to distinguish healthy and defected geared systems and to identify the defective components. In this part, the effect of local damage and profile error on the geared system (gear 12) on the dynamic behavior of different components of the drivetrain will be investigated.

4.1. Effect of local damage in spur gear on the dynamic response

The main purpose of this Section is to investigate the effects of introduction of the local damage into the geared system on the dynamic response. In the presence of a local damage defect, the meshing stiffness variations give important information about the dynamic behavior of the system. For the modeling of the local gear defect, three approaches have been used in the literature. The first approach is based on the fact that tooth wear can cause loss of contact due to deviation of the ideal profile, resulting in a periodic decrease in the tooth stiffness. The second approach assumes that wear causes reduction of the driving ratio from where it delays the phase where two pairs of teeth come into contact with a decrease in the amplitude of the maximum stiffness associated with this phase. The third approach consists in reducing the two extreme values of the stiffness in addition to the reduction of the driving ratio at the level of the period affected by this defect. The first two approaches are the most used in the research work.

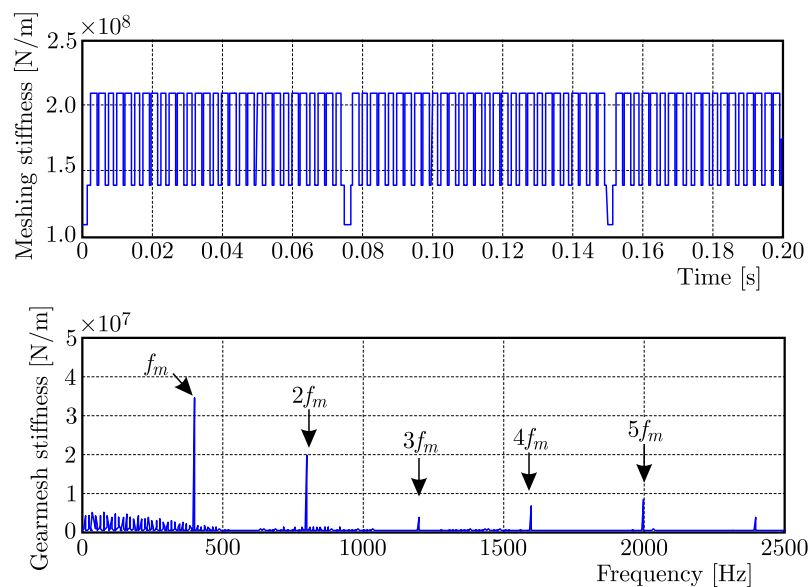


Fig. 6. Gear mesh stiffness for local defect pinion tooth: (a) time response, (b) corresponding spectrum

The tooth damage is modeled by a loss in the mesh stiffness, and it is shown in Fig. 6a. In the presence of a local defect, the corresponding spectrum (Fig. 6b) shows that the effect of defect on the vibration signal is the amplitude modulation around the meshing frequency f_m and a comb lines whose pitch corresponds to the pinion rotation frequency f_p .

Using the parameter values illustrated in Table 2, the velocity vibration signals of the second bearing along the y direction (\dot{y}_2) and the speed time response ($\dot{\theta}_{12}$) of defected gear 12 in the two cases; for both the perfect working condition and in the presence of the local defect on gear 12 are shown in Figs. 7a and 7b, respectively. The local damage occurred on the gear tooth and generated a short duration impulsive signal. The impulse period is 0.075 s, which is equal to the rotational frequency of the defected wheel (gear 12). The local impulse in the vibration signal is periodic and repeated every rotation of gear 12 resulting an additional amplitude and phase modulation.

In the following, we are interested in studying the effects of faults on each subsystem and in selecting different terms. In the gearbox, we study variation of the dynamic transmission error (DTE) which is defined in Eq. (4.1). From the literature, it seems clear that the transmission error represents an interesting indicator of the vibratory behavior of a gear train. On the other hand, deformations of bodies, teeth as well as other components such as shafts and bearings are encompassed in this concept. To investigate the clutch dynamic behavior, tangential forces

Table 2. Values of parameters for numerical studies of the system

Torque excitation T_p, T_{pm} [Nm]	$T_p = 300, T_{pm} = 250$
Engine speed Ω_e [rpm]	$\Omega_e = 800$ rpm
Masses m_{b1}, m_{b2}, m_{b3} [kg]	$m_{b1} = 0.5, m_{b2} = 3, m_{b3} = 10$
Inertias I_1, I_2, I_3, I_4 [kg m ²]	$I_1 = 0.2, I_2 = 12 \cdot 10^{-3}, I_3 = 8 \cdot 10^{-4}, I_4 = 2 \cdot 10^{-4}$
Torsional stiffness [Nm/rad]	$k_{12} = 8 \cdot 10^4, K_1 = K_2 = K_3 = 3 \cdot 10^5$
Bearing stiffness [N/m]	$k_{xi} = k_{yi} = 10^8, i = 1, 2, 3$
Number of teeth	$Z_{12} = 30, Z_{21} = 45$
Normal load [N]	$N = 1000$

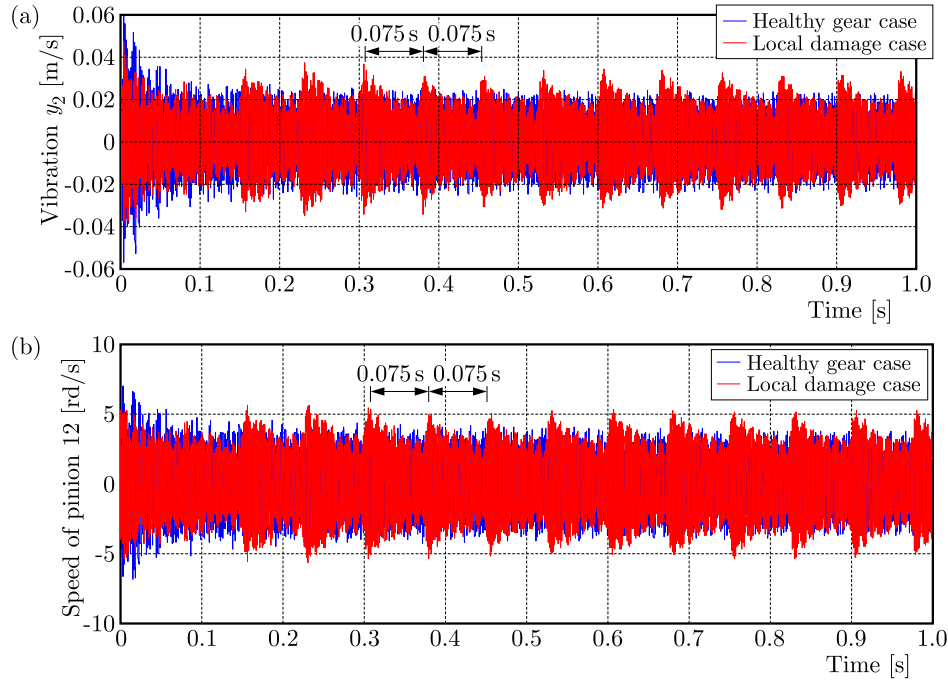


Fig. 7. Time response of the second bearing speed along the y direction (a) and of the pinion speed (b); red line – case with the defect, blue line – case without the defect

applied to the friction disc are taken into account which allows us to give an idea on the torque transmitted by the clutch. The disc brake is treated by studying disc vibration since the disc undergoes the most important vibration

$$\text{DTE} = \theta_{12} - \frac{Z_{21}}{Z_{12}} \theta_{21} \quad (4.1)$$

where Z_{12} and Z_{21} represents, respectively, the teeth number of pinions 12 and 21.

On the temporal signal, the dynamic transmission error DTE magnitude does not give a significant change with the presence of a fault. It is hard to detect clear symptoms of any error in the system from the time domain only, especially when the system is complex. The frequency domain can be used and it is the most popular approach to diagnosis of defects of the gear. The spectrum of the DTE in two cases, healthy and defected pinions, are shown in Fig. 8. In the frequency spectrum in Fig. 9, two frequencies appear: frequency of the meshing stiffness f_m and its harmonics, and frequency of rotation of the pinion f_p . The spectrum shows peaks corresponding to the harmonic frequencies f_p . The other peaks represent the natural frequencies of the system.

The dynamic behavior of the clutch affects not only the dynamics of the drivetrain system but also the transfer of the excitation to drive wheels. Figure 9 shows the temporal signals

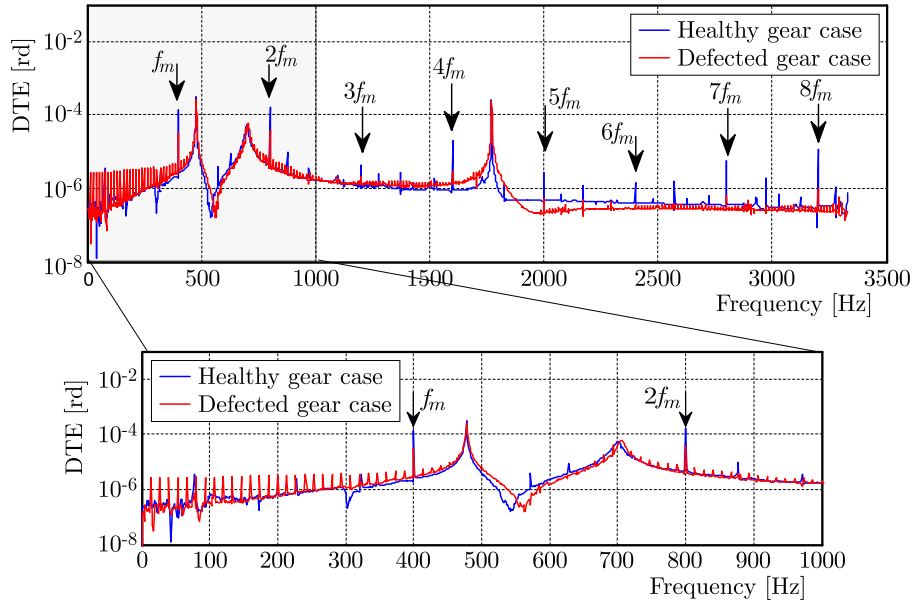


Fig. 8. Spectrum of the dynamic transmission error; red line – case with the defect, blue line – case without the defect

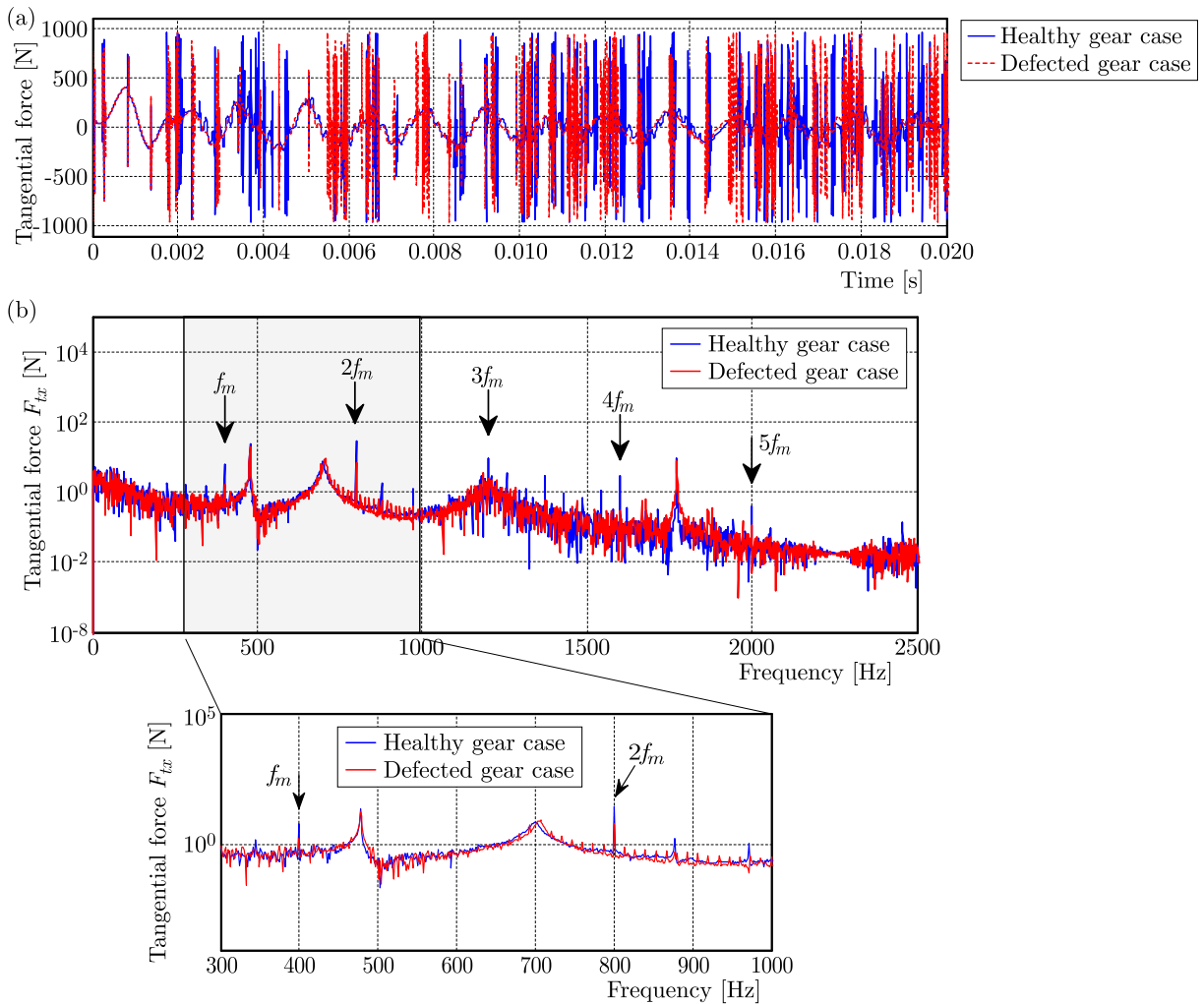


Fig. 9. Nonlinear tangential force $F_{T_{x2/3}}$ along the x direction: (a) time response, (b) corresponding spectrum; red line – case with the defect, blue line – case without the defect

and the frequency spectrum of the clutch tangential force $F_{Tx2/3}$ along the x direction. In the case without the defect, the spectra show peaks around the meshing frequency f_m and some eigenfrequencies (in the frequency band 300 Hz to 1000 Hz). The dynamic model in this case is excited only by the periodic time varying meshing stiffness (internal excitation). In the presence of local damage, there appears in the spectrum a new peak at the frequency f_p , which corresponds to the frequency of rotation of gear 12.

Figure 10 shows spectra of the two tangential forces applied by the second block on the third block and defined by Eq. (3.10) in the case with the defect. In the presence of the gear fault, the same remarks are available for $F_{Ty2/3}$ with $F_{Tx2/3}$, and we can interpret that the force amplitude along the y direction is slightly higher than the force along the x direction.

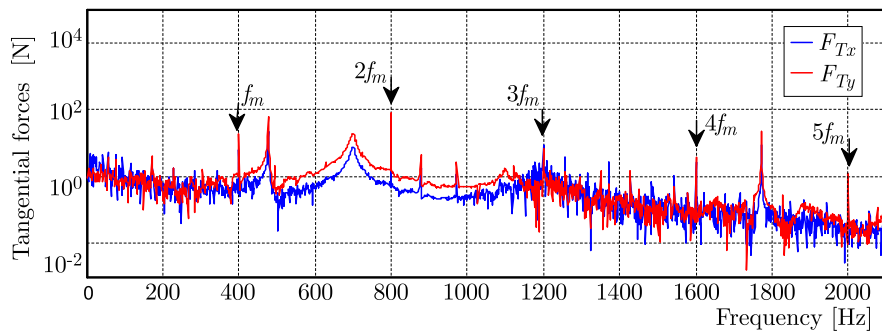


Fig. 10. Nonlinear tangential forces along x and y directions; blue line – F_{Tx} , red line – F_{Ty}

Figure 11 represents the frequency response of linear rotation of the brake disc. We can clearly see the presence of several peaks corresponding to the mesh frequency with their harmonic and natural frequency of the system. Also, other peaks can be shown which represent the frequency of pinion rotation f_p . This is due to local damage of the gearbox.

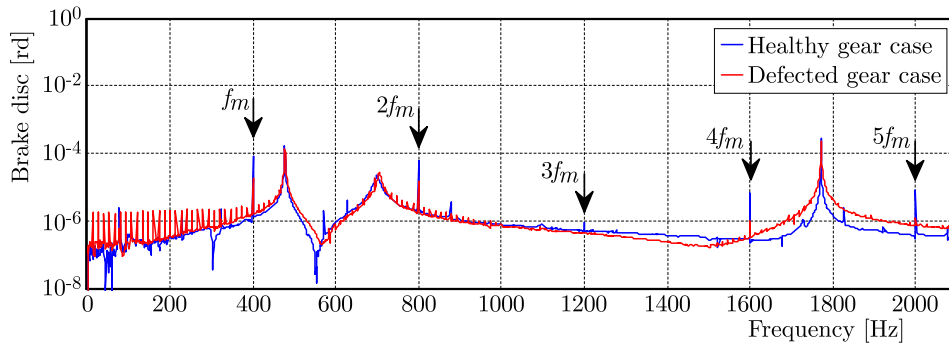


Fig. 11. Spectrum of the brake disc vibration; red line – case with the defect, blue line – case without the defect

4.2. Effect of the profile error in spur gear on the dynamic response

In gear systems, the profile defect is characterized by deviation of shape between the ideal profile of a tooth and the theoretical profile in the form of a circle. This defect often comes from the process of machining of teeth. The profile defect is introduced into equations of motion by adding the exciting term of the displacement type denoted by e_{12} at the level of tooth deflection on the line of action. This defect is modelled in Fig. 12.

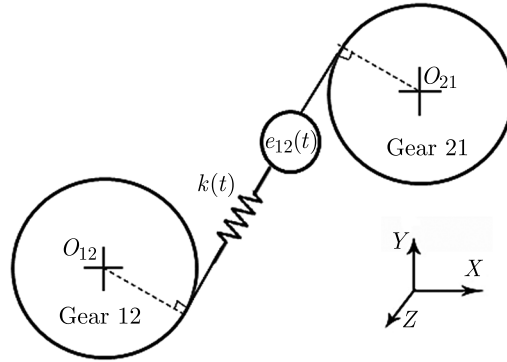


Fig. 12. Profile error modelling

The profile error is assumed to be uniform over all teeth. Transmission error due to this defect can be assimilated by a function which varies periodically with the meshing period T_m as

$$e_{12}(t) = e_{12} + \sum_{i=1}^{\infty} e_{12} \sin(2\pi i f_m t) \tag{4.2}$$

where e_{12} , f_m and t are, respectively, the error profile amplitude, meshing frequency and time variation.

The introduction of this excitation into the equations of motion gives rise to a supplementary force of external origin given by

$$\mathbf{F}_{sup} = k(t)e_{12}(t)\mathbf{L}_\delta \tag{4.3}$$

The profile error of the gear with the amplitude $e_{12} = 50 \mu\text{m}$ will amplify the amplitude of the transmission error. This result is illustrated in Fig. 13a. The logarithmic representation of the spectrum shows that the meshing frequency is amplified and will be clear in the frequency shape with detecting other peaks in the signal (Fig. 13b).

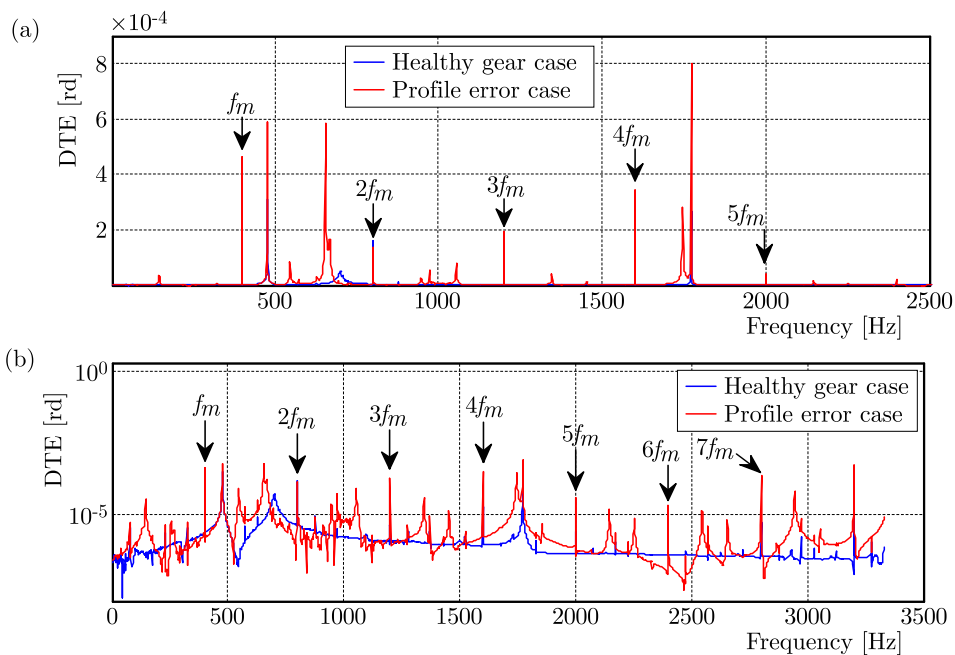


Fig. 13. Spectrum of the dynamic transmission error: (a) linear scale, (b) logarithmic scale; red line – case with the profile error, blue line – case without the defect

These results are validated with the spectrum frequency of the tangential force of the clutch and brake disc vibration in Figs. 14 and 15. The frequency level increases but the signal will be more complex and difficult to treat especially with the logarithmic representation.

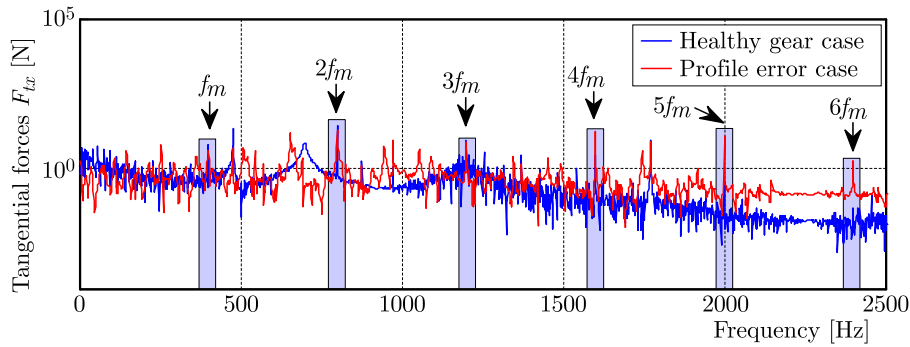


Fig. 14. Spectrum of nonlinear tangential forces $F_{Tx2/3}$ along the x direction; red line – case with the profile error, blue line – case without the defect

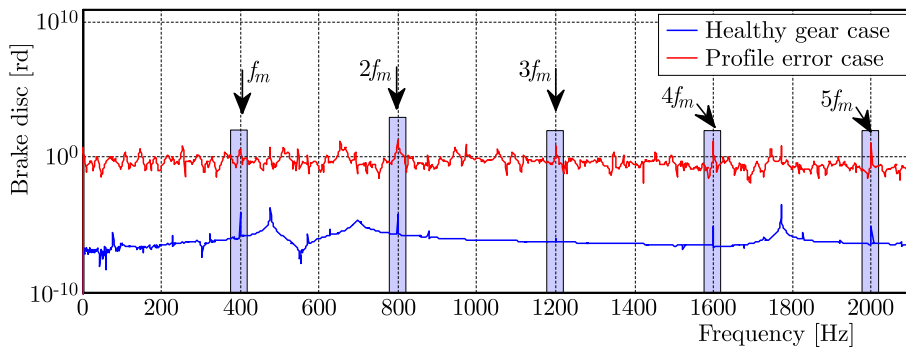


Fig. 15. Spectrum of brake disc vibration; red line – case with the profile error, blue line – case without the defect

4.3. Effect of the two gear defects on the dynamic response

Figures 16, 17 and 18 represent the frequency response on the dynamic components of the transmission error, clutch tangential force and brake disc torsional vibration in the two case studies. We conclude that the effects of the two faults are clear in the spectrum representation, especially in the DTE signal. The local damage detected by appearing as side bands of the fundamental frequency and the profile error can be diagnosed by amplification of the frequency. Another interpretation can be noticed that the peaks due to the local defect are also amplified.

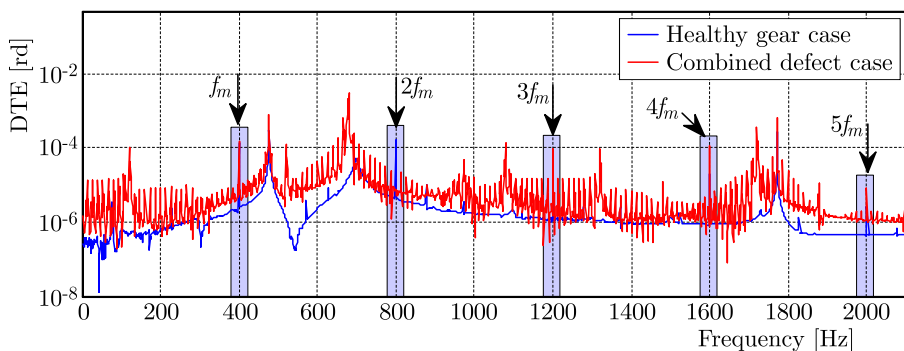


Fig. 16. Spectrum of the dynamic transmission error; red line – with two defects, blue line – without defects

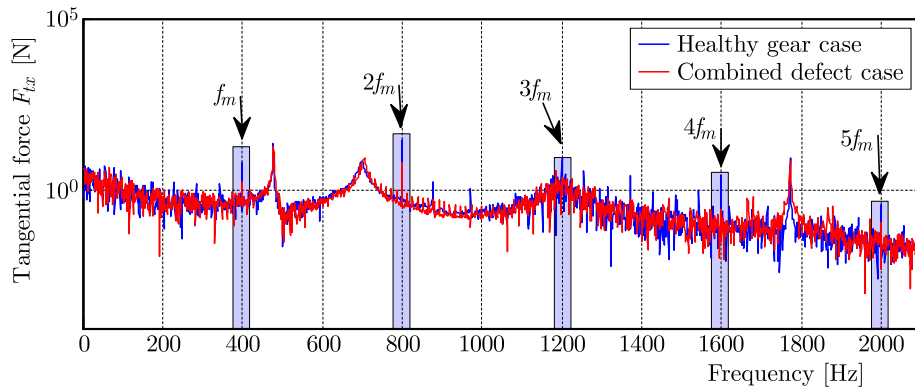


Fig. 17. Spectrum of the tangential force $F_{T_{x2/3}}$ along the x axis; red line – with two defects, blue line – without defects

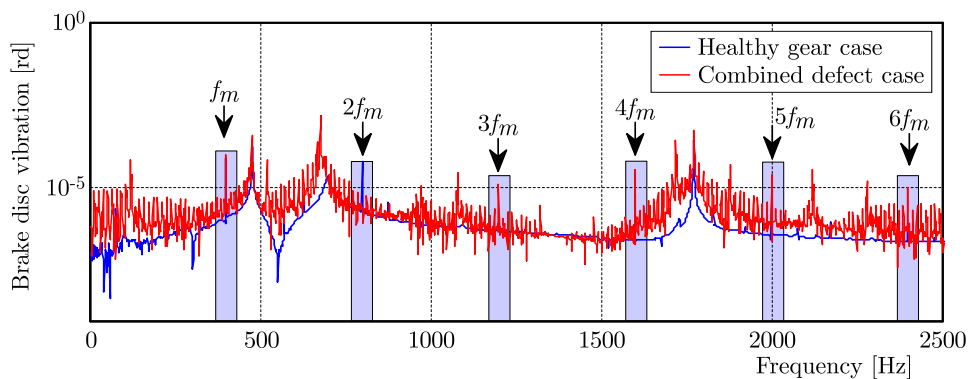


Fig. 18. Spectrum of brake disc vibration; red line – with two defects, blue line – without defects

5. Conclusion

The purpose of this research work is to develop a nonlinear dynamic model of a vehicle drivetrain system, introduce two typical defects and investigate the effect of these faults on the dynamic response of the system. To achieve this outcome, the developed model with thirteen degrees of freedom that includes engine excitation, clutch, gearbox and disc brake is detailed and the differential governing equation is solved by the Runge Kutta integration method. The dynamic behavior of both the faultless drivetrain (without defect), and the mechanism with the local damage and profile error of the gear is compared in time and frequency domains. In the faultless mechanism, the spectrum reveals peaks at the meshing frequencies f_m and the dominant eigenfrequency. In the presence of the local defect, amplitude modulation occurs in the time signal of the bearing and the gear. From the FFT spectrum, it is observed that the effect of the local fault appears in the frequency domain signal as sidebands of the pinion rotation frequency. Introducing the profile error, the signal vibratory level increases. These results are verified in the literature. Finally, the two defects are integrated together and despite the complexity of the system, the two faults in the frequency representation can be detected. Comparison of these frequency spectra at the healthy and defected condition of the gear transmission reflects significant symptoms of local damage and profile errors on the vibrational behavior of the system.

References

1. ABOUEL-SEoud S., IBRAHIM A., MOHAMED K., 2012, An experimental study on the diagnostic capability of vibration analysis for wind turbine planetary gearbox, *International Journal of Modern Engineering Research*, **2**, 3, 667-675

2. AHERWAR A., KHALID MD.S., 2012, Vibration analysis techniques for gearbox diagnostic: a review, *International Journal of Advanced Engineering Technology*, **3**, 2, 4-12
3. AHMED I., 2011, Analysis of disc brake squeal using a ten-degree-of-freedom model, *International Journal of Engineering, Science and Technology*, **3**, 142-155
4. BEMPORAD A., BORRELLI F., GLIELMO L., VASCA F., 2001, Optimal piecewise-linear control of dry clutch engagement, *IFAC Workshop Advances in Automotive Control*, 33-38
5. BRANCATI R., ERNESTO R., RICCARDO R., 2007, An analysis of the automotive driveline dynamic behaviour focusing on the influence of the oil squeeze effect on the idle rattle phenomenon, *Journal of Sound and Vibration*, **303**, 858-872
6. CHAARI F., BACCAR W., ABBES M.S., HADDAR M., 2008, Effect of spalling or tooth breakage on gear mesh stiffness and dynamic response of a one-stage spur gear transmission, *European Journal of Mechanics-A/Solids*, **27**, 691-705
7. DIVANDARI M., AGHDAM B.H., BARZAMINI R., 2012, Tooth profile modification and its effect on spur gear pair vibration in presence of localized tooth defect, *Journal of Mechanics*, **28**, 373-381
8. DRISS Y., FAKHFAKH T., HADDAR M., 2007, Effect of eccentricity on a clutch system under a harmonically varying normal load, *Journal of Failure Analysis and Prevention*, **7**, 127-136
9. FAKHFAKH T., CHAARI F., HADDAR M., 2005, Numerical and experimental analysis of a gear system with teeth defects, *The International Journal of Advanced Manufacturing Technology*, **25**, 542-550
10. FAKHFAKH T., WALHA L., LOUATI J., HADDAR M., 2006, Effect of manufacturing and assembly defects on two-stage gear systems vibration, *The International Journal of Advanced Manufacturing Technology*, **29**, 1008-1018
11. FOSBERRY R.A.C., HOLUBECKI Z., 1961, *Disc Brake Squeal: its Mechanism and Suppression*, Motor Industry Research Association
12. GAILLARD C.L., SINGH R., 2000, Dynamic analysis of automotive clutch dampers, *Applied Acoustics*, **60**, 399-424
13. GHORBEL A., ABDENNADHER M., ZGHAL B., WALHA L., HADDAR M., 2017, Modal analysis and dynamic behavior for analytical drivetrain model, *Journal of Mechanics*, DOI: 10.1017/jmech.2017.23
14. HOWARD I., JIA S., WANG J., 2011, The dynamic modelling of a spur gear in mesh including friction and a crack, *Mechanical Systems and Signal Processing*, **15**, 831-853
15. KHABOU M.T., KSENTINI O., JARRAYA A., ABBES M.S., CHAARI F., HADDAR M., 2014, Influence of disk brake friction on the dynamic behaviour of a directly coupled spur gear transmission, *Multidiscipline Modeling in Materials and Structures*, **10**, 146-162
16. KIM W., YOO H.H., CHUNG J., 2010, Dynamic analysis for a pair of spur gears with translational motion due to bearing deformation, *Journal of Sound and Vibration*, **329**, 4409-4421
17. KOBRA H., HOJAT A., OMID M., 2010, Adaptive vibration condition monitoring techniques for local tooth damage in gearbox, *Modern Applied Science, Canadian Center of Science and Education*, **4**
18. KRAK M., JASON D., SINGH R., 2015, Development of a non-linear clutch damper experiment exhibiting transient dynamics, *SAE Technical Paper Series*, 01-2189
19. MASHADI B., MILAD B., 2015, Driveline oscillation control by using a dry clutch system, *Applied Mathematical Modelling*, **39**, 6471-6490
20. RINCON A.F.D., VIADERO F., IGLESIAS M., JUAN A.D., GARCIA P., SANCIBRIAN R., 2012, Effect of cracks and pitting defects on gear meshing, *Proceedings of the Institution of Mechanical Engineers, Part C: Journal of Mechanical Engineering Science*, **226**, 2805-2815
21. SALEH A., KRAK M., JASON D., SINGH R., 2015, Development of refined clutch-damper subsystem dynamic models suitable for time domain studies, *SAE Technical Paper Series*, 01-2180

22. TEMPLIN P., EGARDT B., 2009, An LQR torque compensator for driveline oscillation damping, *18th IEEE International Conference Control Applications*, 352-356
23. WALHA L., FAKHFAKH T., HADDAR M., 2009, Nonlinear dynamics of a two-stage gear system with mesh stiffness fluctuation, bearing flexibility and backlash, *Mechanism and Machine Theory*, **44**, 1058-1069
24. WALHA L., DRISS Y., KHABOU M.T., FAKHFAKH T., HADDAR M., 2011, Effects of eccentricity defect on the nonlinear dynamic behavior of the mechanism clutch-helical two stage gear, *Mechanism and Machine Theory*, **46**, 986-997
25. WU H., GUANGQIANG W., 2016, Driveline torsional analysis and clutch damper optimization for reducing gear rattle, *Shock and Vibration*, **11**, 1-24
26. XUE-LAI L., WEN-BIN S., XINGJIAN J., WAIZUDDIN A., 2016, Vibration isolation analysis of clutches based on trouble shooting of vehicle accelerating noise, *Journal of Sound and Vibration*, **382**, 84-99

Manuscript received May 25, 2017; accepted for print December 4, 2017

NUMERICAL ANALYSIS OF THE DEEP DRAWING PROCESS INCLUDING THE HISTORY OF STRESS AND STRAIN

PAWEL KALDUNSKI

Koszalin University of Technology, Koszalin, Poland

e-mail: pawel.kaldunski@tu.koszalin.pl

This paper discusses the results of a numerical study of circular cup drawing of steel sheets using finite element method. The drawing process is considered as a geometrical and physical nonlinear problem with unknown boundary conditions in the contact area of the system, such as the tool and the workpiece. The updated Lagrangian description is used to characterize these nonlinear phenomena on a typical incremental step time. Numerical results are obtained using an explicit method in Ansys/Ls-Dyna program. The constitutive Cowper-Symonds material model with linear hardening strain to predict material plasticity is used. The results of implementation of stresses and strains from a blanking operation flat disc of a sheet of metal for deep-drawing process are presented. After the blanking process simulation, an implicit springback analysis is performed. Then a numerical analysis of cup forming from this flat disc plate was carried out. The analysis results are compared with one another through reading of the sheet thickness in several characteristic points and the overall height of the product.

Keywords: deep drawing, modeling, numerical analysis, FEM, stress history, strain history

1. Introduction

At present, in metal forming industry, preparation of three-dimensional models for the drawing is very important to explain and to understand specific forming processes which occur in the drawpiece. There are many different methods of building finite element models of drawing examples using 2D numerical and analytical models (Yao and Cao, 2001). Currently, in the modelling and simulation of drawing processes, the influence on state of stress and strain prior treatments is mainly omitted (Nagasekhar *et al.*, 2006; Trzepiecinski and Gelgele, 2011). Apart from the unknown state after sheet rolling (Kim and Olver, 1998), during the blanking process, additional stress is placed on the disc periphery. The blanking process is understood as cutting out a flat disc from a flat metal sheet (Bohdal *et al.*, 2014). As the tool, a die and a punch with cutting edges were used, and to prevent possible warping of the disc after cutting out, a blankholder was used (Urriolagoitia-Sosa *et al.*, 2011). Then, the drawpiece without a flange was formed from the flat disc.

This paper presents the results of a comprehensive modelling of the drawing process including the history of stress and strain. The blanking process modelling has been carried out, which takes into account a springback phenomenon that occurs after the load is removed. Such an analysis allows a more accurate determination of the finished product dimensions, the drawing force in the whole process, and it permits one to determine the state of stress at any place of the drawpiece. From the mechanical perspective, this process is treated as a doubly nonlinear initial-boundary value problem with movable nonlinear sources and boundaries and only partial knowledge of the boundary conditions. The following nonlinearities occur in the process: geometric, physical and boundary conditions in the area of tool-sheet contact. The geometric nonlinearity, which is thought to be a nonlinear dependence between the strain and displacement, results from a change

in the object geometry. The physical (i.e., material) nonlinearity is caused by nonlinearity of the mechanical properties of the material. A mathematical description of these nonlinear phenomena requires the use of rules regarding formulation of boundary and initial problems.

2. Finite element modelling

The description of nonlinearity of the material is conducted using an incremental model that takes into account the influence of the history of strains. The object is treated as a body in which elastic strains may occur (in the scope of reversible strains) together with plastic strains (in the scope of irreversible strains) with nonlinear hardening (Gambin and Kowalczyk, 2003). For the purpose of constructing a material model, the following are used: Huber-Mises-Hencky's nonlinear plasticity condition, the associated flow law and isotropic hardening (Jemiolo and Gajewski, 2014). The state of the material after the aforementioned processing is taken into account by introducing the following initial states: displacement, stresses and strains. The states of strains are described with nonlinear dependences and no linearization (Simo and Hughes, 1998). In this description, adequate measures are used for an increment of strains and for an increment of stresses (i.e., an increment of the Green-Lagrange strain tensor and an increment of the second Piola-Kirchhoff symmetric stress tensor). The incremental contact model covers contact forces, contact rigidity, contact boundary conditions and friction coefficients in this area. The mathematical model is supplemented with incremental equations of motion of the object and uniqueness conditions. An incremental function of the total energy of the system is introduced. From the stationary condition of this function, it is possible to derive a variational nonlinear equation to describe motion and deformation of the object for a typical incremental step. This equation is untangled with spatial discretization using the finite element method, which results in discrete systems of equations for motion and deformation of the object in the drawing process (Zienkiewicz and Taylor, 2006).

2.1. Basic relationships

Components of the Green-Lagrange strain tensor increment for a typical time step Δt and for a non-linear isotropic material with mixed hardening are calculated from the formula (Bohdal and Kukielka, 2014; Bohdal, 2015)

$$\Delta\varepsilon_{ij} = \frac{1}{1 - \tilde{S}^{**}} \left(D_{ijkl}^{(E)} \Delta\sigma_{kl} - \frac{\frac{2}{3}\sigma_Y(\cdot) \dot{E}_T \Delta\dot{\varepsilon}_e \tilde{S}_{ij}}{\tilde{S}_{ij} C_{ijkl}^{(E)} \tilde{S}_{kl} + \frac{2}{3}\sigma_Y^2(\cdot) (\tilde{C}(\cdot) + \frac{2}{3}E_T)} \right) \quad (2.1)$$

Components of the Piola-Kirchhoff stress tensor increment for a typical time step Δt and for a non-linear material with mixed hardening are calculated using the formula

$$\Delta\sigma_{ij} = C_{ijkl}^{(E)} \left(\Delta\varepsilon_{kl} - \psi \frac{\tilde{S}_{kl} \left(\tilde{S}_{ij} C_{ijkl}^{(E)} \Delta\varepsilon_{kl} - \frac{2}{3}\sigma_Y(\cdot) \dot{E}_T^{(VP)} \Delta\dot{\varepsilon}_z^{(VP)} \right)}{\tilde{S}_{ij} C_{ijkl}^{(E)} \tilde{S}_{kl} + \frac{2}{3}\sigma_Y^2(\cdot) (\tilde{C}(\cdot) + \frac{2}{3}E_T)} \right) \quad (2.2)$$

where ψ is the load factor and is $\psi = 1$ for loading and $\psi = 0$ for unloading processes, $\tilde{S}^{**} = \tilde{S}_{ij}^* C_{ijmn}^{(E)} \tilde{S}_{mn}$ is a positive scalar variable, $\tilde{S}_{ij} = S_{ij} - \alpha_{ij}$ ($i, j = 1, 2, 3$) are the stress deviator components, $\tilde{\mathbf{D}}_\sigma$ and $D_{ijkl}^{(E)}$ are components of the tensor $\mathbf{D}^{(E)} = \mathbf{C}^{(E)-1}$ in time t , $C_{ijkl}^{(E)}$ are the elastic constitutive tensor components $\mathbf{C}^{(E)}$, $\tilde{C}(\cdot) = \tilde{C}(\varepsilon_e^{(VP)}, \dot{\varepsilon}_e^{(VP)})$ is the temporary translation hardening parameter in time t . $\sigma_Y(\cdot) = \sigma_Y(\varepsilon_e^{(VP)}, \dot{\varepsilon}_e^{(VP)})$ is the accumulated material yield stress which depends on the history

of viscoplastic strain and strain rate, $\varepsilon_e^{(VP)}$ and $\dot{\varepsilon}_e^{(VP)}$ are the cumulative effective viscoplastic strain and strain rates, respectively, E_T is the strain hardening modulus at time t , \dot{E}_T is the strain hardening modulus rate at time t (Bohdal, 2015).

In the analysis of the deep drawing process, the bilinear model is used. This material model has a linear hardening relationship between stress and strain described with the empirical model: $\sigma_Y = \sigma_{Y0} + E_{tan}\varepsilon_{eq}^{(P)}$, where σ_{Y0} is the initial yield stress, $E_{tan} = (E_T E)/(E - E_T)$ is the material parameter dependent on the modulus of plastic hardening $E_T = d\sigma_Y/d\varepsilon_{eq}^{(P)}$ and Young's elastic modulus E , $\varepsilon_{eq}^{(P)}$ is the equivalent plastic strain. The Cowper-Symonds elastic/viscoplastic material model is used for computer simulation of the cutting process. According to the strain criterion, material separation occurs when the strain value of the leading node is greater than or equal to a limiting value. The limiting strain used is $\varepsilon_f = 1$. When an element of the matrix material reaches the limiting strain value, the corresponding element will be deleted. The Cowper-Symonds model allows for linear isotropic ($\beta = 1$) assumed in simulations, kinematic ($\beta = 0$) or mixed ($0 < \beta < 1$) plastic strain hardening, and the effect of the plastic strain velocity is given by the following power relation

$$\sigma_p = \left(1 + \frac{\dot{\varphi}_i^{(p)}}{C}\right)^m (R_e + \beta E_p \varphi_i^{(p)}) \quad (2.3)$$

where β is the plastic strain hardening parameter, R_e [MPa] is the initial static yield point, $\dot{\varphi}_i^{(p)}$ [s^{-1}] is the plastic strain rate, C [s^{-1}] is the material parameter defining the effects of the plastic strain rate, $m = 1/P$ is the material constant defining the sensitivity of the material to the plastic strain rate, $\varphi_i^{(p)}$ [-] is the plastic strain intensity, and $E_p = (E_T E)/(E - E_T)$ is a material parameter dependent both on the plastic strain hardening modulus, $E_T = \partial\sigma_p/\partial\varphi_i^{(p)}$, and Young's modulus E .

3. Numerical model and results

The blanking and drawing tools are treated as non-deformable bodies, i.e., $E \rightarrow \infty$. The following material parameters are assumed for DC01 deep-drawing steel (Kaldunski, 2009): Young's modulus $E = 210$ GPa, Poisson's ratio $\nu = 0.29$, density $\rho = 8000$ kg/m³, yield stress $R_e = 200$ MPa, tangent modulus $E_{tan} = 1050$ MPa.

In this study, the objects are meshed with an 8-node SOLID 164 element type with reduced integration and hourglass control. The sheet has been divided into cubic elements to eliminate the influence of non-uniform mesh on the final results. The contact between ideally rigid tools and the deformable sheet metal is described using Coulomb's friction model according to the formula

$$\mu_c = F_D + (F_S - F_D)e^{-D_C|v_{rel}|} \quad (3.1)$$

where F_D is the dynamic friction coefficient, F_S – static friction coefficient, D_C – exponential decay coefficient, e – Euler's number, v_{rel} – relative velocity of the surfaces in contact.

The following coefficients of friction in the contact zone between the stamp and sheet have been adopted: static friction coefficient $\mu_s = 0.2$, dynamic friction coefficient $\mu_d = 0.1$.

The following coefficients of friction in the contact zone between the die block and sheet have been adopted: static friction coefficient $\mu_s = 0.1$, dynamic friction coefficient $\mu_d = 0.01$.

The D_C exponential decay coefficient is 10. The dependence of the coefficients of friction between the sheet and the stamp on the relative velocity of the surfaces in contact is presented with the solid line on the graph (Fig. 1), while the dotted line shows the dependence of the friction coefficients between the sheet and the die block.

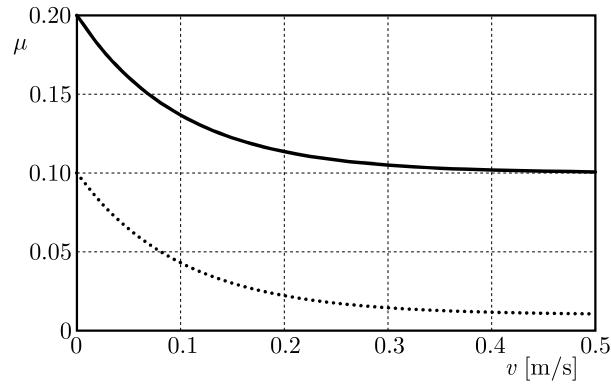


Fig. 1. Friction coefficient as a function of relative velocity of the surfaces in contact

An additional blankholder is applied from the bottom, which eliminates the bulge out effect of the blanked element. The type of the material used for this calculation is sheet metal stamping DC 01 with thickness $g = 2$ mm. Diameter of the blanked disc $D = 70$ mm. Figure 2 shows the initial mesh of the blanking process. The cutting areas of the die and punch are divided on a denser mesh to increase the calculation accuracy.

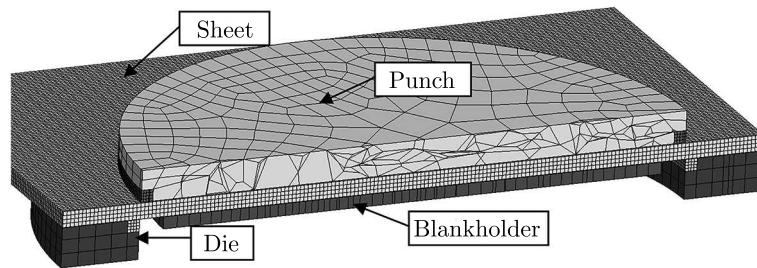


Fig. 2. Initial mesh of the blanking process

Figure 3 shows the equivalent stress distribution in the blanked disc. It may be observed that the maximum stress values are located on the disc periphery in the cutting area.

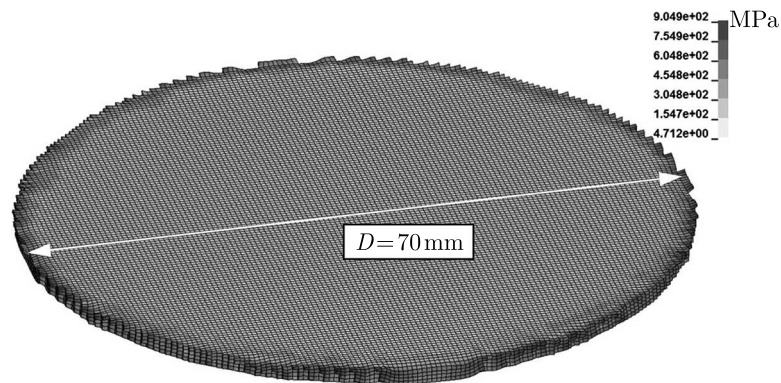


Fig. 3. Equivalent stress distribution in the blanked disc

Figure 4 shows the equivalent stress distribution in the disc after unloading. This analysis is necessary in a multistage process. Otherwise, in further simulations, it does not receive any correct results. It can be observed that the values of the equivalent stress at the periphery of the disc after removing the elastic strain is almost 3 times reduced.

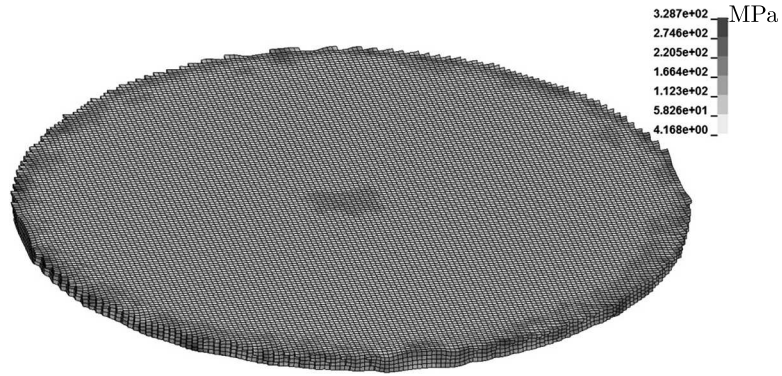


Fig. 4. Equivalent stress distribution in the blanked disc after springback

3.1. Deep drawing without the history of stress and strain

Figure 5 shows a cross-sectional view of a discrete model of the drawing process (Kaldunski and Kukielka, 2014). The die which is used has rounding radius $r_d = 16$ mm and internal diameter $d = 40$ mm. The punch diameter has rounding radius $r_p = 4$ mm and its diameter is equal to $d_p = 35$ mm. The clearance die is therefore 2.5 mm. An acceptable reduction of the diameter in the drawing process determined by the m_1 coefficient for the ratio $D/g = 35$ equals $m_1 = 0.5$ (Table 1). This means that the value $m_1 = d/D = 0.57$ is acceptable.

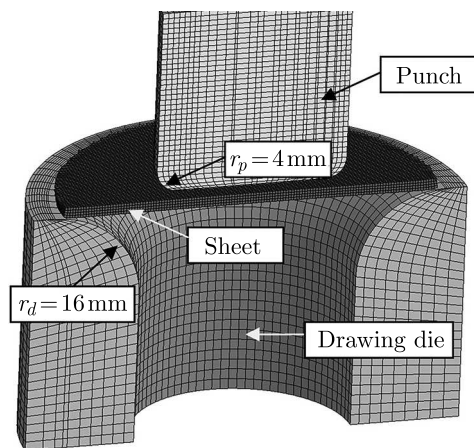


Fig. 5. A discrete model of the drawing process

Table 1. Acceptable reduction of the diameter in the drawing process for the ratio D/g (Marciniak, 1998)

D/g	$m_1 = d/D$
630	0.62
400	0.60
250	0.58
160	0.56
100	0.54
63	0.52
40	0.50
25	0.48

At first, analysis of the numerical drawing process without taking into account the history of stress and strain from the blanking has been performed. Thus, the initial values of stress and strain in all elements and nodes were 0. What was left was only the mesh deformation of the disc as a result of blanking. Figure 6a shows a map of the equivalent stresses in the finished drawpiece. It can be observed that the values are rising from the bottom transition area through the side wall to the periphery. The maximum values of stresses during the drawing process occur at the periphery as a result of circumferential compressive stresses. Unevenness on the edge results from sheet discretization.

After the drawpiece forming simulation, a springback type analysis has been performed. It is analysis performed with the implicit integration method. It enables removal of all the nodes and elements of elastic strains, and it simulates the release of the product from the die. As a result of the removal of elastic strains, the product undergoes expansion, and its external diameter increases from 40 mm (Fig. 6a) to 40.13 mm (Fig. 6b). Also, the stresses occurring at the periphery of the drawpiece are reduced by approximately 25%. Moreover, their location change. They occur in around half of the product height.

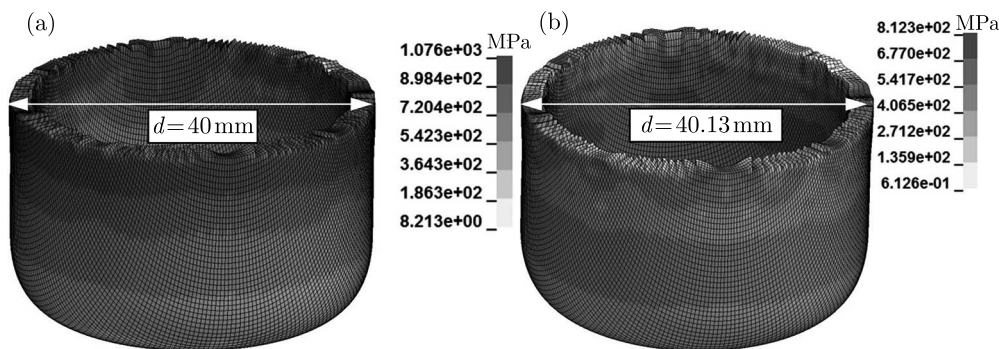


Fig. 6. Maps of the equivalent stress in the drawpiece without history: (a) before springback, (b) after springback

3.2. Deep drawing with the history of stress and strain

To simulate the drawing process including the history of stress and strain, the disc after blanking and after springback analysis has been imported. To simulate the drawing process including the history of stress and strain, in the disc after blanking and after springback, analysis was performed taking into account the stress and strain values. All the conditions for the process, that is: diameters and radii remained unchanged. Figure 7a shows maps of the equivalent stress in the finished product. It can be seen that also in this case, the maximum stresses are located on the periphery of the product. However, the values are about 66% higher than in the case without including the history of stress and strain. In addition, the process of shaping the product proceeded in the same manner as in the previous case. The obtained diameter of the drawpiece corresponds to the internal die diameter, i.e. 40 mm.

At the next stage, the springback analysis has been performed (Fig. 7b). The product behaved in a similar manner as in the case without including the history. The maximum stress value was migrated from the periphery to about half of the drawpiece height and decreased by 45%. The diameter of the product was increased to 40.11 mm, so that was almost the same as without including the stress and strain history.

3.3. Comparison of two examples

The next step is a detailed comparison of the drawpiece obtained without including the history of stress and strain with the drawpiece in which that history is included. Figure 8 shows

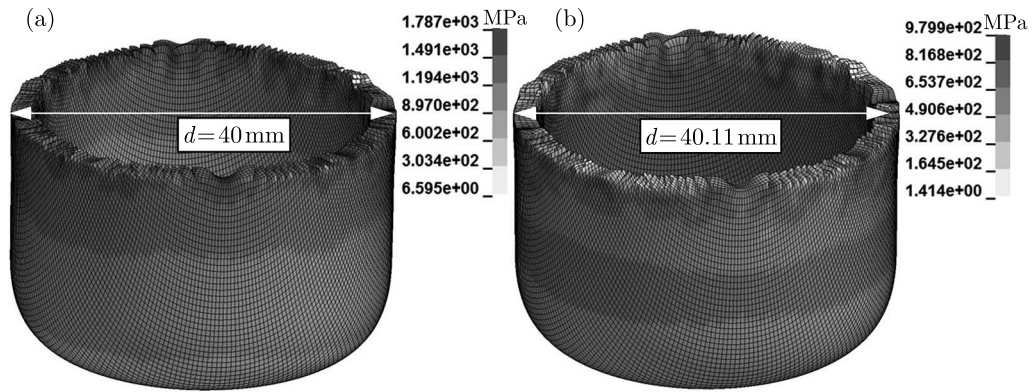


Fig. 7. Maps of the equivalent stress in the drawpiece with history: (a) before springback, (b) after springback

the graph of the drawing force as a function of punch displacement for these two cases. The solid line represents the dependence with including the history. The dotted line represents the dependence without including the history. It can be observed that the two graphs are similar in characteristics. The differences are only in terms of the value, and there is a slight shifting. The fluctuations at the first stage of the graph are probably a result of discontinuous contact at the beginning of the drawing process. The maximum drawing force in the case with the history included is equal to 65 kN, without including the history it is less by about 7 kN. The difference in the value due to the fact that the disc has hardening at the periphery after blanking. This requires a greater force to deform it further. In both cases, the achievement of the maximum drawing force occurred at the punch displacement being equal to 25 mm. This is the moment where there is the greatest peripheral drawpiece flange compression.

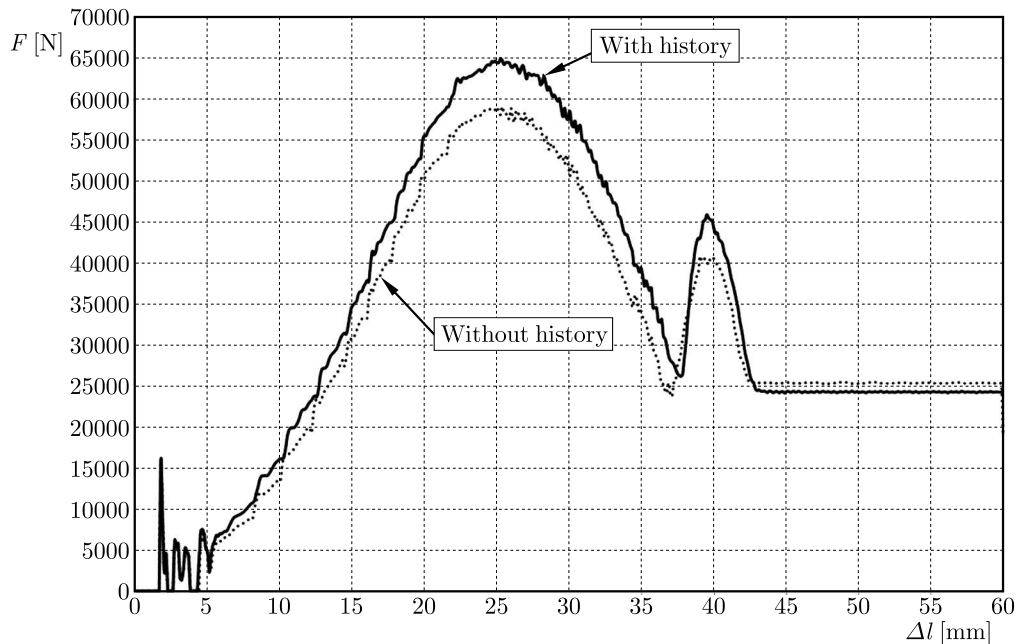


Fig. 8. Dependence of the drawing force from punch displacement

Figure 9 shows the deformation of the product for the maximum drawing force without including the history of stress and strain. After passing the maximum value of the drawing force, its value decreases until the periphery of the drawpiece is located directly between the die and the punch. At this point, the drawing force increases again, in the case with including

the history up to 46 kN, and for the case without the history up to 41 kN. This increase results directly from the clearance between the die and the punch. In this case, this is adopted less intentionally to observe the effect it would have on the formation of the product. This moment is illustrated in Fig. 10. The final step of drawpiece forming can be observed, which consists in compression of the drawpiece peripheral to the size of the clearance equal to 2.5 mm. An improper selection of the clearance may cause at this point, during the experiment on the hydraulic press, jamming and damage of the tools.

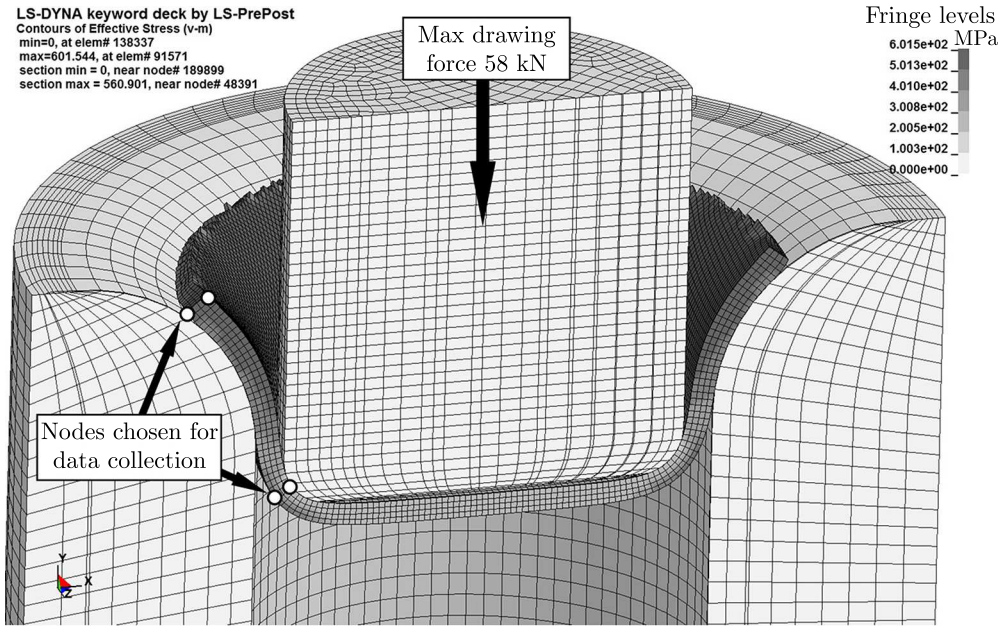


Fig. 9. Deformation of the product for the maximum drawing force without the history of stress and strain

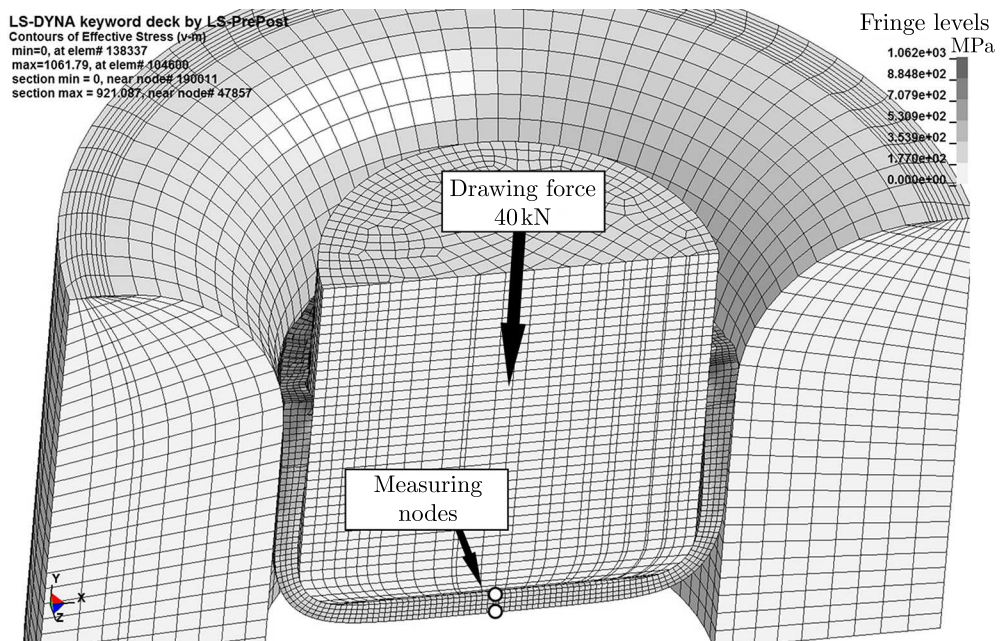


Fig. 10. Final drawpiece formation without the history of stress and strain

Apart from the drawing force, it is also possible to compare products in terms of their geometry and shape. Namely, the two drawpieces sheet thicknesses in characteristic locations and their total heights are compared. The reading is performed between the same nodes in each case. This proceeding allows us to eliminate errors of the mesh deformation, or other reading inaccuracies. Figure 11a shows a graph of the sheet thickness changes at the drawpiece periphery as a function of the punch displacement. It can be observed that the drawpiece, almost from the beginning of the drawing process with the history included, has a greater thickness at its periphery. This is due to the fact that the compressive circumferential stress during the process is cumulative with the stress after blanking. The compression of such a tensioned material is difficult, therefore, some of the material moves inwards or outwards and causes enlargement of the sheet thickness. The maximum difference in the thickness of the sheet metal at the periphery occurs before the punch and reaches a 40 mm displacement. For the drawpiece with the history included, the thickness is equal to 2.77 mm, whereas without the history is equal to 2.68 mm. This situation occurs immediately before the moment the periphery is compressed between the punch and the die, as shown in Fig. 10. Then, after forming the drawpiece walls to the cylindrical form, the edge thickness is nearly identical for the two cases and it is 2.54 mm for the case with and 2.53 mm without the history. The value at end in both cases that is larger than the clearance value equal to 2.5 mm is due to friction. The nodes between which the reading is made are not in a perfectly horizontal position. As a result of sliding friction on the die and static on the punch, its minor displacement occurs.

Another dimension that is compared in both cases is the sheet thickness measured at the center of the drawpiece bottom. The reading has been conducted in the same manner as before. What is measured during the whole process is the distance between nodes, at the outer and inner surface, in the middle of the disc. The reading results are presented in the graph in Fig. 11b. The reading starts from the initial value of the sheet thickness of 2.01 mm. Then, during the process, small thinning follows in the bottom sheet. In the case where the history of stress and strain is included, the thickness in the final product is 1.96 mm, whereas without history it is 1.97 mm. A reduction in the sheet thickness in this area is due to radial extension of the bottom during the drawing process. This is often so slight thinning that besides the reading of the simulation result it is very difficult to observe. Also in this case, the difference on the level of 0.01 mm is only a general value, that the history of stress and strain causes a marginal effect on the change in the thickness of the bottom drawpiece.

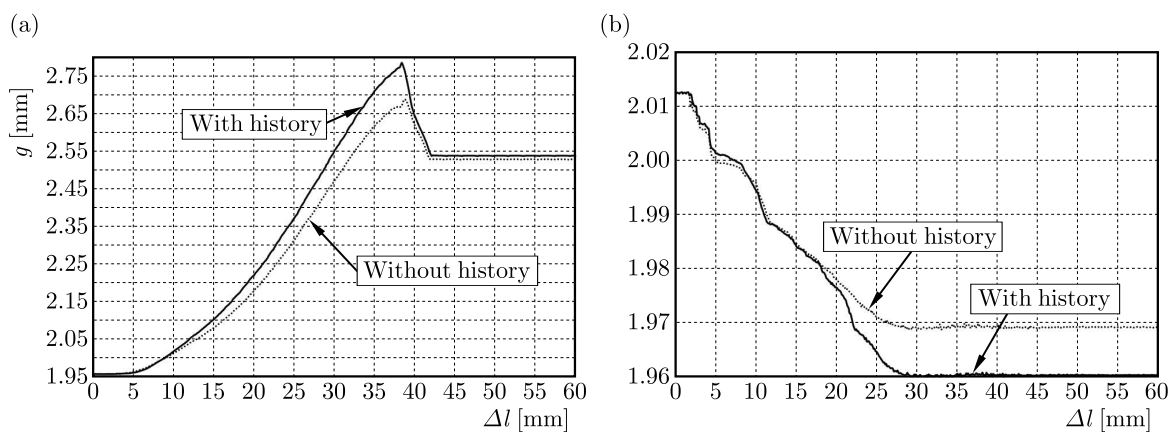


Fig. 11. Dependence of: (a) edge thickness from punch displacement, (b) bottom thickness from punch displacement

Much more important is the reading of the sheet metal thickness on the curved edge of the drawpiece, where the bottom passes into the cylindrical wall. An improper selection of the clearance or a too large diameter of the output disc in relation to the internal die diameter may

cause bottom break off during the drawing process. The bottom break off occurs most frequently in the area where the bottom passes into the cylindrical wall, because there occurs the greatest thickness reduction of the sheet. The dependence of the sheet thickness changes as a function of the punch displacement is plotted in Fig. 12a. The reading starts from the initial value of the sheet thickness of 2.01 mm. Larger sheet thinning occurred when including the history of stress and strain. The sheet thickness decreases to 1.74 mm. This is due to significant hardening of the drawpiece periphery, which makes entry into the die difficult, and this, in turn, promotes thinning of the sheet metal at its rounding. In the case without the history included, the sheet thickness in this area is 1.76 mm. Similarly, as for measuring of the bottom thickness, these differences are difficult to observe and are measured in a traditional experiment.

The last element which is compared is the drawpiece height. The dependence, as a function of the drawpiece height from the punch displacement, is shown in the graph in Fig. 12b. Both characteristics are almost identical to the punch displacement of 40 mm. The last stage of the drawing process is from the displacement 40 mm where a noticeable difference between the heights are plotted in Fig. 12c. The drawpiece height shaped with the history included is equal to 26.21 mm, whereas without the history it is 25.96 mm. Marginally larger height of the product with the history included may result directly from the hardening of the drawpiece periphery. This hardening, in turn, influences substantial thickening of the periphery. This, in turn, at the final stage makes the transition difficult between the die and the punch. This affects the greater flow on the sidewall, bottom and the area where the bottom passes into the cylindrical wall. Similarly as in the reading of the sheet thickness at the periphery of drawpiece, in the bottom and rounding, the differences are minor and difficult to measure in a traditional experiment. Numerical analysis allows one to detect these slight size differences.

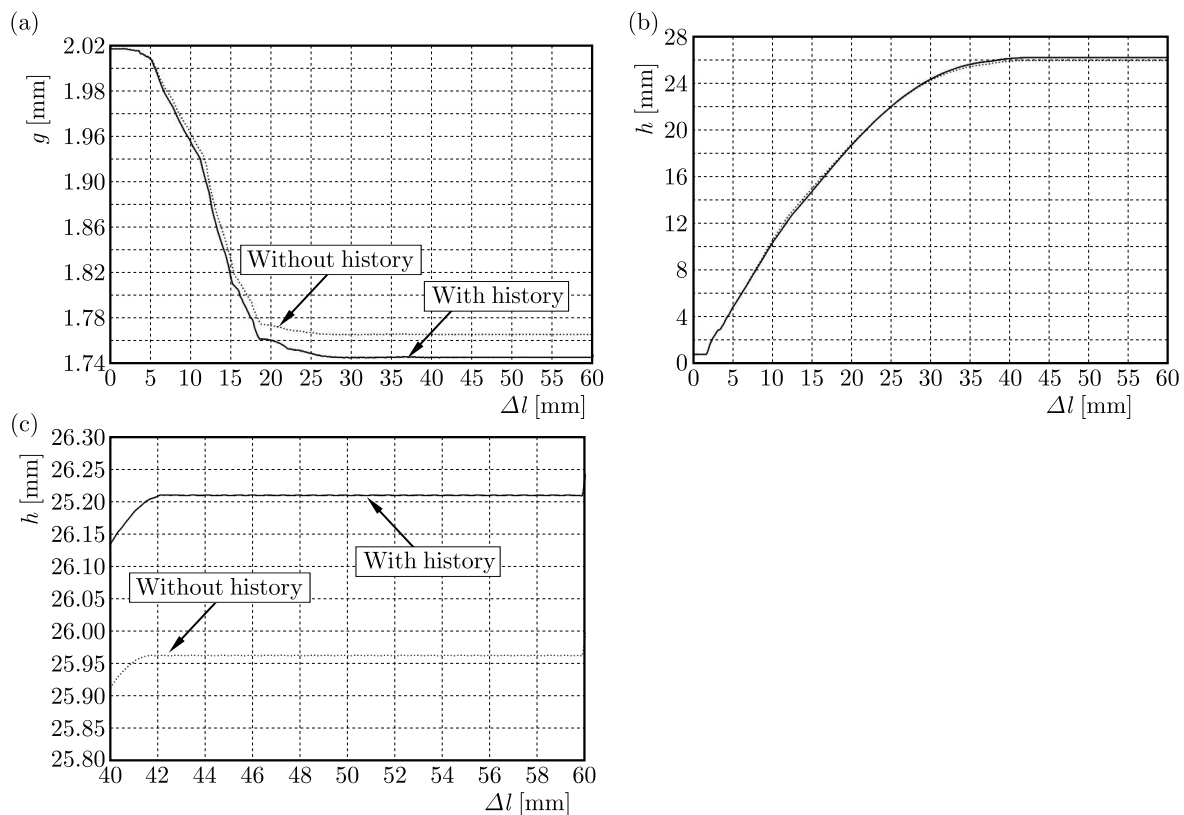


Fig. 12. Dependence of: (a) rounding thickness from punch displacement, (b) drawpiece height from punch displacement, (c) drawpiece height from punch displacement (zoom)

4. Conclusions

In this paper, the results of numerical complex modelling of the blanking and drawing processes have been compared. After blanking simulation, a springback analysis has been conducted. Then, two analyses of drawing were carried out and the results were compared. One with the history included of stress and strain after the blanking process, and the other one without that history. The comparative elements between the analyses were: the drawing force as a function of punch displacement, changing of the sheet thickness at the bottom, at the periphery and the rounding, and also the final drawpiece height. In addition, the equivalent stress distributions in the drawpieces were compared.

It was observed that including the history in the drawing process caused an increase of the maximum drawing force by 12%. There were also marginal differences in the drawpiece dimensions, which were impossible to measure with traditional methods during the experiment. The sheet thickness on the periphery, until the whole drawpiece had been formed, was higher by 3.4%. The drawpiece bottom thickness decreased by 0.5%. Also, the rounding thickness decreased by 1.1%. The product with the history included was 1% higher than without the history. The most significant difference was noted in the stress values. The drawpiece with the history included had a 66% higher stress values in the last step of the analysis. After the springback analysis, the stress values was higher by 20.7% than in the analysis without the history.

References

1. BOHDAL L., 2015, Application of FEM and vision-based methods to analysis of shearing processes in the aspect of scrap reduction, *Annual Set the Environment Protection*, **17**, 90-103
2. BOHDAL L., KUKIELKA L., 2014, Application of variational and FEM methods to the modelling and numerical analysis of guillotining process for geometrical and physical nonlinearity, *Mechanics*, **20**, 2, 197-204
3. BOHDAL L., KUKIELKA L., KUKIELKA K., KULAKOWSKA A., MALAG L., PATYK R., 2014, Three dimensional finite element simulation of sheet metal blanking process, *Applied Mechanics and Materials*, **474**, 430-435
4. GAMBIN W., KOWALCZYK K., 2003, *Plasticity of Metals* (in Polish), Warsaw University of Technology Publishing House
5. JEMIOLO S., GAJEWSKI M., 2014, *Hyperelasto-Plasticity* (in Polish), Warsaw University of Technology Publishing House
6. KALDUNSKI P., 2009, Modelling and simulation forming of circularly-symmetrical drawpieces without flange with the regard for the geometrical and physical nonlinearity (in Polish), PhD Thesis, Koszalin
7. KALDUNSKI P., KUKIELKA L., 2014, Numerical analysis and simulation of drawpiece forming process by Finite Element Method, *Applied Mechanics and Materials*, **474**, 153-158
8. KIM T.H., OLVER A.V., 1998, Stress history in rolling-sliding contact of rough surfaces, *Tribology International*, **31**, 12, 727-736
9. MARCINIAK Z., 1998, *Technology of the Drawpieces and die Design. Notebook Problems* (in Polish), Technical Center A. Marciniak, Warszawa
10. NAGASEKHAR A.V., TICK-HON YIP, LI S., SEOW H.P., 2006, Stress and strain histories in equal channel angular extrusion/pressing, *Materials Science and Engineering: A*, **423**, 143-147
11. SIMO J.C., HUGHES T.J.R., 1998, *Computational Inelasticity*, Springer-Verlag, New York

12. TRZEPIECINSKI T., GELGELE H.L., 2011, Investigation of anisotropy problems in sheet metal forming using finite element method, *International Journal of Material Forming*, **4**, 357-369
13. URRIOLAGOITIA-SOSA G., ROMERO-ANGELES B., HERNANDEZ-GOMEZ L.H., TORRES-TORRES C., URRIOLAGOITIA-CALDERON G., 2011, Crack-compliance method for assessing residual stress due to loading/unloading history: Numerical and experimental analysis, *Theoretical and Applied Fracture Mechanics*, **56**, 188-199
14. YAO H., CAO J., 2001, Assessment of corner failure depths in the deep drawing of 3D panels using simplified 2D numerical and analytical models, *Journal of Manufacturing Science and Engineering*, **123**, 248-257
15. ZIENKIEWICZ O.C., TAYLOR R.L., 2006, *The Finite Element Method for Solid and Structural Mechanics*, Elsevier, 6th edition

Manuscript received September 30, 2015; accepted for print December 21, 2017

MATHEMATICAL MODEL OF LEVITATING CART OF MAGNETIC UAV CATAPULT

ANNA SIBILSKA-MROZIEWICZ, EDYTA ŁADYŻYŃSKA-KOZDRAŚ

Warsaw University of Technology, Faculty of Mechatronics, Warsaw, Poland

e-mail: a.sibilska@mchtr.pw.edu.pl; e.ladyzynska@mchtr.pw.edu.pl

The article presents the steps of modeling of the dynamics of a levitating cart of an unmanned aerial vehicle (UAV) magnetic catapult. The presented in the article innovative catapult is based on the Meissner effect occurring between high-temperature superconductors (HTS) and a magnetic field source. The catapult suspension system consists of two elements: fixed to the ground base with magnetic rails and a moving cart. Generating magnetic field rails are made of neodymium magnets. Levitation of the launcher cart is caused by sixteen superconductors YBCO, placed in the cart frame supports. Described in the article model contains the system of Cartesian reference frames, kinematic constraints, equations of motion and description of forces acting on the cart as well as exemplary numerical simulation results.

Keywords: magnetic catapult, equations of motion, Meissner effect

1. Introduction

The growing demand for commercial unmanned aerial vehicles (UAV) requires exploration of innovative technical solutions associated with critical aspects of the use of such facilities. Safe procedures for UAV take-off and landing are one of such issues. Most of unmanned aerial vehicles have neither sufficient power supply nor a structure for self-start, especially in the field of uneven ground and insufficient runway.

Only a few of UAVs such as Predator have a chassis system allowing for self-start and landing. The chassis system, however, increases mass of the vehicle, makes its construction more complicated and requires implementation of advanced algorithms of control during take-off and landing. Moreover, the take-off procedure itself requires significant reserves of power. Take-off of an unmanned aerial vehicle can also be done by throwing it from a human hand. However, this way is only possible in the case of small and lightweight UAVs such as Raven used by the US Army.

In other cases it is necessary to use a separate device called a launcher or airplane catapult. Nowadays, it is common to use rocket systems (RATO-Rocket Assisted Take Off), bungee cord, hydraulic and pneumatic launchers (Fahlstrom and Gleason, 2012). An attractive alternative to current systems are magnetic catapults. Magnetic catapults compared with classical solutions enable safe, non-impact service of the UAV launch process and allow achieving much bigger final UAV speed. NASA plans using electrodynamic catapults to launch spacecraft (Polzin *et al.*, 2013) and hypersonic planes. Magnetic catapults are also planned to replace steam catapults used on aircraft carriers (Bertoncelli *et al.*, 2002).

Nowadays, magnetic suspension systems are used in high-speed trains (Mag-Lev). Currently, two types of Mag-Lev technology are developed commercially (Liu *et al.*, 2015). Electromagnetic suspension (EMS) developed by the German Transrapid system. The suspension is based on the strength attraction force between metal rails and mounted on the underside of the train

electromagnets. Built in 2004 Shanghai Maglev train uses the EMS technology. The second solution is an electrodynamic suspension system (EDS) proposed by Central Japan Railway Company. The EDS system uses strong repulsive forces generated by strong superconducting electromagnets built into the train path and trains chassis. Built in Japan Chuo Shinkansen line, which is the fastest train in the world (Coates, 2007), is based on the EDS technology. An alternative to EMS and EDS systems are passive suspensions using diamagnets.

This paper presents a mathematical model of a new UAV catapult prototype based on “out of the box” idea, using HTS in the launcher suspension system. According to the Meissner effect, superconductors cooled down below the critical temperature shield the external magnetic field generated by permanent magnets or electromagnets. The Meissner effect ensures spectacular levitation of the superconductor above the source of the magnetic field (Fig. 1).

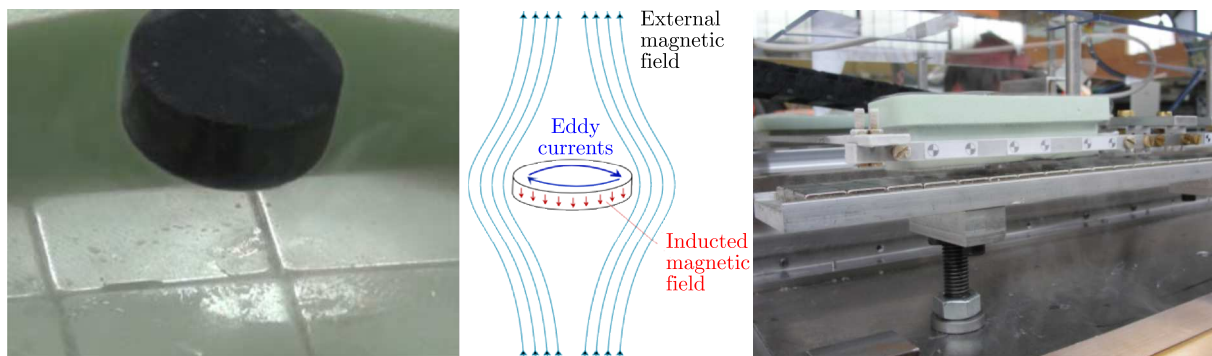


Fig. 1. Meissner effect

The initial part of the article presents a prototype of a magnetic UAV catapult using the Meissner effect. The following considerations include itemized assumptions regarding physical model and description of the system of Cartesian coordinate frames. Subsequent discussion contains equations of motion of the levitating cart and description of kinematic constraints and loads acting on the cart. The considerations are closed by results of numerical simulations.

2. Catapult prototype

Figure 2 shows photographs of the prototype of a magnetic launcher designed within FP7, EU GABRIEL (Integrated Ground and on-board system for Support of the Aircraft Safe Take-off and Landing) (Rohacs, 2015), (Falkowski, 2016), (Falkowski, Sibilski, 2013). During the take-off procedure, the UAV is attached to the levitating cart which is a movable part of the launcher. The cart is driven by a linear motor. The construction of the cart consists of a rigid frame made of duralumin and four containers. In each container, there are four high-temperature superconductors YBCO with a critical temperature of 92 K. These superconductors have a cylindrical shape with diameter of 21 mm and height of 8 mm. After filling the containers with liquid nitrogen, superconductors transit into superconducting state and start hovering over the launcher tracks due to the Meissner phenomena. Levitation phenomenon ends when the YBCO temperature exceeds the critical temperature of 92K. Therefore, the material of the container should provide the maximum thermal isolation. The starting path, mounted to the launcher base, consists of two parallel rails, each made of three rows of permanent magnets. To build the prototype, rectangular neodymium magnets polarized top-down have been used.

Potential use of passive suspensions, based on HTS in transportation systems, would bring many benefits. The levitation phenomenon enables frictionless longitudinal movement of the cart. The levitation gap remains stable without any feedback loop, and low complexity of the system would improve its reliability. The biggest defect of the solution is the need of cooling

down and maintaining superconductors in low temperatures. Systems which use passive magnetic suspension, despite growing popularity, have not been used so far in professional and commercial technical solutions. However, there is a small number of academic research projects on the use of HTS in transportation systems, including SupraTrans (Schultz *et al.*, 2005), Cobra Tram (Sotelo *et al.*, 2011) and SuperMaglev (Wang *et al.*, 2005).

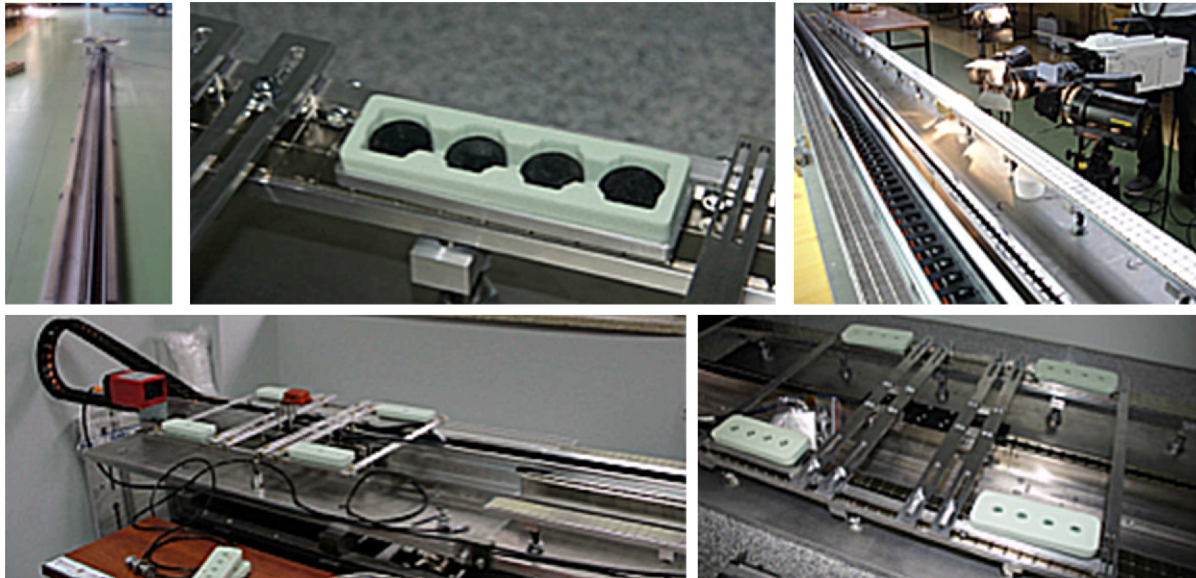


Fig. 2. Prototype of a magnetic UAV catapult using the Meissner effect

3. Physical model

An extremely important step in the modeling procedure (Ładyżyńska-Kozdraś, 2011) is definition of the physical model being the basis of formulation of the mathematical model. The proposed physical model of the levitating cart assumes the following simplifications:

- the levitating cart is an axisymmetric solid body with six degrees of freedom;
- mass and center of mass of the cart do not change during movement, however, the position of the taking off airplane may change;
- the system motion is considered only in a no wind environment;
- motion of the cart is controlled in only one direction by a linear motor;
- the cart is levitating above magnetic rails due to the Meissner effect;
- cart movement results from gravitational, magnetic and propulsion forces acting on the cart itself and gravitational, aerodynamical and propulsion forces acting on the taking off airplane;
- mass of evaporating nitrogen is not considered.

4. Reference frames

In order to describe the dynamics of the levitating cart, the following clockwise Cartesian coordinates frames are attached to the following parts of the UAV magnetic launcher:

- The motionless base system $Ox_f y_f z_f$ is a rectangular Cartesian coordinate system rigidly connected with the ground. The Oz_f axis is directed vertically downward, in the direction of gravitational acceleration; the Ox_f axis coincides with the horizontal projection of the

aircraft taking-off path; the Oy_f axis completes the right-handed coordinate system. The base frame origin coincides with the starting point of the catapult cart. The position of the levitating cart, along the Ox_f frame, could be measured by a laser sensor.

- The magnetic reference frame $Ox_my_mz_m$ is a coordinate system in which magnetic interactions and cart propulsion forces are modeled. The Ox_m axis covers the catapult axis of symmetry; the Oz_m axis points down perpendicularly to the catapult base; the Oy_m axis connects the left and right catapult rails. The system origin is moving along the catapult axis of symmetry Ox_m and covers the projection of the levitating cart center of mass into the Ox_m axis. Orientation of the magnetic reference frame, due to the fixed system $Ox_fy_fz_f$, is described by two angles $\theta_{m/f}$ and $\phi_{m/f}$. The angle $\theta_{m/f}$ corresponds to deliberate inclination of the catapult base, relative to the horizontal plane. A non zero value of the $\phi_{m/f}$ angle is caused by imbalances of the substrate on which the launcher is placed.
- The $Ox_sy_sz_s$ coordinate system describes the position and orientation of the levitating cart. The origin of the cart coordinate system is fixed with the cart center of mass, and its axes are rigidly connected with the cart frame. The Ox_s axis points along the longitudinal cart dimension; the Oz_s axis is perpendicular to the cart surface and points downward; the Oy_s axis is parallel to the lateral cart dimension and completes the right-handed coordinate system. Orientation of the launcher cart with respect to the magnetic coordinate system is described by three quasi-Euler angles $\theta_{s/m}$, $\psi_{s/m}$ and $\phi_{s/m}$.

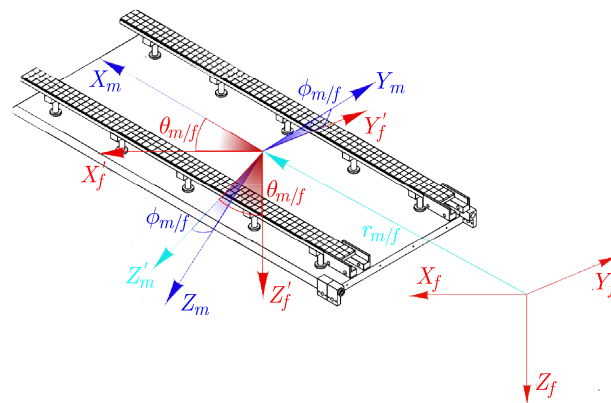


Fig. 3. Coordinate systems fixed with the magnetic launcher: inertial $Ox_fy_fz_f$ and magnetic $Ox_my_mz_m$

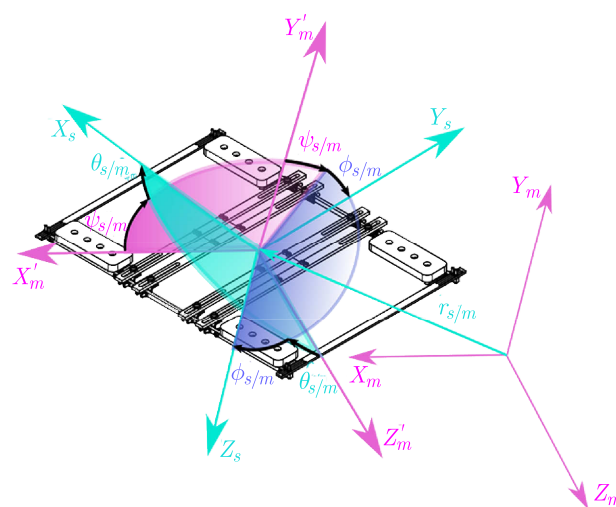


Fig. 4. The coordinate system fixed with the levitating cart $Ox_sy_sz_s$

- The axes of the gravitational reference frame $Ox_gy_gz_g$ are parallel to the inertial frame $Ox_fy_fz_f$. The system origin is fixed with the cart center of mass. In that system, the gravitational forces and torques are described.
- The reaction forces and torques acting between the cart and taking-off airplane are described in the $Ox_cy_cz_c$ coordinate system. The system origin and its orientation is dictated by the way of attaching the UAV into the cart frame.

5. Kinematic constrains

Motion of the cart is described by time and space coordinates located in the event space. The cart position, at the particular moment, is unambiguously described by linear and angular coordinates and velocities. Those coordinates change with time and are coupled by kinematic constrains. It is important to maintain a mutual coordinate system while describing the function of particular coordinates. Delivered below equations describing cart kinematic constrains are described in the $Ox_sy_sz_s$ system fixed with the cart center of mass.

The vector of the current cart position in the fixed to the ground inertial frame $Ox_fy_fz_f$ is described by

$$\mathbf{r} = x_f \mathbf{i}_f + y_f \mathbf{j}_f + z_f \mathbf{k}_f \quad (5.1)$$

The vector of instantaneous linear velocity \mathbf{V} described in the frame fixed with the cart frame $Ox_sy_sz_s$ has three components: longitudinal U , lateral V and climb speed W

$$\mathbf{V} = U \mathbf{i}_s + V \mathbf{j}_s + W \mathbf{k}_s \quad (5.2)$$

The vector of instantaneous angular velocity $\mathbf{\Omega}$ described in the fixed to the cart frame system $Ox_sy_sz_s$ has the following components: roll rate P , pitch rate Q and yaw rate R

$$\mathbf{\Omega} = P \mathbf{i}_s + Q \mathbf{j}_s + R \mathbf{k}_s \quad (5.3)$$

Kinematic constraints between linear velocity components measured relative to the inertial coordinate system $Ox_fy_fz_f$, and linear velocities U , V , W measured relative to the coordinate system $Ox_sy_sz_s$, fixed to the cart, have the following form

$$\begin{bmatrix} U \\ V \\ W \end{bmatrix} = R_{s/m} R_{m/f} \begin{bmatrix} \dot{x}_f \\ \dot{y}_f \\ \dot{z}_f \end{bmatrix} \quad (5.4)$$

The rotation matrices $\mathbf{R}_{s/m}$ and $\mathbf{R}_{m/f}$ are described by equations (5.5) with notations: $c\alpha = \cos \alpha$ and $s\alpha = \sin \alpha$

$$\mathbf{R}_{s/m} = \begin{bmatrix} c\theta_{s/m} c\psi_{s/m} & c\theta_{s/m} s\psi_{s/m} & -s\theta_{s/m} \\ s\phi_{s/m} s\theta_{s/m} c\psi_{s/m} - c\phi_{s/m} s\psi_{s/m} & s\phi_{s/m} s\theta_{s/m} s\psi_{s/m} + c\phi_{s/m} c\psi_{s/m} & s\phi_{s/m} c\theta_{s/m} \\ c\phi_{s/m} s\theta_{s/m} c\psi_{s/m} + s\phi_{s/m} s\psi_{s/m} & c\phi_{s/m} s\theta_{s/m} s\psi_{s/m} - s\phi_{s/m} c\psi_{s/m} & c\phi_{s/m} c\theta_{s/m} \end{bmatrix} \quad (5.5)$$

$$\mathbf{R}_{m/f} = \begin{bmatrix} c\theta_{s/m} & 0 & -s\theta_{s/m} \\ s\phi_{s/m} s\theta_{s/m} & c\phi_{s/m} & s\phi_{s/m} c\theta_{s/m} \\ c\phi_{s/m} s\theta_{s/m} & -s\phi_{s/m} & c\phi_{s/m} c\theta_{s/m} \end{bmatrix}$$

The components of instantaneous angular velocities P , Q , R are combinations of generalized velocities $\dot{\theta}_{s/m}$, $\dot{\psi}_{s/m}$, $\dot{\phi}_{s/m}$ and trigonometric functions of angles: $\theta_{s/m}$, $\psi_{s/m}$ and $\phi_{s/m}$, according to the relation

$$\begin{bmatrix} P \\ Q \\ R \end{bmatrix} = \begin{bmatrix} 1 & 0 & -\sin \theta_{s/m} \\ 0 & \cos \phi_{s/m} & \sin \phi_{s/m} \cos \theta_{s/m} \\ 0 & -\sin \phi_{s/m} & \cos \phi_{s/m} \cos \theta_{s/m} \end{bmatrix} \begin{bmatrix} \dot{\phi}_{s/m} \\ \dot{\theta}_{s/m} \\ \dot{\psi}_{s/m} \end{bmatrix} \quad (5.6)$$

6. Equations of motion

To derive equations of motion for objects treated as rigid bodies, mostly Newtonian approach is used, i.e. forces, momentum and angular momentum conservation laws. Examples could be found in (Baranowski, 2016). Sometimes, more involved theoretical mechanics is used, e.g. Lagrangian formulation, see (Koruba *et al.*, 2010), Boltzmann-Hamel equations like in (Ładyżyńska-Kozdraś and Koruba, 2012) or Maggi equations (Ładyżyńska-Kozdraś, 2012).

In the presented consideration, the levitating cart is treated as a rigid body with six degrees of freedom. The proposed equations of motions are described in the coordinate frame fixed to the cart center of mass $Ox_s y_s z_s$. The presented mathematical model is developed according to principal mechanical laws: the momentum and angular momentum conservation principles.

— The derivative of the momentum $\mathbf{\Pi}$ with respect to time

$$\frac{\partial \mathbf{\Pi}}{\partial t} + \mathbf{\Omega} \times \mathbf{\Pi} = \mathbf{F} \quad (6.1)$$

— The derivative of the angular momentum \mathbf{K} with respect to time

$$\frac{\partial \mathbf{K}}{\partial t} + \mathbf{\Omega} \times \mathbf{K} + \mathbf{V} \times \mathbf{\Pi} = \mathbf{M} \quad (6.2)$$

The principle of conservation of the momentum and angular momentum can be applied to the problem in two ways. Firstly, the levitating cart and taking-off airplane are treated as a single undivided rigid body. The momentum and angular momentum of that body is defined for the entire object, relative to the one arbitrarily chosen pole which does not necessarily coincide with the center of mass. The second way is to designate moments and angular moments separately for the taking off plane and the levitating cart. The presented equations consider both movable parts of the catapult as a one rigid body.

The general form of equations of motion of the cart in the three dimensional space is expressed by the relationship (Ładyżyńska-Kozdraś, 2011)

$$\mathbf{M}\dot{\mathbf{V}} + \mathbf{K}\mathbf{M}\mathbf{V} = \mathbf{Q} \quad (6.3)$$

where:

— matrix of inertia

$$\mathbf{M} = \left[\begin{array}{ccc|ccc} m & 0 & 0 & 0 & S_z & -S_y \\ 0 & m & 0 & -S_z & 0 & S_z \\ 0 & 0 & m & S_y & -S_x & 0 \\ \hline 0 & -S_z & S_y & I_x & -I_{xy} & -I_{xz} \\ S_z & 0 & -S_x & -I_{yx} & I_y & -I_{yz} \\ -S_y & S_x & 0 & -I_{zx} & -I_{zy} & I_z \end{array} \right] \quad (6.4)$$

— matrix of kinematic constrains

$$\mathbf{K} = \left[\begin{array}{ccc|ccc} 0 & -R & Q & 0 & 0 & 0 \\ R & 0 & -P & 0 & 0 & 0 \\ -Q & P & 0 & 0 & 0 & 0 \\ \hline 0 & -W & V & 0 & -R & Q \\ W & 0 & -U & R & 0 & -P \\ -V & U & 0 & -Q & P & 0 \end{array} \right] \quad (6.5)$$

— vector of linear and angular accelerations

$$\dot{\mathbf{V}} = [\dot{U}, \dot{V}, \dot{W}, \dot{P}, \dot{Q}, \dot{R}]^T \quad (6.6)$$

— vector of linear and angular velocities

$$\mathbf{V} = [U, V, W, P, Q, R]^T \quad (6.7)$$

— vector of external forces and torques

$$\mathbf{Q} = \begin{bmatrix} \mathbf{F} \\ \mathbf{M} \end{bmatrix} \quad (6.8)$$

After determining kinematic constraints as well as forces \mathbf{F} and torques \mathbf{M} acting on the levitating cart, a general model of the system dynamics is obtained.

7. Forces and torques acting on levitating cart

Forces and torques acting on the considered system results from interactions between the taking-off UAV, levitating cart and the generated by the catapult rails magnetic field. The vector of external forces and torques \mathbf{Q} can be described by superposition of the vectors of forces and torques: acting only on the cart frame \mathbf{Q}^S , acting on the UAV alone \mathbf{Q}^B , and describing the method of attachment of the taking-off UAV into the cart frame

$$\mathbf{Q} = \mathbf{Q}^S + \mathbf{Q}^B + \mathbf{Q}^{SB} \quad (7.1)$$

The cart frame undergoes the gravitational pull \mathbf{Q}_g^S , propulsion forces \mathbf{Q}_T^S , aerodynamic interactions \mathbf{Q}_A^S and the load resulting from the Meissner effect, called levitation forces $\mathbf{Q}_{L_i}^S$. The levitation forces depend on the position of the box with superconductors relative to the rails generating magnetic field. This distance is called the levitation gap. Taking into account changes in the orientation of the cart, the levitation forces $Q_{L_i}^S$ are determined separately for each of four containers with superconductors

$$\mathbf{Q}^S = \mathbf{Q}_g^S + \mathbf{Q}_T^S + \mathbf{Q}_A^S + \sum_{i=1}^4 \mathbf{Q}_{L_i}^S \quad (7.2)$$

The taking-off UAV moves under the influence of the gravitational pull \mathbf{Q}_g^B , propulsion forces \mathbf{Q}_T^B , aerodynamic interactions \mathbf{Q}_A^B and the load resulting from the UAV control system \mathbf{Q}_δ^B

$$\mathbf{Q}^B = \mathbf{Q}_g^B + \mathbf{Q}_T^B + \mathbf{Q}_A^B + \mathbf{Q}_\delta^B \quad (7.3)$$

The loads \mathbf{Q}_g^S and \mathbf{Q}_g^B are described in the gravitational system $Ox_g y_g z_g$. The linear drive propulsion forces \mathbf{Q}_T^S and levitation forces $\mathbf{Q}_{L_i}^S$ are considered in relation to the magnetic system $Ox_m y_m z_m$. Therefore, it is necessary to transform the individual vectors to the coordinate system attached to the levitating cart, by multiplying them by the corresponding transformation matrix. The value of the nonlinear levitation force depends on the gap between the cart support and magnetic rails. The smaller the gap, the greater the force. The levitation force is modeled as a concentrated force acting on the center of the box with superconductors.

8. Preliminary numerical simulation

The use of the momentum and angular momentum laws of conservation for mechanical systems makes it possible to develop the dynamical model of the take-off of an unmanned aircraft.

During the take-off procedure, the UAV is attached to the levitating cart, which is a movable part of the launcher. In the analysis, the UAV class micro Bell 540 has been taken into account. In the research, it is assumed that the linear-driven cart moves with constant horizontal acceleration.

The presented in the article mathematical model of the levitating cart of the magnetic UAV catapult is the theoretical basis for preliminary numerical simulations. The obtained numerical results show correctness of the developed mathematical model. As shown in Figs. 5 and 6, the unmanned aircraft take-off takes place in a proper manner. It maintains the preset parameters resulting from the adopted guidance parameters of the levitating cart of the magnetic UAV catapult.

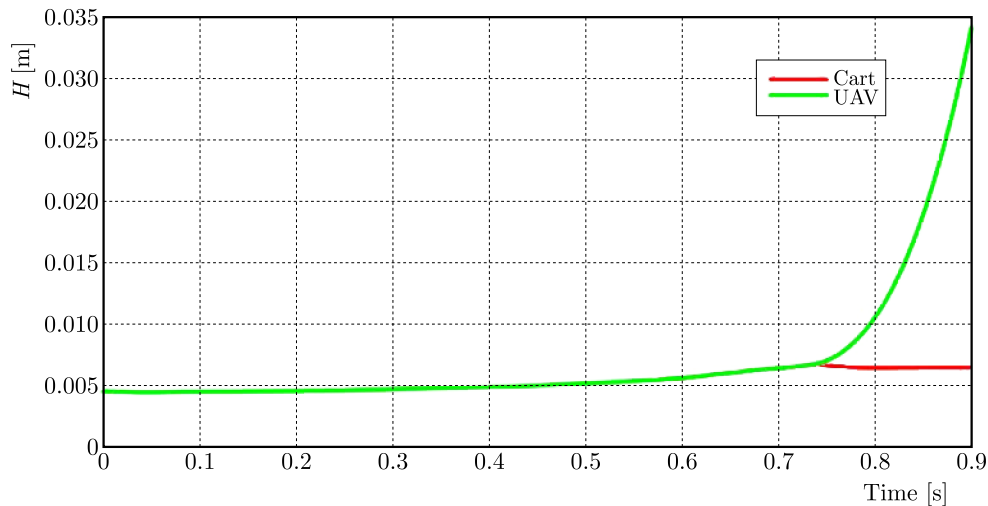


Fig. 5. The course of changes in height of the levitating cart and UAV at the moment of take-off

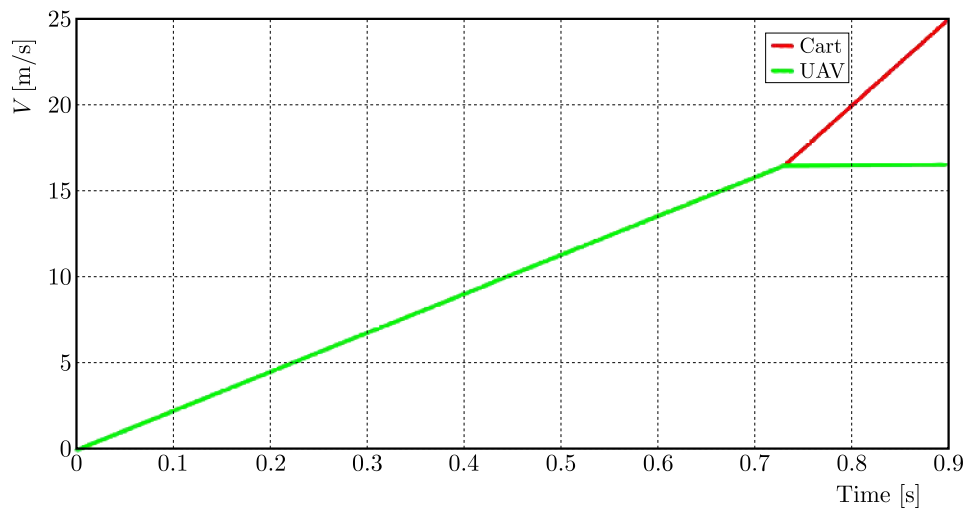


Fig. 6. Velocity of the levitating cart and UAV at the moment of take-off

9. Conclusions

The paper is addressing an interesting subject related to dynamics and modelling methodology of the levitating cart of a magnetic UAV catapult. The presented mathematical model has been developed according to principal mechanical laws – the momentum and angular momentum of conservation. The considerations are closed by exemplary numerical results.

Described work is a prelude to wider research on the mechanical properties of the launcher levitating cart, being under the influence of forces, generated by levitation of HTS in the magnetic field.

The presented in this article model does not take into consideration the non-uniformness of magnetic field and the flux pinning effect occurring in II type superconductors. Description of levitation forces and torques, based on both theoretical investigations and laboratory tests, will be the next step of research as well as development of a more general mathematical model including UAV dynamics and non-uniformness of the magnetic field distribution.

References

1. BARANOWSKI L., 2016, Explicit “ballistic M-model”: a refinement of the implicit “modified point mass trajectory model”, *Bulletin of the Polish Academy of Sciences Technical Sciences*, **64**, 1
2. BERTONCELLI T., MONTI A., PATTERSON D., DOUGAL R., 2002, Design and simulation of an electromagnetic aircraft launch system, *Power Electronics Specialists Conference, 2002. pesc 02. 2002 IEEE 33rd Annual*, **3**, 1475-1480
3. COATES K.C., 2007, *TGV's 357Mph Demo Proves HSM's Superiority*, North American Maglev Transport Institute
4. FAHLSTROM P., GLEASON T., 2012, *Introduction to UAV Systems*, Wiley, Aerospace Series, ISBN 978-11-1839-681-0
5. FALKOWSKI K., 2016, *Passive Magnetic Suspension* (in Polish), Military University of Technology, ISBN 978-83-7938-115-9
6. FALKOWSKI K., HUŚCIO T., 2009, Modelling of the magnetic attraction force of the electromagnetic module in the relative base – air-gap – absolute base system, *Solid State Phenomena*, **144**, 53-58
7. FALKOWSKI K., SIBILSKI K., 2013, Magnetic levitation system for take-off and landing airplane – project GABRIEL, *COMSOL Conference 2013*, Rotterdam
8. KORUBA Z., DZIOPA Z., KRZYSZTOFIK I., 2010, Dynamics and control of a gyroscope-stabilized platform in a self-propelled anti-aircraft system, *Journal of Theoretical and Applied Mechanics*, **48**, 1, 5-26
9. LICHOTA P., SIBILSKI K., OHME P., 2016, D-optimal simultaneous multistep excitations for aircraft parameter estimation, *Journal of Aircraft*, <http://dx.doi.org/10.2514/1.C033794>
10. LIU Z., LONG Z., LI X., 2015, *MagLev Trains: Key Underlying Technologies*, Springer Tracts in Mechanical Engineering, ISBN 978-3-662-45673-6
11. ŁADYŻYŃSKA-KOZDRAŚ E., 2011, The modelling and numerical simulation of the controlled, movable objects with imposed non-holonomic constraints treated as control laws (in Polish), *Mechanika*, **237**, Oficyna Wydawnicza Politechniki Warszawskiej
12. ŁADYŻYŃSKA-KOZDRAŚ E., 2012, Modeling and numerical simulation of unmanned aircraft vehicle restricted by non-holonomic constraints, *Journal of Theoretical and Applied Mechanics*, **50**, 1, 251-268
13. ŁADYŻYŃSKA-KOZDRAŚ E., KORUBA Z., 2012, Model of the final section of navigation of a self-guided missile steered by a gyroscope, *Journal of Theoretical and Applied Mechanics*, **50**, 2, 473-485
14. POLZIN K.A., ADWAR J.E., HALLOCK A.K., 2013, Optimization of electrodynamic energy transfer in coilguns with multiple, uncoupled stages, *IEEE Transactions on Magnetics*, **49**, 4, 1453-1460
15. ROHACS D., ROHACS J., 2015, Magnetic levitation assisted aircraft take-off and landing (feasibility study – GABRIEL concept), *Progress in Aerospace Sciences*, ISSN 0376-0421

16. SCHULTZ L., DE HAAS O., VERGES P., BEYER C., ROHLIG S., OLSEN H., KUHN L., BERGER D., NOTEBOOM U., FUNK U., 2005, Superconductively levitated transport system – the SupraTrans project, *IEEE Transactions on Applied Superconductivity*, **15**, 2, 2301-2305
17. SOTELO G.G., DIAS D.H.N., DE ANDRADE R., STEPHAN R.M., 2011, Tests on a superconductor linear magnetic bearing of a full-scale MagLev vehicle, *IEEE Transactions on Applied Superconductivity*, **21**, 1464-1468
18. WANG J., WANG S., DENG C., ZENG Y., SONG H., HUANG H., 2005, A superhigh speed has MagLev vehicle, *International Journal of Modern Physics B*, **19**, 01n03, 399-401

Manuscript received July 10, 2016; accepted for print December 28, 2017

3D FE ANALYSIS OF THE BEHAVIOR OF ELLIPTICAL CRACKS ON ORTHOPEDIC CEMENT OF THE TOTAL HIP PROSTHESIS

ALI BENOUIS

*LMPM, Department of Mechanics, Faculty of Engineering, University of Sidi-Bel-Abbes, Algeria and
University of Saida, Saida, Algeria; e-mail: aly_ouis@hotmail.fr*

MOHAMMED EL SALLAH ZAGANE

LMPM, Department of Mechanics, Faculty of Engineering, University of Sidi-Bel-Abbes, Algeria

ABDELKADER BOULENOUAR

Djillali Liabes University of Sidi Bel-Abbes, Mechanical Engineering Department, LMRS, Algeria

BOUALEM SERIER, MOHAMED ELNEDHIR BELGHERRAS

LMPM, Department of Mechanics, Faculty of Engineering, University of Sidi-Bel-Abbes, Algeria

An explicit analysis conducted on the crack behavior in surgical cement (Polymethylmethacrylate – PMMA) used for Total Hip Prosthesis (THP) is of great importance in collecting information about the nature of the phenomenon of loosening of the cement application. The rupture of the orthopedic cement is practically the main cause of this loosening. Understanding different rupture mechanisms give a great value in advancing the durability of the cemented total prosthesis. The purpose of this study is to analyse cracks behavior, initiated in the cement that links the femoral-stem with the bone, using the Finite Element Analysis Method (FEM). The present study brings into focus the variation of the stress intensity factor in modes I, II and III. This rupture criterion is used according to the nature of crack, its orientation and its location in the orthopedic cement. At first, the level and distribution of the equivalent von Mises stress is analysed, which is induced in the medial, proximal and distal parts of the bone cement. Then, the behavior of different geometric forms of an elliptical crack is evaluated which are located and initiated within the body of these three parts.

Keywords: cement, implant, crack size, stress intensity factors (SIFs), X-FEM

1. Introduction

The bone cement does not act as a glue, but rather as a filling material. Currently, the most common bone cement material is polymethylmethacrylate (PMMA), which is a self-curing polymer compound. In the assembly method, the bone cement is used to connect the hip prosthesis with the femur. The cemented type of Total Hip Replacement (THR) offers a better stress distribution in femur compared to a cementless type. In addition, the hip prosthesis with a shorter stem distributes stresses evenly in the femur. Also, different cancellous density does not significantly affect the stresses. Fatigue failure of the cement mantle have been identified as a possible loosening mechanism for the prosthesis, which can lead to revision surgery. In vivo, surface morphology fracture of the bone cement, related to PMMA fracture micromechanics, despite the higher cement stresses with deboned stems, polished prostheses do not provoke the damage accumulation failure scenario, according to studies which used the extrapolation method to predict the creep behavior of the PMMA bone cement (Topoleski *et al.*, 1990; Lennon *et al.*, 2004; Morgan *et al.*, 2003). Benouis *et al.* (2016) used 2D-FEM to analyse the behavior of cracks interaction with the orthopedic cement by computing SIFs. Benbarek *et al.* (2013)

used numerical analysis to examine the orthopedic cement on the acetabular part. Specifically, the behavior of a crack was examined, emanating from a cavity that was found in several locations in the cement, in order to examine the variation of the SIF, loading, and orientation, and finally to predict the angle and optimum loading for crack propagation, using X-FEM (The Extended Finite Element Method). Abdel-Wahab and Silberschmidt (2011) experimentally and numerically studied the dynamic behavior of a fracture impact in the cortical bone tissue, using X-FEM. Another study by Bouziane *et al.* (2013) showed that the stress intensity factor of a crack, emanating from a cavity, was higher than the one emanating from an inclusion. Ramos *et al.* (2013) experimentally observed that the position of an implant in the femur and assemblage with the femoral canal were two important issues of the formation mechanism of cracks between the two surfaces (os-cement, cement-implant). Griza *et al.* (2013) analysed with FEM the stress distribution of the acetabular part in the PTH using screw fixation. The analysis showed that it took a large amount of computational force to predict screw fracture in the case of the unbounded metal-backed and bone interface. Taylor *et al.* (2003) used analytical and numerical methods to predict damage of the bone. Najafi *et al.* (2011) simulated the presence of micro-cracks in the cortical bone. It was proved that the propagation of those cracks was strongly influenced by the bone density, thus, suggesting that the fracture toughness of the bone should be provided, at least in part, in order that bone density could be quantified. Benouis *et al.* (2015) presented a numerical model of the crack propagation trajectory in the cement of the acetabular part. The crack direction is evaluated as a function of displacement extrapolation and the strain energy density criterion. The low-modulus bone cement of the total hip prosthesis, combined with its mechanical behavior, determines, inter alia, the lifetime of these prostheses. Several experimental procedures have been conducted on the cement, showing the existence of cracks emanating from cavities within the body (McCormack and Prendergast, 1999). These cracks are mainly responsible for the loosening of the total hip prostheses.

This study aims to analyse the behavior of different geometrical forms of elliptical cracks in the orthopedic cement of the femur THP, and to compute the evolution of SIFs at the cracks tip using X-FEM. The effects of the location and orientation of these cracks are highlighted.

2. Methods

2.1. Geometry

There is currently a variety of product types in the global market of total hip replacement, which are: CMK, BM, FRAM A, etc. For the experimental part of this study, CMK3 has been used (third generation of Charnley KERBOULL prosthesis) due to its availability in the local market. In this study, three-dimensional (3D) Finite Element Method (FEM) has been used in order to examine the behavior of cracks initiated in the bone cement with femoral implant Charnley (Fig. 1).

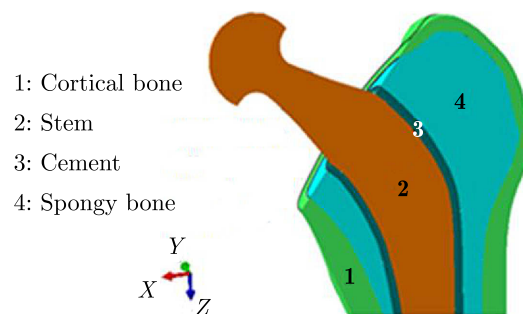


Fig. 1. Three-dimensional femur stems for Charnley

2.2. Finite element model

Three-dimensional (3D) finite element models have been produced for femur, bone cement, implant, and meshed using C3D4 (a 4 node linear tetrahedron). The whole model (stem, bone cement, and femur) has been discretized in 1173459 elements as shown in Fig. 2. To assure reliability of the results, an extremely fine mesh has been imposed around the region of cement cracks.

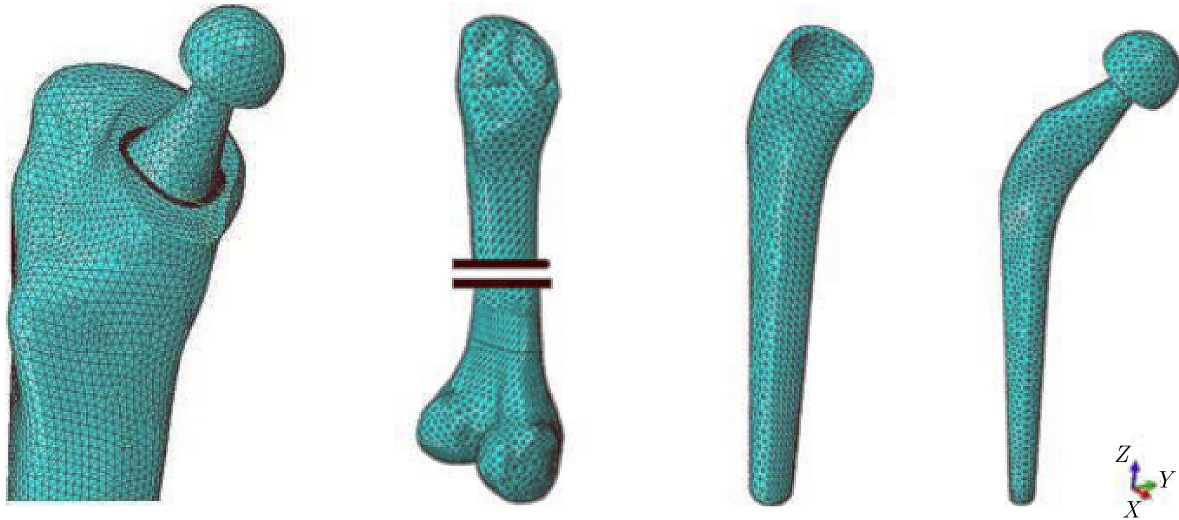


Fig. 2. Boundary conditions and muscle-forces applied in the THP

2.3. Material model

Mechanical properties of the materials are presented in Table 1. The cortical bone is considered as a transversely isotropic elastic material, whereas the spongy bone, cement and Charnley stem, are considered as linear isotropic elastic materials. To assign the material properties to the cortical bone, elastic properties are inserted into ABAQUS. Cement properties are: tensile strength 25 MPa, compressive strength 80 MPa (Rodríguez *et al.*, 2014), shear strength 40 MPa (Merckx, 1993) and fatigue (108 cycles) 14 MPa (Pilliar *et al.*, 1982; Soltész, 1994). Ries *et al.* (2006) found that the critical stress intensity factors K_{IC} are between $0.96 \text{ MPa}\sqrt{\text{m}}$ to $1.76 \text{ MPa}\sqrt{\text{m}}$.

Table 1. Material, properties of THP (Waanders *et al.*, 2012)

Part of model	Elastic modulus [GPa]	Poisson's ratio [-]	Density [kg/m ³]
Stem	210	0.3	7900
Cement	2.4	0.3	1200
Cancellous bone	0.4	0.3	1990
Cortical bone	$E_x, E_y = 7.0, E_z = 11.5$ $G_{xy} = 2.6, G_{yz}, G_{zx} = 3.5$	$\nu_{xy}, \nu_{zy}, \nu_{zx} = 0.4$	600

2.4. Boundary conditions and loading

The values of the applied loads are taken from Bergman *et al.* (1993), as it is illustrated in Fig. 3. These values represent loading variation during normal walking. In static analysis, the maximum force of stumbling activity is employed to simulate simplified loading on the implant. This load analysis is based on a selection of the peak-load during stumbling activity.

The normal walking resultant force F acting on the head of the femur is 8.7 times the body weight ($BW = 70 \text{ kg}$) at 58% of the gait cycle.

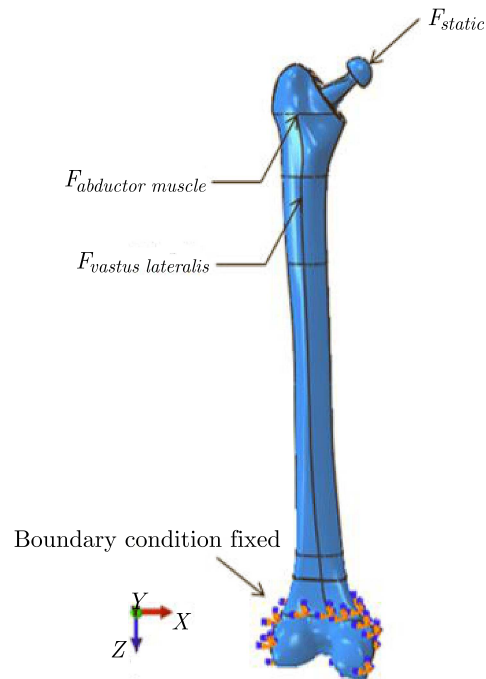


Fig. 3. Boundary conditions and loading of the hip prosthesis

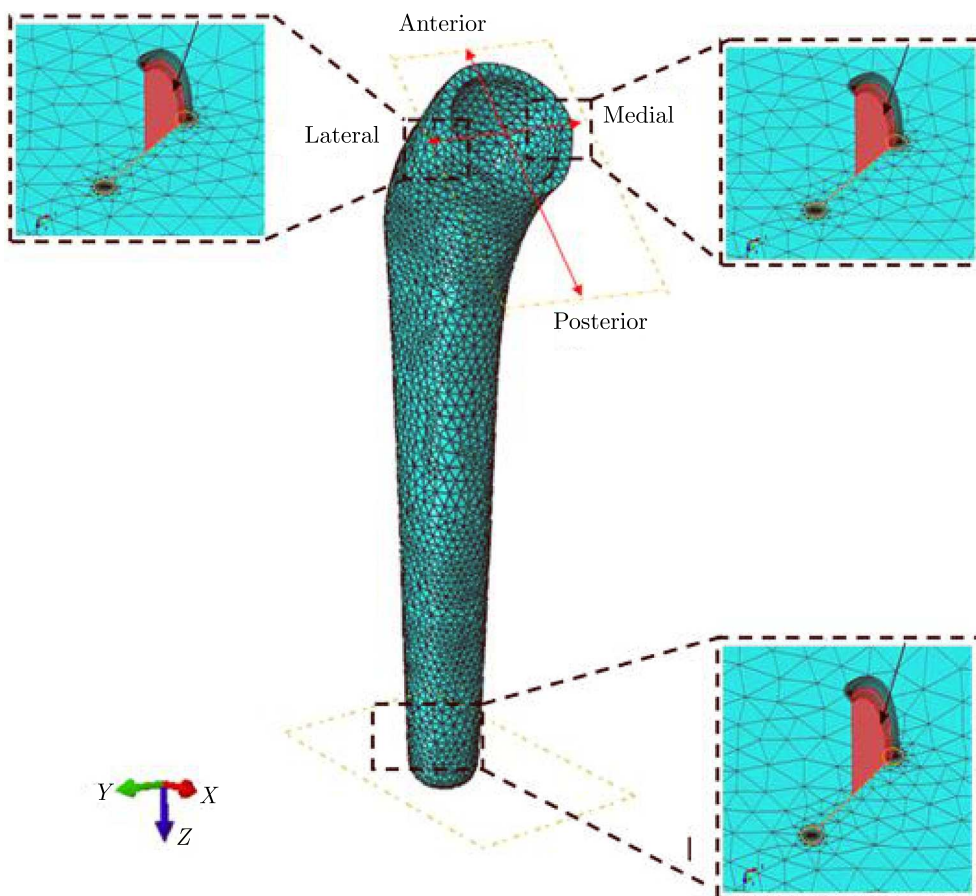


Fig. 4. Three-dimensional model of the crack location

In this study, the magnitudes and directions of muscles are based on data by Bregmann *et al.* (2001). The abductor muscle load $F_{abductor-muscle}$ is applied to the proximal part of the greater trochanter. The iliotibial-tract load $F_{iliotibial-tract}$ is applied to the bottom of the femur in the longitudinal femur direction as presented in Table 2. The boundary condition is applied by fixing the distal epiphysis, which is the distal end of the femur that is connected to the knee (El-Sheikh *et al.*, 2006). Figure 3 shows the coordinate system where the forces components refer to. The analysis of cracks in different parts of the cement (proximal and distal) is shown in Fig. 4. Real cracks are simulated (Fig. 6), according to the dimensions shown in Fig. 5.

Table 2. Maximum loading configuration of the major muscles (Bergmann *et al.*, 2001)

Force [N]	X	Y	Z	F
Joint contact force	-433.8	-263.8	-1841.3	F_{static}
Abductor muscle	465.9	34.5	695.0	F_1
Vastus lateralis muscle	-7.2	148.6	-746.3	F_2

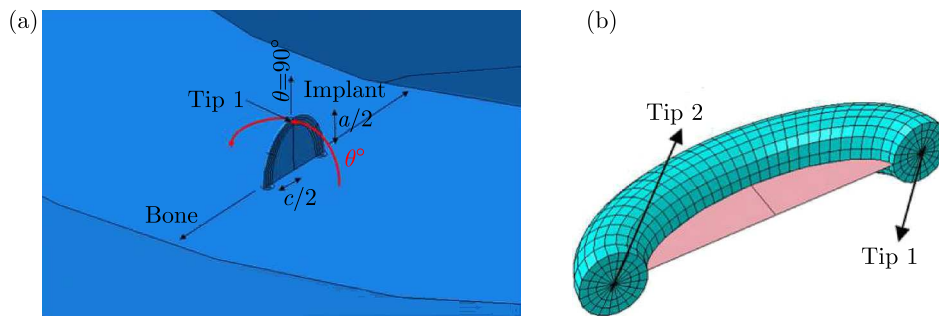


Fig. 5. (a) Dimension and orientation of the crack. (b) Mesh adapted to X-FEM

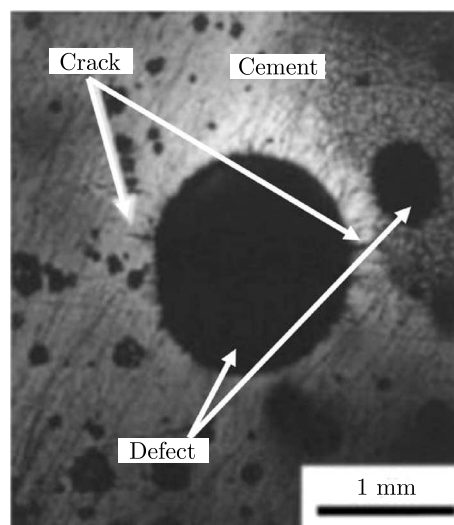


Fig. 6. Cracks in acrylic bone cement observed under transmitted light (McCormack and Prendergast, 1999)

3. Analysis and results

3.1. Stress distribution in the cement

A three-dimensional finite element analysis model of von Mises stress applied to the three parts (proximal, medial, lateral, and distal) of the bone cement is shown in Fig. 7. This figure clearly shows that the major stresses are found in the upper region (proximal) where the cement is the most heavily solicited. The other two parts are exposed to lower stresses. The presence of a fragment of the body in this area (cavities, blood bag or bone debris) may be dangerous for stability of the total hip prosthesis. Indeed, such imperfections are the reason for stress concentration by the notch effect. These local stresses can exceed the maximum principal stress of the crack initiation, which can lead to creation and, later, propagation of cracks caused by fatigue. This promotes the risk of the loosening of the total hip prosthesis. Knowing that the cement material has a lower mechanical tensile strength by about 24 MPa, one may conclude that stress concentration in the proximal part of the cement, by the notch effect, can lead to total destruction. Later in this paper, this crack behavior is examined thoroughly. This study is carried out by locating the crack initiation area and its orientation in the orthopedic cement.

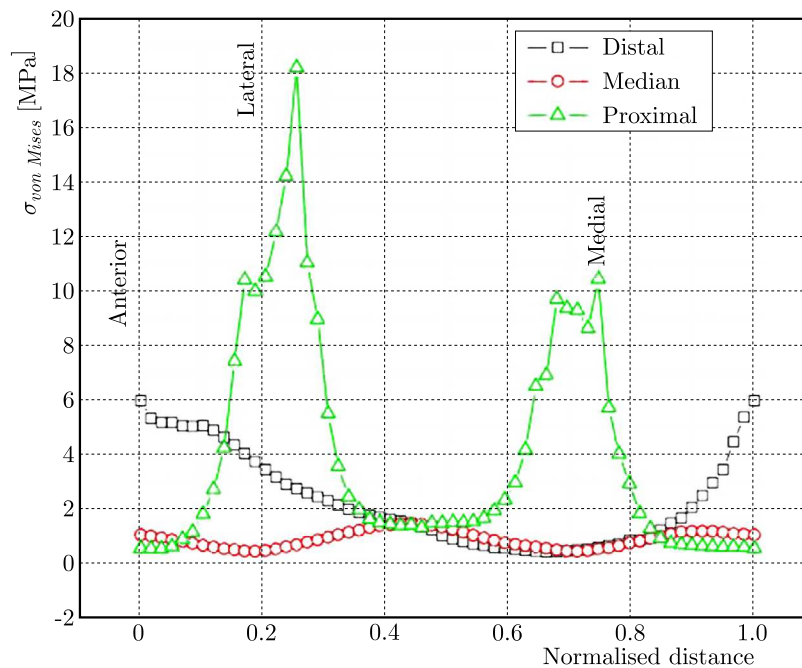


Fig. 7. The equivalent von Mises stress distribution around the cement perimeter in different parts (proximal, medial and distal)

3.2. Effect of the crack initiation site

The first elliptical cracks of various geometrical forms are firstly observed at the heart of the cement between the interfaces of the femoral implant-cement and the cement-bone. The analysis of their behavior starts at that area. At first, cracks take place in three areas: proximal (medial, lateral), and distal. This behavior is evaluated in terms of variation of the stress intensity factor and the results obtained are shown in Figs. 8, 9 and 10. Later in this paper, the variation of this rupture criterion is presented in mode I, II and III, according to the size of the crack initiated in these three areas, respectively. The size of the defect is defined by the ratio of the diameters a/c . Figure 8 shows the effect of steady progress in the opening mode (mode I) of the crack, located in these three areas, in terms of mechanical energy K_I in crack tip 1 and tip 2 (see Fig. 5). This

figure clearly shows that crack propagation in the direction of tip 1 increases the stress intensity factor in mode I. The criterion of rupture is significant as the crack arises in the lower part of the orthopedic cement, and this practically enlarges the crack (Fig. 5a). The growth of the crack in mode I, following the direction of tip 2, is stopped. The crack tip is stable. The crack propagates practically towards the evolution of point 1 independently of its point of start (Fig. 5b).

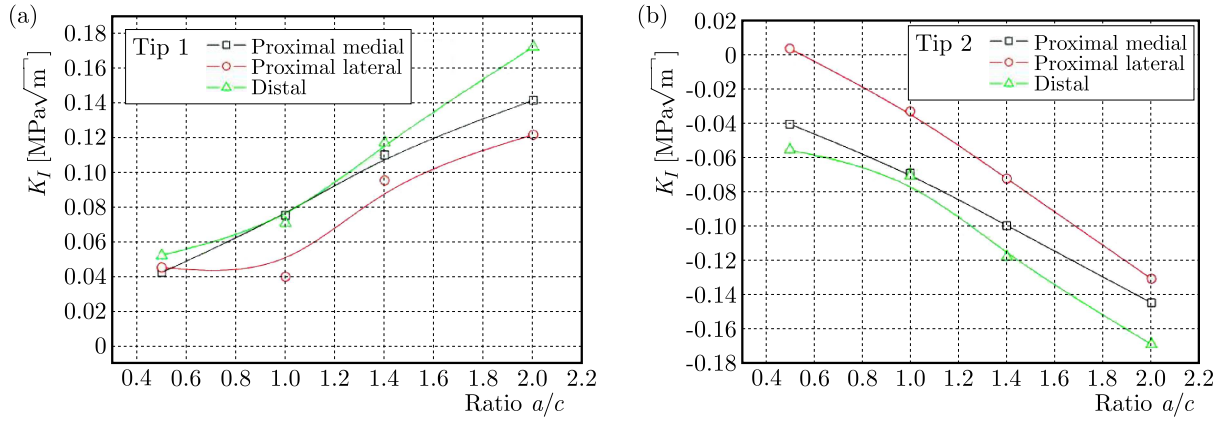


Fig. 8. Stress intensity factors K_I in tip 1 and tip 2 for different crack size and priming site

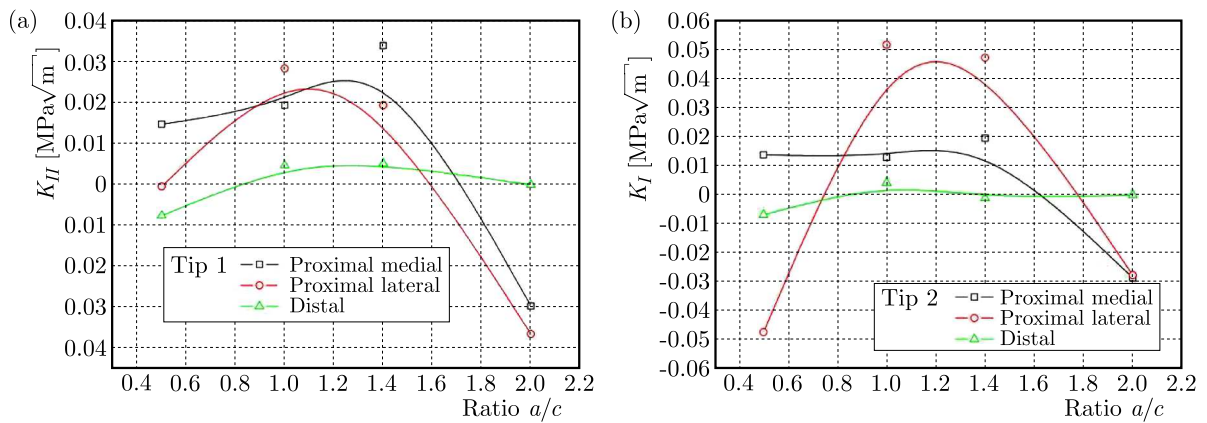


Fig. 9. Stress intensity factors K_{II} in tip 1 and tip 2 for different crack size and its priming site

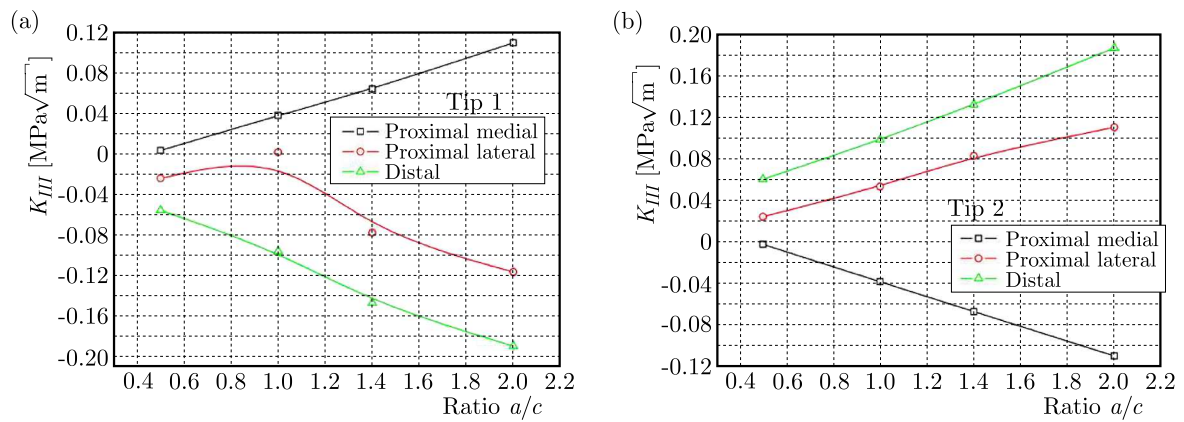


Fig. 10. Stress intensity factors K_{III} tip 1 and tip 2 for different crack size and its priming site

In Fig. 9, variation of the stress intensity factor is illustrated in crack tips 1 and 2 in mode II according to the size and location of initiation. A crack in the lateral proximal area follows the

most important rupture criterion. Such a crack is developed by shear (mode II) in its two tips. Variation of the stress intensity factor in mode III to of crack tips 1 and 2 as a function of the geometric form of the cracks is in the three parts of the cement, as shown in Fig. 10. This figure shows that this rupture parameter increases as the crack evolves independently of its starting point. This evolution is observed in the two tips of this defect. It is the distal part where the crack is unstable. The results obtained in this part of the work show that a crack initiated at the distal part of the cement propagates essentially in mode I and in mode III (mixed mode). In mode II, the crack growth kinetics is virtually null. A crack initiated at the proximal part (medial and lateral) is developed in mode I, in mode II and in mode III (mixed mode). Compared to tip 1, in tip 2, the stress intensity factor is higher. Such a crack propagates essentially according to crack tip 2.

3.3. Effect of crack orientation

The crack initiated in the cement, in its proximal (medial, lateral) and distal parts, undergoes rotation around its center of gravity. The effect of this rotation can be estimated by the stress intensity factor in tips 1 and 2 in mode I, mode II and in mode III. The results obtained are shown in Figs. 11, 12 and 13, respectively. This criterion of rupture in mode I at tip 1 reaches its maximum intensity when the crack is initiated at the distal part and is oriented at an angle of 20° up to 160° . This crack tip is estimated by the most important intensity factor in mode I, when its rotation is 160° , independently of the area in which it propagates (Fig. 11).

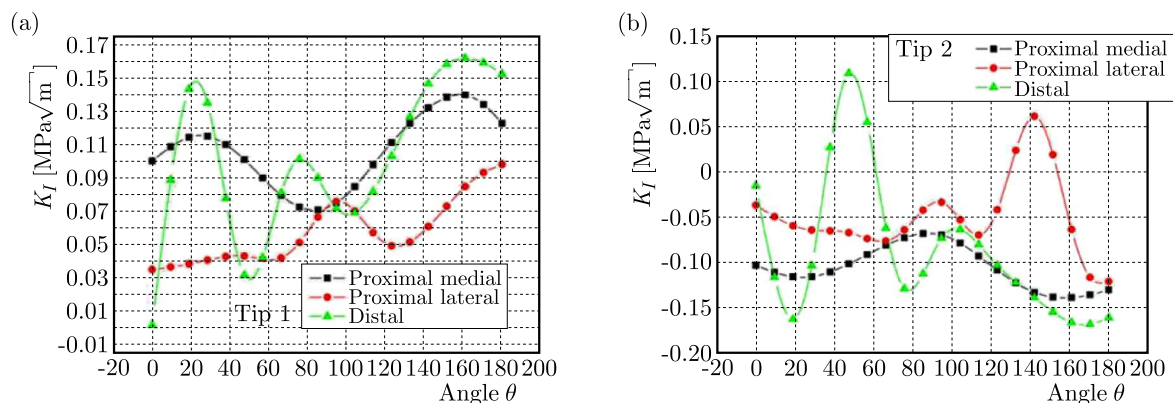


Fig. 11. Stress intensity factors K_I tip 1 and tip 2 depending on their orientation and priming crack site; $a = 1$ mm and $c = 0.5$ mm

In this case, this factor gradually drops from the distal part to the proximal part, the medial than the lateral. This criterion of rupture at crack tip 2 takes maximum values when the crack is located at the distal part and is oriented at an angle of approximately 50° . Therefore, there are orientations for which this crack tip is stable, characterized by negative values of the factor (Fig. 11). In mode II, crack tip 1 dominates in the lateral proximal part of the cement, and the greatest important stress intensity factor is obtained in orientations of 20° , 50° , 80° and 180° (Fig. 12a). This criterion of rupture at the crack tip 1, located at the distal part, reaches the greatest intensities, when this defect is oriented at angles of 145° and 110° . The orientation of the crack, initiated in the medial proximal part at 120° , leads to high factor values in this region of the cement (Fig. 12a). The rupture factor in mode II in crack tip 1, results in a crack located in the lateral proximal part oriented by 20° . Similar behavior is observed for crack tip 2 propagating in mode II as shown in Fig. 12b.

The variation of the stress intensity factor in mode III at crack tips 1 and 2, for the three parts of the cement, is shown in Fig. 13. Figure 13a shows that this rupture criterion at the crack tip 1 is maximum when the crack is initiated at the distal part and oriented at an angle

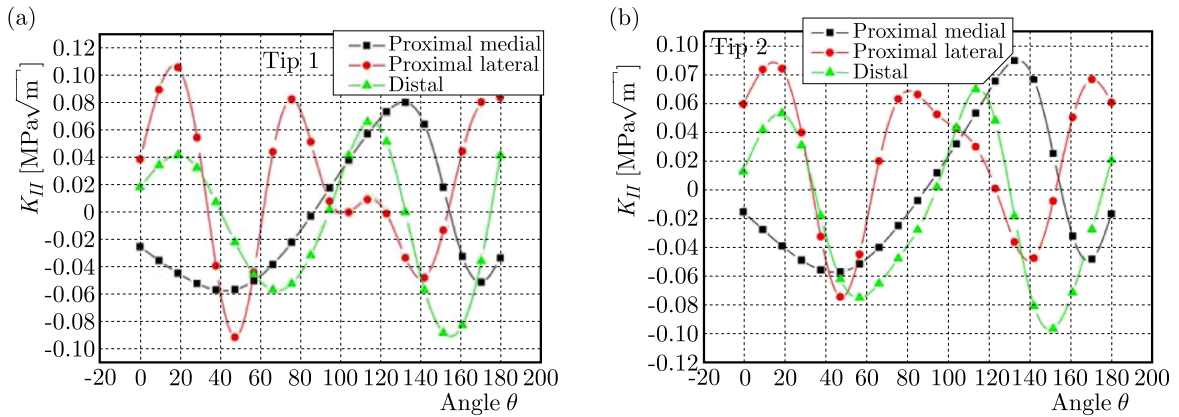


Fig. 12. Stress intensity factors K_{II} tip 1 and tip 2 depending on their orientation and priming crack site; $a = 1$ mm and $c = 0.5$ mm

of 45° . Compared to other locations of initiation, such a location of the crack leads to high values of the mechanical energy in mode III. A localization of this crack tip in the lateral proximal part leads to a higher intensity, when this defect is oriented at an angle of 25° . This rupture parameter varies among different orientations of the crack initiated in the medial proximal part (Fig. 13a). The stress intensity factor in mode III at crack tip 2 gives the most intense results from the crack tip located in the lateral proximal part of the cement when it is inclined at an angle of 0° up to 180° (Fig. 13b), i.e. when the main axis of this crack is parallel to that of the femoral implant. In the distal part, the factor presents two maxima for orientations of 45° and 90° , that is to say, when the crack is inclined by 45° on each side of the femoral implant axis. A localization of the crack in the medial proximal part leads to relatively low intensities of the factor.

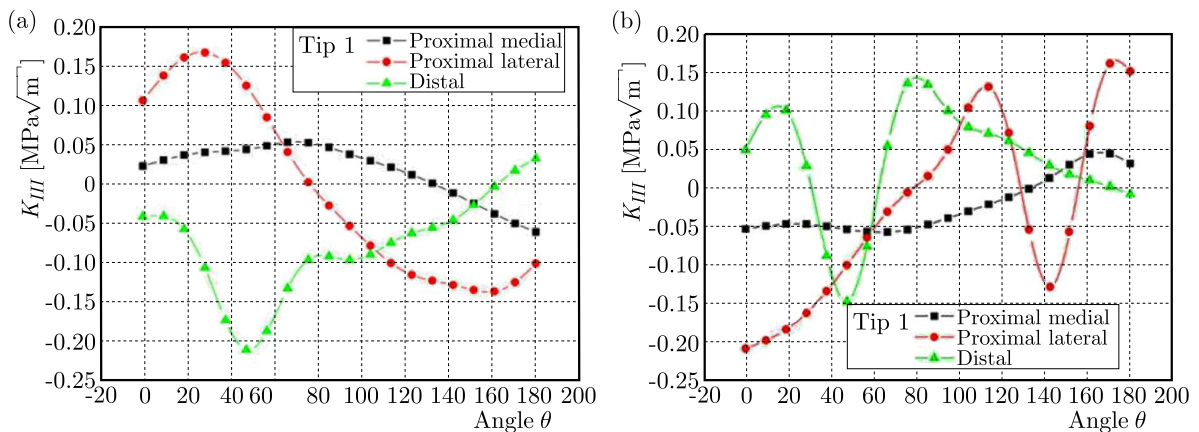


Fig. 13. Stress intensity factors K_{III} tip 1 and tip 2 depending on their orientation and priming crack site; $a = 1$ mm and $c = 0.5$ mm

4. Conclusion

The results obtained in this work make it possible to extract the following conclusions:

- The equivalent von Mises stresses in the cement are strongly localized in its proximal parts.
- The stress intensity factor in crack tips 1 and 2 depends on the location where the defect is initiated in the orthopedic cement.
- The crack tip 1 initiated at the distal part of the cement propagates essentially in mode I and in mode III (mixed mode). The growth kinetics in mode II is virtually negligible.

- A crack initiated at the proximal part (medial and lateral) can be developed in mode I, mode II and mode III (mixed mode). In the proximal part, the crack tip propagates in mixed mode I, II and III. Mode I is predominant.
- Crack tip 2, located in the distal part, evolves practically in mode III. Such a tip located at the proximal part develops essentially in mixed mode (II and III).
- The stress intensity factor in mode I, II and III, resulting from crack tips initiated in the cement in its proximal and distal parts, depends on the orientation of the crack. The orientation of 20° results practically in the highest values of the criterion of rupture in modes I, II and III.

References

1. ABAQUS Ver 9-11, 2011, User Guide
2. ABDEL-WAHAB A.A., SILBERSCHMIDT V.V., 2011, Numerical modeling of impact fracture of cortical bone tissue using X-FEM, *Journal of Theoretical and Applied Mechanics*, **49**, 3, 599-619
3. BENBAREK S., BACHIR BOUIADJRA B., BOUZIANE M.M., ACHOUR T., SERIER B., 2013, Numerical analysis of the crack growth path in the cement mantle of the reconstructed acetabulum, *Materials Science and Engineering C*, **33**, 543-549
4. BENOUIS A., BOULENOUAR A., BENSEDDIQ N., SERIER B., 2015, Numerical analysis of crack propagation in cement PMMA: application of SED approach, *Structural Engineering and Mechanics*, **55**, 1, 93-109
5. BENOUIS A., BOULENOUAR A., SERIER B., 2016, Finite element analysis of the behaviour of a crack in the orthopedic cement, *Journal of Theoretical and Applied Mechanics*, **54**, 1, 277-284, DOI: 10.15632/jtam-pl.54.1.277
6. BERGMANN G., DEURETZBACHIR G., HELLER M., GRAICHEN F., ROHLMANN A., STRAUSS J., DUDA G.N., 2001, Hip contact forces and gait patterns from routine activities, *Journal of Biomechanics*, **34**, 859-871
7. BERGMANN G., GRAICHEN F., ROHLMANN A., 1993, Hip joint loading during walking and running, measured in two patients, *Journal of Biomechanics*, **26**, 969-990
8. BOUZIANE M.M., BACHIR BOUIADJRA B., BENSEDDIQ N., TABETI E.M.H., SERIER B., BENBAREK S., 2013, The effects of cracks emanating from micro-void and bone inclusion in cemented total hip replacement, *Advances in Bio-Mechanical Systems and Materials, Advanced Structured Materials*, **40**, DOI: 10.1007/978-3-319-00479-2_4
9. EL-SHEIKH H.F., MACDONALD J.B., HASHMI M.S.J., 2002, Material selection in the design of the femoral component of cemented total hip replacement, *Journal of Materials Processing Technology*, **122**, 309-317
10. GRIZA S., AZEVEDO T.F., DOS SANTOS S.V., TENTARDINI E.K., STROHAECKER T.R., 2013, Metallurgical failure analysis of acetabular metal-backed screws, *Engineering Failure Analysis*, **32**, 178-187
11. LENNON A.B., MCCORMACK B.A.O., PRENDERGAST P.J., 2004, The relationship between cement fatigue damage and implant surface finish in proximal femoral prostheses, *Medical Engineering and Physics*, **25**, 833-841
12. MCCORMACK B.A.O., PRENDERGAST P.J., 1999, Microdamage accumulation in the cement layer of hip replacements under flexural loading, *Journal of Biomechanics*, **32**, 5, 467-475
13. MERCKX D., 1993, Les ciments orthopédiques dans la conception des prothèses articulaires, *Biomécanique et biomatériaux, Cahiers d'enseignement de la SOFCOT, Expansion scientifique française*, **44**, 67-76

14. MORGAN R.L., FARRAR D.F., ROSE J., FORSTER H., 2003, Creep behavior of bone cement: a method for time extrapolation using time-temperature equivalence, *Journal of Materials Science: Materials in Medicine*, **14**, 321-325
15. NAJAFI A.R., SAFFAR K.P.A., ARSHI A.R., MALLAKIN E., KATOUZIAN H.R., ESLAMI M.R., MOEINZADEH M.H., 2011, Propagation of microcracks in bovine osteonal cortical bone, *Akademeia*, **1**, 1, 1923-1504
16. PILLIAR R.M., VOWLES R., WILLIAMS D.F., 1982, Fracture toughness testing of biomaterials using a mini-short rod specimen design, *Journal of Biomedical Materials Research*, **21**, 145-154
17. RAMOS A., RELVAS C., COMPLETO A., SIMÕES J.A., 2013, The formation of cracks at cement interfaces of different femoral stem designs, *European Orthopaedics and Traumatology*, **4**, 205-215, DOI: 10.1007/s12570-013-0190-6
18. RIES M.D., YOUNG E., AL-MARASHI L., GOLDSTEIN P., HETHERINGTON A., PETRIE T., PRUITT L., 2006, In vivo behavior of acrylic bone cement in total hip arthroplasty, *Biomaterials*, 256-261
19. RODRIGUEZ L.C., CHARI J., AGHYARIAN S., GINDRI I.M., KOSMOPOULOS V., RODRIGUES D.C., 2014, Preparation and characterization of injectable brushite filled-poly (methyl methacrylate) bone cement, *Materials*, **7**, 6779-6795
20. SOLTÉSZ U., 1994, The influence of loading conditions on the lifetimes in fatigue testing of bone cements, *Journal of Materials Science: Materials in Medicine*, **5**, 654-656
21. TAYLOR D., HAZENBERG J.G., LEE T.C., 2003, The cellular transducer in damage-stimulated bone remodelling: a theoretical investigation using fracture mechanics, *Journal of Theoretical Biology*, **225**, 65-75
22. TOPOLESKI L.D., DUCHEYNE P., CUCKLER J.M., 1990, A fractographic analysis of in vivo poly-methyl-methacrylate bone cement failure mechanisms, *Journal of Biomedical Materials Research*, **24**, 2, 135-154
23. WAANDERS D., JANSSEN D., MANN K.A., VERDONSCHOT N., 2012, The behavior of the micro-mechanical cement-bone interface affects the cement failure in total hip replacement, *Journal of Biomechanics*, **44**, 2, 228-234

Manuscript received June 25, 2017; accepted for print January 10, 2018

PRIMARY PARAMETRIC RESONANCE OF AN AXIALLY ACCELERATING BEAM SUBJECTED TO STATIC LOADS

YUDA HU, YANTIAN RONG

School of Civil Engineering and Mechanics, Yanshan University, Qinhuangdao, China

Hebei Provincial Key Laboratory of Mechanical Reliability for Heavy Equipments and Large Structures, Yanshan University, Qinhuangdao, China

e-mail: huyuda03@163.com; Tiffany_rong@163.com

JING LI

School of Civil Engineering and Mechanics, Yanshan University, Qinhuangdao, China

Department of Basic Teaching, Tangshan University, Tangshan, China

e-mail: jingamanda721@163.com

Primary parametric resonance and stability of an axially accelerating and current-carrying beam subjected to static loads in magnetic field are investigated. The nonlinear magneto-elastic vibration equation is derived. The approximate solution of the static problem and the disturbance differential equation of the beam with two sides simply supported are obtained. The frequency-response equation of primary parametric resonance is further achieved by a multi-scale method. According to stability conditions, the stability of the steady-state solution is also discussed. By numerical examples, the amplitude versus different parameter curves and the bifurcation diagrams of the amplitude are acquired. The effects of magnetic induction intensity, axial speed, detuning parameter and static loads on nonlinear vibration characteristics are also analyzed.

Keywords: current-carrying beam, primary parametric resonance, magnetic field, axial movement, static loads

1. Introduction

In modern engineering life, with the rapid development of science and technology and wide application of axially moving systems, electromagnetic structures have been gradually applied in many significant industrial fields, for instance, aerospace and heavy-duty machinery. When interfered by electromagnetic field, mechanical field and parametric resonance, magneto-elastic structures may cause large amplitude vibration or even result in the loss of stability. Therefore, it is important to analyze nonlinear dynamic characteristics of axially accelerating beams in magnetic field when the beams are under coupled vibration. The nonlinear vibration model of electroconductive plate in the magnetic field has been established (Hasanyan *et al.*, 2001) and the investigation of vibrational behaviors have also been made by means of the Hamilton principle and multi-scale method (Hasanyan *et al.*, 2005). The dynamic stability and nonlinear subharmonic resonance of conductive plates under magnetic field have been investigated (Zheng *et al.*, 2005; Hu and Li, 2009). Wang *et al.* (2003) analyzed magneto-thermo-elastic instability of simply supported ferromagnetic plates subjected to thermal and magnetic loadings and investigated effects of thermal and magnetic fields in some detail. Hu *et al.* (2015) analyzed the strong nonlinear subharmonic resonance of an axially moving plate and employed the singularity theory to analyze the corresponding transition variety and the effects of parameters on system bifurcation. Ghayesh and Balar (2008) studied the stability condition of the Rayleigh beam by

the Routh-Hurwitz criterion. Non-linear parametric vibration and stability of an axially moving Timoshenko beam with two dynamic models were investigated by Ghayesh and Balar (2010). Principal parametric resonance of an axially accelerating viscoelastic beam was studied with two models: one was partial differential nonlinear model and the other an integro-partial differential nonlinear model (Chen and Yang, 2005). Chakraborty and Mallik (1998) investigated the effects of the parametrically excited nonlinear moving beam with and without an external harmonic excitation. Based on the Timoshenko model, parametric resonance of axially moving beams and dynamic stability of a viscoelastic variable motion beam were studied (Tang *et al.*, 2009; Chen *et al.*, 2010). Hu and Zhang (2013) analyzed the primary parametric resonance of a rectangular thin plate in magnetic field and the effect of different parameters on dynamic behaviors. The nonlinear resonance of a rotating circular plate with initial deflection in magnetic field was studied by Hu and Wang (2015). Wang and Chen (1998) applied the Galerkin integral method to obtain the differential equation of flexible circular plates and discussed the influence of initial deflection on vibration characteristics. The effect of initial deflections on natural vibration frequencies of shells was analyzed by Matsner (1978). However, these investigations are all limited to primary parametric resonance of current-carrying structures with initial deflection. Thus it is still imperative to understand nonlinear dynamic behaviors of axially accelerating structures subjected to static loads under magnetic field.

In this article, the primary parametric resonance of an axially accelerating and current-carrying beam subject to static loads under magnetic field is investigated and the stability of the steady-state solution is also discussed. Detailed numerical examples are employed to demonstrate that the system presents typical nonlinear vibration characteristics and complex dynamic behaviors.

2. Magneto-elastic vibration equations of the axially moving and current-carrying beam

An isotropic current-carrying beam under a magnetic field $\mathbf{B} = [0, B_{0y}, 0]$, a uniformly distributed axial tension F_{0x} and a uniformly distributed transverse load P_z , travels along the centroidal axis x -direction with an axial speed C . As shown in Fig. 1, the beam with length l , width b , thickness h and mass density ρ is charged with the electric current density vector $\mathbf{J}_e = [J_{0x}(t), 0, 0]$. And t is time variable.

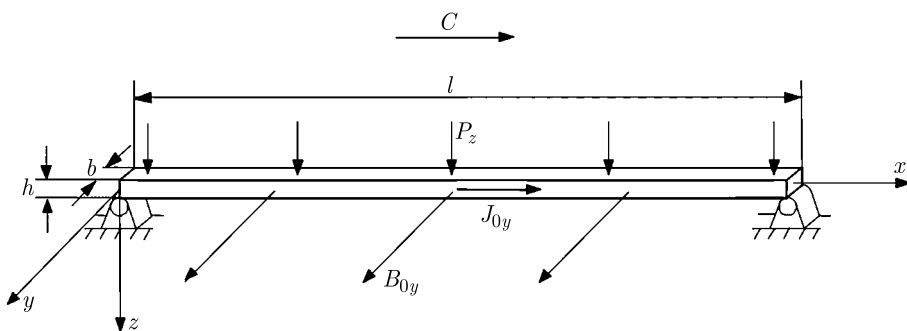


Fig. 1. Mechanical model of an axially accelerating and current-carrying beam in magnetic field

2.1. Kinetic energy

The transverse velocity of the axially accelerating beam can be expressed as follows

$$V_{0z} = \frac{dw}{dt} = \frac{\partial w}{\partial t} + C \frac{\partial w}{\partial x} \quad (2.1)$$

where $w(x, t)$ is the transverse displacement.

For this system, the total kinetic energy T is

$$T = \frac{1}{2}\rho \int_{-\frac{h}{2}}^{\frac{h}{2}} \int_{-\frac{b}{2}}^{\frac{b}{2}} \int_0^l (C^2 + V_{0z}^2) dx dy dz = \frac{1}{2}\rho A \int_0^l \left[C^2 + \left(\frac{\partial w}{\partial t} + C \frac{\partial w}{\partial x} \right)^2 \right] dx \quad (2.2)$$

where $A = b \times h$ is the cross-sectional area of the beam.

2.2. Potential energy

According to the Euler-Bernoulli beam theory, the total potential energy of the beam is composed of three parts, namely, the strain potential energy U_1 induced by axial tension, the bending strain potential energy U_2 and the in-plane strain potential energy U_3 . The total potential energy of the beam can be represented as follows

$$\begin{aligned} U &= U_1 + U_2 + U_3 \\ &= \int_0^l F_{0x} \varepsilon_x dx + \frac{1}{2} \int_{-\frac{h}{2}}^{\frac{h}{2}} \int_{-\frac{b}{2}}^{\frac{b}{2}} \int_0^l E \left(-\frac{\partial^2 w}{\partial x^2} z \right)^2 dx dy dz + \frac{1}{2} \int_{-\frac{h}{2}}^{\frac{h}{2}} \int_{-\frac{b}{2}}^{\frac{b}{2}} \int_0^l E \varepsilon_x^2 dx dy dz \\ &= \int_0^l \left[F_{0x} \varepsilon_x + \frac{1}{2} EI \left(\frac{\partial^2 w}{\partial x^2} \right)^2 + \frac{1}{2} EA \varepsilon_x^2 \right] dx \end{aligned} \quad (2.3)$$

where $\varepsilon_x = (\partial w / \partial x)^2 / 2$ is the normal strain component of the beam, E is Young's modulus, $I = \int_{-h/2}^{h/2} \int_{-b/2}^{b/2} z^2 dy dz$ is the cross sectional moment of inertia.

2.3. Virtual work by the external force

Transverse external forces acting on the beam include the transverse uniformly distributed forced excitation P_z and electromagnetic force F_z . Hence, the virtual work generated by P_z can be expressed as

$$\delta W_1 = \int_0^l P_z \delta w dx \quad (2.4)$$

Neglecting the effect of magnetization and displacement current, the Lorentz force of a good conductor can be expressed as

$$\mathbf{f} = \mathbf{J} \times \mathbf{B} \quad (2.5)$$

where \mathbf{J} is the electric current density in the beam.

Equation (2.5) can be rewritten as below

$$\mathbf{f} = \mathbf{J}_{0x} \times \mathbf{B} + \mathbf{J}_x \times \mathbf{B} = \begin{vmatrix} \mathbf{i} & \mathbf{j} & \mathbf{k} \\ J_{0x} + J_x & 0 & 0 \\ 0 & B_{0y} & 0 \end{vmatrix} = (J_{0x} B_{0y} + J_x B_{0y}) \mathbf{k} \quad (2.6)$$

where \mathbf{i} , \mathbf{j} , and \mathbf{k} are the unit vectors in the x , y , and z directions, respectively, $J_x = -\sigma_0 V_{0z} B_0$ is the induced current density component in the conductive beam due to the external magnetic field along the x axis, and σ_0 is the electric conductivity.

The electromagnetic force per unit length can be derived from Eq. (2.6)

$$F_z = \int_{-\frac{b}{2}}^{\frac{b}{2}} \int_{-\frac{b}{2}}^{\frac{b}{2}} (J_{0x} B_{0y} + J_x B_{0y}) dy dz \quad (2.7)$$

So, the virtual work due to the electromagnetic force can be represented as

$$\delta W_2 = \int_0^l F_z \delta w dx \quad (2.8)$$

2.4. Establishing the vibration equation by the Hamilton principle

Based on the Hamilton principle, which is one of the most important integral principles of mechanics, one can get

$$\int_{t_1}^{t_2} (\delta T - \delta U + \delta W_1 + \delta W_2) dt = 0 \quad (2.9)$$

where δT is the variational expression of kinetic energy and δU is the variational expression of potential energy.

Substitution of Eqs. (2.2), (2.3), (2.4) and (2.8) into Eq. (2.9) yields the nonlinear magneto-elastic vibration equation of the axially accelerating beam

$$\begin{aligned} \rho A \frac{\partial^2 w}{\partial t^2} + 2\rho AC \frac{\partial^2 w}{\partial x \partial t} + \rho AC^2 \frac{\partial^2 w}{\partial x^2} + \rho A \frac{\partial C}{\partial t} \frac{\partial w}{\partial x} - F_{0x} \frac{\partial^2 w}{\partial x^2} \\ - \frac{3}{2} EA \left(\frac{\partial w}{\partial x} \right)^2 \frac{\partial^2 w}{\partial x^2} + EI \frac{\partial^4 w}{\partial x^4} = F_z + P_z \end{aligned} \quad (2.10)$$

where

$$F_z = AB_{0y} J_{0x} - A\sigma_0 B_{0y}^2 \left(\frac{\partial w}{\partial t} + C \frac{\partial w}{\partial x} \right)$$

3. Disturbance differential equation of the axially accelerating beam subjected to static loads

When a system is under a constant forced excitation ($P_z = P_c$) and a constant magnetic induction intensity ($B_{0y} = B_0$) and charged with a direct current ($J_{0x} = J_c$), the value of $AB_{0y} J_{0x}$ is constant. Let $Q_z = AB_0 J_c$, $Q = P_c + Q_z$, and Q is a uniformly distributed static load. Equation (2.10) can be expressed in the following form

$$\begin{aligned} \rho A \frac{\partial^2 w}{\partial t^2} + 2\rho AC \frac{\partial^2 w}{\partial x \partial t} + \rho AC^2 \frac{\partial^2 w}{\partial x^2} + \rho A \frac{\partial C}{\partial t} \frac{\partial w}{\partial x} - F_{0x} \frac{\partial^2 w}{\partial x^2} - \frac{3}{2} EA \left(\frac{\partial w}{\partial x} \right)^2 \frac{\partial^2 w}{\partial x^2} \\ + EI \frac{\partial^4 w}{\partial x^4} + A\sigma_0 B_0^2 \left(\frac{\partial w}{\partial t} + C \frac{\partial w}{\partial x} \right) = Q \end{aligned} \quad (3.1)$$

It is assumed that the beam has a tiny static deflection w_0 under the uniformly distributed static load Q and a deflection w_1 when it vibrates. Therefore, the total deflection of the system can be given as below

$$w = w_0 + w_1 \quad (3.2)$$

Therefore, Eq. (3.1) can be rewritten as

$$\begin{aligned} &\rho A \frac{\partial^2 w_1}{\partial t^2} + 2\rho AC \frac{\partial^2 w_1}{\partial x \partial t} + \rho AC^2 \left(\frac{\partial^2 w_0}{\partial x^2} + \frac{\partial^2 w_1}{\partial x^2} \right) + \rho A \frac{\partial C}{\partial t} \frac{\partial w_1}{\partial x} \\ &- F_{0x} \left(\frac{\partial^2 w_0}{\partial x^2} + \frac{\partial^2 w_1}{\partial x^2} \right) - \frac{3}{2} EA \left(\frac{\partial w_0}{\partial x} + \frac{\partial w_1}{\partial x} \right)^2 \left(\frac{\partial^2 w_0}{\partial x^2} + \frac{\partial^2 w_1}{\partial x^2} \right) \\ &+ EI \left(\frac{\partial^4 w_0}{\partial x^4} + \frac{\partial^4 w_1}{\partial x^4} \right) + A\sigma_0 B_0^2 \left[\frac{\partial w_1}{\partial t} + C \left(\frac{\partial w_0}{\partial x} + \frac{\partial w_1}{\partial x} \right) \right] = Q \end{aligned} \tag{3.3}$$

The initial deflection w_0 satisfies the following equation

$$\rho AC^2 \frac{\partial^2 w_0}{\partial x^2} - F_{0x} \frac{\partial^2 w_0}{\partial x^2} - \frac{3}{2} EA \left(\frac{\partial w_0}{\partial x} \right)^2 \frac{\partial^2 w_0}{\partial x^2} + EI \frac{\partial^4 w_0}{\partial x^4} + A\sigma_0 B_0^2 C \frac{\partial w_0}{\partial x} = Q \tag{3.4}$$

According to the axially moving beam simply supported on two sides, its boundary conditions are

$$\begin{aligned} x = 0 : \quad &w = 0 & \frac{\partial^2 w}{\partial x^2} = 0 \\ x = l : \quad &w = 0 & \frac{\partial^2 w}{\partial x^2} = 0 \end{aligned}$$

Assume that the static deflection displacement satisfies the boundary condition

$$w_0 = f_0 \sin \frac{\pi x}{l} \tag{3.5}$$

After substituting Eq. (3.5) into Eq. (3.4) and using the Galerkin method, we can get

$$\begin{aligned} &\int_0^l \left[\rho AC^2 \frac{\partial^2 w_0}{\partial x^2} - F_{0x} \frac{\partial^2 w_0}{\partial x^2} - \frac{3}{2} EA \left(\frac{\partial w_0}{\partial x} \right)^2 \frac{\partial^2 w_0}{\partial x^2} \right] \sin \frac{\pi x}{l} dx \\ &+ \int_0^l \left(EI \frac{\partial^4 w_0}{\partial x^4} + A\sigma_0 B_0^2 C \frac{\partial w_0}{\partial x} - Q \right) \sin \frac{\pi x}{l} dx = 0 \end{aligned} \tag{3.6}$$

After integration, the following formula is obtained

$$a_2 f_0^3 - (a_3 - a_1) f_0 + a_4 Q = 0 \tag{3.7}$$

where

$$a_1 = \frac{EI\pi^4}{2l^3} \quad a_2 = \frac{3EA\pi^4}{16l^3} \quad a_3 = \frac{\rho AC^2\pi^2 - F_{0x}\pi^2}{2l} \quad a_4 = -\frac{2l}{\pi}$$

The real root of Eq. (3.7) is

$$f_0 = Z_0 - \frac{a_1 - a_3}{3a_2 Z_0} \tag{3.8}$$

where

$$Z_0 = \sqrt[3]{\sqrt{\left(\frac{a_1 - a_3}{3a_2}\right)^3 + \left(\frac{a_4 Q}{2a_2}\right)^2} - \frac{a_4 Q}{2a_2}}$$

Considering Eq. (3.4) for the initial static deflection w_0 in Eq. (3.3), we can write the following equation for the deflection w_1

$$\begin{aligned} & \rho A \frac{\partial^2 w_1}{\partial t^2} + 2\rho AC \frac{\partial^2 w_1}{\partial x \partial t} + \rho AC^2 \frac{\partial^2 w_1}{\partial x^2} + \rho A \frac{\partial C}{\partial t} \frac{\partial w_1}{\partial x} - F_{0x} \frac{\partial^2 w_1}{\partial x^2} \\ & - \frac{3}{2} EA \left[2 \frac{\partial w_0}{\partial x} \frac{\partial w_1}{\partial x} \left(\frac{\partial^2 w_0}{\partial x^2} + \frac{\partial^2 w_1}{\partial x^2} \right) + \left(\frac{\partial w_1}{\partial x} \right)^2 \frac{\partial^2 w_0}{\partial x^2} + \left(\frac{\partial w_0}{\partial x} \right)^2 \frac{\partial^2 w_1}{\partial x^2} \right. \\ & \left. + \left(\frac{\partial w_1}{\partial x} \right)^2 \frac{\partial^2 w_1}{\partial x^2} \right] + EI \frac{\partial^4 w_1}{\partial x^4} + A\sigma_0 B_0^2 \left(\frac{\partial w_1}{\partial t} + C \frac{\partial w_1}{\partial x} \right) = 0 \end{aligned} \quad (3.9)$$

For the axially accelerating beam, its axial speed and axial tension can be assumed as follows, respectively

$$C = C_0 + C_1 \cos(\omega_1 t) \quad F_{0x} = F_0 + F_1 \cos(\omega_2 t) \quad (3.10)$$

According to the simply supported boundary condition, the deflection w_1 can be denoted as

$$w_1 = s(t) \sin \frac{\pi x}{l} \quad (3.11)$$

where C_0 is the axial constant speed, C_1 is the amplitude of the time-variant axial speed, F_0 is the axial constant tension, F_1 is the amplitude of the time-variant axial tension, and ω_1 and ω_2 are the frequencies of the time-variant axial speed and time-variant axial tension, respectively.

Substituting Eqs. (3.10) and (3.11) into Eq. (3.9) and using the Galerkin method yields the dimensionless magneto-elastic parametric vibration differential equation

$$\ddot{q}(\tau) + 2\tilde{\zeta}\dot{q}(\tau) + \omega_0^2 q(\tau) - [\tilde{k}_1 \cos(2\tau) + \tilde{k}_2 \cos(4\tau) - \tilde{k}_3 \cos(2\tau)]q(\tau) - \tilde{\alpha}_4 q^2(\tau) + \tilde{\alpha}_3 q^3(\tau) = 0 \quad (3.12)$$

where

$$\begin{aligned} q &= \frac{s}{h} & 2\tau &= \omega_1 t & 2\tau &= \omega_2 t & \tilde{\zeta} &= \frac{\sigma_0 B_0^2}{\rho \omega_1} \\ \tilde{k}_1 &= \frac{8C_0 C_1 \pi^2}{\omega_1^2 l^2} & \tilde{k}_2 &= \frac{2C_1^2 \pi^2}{\omega_1^2 l^2} & \tilde{k}_3 &= \frac{4\pi^2 F_1}{\rho A \omega_1^2 l^2} \\ \omega_0^2 &= \frac{4\pi^2 F_0 l^2 + 4\pi^4 EI + \frac{9}{2} EA \pi^4 f_0^2 - 2\rho Al^2 \pi^2 C_1^2 - 4\rho Al^2 \pi^2 C_0^2}{\rho Al^4 \omega_1^2} \\ \tilde{\alpha}_4 &= \frac{9f_0 E \pi^4 h}{2\rho \omega_1^2 l^4} & \tilde{\alpha}_3 &= \frac{3E \pi^4 h^2}{2\rho \omega_1^2 l^4} \end{aligned}$$

4. Solving the primary parametric vibration problem by the method of multiple scales

In order to analyze the problem of principal parametric resonance of Eq. (3.12), a small parameter ε is introduced

$$\ddot{q}(\tau) + 2\varepsilon\zeta\dot{q}(\tau) + \omega_0^2 q(\tau) - \varepsilon[k_1 \cos(2\tau) + k_2 \cos(4\tau) - k_3 \cos(2\tau)]q(\tau) - \varepsilon\alpha_4 q^2(\tau) + \varepsilon\alpha_3 q^3(\tau) = 0 \quad (4.1)$$

where

$$\zeta = \frac{\tilde{\zeta}}{\varepsilon} \quad k_1 = \frac{\tilde{k}_1}{\varepsilon} \quad k_2 = \frac{\tilde{k}_2}{\varepsilon} \quad k_3 = \frac{\tilde{k}_3}{\varepsilon} \quad \alpha_3 = \frac{\tilde{\alpha}_3}{\varepsilon} \quad \alpha_4 = \frac{\tilde{\alpha}_4}{\varepsilon}$$

When solving the problem of the principal parametric resonance, we let

$$\omega_0 = 1 + \varepsilon\sigma \tag{4.2}$$

where σ is the detuning parameter.

The first-order approximate solution to the vibration differential equation can be found through the method of multiple scales (Nayfeh and Mook, 1979). Meanwhile, the fast time scale $T_0 = \tau$ and the low time $T_1 = \varepsilon\tau$ scale are introduced. The approximate analytical solution of parametric resonance can be drawn as

$$q(\tau, \varepsilon) = q_0(T_0, T_1) + \varepsilon q_1(T_0, T_1) \tag{4.3}$$

Substituting Eqs. (4.2) and (4.3) into Eq. (4.1), and equating the coefficients of ε^0 and ε^1 on both sides, one can conclude that

$$\begin{aligned} D_0^2 q_0 + q_0 &= 0 \\ D_0^2 q_1^2 + q_1 &= -2D_0 D_1 q_0 - 2\zeta D_0 q_0 - 2\sigma q_0 \\ &+ [k_1 \cos(2\tau) + k_2 \cos(4\tau) - k_3 \cos(2\tau)]q_0 - \alpha_3 q_0^3 + \alpha_4 q_0^2 \end{aligned} \tag{4.4}$$

where $D_0 = \partial/\partial T_0$ and $D_1 = \partial/\partial T_1$.

The general solution of zero-order approximate Eq. (4.4)₁ can be expressed as follow

$$q_0 = A_0(T_1)e^{iT_0} + \bar{A}_0(T_1)e^{-iT_0} \tag{4.5}$$

where $i^2 = -1$, A_0 is an unknown complex number and \bar{A}_0 is the conjugate complex of A_0 . Substitution of Eq. (4.5) into first-order approximate Eq. (4.4)₂ gives

$$\begin{aligned} D_0^2 q_1^2 + q_1 &= -2iA_0' e^{iT_0} - 2i\zeta A_0 e^{iT_0} - 2\sigma A_0 e^{iT_0} - 3\alpha_3 A_0^2 \bar{A}_0 e^{iT_0} + \alpha_4 A_0^2 e^{i2T_0} + A_0 \bar{A}_0 \\ &- \alpha_3 A_0^3 e^{i3T_0} + \frac{k_1 - k_3}{2}(A_0 e^{i3T_0} + \bar{A}_0 e^{iT_0}) + \frac{k_2}{2}(A_0 e^{i5T_0} + \bar{A}_0 e^{i3T_0}) + cc \end{aligned} \tag{4.6}$$

where $A_0' = \partial A_0/\partial T_1$, cc stands for the conjugate complex part of the function on the right-hand side of Eq. (4.6).

Eliminating the secular term from the particular solution to Eq. (4.6)

$$-2iA_0' - 2i\zeta A_0 - 2\sigma A_0 - 3\alpha_3 A_0^2 \bar{A}_0 + \frac{k_1 - k_3}{2} \bar{A}_0 = 0 \tag{4.7}$$

Express now A_0 of Eq. (4.7) in the polar form

$$A_0 = \frac{1}{2}a(T_1)e^{i\varphi(T_1)} \tag{4.8}$$

where a and φ are real.

Substituting Eq. (4.8) into Eq. (4.7) we separate the conclusion into its real and imaginary parts, and arrive at

$$a' = -\zeta a + \frac{k_1 - k_3}{4}a \sin(2\varphi) \quad a\varphi' = \sigma a + \frac{3\alpha_3}{8}a^3 - \frac{k_1 - k_3}{4}a \cos(2\varphi) \tag{4.9}$$

There are $a' = 0$ and $\varphi' = 0$ according to steady state motion of the system. So, we conclude

$$\zeta a = \frac{k_1 - k_3}{4}a \sin(2\varphi) \quad \sigma a + \frac{3\alpha_3}{8}a^3 = \frac{k_1 - k_3}{4}a \cos(2\varphi) \tag{4.10}$$

The frequency-response equation is achieved according to Eqs. (4.10)

$$(\zeta a)^2 + \left(\sigma a + \frac{3\alpha_3}{8}a^3\right)^2 = \left(\frac{k_1 - k_3}{4}a\right)^2 \tag{4.11}$$

5. Stability analysis of steady state motion

We determine the stability of steady-state motion by investigating the nature of the singular points of Eqs. (4.9). To accomplish this, we let

$$a = a_0 + a_s \quad \varphi = \varphi_0 + \varphi_s \quad (5.1)$$

where a_0 and φ_0 are equilibrium solutions of the steady motion, a_s and φ_s are tiny disturbance values.

Substituting Eqs. (5.1) into Eqs. (4.9), expanding for small a_s and φ_s , noting that a_s and φ_s satisfy Eqs. (4.10) and keeping linear in a_s and φ_s , we obtain

$$a'_s = -2a_0\left(\sigma + \frac{3\alpha_3}{8}a^2\right)\varphi_s \quad \varphi'_s = \frac{3\eta_3 a_0}{4}a_s - 2\zeta\varphi_s \quad (5.2)$$

Thus, the stability of steady-state motions depends on the eigenvalues of the coefficient matrix on the right-hand sides of Eqs. (5.2). Using Eqs. (4.10), one can obtain the following eigenvalue equation

$$\begin{vmatrix} -\lambda & -2a_0\left(\sigma + \frac{3\eta_3}{8}a_0^2\right) \\ \frac{3\eta_3 a_0}{4} & -2\zeta - \lambda \end{vmatrix} = 0 \quad (5.3)$$

The solution of the system is stable only if the real parts of the eigenvalues are negative according to the stability theory. Based on the Routh-Hurwitz criteria, we conclude

$$\frac{3\alpha_3}{2}a_0^2\left(\sigma + \frac{3\alpha_3}{8}a_0^2\right) > 0 \quad (5.4)$$

6. Analysis of numerical illustrations

The numerical results are based on a copper beam model with length $l = 0.3$ m, width $b = 0.02$ m, thickness $h = 0.01$ m, Young's modulus $E = 108$ GPa, mass density $\rho = 8920$ kg/m³, Poisson's ratio $\mu = 0.33$, and electric conductivity $\sigma_0 = 5.7143 \cdot 10^7$ ($\Omega \cdot \text{m}$)⁻¹. Figures 2-7 represent the response curve of amplitude a versus the detuning parameter $\varepsilon\sigma$, the amplitude of time-variant axial tension F_1 and the static load Q . The solid lines represent the stable solutions and the dotted lines represent the unstable solutions. Figure 8 demonstrates the bifurcation diagram of the amplitude.

6.1. The curve of the amplitude-detuning parameter

For the given range in Fig. 2 in which the detuning parameter $\varepsilon\sigma$ changes from negative to positive, the amplitude a drops gradually to zero. The unstable solutions have tend to decrease as the axial constant velocity C_0 , the amplitude of the time-variant axial speed C_1 , the amplitude of the time-variant axial tension F_1 increase and the magnetic induction intensity B_0 , the static load Q decrease. It is also noted that the resonance region between the unstable solutions and the stable solutions broadens as C_0 , C_1 and F_1 increase and B_0 decreases. In Figs. 2a and 2e, the curves intersect and have different variation on both sides of the intersection point due to the value of $k_1 - k_3$ and ω_0 varying with C_0 . An increase of the static load Q leads an increase of ω_0 (Eqs. (3.8) and (3.12)). In Figs. 2b, 2c and 2d, we can note that the amplitudes of the stable solutions increase as C_1 and F_1 go up and B_0 comes down.

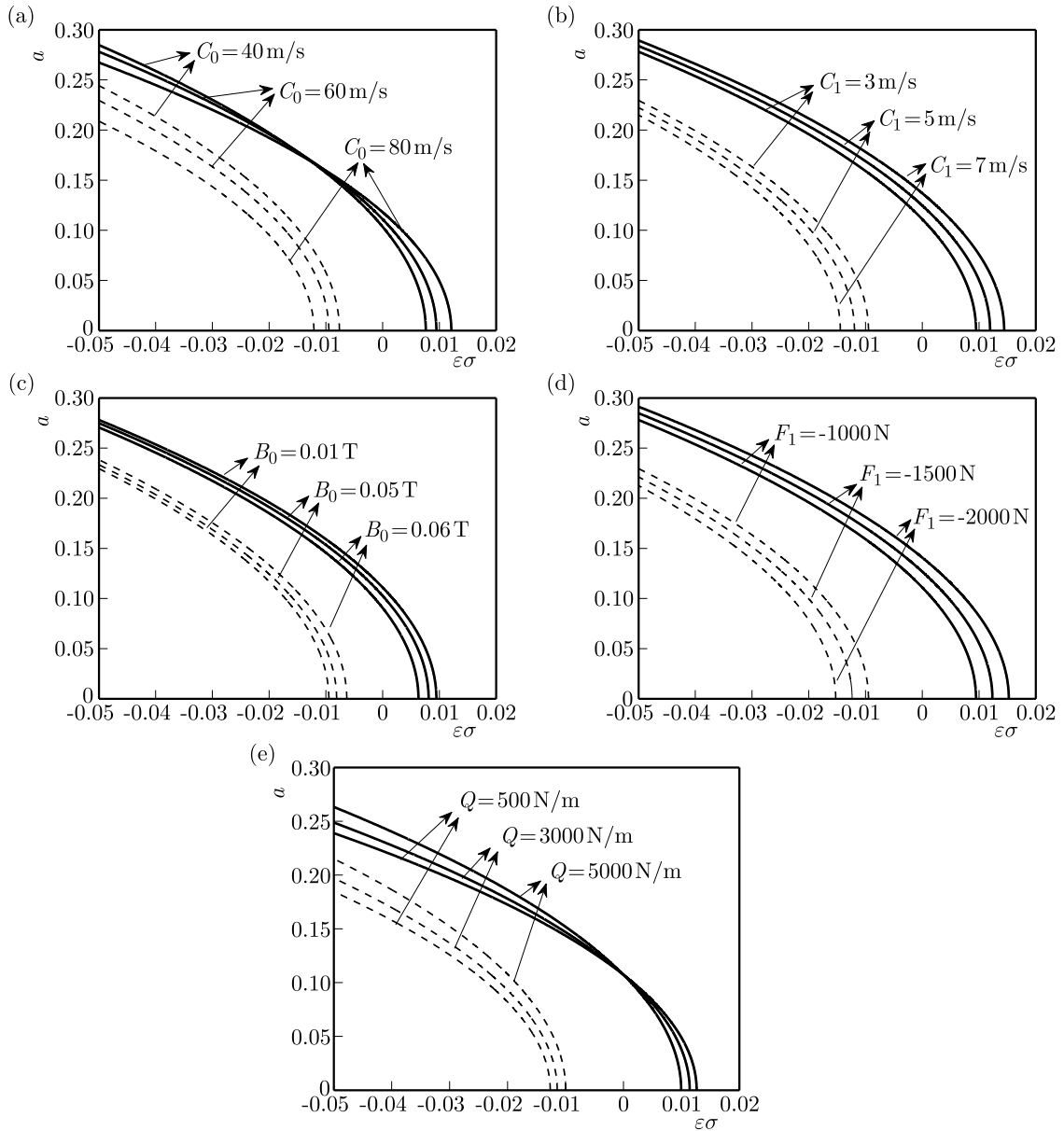


Fig. 2. The curve of amplitude frequency, $J_c = 0.02 \text{ A/mm}^2$:
 (a) $C_1 = 3 \text{ m/s}$, $B_0 = 0.01 \text{ T}$, $F_1 = -1000 \text{ N}$ when $P_c = 0 \text{ N/m}$ and $F_0 = 30 \text{ kN}$;
 (b) $C_0 = 60 \text{ m/s}$, $B_0 = 0.01 \text{ T}$, $F_1 = -1000 \text{ N}$ when $P_c = 0 \text{ N/m}$ and $F_0 = 30 \text{ kN}$;
 (c) $C_0 = 60 \text{ m/s}$, $C_1 = 3 \text{ m/s}$, $F_1 = -1000 \text{ N}$ when $P_c = 0 \text{ N/m}$ and $F_0 = 30 \text{ kN}$;
 (d) $C_0 = 60 \text{ m/s}$, $C_1 = 3 \text{ m/s}$, $B_0 = 0.01 \text{ T}$ when $P_c = 0 \text{ N/m}$ and $F_0 = 30 \text{ kN}$;
 (e) $C_0 = 50 \text{ m/s}$, $C_1 = 3 \text{ m/s}$, $B_0 = 0.01 \text{ T}$, $F_1 = -1000 \text{ N}$ when $F_0 = 15 \text{ kN}$

6.2. The curve of the amplitude-parametric excitation

Figure 3 represents the response curve of the amplitude a versus the parametric excitation F_1 under the influence of magnetic induction intensity B_0 . The zero solution region becomes wide when the magnetic induction intensity B_0 goes up, that is, the non-resonance region broadens. From Fig. 3, we note that the system has stable nontrivial solutions when the detuning parameter $\varepsilon\sigma = 0$, and the unstable nontrivial solutions when the detuning parameter $\varepsilon\sigma \neq 0$. All curves in Fig. 3 are symmetrically distributed with $F_0 = 0 \text{ N/m}$ line when the amplitude of the time-variant axial speed $C_1 = 0 \text{ m/s}$. When $C_1 = 1 \text{ m/s}$, the symmetry axis shifts towards right.

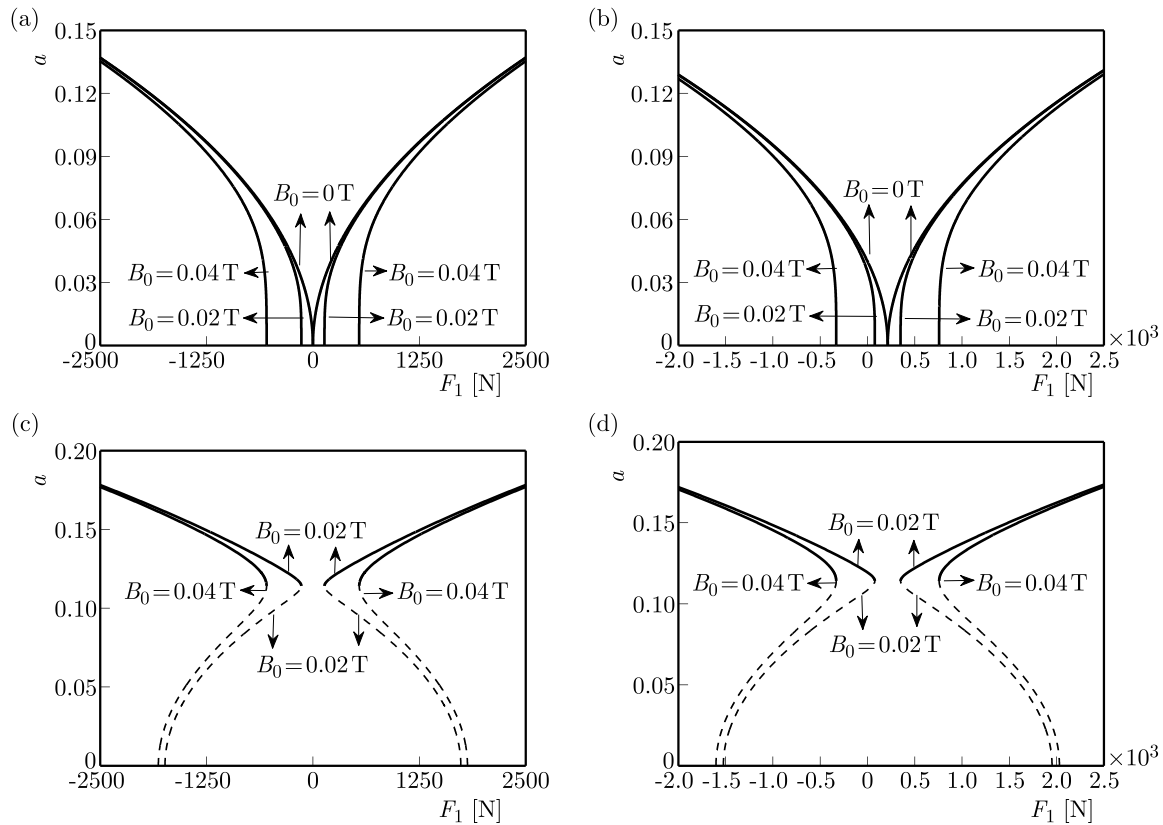


Fig. 3. The curve of the amplitude-parametric excitation, $F_0 = 30 \text{ kN}$, $J_c = 0.02 \text{ A/mm}^2$, $P_c = 0 \text{ N/m}$:
 (a) $\varepsilon\sigma = 0$, $C_0 = 60 \text{ m/s}$, $C_1 = 0 \text{ m/s}$; (b) $\varepsilon\sigma = 0$, $C_0 = 60 \text{ m/s}$, $C_1 = 1 \text{ m/s}$;
 (c) $\varepsilon\sigma = -0.01$, $C_0 = 60 \text{ m/s}$, $C_1 = 0 \text{ m/s}$; (d) $\varepsilon\sigma = -0.01$, $C_0 = 60 \text{ m/s}$, $C_1 = 1 \text{ m/s}$

According to the frequency-response equation, the square item in the right-side contains F_1 . Due to F_1 varying from a positive to a negative value, the curves present symmetrical distribution. And the existence of the time-variant axial speed can cause the curves shift towards right. Similar phenomena are also observed in Figs. 4-6.

Figure 4 represents the response curve of the amplitude a versus the parametric excitation F_1 under the influence of the amplitude of the time-variant axial speed C_1 . In Fig. 4, for the stable solutions on the left side, the greater C_1 is, the larger the vibration amplitude a becomes. However, it has the opposite result on the right side.

Figure 5 represents the response curve of the amplitude a versus the parametric excitation F_1 under the influence of the detuning parameter $\varepsilon\sigma$. In Figs. 5a, 5b and 5c, as the absolute value of the detuning parameter $\varepsilon\sigma$ gets greater, the vibration amplitude a becomes larger. In Figs. 5d, 5e and 5f, with a gradual increase of the magnetic induction intensity B_0 , the zero solution region appears and gets broader.

Figure 6 represents the response curve of the amplitude a versus the parametric excitation F_1 under the influence of the static load Q . Figure 6a shows that the increasing static load Q makes the vibration amplitude a decrease. However, the tendency in Fig. 6b is opposite.

6.3. The curve of amplitude – static load

Figure 7 shows that the system has only stable nontrivial solutions, and the increasing static load Q decreases the vibration amplitude a . We can also see that the vibration amplitude a is increasing when the axial constant velocity C_0 , the amplitude of time-variant axial speed C_1 , the amplitude of the time-variant axial tension F_1 increase and the magnetic induction intensity B_0

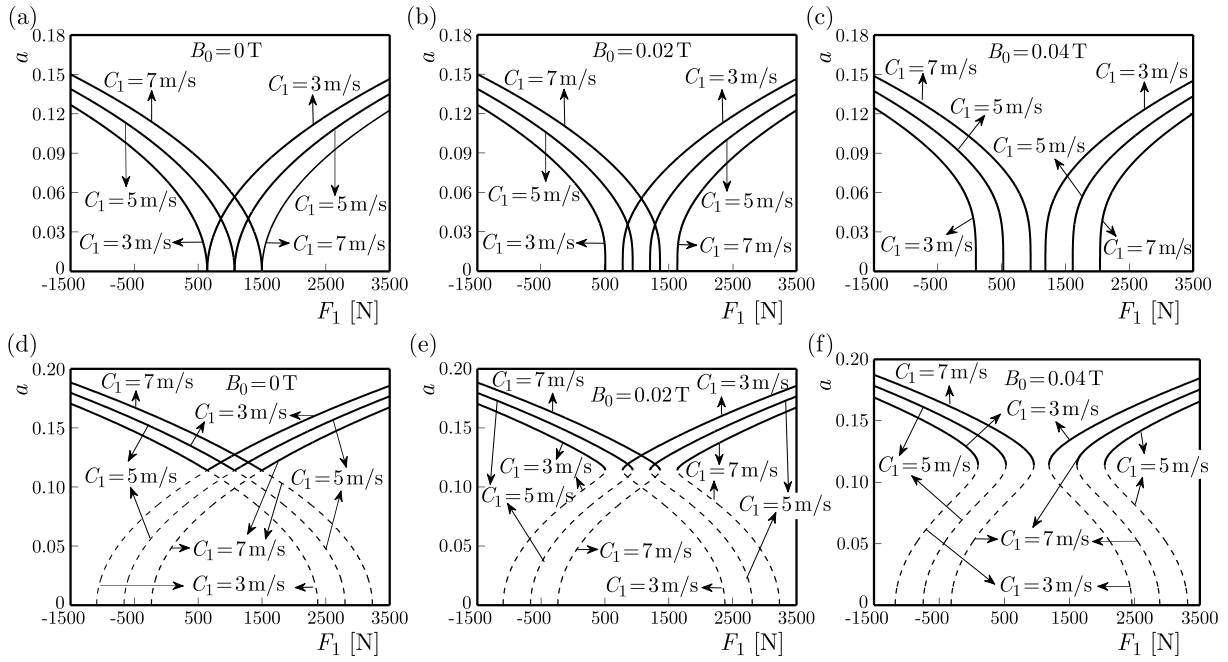


Fig. 4. The curve of the amplitude-parametric excitation, $F_0 = 30 \text{ kN}$, $J_c = 0.02 \text{ A/mm}^2$, $P_c = 0 \text{ N/m}$:
 (a) $\varepsilon\sigma = 0$, $C_0 = 60 \text{ m/s}$; (b) $\varepsilon\sigma = -0.01$, $C_0 = 60 \text{ m/s}$

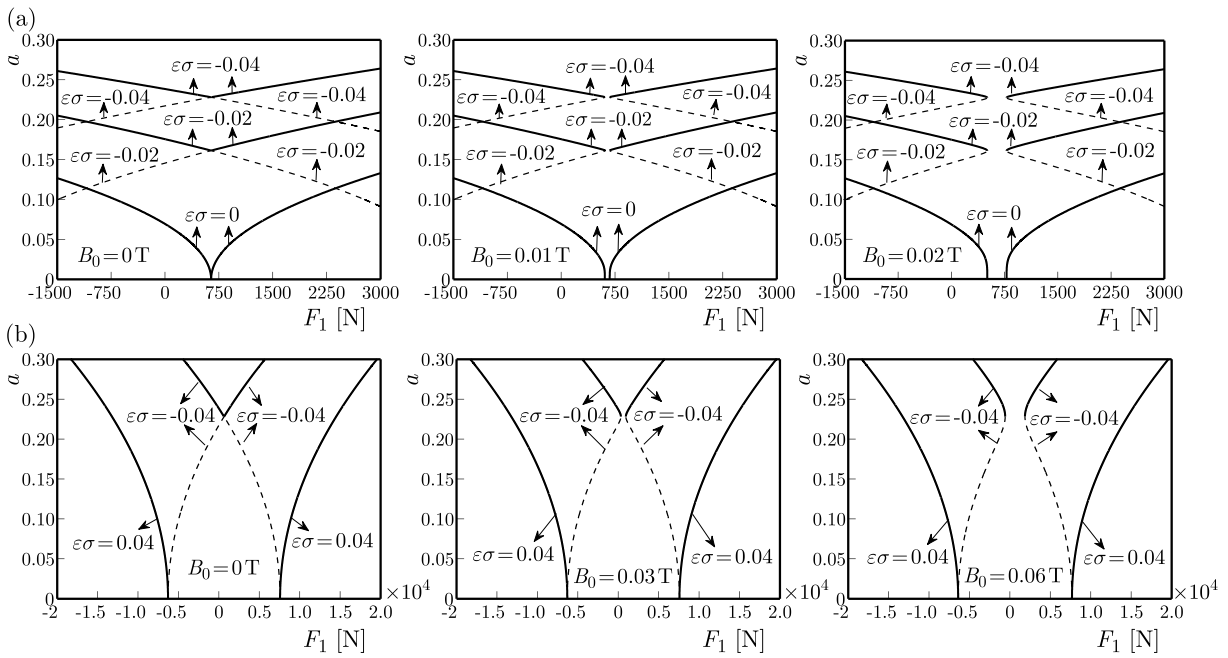


Fig. 5. The curve of the amplitude-parametric excitation, $F_0 = 30 \text{ kN}$, $J_c = 0.02 \text{ A/mm}^2$, $P_c = 0 \text{ N/m}$:
 (a) $C_0 = 60 \text{ m/s}$, $C_1 = 3 \text{ m/s}$ when $\varepsilon\sigma = 0, -0.02$ and -0.04 ; (b) $C_0 = 60 \text{ m/s}$, $C_1 = 3 \text{ m/s}$ when $\varepsilon\sigma = 0.04$ and -0.04

decreases. In Figs. 7a, 7b and 7c, the curves become leveling off when the static load Q increases to a certain value. The changes of the amplitude of the time-variant axial speed C_1 and the amplitude of the time-variant axial tension F_1 have a more significant effect on the vibration amplitude than that of the magnetic induction intensity B_0 .

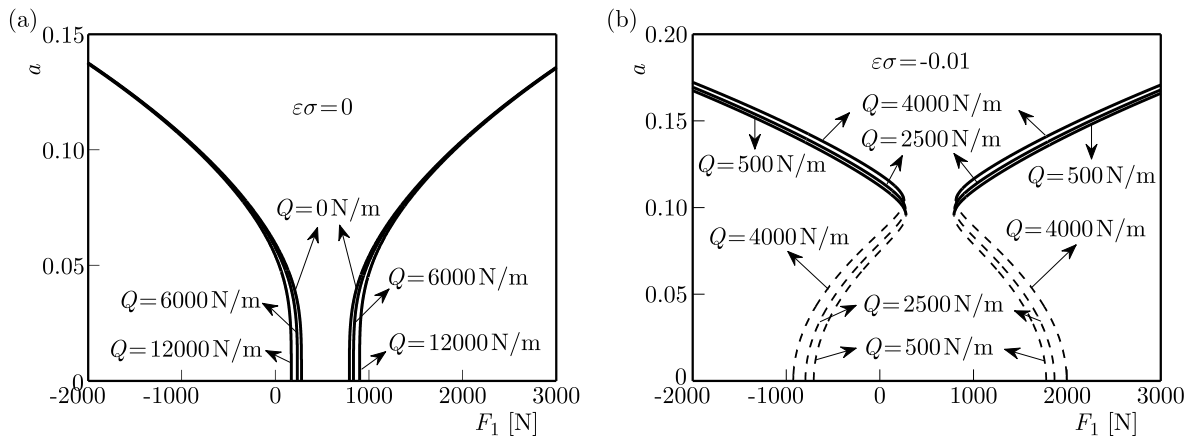


Fig. 6. The curve of amplitude-parametric excitation, $F_0 = 15 \text{ kN}$, $J_c = 0.02 \text{ A/mm}^2$:
 (a) $C_0 = 50 \text{ m/s}$, $C_1 = 3 \text{ m/s}$, $B_0 = 0.03 \text{ T}$; (b) $C_0 = 50 \text{ m/s}$, $C_1 = 3 \text{ m/s}$, $B_0 = 0.03 \text{ T}$

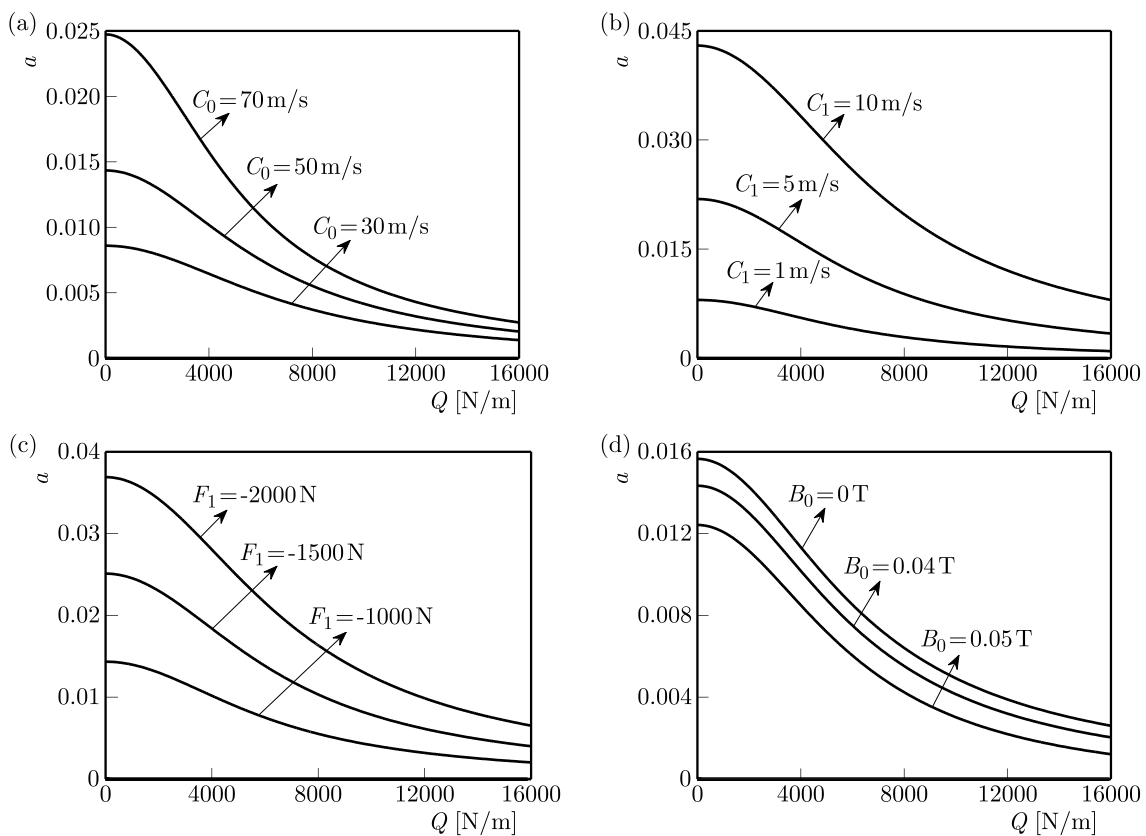


Fig. 7. The curve of amplitude - static load, $F_0 = 15 \text{ kN}$, $J_c = 0.02 \text{ A/mm}^2$, $\varepsilon\sigma = 0.01$:
 (a) $C_1 = 3 \text{ m/s}$, $F_1 = -1000 \text{ N}$, $B_0 = 0.04 \text{ T}$; (b) $C_0 = 50 \text{ m/s}$, $F_1 = -1000 \text{ N}$, $B_0 = 0.04 \text{ T}$;
 (c) $C_0 = 50 \text{ m/s}$, $C_1 = 3 \text{ m/s}$, $B_0 = 0.04 \text{ T}$; (d) $C_0 = 50 \text{ m/s}$, $C_1 = 3 \text{ m/s}$, $F_1 = -1000 \text{ N}$

6.4. The bifurcation diagram of the amplitude

In Fig. 8, the critical point of excitation is the intersection point of the trivial solution and resonance solutions (including both the stable and unstable solutions) of the system. As the figures show, in the upper region of each curve, the system has both a stable and an unstable solution, and in the lower part, the system has no solution. In the given range of the amplitude of the time-variant axial speed C_1 , the time-variant axial tension F_1 of critical bifurcation increases with the growth of the magnetic induction intensity B_0 . Given a certain range for B_0 , the time-variant axial tension F_1 shows the same result as C_1 increases.

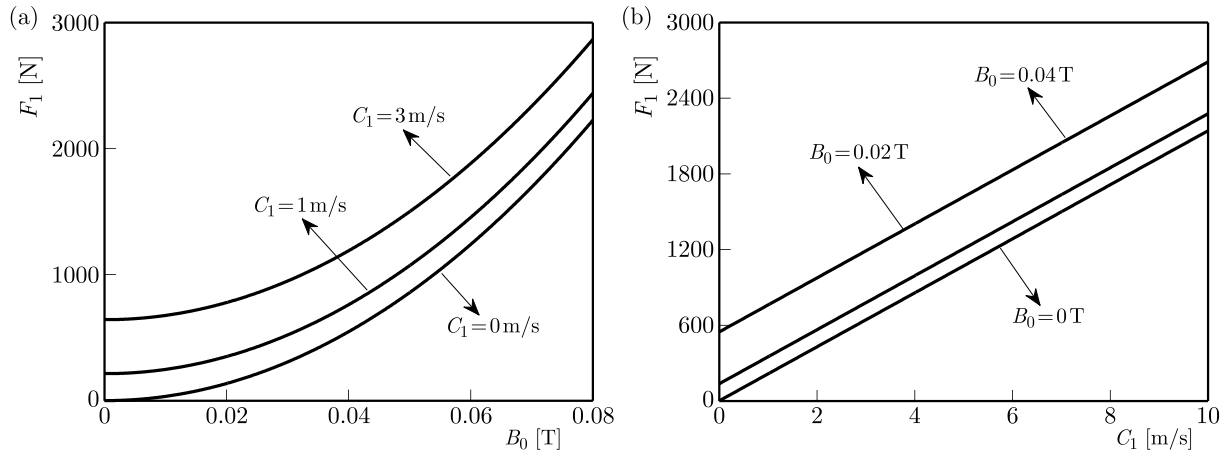


Fig. 8. The bifurcation diagrams of the amplitude, $C_0 = 60$ m/s, $F_0 = 30$ kN, $J_c = 0.02$ A/mm², $P_c = 0$ N/m and $\varepsilon\sigma = -0.01$: (a) $F_1 - B_0$ bifurcation diagram of the amplitude; (b) $F_1 - C_1$ bifurcation diagram of the amplitude

In Fig. 8a, the curves which correspond to Figs. 3c and 3d, show a rising trend with the increase of the amplitude of the time-variant axial speed C_1 . The bifurcation diagrams of the time-variant axial tension F_1 versus the axial constant velocity C_0 , which correspond to Figs. 4d, 4e and 4f, are distributed in a parallel line pattern with a change of the magnetic induction intensity B_0 in Fig. 8b.

7. Conclusions

In this article, the primary parametric resonance and stability of an axially accelerating current-carrying beam under magnetic field are investigated. The effects of the detuning parameter, axial velocity, axial tension, magnetic induction intensity and static load on nonlinear characteristics of the system are discussed. The following conclusions can be drawn:

- The vibration amplitude varies with the physical parameters, and the system exhibits typical primary parametric resonance characteristics.
- The external magnetic field has a significant effect on the vibration of the system, and the vibration amplitude control can be achieved by controlling the value of magnetic induction intensity.
- When the axial time-variant speed is not zero, the symmetry axis of the resonant characteristic curve shifts towards right.
- The vibration amplitude under parametric resonance decreases with an increase of the static loads.

Acknowledgment

This work was supported by the Project of National Natural Science Foundation of China (No. 11472239), Hebei Provincial Natural Science Foundation of China (No. A2015203023) and the Key Project of Science and Technology Research of Higher Education of Hebei Province of China (No. ZD20131055).

References

1. CHAKRABORTY G., MALLIK, A.K., 1998, Parametrically excited non-linear traveling beams with and without external forcing, *Nonlinear Dynamics*, **17**, 4, 301-324

2. CHEN L.Q., TANG Y.Q., LIM C.W., 2010, Dynamic stability in parametric resonance of axially accelerating viscoelastic Timoshenko beams, *Journal of Sound and Vibration*, **329**, 5, 547-565
3. CHEN L.Q., YANG X.D., 2005, Steady-state response of axially moving viscoelastic beams with pulsating speed: comparison of two nonlinear models, *International Journal of Solids and Structures*, **42**, 1, 37-50
4. GHAYESH M.H., BALAR S., 2008, Non-linear parametric vibration and stability of axially moving visco-elastic Rayleigh beams, *International Journal of Solids and Structures*, **45**, 25-26, 6451-6467
5. GHAYESH M.H., BALAR S., 2010, Non-linear parametric vibration and stability analysis for two dynamic models of axially moving Timoshenko beams, *Applied Mathematical Modelling*, **34**, 10, 2850-2859
6. HASANYAN D.J., KHACHATURYAN G.M., PILIPOSYAN G.T., 2001, Mathematical modeling and investigation of nonlinear vibration of perfectly conductive plates in an inclined magnetic field, *Thin-Walled Structures*, **39**, 1, 111-123
7. HASANYAN D., LIBRESCU L., QIN Z., AMBUR D.R., 2005, Nonlinear vibration of finitely-electroconductive plate strips in an axial magnetic field, *Computers and Structures*, **83**, 15, 1205-1216
8. HU Y.D., HU P., ZHANG J.Z., 2015, Strongly nonlinear subharmonic resonance and chaotic motion of axially moving thin plate in magnetic field, *Journal of Computational and Nonlinear Dynamics*, **10**, 2, 1-12
9. HU Y.D., LI J., 2009, The magneto-elastic subharmonic resonance of current-conducting thin plate in magnetic field, *Journal of Sound and Vibration*, **319**, 3, 1107-1120
10. HU Y.D., WANG T., 2015, Nonlinear resonance of the rotating circular plate under static loads in magnetic field, *Chinese Journal of Mechanical Engineering*, **28**, 6, 1277-1284
11. HU Y.D., ZHANG J.Z., 2013, Principal parametric resonance of axially accelerating rectangular thin plate in magnetic field, *Applied Mathematics and Mechanics (English Edition)*, **34**, 11, 1405-1420
12. MATSNER V.I., 1978, Effect of initial deflections on the natural vibration frequencies of shells under axial compressive loads, *Soviet Applied Mechanics*, **14**, 5, 528-531
13. NAYFEH A.H., MOOK D.T., 1979, *Nonlinear Oscillations*, Wiley, New York
14. TANG Y.Q., CHEN L.Q., YANG X.D., 2009, Parametric resonance of axially moving Timoshenko beams with time-dependent speed, *Nonlinear Dynamics*, **58**, 4, 715-724
15. WANG J.Y., CHEN K.J., 1993, Vibration problems of flexible circular plates with initial deflection, *Applied Mathematics and Mechanics (English Edition)*, **14**, 2, 177-184
16. WANG X.Z., LEE J.S., ZHENG X.J., 2003, Magneto-thermo-elastic instability of ferromagnetic plates in thermal and magnetic fields, *International Journal of Solids and Structures*, **40**, 22, 6125-6142
17. ZHENG X.J., ZHANG J.P., ZHOU Y.H., 2005, Dynamic stability of a cantilever conductive plate in transverse impulsive magnetic field, *International Journal of Solids and Structures*, **42**, 8, 2417-2430

Manuscript received July 12, 2016; accepted for print January 10, 2018

MODELLING OF FGM PLATES

GRZEGORZ JEMIELITA

Warsaw University of Life Sciences, Faculty of Civil and Environmental Engineering, Warsaw, Poland

e-mail: g.jemielita@il.pw.edu.pl

ZOFIA KOZYRA

Warsaw University of Technology, Faculty of Civil Engineering, Warsaw, Poland

e-mail: z.kozyra@il.pw.edu.pl

The paper presents formulation of the problem of layered plates composed of two various isotropic materials. We assume that the first material M_1 is characterized by the following parameters: Young's modulus E_1 and Poisson's ratio ν_1 , whereas the second one by E_2 and ν_2 , respectively. Let us consider two modelling cases for functionally graded material (FGM) plates. These cases are related to an appropriate distribution of the material within two-layer and three-layer systems. Our objective is to compare the stiffness of both the two-layer and three-layer plates with the FGM plate containing various proportions between the material components M_1 and M_2 .

Keywords: modelling, layer plate, FGM plate, stiffness of the plate

1. Introduction

The effect of a continuous change in the plate properties (through the thickness) can be obtained in various ways. The overall properties of FGMs are unique and differ from any of the individual material forming it (Mahamood *et al.*, 2012).

Usually, we assume isotropic plates with variation of two constituents: ceramic and metal (Mokhtar *et al.*, 2009). Another possibility is to assume aluminium-alumina FGM plates (Rohit Saha and Maiti, 2012).

Thus, the created plate material is inhomogeneous with both the composition and material properties varying smoothly through thickness of the plate. The material properties along the thickness direction of the FGM plate vary in accordance to a power-law function, exponential function, sigmoid function, etc. Another modelling examples known in the literature are related to asymptotic and tolerance modelling (Woźniak, 1995; Nagórko, 1998, 2010; Wągrowaska and Woźniak, 2015; Woźniak *et al.*, 2016).

Most material properties through the plate thickness are expressed by

$$p(z) = (p_1 - p_2)f(z) + p_2 \quad (1.1)$$

where

$$f(z) = \left(\frac{1}{2} + \frac{z}{h}\right)^n \quad p = \rho, E, \nu \quad (1.2)$$

where h is the plate thickness, the subscripts 1 and 2 indicate the top $z = h/2$ and bottom $z = -h/2$ surfaces, E – Young's modulus, ν – Poisson's ratio, ρ is mass density, n – material

parameter (Reddy, 2000; Efraim, 2011; Kim and Reddy, 2013; Kumar *et al.*, 2011). Mokhtar *et al.* (2009) use the following definition of the function $p(z)$

$$p(z) = \begin{cases} f_1(z)p_c + [1 + f_1(z)]p_m & \text{for } 0 \leq z \leq \frac{h}{2} \\ f_2(z)p_c + [1 + f_2(z)]p_m & \text{for } -\frac{h}{2} \leq z \leq 0 \end{cases} \quad (1.3)$$

where

$$f_1(z) = 1 - \frac{1}{2} \left(1 - \frac{2z}{h}\right)^n \quad f_2(z) = \frac{1}{2} \left(1 + \frac{2z}{h}\right)^n \quad (1.4)$$

Delale and Erdogan (1983) and Rohit Saha and Maiti (2012) used an exponential function in order to describe the variation of Young's modulus in the following form

$$E(z) = E_m \exp\left(z + \frac{h}{2}\right) \quad B = \frac{1}{h} \ln \frac{E_c}{E_m} \quad -\frac{h}{2} \leq z \leq \frac{h}{2} \quad (1.5)$$

In this work, we present a new FGM plate model formulated by using an appropriate modelling related to double-layer and three-layer plates.

2. modelling of an FGM plate developed from a two-layer plate

Let us assume a two-layer plate whose scheme is shown in Fig. 1.

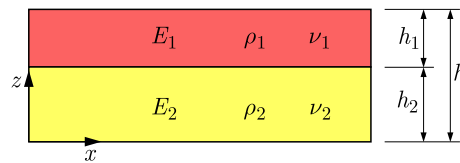


Fig. 1. A scheme of the two-layer plate

Our aim is to construct a gradient plate developed from a two-layer plate as well as to compare the stiffnesses of both systems in the case of any quotient $\eta = h_1/h$.

2.1. Plate geometry

The function describing the properties of the plate is defined as follows

$$p(z) = \begin{cases} p_1 & \text{for } 1 - \eta \leq \xi \leq 1 \\ p_2 & \text{for } 0 \leq \xi \leq 1 - \eta \end{cases} = p_2[1 + \varepsilon s(\xi)] \quad p = \rho, E, \nu \quad (2.1)$$

where

$$s(\xi) = \begin{cases} 0 & \text{for } 0 \leq \xi \leq 1 - \eta \\ 1 & \text{for } 1 - \eta \leq \xi \leq 1 \end{cases} \quad (2.2)$$

where ρ denotes density, E – Young's modulus, ν – Poisson's ratio, $\varepsilon = (p_1 - p_2)/p_2$, $\xi = z/h$, $\eta = h_1/h$, $0 \leq \eta \leq 1$, $h = h_1 + h_2$. Visualization of the discontinuous function $s(\xi)$ (defined via Eq. (2.2)) is presented in Fig. 2.

We are looking for a continuous-density function $\rho(\xi)$ satisfying the following conditions:
— the law of mass conservation

$$\int_0^1 \rho(\xi) d\xi = \frac{\rho_1 h_1 + \rho_2 h_2}{h} = \rho_2(1 + \varepsilon \rho \eta) \quad \varepsilon_\rho = \frac{\rho_1 - \rho_2}{\rho_2} \quad \eta = \frac{h_1}{h} \quad (2.3)$$

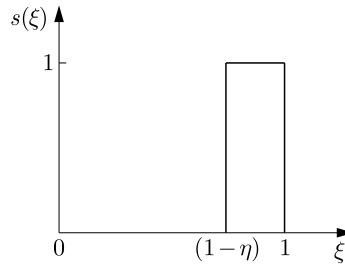


Fig. 2. Discontinuous function $s(\xi)$, see Eq. (1.2)

— positive-density condition

$$\rho(\xi) \geq 0 \quad 0 \leq \xi \leq 1 \tag{2.4}$$

— boundary conditions

$$\rho(0) = \rho_2 \quad \rho(1) = \rho_1 \tag{2.5}$$

The function under consideration $\rho(\xi)$ can be described as follows

$$\rho(\xi) = \rho_2[1 + \varepsilon_\rho f(\xi)] \tag{2.6}$$

where the function $f(\xi)$ satisfies the conditions as follows

$$\int_0^1 f(\xi) d\xi = \int_0^1 s(\xi) d\xi = \eta \tag{2.7}$$

$$f(0) = 0 \quad f(1) = 1 \quad f(\xi) \geq 0 \quad 0 \leq \xi \leq 1$$

The functions characterizing elastic properties of the FGM material, i.e. Young’s modulus $E(\xi)$ and Poisson’s ratio $\nu(\xi)$, should satisfy the following conditions

$$\begin{aligned} E(\xi) &\geq 0 & 0 \leq \xi \leq 1 & & E(0) &= E_2 & & E(1) &= E_1 \\ \nu(\xi) &\geq 0 & 0 \leq \xi \leq 1 & & \nu(0) &= \nu_2 & & \nu(1) &= \nu_1 \end{aligned} \tag{2.8}$$

The forms of analyzed functions $E(\xi)$ and $\nu(\xi)$ differ. In the case of metallic alloys, one can assume $\nu_1 = \nu_2 = \nu$ because of small differences between Poisson’s ratios and the fact that the effect of Poisson’s ratio on the deformation is much less than that of Young’s modulus (Delale, Erdogan, 1983). However, analyzing the plates, it can be assumed that the function $E(\xi)/[1 - \nu^2(\xi)]$ is analogous to the form of the density function expressed by Eq. (2.6)

$$\frac{E(\xi)}{1 - \nu^2(\xi)} = \frac{E_2}{1 - \nu_2^2} [1 + \varepsilon_E f(\xi)] \quad \varepsilon_E = \alpha - 1 \quad \alpha = \frac{E_1(1 - \nu_2^2)}{E_2(1 - \nu_1^2)} \tag{2.9}$$

and the function $f(\xi)$ satisfies conditions (2.7).

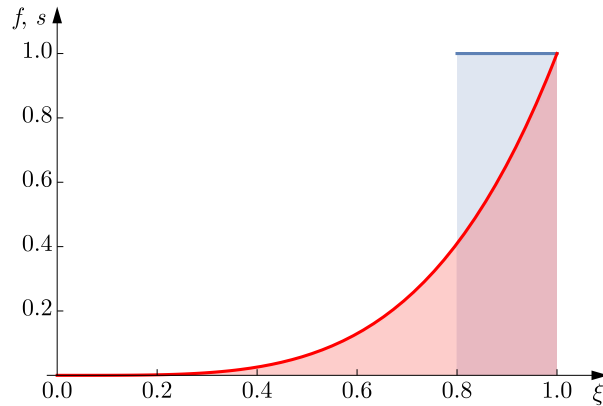
Let us note that taking the function $E(\xi)/[1 - \nu^2(\xi)]$ along with conditions (2.8)₁ leads to a simple interpretation of the static problem. Tensile strength of the FGM cross-section with Young’s modulus and Poisson’s ratio described by Eqs. (2.9) is the same as for the cross-section shown in Fig. 1.

Figure 3 shows the functions s and f satisfying conditions (2.7) for $\eta = 0.2$.

We anticipate the following form of $f(\xi)$

$$f(\xi) = f_r(\xi) = \xi^r (a_1 \xi + a_2) \tag{2.10}$$

where $r = n$ or $r = 1/n$, and n is an arbitrary natural number.

Fig. 3. The functions f and s

The proposed function satisfies boundary condition (2.7)₂, whereas condition (2.7)₃ is satisfied

$$\forall r \neq 0 \quad \text{if} \quad a_2 = 1 - a_1 \quad \Rightarrow \quad f_r(\xi) = \xi^r [a_1(\xi - 1) + 1] \quad (2.11)$$

As a special case $r = n = 0$, condition (2.7)₃ will be satisfied with $a_1 = 1$.

Condition (2.7)₁ gives

$$\int_0^1 f(\xi) d\xi = \int_0^1 \xi^r [a_1(\xi - 1) + 1] d\xi = \frac{2 + r - a_1}{(1 + r)(2 + r)} = \eta \quad (2.12)$$

what implies

$$a_1 = (2 + r)[1 - \eta(1 + r)] \quad (2.13)$$

Taking condition (2.7)₄

$$\xi^r [a_1(\xi - 1) + 1] \geq 0 \quad (2.14)$$

it follows that at $n > 0$, $f(\xi) \geq 0$ for

$$-r \leq a_1 \leq 1 \quad \frac{1}{r + 2} \leq \eta \leq \frac{2}{r + 2} \quad (2.15)$$

It is obvious that for each η , we can find an appropriate natural number n for $r = n$ or $r = 1/n$.

Thus, $f(\xi)$ is written as follows

$$f(\xi) = f_r(\xi) = \xi^r \{1 - (1 - \xi)(2 + r)[1 - \eta(1 + r)]\} \quad (2.16)$$

As a special case of $f_0(\xi)$, we obtain $\eta = 1/2$, $f_0(\xi) = \xi$. Taking $r = 1$

$$f_1(\xi) = \xi [1 - (1 - \xi)3(1 - 2\eta)] \quad \text{for} \quad \frac{1}{3} \leq \eta \leq \frac{2}{3} \quad (2.17)$$

For $n \geq 2$, we have two different functions

$$f_n(\xi) = \xi^n \{1 - (1 - \xi)(2 + n)[1 - \eta(1 + n)]\} \quad (2.18)$$

or

$$g_n(\xi) = f_{1/n}(\xi) = \xi^{\frac{1}{n}} \left\{ 1 - (1 - \xi) \left(2 + \frac{1}{n} \right) \left[1 - \eta \left(1 + \frac{1}{n} \right) \right] \right\} \quad (2.19)$$

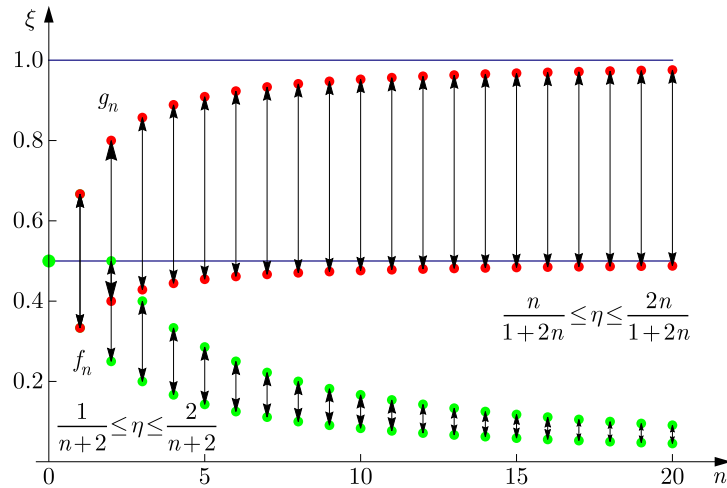


Fig. 4. Ranges of η for $f_n(\xi)$ and $g_n(\xi)$ satisfying conditions (2.7)

For a given value η , one can find such a value n at which the functions $f_n(\xi)$ or $g_n(\xi)$ meet conditions (2.7). Figure 4 shows such ranges of η at which the functions $f_n(\xi)$ and $g_n(\xi)$ satisfy the conditions expressed via Eqs. (2.7).

For $\eta = 1/3$, Fig. 4 depicts four possible values of n , i.e. $n = 1, 2, 3, 4$. On the other hand, we have three functions to be shown in Fig. 5a. In the case of $\eta = 0.2$, we obtain six functions satisfying conditions (2.7) for $n = 3, 4, 5, 6, 7, 8$ (see graphs visualized in Fig. 5b). It is obvious that for any η it gives a collection of functions satisfying conditions (2.7).

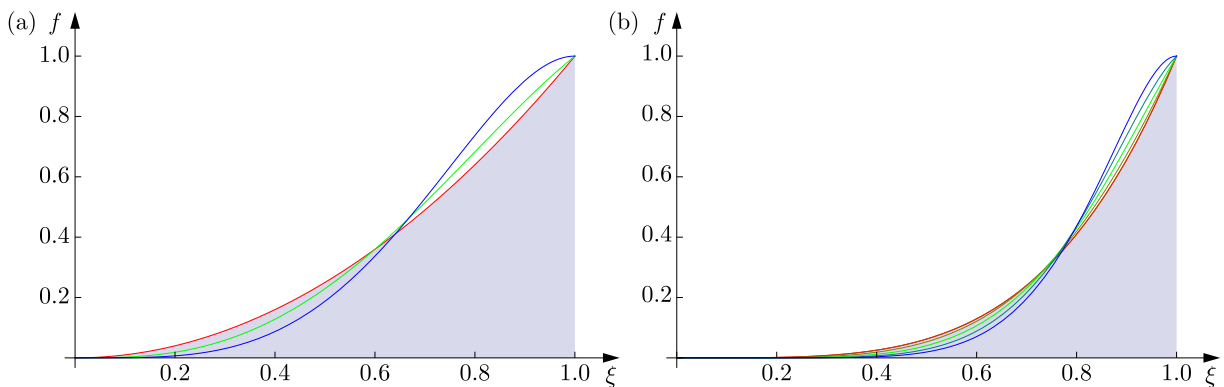


Fig. 5. Graphs of $f_n(\xi)$ for: (a) $\eta = 1/3$ and $n = 1, 2, 3, 4$; (b) $\eta = 0.2$ and $n = 3, 4, 5, 6, 7, 8$

Moving back to the graph illustrated in Fig. 4, it is obvious that for $1/2 \leq \eta \leq 1$ we get an infinite number of functions satisfying conditions (2.7). Figure 6 shows variation of functions $E(\xi)(1 - \nu_2^2)/\{E_2[1 - \nu^2(\xi)]\} = 1 + \varepsilon_E f(\xi)$, $f(\xi) = f_n(\xi)$ or $g(\xi) = g_n(\xi)$ for $\alpha = 2$, $\eta = 1/5, 1/6, 1/3$ along the FGM plate thickness.

2.2. Stiffness of the two-layer and FGM plates

The stiffness of the two-layer plate is expressed by the formula

$$D_w = \frac{E_2 h^3}{12(1 - \nu^2)} \left[\eta^3 \alpha + (1 - \eta)^3 + \frac{3(1 - \eta)\alpha\eta}{1 - \eta(1 - \alpha)} \right] \tag{2.20}$$

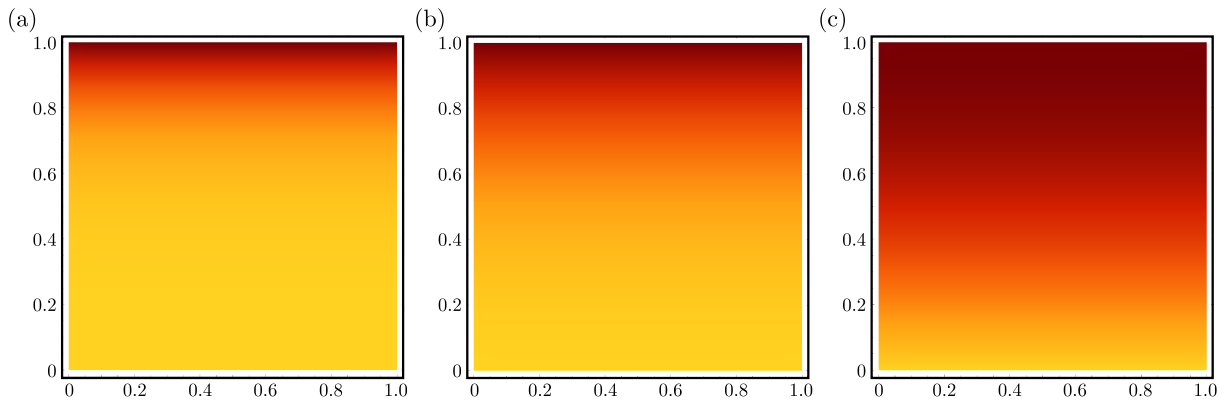


Fig. 6. Cross section of the FGM two-component plate: (a) $\alpha = 2$, $n = 3$, $\eta = 1/5$,
 (b) $\alpha = 2$, $n = 1$, $\eta = 1/3$, (c) $\alpha = 2$, $n = 1$, $\eta = 2/3$

The stiffness of the FGM plate depends on the functions f or g . These functions depend, in turn, on the variable ξ , on the parameter $\eta = h_1/h$ and on the natural number n

$$E_f(\xi, \alpha, n, \eta) = \frac{E}{1 - \nu^2}(\xi, \alpha, n, \eta) = \frac{E_2}{(1 - \nu_2^2)}[1 + (\alpha - 1)f_n(\xi)] \quad (2.21)$$

or

$$E_g(\xi, \alpha, n, \eta) = E_f\left(\xi, \alpha, \frac{1}{n}, \eta\right) = \frac{E_2}{1 - \nu_2^2}[1 + (\alpha - 1)g_n(\xi)] \quad (2.22)$$

The stiffness of the FGM plate material is expressed via formulas:

— for $\frac{1}{n+2} \leq \eta \leq \frac{2}{n+2}$

$$D_{f(FGM)}(\alpha, n, \eta) = \frac{E_2 h^3}{1 - \nu_2^2} \int_{-e_f}^{1-e_f} [1 + (\alpha - 1)f_n(\xi + e_f)] \xi^2 d\xi \quad (2.23)$$

$$= \frac{1}{3} - e_f + e_f^2 + (\alpha - 1) \left(\eta e_f^2 + \frac{2 + (1+n)(2+n)\eta}{(3+n)(4+n)} - \frac{2e_f[1 + (1+n)(2+n)\eta]}{(2+n)(3+n)} \right)$$

— for $\frac{n}{1+2n} \leq \eta \leq \frac{2n}{1+2n}$

$$D_{g(FGM)}(\alpha, n, \eta) = D_{f(FGM)}\left(\alpha, \frac{1}{n}, \eta\right) = \frac{E_2 h^3}{1 - \nu_2^2} \int_{-e_g}^{1-e_g} [1 + (\alpha - 1)g(\xi + e_g)] \xi^2 d\xi = \frac{1}{3} - e_g$$

$$+ e_g^2 + (\alpha - 1) \left(\frac{2n^2 + \eta\{(1 - e_g)[1 - e_g + n(3 - 7e_g)] + 2n^2(1 - 4e_g + 6e_g^2)\}}{(1 + 3n)(1 + 4n)} \right) \quad (2.24)$$

$$- \frac{2n^2 e_g}{(1 + 2n)(1 + 3n)}$$

whereas

$$e_f(\alpha, \eta, n) = \frac{4 + 5n + n^2 + 2\alpha + 2(1+n)(2+n)(\alpha - 1)\eta}{2(2+n)(3+n)[1 + (\alpha - 1)\eta]} \quad (2.25)$$

$$e_g = e_f\left(\alpha, \eta, \frac{1}{n}\right) = \frac{1 + 5n + 4n^2 + 2n^2\alpha + 2(1+n)(1+2n)(\alpha - 1)\eta}{2(2n+1)(3n+1)[1 + (\alpha - 1)\eta]}$$

In general, we have the following inequalities

$$\begin{aligned}
 D_{f(FGM)}\left(\alpha, n, \eta = \frac{2}{2+n}\right) &\neq D_{f(FGM)}\left(\alpha, n+1, \eta = \frac{1}{2+n}\right) \\
 D_{g(FGM)}\left(\alpha, n, \eta = \frac{2n}{2n+1}\right) &\neq D_{g(FGM)}\left(\alpha, n+1, \eta = \frac{n}{2n+1}\right)
 \end{aligned}
 \tag{2.26}$$

but there always exists such $\hat{\eta}$ meeting the following equality for each α

$$D_{FGM}(\alpha, n, \hat{\eta}) = D_{FGM}(\alpha, n+1, \hat{\eta})
 \tag{2.27}$$

For each α , the following equality is satisfied

$$D_{f(FGM)}\left(\alpha, n, \eta = \frac{1}{2+n}\right) = D_{f(FGM)}\left(\alpha, n+1, \eta = \frac{1}{2+n}\right)
 \tag{2.28}$$

In the case of $n/(1+2n) \leq \eta \leq 2n/(1+2n)$, there exist such values of $\hat{\eta}$ satisfying the following equalities

$$D_{g(FGM)}(\alpha, n, \hat{\eta}) = D_{g(FGM)}(\alpha, n+1, \hat{\eta})
 \tag{2.29}$$

For example: $D_{g(FGM)}(\alpha = 2, n = 1, \hat{\eta}) = D_{g(FGM)}(\alpha = 2, n = 2, \hat{\eta})$, for $\hat{\eta} = 0.424472$.

Figure 7 presents diagrams of the function $r(\eta)$ describing the stiffness of the plate $D = E_2 h^3 r(\eta) / [12(1 - \nu_2^2)]$ for $\alpha = 2$ where D_w and D_{FGM} denote the two-layer plate and the graded material plate, respectively.

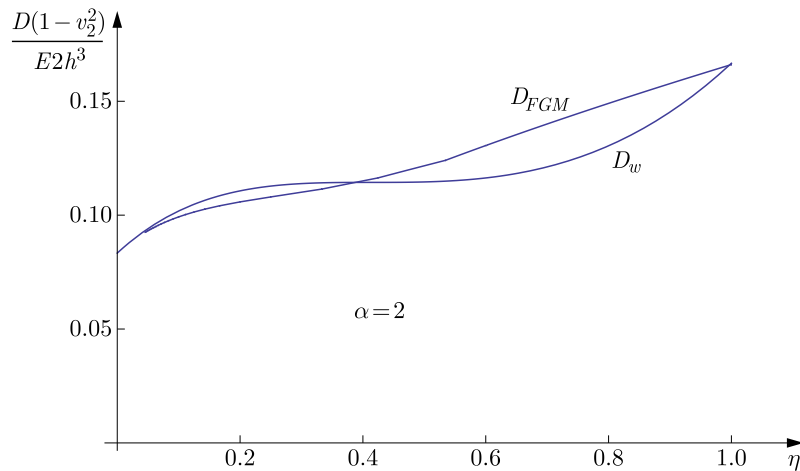


Fig. 7. A diagram of the function $r(\eta)$

3. modelling of the gradient plate developed from the three-layer plate

Let us consider a three-layer plate with a symmetrical arrangement of layers. In such a case, it is convenient to take the intermediate layer thickness equal to $2h_2$ (Fig. 8).

3.1. Determining the functions f_n, g_n

Similarly, as in the case of two-layer plate, we assume that Eqs. (2.9) hold provided that the functions f_n and g_n have the following forms

$$f_n(\xi) = \xi^{2n}[1 - a_1(1 - \xi^2)] \quad g_n(\xi) = (\xi^2)^{\frac{1}{n}}[1 - b_1(1 - \xi^2)]
 \tag{3.1}$$

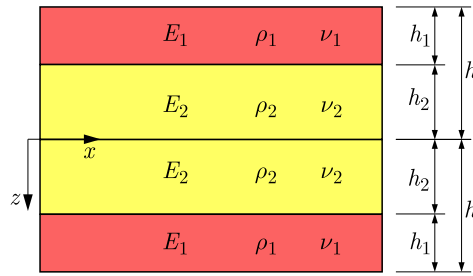


Fig. 8. A scheme of the three-layer plate

Satisfying the following conditions (see (2.7))

$$\int_0^1 f(\xi) d\xi = \int_0^1 s(\xi) d\xi = \eta = \frac{h_1}{h} \tag{3.2}$$

$$f(\pm 1) = 1 \quad f(0) = 0 \quad f(\xi) \geq 0 \quad -1 \leq \xi \leq 1$$

we obtain the functions f_n and g_n of the form:

— for $\frac{1}{3+2n} \leq \eta \leq \frac{3+4n}{(1+2n)(3+2n)}$

$$f_n(\xi) = \xi^2 n \left(1 - \frac{1}{2}(3+2n)[1 - \eta(1+2n)](1 - \xi^2) \right) \tag{3.3}$$

— for $\frac{n}{2+3n} \leq \eta \leq \frac{n(3n+4)}{(2+n)(2+3n)}$

$$g_n(\xi) = f_{1/n}(\xi) = (\xi^2)^{\frac{1}{n}} \left(1 - \frac{1}{2n^2}(2+3n)[n(1-\eta) - 2\eta](1 - \xi^2) \right) \tag{3.4}$$

Figure 9 shows the ranges of η for the functions $f_n(\xi)$ and $g_n(\xi)$ satisfying conditions (2.7).

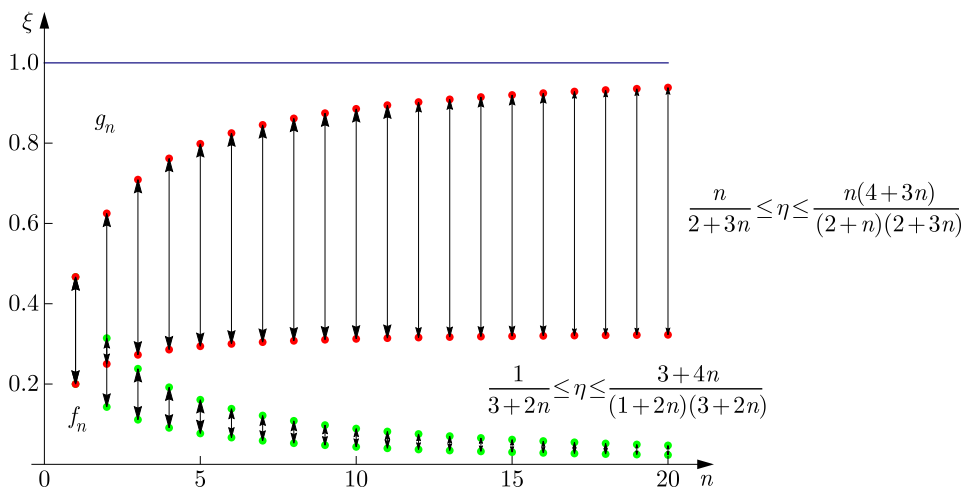


Fig. 9. Ranges of η for $f_n(\xi)$ and $g_n(\xi)$ satisfying conditions (2.7)

Figure 10a presents functions $f_1 = g_1$ within the range of validity $3/15 \leq \eta \leq 7/15$, whereas the functions g_{10} for $30/96 \leq \eta \leq 85/96$ are visualized in Fig. 10b.

Similarly, as in Section 3, the function $E(\xi)/[1 - \nu^2(\xi)]$ can be expressed as follows

$$\frac{E(\xi)}{1 - \nu^2(\xi)} = \frac{E_2}{1 - \nu_2^2} [1 + \varepsilon_E f(\xi)] \tag{3.5}$$

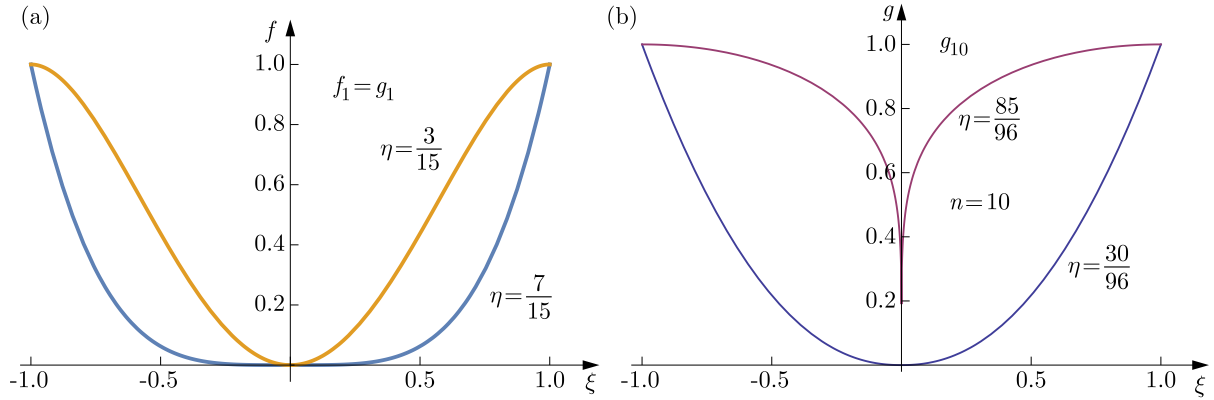


Fig. 10. (a) Functions $f_1 = g_1$ for $3/15 \leq \eta \leq 7/15$, (b) functions g_{10} for $30/96 \leq \eta \leq 85/96$

where the following designations are adopted

$$\varepsilon_E = \alpha - 1 \quad \alpha = \frac{E_1(1 - \nu_2^2)}{E_2(1 - \nu_1^2)} \quad f(\xi) = f_n(\xi) \quad \text{or} \quad f(\xi) = g_n(\xi) \quad (3.6)$$

Figure 11 presents variations of the function $E(\xi)(1 - \nu_2^2)/\{E_2[1 - \nu^2(\xi)]\} = 1 + \varepsilon_E f(\xi)$, $f(\xi) = f_n(\xi)$ or $g(\xi) = g_n(\xi)$ for $\alpha = 2$, $\eta = 1/5, 7/15, 5/8$ along the FGM plate thickness.

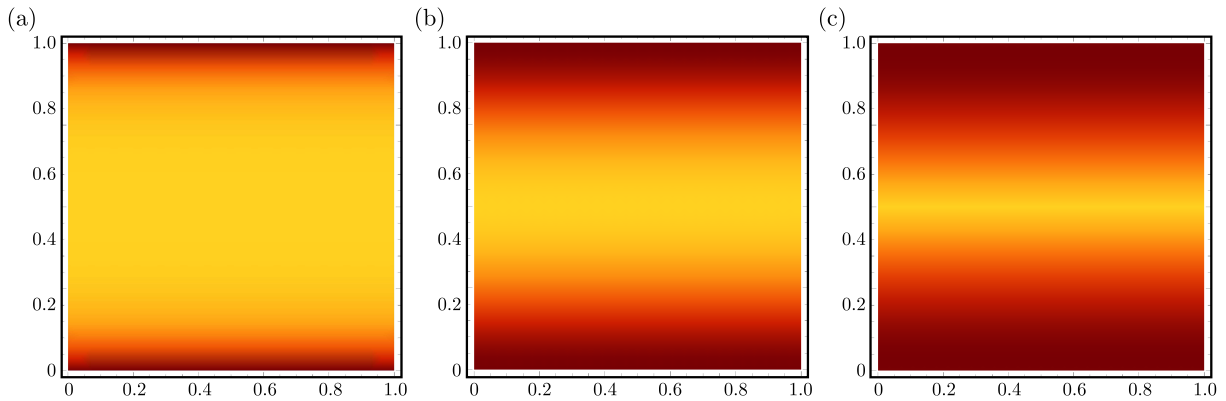


Fig. 11. Cross section of the FGM two-component plate: (a) $f_1(\alpha = 2, \eta = 1/5)$, (b) $f_1(\alpha = 2, \eta = 7/15)$, (c) $g_2(\alpha = 2, \eta = 5/8)$

3.2. Stiffness of the three-layer FGM plate

The stiffness of the three-layer plate D_w can be described as follows

$$D_w = \frac{2E_2h^3}{3(1 - \nu_2^2)} [(1 - \eta)^3 + \alpha\eta(3 - 3\eta + \eta^2)] \quad (3.7)$$

In the case of the FGM plate, the following formulas can be applied:

— for $\frac{1}{3+2n} \leq \eta \leq \frac{3+4n}{(1+2n)(3+2n)}$

$$D_{f(FGM)}(\alpha, n, \eta) = \frac{2E_2h^3}{3(1 - \nu_2^2)} \frac{3(3 + 2\alpha) + 4n(4 + n) + 3\eta(\alpha - 1)[3 + 4n(2 + n)]}{(3 + 2n)(5 + 2n)} \quad (3.8)$$

— for $\frac{n}{2+3n} \leq \eta \leq \frac{n(4+3n)}{(2+n)(2+3n)}$

$$D_{g(FGM)}(\alpha, n, \eta) = \frac{2E_2h^3}{3(1 - \nu_2^2)} \frac{4 + 16n + 9n^2 + 6\alpha n^2 - 3\eta(2 + n)(2 + 3n)(\alpha - 1)}{(2 + 3n)(2 + 5n)} \quad (3.9)$$

The stiffnesses of the layered plate D_w and the FGM plate D_{FGM} as a function of η for $\alpha = E_1/E_2 = 2$ are visualized in Fig. 12.

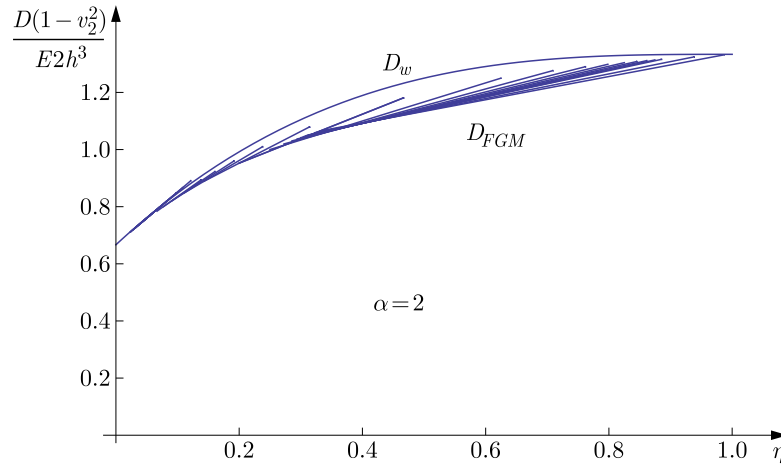


Fig. 12. Layered plate stiffness D_w and FGM plate stiffness D_{FGM} as a function of η for $\alpha = E_1/E_2 = 2$

4. Conclusions

Figure 7 shows the dependence of the stiffness of a two-layer plate and an FGM plate on the parameter η . Analyzing this graph, one concludes that taking two plates (the two-layer and FGM) with the same amount of the material and for certain values of the parameter η , the stiffness of the FGM plate is greater than the stiffness of the two-layer plate. It proves that we can construct an FGM plate, according to the procedure outlined in Section 2, with a higher stiffness of the two-layer plate and with the same amount of the material for both plates. In the case of the three-layer plate and its corresponding FGM plate, the FGM plate stiffness is less than the stiffness of the three-layer plate for all values of the parameter η , except for $\eta = 0$ and $\eta = 1$, for which the stiffnesses are the same.

References

1. DELALE F., ERDOGAN F., 1983, The crack problem for a nonhomogeneous plane, *ASME Journal of Applied Mechanics*, **50**, 609-615
2. EFRAIM E., 2011, Accurate formula for determination of natural frequencies of FGM plates basing on frequencies of isotropic plates, *Procedia Engineering*, **10**, 242-247
3. KIM J., REDDY J.N., 2014, Analytical solutions for bending, vibration, and buckling of FGM plates using a couple stress-based third-order theory, *Composite Structures*, **103**, 86-98
4. KUMAR J.S., REDDY B.S., REDDY C.E., KUMAR REDDY K.V., 2011, Geometrically non linear analysis of functionally graded material plates using higher order theory, *International Journal of Engineering Science and Technology*, **3**, 1, 279-288
5. MAHAMOOD R.M., ESTHER T. AKINLABI E.T., SHUKLA M., PITYANA S., 2012, Functionally graded material: an overview, *Proceedings of the World Congress on Engineering, WCE 2012*, **III**, London, U.K.
6. MOKHTAR B., ABEDLOUAHED T., ABBAS A.B., ABDELKADER M., 2009, Buckling analysis of functionally graded plates with simply supported edges, *Leonardo Journal of Sciences*, **16**, 21-32

7. NAGÓRKO W., 1998, Two methods of modeling of periodic nonhomogeneous elastic plates, *Journal of Theoretical and Applied Mechanics*, **36**, 291-303
8. NAGÓRKO W., 2010, Asymptotic modeling in elastodynamics of FGM, [In:] *Mathematical Modelling and Analysis in Continuum Mechanics of Microstructured Media*, Woźniak C. et al. (Edit.), Silesian University of Technology, Gliwice, 143-151
9. REDDY J.N., 2000, Analysis of functionally graded plates, *International Journal for Numerical Methods in Engineering*, **47**, 663-684
10. ROHIT SAHA, MAITI P.R., 2012, Buckling of simply supported FGM plates under uniaxial load, *International Journal of Civil and Structural Engineering*, **2**, 4, 1035-1050
11. WĄGROWSKA M., WOŹNIAK C., 2015, A new 2D-model of the heat conduction in multilayered medium-thickness plates, *Scientiarum Polonorum Acta Architectura*, **14**, 1, 37-44
12. WOŹNIAK C., 1995, Microdynamics: continuum modeling the simple composite materials, *Journal of Theoretical and Applied Mechanics*, **33**, 267-289
13. WOŹNIAK C., WĄGROWSKA M., SZLACHETKA O., 2016, On the tolerance modelling of heat conduction in functionally graded laminated media, *Journal of Applied Mechanics and Technical Physics*, **56**, 2, 274-281

Manuscript received August 22, 2016; accepted for print February 7, 2018

LOW-FREQUENCY PRESSURE FLUCTUATION DAMPER BASED ON HYDROPNEUMATIC SPRING WITH CONSTANT STIFFNESS

ANDRZEJ FIGIEL, ZYGMUNT KUDŹMA, MICHAŁ STOSIAK

Wrocław University of Science and Technology, Faculty of Technology and Engineering, Wrocław, Poland
e-mail: andrzej.figiel@pwr.edu.pl; michal.stosiak@pwr.edu.pl

A wide spectrum of pressure fluctuation frequencies occurs in hydraulic systems. Particularly hazardous and difficult to eliminate are pressure fluctuations in the range up to 50 Hz, resulting in the generation of infrasounds by machines equipped with a hydrostatic drive. The best protection against the harmful effect of ultrasounds is to suppress them at the very source, i.e. to eliminate the causes of the generation of this noise. This paper presents a concept of reducing pressure fluctuation in the range of low excitation frequencies by means of a low-frequency damper of special design. The basis for designing pressure fluctuation dampers effective in reducing pressure fluctuation amplitudes in the range of low frequencies (< 50 Hz), which also function as acoustic filters of the generated infrasounds, is provided. The effectiveness of the low-frequency damper in reducing pressure fluctuation amplitudes has been experimentally tested. The damper was found to be most effective when its eigenfrequency coincided with the excitation frequency to be reduced.

Keywords: damper, pressure fluctuation, infrasounds

1. Introduction

Pressure fluctuation, on the one hand, is a consequence of the periodically changing rate of flow of the working medium due to cyclicity of operation of pump displacement elements and, on the other hand, it is a result of external excitations in the form of mechanical vibrations acting on the hydraulic system components mounted on various supporting structures (e.g. loader frame). Fluctuations in the output, and so in pressure, in a hydraulic system are undesirable since they can cause many disturbances to normal operation and be a source of excessive noise, see Michałowski and Stolarski (1998). One of the most serious consequences of pressure fluctuations are vibrations of flexible pipes (German *et al.*, 2000; Stosiak, 2011; Czerwinski and Luczko, 2015) and, in some cases, of hydraulic system control elements (Kollek *et al.*, 2010). In order to confirm the coincidence between pressure fluctuations and the emitted noise, Osiński and Kollek (2013) recommend to locate the noise sources by means of a two-microphone probe. In this way, one can obtain a map of noise intensity around the investigated device and indicate the noisiest places which, as a rule, coincide with the areas where the maximum pressure fluctuation amplitude occurs.

A wide pressure fluctuation frequency spectrum, in both the infrasonic (up to 50 Hz) range and the audible range (up to 2 kHz), occurs in hydraulic systems (Ijas, 2007; Kollek *et al.*, 2009; Mikota, 2000; Earnhart and Cunefare, 2012).

The necessity to reduce low-frequency pressure fluctuation on the one hand is dictated by ergonomics and on the other by reduction of low-frequency excitations leading to minimization of the resonant vibration of hydraulic system components such as flexible pipes, valves, controllers and distributors, whose eigenfrequencies are in the low-frequency range. Especially hazardous and difficult to eliminate are pressure fluctuations in the range up to 50 Hz, resulting in the generation of infrasounds by machines equipped with a hydrostatic drive system (Kudźma, 2012).

The best protection against the harmful effect of ultrasounds is to suppress them at the very source, i.e. to eliminate the causes of the generation of this noise. Various hydropneumatic accumulators are commonly used to reduce pressure fluctuation amplitudes in the low frequency range (Dindorf, 2004; Palczak and Pomowski, 2006; Ijas, 2007; Earnhart and Cunefare, 2012; Kollek *et al.*, 2009; Garbacik *et al.*, 1986). However, the limitation of this solution is that hydropneumatic accumulators are most effective in reducing pressure fluctuation amplitudes when the accumulator resonance frequency coincides with the fluctuation frequency which is to be reduced. It should be noted that the accumulator free vibration frequency to a large extent depends on the magnitude of pressure in the hydraulic system incorporating this component. This means that hydropneumatic accumulators act selectively and so as dampers they are narrow-band filters, and their actual effectiveness in reducing pressure fluctuation is limited to practically a single excitation frequency equal to the hydropneumatic accumulator resonance frequency changing with the load of the drive system which incorporates the accumulator. Damping effectiveness tends to rapidly decrease already at slight deviations from the resonance frequency (Ortwig *et al.*, 1999; Kudźma, 2012; Garbacik *et al.*, 1986). The minimization of pressure fluctuations in hydraulic systems through the use of various dampers has been investigated by, among others, Dindorf (2004), Ijas (2007), Kudźma (2012), Kudźma and Kudźma (2015), Kollek *et al.* (2009), Earnhart and Cunefare (2012), Garbacik *et al.* (1986), Mikota (2000), Ortwig *et al.* (1999), Singh (2005), Skaistis (1988). Most of the above authors found that passive chamber dampers of the bypass, branch and Helmholtz resonator type were usable at excitation frequencies above 150 Hz. This limitation is due to the fact that for lower excitation frequencies the above dampers assume overall geometrical dimensions which eliminate them from the use in real hydrostatic drive systems of machines. A Helmholtz resonator with flexible lining of its walls, effective in reducing amplitudes of low (below 50 Hz) pressure fluctuation frequencies, but at the maximum pressure in the system limited to a few MPa, was presented by Earnhart and Cunefare (2012). The application of active damping consisting in pressure fluctuation generation by means of complex electrohydraulic systems in counterphase to the pressure fluctuation which is to be reduced, was presented by Changbin and Zongxia (2014), Pan (2013). By properly adjusting the phase and amplitude of the additional fluctuation it is possible to effectively reduce the fluctuation generated by the pump in the whole frequency range. Because of its complicated structure, the active damping of pressure fluctuation has not gone beyond laboratory tests.

This paper presents a concept for reducing pressure fluctuation in the range of low excitation frequencies through a special design of the low-frequency damper effective in the whole range of loads.

2. Low-frequency pressure fluctuation damper

In order to reduce low-frequency pressure fluctuation amplitudes, a damper whose design (laboratory version) is shown in Fig. 1 has been used. In comparison with the patent damper, this design was modified by introducing an additional piston rod to enable a simple change of the total vibrating system weight and measurements of piston displacements during damper operation. The damper is a kind of bypass in the hydraulic system, performing function of a reactive filter and a filter absorbing changes in energy resulting from output and pressure fluctuations. It reduces low-frequency output fluctuations. Thanks to the use of two hydropneumatic accumulators differently charged with gas, the damper effectively performs its function in a wide range of operational system pressures.

The low-frequency fluctuation damper shown in Fig. 1 operates as described below. After the cylinder is filled with the hydraulic oil, hydropneumatic accumulators 1 and 2 mounted in top cover 9 are precharged with nitrogen to pressure $p_{g02} > p_{g01}$. The damper is connected

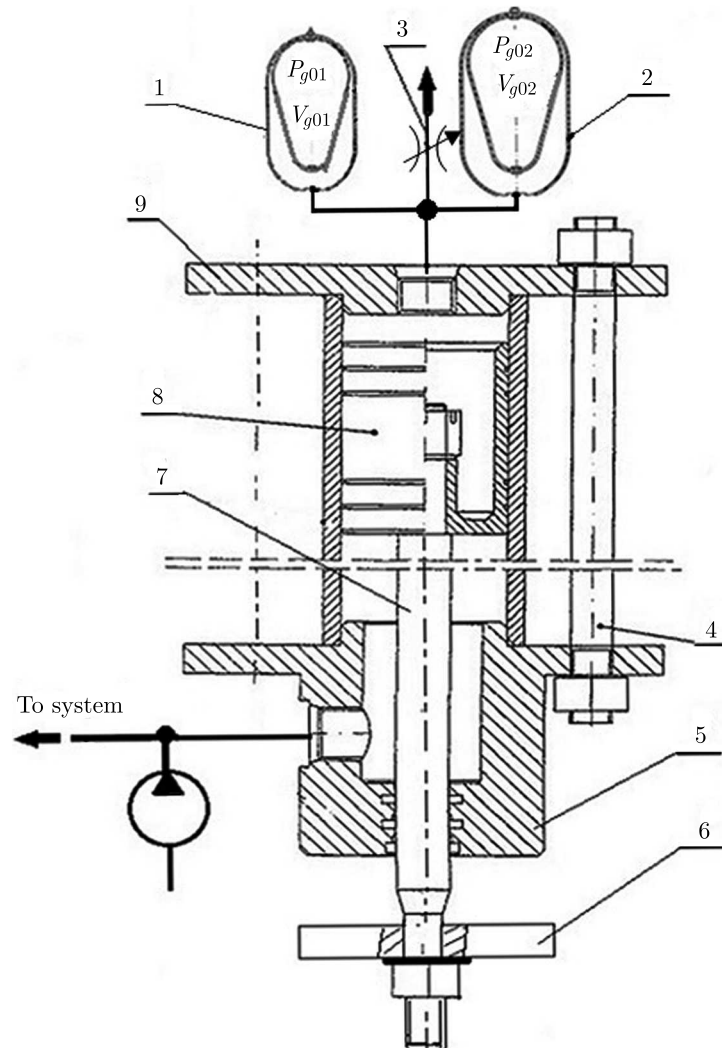


Fig. 1. Active low-frequency pressure fluctuation damper in its laboratory version:
 1 – hydraulic accumulator, 2 – hydraulic accumulator, 3 – vent and cut-off valve, 4 – pin,
 5 – bottom cover, 6 – loading disk, 7 – piston rod, 8 – piston, 9 – top cover

in parallel via a threaded hole in bottom cover 5 to the pump pressure conduit. The principle of operation of the damper comes down to taking over output fluctuation (generating pressure fluctuation) excitations. The excitations are taken over by the system: the movable piston with the piston rod – a hydropneumatic spring. The hydropneumatic spring is made up of at least two hydraulic accumulators differing in their initial gas volumes and precharge pressures. Owing to this, the hydropneumatic spring stiffness is approximately constant in the whole range of pressures generated by the driver element of the hydraulic system and, consequently, the low-frequency damper effectiveness is constant in the whole range of loads. Because of the patent application being processed, the low-frequency damper is only generally described here.

3. Mathematical model

3.1. First stage in damper operation

The operation of the low-frequency damper can be divided into two stages. The first stage covers the period from starting the system to the instant when the average pressure p_{av} is lower

than the precharge pressure p_{g02} in accumulator 2 (Fig. 1) – only one accumulator operates. The second stage begins when the average system pressure $p_{av} > p_{g02}$ – both accumulators operate.

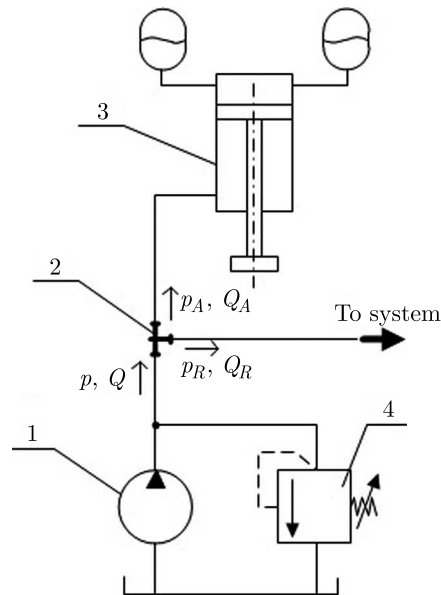


Fig. 2. Way of installing the low-frequency damper in the system: 1 – displacement pump, 2 – tee TT (feed node), 3 – low-frequency damper, 4 – safety valve

The particular symbols in Fig. 2 stand for: Q – the rate of pump delivery, Q_A – rate of flow to the low-frequency damper, Q_R – rate of flow to the pipeline feeding the system, and $p \cong p_A \cong p_R$ – pressure deviations in tee (tee arms).

Analysis of the hydraulic system with the low-frequency damper begins with calculation of the operational impedance $Z_T(s)$ in the feed node T_T

$$Z_T(s) = \frac{p_A(s)}{Q_A(s)} \quad (3.1)$$

where $p_A(s)$ and $Q_A(s)$ are the Laplace transforms of the pressure p_A and flow rate Q_A , s is the Laplace variable.

On the basis of the calculated impedance one selects such its value which would ensure minimal changes in Q_R and in pressure p_R . The parameters are a result of the pulsatory flow rate in the infrasonic range.

Moreover, the following simplifying assumptions are made:

- the system operates at thermal equilibrium with its surroundings;
- compressibility of the oil and elasticity of the conduits are neglected as being small in comparison with elasticity of the gas in the accumulator, also leakage losses are neglected;
- the safety valve remains closed over the whole load range;
- at low Q_A values, the flow in the low-frequency damper and the hydraulic accumulators connections is laminar.

For the feed node T_T , on the above assumptions, the equation of continuity for a nonuniform flow can be expressed through constant flow components Q_{AS} , Q_{RS} , Q_S and variable flow components Q_A , Q_R and Q

$$Q_S + Q = Q_{RS} + Q_R + Q_{AS} + Q_A \quad (3.2)$$

For the system shown in Fig. 2, one can assume that the whole flow generated by the pump goes via connection T to the system: damper-pipeline feeding the system. Thus the equation of

flow continuity assumes form (3.2): $Q + Q_S = Q_{RS} + Q_R + Q_{AS} + Q_A$. Moreover, the whole (mean) constant flow (Q_S) in steady operating conditions goes to the pipeline which feeds the system: $Q_S = Q_{RS}$. Thus the value of the constant component going to the damper is $Q_{AS} = 0$. Therefore, equation (3.2) can be written as

$$Q = Q_A + Q_R \tag{3.3}$$

The tee transmittances can be presented in the form of the matrix equation, see Kudźma (2012), Earnhart and Cunefare (2012)

$$\begin{bmatrix} p \\ Q \end{bmatrix} = \begin{bmatrix} 1 & 0 \\ Z_T^{-1} & 1 \end{bmatrix} \begin{bmatrix} p_R \\ Q_R \end{bmatrix} \tag{3.4}$$

where $Z_T = p_A/Q_A$ is the impedance of the damping system.

The expansion of equation (3.4) yields

$$Q_R = Q - \frac{p_R}{Z_T} \tag{3.5}$$

The mathematical model of the low-frequency damper is used to determine the structural parameters of the latter ensuring the maximum elimination of system output fluctuations with a given frequency, i.e. $Q_R(t) = \min$.

The flow caused by compressibility of the gas in the accumulator is defined by the equation (Dindorf, 2004)

$$Q_A = C_A \frac{dp_g}{dt} \tag{3.6}$$

where C_A is the capacitance of the hydraulic accumulator, p_g – pressure of the gas in the accumulator.

The capacitance of the hydraulic accumulator and its dynamic properties depend on the mass of the partition (membrane, etc.), compressibility of the gas and the inertia and resistance of the flow of the oil. For a constant entropy $S = \text{const}$, the accumulator capacitance can be written as (Dindorf, 2004; Kudźma, 2012)

$$C_A = \left(\frac{\partial V_g}{\partial p_g} \right)_S \tag{3.7}$$

where V_g is the volume of the gas in the accumulator.

Taking into account:

- (active) damper resistance R_{0T} which includes the effect of fluid resistance and piston motion resistance,
- piston hydraulic inductance L_T (passive resistance) which includes the effect of inertia of the fluid and moving piston components, one can determine the pressure drop (Palczak and Pomowski, 2006)

$$p_A - p_g = L_T \frac{dQ_A}{dt} + R_{0T} Q_A \tag{3.8}$$

From the assumption that hydraulic resistances, expressed by the last term of equation (3.8), have a quasi-stationary character it follows that the fluid friction loss coefficient for the steady flow and for the unsteady flow in the conduit at the same fluid flow velocity has an identical value. Consequently, considering the low flow rate fluctuation frequencies and the relatively large radius of the conduit, the effect of fluid motion nonstationarity in the conduit on frictional resistances is neglected.

Having differentiated both sides of expression (3.8), one gets

$$\frac{dp_A}{dt} - \frac{dp_g}{dt} = L_T \frac{d^2 Q_A}{dt^2} + R_{0T} \frac{dQ_A}{dt} \quad (3.9)$$

Using equation (3.6) and rearranging (3.9), one gets

$$C_A \frac{dp_A}{dt} = C_A L_T \frac{d^2 Q_A}{dt^2} + C_A R_{0T} \frac{dQ_A}{dt} + Q_A \quad (3.10)$$

Having applied the Laplace transformation to equation (3.10) at zero initial conditions, one gets the low-frequency damper operational transmittance $G_T(s)$

$$G_T(s) = \frac{Q_A(s)}{p_A(s)} = \frac{C_A s}{C_A L_T s^2 + C_A R_{0T} s + 1} \quad (3.11)$$

Assuming the damper eigenfrequency

$$\omega_{0T} = \sqrt{\frac{1}{C_A L_T}} \quad (3.12)$$

and the damping number

$$\xi_T = \frac{1}{2\omega_{0T}} C_A R_{0T} \quad (3.13)$$

one gets

$$G_T(s) = \frac{C_A s}{\frac{1}{\omega_{0T}^2} s^2 + 2\xi_T \omega_{0T} s + 1} \quad (3.14)$$

The amplitude-frequency characteristics of the low-frequency damper are determined on the basis of its initial impedance $Z_T(s)$ in spectral form $|Z_T(\omega)|$. Therefore, $s = j\omega$ is substituted into the transition function $G_T(s)$ (3.11) and inverse of the latter is specified, whereby one gets

$$Z_T(\omega) = \frac{p_A(\omega)}{Q_A(\omega)} = \frac{1}{C_A \omega_{0T}} \left[2\xi_T \omega_{0T}^2 + j \left(\frac{\omega}{\omega_{0T}} - \frac{\omega_{0T}}{\omega} \right) \right] \quad (3.15)$$

j is the imaginary unit.

Assuming constant coefficients related to the low-frequency damper design

$$\Phi = \frac{1}{C_A \omega_{0T}} \quad \Psi_T = 2\xi_T \omega_{0T}^2 \quad (3.16)$$

from formula (3.15), one calculates the impedance modulus

$$|Z_T(\omega)| = \Phi \sqrt{\Psi_T^2 + \left(\frac{\omega}{\omega_{0T}} - \frac{\omega_{0T}}{\omega} \right)^2} \quad (3.17)$$

In order to generalize the above analysis, relation (3.17) is presented in the dimensionless form

$$|Z_{TB}| = \frac{|Z_T|}{\Phi} = \sqrt{\Psi_T^2 + \left(\frac{\omega}{\omega_{0T}} - \frac{\omega_{0T}}{\omega} \right)^2} \quad (3.18)$$

In order to determine the low-frequency damper impedance minimum corresponding to the maximum damping of pressure fluctuations in the connection node, and to relate this value to the

damper structural parameters, one should define such parameters as: hydraulic inductance L_T , capacitance C_A and damper connection (tee+pipe) resistance R_{0T} .

The hydraulic inductance L_T is defined by the expression (Backé and Murrenhoff, 1994)

$$L_T = \frac{M_{zr}}{A_A^2} \quad (3.19)$$

where M_{zr} is the mass reduced to the damper piston face area, A_A – active damper piston face area.

The reduced mass M_{zr} of the vibrating system is the sum of the piston mass, loading disk mass, mass of the fluid in the damper cylinder and the reduced-to-the-piston-face-surface mass of the fluid in the connection.

In accordance with the assumptions, the resistance of the damper is calculated from the Hagen-Poiseuille relation (Palczak and Pomowski, 2006)

$$R_0 = \frac{8\pi\mu L_c}{F_p^2} \quad (3.20)$$

where μ is the dynamic viscosity of the working medium, F_p – cross sectional area of the connection, L_c – total length of the connection.

Each accumulator has its specific capacitance C_A . By analogy to pneumomechanics, the flexibility of the hydropneumatic spring is $C_S = C_A/A_A^2$. The spring flexibility, in turn, is the inverse of its stiffness, i.e. stiffness K_S of the hydropneumatic spring according to Dindorf (1998) is

$$K_S = \frac{1}{C_S} = \frac{A_A^2}{C_A} \quad (3.21)$$

The stiffness of the hydropneumatic spring should be related to the damper structural parameters A_A , pressure p_{g01} and the initial gas volume V_{g01} . Changes in the gas pressure and volume in the hydropneumatic accumulator in quick-variable processes are interrelated by the polytropic equation (Backé and Murrenhoff, 1994)

$$p_{g01}V_{g01}^n = p_{1g}V_{1g}^n \quad (3.22)$$

where p_{g01} is the initial gas pressure, V_{g01} – initial gas volume, p_{1g} – ultimate gas pressure, V_{1g} – ultimate gas volume, n – polytropic exponent.

The change in the gas volume (ΔV_g) is interrelated with the piston displacement x through the expression

$$\Delta V_g = A_A x \quad (3.23)$$

Hence, one can write

$$V_{1g} = V_{g01} - A_A x \quad (3.24)$$

On the basis of equations (3.22) and (3.24), one can determine the ultimate pressure p_{1g} depending on the initial pressure p_{g01} , initial volume V_{g01} and piston displacement x

$$p_{1g} = \frac{p_{g01}}{\left(1 - \frac{A_A}{V_{g01}}x\right)^n} \quad (3.25)$$

Multiplying equation (3.25) by the active piston surface A_A , one gets the relation for the hydropneumatic spring force P_{sh} as a function of the displacement x

$$P_{sh} = \frac{A_A p_{g01}}{\left(1 - \frac{A_A}{V_{g01}}x\right)^n} \quad (3.26)$$

Having linearized equation (3.26), using the expansion into a Maclaurin series and taking the first terms into account, one gets

$$\Delta P_{sh} = \frac{nA_A^2 p_{g01}}{V_{g01}} \Delta x + A_A p_{g01} \quad (3.27)$$

where ΔP_{sh} is an increase in the hydropneumatic spring force, Δx – an increase in the piston displacement. The value of the error due to the Lagrange remainder in the Maclaurin formula depends on the A_A/V_{g01} ratio and it approaches its maximum when approaching the value of the inverse to the A_A/V_{g01} ratio because

$$\frac{p_{g01}}{\left(1 - \frac{A_A}{V_{g01}}x\right)^n} = p_{g01} + \frac{A_A n p_{g01}}{V_{g01}}x + \frac{A_A^2 n(n+1)p_{g01}}{2V_{g01}^2 \left(1 - \frac{A_A}{V_{g01}}c\right)^{n+3}}x^2 \quad (3.28)$$

hence

$$\left| \frac{A_A^2 n(n+1)p_{g01}}{2V_{g01}^2 \left(1 - \frac{A_A}{V_{g01}}c\right)^{n+3}} x^2 \right| \leq Mx^2 \quad \left| \frac{A_A^2 n(n+1)p_{g01}}{2V_{g01}^2 \left(1 - \frac{A_A}{V_{g01}}c\right)^{n+3}} \right| \leq M \quad (3.29)$$

where $c \in (0, x)$.

Using the system stiffness defining relation

$$K_s \stackrel{\text{def}}{=} \frac{\partial P_{sh}}{\partial \Delta x} \quad (3.30)$$

one gets the final form of the expression describing the stiffness of the hydropneumatic spring

$$K_s = \frac{nA_A^2 p_{g01}}{V_{g01}} \quad (3.31)$$

Returning to equation (3.21) and using relation (3.31), after transformations, one gets

$$(3.32) C_A = \frac{V_{g01}}{n p_{g01}} \quad (3.32)$$

Equation (3.32) describes the capacitance of the hydroaccumulator in the neighbourhood of the point $x = 0$ and for slight changes in the location of this point.

3.2. Second stage in damper operation

When the drive unit load increases, the average operating hydrostatic system pressure and the gas pressure in the accumulator change from p_{01g} to p_{kg} . Since the accumulator fills with the oil slowly, one can assume that compression of the gas is an isothermal process in accordance with the equation

$$p_{g01} V_{g01} = p_{kg} V_{kg} \quad (3.33)$$

and so as the load increases, motion of the damper piston takes place at the average pressure p_{kg} , and the volume of the gas in the accumulator amounts to

$$V_{kg} = \frac{p_{g01} V_{g01}}{p_{kg}} \quad (3.34)$$

Substituting p_{kg} for p_{01g} and V_{kg} for V_{g01} (a new balance point) in equation (3.31), one gets

$$K_{s1} = \frac{nA_A^2 p_{kg}}{p_{g01} V_{g01}} \quad (3.35)$$

Relation (3.35) describes the stiffness of the hydropneumatic spring of the active damper operating at the average pressure p_k in the system. Returning to equation (3.21), in new conditions of the equilibrium, one gets an expression for the accumulator capacitance C_{A1}

$$C_{A1} = \frac{p_{g01} V_{g01}}{n p_{kg}^2} \tag{3.36}$$

The change in the accumulator capacitance as a result of an increase in the average pressure from p_{01g} to p_{kg} , and so the change in the accumulator eigenfrequency $\omega_{\delta T}$ and in damping effectiveness, amounts to

$$\frac{C_{A1}}{C_A} = \left(\frac{p_{g01}}{p_{kg}} \right)^2 \tag{3.37}$$

In order to reduce the effect of variation in the average system pressure on the accumulator eigenfrequency at the instant when a certain pressure p_{kg} is reached, the volume of the other accumulator whose precharge pressure amounts to p_{kg} is added. This is the essence of the proposed low-frequency damper solution. In order to prove this thesis, experiments consisting in determining the capacitance for a single accumulator and, starting from a certain pressure value, for a system of two accumulators connected in parallel, have been carried out. A diagram of the measuring system for determining the capacitance of the hydraulic accumulators is shown in Fig. 3.

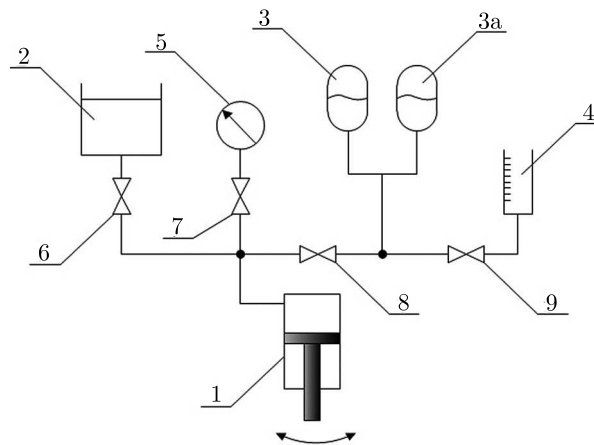


Fig. 3. Diagram of the system for determining the hydropneumatic accumulator capacitance in stationary conditions: 1 – hand-operated pump, 2 – priming tank, 3, 3a – tested hydroaccumulators, 4 – calibrating tank, 6, 7, 8, 9 – cut-off valves, initial accumulator operating conditions 3: $V_0 = 0.5 \text{ dm}^3$, $p_0 = 2 \text{ MPa}$; for accumulator 3a: $V_0 = 0.7 \text{ dm}^3$, $p_0 = 8 \text{ MPa}$

Using defining relation (3.7) and replacing the partial derivatives with increments, one can experimentally determine the capacitance of the hydropneumatic accumulator via volume changes ΔV_g caused by pressure increment. This is shown in Fig. 3. In order to obtain the required pressure value, hand-operated pump 1 (pressure gauge calibration press) has been used while the volume change ΔV_g was determined using graduated vessel 4 and properly set the cut-off valves (Fig. 4).

Relation $\Delta V_g = f(p_g)$ in the pressure range of 2-16 MPa for the two hydropneumatic accumulators was linearized with a secant, and a constant capacitance value $C_A = 0.56 \cdot 10^{-10} \text{ m}^5/\text{N}$ was obtained.

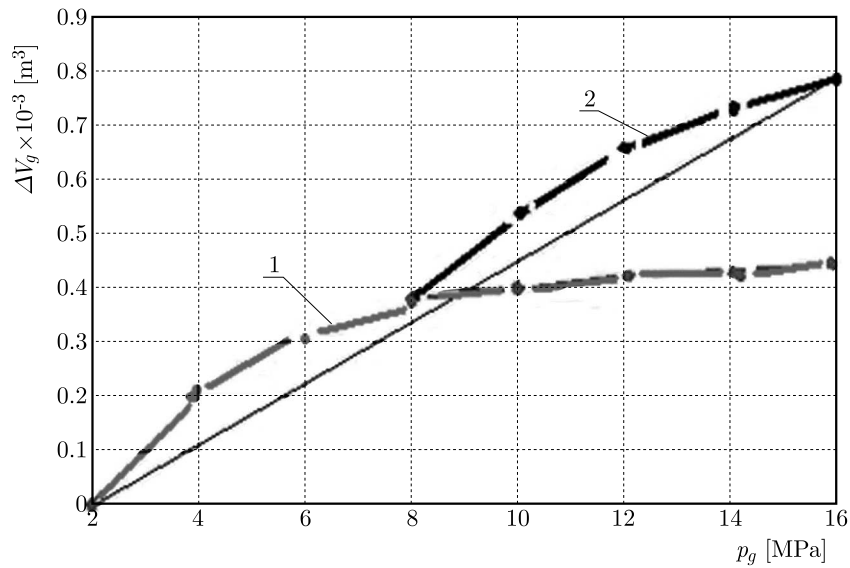


Fig. 4. Change ΔV_g in gas volume in the hydraulic accumulators connected in parallel versus pressure; one accumulator I, $p_{0g1} = 2$ MPa, $V_{0g1} = 0.5$ dm³, two accumulators connected in parallel I+II, $p_{0g2} = 8$ MPa, $V_{0g2} = 0.7$ dm³

4. Solution of the mathematical low-frequency damper model

The solution of the mathematical active damper model, based on relation (3.18), is presented graphically using Mathematica 5.1 and Origin v. 7.5 Pro software. Before solving the model, it was necessary to determine the particular coefficients and their variation ranges, which was done analytically or experimentally. The values of some of the major coefficients are: resultant reduced mass $M_{zr} = 2.87$ kg, inductance $L_T = 0.65 \cdot 10^6$ kg/m⁴, connection resistance $R_{0T} = (1.5 - 50) \cdot 10^8$ Ns/m⁵, range of dynamic viscosity $\mu = (30 - 1000) \cdot 10^{-3}$ Ns/m², total length $L_c = 0.86$ m, capacitance $C_A = 0.56 \cdot 10^{-10}$ m⁵/N, eigenfrequency according to formula (3.12) $\omega_{0T} = 158$ s⁻¹ (corresponds to eigenfrequency $f_{0T} = 25$ Hz and so to the rotational speed $n_p = 1500$ rpm of the motor driving the displacement pumps in the experiments) and damping number $\xi_T = 2.9 \cdot 10^{-5}$ s².

Figure 5a shows the effect of oil viscosity on the impedance modulus of the active damper in dimensionless coordinates (other parameters remain unchanged). Figure 5b illustrates the damper impedance modulus-dimensionless frequency relationship for viscosity $\mu = 30 \cdot 10^{-3}$ Ns/m².

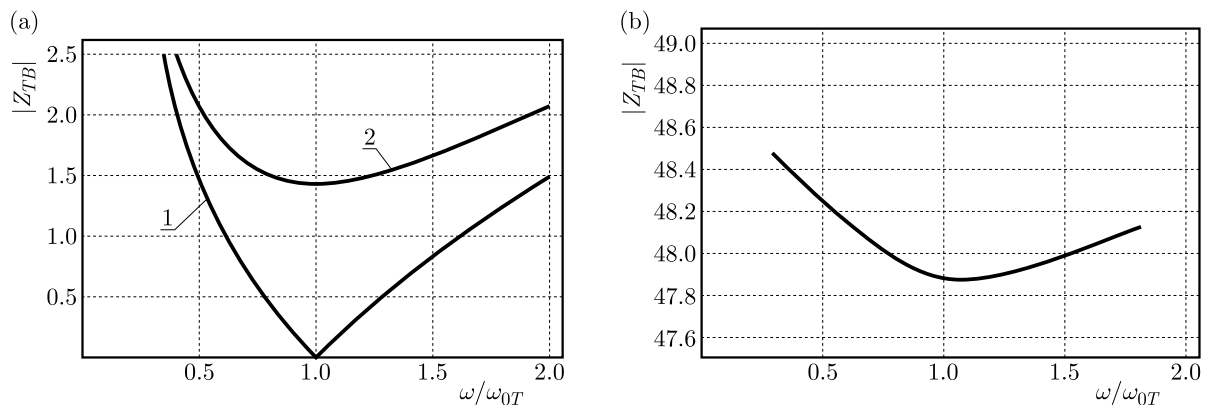


Fig. 5. (a) Low-frequency impedance modulus in dimensionless coordinates: 1 – oil viscosity $\mu = 0$; 2 – oil viscosity $\mu = 30 \cdot 10^{-3}$ Ns/m²; low-frequency damper impedance modulus in dimensionless coordinates for oil viscosity $\mu = 200 \cdot 10^{-3}$ Ns/m²

5. Experimental verification

Hydraulic pressure fluctuation tests involving the low-frequency damper have been carried using a test setup (Fig. 6) designed by the authors. The setup made it possible to determine amplitude-frequency characteristics of the investigated damper. A single-stage VCD (VoiceCoilDrive) Parker-Hannifin D1FPE01MC9NB00 proportional distributor was used as the pressure fluctuation inducing element. This means that, as opposed to conventional proportional distributors, it is not an electromagnet core, but a moving coil which acts on the spool. Consequently, the dynamic performance of the valve is significantly better owing to a substantial reduction in the moving mass (Kolvenbach and Krips, 2004). The distributor specifications were as follows: hysteresis $< 0.05\%$ and the cut-off frequency at 5% of the command signal – 350 Hz at the amplitude damping by 3 dB (Kudźma *et al.*, 2014). Dedicated software called HydroSter was developed to control the proportional valve in the test setup. A sinusoidal command signal with the set amplitude and frequency, generated by the HydroSter software, fed to the distributor coil would induce pressure fluctuations with a specified amplitude and frequency. The structure and operation of the HydroSter software are described in more detail in Kudźma (2012).

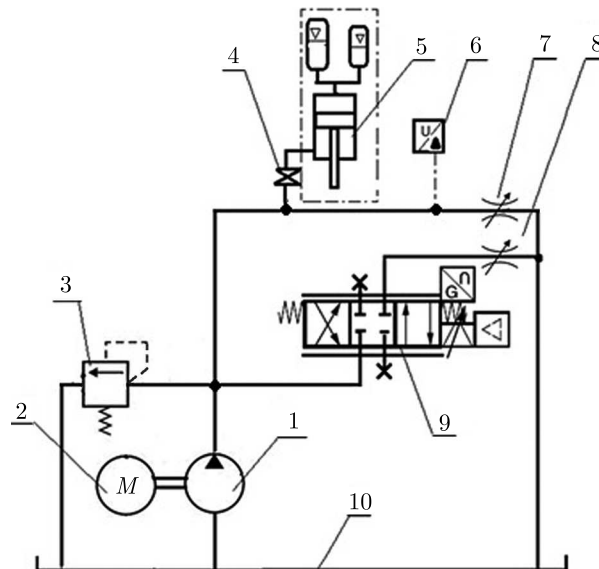


Fig. 6. Hydraulic diagram for determination of frequency characteristics of a low-frequency damper: 1 – displacement pump, 2 – electric motor, 3 – safety valve, 4 – cut-off valve, 5 – low-frequency damper, 6 – pressure transducer, 7, 8 – throttle valve, 9 – proportional distributor, 10 – tank

The experimental verification consisted in recording pressure fluctuations over time while generating pressure fluctuations with the set frequency and amplitude, with the low-frequency damper installed and without the damper, in identical operating conditions. In the system shown in Fig. 6, the sources of excitations in the form of output and pressure fluctuations were: working displacement pump 1 (with a constant delivery and a fixed driving shaft speed) and proportional distributor 9 to whose coils a time-varying command signal with the set amplitude, constant value and frequency was fed. The presence of the damper in the system was determined by opening of cut-off valve 4 (Fig. 6). In the laboratory version of the damper, a displacement transducer was used to measure the displacement of the damper piston. Sample results of pressure fluctuation measurements are presented in Figs. 7-9.

Then the effectiveness of the damper was experimentally verified by determining the amplitude-frequency characteristic for the input pressure fluctuation amplitude Δp and the output piston displacement Δx . As a part of the investigations, the resonance frequency corre-

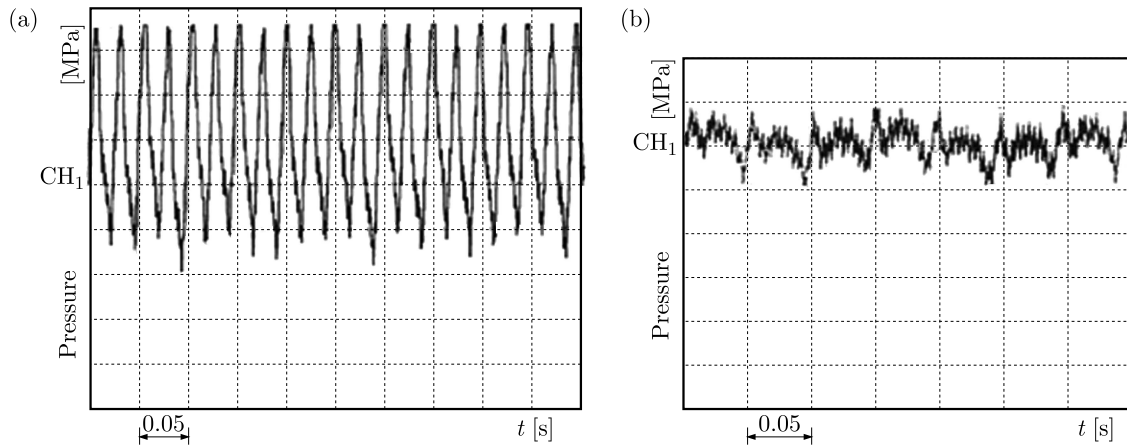


Fig. 7. Pressure fluctuations in the hydraulic system. Frequency of the pressure fluctuation excitation with a harmonic exciter $f_w = 25$ Hz. Forcing pressure $p_t = 12$ MPa: (a) system without the damper, (b) system with the damper (the scales in the two figures are identical)

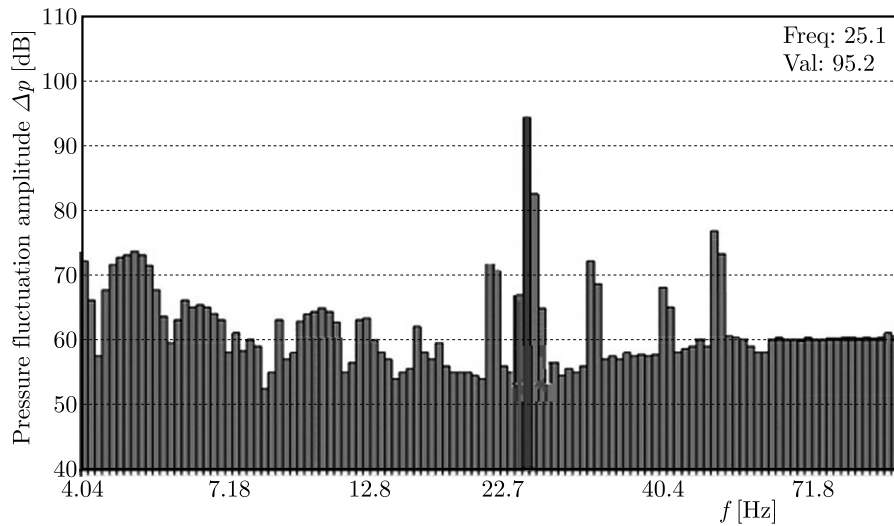


Fig. 8. Narrow-band analysis of pressure fluctuation in the hydraulic system without the low-frequency damper. Frequency of the pressure fluctuation excitation with a harmonic exciter $f_w = 25$ Hz. Forcing pressure $p_t = 12$ MPa

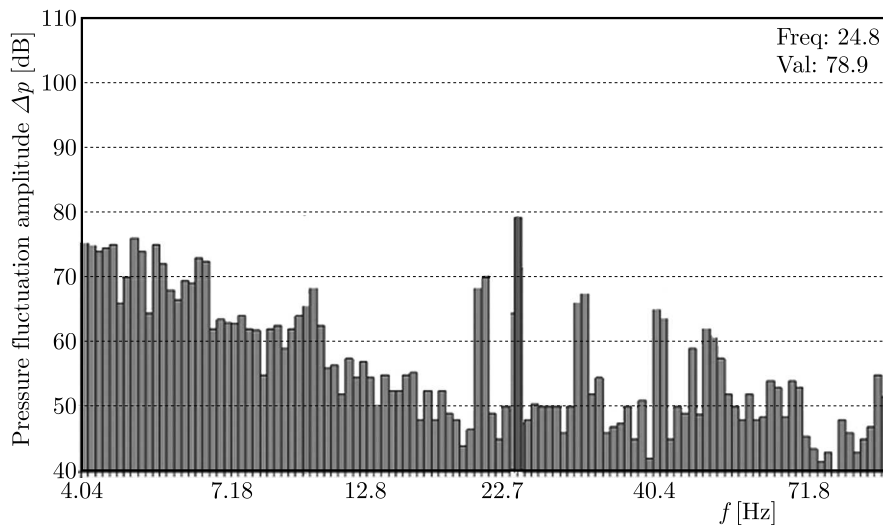


Fig. 9. Narrow-band analysis of pressure fluctuation in the hydraulic system with the low-frequency damper. Frequency of the pressure fluctuation excitation with a harmonic exciter $f_w = 25$ Hz. Forcing pressure $p_t = 12$ MPa

sponding to the maximum transmittance was determined, whereby it was confirmed that the active damper was most effective at the resonance frequency (Fig. 10).

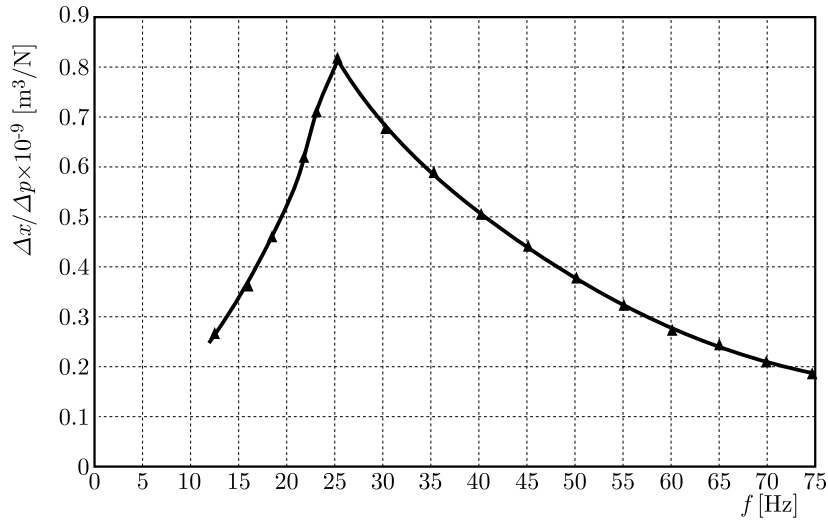


Fig. 10. Amplitude-frequency characteristic of the low-frequency damper at a forcing pressure of 12 MPa

6. Conclusion

A wide spectrum of pressure fluctuations occurs in hydraulic systems. Particularly hazardous and difficult to eliminate are pressure fluctuations in the range up to 50 Hz, resulting in generation of infrasounds by machines equipped with a hydrostatic drive system.

Various hydropneumatic accumulators are commonly used to reduce pressure fluctuation amplitudes in the low-frequency range. The drawback of this solution is that hydropneumatic accumulators are most effective in reducing pressure fluctuation amplitudes when the accumulator resonance frequency coincides with the fluctuation frequency which is to be reduced. It should be noted that the accumulator eigenfrequency to a large extent depends on the magnitude of pressure in the hydraulic system incorporating this component. This means that hydropneumatic accumulators act selectively and so, as dampers, they are narrow-band filters, and their actual effectiveness in reducing pressure fluctuation is limited to practically a single excitation frequency equal to the hydropneumatic accumulator resonance frequency. Damping effectiveness has been observed to rapidly decrease already at slight deviations from the resonance frequency.

A concept of a pressure fluctuation damper whose key component is a hydropneumatic spring, effective in the range of low frequencies, has been presented in this paper. The axial cross section of the low-frequency damper, whose characteristic feature is that two hydropneumatic accumulators differing in their volume and gas precharge pressure form the hydropneumatic spring, is shown in Fig. 1. Owing to this solution, the hydropneumatic spring has an approximately constant stiffness in the whole load range, whereby its resonance frequency remains unchanged. Also, a mathematical model of the damper has been provided and effectiveness of the latter has been verified using a specially designed experimental setup enabling generation and recording of harmonic pressure fluctuations in a wide range of excitation frequencies. Theoretical analysis and verification results show that the low-frequency damper is most effective when its resonance frequency coincides with the frequency to be reduced. The damper resonance frequency, expressed by relation (3.12), depends on the equivalent capacitance of at least two hydroaccumulators (under heavier drive system loads), experimentally determined using defining relation (3.7) and on the hydraulic inductance described by relation (3.19).

In hydrostatic drive systems, the low-frequency damper performs function of an acoustic filter, especially in low frequencies. This is evidenced by the chart in Fig. 11, showing a comparison between the third octave spectra of the sound pressure level L_m of the actual hydraulic system lifting the jib of loader Ł-200, with and without the low-frequency damper. The measurements have been carried out in a sound chamber in which the Ł-200 loader jib lifting system was placed. The chamber and the way in which the measurements were performed were described in detail in Kudźma (2012). The resonance frequency of the damper installed in the lifting system amounted to 25 Hz, which corresponded to the pump driving motor rotational speed $n_p = 1500$ rpm. In order to reduce the pressure fluctuation amplitude for higher frequencies, one should install the passive damper described in, e.g., Kudźma and Kudźma (2015).

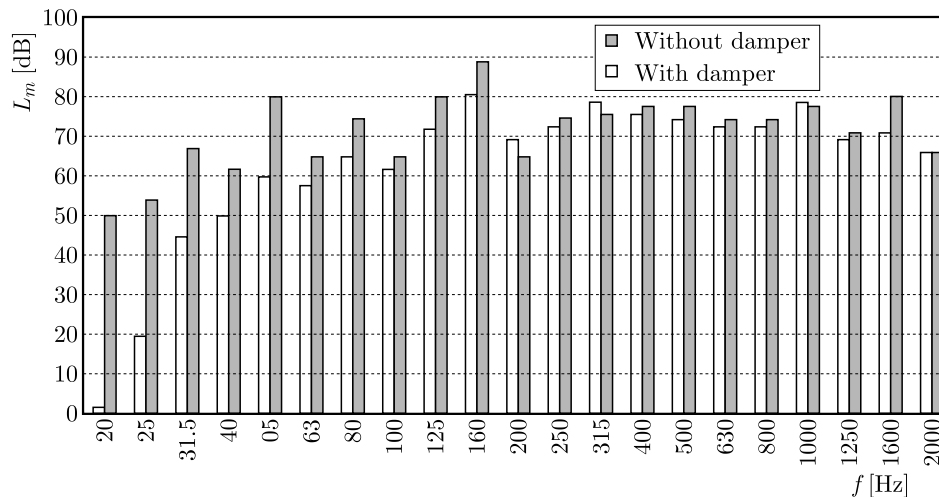


Fig. 11. Comparison between the third octave spectra of the sound pressure level L_m of the actual Ł-200 loader jib lifting hydraulic system with and without the low-frequency damper, pump shaft rotational speed $n_p = 1500$ rpm, forcing pressure $p_t = 12$ MPa

References

1. BACKÉ W., MURRENHOF H., 1994, *Grundlagen der Ölhydraulik*, Lecture notes: Institut für Fluidtechnische Antriebe und Steuerungen, RWTH Aachen, Germany
2. CHANGBIN G., ZONGXIA J., 2014, A piezoelectric direct-drive servo valve with a novel multi-body contacting spool-driving mechanism. Design, modelling and experiment, *Proceedings of the Institution of Mechanical Engineers, Part C: Journal of Mechanical Engineering Science*, **228**, 1, 169-185
3. CZERWINSKI A., LUCZKO J., 2015, Parametric vibrations of flexible hoses excited by a pulsating fluid flow, Part II: Experimental research, *Journal of Fluids and Structures*, **55**, 174-190
4. DINDORF R., 2004, *Modelling and Simulation of Nonlinear Control Elements and Systems of Fluid Drives* (in Polish), Kielce University of Technology Publishing House, Kielce
5. EARNHART N.E., CUNEFARE K.A., 2012, Compact Helmholtz resonators for hydraulic systems, *International Journal of Fluid Power*, **13**, 41-50
6. GARBACIK A., LISOWSKI E., SZEWCZYK K., 1986, Hydraulic accumulator as pressure fluctuation damper (in Polish), *Sterowanie i Napęd Hydrauliczny*, **4**, 9-13
7. GERMAN D.G., REESE J.M., ZHANG Y.L., 2000, Vibration of a flexible pipe conveying viscous pulsating fluid flow, *Journal of Sound and Vibration*, **230**, 2, 379-392
8. IJAS M., 2007, *Damping of Low Frequency Pressure Oscillation*, Tampere University of Technology Publication 656, Tampere

9. KOLLEK W., KUDŹMA Z., OSIŃSKI P., STOSIAK M., 2009, Low-frequency noise of heavy engineering machinery (in Polish), *Napędy i Sterowanie*, **1**, 50-55
10. KOLLEK W., KUDŹMA Z., RUTAŃSKI J., STOSIAK M., 2010, Acoustic problems relating to microhydraulic components and systems, *The Archive of Mechanical Engineering*, **57**, 3, 293-308
11. KOLVENBACH H., KRIPS W., 2004, Revolution in Dynamik und Kraft: Neue Antriebs technologie für Stetigventile, *4th International Fluid Power Conference "Intelligent Solutions by Fluid Power"*, Dresden
12. KUDŹMA Z., 2012, *Pressure Fluctuation and Noise Damping in Hydraulic Systems in Transient and Steady States* (in Polish), Wrocław University of Technology Publishing House, Wrocław
13. KUDŹMA S., KUDŹMA Z., 2015, Refined model of passive branch damper of pressure fluctuations, *Journal of Theoretical and Applied Mechanics*, **53**, 3, 557-567
14. KUDŹMA Z., STOSIAK M., HEROK S., 2014, Setup for determining static and dynamic characteristics of proportional valves (in Polish), *Pomiary Automatyka Robotyka*, **18**, 3, 112-119
15. MICHAŁOWSKI S., STOLARSKI B., 1998, *Suppression of Vibration and Noise in Heavy Engineering Machinery* (in Polish), Monograph, Cracow University of Technology Publishing House, Cracow
16. MIKOTA J., 2000, Comparison of various designs of solid body compensators for the filtering of fluid flow pulsations in hydraulic systems, *Proceedings of 1 FPNI-PhD Symposium*, Hamburg
17. ORTWIG H., GOEBELS K., SCHWARZ T., 1999, Hydroämpfer zur Geräuschreduzierung in hydraulischen Anlagen, *Ölhydraulik und Pneumatik*, **9**, 652-656
18. OSIŃSKI P., KOLLEK W., 2013, Assessment of energetic measuring techniques and their application to diagnosis of acoustic condition of hydraulic machinery and equipment, *Archives of Civil and Mechanical Engineering*, **13**, 3, 313-321
19. PALCZAK E., POMOWSKI J., 2006, Transient states of hydraulic system with accumulator (in Polish), *Inżynieria Maszyn, Rozwój Maszyn i Urządzeń Hydraulicznych*, **2-3**, 29-38

Manuscript received July 29, 2016; accepted for print February 13, 2018

INVESTIGATIONS OF MATERIAL BEHAVIOUR UNDER MONOTONIC TENSION USING A DIGITAL IMAGE CORRELATION SYSTEM

TADEUSZ SZYMCZAK

Motor Transport Institute, Centre for Material Testing, Warsaw, Poland

e-mail: tadeusz.szyczak@its.waw.pl

The paper reports behaviour of engineering materials for different kinds of notches, i.e. having U , V shapes. Their variants with respect to dimensions are illustrated in static and fatigue tests. The influence of these types of geometrical imperfections on material fatigue is presented using variations of the Wöhler curve, number of cycles to failure and the fatigue notch factor. Results of experiments conducted by the use of the Digital Image Correlation system called 4M Aramis are illustrated. Courses of tensile characteristics of the 41Cr4 steel, obtained by means of both techniques: extensometer and DIC are compared. They indicated that the DIC technique can be a good tool for determination of mechanical properties. The equivalent strain full-field distributions on specimens tensioned with and without imperfections up to material fracture are presented. The influence of U and V notches on variations of tensile curves is shown.

Keywords: geometrical imperfection, notch, extensometer, DIC, non-contact technique

1. Introduction

Determination of behaviour of materials under various loading types can be reached by the use of different measurement techniques. The extensometer method is the most popular approach applied in static and fatigue tests for measuring strain state components versus time. Nevertheless, this technique registers strain variations in one direction indicated at the beginning of the experiment with respect to the load direction. These results are important for typical engineering calculations focused on the assessment of material behaviour in a one-axis coordinate system. For material examination under more complex types of loading, these data are insufficient because many materials exhibit anisotropy of mechanical properties. Moreover, observation of damage zones and strain fields is not possible and, nowadays, these material features can be followed using a modern, non-contact optical method, such as Digital Image Correlation (DIC).

The DIC method recommended for 3D measurements is a stereoscopic technique employing two CCD cameras, light sources and advanced software (GOM source). This method involves applying a special pattern represented by black dots on a grey background (Chu *et al.*, 1985; Lord, 2009). A mathematical description of the DIC is available in the literature (Chu *et al.*, 1985, for example). Markers are chosen by a DIC device for obtaining x , y and z coordinates, and are followed by the DIC system up to specimen fracture. The DIC can employ a pattern of rectangles or squares whose origins are directly selected for calculations of displacement/strain. Results are presented as full-field maps expressing distribution of strain from the test beginning up to the specimen fracture (Lord, 2009; Kamaya and Kawakubo, 2011). The maps can be compared with the FEA results (Toussaint *et al.*, 2008; Gower and Shaw, 2010; Kamaya and Kawakubo, 2011) to validate material models or constitutive equations. The Digital Image Correlation is recommended for static and fatigue tests conducted under various types of loading. In the case of static experiments, a DIC device can be used more flexibly than in experiments on cyclic

loading. This is due to the limited number of stages offered by the DIC software to be recorded. Therefore, a concept to follow strain variations due to cyclic loading should be formulated before testing with the use software targets or commands in C++.

Results from various research groups show that the DIC is employed for examination of material behaviour under typical tensile and compression tests (Forster *et al.*, 2010), fracture toughness examinations (Durif *et al.*, 2012) and experiments focused on determination of the effects of geometrical imperfection such as notches (Kamaya and Kawakubo, 2011) and holes. Data on monotonic tension are usually represented by full-field maps expressing strain distribution and its values up to the moment of fracture appearance. The results from fracture toughness experiments present the strain distribution close to the fatigue crack and stress intensity factors.

1.1. Specimens with notches

Notches are defined as geometrical imperfections of structural components. Their geometry is represented by the angle between their edges, radius and depth. Many results express values of the stress concentration factor (SCF) obtained by analytical or numerical calculations. This enables the assessment of influence of the stress concentration factor on stress values appeared in the notch tip, in a one-dimensional coordinates system. The second widely used method for determination of SCF influence comes as a result of the development of Finite Element Analysis (FEA). In this case, advanced engineering software is used to solve problems caused by different kinds of geometrical discontinuities. In the case of this method, many advantages can be stated, i.e. application of various 2D or 3D elements and analysis of macro- and micro-scales. Its main drawbacks are material definitions in the elastic-plastic state, as FEA requires definition of material hardening or softening reached not only in one axial stress state, but also in a complex one. Despite the use of modern biaxial testing machines, material examination under various combination of stress components is not easy and is still being developed.

Notches are classified by many branches of industry as geometric discontinuities that can influence material behaviour and reduce lifetime of components. They appear in drive shafts, engines, car bodies, turbines and others elements as well as constructions having complicated shapes. One effect of notches, strongly related to their radius, angle, fillet at the tip and other dimensions, is that the size of these features can influence the concentration of stress/strain state components, time to fracture and failure type of the material.

Worth to distinguish round and flat specimens with macro- (Fig. 1) and micro-notches (Maruno *et al.*, 2004; Whaley, 1964). The size of geometric discontinuities is unique for each type of specimen and depends on details of the experimental procedure. In the case of round specimens, notches are machined around the major axis of the specimen (Figs. 1 and 2) but for flat specimens, geometric discontinuities are located on one (Whaley, 1964) or both sides of the specimen (Fig. 2).

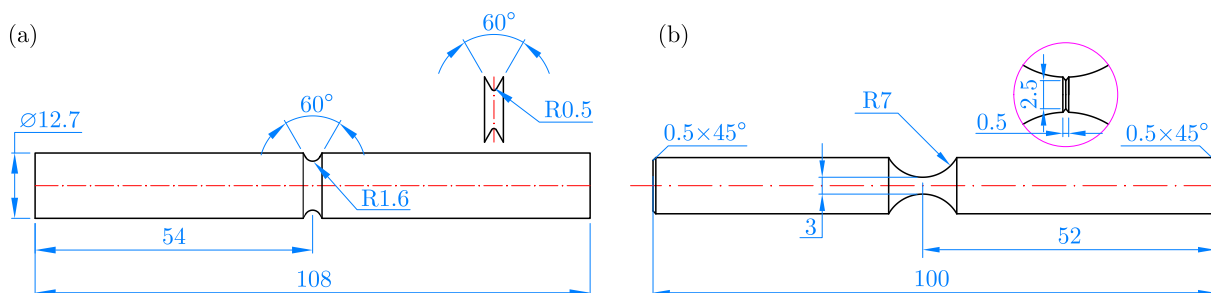


Fig. 1. Notched round specimens for fatigue testing: (a) Fatemi *et al.* (2004), (b) Pluingae and Gjonaj (2001)

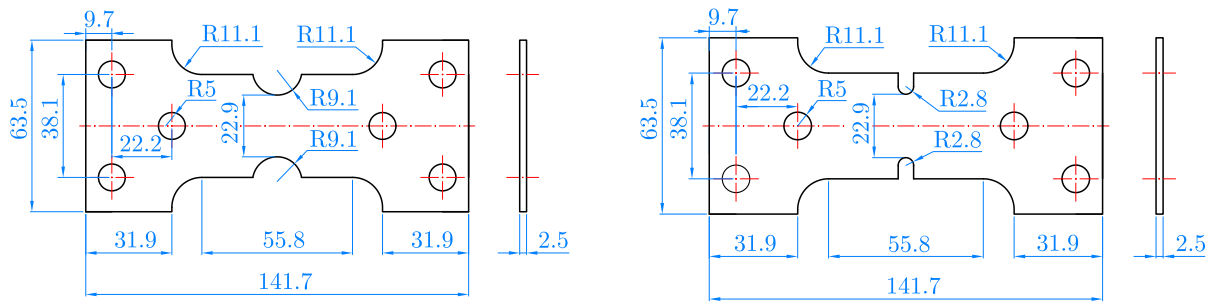


Fig. 2. Double-notched flat specimens used for examination of material behaviour under cyclic loading (Fatemi *et al.*, 2004)

1.2. Material behaviour due to notches and holes

Great efforts of many research groups (Wahl *et al.*, 1930; Mazdumar and Lawrence, 1981; Lanning *et al.*, 1999; Milke *et al.*, 2000; Fatemi *et al.*, 2002, 2004; da Silva *et al.*, 2012) are made to describe phenomenology of the influence of notches on material behaviour under various loading types up to fracture. As previously mentioned, notched specimens represent individual projects of research groups.

Experimental results from tests concentrated on determination of the influence of notches on material fatigue show the significant effect of geometric discontinuities on lifetime (Figs. 3-6). The differences between material lifetime due to various stress levels can be equal to 80% (Fig. 3). Moreover, contrary to the results from tests on smooth specimens, the data for notched specimens indicate some difficulties in the machining of the notches. Boroński (2007) assumed that the fatigue life determined at the notch bottom was the same as the life for a smooth specimen when strains waveforms for the both specimens type were the same.

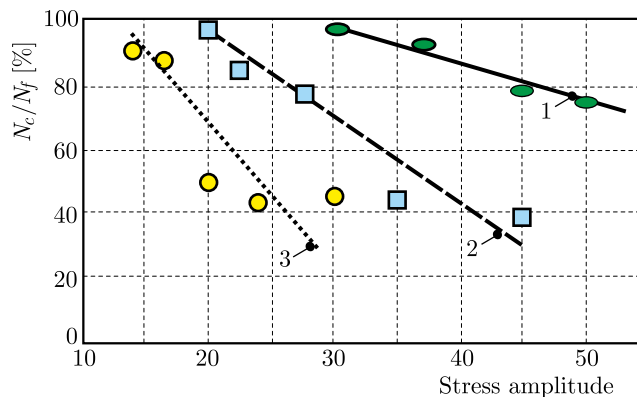


Fig. 3. The influence of notch radius on the proportion of cycle numbers to initiation of the first crack N_c and fracture N_f at various stress amplitudes for the specimens: 1 – un-notched, 2 – notched with radius 1.5 mm, 3 – notched with radius 6.35 mm; material: 24S-T4 aluminium alloy (Bennett and Weinberg, 1954)

The results presented in Fig. 4 illustrate variations of the fatigue notch factor for values of the stress ratio R within a range of 0.5-1.0 due to the radius of the notch machined in cylindrical and flat specimens. In the case of flat specimens, an increase of this parameter is clearly visible. For the cylindrical specimen, the value of the fatigue notch factor achieved a constant level.

Experimental procedures are also designed to capture Wöhler curve variations at stress controlled tests, applying notches with different values of stress concentration factors (Fig. 5). These investigations are usually carried out using round or flat specimens. As can be seen in the paper by Fatemi *et al.* (2002, 2004), a great decrease of the cycle number to failure was achieved

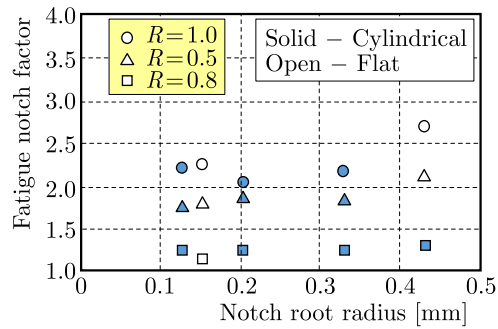


Fig. 4. Fatigue notch factor versus notch root radius for cylindrical and flat specimens with notches for a stress ratio within a range from 0.5 to 1; material used: Ti-6Al-4V (Lanning *et al.*, 1999)

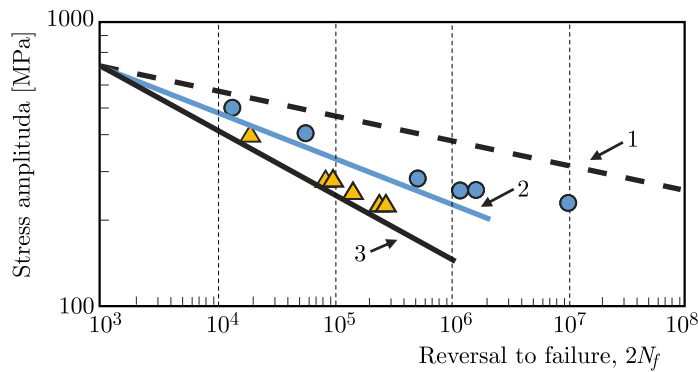


Fig. 5. Wöhler curve determined on circumferentially notched round bars for stress concentration factors equal to: 1 - 1.0, 2 - 1.787, 3 - 2.833; material: 1141 medium carbon steel micro-alloyed with Vanadium (Fatemi *et al.*, 2002, 2004)

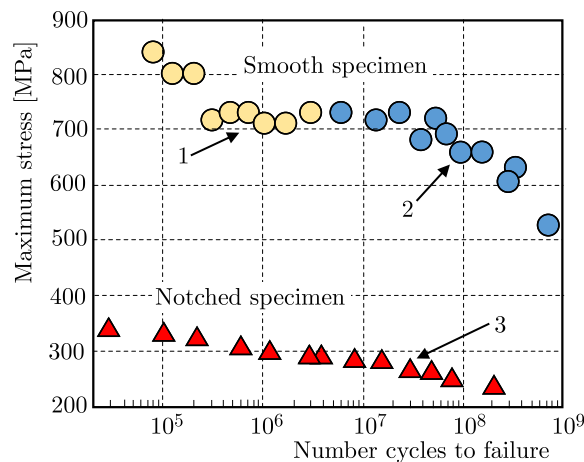


Fig. 6. Wöhler curve of 40Cr steel obtained for smooth and notched specimen with modes crack initiation: 1, 3 - surface, 2 - subsurface (Qian *et al.*, 2010)

when the SCF increased three times. Distribution of experimental points from tests performed on flat specimens with the notch having a stress concentration factor equal to 1.787, expressed low agreement with a semi-logarithmic approximated function. The reason for this disagreement is usually related to the specimen machining process and their mounting in testing machines.

Other experiments were conducted to determine the zone of initiation of cracks during fatigue (Fig. 6). In that case, the stress signal was used to control the testing machine. Both smooth and notched specimen geometries were applied (Chen, 2004). The application of smooth specimens in tests performed at various stress levels allowed following the initiation and propagation of

cracks from the surface to the subsurface. In the case of notched specimens, the cracks appeared on the surface only.

Analytical and numerical calculations are concentrated on determination of stress gradients in the tip of the notch (Siebel and Stieler, 1955; Peterson, 1959; DuQuensay *et al.*, 1986; Filippini, 2000; Milke *et al.*, 2000). Their magnitude are calculated using an equation representing dimensions of notches (Siebel and Stieler, 1955; Peterson, 1959; Pilkey, 1997), Neuber's theory (Neuber, 1958, 1961; Filippini, 2000; Topper *et al.*, 1967), and proportion of stress and nominal stress in the notch (Peterson, 1959; DuQuensay *et al.*, 1986).

In FEM analysis, the influence of notches is calculated for specimens with narrow geometrical discontinuities like V or U shapes (Pluingae and Gjonaj, 2001; Andersson, 2013; da Silva *et al.*, 2012). The maximum stress in the tip of a notch (da Silva *et al.*, 2012; Andersson, 2013) and the stress concentration factor are parts of the results (da Silva *et al.*, 2012) as well as an estimation of fatigue strength (Andersson, 2013).

2. Details of the experiment

The experimental procedure elaborated for application of the DIC system contained three stages as follows:

- a) determination of the stress-strain curve, Young's modulus, yield point and ultimate tensile strength;
- b) investigation of the full-field strain distribution close to U and V notches;
- c) examination of the influence of dimensions of U or V notches and their interactions with material behaviour.

All tests were carried out at room temperature using servohydraulic 8802 Instron and electro-dynamic Electropuls E10000 Instron testing machines. The Aramis 4M Digital Image Correlation system was employed to follow distribution of the strain state. Before testing, the DIC device was calibrated. In the testing stages focused on determination of mechanical properties and material behaviour with the assistance of geometrical imperfections and various tensile rates, an extensometer and the 4M Aramis were used simultaneously. The assessment of the DIC system used for the determination of mechanical properties was made on the basis of a comparison of data obtained by the extensometer and by virtual tensometers defined in the DIC software.

Application of the Digital Image Correlation technique required the following stages:

- a) adjustment of the distance between two cameras, its angle indicated in guidelines of technical data;
- b) positioning the 4M Aramis with respect to the centre of the measurement zone;
- c) selection of a calibration plate, which should be chosen on the basis of dimensions of the region for which the displacement is considered to be determined;
- d) performing the calibration procedure by applying the plate which takes various orientations in the 3D coordinate system, and recording its positions;
- e) mounting the specimen, having an artificial measuring zone represented by black dots stochastically arranged on the grey layer, in grips of the testing machine;
- f) capturing the first photo and establishing it as the reference one for displacement determination and strain calculations.

Technical data (GOM folders) for calibration of the DIC system are delivered by the producer of this device type and contain the following features: measuring volume (height, length, width), minimum length camera support, distance ring (it enables one to change camera lens), measuring distance (from the central section of the DIC device to the centre of the measuring zone), slider

distance (determined by two technical points on the cameras), camera angle (it determines the centre of the measuring zone), calibration object (a plate with special regular markers having determined coordinates, which should be identified by the cameras during the calibration process).

In the case of the experiments, the 4M Aramis was used with the following technical parameters:

- initial measuring zone determined on the basis of the specimen tested 25 mm × 10 mm × 3 mm;
- calibration plate 25 mm × 18 mm;
- slider distance 37.5 mm;
- camera lens 75 mm + slider distance;
- camera angle 25°;
- sampling rate 2 photos/s.

3. Results

Comparison of tensile curves obtained by the use of the flat specimen and the extensometer as well as the DIC system is presented in Fig. 7. The axial stress is calculated as a proportion of the axial force to the cross-section of the measurement zone. Values of the axial strain are calculated for the same base, close to 25 mm.

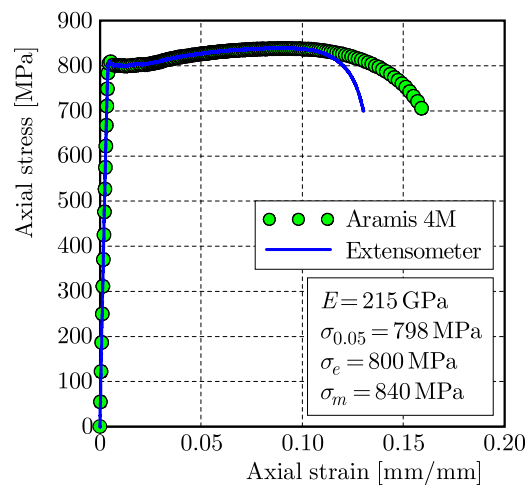


Fig. 7. Comparison of tensile characteristics determined by the use of the extensometer and Aramis 4M; material: high strength steel

A digital image correlation device and the extensometer technique have been simultaneously employed in the monotonic test. For DIC calculations, two virtual tensometers were selected to define the gauge length for determination of the axial strain. A comparison of the results from the extensometer and the DIC technique expressed high agreement in the stress-strain curves from the beginning of testing up to the ultimate tensile strength occurrence. Differences in the last section of those relationships are related to appearance of the neck, which is close to the extensometer edge.

Mechanical properties calculated on the basis of the data obtained by means of both applied techniques are listed in Fig. 7. Differences between tensile characteristics (Figs. 7 and 8) are very small, indicating the DIC system to be recommend not only for capturing strain maps (Fig. 9), but also for determination of typical mechanical parameters.

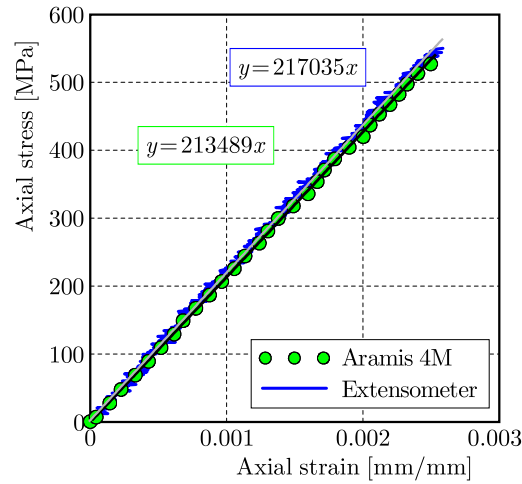


Fig. 8. Linear relationship of tensile curves illustrated in Fig. 7

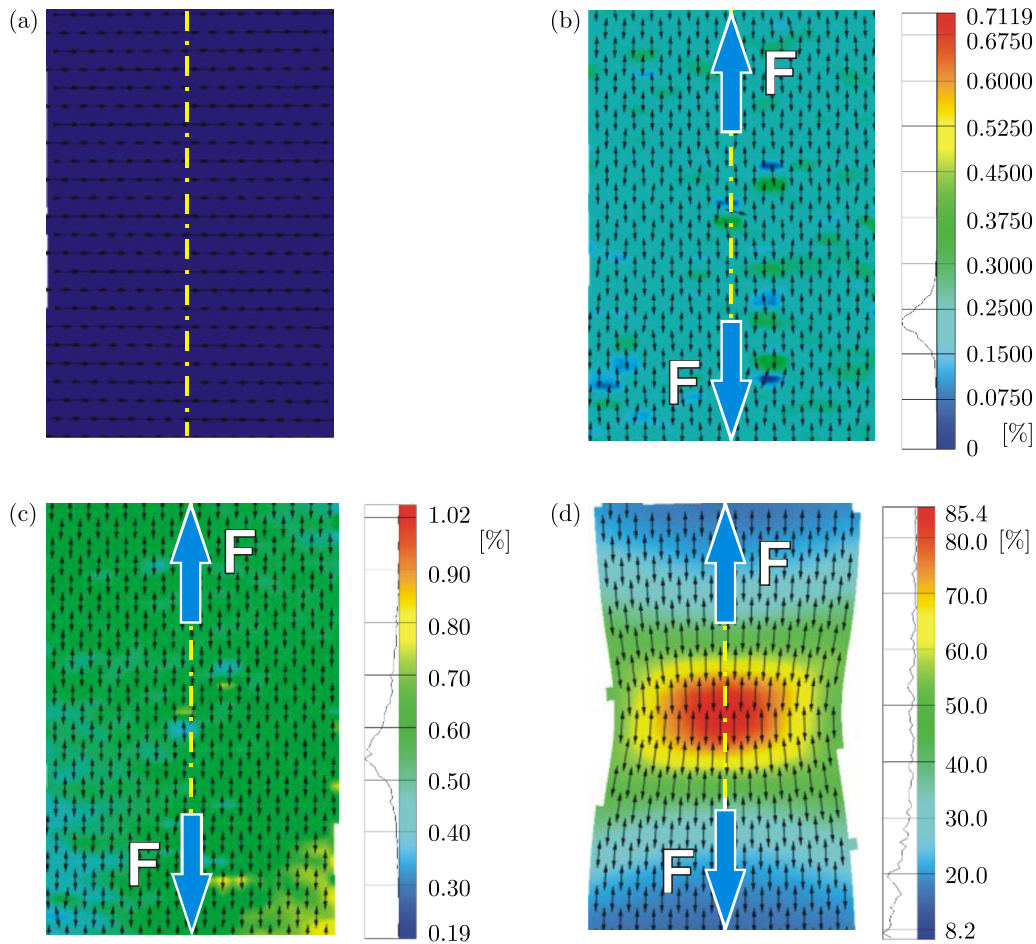


Fig. 9. Distribution of axial strain in a flat specimen under monotonic tension at various stages of the testing: (a) specimen mounted in the testing machine before the experiment, (b) at the strain-determined proportional limit, (c) at the strain-determined yield point, (d) before fracture

The main advantage of the DIC system is presented in Fig. 9, which shows variations of the axial strain distribution at various stages of tension. On the basis of these results, the damage zone can be followed up to the specimen fracture (Figs. 9b-d). It is also worth noticing that the distribution of the major strain (black vectors) at the beginning of tensile testing enables the assessment of quality mounting of a specimen in the testing machine (Fig. 9a).

Another application of the DIC method is illustrated in Fig. 10. These figures show the equivalent strain distributions for the specimen with a U -shaped notch at various material states. The 4M Aramis system employs the equation as follows

$$\varepsilon_{eq} = \sqrt{\frac{2}{3} (\varepsilon_{1,true}^2 + \varepsilon_{2,true}^2 + \varepsilon_{3,true}^2)} \quad (3.1)$$

where ε_i represents the major true strains, $i = 1, 2, 3$. The major strains are expressed by the following equation $\varepsilon_{i,true} = \ln(1 + \varepsilon)$, for which $\varepsilon = (\Delta l)/l_0$ is the engineering strain, where l_0 is gauge length, Δl – elongation. Equation (3.1) presents the stress state in the strain coordinate system. It can be reached on the basis of theory of plasticity (Westergaard, 1952; Olszak, 1965; Chen, 2004).

It should be emphasized that equation (3.1) can be used when the straining is proportional, i.e. expressed by constant ratios of $d\varepsilon_{1,true}/d\varepsilon_{2,true}/d\varepsilon_{3,true}$.

Both initial images present the specimen at the beginning of the test, i.e. the referential stage with zero loading and in the elastic state (Figs. 10a,b). The elastic-plastic state, shown in Fig. 10c, expresses the equivalent strain distribution and indicates the deformation zone located close to the centres of U -notches as initiators of maximum strain.

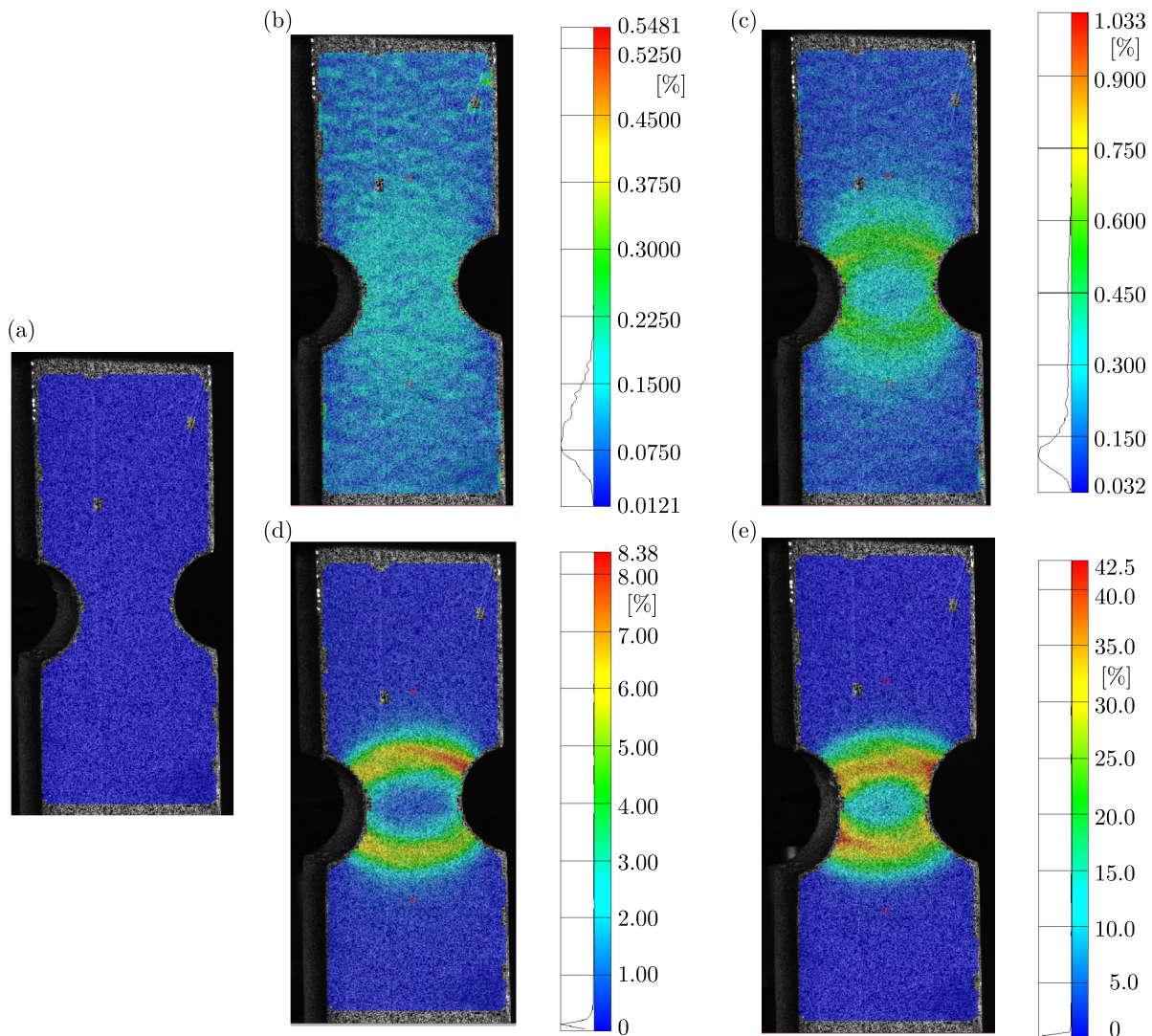


Fig. 10. The equivalent strain distribution in the U -notched specimen; material: aluminium

These arc-shaped deformation regions appear where the growing damage occurs. It is strongly evidenced in the following stages of specimen tension, presenting the material behaviour before fracture (Figs. 10d,e). As it can be noticed in Figs. 10c-e, the strain distribution is expressed by the zone in form of an arc at the test beginning up to the specimen fracture. It shows that besides the strain concentration, which can be captured in the DIC experiments, the shape of strain should be taken into account as data for further analysis of the effects related to the *U*-shaped notch.

The making use of the DIC system has also been examined in the test on determination of the influence of dimensions of geometrical imperfections in *U*-shaped (Figs. 11 and 12) and *V*-shaped specimens (Figs. 15 and 16) on the material fracture. The depth of the notches was the same and equal to 1.3 mm. The radii of the *U*-notches were of 0.75 mm, 1.5 mm and 2.5 mm. The angles between the edges of the *V*-notches were 30°, 60° and 90°, respectively.

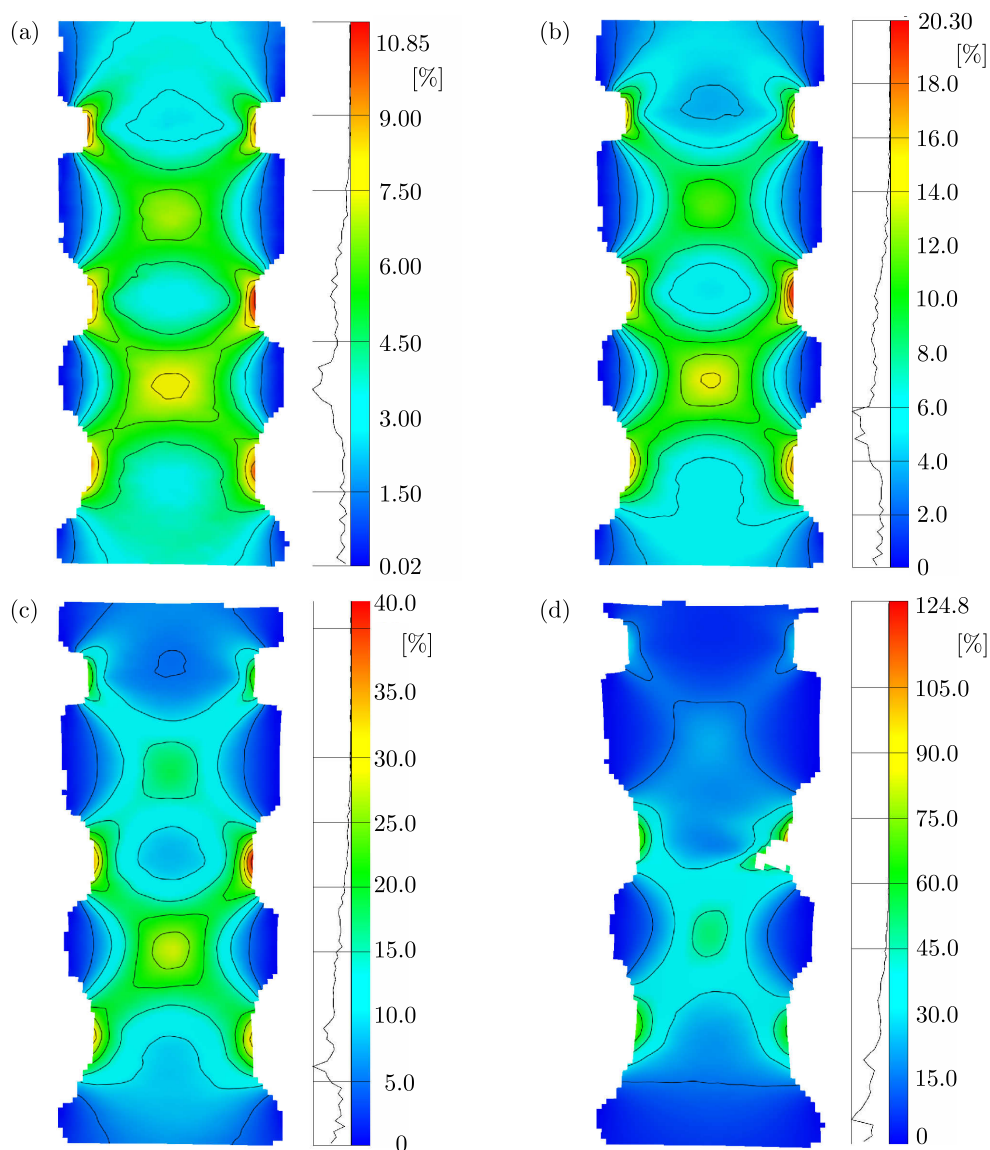


Fig. 11. The equivalent strain distribution in the *U*-shaped multi-notched specimen at various stages of monotonic tension: (a), (b), (c) elastic-plastic state, (d) elastic-plastic state before fracture; material: the 41Cr4 steel

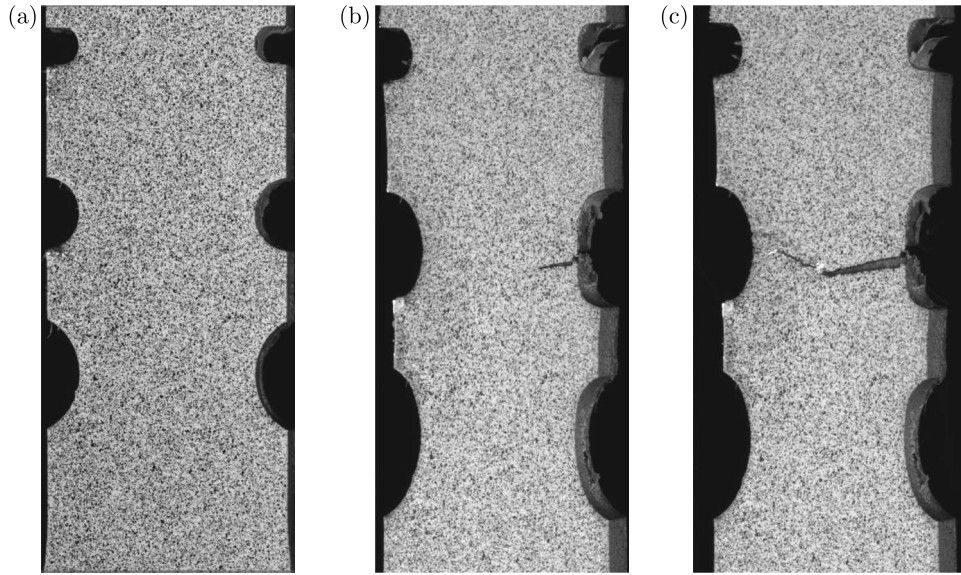


Fig. 12. Three stages of the U -notched specimen during monotonic tension: (a) before loading, (b) crack appearing, (c) crack growing

Effects resulting from the dimensions of the U and V notches have been determined based on variations of the equivalent strain isolines (Figs. 11 and 15). In the case of the U multi-notched specimen, the interaction between the notches became more significant with an increase of their radius (Fig. 11b). The results achieved for further tension also expressed that effect (Fig. 11c). It disappeared when the damage zone became greater (Fig. 11d), and it vanished with growing of the cracks. The cracks can also be followed on the basis of typical photos from the DIC of CCD camera (Fig. 12). This is very important for the final stage of testing, because crack growing causes a fracturing measurement pattern and, therefore, the digital correlation is not possible to be done (Figs. 11d and 12b,c).

Assessment of the effects of notches has been followed by using analytical equations for the stress concentration factor and the maximum stress (Pilkey, 1997). Their form for the multi-notched U specimens is noted in Eqs. (3.2), where K_{tU} is the stress concentration factor, r is the notch radius, d is the distance between the centre of opposite notches, D is specimen width, and L is the distance between the notches

$$\begin{aligned}
 K_{tU} &= C_1 + C_2 \frac{2r}{L} + C_3 \left(\frac{2r}{L}\right)^2 + C_4 \left(\frac{2r}{L}\right)^3 \\
 C_1 &= 3.1055 - 3.4287 \frac{2r}{D} + 0.8522 \left(\frac{2r}{D}\right)^2 \\
 C_2 &= -1.4370 - 10.5053 \frac{2r}{D} - 8.7547 \left(\frac{2r}{D}\right)^2 - 19.6237 \left(\frac{2r}{D}\right)^3 \\
 C_3 &= -1.6753 - 14.0851 \frac{2r}{D} + 43.6575 \left(\frac{2r}{D}\right)^2 \\
 C_4 &= 1.7207 + 5.7974 \frac{2r}{D} - 27.7463 \left(\frac{2r}{D}\right)^2 + 6.0444 \left(\frac{2r}{D}\right)^3
 \end{aligned} \tag{3.2}$$

Variations of the stress concentration factor versus notch radius express a linear reduction of its value with the radius increase, Fig. 14a. The same course is noticed for the maximum stress, as can be seen in Fig. 14b. This magnitude has been reached applying the following formula

$$\sigma_{max} = K_{tU} \sigma_{nom} \tag{3.3}$$

where $\sigma_{nom} = F/A_0$ is the nominal stress, A_0 – area of the specimen cross section for the measurement zone.

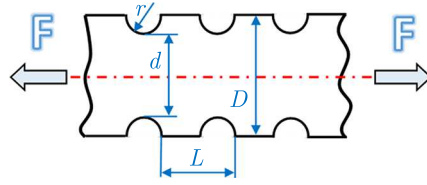
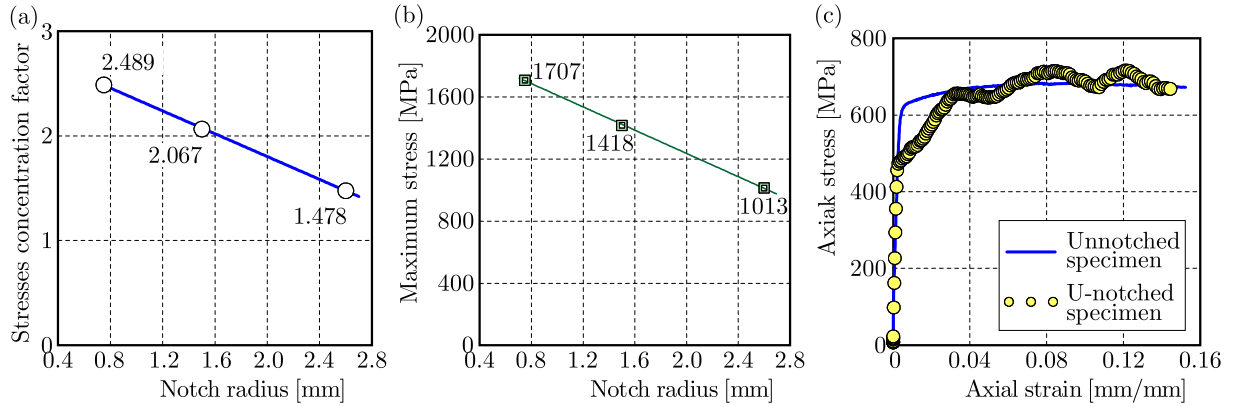
Fig. 13. U multi-notched specimen with the dimensions (Pilkey, 1997)

Fig. 14. Results for the multi-notched U specimen: (a) and (b) stress concentration factor and maximum stress as a function of notch radius, respectively, (c) tensile curve variations calculated by employing the cross section of the specimen

Looking at these results, it is easy to indicate the notches which are the dominant geometrical imperfections for the crack appearance, i.e. having a radius of 0.75 mm. This fact has not been confirmed by the DIC results in the final stages of tension (Figs. 11c,d), where the main crack occurred in the middle notch, for which the calculated maximum stress was lower (close to 300 MPa) than for the smallest radius considered.

The effects resulting from the presence of V -notches can also be captured by means of the DIC (Fig. 15). For this type of geometrical imperfections, the full-field equivalent strain distributions close to the tip of the notches and the entire measurement section can be observed (Fig. 15b). Besides different values of the V -notch angle, the indication of the main concentrator for the maximum strain is difficult. The 30° and 60° notches appear to have a very similar influence on the strain distribution at the beginning of the test. Further tension leads to an increase of the strain level in both notches diagonal arrangement which appear to be geometrical imperfections for the main damage zones (Figs. 15c, 16b). In these sections, the equivalent strain increases, causing a fracture in the middle notch and then in the diagonal one (Figs. 15d, 16c).

For this type of geometrical imperfections, the stress concentration factor and the maximum stress have been calculated by the use of the following formulas (Pilkey, 1997)

$$\begin{aligned}
 K_{tV} &= C_1 + C_2\sqrt{K_{tU}} + C_3K_{tU} \\
 C_1 &= -10.01 + 0.1534\alpha - 0.000647\alpha^2 \\
 C_2 &= 13.60 - 0.2140\alpha + 0.000973\alpha^2 \\
 C_3 &= -3.781 + 0.07873\alpha - 0.000392\alpha^2
 \end{aligned} \tag{3.4}$$

where K_{tV} , K_{tU} are the stress concentration factors for the V and U notches, respectively; C_i are coefficients, and α is the angle between the edges of the notches. The maximum stress is found

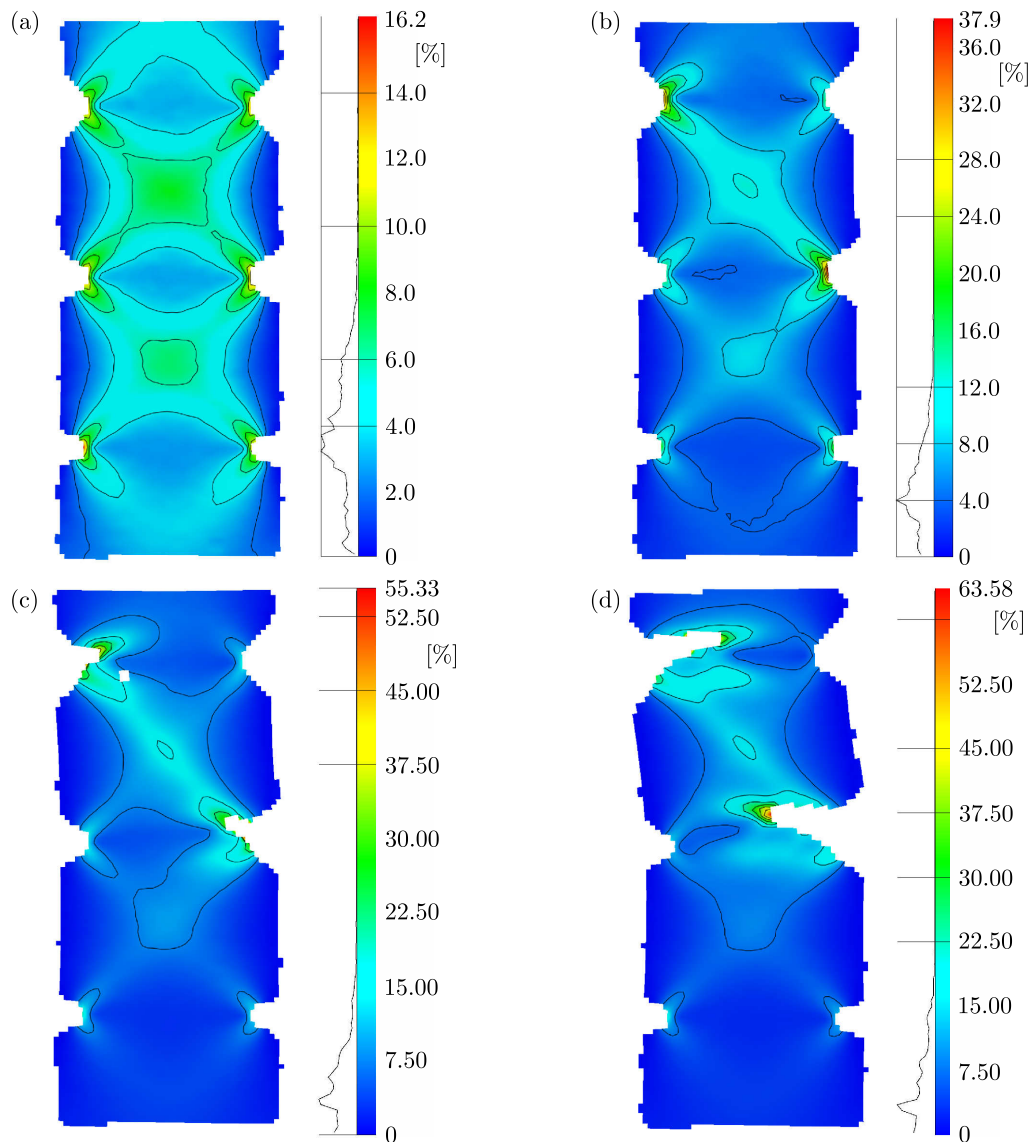


Fig. 15. The equivalent strain distribution in the multi-notched V specimen at various stages of monotonic tension: (a), (b) elastic-plastic state, (c), (d) elastic-plastic state before fracture; material: the 41Cr4 steel

applying the following relationship $\sigma_{max} = K_{tV}\sigma_{nom}$. The results express small lowering of the stress concentration factor and the maximum stress with the decreasing notch angle, Fig. 17. These data strongly correspond with the final stage of tension of the multi-notched V specimen (Figs. 15c,d). Small differences between the values of the stress concentration factor and the maximum stress at various notch angles show that all of the examined V notches are also the places where the damage zones can occur.

The influence of the V -notch on material straining during tension is illustrated in Fig. 17c presenting a comparison of tensile curves determined by the use of smooth and V multi-notched specimens. It is easy to notice that the presence of this type geometrical imperfection caused a 50% reduction of elongation and 30% lowering of the yield point.

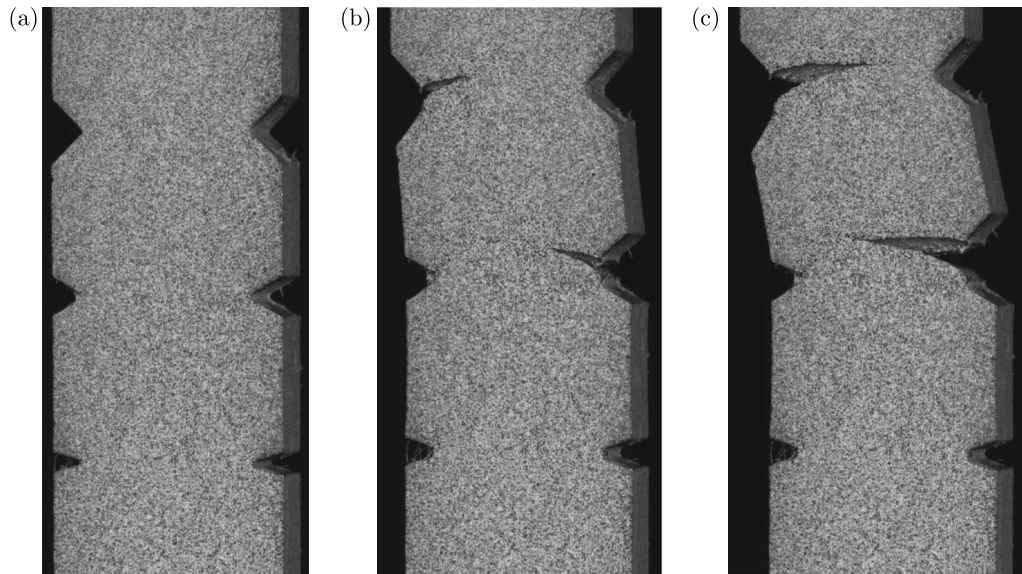


Fig. 16. Three stages of the multi-notched V specimen during monotonic tension: (a) before loading, (b) crack initiation, (c) crack growth

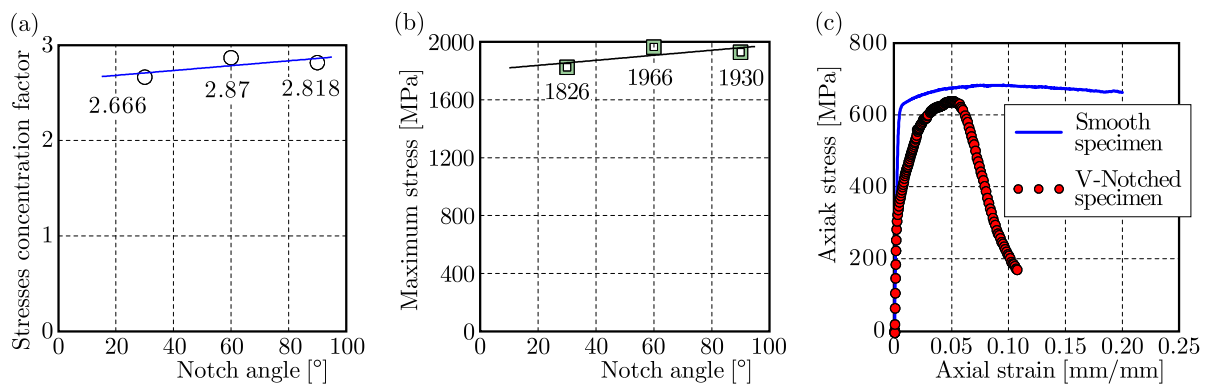


Fig. 17. Results for the multi-notched V specimen: (a) and (b) stress concentration factor and the maximum stress as a function of notch radius for the V-notched specimen, (c) tensile curve variations with respect to dimension of the cross section of the specimen; respectively

4. Summary

The Digital Image Correlation method can be employed for tests on specimens with or without geometrical imperfections. This technique allows capturing damage zones up to specimen fracture.

The DIC method follows the interaction of strain fields resulting from the presence of notches. Isolines created in a multi-notched specimen occur at the initial stage of tension and disappear at the moment of damage zones focusing and crack appearing.

Independently of the type of geometrical imperfections considered, a significant reduction of the proportional limit and yield point has been observed.

A typical DIC device is able to reach strain distribution close to the notch in the elastic-plastic state. In the case of the elastic state, the micro-DIC method using a microscope device is more recommended.

The Digital Image Correlation technique can be successfully used for determination of the Young's modulus, yield point, ultimate tensile strength and elongation.

Acknowledgement

The paper was partly carried out in the framework of the project No. 2014/15/B/ST8/04368 founded by the National Science Centre.

References

1. ANDERSSON M., 2013, The influence of notches on fatigue of heat treated sintered steel, *EURO PM 2013*, Gothenburg, 6 p.
2. BENNETT J.A., WEINBERG J.G., 1954, Fatigue notch sensitivity of some aluminium alloys, *Journal of Research of the National Bureau of Standards*, **52**, 5, 235-245
3. BOROŃSKI D., 2007, *Methods for Examination of Strain and Stress under Fatigue of Material and Structures* (in Polish), Institute for Sustainable Technologies, National Research Institute, Bydgoszcz-Radom, Poland, 190 p.
4. CHU T.C., RANSON W.F., SUTTON M.A., PETERS W.H., 1985, Application of digital-image-correlation techniques to experimental mechanics, *Experimental Mechanics*, **25**, 3, 232-244
5. CHEN C., 2004, General theory, *ME631*, UAF, 15 p.
6. DA SILVA B.L., FERREIRA J.L.A., ARAJO J.A., 2012, Influence of notch geometry on the estimation of the stress intensity factor threshold by considering the Theory of Critical Distances, *International Journal of Fatigue*, **42**, 258-270
7. DUQUENSAY D.L., TOPPER T.H., YU M.T., 1986, The effect of notch radius on the fatigue notch factor and the propagation of short cracks, [In:] *The Behaviour of Short Fatigue Cracks*, Edited by K.J. Miller and E.R. de los Rios, EGF Pub., Mechanical Engineering Publications, London, 323-335
8. DURIF E., RÉTHORÉ J., COMBESURE A., FREGONESE M., CHAUDET P., 2012, Controlling stress intensity factors during a fatigue crack propagation using digital image correlation and a load shedding procedure, *Experimental Mechanics*, **52**, 8, 1021-1031
9. FATEMI A., FANG D., ZENG Z., 2002, Notched fatigue behaviour under axial and torsion loads: experiment and predictions, *8th International Fatigue Congress*, Stockholm, Sweden, 3, 1905-1914
10. FATEMI A., ZENG Z., PLASEIED A., 2004, Fatigue behaviour and life predictions on notched specimens made of QT and forged microalloyed steels, *International Journal of Fatigue*, **26**, 6, 663-672
11. FILIPPINI M., 2000, Stress gradient calculations at notches, *International Journal of Fatigue*, **22**, 5, 397-409
12. FORSTER J., THEOBALD A., ENGEL S., PASMANN R., 2012, Using optical measuring system for identification of material parameters for Finite Element Analysis, *11. LS-DYNA*, Ulm, Germany, 9 p.
13. GOWER M.R., SHAW R.M., 2010, Towards a planar cruciform specimen for biaxial characterization of polymer matrix composites, *Applied Mechanics and Materials*, **24-25**, 115-120
14. KAMAYA M., KAWAKUBO M., 2011, A procedure for determining the true stress-strain curve over a large range of strains using digital image correlation and finite element analysis, *Mechanics of Materials*, **43**, 5, 243-253
15. LANNING D.B., HARITOS G.K., NICHOLAS T., 1999, Influence of stress state on high cycle fatigue of notched Ti-6Al-4V specimens, *International Journal of Fatigue*, **21**, 1, S87-S95
16. LORD J.D., 2009, Digital Image Correlation (DIC), Modern stress and strain analysis, [In:] *A State of the Art Guide to Measurement Techniques*, BSSM Technical Editors: J. Eaton Evans, J.M. Dulie-Barton, R.L. Burguete, 14-15
17. MARUNO Y., MIYAHARA H., NOGUCHI H. AND OGI K., 2004, Notch size effects in the fatigue characteristics of Al-Si-Cu-Mg cast alloy, *Materials Transactions*, **45**, 3, 839-843

18. MAZDUMAR P.K., LAWRENCE F.V. JR., 1981, An analytical study of the fatigue notch size effect, A Report of the Fracture Control Program, College of Engineering, University of Illinois, Urbana, Illinois 6180
19. MILKE J.G., BEUTH J.L., BIRY N.E., 2000, Notch strengthening in titanium alumini dies under monotonic loading, *Experimental Mechanics*, **4**, 4, 415-424
20. NEUBER H., 1958, *Kerbspannungslehre*, 2nd ed., Berlin, Springer-Verlag
21. NEUBER H., 1961, *Theory of Notch Stresses*, Office of Technical Services, U.S. Department of Commerce, Washington, DC
22. OLSZAK W., 1965, *Theory of Plasticity*, PWN, Warsaw
23. PETERSON R.E., 1959, Analytical approach to stress concentration effect in fatigue of aircraft materials, *Proceedings on Fatigue of Aircraft Structure*, WADC Technical Report No. 59-507, August 1959, 273-299
24. PILKEY W.D., 1997, *Peterson's Stress Concentration Factors*, Wiley, New York
25. PLUVINGAE G., GJONAJ M., 2001, *Notch Effects in Fatigue and Fracture*, NATO Science Series, Series II: Mathematics, Physics and Chemistry, 11, Springer Science+Business Media, B.V.
26. QIAN G., HONG Y., ZHOU CH., 2010, Investigation of high cycle and very-high-cycle fatigue behaviors for a structural steel with smooth and notched specimens, *Engineering Failure Analysis*, **17**, 7-8, 1517-1525
27. SIEBEL E., STIELER M., 1955, Ungleichformige spannungsverteilung bei schwingender beanspruchung, *Zeitschrift des Vereines Deutscher Ingenieure*, *VDI-Z*, **97**, 5, 121-126
28. TOPPER T.H., WETZEL R.M., MORROW J., 1967, Nuber's rule applied to fatigue of notched specimens, Report No. NAEC-ASL-1114, Aeronautical Structures Laboratory, 15 p.
29. TOUSSAINT F., TABOUROT L., VACHER P., 2008, Experimental study with a Digital Image Correlation (DIC) method and numerical simulation of an anisotropic elastic-plastic commercially pure titanium, *Archives of Civil and Mechanical Engineering*, **8**, 3, 131-143
30. WAHL A.M., BEUWKES R., PITTSBURGH E., 1930, Stress concentration produced by holes and notches, *Applied Mechanics*, **56**, 11, 617-623
31. WESTERGAARD H.M., 1952, *Theory of Elasticity and Plasticity*, New York, John Wiley
32. WHALEY R.E., 1964, Fatigue and static strength of notched and un-notched aluminium alloy and steel specimens, *Experimental Mechanics*, 329-334
33. www.gom.com

THE INFLUENCE OF NON-AXISYMMETRIC PULSE SHAPER POSITION ON SHPB EXPERIMENTAL DATA

ROBERT PANOWICZ

Military University of Technology, Faculty of Mechanical Engineering, Warsaw, Poland
e-mail: robert.panowicz@wat.edu.pl

JACEK JANISZEWSKI, KRZYSZTOF KOCHANOWSKI

Military University of Technology, Faculty of Mechatronics and Aviation, Warsaw, Poland

The results of experimental and numerical analysis of the influence of the non-axisymmetric pulse shaper position on recorded wave signals in the split Hopkinson pressure bar experiment are presented. The paper focuses attention on the problem of wave signal disturbances caused by a bending wave resulting from non-axisymmetric pulse shaper positions and, moreover, different shaper thickness, striker impact velocities and Wheatstone bridge configurations. The obtained results of analyses indicate that the effect of the non-axisymmetric pulse shaper position may be neglected if deviation from the bar axis does not exceed 20%.

Keywords: split Hopkinson pressure bar, pulse shaping technology, high-strain-rate testing

1. Introduction

The most popular experimental arrangement for investigating dynamic behaviour of materials at high strain rates within the range 10^2 to $5 \cdot 10^4 \text{ s}^{-1}$ is the split Hopkinson pressure bar (SHPB), also known as Kolsky bar. The original setup of SHPB in compression was constructed by Herbert Kolsky, who developed in 1949 also the theoretical basis of the method (Kolsky, 1949). In general, the SHPB technique has been widely used to determine dynamic properties of a variety of engineering materials such as metals and their alloys, ceramics, polymers and elastomers, composites, shape memory alloys, foams, and even biological tissues (Chen and Song, 2011).

The SHPB setup usually consists of the striker bar and two long bars called the input and output bars with the same diameter and material (typically high strength material like maraging steel). The material sample is placed between the bars, and it is loaded by a stress impulse generated by the striker impact applied to the front surface of the input bar. This generates a trapezoidal stress impulse (incident wave) which travels through the impacted bar. When the elastic wave reaches the specimen, due to mismatch of mechanical impedances between the bar and the specimen material, a part of the incident wave is reflected back (reflected wave) and the rest of the incident wave is transmitted through the specimen. It compresses the specimen with high rates, and rest of the wave travels to the output bar as a transmitted wave. The incident and reflected signals are recorded by strain gages which are glued on the input bar, whereas the transmitted signals are sensed by strain gages located on the output bar.

In split Hopkinson pressure bar (SHPB) experiments, besides specimen geometry, the profile of the incident pulse is the only controllable parameter to subject the specimen to the desired testing conditions. The shape of the incident stress wave is usually controlled through pulse techniques (Chen and Song, 2011). There are different techniques of incident pulse shaping, such as modification of the striker geometry (Bekker *et al.*, 2015; Cloete *et al.*, 2009), using a preloading bar (Ellwod *et al.*, 1982; Foley *et al.*, 2010) or by using a pulse shaper method (Chen

and Luo 2004; Lu and Li, 2010; Chen and Song, 2011), where a small disc made of a ductile material is glued with grease on the impact end of the input bar (Fig. 1). This technique is mainly used for facilitating stress equilibrium and constant strain rate deformation in the specimen (Vecchio and Jiang, 2007). Moreover, the dispersion of incident and reflected waves propagated in SHPB bars can be physically minimized through a pulse shaper, which plays role of a mechanical filter to damp undesired high-frequency signal components in the incident pulse (Chen and Song, 2011).

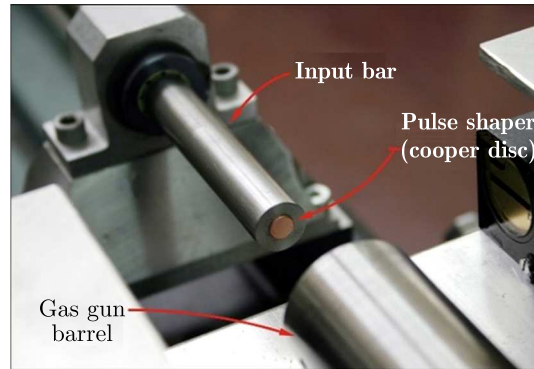


Fig. 1. View of a pulse shaper placed on the impact face of the input bar

Nowadays, the pulse shaper technique is a well-known and commonly used method. The experimental studies have been carried out using pulse shapers not only for metal specimens but also for materials such as rubber (Song and Chen, 2005), plexiglass (Naik and Yernamma, 2008), fabric (Hsiao and Daniel, 1998) and ceramic (Chen and Luo, 2004).

One of the first works devoted to this technique were published by Franz and Follansbee (1984) and Follansbee (1985). They investigated the influence of pulse shaper thicknesses ranging from 0.1 to 2.0 mm on shaping the incident pulse, minimization of dispersion effects and dynamic stress equilibrium in the sample. More recently, the pulse shaper technique was widely considered by Chen *et al.* (2003). They used a layered pulse shaper consisting of two disks made of copper/mild steel to investigate small-strain behaviour of mild steel, i.e., through a material dynamic test in the initial stage of both elastic and plastic deformation. The above-mentioned authors proposed also an original use of the pulse shaper technique to determine dynamic stress-strain loops for engineering materials (Song and Chen, 2004). They used an arrangement of two pulse shapers placed in front of and behind the flange for precise control of loading and unloading a portion of the incident pulse. Thanks to this, it was possible to obtain a similar rise and fall loading time of the stress wave.

Great contribution to the development of the pulse shaping technique was brought by a team headed by Vecchio. For example, Vecchio and Jiang (2007) proposed making use of a pulse shaper made of a high strength, high-work-hardening rate material to obtain a half sinusoidal incident pulse.

The issue of the pulse shaper in the SHPB was based on analytical and numerical considerations. The analytical model of the influence of a deformable pulse shaper made of OFHC copper on the incident pulse was developed by Nemat-Nasser *et al.* (1991). The analytical model was also developed by Frew *et al.* (2002, 2005) for homogeneous and layered pulse shapers made of different materials. In turn, Ramirez and Rubio-Gonzalez (2006) used the finite element method to study the effect of incident pulse rise time and the selection of materials and geometric parameters of the pulse shaper on wave dispersion. In their research, they used shapers made of copper, 7039 aluminum and 4340 steel. Application of the copper pulse shaper allowed alleviating the wave dispersion. In turn, the influence of diameter and thickness of a pulse shaper made of C10200 copper as a function of the striker velocity was investigated by Naghdabadi *et al.*

(2012) using numerical analysis and experimental research. On the basis of the research results, they formulated general guidelines to properly design a pulse shaper.

A proper choice of the pulse shaper geometry and material is particularly important in the case of brittle materials for which the value of failure strain is less than 1%. In this case, special attention should be paid to minimization of the wave dispersion, quick receiving of dynamic stress equilibrium and nearly constant strain rates over most of the test duration. Therefore, the technique of shaping the incident pulse needs to guarantee the possibility of receiving a stress wave of a suitable shape. Ellwood *et al.* (1982), Li and Xua (2009), and Shemirani *et al.* (2016) demonstrated that a half sinusoidal incident pulse is suitable for testing brittle materials.

Despite the development of the analytical model and many numerical models concerning the influence of the pulse shaper geometry on the incident pulse, the problem of selection of a pulse shaper for testing different materials is usually solved via try and error approach.

The basic requirement for the desired application of a pulse shaper is to place the pulse shaper on the front face of the input bar axisymmetrically. However, in routine experimental practice, no special attention is paid to the pulse shaper positioning and, it is usually carried out more or less carefully. It may be supposed that the non-axisymmetrical fixing of the pulse shaper will cause additional disturbances of measured signals arising from formation and propagation of bending waves in the bars. These disturbances will occur especially when the measurement system is based on a Wheatstone bridge arrangement as a quarter- or half-bridge circuit. The half-bridge is commonly used in the SHPB experimental technique, in which bars with small diameter (3-6 mm) are used. In these cases, problems with gluing strain gauges required to obtain a full Wheatstone bridge occur. It can be also supposed that the disturbances caused by the non-axisymmetrical position of the pulse shaper will be significant for bars with low stiffness (e.g. plexiglas). It appears that the errors resulting from these conditions will be mainly expressed in the incorrect determination of the strain value in the sample. Therefore, in this paper, experimental investigation and numerical analysis are undertaken to estimate the effect of the pulse shapers non-axisymmetric position on stress waves in SHPB and the material dynamic response.

The influence of different pulse shaper positions and different shaper thickness for a quarter- and a half-Wheatstone bridge configuration and three impact velocities of 10, 12.5 and 15 m/s are subjected to considerations.

The paper is organized as follows: Section 2 is dedicated to the methodology of numerical and experimental investigations. Numerical and experimental results are collected in Section 3, where the influence of different pulse shapers positions and different thickness of the shapers are analyzed. Moreover, the influence of striker velocity on the pulse propagation and the sample dynamic response depending on the non-axisymmetric pulse shaper position is also considered. A summary and conclusions are presented in the final Section.

2. Methodology of experimental and numerical investigations

2.1. Experimental setup

Numerical analysis of the main problem of the present paper has been verified experimentally with the use of a split Hopkinson pressure bar stand presented in Fig. 2. It mainly consists of a launching system (air pressure gun), striker bar, input bar, output bar (bar system), velocity measuring device and a computer-controlled high-frequency data acquisition system.

The input bar and the output bar are 1200 mm long, while the striker length is 250 mm. Both the bars and the striker have a common diameter of 12.05 mm and are made of maraging steel of grade MS350 (nominal quasi-static yield strength $R_{0.2} = 2300$ MPa, sound speed

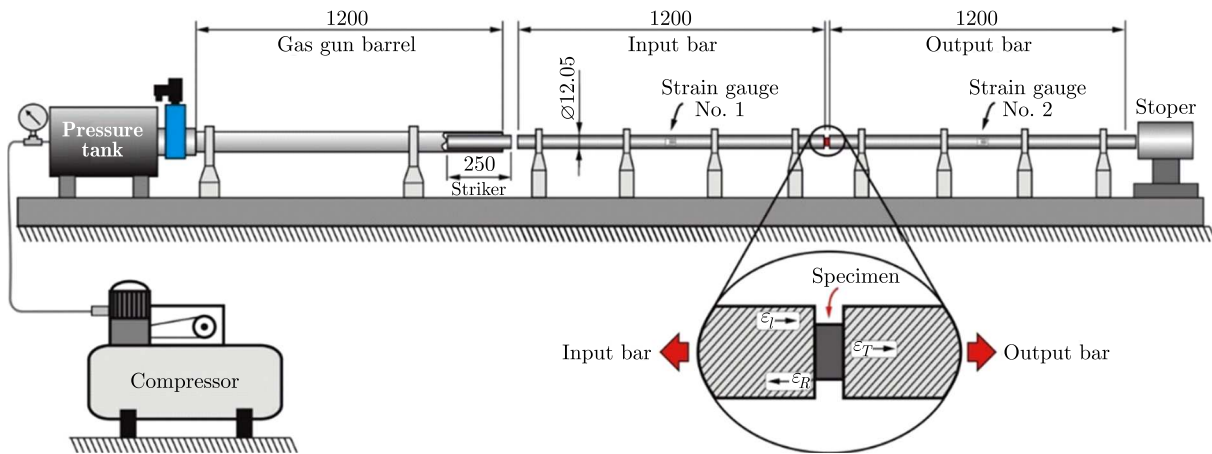


Fig. 2. Schematic diagram of the compression SHPB set-up (recording system not shown)

$C_0 = 4866$ m/s). Each bar is supported by four linear bearing stands which are mounted on an optical bench allowing precise alignment of the bars system.

The wave signals in the input and output bars are captured using a pair of strain gauges attached symmetrically to the opposite surfaces of the bars. The strain gauges are connected to the opposite legs of the Wheatstone bridge, which is a typical half-bridge configuration. In the other legs of the bridge, dummy resistors are mounted, the resistance of which matches the strain gauges resistance (350Ω). The foil strain gauges of 1.6 mm gauge length are used. The amplified signals of the strain gauges are recorded with a high cut-off frequency of 1 MHz with the use of a signal conditioning unit and a high-speed digital oscilloscope.

2.2. Numerical modelling

It results from the principle of SHPB operation that a phenomenon occurring at a high strain rate is considered. In such cases, explicit time integration schemes are used in numerical analysis. In most cases, due to accuracy of the scheme, a central difference time integration scheme is used. A local truncation error of this method is of the order of Δt^2 .

Such schemes are conditionally stable. The stability criteria are defined by the Courant-Friedrichs-Levy (CFL) principle (Courant *et al.*, 1967):

$$\Delta t \leq C_{CFL} \frac{\Delta x}{\sqrt{v_{adv}^2 + c_{group}^2}} \quad (2.1)$$

where Δt is the time step, Δx – length interval, C_{CFL} – Courant or CFL number, v_{adv} – advection velocity, c_{group} – group velocity. In the case of typical analyses $C_{CFL} = 0.9$. For analysis of phenomena in which detonation of explosives is considered, the blast wave interaction with the structure is equal to 0.67. Whereas, in the case of numerical modeling of the phenomena taking place at very high strain rates, such as formation of an explosively formed projectile or shape charge jet generation, the adopted coefficient is even smaller.

The authors used the Finite Element Method (FEM) with a central difference time integration scheme implemented in explicit LS-Dyna to carry out numerical simulations (Hallquist, 2006).

The finite element model of the SHPB contains all components of the arrangement (Fig. 3). In addition to the main part of the set-up (bars, sample, striker), the model includes: pulse shaper, slide bearings and barrel. All parts, except for the sample and the pulse shaper, are described by eight-node solid elements with one point integration. Whereas, fully integrated solid elements with formulation for elements with a poor aspect ratio and accurate formulation

are used to describe the sample and the pulse shaper (Hallquist, 2006). In order to reduce the number of finite elements and shorten computation time, symmetry of the model is utilized. In simulation, the dimensions of all elements of the SHPB are the same as in the experiments.

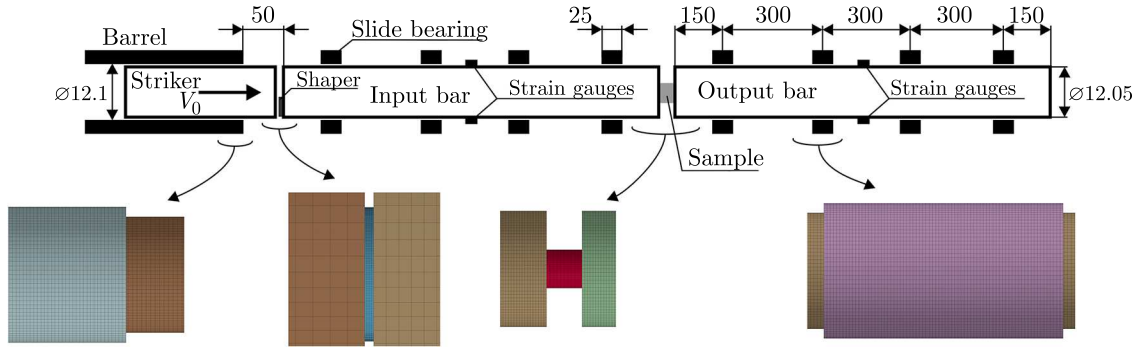


Fig. 3. A schematic diagram of the SHPB set-up used in numerical analysis

Between the interacting surfaces, there is defined contact based on a contact-impact algorithm the parameters of which have been established on the basis of the authors' own previous works (Panowicz, 2013). A segment-to-segment method (a mortar method) has been used to describe contact between the surfaces. This approach is based on the projection of integration points onto the master segment with penalty regularization of contact tractions (Fischer and Wriggers, 2006; Konyukhov and Schweizerhof, 2013). For the mortar method, the contact constraints are fulfilled in a weak manner. It shows optimal convergence behaviour compared to node-to-segment methods. Additionally, the Coulomb law is used to predict friction between the interacting surfaces. The friction coefficient is equal to 0.1, which corresponds to greased surfaces.

The bars, striker, barrel and slide bearings are given material properties of maraging steel: Young's modulus $E_B = 196$ GPa, Poisson's ratio $\nu_B = 0.3$, and density $\rho_B = 7800$ kg/m³.

In this paper, the Johnson-Cook constitutive model (Rule and Jones, 1998) is used in the following form

$$\sigma_{flow} = (A + B\varepsilon_p^n)(1 + C \ln \varepsilon^*)(1 - T^{*m}) \quad T^* = \frac{T - T_r}{T_m - T_r} \quad (2.2)$$

where $\varepsilon^* = \dot{\varepsilon}/\dot{\varepsilon}_0$ is the normalized strain rate, T^* is the homologous temperature and other symbols mean: T – specimen temperature, T_m – melting temperature of the specimen, T_r – room temperature, $\dot{\varepsilon}$ – strain rate, $\dot{\varepsilon}_0$ – referenced strain rate usually equal to 1 s⁻¹, ε_p – plastic strain, and five material constants A , B , n , C , m are applied to the sample and the pulse shaper. The first bracket in the Johnson-Cook constitutive equation describes strain hardening, the second – strain rate hardening, and the third one – thermal softening.

The constitutive relation is complemented by the hydrodynamic equation of state in the Gruneisen form (Steinberg, 1996; Hallquist, 2006)

$$p = \begin{cases} \frac{\rho_0 C_0^2 \mu \left[1 + \left(1 - \frac{\gamma_0}{2} \right) \mu - \frac{a}{2\mu^2} \right]}{1 - (S_1 - 1)\mu - \frac{S_2 \mu^2}{\mu + 1} - \frac{S_3 \mu^3}{(\mu + 1)^2}} + (\gamma_0 + a\mu)E & \text{for } \mu \geq 0 \\ \rho_0 C_0^2 \mu + (\gamma_0 + a\mu)E & \text{for } \mu < 0 \end{cases} \quad (2.3)$$

where $\mu = \rho/\rho_0 - 1$, ρ is density, ρ_0 – initial density, C_0 – bulk sound speed, γ_0 – initial value of Gruneisen gamma, a – coefficient of the volume dependence of gamma, S_1, S_2, S_3 – Hugoniot coefficients, E – energy per volume.

The material constants determining the behaviour of the semi-hard copper pulse shaper and the sample made of Ti-6Al-4V have been taken from literature (Ozel and Sima, 2010; Grazka and Janiszewski, 2012) and are shown in Tables 1 and 2.

Table 1. Material constants of copper and Ti-6Al-4V (Ozel and Sima, 2010; Grazka and Janiszewski, 2012)

Physical parameters	Cu	Ti-6Al-4V	J-C constants	Cu	Ti-6Al-4V
ρ [kg/m ³]	8940	4430	A [MPa]	99.7	862.5
E [GPa]	100	114	B [MPa]	262.8	331.2
ν [-]	0.31	0.3	n [-]	0.23	0.34
T_m [K]	1338	1953	C [-]	0.029	0.012
c_p [J/(kg K)]	385	546	m [-]	0.98	0.8

Table 2. EOS of copper and Ti-6Al-4V (Steinberg, 1996)

	Cu	Ti-6Al-4V		Cu	Ti-6Al-4V
C_0 [m/s]	3940	5130	γ_0 [-]	2.02	1.23
S_1 [-]	1.489	1.028	a [-]	0.47	0.17
S_2 [-]	0.0	0	S_3 [-]	0.0	0

In the numerical analysis, the influence of the non-axisymmetric position of the pulse shaper as a function of its location, thickness and velocity of the striker is examined. The non-axisymmetric position of the pulse shaper is defined by the parameter δ which expresses the percentage offset of the shaper center relative to the longitudinal axis of the input bar

$$\delta = \frac{h}{R-r} \cdot 100\% \quad (2.4)$$

where R is the bar radius, r – shaper radius equal to 1.5 mm, h – distance between the shaper center and the symmetry axis of the bar.

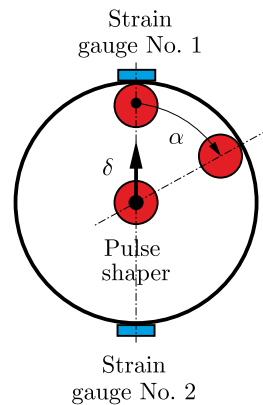


Fig. 4. Front surface of the incident bar from the striker side; δ – direction of the pulse shaper position change, α – angle between the gauge and the pulse shaper

Figure 4 shows schematically a change in the shaper position relative to the bar and strain gauges (parameter δ). Considered are cases for the following values of the parameter δ : 0, 20, 40 and 60% for four shaper thicknesses $d = 0.101, 0.201, 0.311, 0.441$. The values of the shaper thickness are taken based on the measurements of thickness of the metal sheets the shaper is made of. Moreover, the above variants are examined in relation to different impact velocities V_0 of the striker, which are 10, 12.5 and 15 m/s.

The validation process of the developed numerical model is based on a comparative analysis of the profiles of experimental and numerical incident waves. The validations have been performed for the experimental conditions shown in Table 3. The results of the experiments and their corresponding simulations collected in Figs. 5 and 6 show very good agreement.

Table 3. The experimental data

Shaper thickness [mm]	Shaper location δ [%]	Shaper velocity [m/s]
0.101	0	15.25
0.101	100	15.03
0.201	0	11.76
0.201	100	12.62
0.311	0	14.16
0.311	100	15.06
0.441	0	11.24
0.441	100	14.6

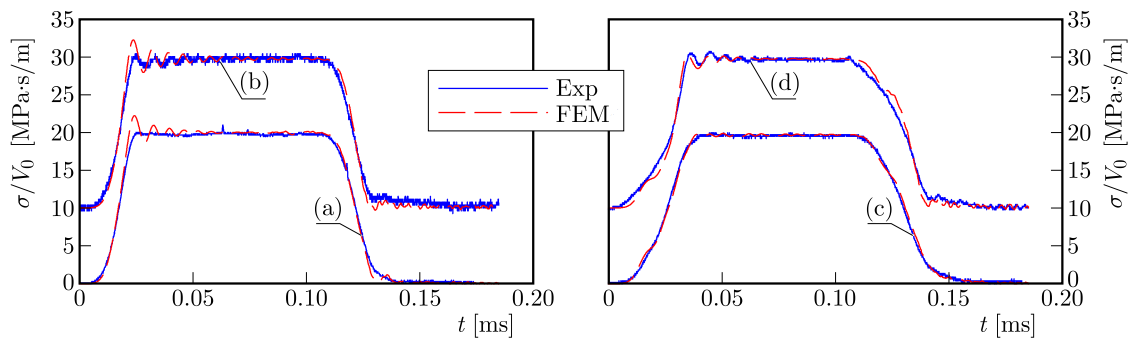


Fig. 5. Comparison of the normalized incident wave profiles obtained from numerical (FEM) and experimental (Exp.) analysis: (a) $d = 0.101$, $\delta = 0\%$, (b) $d = 0.101$, $\delta = 100\%$, (c) $d = 0.201$, $\delta = 0\%$, (d) $d = 0.201$, $\delta = 100\%$, curves b and d are shifted upwards for better illustration of the results

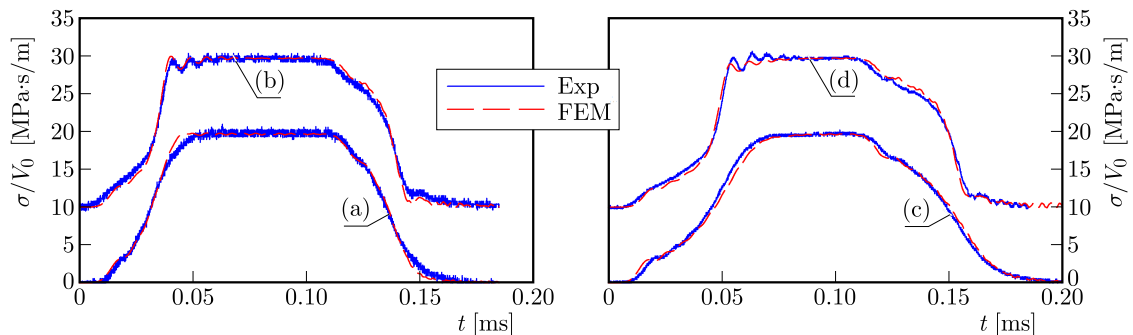


Fig. 6. Comparison of the normalized incident wave profiles obtained from numerical (FEM) and experimental (Exp.) analysis: (a) $d = 0.311$, $\delta = 0\%$, (b) $d = 0.311$, $\delta = 100\%$, (c) $d = 0.441$, $\delta = 0\%$, (d) $d = 0.441$, $\delta = 100\%$, curves b and d are shifted upwards for better illustration of the results

3. Results and discussion

The plain fact is that in the case of a half- or a full-Wheatstone bridge, a non-axisymmetric placement of the pulse shaper is not clearly reflected in the shape of the wave profiles recorded by strain gauges. In fact, it is a consequence of the compensation effect resulting from the position of the strain gauges on the opposite side surfaces of the bar. However, in the case of application of the Wheatstone bridge arrangement based on the quarter-bridge circuit (commonly used in SHPB experiments), disturbances resulting from the non-axisymmetric position of the pulse shaper become significant. Figure 7 presents summary profiles of the incident, reflected and transmitted waves depending on the relative position of the pulse shaper and strain gauges.

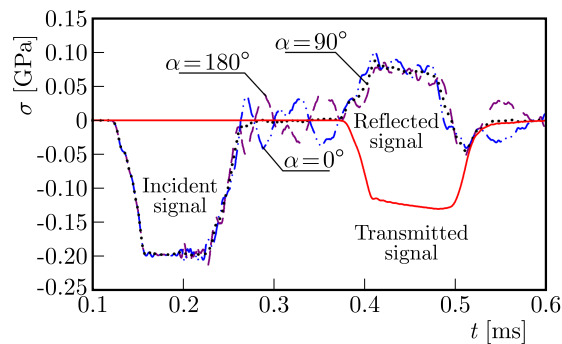


Fig. 7. Disturbances of waves signals depending on the relative position of the pulse shaper and strain gauges (parameter $\delta = 60\%$, $\alpha = 0^\circ$, 90° and 180° , pulse shaper thickness $d = 0.211$ mm, impact velocity $V_0 = 10$ m/s)

As expected, with the increasing parameter δ , the disturbance amplitudes of the incident and reflected signals are also increasing. However, only a part of the incident signal is disturbed, whereas the whole reflected signal profile is distorted by bending waves. In turn, when the non-axisymmetric position of the pulse shaper is not in the direction of the strain gauge but inclined at some angle α , the recorded disturbance amplitudes of wave signals decrease with the increasing angle of deflection. The smallest oscillations of wave signals occur when the deflection angle is equal to 90° (green line).

On the basis of Fig. 7, it can also be seen that the transmitted signal is noise-free and does not depend on the non-axisymmetric position of the pulse shaper. Such a situation takes place and is preferable in the case of high-strain-rate material testing, when the material specimen is not permanently connected to the contact surfaces of the bars, for example, in uniaxial compression. However, when tensile or torsion tests are conducted, the transmitted signal will also be disturbed by the bending waves.

For a typical half-bridge configuration (strain gauges are connected to the opposite bridge legs), disturbances caused by the non-axisymmetric position of the pulse shaper have a different character and their amplitude is significantly smaller. This is due to cancellation of the bending effect (flexural mode of vibration) by averaging strain (Fig. 4). In Fig. 8, it can be observed that the incident wave shapes differ to a small extent for different values of the parameter δ (Figs. 8b and 8d), whereas for the pulse shaper with thickness of 0.441, the differences are larger compared to the same profiles obtained for the shaper with thickness of 0.201. Furthermore, characteristic/additional disturbances resembling concavity in the incident wave profiles for their plateau parts are observed (Fig. 8d). The greater concavity, the higher value of the parameter δ . A similar effect of the non-axisymmetric pulse shaper position is observed for reflected waves (Fig. 9). However, the magnitudes of the observed disturbances of the reflected wave profile are smaller.

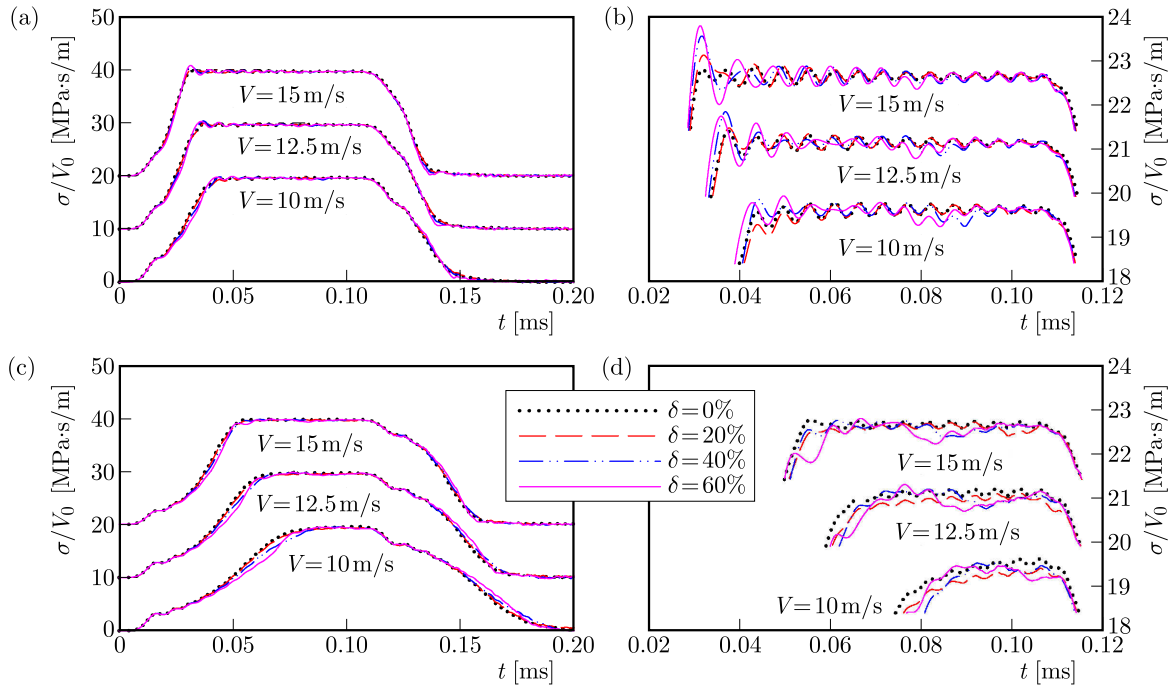


Fig. 8. The incident stress waves normalized to impact velocity: shaper thickness $d = 0.201$ mm (a), (b) and $d = 0.441$ mm (c), (d), curves for $V = 12.5$ m/s and $V = 15$ m/s are shifted upwards for better illustration of the results

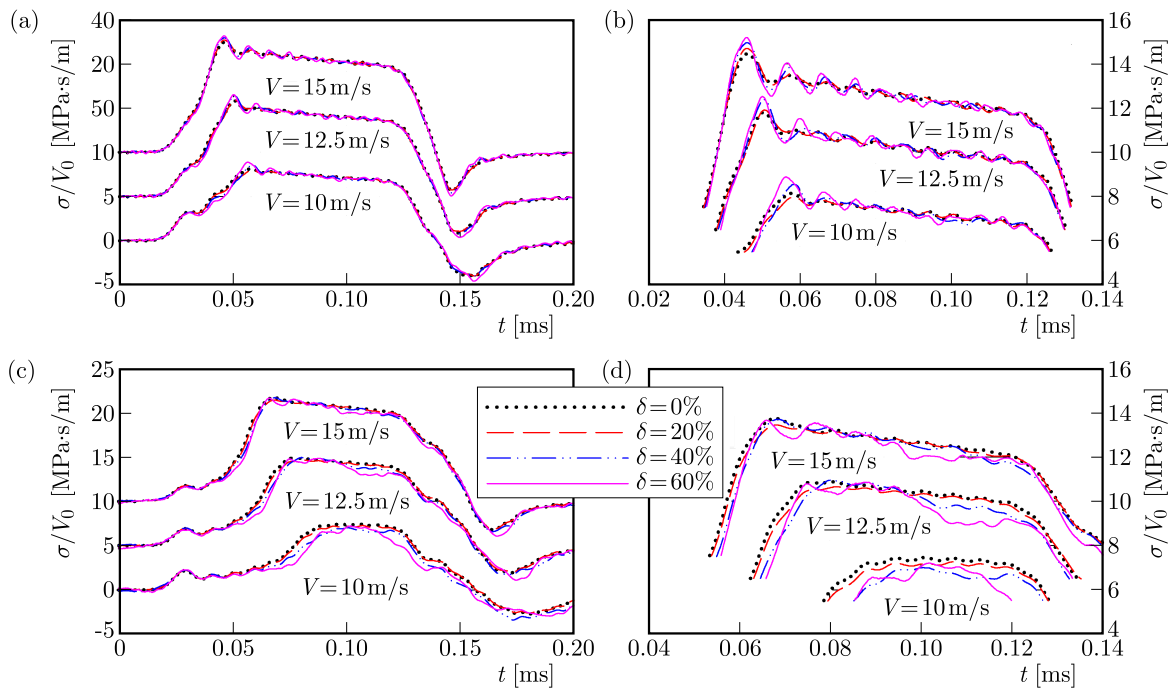


Fig. 9. The normalized reflected stress waves normalized to impact velocity: shaper thickness $d = 0.201$ mm (a), (b) and $d = 0.441$ mm (c), (d), curves for $V = 12.5$ m/s and $V = 15$ m/s are shifted upwards for better illustration of the results

For small pulse shaper thickness, the influence of the non-axisymmetric position of the pulse shaper is manifested in the incident waves, particularly, by larger initial amplitudes of the Pochhammer and Chree disturbances (Fig. 10). This effect decreases with the increasing velocity of the striker and an increase in the pulse shaper thickness. If a thicker pulse shaper is used,

the disturbance occurs in the form of concavity in the other half of the signal plateau. It is found that the concavity magnitude is less dependent on the striker velocity. Moreover, the non-axisymmetric position of the pulse shaper affects the rise time of the incident pulse especially for lower striker velocity and the thicker pulse shaper. Similar relations are also observed for the reflected signals.

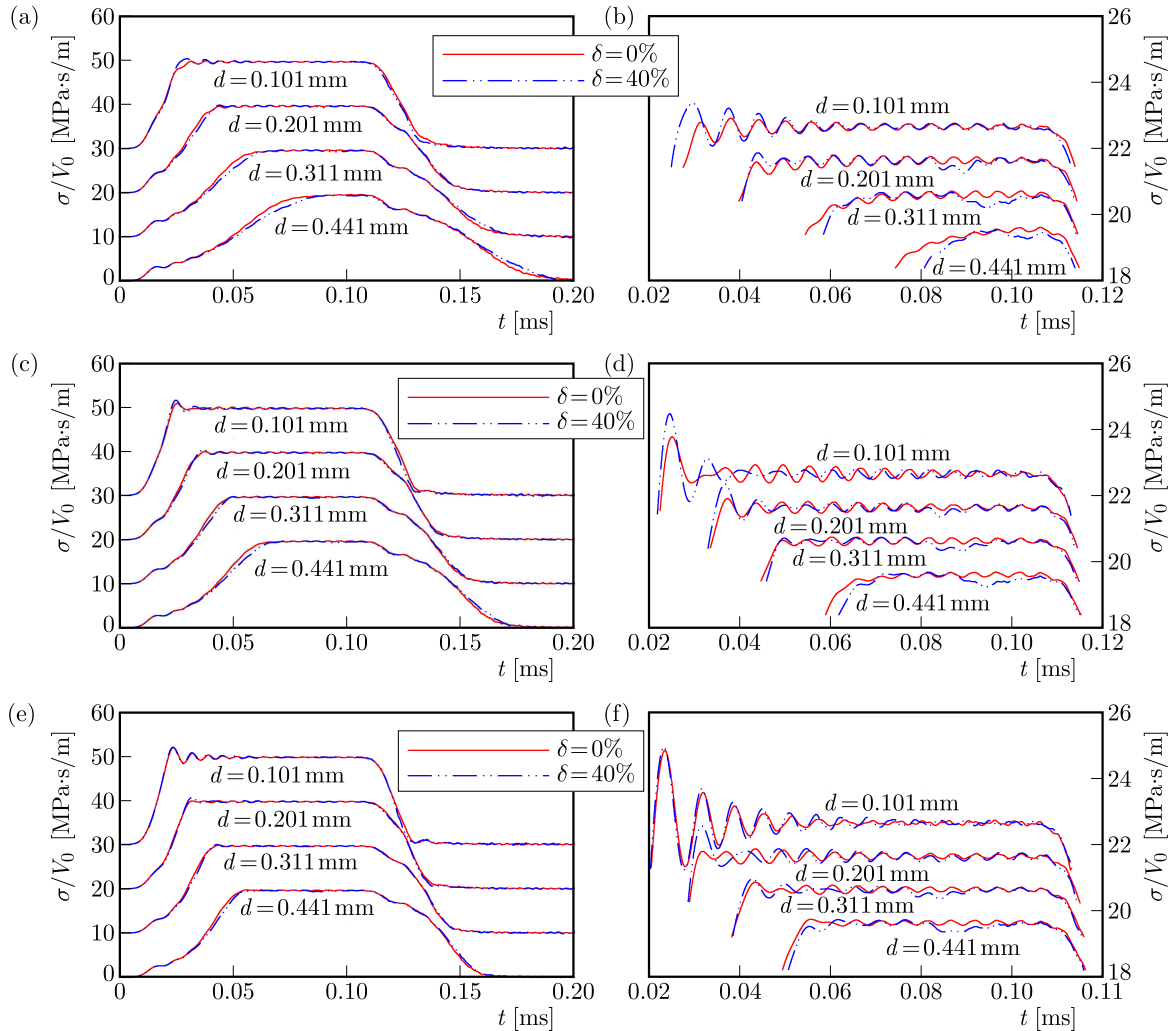


Fig. 10. Incident stress waves for $\delta = 0\%$ and 40% and different shaper thickness: (a), (b) $V_0 = 10$ m/s, (c), (d) $V_0 = 12.5$ m/s, (e), (f) $V_0 = 15$ m/s, curves for d from 0.101 to 0.311 mm are shifted upwards for better illustration of the results

In order to fully assess the impact of the non-axisymmetric position of the pulse shaper, the σ - ε curves for Ti-6Al-4V have been determined according to Kolsky's theory using 3-wave analysis

$$\varepsilon = \frac{C_B}{L_S} \int_0^t (\varepsilon_I - \varepsilon_R - \varepsilon_T) d\tau \quad \sigma = \frac{1}{2} \frac{A_B}{A_S} E_B (\varepsilon_I + \varepsilon_R + \varepsilon_T) \quad (3.1)$$

where E_B , C_B – longitudinal elastic wave speed and Young's modulus of the bar material, L_S – initial length of the specimen, A_B , A_S – cross-sectional areas of the bars and the specimen, respectively; and of the bar material, ε_I , ε_R and ε_T – incident, reflected and transmitted strain, respectively.

Figures 11 and 12 show the influence of the non-axisymmetric position of the pulse shaper expressed with the parameter δ and thickness d of the pulse shaper as a function of the striker velocity on the σ - ε curve profile. These figures illustrate that the non-axisymmetric position of the pulse shaper generates a deviation in flow stress and the final strain values from the perfect condition ($\delta = 0$) in the initial loading. In the case of a thin pulse shaper ($d = 0.101$ and 0.201 mm), the deviations are smaller than for shaper thickness of 0.311 and 0.441 mm (Fig. 12). Visible

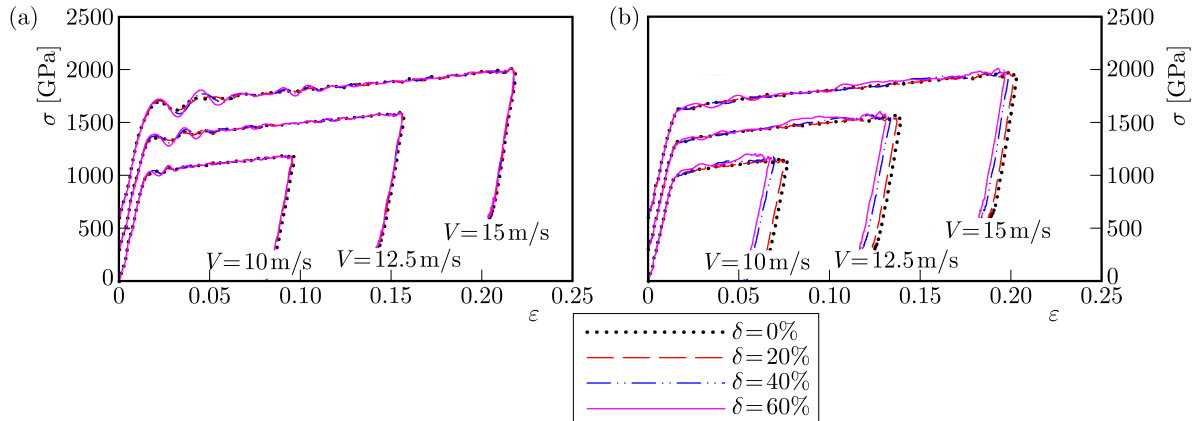


Fig. 11. The comparison of stress-strain curves for different parameters δ and pulse shaper thickness: (a) $d = 0.201$ mm, (b) $d = 0.441$ mm, curves for d from 0.101 to 0.311 mm are shifted for better illustration of the results

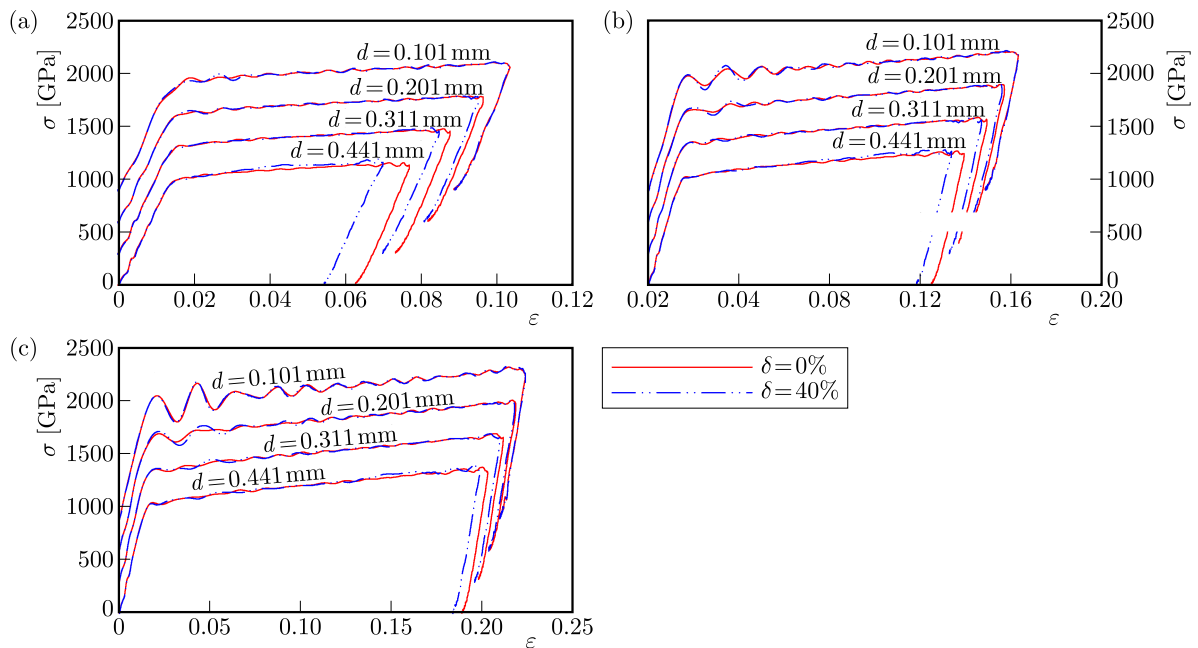


Fig. 12. The comparison of stress-strain curves for parameters $\delta = 0$ and 40% : (a) $V_0 = 10$ m/s, (b) $V_0 = 12.5$ m/s, (c) $V_0 = 15$ m/s, curves for d from 0.101 to 0.311 mm are shifted upwards for better illustration of the results

deviations in Fig. 11b constitute a fragment of the plateau portion of the curve σ - ε (flow stresses at the latter period) and a curve part showing the final strain values. It should be noted that for the lowest velocity of the striker ($V_0 = 10$ m/s), the deviations are significantly higher than for higher striker velocity ($V_0 = 12.5$ m/s and 15 m/s), and it can be supposed that with the increasing impact velocity, the deviation will decrease. Maximum deviations for $\delta = 60\%$ in the σ - ε curve plateau part are 57 , 53 , 21 MPa for the striker velocity of 10 , 12.5 and 15 m/s, respec-

tively, and the final strain values for $\sigma = 800$ MPa level are 0.0092, 0.0086, 0.0066, respectively. In the case of the parameter $\delta = 20\%$, such disturbances are very small and can be neglected. It is also possible to neglect the impact of the aforementioned parameters on the flow stresses in the elastic regime. No disturbances in this area can be explained by the fact that the flexural wave velocity is relatively small compared to the longitudinal wave velocity and interferes only with the waves at the later period, producing highly distorted data. In turn, the deviation in the final strain is due to some portions of the impact energy being dissipated as flexural energy.

4. Conclusion

The influence of the non-axisymmetric pulse shaper position in the split Hopkinson pressure bar technique has been investigated numerically. Our studies show that the distorted signal of the SHPB is mainly due to the presence of flexural modes of vibration, like in the misalignment bars effect (Kariem *et al.*, 2012). The results of analysis of a wide range of numerical experiments indicate that the effect of the non-axisymmetric pulse shaper position may be neglected if deviation from the input bar axis does not exceed 20%, which corresponds to the position deviation (distance between the shaper centre and symmetry bar axis) equal to approximately 15% of the input bar radius.

It should be emphasised that the above discussion has shown only one configuration of the bars supports position, i.e., the number of supports and the distance between them. In the case of another configuration, especially in the case of a smaller number of the bars supports, the non-axisymmetric pulse shaper position will produce a different deviation of SHPB data. A similar situation will take place when only one strain gauge configuration in the SHPB arrangement is considered. In that case, the deviation amplitude of the measured signals will be larger and, in consequence, bigger errors will appear in the SHPB data (stress-strain curve).

Acknowledgement

The paper has been partially founded within the project DOBR-BIO4/031/13249/2013 supported by the National Centre for Research and Development. This support is gratefully acknowledged.

References

1. BEKKER A., CLOETE T.J., CHINSAMY-TURAN A., NURICK G.N., KOK S., 2015, Constant strain rate compression of bovine cortical bone on the split-Hopkinson pressure bar, *Materials Science and Engineering C*, **46**, 1, 443-449
2. CHEN W., LUO H., 2004, Dynamic compressive responses of intact and damaged ceramics from a single split Hopkinson pressure bar experiment, *Experimental Mechanics*, **44**, 3, 295-299
3. CHEN W., SONG B., 2011, *Split Hopkinson (Kolsky) Bar: Design, Testing and Applications*, Berlin, Springer
4. CHEN W., SONG B., FREW D.J., FORRESTAL M.J., 2003, Dynamic small strain measurements of a metal specimen with a split Hopkinson pressure bar, *Experimental Mechanics*, **43**, 1, 201-23
5. CLOETE T.J., VAN DER WESTHUIZEN A., KOK S., NURICK G.N., 2009, A tapered striker pulse shaping technique for uniform strain rate dynamic compression of bovine bone, *EDP Sciences*, **1**, 901-907
6. COURANT R., FRIEDRICHS K.O., LEWY H., 1967, Ueber die partiellen Differenzgleichungen der mathematischen Physik, *Mathematische Annalen* (1928), **100**, 32-74. Translated as: On the partial difference equations of mathematical physics, *IBM Journal of Research and Development*, **11**, 215-234

7. ELLWOOD S., GRIFFITHS L.J., PARRY D.J., 1982, Materials testing at high constant strain rates, *Journal of Physics, E*, **15**, 280-282
8. FISCHER K.A., WRIGGERS P., 2006, Mortar based frictional contact formulation for higher order interpolations using the moving friction cone, *Computer Methods in Applied Mechanics and Engineering*, **195**, 5020-5036
9. FOLEY J.R., DODSON J.C., MCKINION C.M., 2010, Split Hopkinson bar experiments of preloaded interfaces, *Proceedings of the IMPLAST 2010 Conference*
10. FOLLANSBEE P.S., 1985, *The Hopkinson Bar in Mechanical Testing and Evaluations*, ASM Handbook, 9th ed. ASM Int., Materials Park Ohio
11. FRANTZ C.E., FOLLANSBEE P.S., 1984, Experimental techniques with the split Hopkinson pressure bar, *Proceedings of the 8th International Conference on High Energy Rate Fabrication*, San Antonio, Texas, 229-236
12. FREW D.J., FORRESTAL M.J., CHEN W., 2002, Pulse shaping techniques for testing brittle materials with a split Hopkinson pressure bar, *Experimental Mechanics*, **42**, 1, 93-106
13. FREW D.J., FORRESTAL M.J., CHEN W., 2005, Pulse shaping techniques for testing elastic-plastic materials with a split Hopkinson pressure bar, *Experimental Mechanics*, **45**, 186-195
14. GRAZKA M., JANISZEWSKI J., 2012, Identification of Johnson-Cook equation constants using finite element method, *Engineering Transactions*, **60**, 215-223
15. HALLQUIST J.O., 2006, *Ls-Dyna. Theoretical Manual*, California, Livermore Software Technology Corporation
16. HSIAO H.M., DANIEL I.M., 1998, Dynamic compressive behavior of thick composite materials, *Experimental Mechanics*, **38**, 172-180
17. KARIEM M.A., BEYNON J.H., RUAN D., 2012, Misalignment effect in the split Hopkinson pressure bar technique, *International Journal of Impact Engineering*, **47**, 60-70
18. KOLSKY H., 1949, An investigation of the mechanical properties of materials at very high rates of strain, *Proceedings of the Physical Society Section B*, **62**, 11, 676-700
19. KONYUKHOV A., SCHWEIZERHOF K., 2013, *Computational Contact Mechanics, Geometrically Exact Theory for Arbitrary Shaped Bodies*, Berlin, Springer
20. LI W., XUA J., 2009, Impact characterization of basalt fiber reinforced geopolymeric concrete using a 100 mm-diameter split Hopkinson pressure bar, *Materials Science and Engineering A*, **513-514**, 145-153
21. LU Y.B., LI Q.M., 2010, Appraisal of pulse-shaping technique in split Hopkinson pressure bar tests for brittle materials, *International Journal of Protective Structures*, **1**, 3, 363-390
22. NAGHDABADI R., ASHRAFIA M. J., ARGHAVANIC J., 2012, Experimental and numerical investigation of pulse-shaped split Hopkinson pressure bar test, *Materials Science and Engineering A*, **539**, 285-293
23. NAIK N. K., YERNAMMA P., 2008, Mechanical behaviour of acrylic under high strain rate tensile loading, *Polymer Testing*, **27**, 504-512
24. NEMAT-NASSER S., ISAACS J.B., STARRETT J.E., 1991, Hopkinson techniques for dynamic recovery experiments, *Proceedings of the Royal Society*, **435**, 371-391
25. OZEL T., SIMA M., 2010, Finite element simulation of high speed machining Ti-6Al-4V alloy using modified material models, *Transactions of NAMRI/SME*, **38**, 49-56
26. PANOWICZ R., 2013, Analysis of selected contact algorithms types in terms of their parameters selection, *Journal of KONES Powertrain and Transport*, **20**, 1, 263-268
27. RAMIREZ H., RUBIO-GONZALEZ C., 2006, Finite-element simulation of wave propagation and dispersion in Hopkinson bar test, *Materials and Design*, **27**, 36-44

28. RULE W.K., JONES S.E., 1998, A revised form for the Johnson-Cook strength model, *International Journal of Impact Engineering*, **21**, 8, 609-624
29. SHEMIRANI A. B., NAGHDABADI R., ASHRAFI M.J., 2016, Experimental and numerical study on choosing proper pulse shapers for testing concrete specimens by split Hopkinson pressure bar apparatus, *Construction and Building Materials*, **125**, 326-336
30. SONG B., CHEN W., 2004, Loading and unloading split Hopkinson pressure bar pulse-shaping techniques for dynamic hysteretic loops, *Experimental Mechanics*, **44**, 6, 622-627
31. SONG B., CHEN W., 2005, Split Hopkinson pressure bar techniques for characterizing soft materials, *Latin American Journal of Solids and Structures*, **2**, 113-152
32. STEINBERG D.J., 1996, Equation of state and strength properties of selected materials, LLNL Report, UCRL-MA-106439
33. VECCHIO K.S., JIANG F., 2007, Improved pulse shaping to achieve constant strain rate and stress equilibrium in split-Hopkinson pressure bar testing, *Metallurgical and Materials Transactions A*, **38**, 2655-2665

Manuscript received April 10, 2017; accepted for print February 27, 2018

STATIC RESONANCE IN ROTATING NANOBARS

UĞUR GÜVEN

Yildiz Technical University, Department of Mechanical Engineering, Istanbul, Turkey

e-mail: uguven@yildiz.edu.tr

In this study, static resonance that occurs in rotating nanobars is addressed. The analysis is based on Eringen's nonlocal elasticity theory and is performed in Lagrangian coordinates. Explicit solutions are given for both clamped-free and clamped-clamped boundary conditions. The present study shows that the static resonance phenomenon is largely a critical case requiring attention for rotating nanobars with small lengths.

Keywords: rotating nanobar, static resonance, nonlocal elasticity, lagrangian coordinates

1. Introduction

The rotating bars have attracted considerable attention in mechanical and aerospace engineering applications as machine elements such as turbines, propellers and helicopter blades. As is known, when the angular velocity of the bar reaches a certain critical value, the static resonance occurs and the longitudinal displacement becomes unbounded. This phenomenon has been first noticed by Bhuta and Jones (1963) and it has been extended by Brunelle (1971) for the rotating disks. As pointed out in (1963), the use of Eulerian coordinates does not even show this resonant character. In those analyses (Bhuta and Jones, 1963; Brunelle, 1971) Lagrangian coordinates were used. Shum and Entwistle (2006) reported that the linear uniaxial model is not representative for the situation at larger strains due to higher angular velocity. The axial deformation of rotating rods was investigated (Hodges and Bless, 1994) by using two simpler nonlinear strain energy models.

Nowadays, the recent developments in science and technology has enabled production of various rotating structures in micro and nano scales. Some publications in this new field can be found (Narendar, 2011, 2012; Narendar and Gopalakrishnan, 2011; Aranda *et al.*, 2012; Danesh and Asghari, 2014) in literature. However, no analytical or numerical study of the static resonance in the nanobars has yet been done. The aim of this work is to investigate the scale effect on the static resonance. In this analysis, the equation of motion is formulated in the Lagrangian coordinates and Eringen's nonlocal elasticity theory is adopted. In this study, the static resonance phenomenon in rotating nanobars is addressed for two boundary conditions: clamped-free (C-F) and clamped-clamped (C-C). It can be seen from the present analysis that the results presented are strongly affected with the boundary conditions (C-F or C-C) and the coordinates systems (Eulerian or Lagrangian).

2. Formulation of the problem and nonlocal elasticity solution

A uniform nanobar of length L rotating statically about the axis of rotation with angular velocity Ω is shown in Fig. 1.

The equation of motion in the Lagrangian coordinates is expressed (Bhuta and Jones, 1963) as

$$\frac{\partial \sigma}{\partial x} + \rho \Omega^2 (u + x) = 0 \quad (2.1)$$

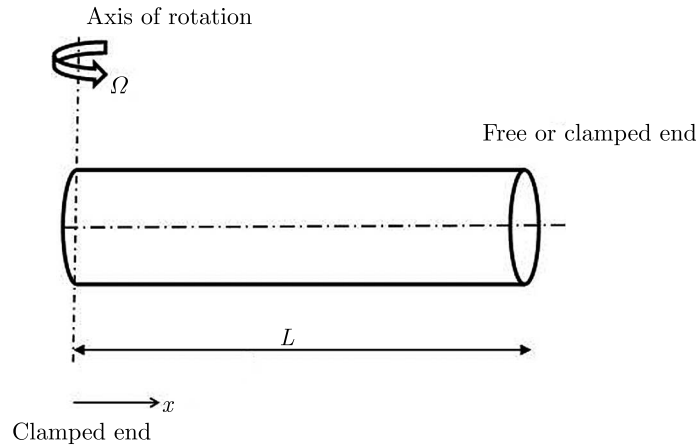


Fig. 1. Sketch of the rotating nanobar

where σ is the nonlocal longitudinal stress, ρ is density, x is the axial distance and u is the longitudinal displacement.

Eringen's nonlocal elasticity theory (Eringen, 2002) for one dimensional case can be expressed in the following form

$$\sigma - (e_0 a)^2 \frac{\partial^2 \sigma}{\partial x^2} = \sigma^{local} = E \frac{\partial u}{\partial x} \quad (2.2)$$

where $e_0 a$ is the small scale coefficient.

By using Eqs. (2.1) and (2.2), the nonlocal longitudinal stress is obtained as follows

$$\sigma = E \frac{\partial u}{\partial x} - (e_0 a)^2 \rho \Omega^2 \left(1 + \frac{\partial u}{\partial x}\right) \quad (2.3)$$

Substituting Eq. (2.3) into Eq. (2.1), the governing equation is given by

$$E \frac{\partial^2 u}{\partial x^2} - (e_0 a)^2 \rho \Omega^2 \frac{\partial^2 u}{\partial x^2} + \rho \Omega^2 u = -\rho \Omega^2 x \quad (2.4)$$

and the general solution to Eq. (2.4) becomes as

$$u = C_1 \sin kx + C_2 \cos kx - x \quad (2.5)$$

where C_1 and C_2 are integration constants and $k^2 = \rho \Omega^2 / [E - (e_0 a)^2 \rho \Omega^2]$.

For the clamped-free boundary conditions, i.e. $u(0) = 0$ and $u'(L) = 0$, the longitudinal displacement u is given by

$$u = \frac{\sin kx}{k \cos kL} \left[1 + \frac{(e_0 a)^2 \rho \Omega^2}{E - (e_0 a)^2 \rho \Omega^2}\right] - x \quad (2.6)$$

provided that Ω does not correspond to a root of

$$\cos kL = 0 \quad (2.7)$$

When Ω corresponds to a root of Eq. (2.7)

$$\Omega_n = \sqrt{\frac{\frac{E}{\rho} \left[(2n-1) \frac{\pi}{2L}\right]^2}{1 + (e_0 a)^2 \left[(2n-1) \frac{\pi}{2L}\right]^2}} \quad (2.8)$$

static resonances occur. The practical value of the critical angular velocity is obtained for $n = 1$.

On the other hand, in the Eulerian coordinates, i.e. neglecting the longitudinal displacement term u in Eq. (2.1), and by repeating the previous similar operations, the final form of the longitudinal displacement is obtained as

$$u = \frac{\rho\Omega^2}{2E} \left\{ [L^2 + 2(e_0a)^2]x - \frac{x^2}{3} \right\} \quad (2.9)$$

Thus, Eq. (2.9) shows clearly that the static resonance phenomenon would not be noticed (i.e., the longitudinal displacement can not become unbounded for a certain value of the angular velocity), for clamped-free boundary conditions when the Eulerian coordinates are used.

Secondly, for the clamped-clamped boundary conditions, i.e. $u(0) = 0$ and $u(L) = 0$, the longitudinal displacement u is given by

$$u = \frac{L \sin kx}{\sin kL} - x \quad (2.10)$$

provided that Ω does not correspond to a root of

$$\sin kL = 0 \quad (2.11)$$

When Ω corresponds to a root of Eq. (2.11)

$$\Omega_n = \sqrt{\frac{\frac{E}{\rho} \left(\frac{n\pi}{L}\right)^2}{1 + \left(e_0a^2 \frac{n\pi}{L}\right)^2}} \quad (2.12)$$

static resonances occurs. The critical angular velocity of practical interest is obtained for $n = 1$.

If the Eulerian coordinates are used in the same analysis, longitudinal displacement expression (2.10) takes the following form

$$u = \frac{\rho\Omega^2}{6E} (L^2 - x^2)x \quad (2.13)$$

Thus, Eq. (2.13) shows clearly that the static resonance phenomenon of motion can not be seen for the clamped-clamped boundary conditions if the Eulerian coordinates are used and, furthermore, the longitudinal displacement is independent of the effect of the small scale coefficient.

3. Numerical example

In this Section, for a numerical example as in (Narendar and Gopalakrishnan, 2011), $a(5,5)$ SWCNT is considered. The diameter is $d = 0.675$ nm, length $L = 10d$, the elasticity modulus $E = 5.5$ TPa and density 2300 kg/m³. In the numerical illustration the following defined ratio is used:

Critical angular velocities ratio = Critical angular velocity calculated from the nonlocal elasticity theory / Critical angular velocity calculated from the classical elasticity theory

Figure 2 shows the critical angular velocities ratio with the dimensionless scale coefficient e_0a/L , for the clamped-free and the clamped-clamped boundary conditions. From Fig. 2 it is found that as the scale coefficient e_0a increases, the critical angular velocity decreases. The classical elasticity solution overestimates the critical angular velocities compared to the nonlocal elasticity solution. In addition, for the clamped-free boundary condition, the critical angular velocities are found to be higher compared to those for the clamped-clamped boundary condition. For the range of small scale parameters in Fig. 2, a detailed previous reference work (Narendar *et al.*, 2011) has been taken into consideration.

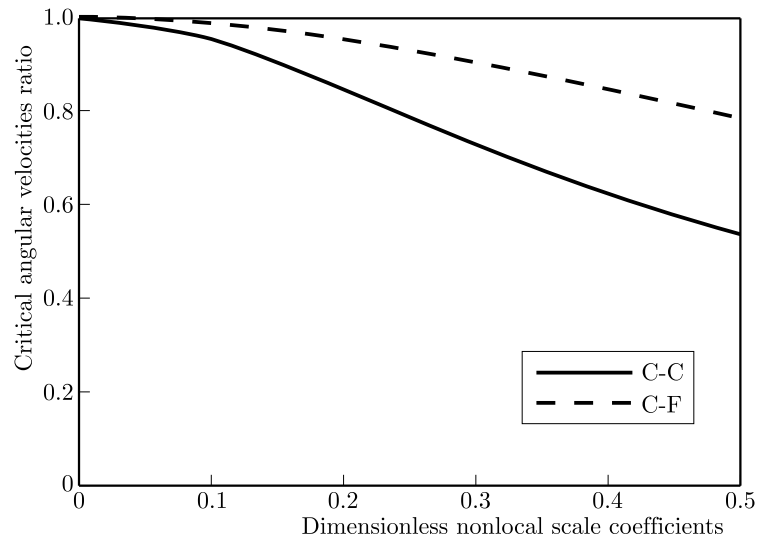


Fig. 2. Critical angular velocities ratio with dimensionless nonlocal scale coefficients

4. Conclusions

In this work, the static resonance phenomenon is investigated for rotating nanobars under clamped-free and clamped-clamped boundary conditions. Here, the classical linear uniaxial model is extended by adopting Eringen's nonlocal elasticity theory, and the equation of motion is formulated in the Lagrangian coordinates. If the critical angular velocities obtained from the nonlocal elasticity calculations are very small, as compared to those from the local elasticity calculations, this linear uniaxial model can be reliably used, as indicated by Hodges and Bless (1994) in detail. Hence, it should be noted that the linear uniaxial model used here will give more reliable results with an increase in the scale coefficient for nanobars with sufficiently small lengths under the clamped-clamped boundary conditions. The present analysis based on the nonlocal elasticity theory shows that the static resonance can be a primary critical case for the rotating nanobars having very small lengths, in contrast to the classical elasticity theory.

References

1. ARANDA-RUIZ J., LOYA J., FERNANDEZ-SAEZ J., 2012, Bending vibrations of rotating nonuniform nanocantilevers using the Eringen nonlocal elasticity theory, *Composite Structures*, **94**, 2990-3001
2. BHUTA P.G., JONES J.P., 1963, On axial vibrations of a whirling bar, *The Journal of the Acoustical Society of America*, **35**, 217-221
3. BRUNELLE E.J., 1971, Stress redistribution and instability of rotating beams and disks, *American Institute Aeronautics Astronautics*, **9**, 758-759
4. DANESH V., ASGHARI M., 2014, Analysis of micro-rotating disk based on the strain gradient elasticity, *Acta Mechanica*, **225**, 1955-1965
5. ERINGEN A.C., 2002, *Nonlocal Continuum Field Theories*, Springer, New York
6. HODGES D.H., BLESS R.R., 1994, Axial instability of rotating rods revisited, *International Journal of Non-linear Mechanics*, **29**, 879-887
7. NARENDAR S., 2011, Mathematical modelling of rotating single-walled carbon nanotubes used in nanoscale rotational actuators, *Defence Science Journal*, **61**, 317-324

8. NARENDAR S., 2012, Differential quadrature based nonlocal flapwise bending vibration analysis of rotating nanotube with consideration of transverse shear deformation and rotary inertia, *Applied Mathematics and Computation*, **219**, 1232-1243
9. NARENDAR S., GOPALAKRISHNAN S., 2011, Nonlocal wave propagation in rotating nanotube, *Results in Physics*, **1**, 17-25
10. NARENDAR S., ROY MAHAPATRA D., GOPALAKRISHNAN S., 2011, Prediction of nonlocal scaling parameter for armchair and zigzag single-walled carbon nanotubes based on molecular structural mechanics, nonlocal elasticity and wave propagation, *International Journal of Engineering Sciences*, **49**, 509-522
11. SHUM W.S., ENTWISTLE R.D., 2006, Longitudinal vibration frequencies of steadily whirling rods, *The Journal of the Acoustical Society of America*, **119**, 909-916

Manuscript received December 1, 2017; accepted for print January 10, 2018

DAMAGE DEVELOPMENT OF INCONEL 718 DUE TO LABORATORY SIMULATED CREEP

KATARZYNA MAKOWSKA, ADAM BRODECKI

Motor Transport Institute, Warsaw, Poland

e-mail: katarzyna.makowska@its.waw.pl; adam.brodecki@its.waw.pl

SŁAWOMIR MACKIEWICZ, ZBIGNIEW L. KOWALEWSKI

Institute of Fundamental Technological Research Polish Academy of Sciences, Warsaw, Poland, and

Motor Transport Institute, Warsaw, Poland

e-mail: smackiew@ippt.pan.pl; zkowalew@ippt.pan.pl; zbigniew.kowalewski@its.waw.pl

The paper presents an attempt of application of the acoustic birefringence coefficient for early stage degradation assessment of Inconel 718 nickel superalloy after short-term creep. It is shown that it can serve as a good damage sensitive parameter and, moreover, it can be well correlated with hardness variation.

Keywords: creep, nickel superalloy, microstructure, pre-deformation, hardness, acoustic birefringence

1. Introduction

Inconel 718 is extensively used in aerospace applications, particularly in aircraft engines (Pollock and Tin, 2006). This is because of the combination of high strength, toughness, resistance to degradation in oxidizing and corrosive environments as well its excellent weldability (Pollock and Tin, 2006). Due to large stress levels and high temperatures taking place during operation of jet engine parts, special materials guarantying adequate creep resistance are required. Such properties exhibits Inconel 718 (Reed and Tao, 2009). Typical conventional non-destructive techniques (based on measurement of ultrasonic wave velocities for example) are sensitive to material damage mainly in the advanced stage of material life. Previous attempts of application of the acoustic birefringence coefficient to damage evaluation provided some encouraging results well reflecting material degradation, sometimes even better than the replica technique and destructive tests.

The acoustic birefringence is based on the velocity difference between two shear waves polarized in mutually perpendicular directions (Szelaźek *et al.*, 2009). Measurements are usually carried out using the same ultrasonic probes, rotated by 90°. The ultrasonic beam goes through the same thickness of the material and reflects from the same area of the opposite surface (Mackiewicz, 2005). In this way, errors coming from structure and heterogeneity of the material can be eliminated (Mackiewicz, 2005).

2. Materials and methods

The material used in all tests has been wrought Inconel 718 nickel superalloy. Chemical analysis was carried out on SpectroMAXx AMETEK. Solution annealing at 968°C was applied following cooling in the air. Subsequently, precipitation hardening at 718°C for 8 hours plus furnace cooling (56°C for 1 hour) to 621°C, held at 621°C for 8 hours, followed by air cooling was performed. The microstructure of the non-deformed material after heat treatment was investigated. Scanning-

-transmission electron microscope STEM Titan 80-300 was used. In order to control the result of heat treatment, the standard tensile test at room temperature was carried out. Also, Vickers hardness tests were performed. In the next step of experimental programme, short-term creep tests under stress of 70 MPa at temperature 850°C were executed on specimens of 40 mm gauge length and 5 mm×7 mm cross-section dimensions. Each creep test was interrupted in the range of selected time periods in order to achieve specimens with the increasing level of pre-strain: 0.5%, 1%, 2.5%, 5%. After each interrupted creep test, ultrasonic inspection was performed to find values of the acoustic birefringence B .

It was calculated according to the following relationship

$$B = 2 \frac{t_{Tl} - t_{Tp}}{t_{Tl} + t_{Tp}} \quad (2.1)$$

where: t_{Tl} – time of propagation of the shear wave polarized in the longitudinal direction of the specimen, t_{Tp} – time of propagation of the shear wave polarized in the perpendicular direction of the specimen.

Ultrasonic measurements were performed in five spots on each specimen along their gauge length and in two reference spots on the gripping parts, aside from the creep stresses. In that way, the maximum value of the acoustic birefringence increase along the gauge length ΔB_{max} could be determined. The measurements were taken by means of a 5 MHz shear wave piezoelectric transducer coupled to the specimen surface by a viscous epoxy couplant (Makowska *et al.*, 2017). The distribution of ultrasonic measurement points on the specimen is schematically presented in Fig. 1.

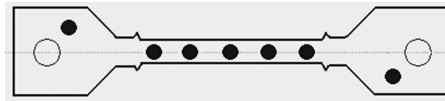


Fig. 1. Spots of ultrasonic measurements

Afterwards, the specimens were subjected to hardness measurements HV0.1. Having had all experimental data, a relationship between the creep strain and the acoustic birefringence coefficient was elaborated. It was shown that HV hardness also exhibited a functional relationship with the variation of the acoustic birefringence coefficient.

3. Results and discussion

The chemical composition of the material tested is shown in Table 1.

Table 1. Chemical composition of Inconel 718 alloy [wt %]

C	Si	Mn	Cr	Ni	Mo	Nb	Ti	Al	Fe
0.082	0.12	0.25	18.24	52.7	3.09	4.68	1.10	0.55	18.59

The representative microstructure of heat-treated Inconel 718 is shown in Fig. 1a,b. Figure 1a shows the structure of the material in a single grain. The area in the square is enlarged and presented in Fig. 1b. According to the diffraction pattern (Fig. 1c,d), the microstructure of Inconel 718 contains a dispersion of γ' and γ'' precipitates in γ matrix, see Fig. 1b. Similar results of microstructural investigations were presented in (Xiao *et al.*, 2004) and (Azadian, 2004). HV hardness of the material reaches 450HV10 after heat treatment, whereas the parameters coming from a static tensile test at the room temperature are as follows: yield point $\sigma_{0.2} = 1114$ MPa, ultimate tensile strength $\sigma_m = 1376$ MPa, elongation $A \approx 25\%$.

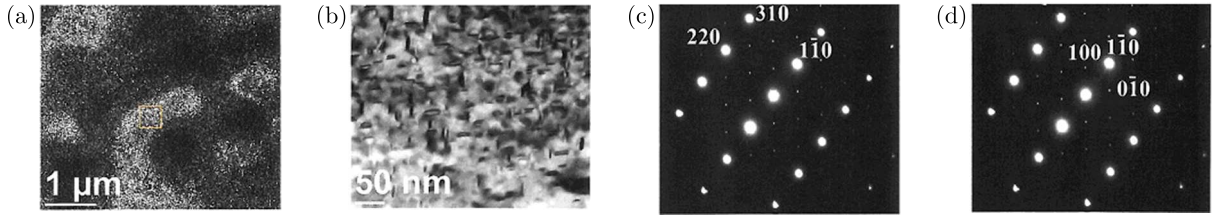


Fig. 2. Microstructure of heat-treated Inconel 718

The results of mechanical tests are shown in Figs. 3 and 4. The creep curve of the alloy is illustrated in Fig. 3a, whereas the mutual relationship between hardness and predeformation of Inconel 718 due to creep in Fig. 3b. The acoustic birefringence coefficient ΔB_{max} representing the maximum increase of the acoustic birefringence on the gauge length due to creep (measured in relation to the gripping section) is shown in Fig. 4a. The values of the parameter are presented as a function of the creep strain. According to the results (Fig. 4a), the ΔB_{max} increases with growth of deformation due to creep. The mutual relationship between the hardness and ultrasonic parameter ΔB_{max} can be well described by an exponential function, see Fig. 4b.

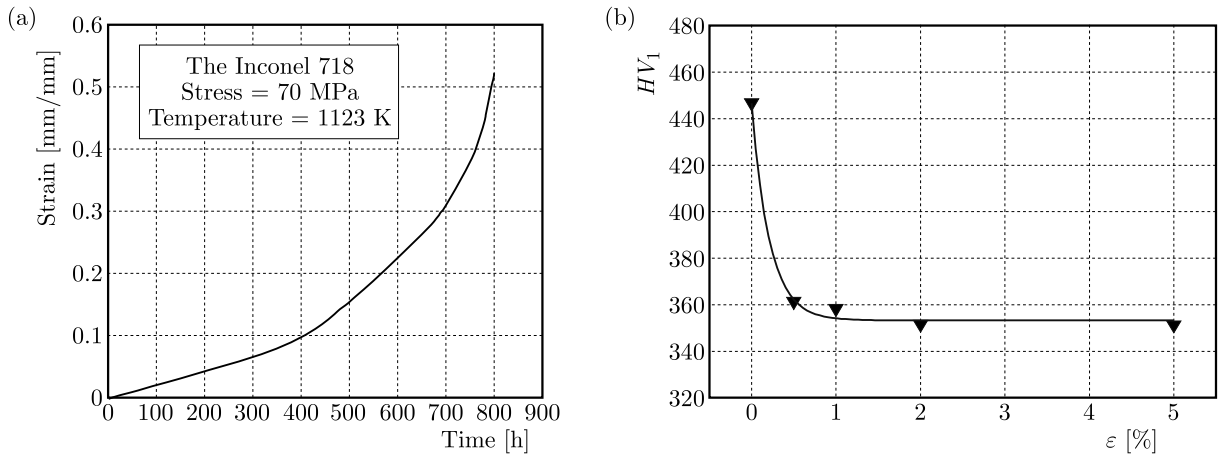
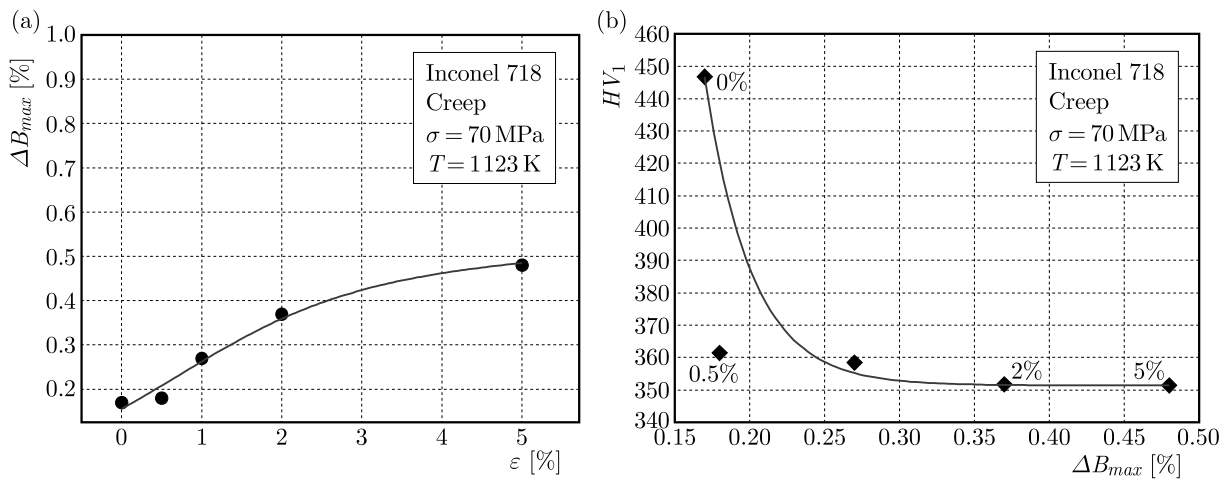


Fig. 3. (a) Creep curve of Inconel 718. (b) Relationship between the hardness and creep strain

Fig. 4. (a) Variation of the acoustic birefringence coefficient ΔB_{max} versus creep strain. (b) Variation of the HV hardness versus the acoustic birefringence coefficient ΔB_{max} ; the numbers 0%-5% denote the level of creep strain

4. Conclusion

The acoustic birefringence coefficient might be useful in assessment of the state of degradation Inconel 718 nickel superalloy in the relatively wide range of material exploitation. The correlation discovered between selected parameters derived from non-destructive and destructive tests may serve as the starting point enabling evaluation of mechanical properties of the materials using only nondestructive investigations.

Acknowledgments

The research was performed within the financial support of the National Science Centre (2013/09/N/ST8/02084).

References

1. AZADIAN S., 2004, Aspects of Precipitation in the Alloy Inconel 718, Doctoral Thesis, Luleå University of Technology, Sweden
2. MACKIEWICZ S., 2005, Possibilities of ultrasonic evaluation of energetic steels as a result long-term exploitation (in Polish), *Conference Book, VII Information and Training Seminar: Diagnostic and Renovations Energetic Devices. New Diagnostic Problems on the Old Power Units*, Ustroń, Poland, 2005
3. MAKOWSKA K., PIOTROWSKI L., KOWALEWSKI Z.L., 2017, Prediction of the mechanical properties of P91 steel by means of magneto-acoustic emission and acoustic birefringence, *Journal of Nondestructive Evaluation*, **35**, 1-10
4. POLLOCK T.M., TIN S., 2006, Nickel-based superalloys for advanced turbine engines: chemistry, microstructure and properties, *Journal of Propulsion and Power*, **22**, 361-374
5. REED R.C., TAO T., 2009, Alloys-by-design: application to nickel-based single crystal superalloys, *Acta Materialia*, **57**, 5898-5913
6. SZELAŻEK J., MACKIEWICZ S., KOWALEWSKI Z.L., 2009, New samples with artificial voids for ultrasonic investigations of material damage due to creep, *NDT&E International*, **42**, 150-156
7. XIAO L., CHEN D.L., CHATURVEDI M.C., 2004, Shearing of γ'' precipitates and formation of planar slip bands in Inconel 718 during cyclic deformation, *Scripta Materiala*, **52**, 603-607

Manuscript received May 9, 2018; accepted for print May 21, 2018

INFORMATION FOR AUTHORS

Journal of Theoretical and Applied Mechanics (JTAM) is devoted to all aspects of solid mechanics, fluid mechanics, thermodynamics and applied problems of structural mechanics, mechatronics, biomechanics and robotics. Both theoretical and experimental papers as well as survey papers can be proposed.

We accept articles in English only. The text of a *JTAM* paper should not exceed **12 pages of standard format A4** (11-point type size, including abstract, figures, tables and references), short communications – **4 pages**.

The material for publication should be sent to the Editorial Office via electronic journal system: <http://www.ptmts.org.pl/jtam/index.php/jtam>

Papers are accepted for publication after the review process. Blind review model is applied, which means that the reviewers' names are kept confidential to the authors. The final decision on paper acceptance belongs to the Editorial Board.

After qualifying your paper for publication we will require L^AT_EX or T_EX or Word document file and figures.

The best preferred form of figures are files obtained by making use of editorial environments employing vector graphics:

- generated in CorelDraw (*.cdr), AutoCad and ArchiCad (*.dwg) and Adobe Illustrator (*.ai). We require original files saved in the standard format of the given program.
- generated by calculation software (e.g. Mathematica) – we need files saved in *.eps or *.pdf formats.
- made in other programs based on vector graphics – we ask for *.eps, *.wmf, *.svg, *.psfiles.

Any figures created without application of vector graphics (scans, photos, bitmaps) are strongly encouraged to be supplied in *.jpg, *.tif, *.png formats with resolution of at least 300 dpi.

Requirements for paper preparation

Contents of the manuscripts should appear in the following order:

- Title of the paper
- Authors' full name, affiliation and e-mail
- Short abstract (**maximum 100 words**) and 3-5 key words (**1 line**)
- Article text (equations should be numbered separately in each section; each reference should be cited in the text by the last name(s) of the author(s) and the publication year)
- References in alphabetical order. See the following:
 1. Achen S.C., 1989, A new boundary integral equation formulation, *Journal of Applied Mechanics*, **56**, 2, 297-303
 2. Boley B.A., Weiner J.H., 1960, *Theory of Thermal Stresses*, Wiley, New York
 3. Canon W., 1955, Vibrations of heated beams, Ph.D. Thesis, Columbia University, New York
 4. Deresiewicz H., 1958, Solution of the equations of thermoelasticity, *Proceedings of Third U.S. National Congress of Applied Mechanics*, 287-305
- Titles of references originally published not in English, should be translated into English and formulated as follows:
 5. Huber M.T., 1904, Specific work of strain as a measure of material effort (in Polish), *Czasopismo Techniczne*, **XXII**, 3, 80-81

All the data should be reported in **SI units**.

Contents

Romaszko M., Sapiński B. — Stiffness and damping characteristics of MR fluid-based sandwich beams: experimental study	571
Gou X., Zhu L., Qi C. — Bifurcation and chaos analysis of a gear-rotor-bearing system	585
Delafrouz P., Pishkenari H.N. — Coarse-graining models for molecular dynamics simulations of FCC metals	601
Ferdek U., Łuczko J. — Nonlinear modeling and analysis of a shock absorber with a bypass	615
Guminiak M., Knitter-Piątkowska A. — Selected problems of damage detection in internally supported plates using one-dimensional Discrete Wavelet Transform	631
Nasiłowska B., Derewońko A., Bogdanowicz Z. — TIG and laser beam welded joints – simplified numerical analyses	645
Said H., Glimm J. — A continuum description of failure waves	657
Olejniak M., Szewc K. — Smoothed particle hydrodynamics modelling of the Rayleigh-Plateau instability	675
Grzybek D., Micek P. — Experimental investigation on the piezoelectric energy harvester as a self-powered vibration sensor	687
Yas M.H., Khorramabadi M.K. — Mechanical buckling of functionally graded polyethylene/clay nanocomposites columns based on the Engesser-Timoshenko beam theory	701
Lekzian E., Parhizkar H., Ebrahimi A. — Study on the effects of preheated wall/plates in microthruster systems	713
Bużantowicz W., Pietrasieński J. — Dual-control missile guidance: a simulation study	727
Zhuang M., Miao C., Wang Z. — Collocation method based on barycentric interpolation iteration for analysis of nonlinear microbeams	741
Dolatabadi H., Aghdam A.H. — Experimental and numerical study of the heat transfer and pressure drop in triangular chevron channels	751
Ghorbel A., Zghal B., Abdennadher M., Walha L., Haddar M. — Effect of the local damage and profile error of the gear on the drivetrain dynamic response	765
Kaldunski P. — Numerical analysis of the deep drawing process including the history of stress and strain	781
Sibilska-Mroziewicz A., Ładyżyńska-Kozdraś E. — Mathematical model of levitating cart of magnetic UAV catapult	793
Benouis A., Zagane M.S., Boulenouar A., Serier B., Belgherras M.E. — 3D FE analysis of the behavior of elliptical cracks on orthopedic cement of the total hip prosthesis	803
Hu Y., Rong Y., Li J. — Primary parametric resonance of an axially accelerating beam subjected to static loads	815
Jemielita G., Kozyra Z. — Modelling of FGM plates	829
Figiel A., Kudźma Z., Stosiak M. — Low-frequency pressure fluctuation damper based on hydropneumatic spring with constant stiffness	841
Szymczak T. — Investigations of material behaviour under monotonic tension using a Digital Image Correlation system	857
Panowicz R., Janiszewski J., Kochanowski K. — The influence of non-axisymmetric pulse shaper position on SHPB experimental data	873
<u>Short Research Communication</u>	
Güven U. — Static resonance in rotating nanobars	887
Makowska K., Brodecki A., Mackiewicz S., Kowalewski Z.L. — Damage development of Inconel 718 due to laboratory simulated creep	893